TP 6660E

TRACK/TRAIN DYNAMICS

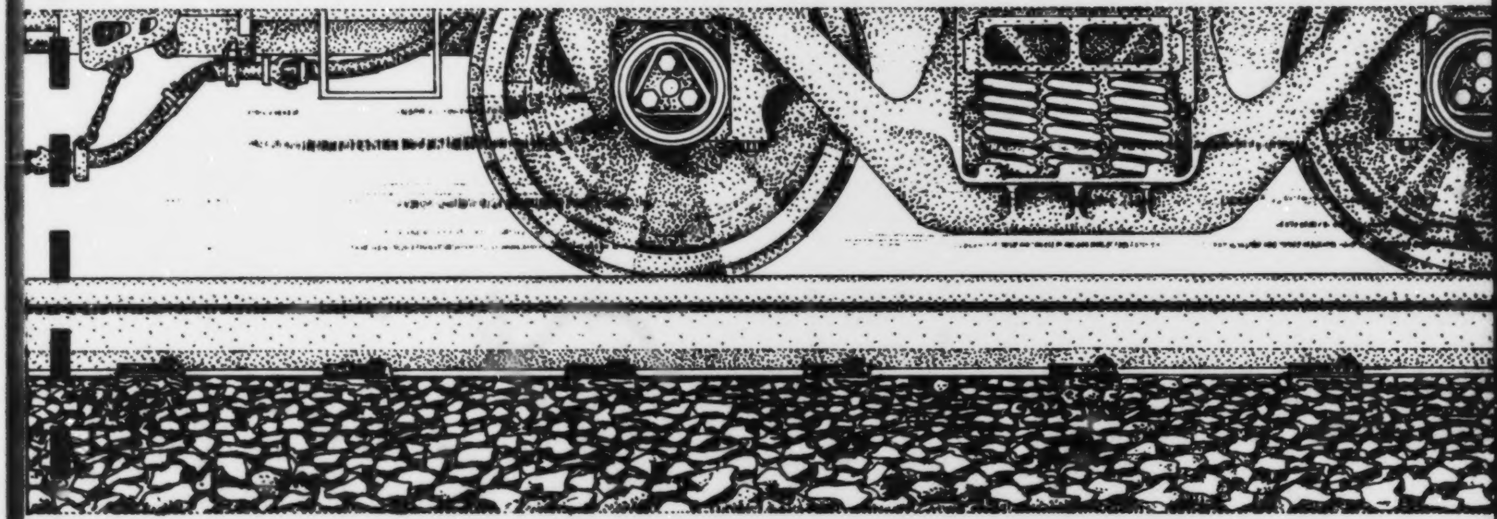

VOLUME 5
1984

TECHNICAL AND OPERATIONS RESEARCH
Canadian Pacific
MONTREAL CANADA

86-0586/

Copyright © 1984,
No part of this publication may be reproduced, stored in a retrieval system or transmitted in any form or by any means: electronic, electrostatic, magnetic tape, mechanical, photocopying, recording or otherwise, without the prior written permission of CP Ltd. or Transport Canada, with the following exception. Full rights to copy are granted for the inclusion of all or part of this publication in a non-profit publication or document provided the information is not used to support a commercial product or service and provided that a proper acknowledgement of the source is included.

Cover Illustration: Eva Krivanek

Un sommaire en français est présenté
dans chacun des rapports ci-inclus.

TP 6660E

TRACK/TRAIN DYNAMICS

VOLUME 5, 1984

Prepared for:

Transportation Development Centre
TRANSPORT CANADA

By:

TECHNICAL AND OPERATIONS RESEARCH
Canadian Pacific
MONTREAL, CANADA

JULY 1985

THE CONTENTS OF THE REPORT REFLECT THE VIEWS OF THE CONTRACTOR
AND NOT NECESSARILY THE OFFICIAL VIEWS OR POLICIES OF THE
TRANSPORTATION DEVELOPMENT CENTRE OF TRANSPORT CANADA

REPORT DOCUMENTATION FORM

1. Transport Canada Report No.
TP 6660E

2. TDC Project No.
6138

3. Recipient's Catalogue No.

4. Title and Subtitle
TRACK/TRAIN DYNAMICS
Volume 5, 1984

5. Report Date
July 1985

6. Performing Organization Report No.
T-888-85

7. Author(s)

8. Transport Canada File No.
D 1465-403-3

9. Performing Organization Name and Address
Canadian Pacific Limited
Planning and Research Department
Windsor Station
Montreal, Quebec

10. DSS File No.
14 SD. T8200-3-3580

11. DSS or Transport Canada Contract No.
OSD83-00193

12. Sponsoring Agency Name and Address
Transportation Development Centre (TDC)
200 Dorchester Blvd. West
Suite 601, West Tower
Montreal, Quebec H2Z 1X4

13. Type of Report and Period Covered
Final; Jan. 1984-Mar.1985

14. Sponsoring Agency Code
TDC 6138

15. Supplementary Notes
Canadian Pacific Limited and Transportation Development Centre equally shared in the cost of this program.

16. TDC Project Officer
D.W. Dibble

17. Abstract

The Planning and Research Department of Canadian Pacific Limited undertakes certain projects of a technical nature which may be of interest to the railway and other industries in general. Some of these projects are conducted under a cost-sharing agreeement between Canadian Pacific Limited and Transportation Development Centre. The results are then published in an annual Track/Train Dynamics report.

Projects covered in this report are rail wear measurement by the Witness Groove Method, evaluation of Japanese Superrail, methods of measuring wheel/rail angles-of-attack, development of a battery operated data logger, measurements of rail stresses due to live loads, evaluation of PACT (slab track), measurements on concrete bridge ties, a study of wheel shelling, a dynamic rail vehicle model, and an evaluation of various types of side-bearings.

Library and Information Centre
Transport Canada

18. Key Words
Witness Groove, Japanese Superrail, Angle-of-Attack, Rail Stresses, Wheel/Rail Forces, PACT, Concrete Bridge Ties, Wheel Shelling, Dynamic Rail Vehicle Model, Side Bearings

19. Distribution Statement
Copies available from Transportation Development Centre.

20. Security Classification (of this report)
Unclassified

21. Security Classification (of this page)
Unclassified

22. No. of Pages
479

23. Price

TDC/CDT 79-005

FORMULE DE DOCUMENTATION POUR RAPPORT

1. Nº du rapport Transports Canada
TP 6660E

2. Nº de l'étude — CDT
6138

3. Nº de catalogue du destinataire

4. Titre et sous-titre
TRACK/TRAIN DYNAMICS
Volume 5, 1984

5. Date du rapport
juillet 1985

6. Nº du rapport de l'organisme exécutant
T-888-85

7. Auteur(s)

8. Nº de dossier Transports Canada
D 1465-403-3

9. Nom et adresse de l'organisme exécutant
Canadien Pacifique Ltée
Departement de recherche
Gare Windsor
Montréal, Québec

10. Nº de dossier — ASC
14 SD. T8200-3-3580

11. Nº de contrat — ASC ou Transports Canada
0SD83-00193

12. Nom et adresse de l'organisme parrain
Centre de développement des transports (CDT)
200 ouest, boul. Dorchester
Suite 601, tour de l'ouest
Montréal, Québec H2Z 1X4

13. Genre de rapport et période visée
Final; jan. 1984-mars.1985

14. Code de l'organisme parrain
CDT 6138

15. Remarques additionnelles
Le CP et le CDT se sont partagés également les coûts de ce projet

16. Agent de projet — CDT
D.W. Dibble

17. Résumé

Le département de recherche et de planification du Canadien Pacifique Ltée entreprend certains projets de nature technique qui pourront être des sujets d'intéret pour le chemin de fer et pour d'autres industries en général. Quelques uns de ces projets sont exécutés dans le cadre de la convention sur le partage des frais conclue entre le Canadien Pacifique et le Centre de développement des transports. Les résultats sont publiés dans un rapport annuel sur les intéractions dynamiques roue-rail.

Les projets presentés dans ce rapport sont: la mesure de l'usure du rail par la méthode de la rainure témoin, l'évaluation du "Superrail" japonais, des méthodes pour mesurer l'angle d'inscription roue-rail, le développement d'un enregisteur/totalisateur fonctionnant sur piles, la mesure des contraintes dans les rails dues à la charge vive, l'évaluation du PACT (Plate-forme ferroviaire en béton), des mesures sur des traverses en béton d'un pont, une étude de l'écaillage de roue, un modèle du comportement dynamique d'un bogie et l'évaluation des différentes glissoires de traverses danseuses.

18. Mots-clés
rainure témoin, "Superrail" japonais, angle d'inscription, contraintes dans les rails, interaction roue-rail, PACT, traverses en béton d'un pont, écaillage de roue, modèle du comportement dynamique d'un bogie

19. Diffusion
Le Centre de développement des transports dispose d'un certain nombre d'exemplaires.

20. Classification de sécurité (de ce rapport)
non-classifié

21. Classification de sécurité (de cette page)
non-classifiée

22. Nombre de pages
479

23. Prix

CDT/TDC 79-005

PREFACE

This report is a continuation of a series of publications issued to present the results of investigations conducted by the Planning and Research Department (Technical and Operations Research Section) of Canadian Pacific Limited related to Track/Train Dynamics.

The principal objective of these research activities is to obtain an improved fundamental understanding of the dynamic interaction between rail vehicles and between these vehicles and the supporting truck structure in order to enhance safety and reduce operation and maintenance expenses.

The following elements of this report describe the methodology, results and recommendations of several track/train dynamics research programs undertaken by the Research Department between January 1, 1984 and March 31, 1985.

Again it is very gratifying to be able to acknowledge the suggestions and assistance provided by many railway personnel and industry colleagues who assisted in these investigations. Cost shared financial support provided by the Transportation Development Centre (Transport Canada) permitted our research efforts to be more extensive and vigorous than would have otherwise been possible.

Assistant Vice-President
Planning and Research

TABLE OF CONTENTS

PAGE

PREFACE i
R. Klein

Measurement of Rail Wear Occurring Over Short Time Periods Using the Witness Groove Method (WGM) and Associated Curving Data 1

Field Evaluation of the Wear Performance of Japanese Head-Hardened Alloy Rail -- Interim Report 78

Modifications of the Angle-of-Attack Measurement System 109

Rail Stresses Developed Due to Live Loads -- Preliminary Results 156

A Battery Powered Data Logger and Acquisition System For Rail/Wheel Measurements 176

Testing of PACT Slab, Mile 106.1 Mountain Subdivision (Albert Canyon) 305

Testing of Bridge 24.0 Winchester Subdivision -- Concrete Bridge Ties 326

Wheel Shelling -- Metallurgical Analysis 350

A Dynamic Rail Vehicle Model 415

In-Service Evaluation of Piggyback Car Truck Stabilizing Devices -- Interim Report 451

MEASUREMENT OF RAIL WEAR OCCURRING OVER SHORT TIME PERIODS USING THE WITNESS GROOVE METHOD (WGM) AND ASSOCIATED CURVING DATA

K. Griffin
Planning and Research Department
Canadian Pacific Limited
Montreal

J. Kalousek
Western Laboratory
Division of Mechanical Engineering
National Research Council
Vancouver

SUMMARY

Short term rail wear (i.e. the wear caused by the passage of one or several unit coal trains) was measured using the Witness Groove Method (WGM) on tangent track and in the middle of the fully developed sections of 2 and 7 degree curves on the Pacific Region of CP Rail in September 1983. Wheelset orientation and wheel/rail forces were also measured for specific trains. The objectives of these tests were to study and evaluate rail wear over a very short time period, to determine the relative influence of different parameters on rail wear and to develop/refine the WGM into a standard wear measurement technique. The WGM test program isolated the effects of track, lubrication, and specific types and tonnages of traffic on short term rail wear.

Trains passing over lubricated track, immediately following sanding, exhibited reduced angle-of-attack values and low lateral forces — relative to those of the prior sanding train. The effect of increased surface roughness, as produced by sanding, on wheel/rail forces and vehicle orientation, was greater than that of the lubricating film. The wheelset orientation and force data was collected, and is presented, on a wheelset-by-wheelset basis; this format illustrates the relationship between angle-of-attack, axle position and low rail lateral forces for the various track, loading and lubrication conditions investigated.

For the present test program, the resolution limit of the WGM (2.5 μm/0.0001 in) did not enable determination of the wear caused by the passage of a single unit coal train over well lubricated rail. The WGM

did, however, successfully measure short term wear. Over the course of the test program 0.3 MGT passed over the test sites; during this time 20 μm(0.0008 in) of wear was measured on the top running surface of tangent track while 40 μm(0.0016 in) of wear was measured on the gauge face of the high rail in the middle of the 7 degree curve.

The top running surfaces of the test section rails all experienced similar low wear rates through a delamination wear mechanism. In addition, there was no appreciable difference in high rail gauge face wear rates between the 2 and 7 degree test curves. This latter observation reflects the fact that these tests were performed in a well lubricated, low wear region and that the gauge face wear experienced here also involved a delamination mechanism.

The WGM may be used, with confidence, in any future test program requiring the short-term measurement of rail wear.

SOMMAIRE

En septembre 1983, l'usure à court terme de rails (c.à.d. l'usure due au passage d'un ou de quelques trains-blocs charbonniers) a été mesurée dans la région Pacifique du CP Rail. Cela a été fait en utilisant la méthode de la rainure témoin le long d'une voie en alignement droit et au milieu de sections de courbes de rayon constant ayant 2 et 7 comme degré de courbure. L'angle d'inscription des essieux et l'interaction roue-rail ont aussi été mesurés pour des trains spécifiques. Les objectifs de ces essais étaient d'étudier et d'évaluer l'usure des rails pendant de très courts laps de temps, de déterminer l'influence relative de différents paramètres sur l'usure des rails, et de développer et raffiner la méthode de la rainure témoin en une technique standard de mesure de l'usure. Pour une usure de rail de courte durée, le programme d'essai de la méthode de la rainure témoin distingue entre les effets de la voie, du régime de lubrification, et ceux d'un trafic de type et de charge variables.

Des trains passant sur une voie lubrifiée, immédiatement aprés avoir été sablée, exposent de faibles valeurs d'angles d'inscription ainsi que de faibles forces latérales - et ce relativement au dernier train de sablage. L'effet d'un accroissement de la rugosité de surface, causée par le sablage, sur l'interaction roue-rail et l'angle d'inscription est plus grand que celui de la péllicule de lubrifiant. Les données d'angles et de forces des essieux ont été regroupées et sont présentées pour chaque essieu; ce format illustre la relation entre l'angle d'inscription, la position de l'essieu par rapport au véhicule et les forces latérales du rail bas et ce pour une étude sur différents types de voies, de chargements et de lubrifications.

Pour le programme d'essai actuel, la limite de résolution de la méthode de la rainure témoin (2.5 µm/0.0001 po.) n'a pas permis de déterminer l'usure sur un rail bien lubrifié dû au passage d'un seul train-bloc charbonnier. La méthode de la rainure témoin a toutefois réussi à mesurer l'usure à court terme. Au cours du programme d'essai les sites ont subi 0.3 MTB de circulation; à ce moment 20 µm (0.0008 po.) d'usure

a été mesurée sur la surface de roulement du rail de la voie en alignement droit tandis que 40 µm (0.0016 po.) d'usure a été mesurée sur le bord interieur du rail haut au centre de la courbe de 7 degrés.

Les surfaces de roulement des profils de rails testés ont toutes montré un taux semblable (peu elévé) d'usure - attribuable à la procédure de délaminage. De plus, il n'y avait pas de différence considérable entre le taux d'usure du bord intérieur du haut rail d'une courbe de 2 degrés et celle de 7 degrés. Cette dernière remarque illustre le fait que ces essais ont été exécutés dans une region bien lubrifiée et de faible usure, et que l'usure du bord intérieur constatée ici implique une procédure de délaminage.

La méthode de la rainure témoin est une méthode de confiance et peut être utilisée pour n'importe quel programme d'essai futur qui éxige une mesure à court terme de l'usure du rail.

ACKNOWLEDGEMENTS

The Planning and Research Department acknowledges the contribution of:

- Officers and personnel of the Pacific Region, CP Rail, for their assistance during the course of this test program.

- Messrs. W. Watson, R. Senn and M. Kryzanowski of the Railway Laboratory, Division of Mechanical Engineering, National Research Council of Canada for their significant contribution in providing instrumentation and data acquisition during the field work. As well, NRCC Western Laboratory personnel provided assistance in the collection and processing of WGM replicas.

- CP Planning and Research personnel, specifically Mr. D. D'Aoust for assistance with measuring angle-of-attack and Mrs. E. Krivanek for illustrations.

- The Transportation Development Center of Transport Canada. This project is part of the cost-shared CP-TDC Track/Train Dynamics Program.

TABLE OF CONTENTS

PAGE

SUMMARY 2

ACKNOWLEDGEMENTS 6

LIST OF TABLES 8

LIST OF FIGURES 10

1.0 INTRODUCTION 14

2.0 TEST DESCRIPTION 16

- 2.1 Test Sites and Measurement Points 16
- 2.2 Wayside Instrumentation and Data Acquisition 17
  - 2.2.1 Lateral and Vertical Force Measurements 17
  - 2.2.2 Angle-of-Attack Measurements 18
  - 2.2.3 WGM Wear Measurements 19
- 2.3 Test Procedure 20

3.0 DATA ANALYSIS 22

- 3.1 Lateral Forces and Angle-of-Attack Measurements 22
  - 3.1.1 Low Rail 24
  - 3.1.2 High Rail 25
- 3.2 Vertical Wheel Load Distribution Characteristics 26
- 3.3 Wear Measurements 26

4.0 CONCLUSIONS 30

REFERENCES 31

LIST OF TABLES

TABLE NO.	DESCRIPTION	PAGE
1	Test Sites for WGM Study	33
2	WGM Study Rail Wear Measurement Points	34
3	Summary of Trains Passing, and Wear Measurements Taken, During Witness Groove Test Program	35
4	Statistical Summary of Low Rail Lateral Forces and Angle-of-Attack Values	37
5	Summary of WG Wear Measurements	38

LIST OF FIGURES

FIGURE NO.	DESCRIPTION	PAGE
1	Test Site #1, 7 Degree Curve, MP 25.1-25.3, Windermere Subdivision	39
2	Test Site #2, Tangent Track, MP 25.4-25.9, Windermere Subdivision	40
3	Test Site #3, 2 Degree Curve, MP 25.9-26.1, Windermere Subdivision	41
4	Hydraulic Loading Device Used for Simultaneous Calibration of Vertical and Lateral Force Circuits	42
5	Sample Output from Brush Chart Recorder of Wheel/Rail Force Measurement Data	43
6	Sign Convention of Angle-of-Attack for a Single Wheelset Travelling in Either Direction and Rail Forces	44
7	Alignment of Magnetic Sensors Used in Angle-of-Attack Measurements	45
8A	Orientation and Approximate Dimension of the Witness Groove	46
8B	Trace of Hypothetical Witness Groove Illustrating Rail Surface Wear Caused by the Passage of Several Trains	46
9A	Lubricant Deposit on Low Rail in Test Site #1	47
9B	Lubricant Deposit on High Rail in Test Site #1	47
10A	Two-Dimensional Frequency Distribution of Wheelset Orientation and Wheel/Rail Force Data, by Axle, Collected in Middle of Fully Developed Section of 2 Degree Curve for the Passage of a Loaded Coal Train (No. 14) -- Rail Condition is Sanded	48
10B	Two-Dimensional Frequency Distribution of Wheelset Orientation and Wheel/Rail Force Data Collected in Middle of Fully Developed Section of 2 Degree Curve for the Passage of a Loaded Coal Train (No. 14) -- Rail Condition is Sanded	49

LIST OF FIGURES CONT'D.

FIGURE NO.	DESCRIPTION	PAGE
11A	Two-Dimensional Frequency Distribution of Wheelset Orientation and Wheel/Rail Force Data, by Axle, Collected in Middle of Fully Developed Section of 2 Degree Curve for the Passage of an Empty Coal Train (No. 16) -- Rail Condition is Sanded	50
11B	Two-Dimensional Frequency Distribution of Wheelset Orientation and Wheel/Rail Force Data Collected in Middle of Fully Developed Section of 2 Degree Curve for the Passage of an Empty Coal Train (No. 16) -- Rail Condition is Sanded	51
12A	Two-Dimensional Frequency Distribution of Wheelset Orientation and Wheel/Rail Force Data, by Axle, Collected in Middle of Fully Developed Section of 2 Degree Curve for the Passage of a Loaded Coal Train (No. 30) -- Rail Condition is Lubricated	52
12B	Two-Dimensional Frequency Distribution of Wheelset Orientation and Wheel/Rail Force Data Collected in Middle of Fully Developed Section of 2 Degree Curve for the Passage of a Loaded Coal Train (No. 30) -- Rail Condition is Lubricated	53
13A	Two-Dimensional Frequency Distribution of Wheelset Orientation and Wheel/Rail Force Data, by Axle, Collected in Middle of Fully Developed Section of 2 Degree Curve for the Passage of a Loaded Coal Train (No. 31) -- Rail Condition is Lubricated	54
13B	Two-Dimensional Frequency Distribution of Wheelset Orientation and Wheel/Rail Force Data Collected in Middle of Fully Developed Section of 2 Degree Curve for the Passage of a Loaded Coal Train (No. 31) -- Rail Condition is Lubricated	55
14A	Two-Dimensional Frequency Distribution of Wheelset Orientation and Wheel/Rail Force Data, by Axle, Collected in Middle of Fully Developed Section of 7 Degree Curve for the Passage of a Loaded Coal Train (No. 38) -- Rail Condition is Sanded	56

LIST OF FIGURES CONT'D.

FIGURE NO.	DESCRIPTION	PAGE
14B	Two-Dimensional Frequency Distribution of Wheelset Orientation and Wheel/Rail Force Data Collected in Middle of Fully Developed Section of 7 Degree Curve for the Passage of a Loaded Coal Train (No. 38) -- Rail Condition is Sanded	57
15A	Two-Dimensional Frequency Distribution of Wheelset Orientation and Wheel/Rail Force Data, by Axle, Collected in Middle of Fully Developed Section of 7 Degree Curve for the Passage of a Loaded Coal Train (No. 39) -- Rail Condition is Lubricated	58
15B	Two-Dimensional Frequency Distribution of Wheelset Orientation and Wheel/Rail Force Data Collected in Middle of Fully Developed Section of 7 Degree Curve for the Passage of a Loaded Coal Train (No. 39) -- Rail Condition is Lubricated	59
16A	Two-Dimensional Frequency Distribution of Wheelset Orientation and Wheel/Rail Force Data, by Axle, Collected in Middle of Fully Developed Section of 7 Degree Curve for the Passage of an Empty Coal Train (No. 40) -- Rail Condition is Lubricated	60
16B	Two-Dimensional Frequency Distribution of Wheelset Orientation and Wheel/Rail Force Data Collected in Middle of Fully Developed Section of 7 Degree Curve for the Passage of an Empty Coal Train (No. 40) -- Rail Condition is Lubricated	61
17	Average Wheelset Orientation and Wheel/Rail Force Data, by Axle, Measured in the Middle of the Fully Developed Section of a 2 Degree Curve due to the Passage of a Loaded Coal Train (No. 14) Under Sanded Track Conditions	62
18	Average Wheelset Orientation and Wheel/Rail Force Data, by Axle, Measured in the Middle of the Fully Developed Section of a 2 Degree Curve due to the Passage of an Empty Coal Train (No. 16) Under Sanded Track Conditions	63

LIST OF FIGURES CONT'D.

FIGURE NO.	DESCRIPTION	PAGE
19	Average Wheelset Orientation and Wheel/Rail Force Data, by Axle, Measured in the Middle of the Fully Developed Section of a 2 Degree Curve due to the Passage of a Loaded Coal Train (No. 30) Under Lubricated Track Conditions	64
20	Average Wheelset Orientation and Wheel/Rail Force Data, by Axle, Measured in the Middle of the Fully Developed Section of a 2 Degree Curve due to the Passage of a Loaded Coal Train (No. 31) Under Lubricated Track Conditions	65
21	Average Wheelset Orientation and Wheel/Rail Force Data, by Axle, Measured in the Middle of the Fully Developed Section of a 7 Degree Curve due to the Passage of a Loaded Coal Train (No. 38) Under Sanded Track Conditions	66
22	Average Wheelset Orientation and Wheel/Rail Force Data, by Axle, Measured in the Middle of the Fully Developed Section of a 7 Degree Curve due to the Passage of a Loaded Coal Train (No. 39) Under Lubricated Track Conditions	67
23	Average Wheelset Orientation and Wheel/Rail Force Data, by Axle, Measured in the Middle of the Fully Developed Section of a 7 Degree Curve due to the Passage of an Empty Coal Train (No. 40) Under Lubricated Track Conditions	68
24	Wear Measurement Locations About the Railhead for High and Low Rails in Curves and for Tangent Track	69
25	Trace of Witness Groove Profiles Illustrating Progressive Rail Surface Wear at Measurement Point 3 (High Rail, Middle of 7 Degree Curve, Test Site 1) Caused by the Passage of Several Trains	70
26	Trace of Witness Groove Profiles Illustrating Progressive Rail Surface Wear at Measurement Point 4 (Low Rail, Middle of 7 Degree Curve, Test Site 1) Caused by the Passage of Several Trains	71

LIST OF FIGURES CONT'D.

FIGURE NO.	DESCRIPTION	PAGE
27	Trace of Witness Groove Profiles Illustrating Progressive Rail Surface Wear at Measurement Point 9 (Tangent Track, Test Site 2) Caused by the Passage of Several Trains	72
28	Trace of Witness Groove Profiles Illustrating Progressive Rail Surface Wear at Measurement Point 10 (Tangent Track, Test Site 2) Caused by the Passage of Several Trains	73
29	Trace of Witness Groove Profiles Illustrating Progressive Rail Surface Wear at Measurement Point 17 (High Rail, Middle of 2 Degree Curve, Test Site 3) Caused by the Passage of Several Trains	74
30	Trace of Witness Groove Profiles Illustrating Progressive Rail Surface Wear at Measurement Point 18 (Low Rail, Middle of 2 Degree Curve, Test Site 3) Caused by the Passage of Several Trains	75
31	Optical Electron Micrographs of Wear Debris Collected in 7 Degree Curve of Test Site 1	76
32	Shelly Surface Exhibited by Low Rail in 7 Degree Curve of Test Site 1	77

1.0 INTRODUCTION

Rail and wheel wear has been investigated theoretically, in laboratories and by field testing by many researchers. Field tests are currently being conducted by the Planning and Research Department, CP Ltd., with the aid of internally developed rail and wheel profilometers. The wear associated with typically several months of regular service is measurable with these instruments and hence the relative performance of the wheels or rails during this period may be evaluated.

It is desirable to also have the capability of measuring the rail or wheel wear occurring during a short time period. The objectives of such testing are fundamentally different from those of tests conducted with existing profilometers. Short term testing would, as an example, yield the rail wear associated with different types of traffic, such as loaded or empty unit coal trains. Long term testing clearly cannot achieve this goal.

In early 1983, the Planning and Research Department formulated a test program to evaluate short term rail wear using the Witness Groove Method (WGM). Research activities were carried out jointly with the Railway Laboratory of the National Research Council of Canada (NRCC) and the NRCC Western Laboratory.

Testwork was aimed at determining rail wear occurring over very short time periods for varying track and loading conditions. The program attempts to isolate the effects of lubrication and specific types and tonnages of traffic. Finally, the test should aid in the development of the WGM into a standard wear measuring technique.

During these tests, Witness Groove (WG) replicas were collected and processed by NRCC Western Laboratory personnel. Lateral and vertical force measurements, calibration and data acquisition were carried out by NRCC Railway Laboratory personnel. Angle-of-attack measurements were collected and processed by CP Planning and Research.

This report presents the results of field measurements of rail wear caused by the passage of limited traffic. Further, the effects of lubrication and different types and vehicle weights of traffic on wheelset orientation, wheel/rail forces and resultant rail wear were investigated and are documented. Also included are descriptions of the test locations and methods of data acquisition and analysis.

2.0 TEST DESCRIPTION

2.1 Test Sites and Measurement Points

All testing was conducted on three test sites located on the Windermere Subdivision between mile points 25.14 and 26.12 (see Table 1, mileages increase in the heavy-haul direction). The test section exhibits a uniform 0.00 grade throughout and contains three distinctly different regions. Track curvatures of 7 and 2 degrees (test sites 1 and 3, respectively) were selected to represent sharp and mild curves; a tangent track section (test site 2) represents a different lateral loading condition.

The three test sites were stringlined with a 62' chord with measurements made at 31' intervals. Track gauge and superelevation were also measured throughout the test sites. The test site track profiles are presented in Figures 1-3. The approximately one mile long test section consisted of continuously welded 132 lb/yd Algoma rail in 1440' strings; chrome and carbon rail metallurgies were employed in the curved and tangent track sections, respectively. All test section rails were rolled in 1971; however, field personnel stated that these rails were installed at different times — 1975 for test site 1, 1981 for test site 2 and 1972 for test site 3. This track was well maintained and the rail well lubricated.

High and low rail wear measurement points were chosen at the 1/3, 1/2 and 2/3 positions (with respect to the heavy-haul direction) along the length of the fully developed curve sections for both test sites 1 and 3, as well as at the mid-point of the long tangent track section in test site 2. At both the high and low rail measurement points corresponding to the mid-points of the 7 and 2 degree full curves, lateral and vertical forces along with wheelset angles-of-attack were measured. These measurement points were all well within the fully developed section of the curves away from rail joints to minimize non-steady state curving behaviour. The locations of these rail wear measurement points are illustrated in Figures 1-3 and presented in Table 2.

2.2 Wayside Instrumentation and Data Acquisition

2.2.1 Lateral and Vertical Force Measurements

Lateral and vertical forces on the high and low rail generated by passing wheelsets during curve negotiation were measured by bonded strain gauge circuits (chevron pattern) applied to the rail at the web and base.

Calibration of the lateral and vertical force circuits were carried out simultaneously using a hydraulic loading device (see Figure 4) developed at the Railway Laboratory of the NRCC. Details of the calibration procedure are reported in Reference 1.

The data from the calibration procedure and from subsequent testwork were recorded on an FM analog tape recorder. A 6-channel brush chart recorder was used to display the data on-site. A sample trace of the lateral and vertical forces measured at measurement points 3 and 4 for the 30 mph passage of a loaded coal train is illustrated in Figure 5. The vertical forces on the high and low rail are calculated from the height of each pulse. The trace of the lateral forces, however, indicates that lateral rail forces occur in both directions. By convention, positive lateral rail forces for high and low rails are defined as forces pushing the rails away from the centre of the curve and are depicted in Figure 6.

2.2.2 Angle-of-Attack Measurements

Angle-of-attack is defined as the instantaneous misalignment angle of a wheelset with respect to the true radial line of a curve over which it is passing. A positive angle-of-attack is defined as shown in Figure 6.

The measurement system employed was an experimental magnetic system consisting of magnetic sensors aligned approximately to the radial line of the curve (see Figure 7). This system measured the angle-of-attack for each passing wheelset as well as the instantaneous translational speed of each axle during curve negotiation. A microcomputer analyzed the signals from the three magnetic sensors and printed out the angle-of-attack and axle speed measurements in the field.

It is very difficult to achieve perfect radial alignment of the angle-of-attack measurement system; a small offset angle (see Figure 7) is normally present and must be accounted for to obtain the true angle-of-attack (depending upon the direction of wheelset travel, this offset should be added to or subtracted from the measured values). According to creep theory, a positive angle-of-attack yields a negative lateral rail force and vice-versa; this relationship was used to determine offset angles in this test program. For each of test sites 1 and 3, offset angles were estimated by examining angle-of-attack values associated with low rail lateral force data close to zero magnitude, normally for the trailing wheels. The principal advantage of examining low, as opposed to high, rail lateral force data is that the lateral forces experienced by low rails are mainly composed of lateral creep. Measured values of high rail lateral forces are actually the resultants of various combinations of lateral loading involving such factors as lateral creep, spin creep, flange force and the lateral component of the tread wheel/rail normal force — it is not possible to isolate the effects of lateral creep on the high rail.

2.2.3 WGM Wear Measurements

The progressive wear at various positions about the railhead surface of high and low rails in curves caused by the passage of limited tonnages was measured using the WGM.

Using a suitable tool and template (see Figure 8A), a reference WG was inscribed laterally across the railhead surface (including the gauge face for high rails in curves) at each wear measurement point. These areas were then cleaned with a solvent, and WG replicas taken using a fast curing (15 minutes), non-shrinking, epoxy. Successive replicas were taken at the various wear measurement points both before and after the passage of selected trains, until the end of the test period. The accuracy of the replication technique is >2.5 μm(>0.0001 in).

A contour profilometer, accurate to 1 μm(0.00004 in), was used to develop the cross-sectional profiles of these replicas. The amount of wear from any particular location alongside the WG was evaluated by superimposing the average profiles taken from two or several replicas. Since the bottom of the WG did not wear, it served as a reference to the material worn from the running surfaces. This approach is illustrated in Figure 8B. Further details of the replication and profile measurement techniques are contained in Reference 2.

2.3 Test Procedure

All rail lubricators from mile points 18.0-41.0 were disconnected on September 22, 1983, five days prior to the start of the WGM test program. According to field personnel, residual lubrication can persist on railhead surfaces for weeks after the disconnection of trackside lubricators; this was the case in the present test program. As Figures 9A and 9B illustrate, substantial lubricant deposits were found on railhead surfaces within the test section (note the difference between washed and unwashed areas) -- in particular toward the field side of low rails (see Figure 9A) and the gauge face area on high rails (see Figure 9B).

An attempt was made to selectively increase lateral forces by cleaning railhead surfaces with solvents and by requesting passing trains to sand. The wheels of trains entering the test section contained substantial amounts of lubricant on their tread surfaces; therefore, cleaning railhead surfaces merely decreased the lubricant film thickness in the rail/wheel interface. Any increase in lateral forces was primarily due to the abrasive action of the sand. In addition, lubrication was being continually re-applied to the test section rails by passing trains which did not sand. While cleaning/sanding railhead surfaces did alter the ratio between the lubricant film thickness and railhead surface roughness, there was no significant modification to the effective lubrication regime or the resulting wear mode.

Arrangements were made with the Chief Dispatcher in Nelson, B.C. to maintain a sequential list of all trains passing through the test sites for the duration of the test program. This list was used in conjunction with information available from the Transportation Department, CP Rail, to get a detailed description of each train passing through the test sites during the test period. This information is summarized in Table 3, along with when (i.e. before or after which trains) and at which measurement points WG's were inscribed and/or replicated.

Reference WG's were inscribed and replicated at the rail wear measurement point locations specified in Section 2.1 (see Table 3, replica no.'s 0, 1 and 4). A number of replicas were then taken at measurement points before and after the passage of various empty and loaded unit coal trains, for both lubricated and sanded railhead conditions, until the end of the test period. As well, angle-of-attack and rail/wheel forces were measured in both the high and low rail test points corresponding to the middle of the 7 and 2 degree full curves for certain of the above trains in order to examine their effect, along with that of lubrication, on rail wear. Specifically, angle-of-attack and rail/wheel forces were measured for the passage of train no.'s 14, 15, 16, 17, 30, 31, 38, 39, and 40 (train no.'s 14-17 and 38 passed over sanded rail). A total of 42 trains, of various types and tonnages, passed over the measurement points at an average speed of 30 mph during the test period — see Table 3.

3.0 DATA ANALYSIS

There is no angle-of-attack or rail/wheel force data available for empty coal trains passing over either lubricated 2 degree or sanded 7 degree curves. Also, the data recorded for train no.'s 15 and 17 was lost because of a tape recorder malfunction which was only discovered during data processing. As explained in Section 2.3, WG replicas were taken at the various measurement points to study the wear associated with the passage of both individual trains and train groupings. Those replicas of WG's located in the middle of the fully developed sections of test sites 1 and 3, and which were specifically associated with (i.e. taken before and/or after) passing trains whose angle-of-attack and lateral and vertical force information was processed and is available (i.e. train no.'s 14, 16, 30, 31, 38, 39 and 40) were analyzed and are reported. For comparison purposes, a limited number of WG replicas corresponding to the mid-point of the long tangent track section in test site 2 were also processed and are reported.

3.1 Lateral Forces and Angle-of-Attack Measurements

Elkins and Eickhoff (see Reference 3) relate the wear in rail/wheel contact to the energy dissipated at the contact patch. This amount of dissipated energy is referred to as the wear index or number. These authors approximate this energy by the sum of the products of lateral force and lateral creepage, and longitudinal force and longitudinal creepage. A similar approach is used by others (see References 4, 5 and 6). These studies primarily relate energy dissipation to wear for dry track. Creepages, however, are extremely difficult to measure, particularly for a large number of wheels, as are longitudinal forces. Wheelset angles-of-attack and lateral forces are routinely measured by CP Planning and Research, primarily to characterize the curving performance of various vehicles. For this reason, angle-of-attack and low rail lateral force measurements were studied on a wheelset-by-wheelset basis; the biaxial frequency distributions for individual wheelsets are shown in Figures 10A, 11A, ..., 16A. Appreciable differences in angle-of-attack and low rail forces are observed between leading and trailing axles, and to a lesser extent between leading and trailing trucks. The frequency distributions for all wheelsets within each of these trains are given in Figures 10B, 11B, ..., 16B.

The average variation between leading and trailing axles for vertical and lateral forces, as well as for average values of angle-of-attack, are shown in Figures 17-23. The data presented in Figures 10A-16B show the appreciable differences which exist in both the mean levels of angle-of-attack and associated lateral forces between lubricated and sanded track, and between empty and loaded trains. For these cases it appears that angles-of-attack and associated low rail lateral forces, for each of leading and trailing axles, are normally distributed. The distributions represented in Figures 10B, 11B, ..., 16B have two difficult-to-distinguish peaks (i.e. one is characteristic of leading axles, the other of trailing axles); however, to assess the effect that loading or lubrication have on angle-of-attack and low rail lateral forces, the complete distributions shown in Figures 10B, 11B, ..., 16B were considered as normal and their arithmetic means ($\overline{X}$) and standard deviations (σ) computed. These statistics are summarized in Table 4.

3.1.1 Low Rail

The curving behaviour observed throughout the test program had the leading axles attaining large positive angle-of-attack values; these generated significant low rail lateral creep forces directed towards the center of the test curves. Trailing axles, relative to leading ones, exhibited small angles-of-attack. The trailing axles of loaded trains attained a more or less radial alignment. The angle-of-attack values of trailing axles on empty trains were quite large, but still significantly lower than those of corresponding lead axles. The loaded train results agree with previous CP test program findings (see Reference 7) which, however, did not include any attempt to investigate empty train performance.

The angle-of-attack values exhibited by both leading and trailing axles decreased, and associated lateral creep forces increased, as loading was increased from the case of an empty train to that of a fully loaded unit coal train. With a loaded car, longitudinal high rail flange steering forces are increased, hence angle-of-attack decreases.

Sanding considerably roughens the running surface of a rail. It is further recognized that, given the same traffic and track, lubrication decreases longitudinal flange steering forces and shifts the vertical load back to the tread contact; this results in an increase in angle-of-attack values and corresponding lateral creep forces on the low rail. The above effect is greater with increasing track curvature. In the present study, trains which passed over lubricated track immediately following sanding exhibited decreased angle-of-attack values and low rail lateral forces, relative to those of the prior sanding train. However, this decrease became more pronounced as residual sand and rail surface asperities were progressively removed from the rail/wheel interface by subsequent trains (see Table 4, 2 degree curve data). Here the effect of the rail running surface roughness overrides that of the lubricating film. As anticipated, angle-of-attack values increased with curvature.

3.1.2 High Rail

Lateral forces measured in the 2 degree curve were low; this agreed with previous CP test program findings (see Reference 7). High forces were associated with the leading axles of trains passing over the 7 degree curve, particularly under sanded track conditions. Corresponding trailing axles generated smaller positive and negative forces, and the zigzagged force pattern shown in Figure 21.

High rail lateral forces increased with loading and, to a lesser extent, with curvature. As noted previously, the leading and trailing axles of empty trains exhibited large positive angle-of-attack values, but flange forces were quite low.

All trains passed over the test section at approximately the balance speed; therefore, the influence of speed on the lateral forces being experienced by high or low rails in curves was not determined.

3.2 Vertical Wheel Load Distribution Characteristics

For both loaded and empty unit coal trains, high and low rails in curves supported, on average, 45 and 55% of the vertical axle load, respectively. Such a distribution reflects the relative low level of lateral forces occurring on test sites 1 and 3, and the fact that the trains passed at approximately the balance speed. This also confirms that there were no large vertical dynamic actions at the measurement points.

3.3 Wear Measurements

The various locations about the railhead at which measurements of the WG profile were performed, for each rail position in both curves and in the tangent track section, are shown in Figure 24. The shapes of these grooves, together with the amount of metal removed/worn following the passage of specific trains, are illustrated in Figures 25-30. The latter Figures do not show profiles corresponding to location d (see Figure 24) because, with the exception of the low rail in the 2 degree curve, location d did not experience measurable wear. The amounts of material progressively removed at the various measurement locations are summarized in Table 5.

The fundamental aim of the wear measurements was the establishment of the rate of material removal at these locations per train. This objective was not achieved since the wear caused by the passage of a single unit coal train over this test section was typically less than the accuracy of the measurement method. Train no. 39 was an exception since it removed a layer ~2.5 μm(~0.0001 in) thick, on average, about the railhead surface in the 7 degree curve. As Table 5 attests, however, the WGM successfully measured short term wear.

Figure 31 presents photomicrographs of wear debris collected in test site 1 (subsequent examination revealed no significant differences between high and low rail wear debris). The wear particles are flakelike material, on average 5 μm(0.0002 in) thick, and consist of particles of both white-etching layer (having no visible crystal structure) and broken down pearlite (deformed lamellae are visible). The shape of the wear debris suggests that the active wear mechanism is either a mild form of adhesive wear or delamination. The overall dimensions of delamination and adhesive wear particles are about the same (see Reference 8), but the delamination wear rate is 1-3 orders of magnitude lower. The number of loading cycles or asperity passages over the flat top section of the delamination particle prior to its release is correspondingly higher than the number of asperity-asperity interactions required to generate a mild adhesive wear particle (50 → 1000 vs. 1000 → 1×10^6 cycles).

From Table 5, 20 μm(0.0008 in) of material, on average, was worn from the various railhead surfaces by the approximately 13,500 wheelsets which passed over the test section. Particles of 5 μm(0.0002 in) average thickness must have been generated by >1000 loading cycles. This, together with the nature of the wear particles presented in Figure 31, suggests that the mode of wear experienced on the WGM test track section was delamination. This same type of delamination wear mechanism was active at the flange contact locations.

In test site 1, a total depth of 40 μm(0.0016 in) of material was removed from the approx. 0.5 cm(0.2 in) wide flange area on the high rail; this translates into a loss of approx. 0.002 cm^2 (0.0003 in^2) from the high rail cross-section. Given that only 0.3 MGT passed over the test section, and assuming that in the extreme case 6.45 cm^2 (1 in^2) of gauge face wear could be tolerated before the rail was condemned, a linear wear projection would yield an expected rail life of 1000 MGT. It must be acknowledged that the product of the depth of wear and the high rail gauge face load bearing area (i.e. the amount of material removed from the high rail cross-section due to gauge face wear) for the 2 and 7 degree test curves are approximately the same. The same approach applied to the case of vertical wear yields a rail life projection of similar duration. In actual service these rails last for an appreciably shorter time than "determined" above; it is apparent that rail replacement in this test section is not governed by wear. It is suggested that rolling contact fatigue, as manifested by flaking and shelly spots (see Figure 32), actually determines the service life of most rails located in this section of track. The investigation of contact fatigue damage, however, was not a part of this study.

Sanding, in addition to increasing lateral forces, considerably roughened the rail running surfaces. This surface roughening caused higher stress concentrations at contacting asperities which resulted in an accelerated rate of delamination. The above effect is shown in WG measurement location b of Figure 25 — train no. 38, which was sanding, removed an amount of material below the resolution limit of the contour profilometer while the subsequent passage of train no. 39 removed an average of +2.5 μm(+0.0001 in) about the railhead surface.

It is recognized that the instantaneous wear rates measured during the WGM test program may be high due to the disconnection of trackside lubricators and the attempts to clean and sand the rail.

4.0 CONCLUSIONS

1. For the present test program, the resolution limit of the WGM did not enable wear determination for the passage of a single unit coal train over a well lubricated rail. The WGM did, however, successfully measure short term rail wear.

2. No appreciable differences in instantaneous wear rates were observed on the top running surfaces of rails located in the tangent track, 2 degree or 7 degree curve test sites. Similarly, no significant difference in gauge face wear rates was observed between the 2 degree and 7 degree test curves.

3. The top running surfaces of the test section rails experienced low wear rates through a delamination wear mode. No wear was measured in the location of grease bands (generally found on high rail gauge face corners and on the field side of low rails in curves).

4. Trains passing over lubricated track, immediately following sanding, exhibited reduced angle-of-attack values and low lateral forces — relative to those of the prior sanding train. The effect of increased surface roughness, as produced by sanding, on wheel/rail forces and vehicle orientation was greater than that of the lubricating film.

REFERENCES

1. "Railroad Dynamics Incorporated (RDI) Truck Evaluation Test", R. Gonsalves, W. Pak and G. Izbinsky, Planning and Research Department, Canadian Pacific Limited, Report No. S670-81, March 1981.

2. "Wear Measurement by Witness Groove Method", H. Ackroyd and J. Kalousek, National Research Council of Canada, Division of Mechanical Engineering Technical Report TR-WE-35, NRC No. 21976, January 1983.

3. "Advances in Nonlinear Wheel/Rail Force Prediction Methods and Their Validation", J.A. Elkins and B.M. Eickhoff, Journal of Dynamic Systems, Measurement and Control, Vol. 104, June 1982, pp. 133-142.

4. "The Design of Bogies for Low Wear on Wheel and Rail in Rapid Transit Applications", D. Lyon and R.J. Weeks, International Symposium on Contact Mechanics and Wear of Rail/Wheel Systems, held in Vancouver, British Columbia, July 1982.

5. "Full Scale Wheel-on-Rail Wear Testing: Comparison with Service Wear and a Developing Theoretical Predictive Method", I.J. McEwen and R.F. Harvey, ASLE/ASME Lubrication Conference in Hartford, Connecticut, October 1983.

6. "Wear of Rail and Tire Steels Under Rolling/Sliding Conditions", P.J. Bolton, P. Clayton and I.J. McEwen, ASLE/ASME Lubrication Conference in San Francisco, California, August 1980.

7. "Single Car Brake Tests", Planning and Research Department, Canadian Pacific Limited, Report No. S795-83, October 1983.

8. "The Effect of Lubrication and Steering on Rail/Wheel Wear and Contact Fatigue", J. Kalousek and H. Ghonem, The Economics and Performance of Freight Car Trucks, Montreal, Canada, October 1983.

Test Sites	Extent of Curve (Miles)	Degree of Curvature (Degrees)	Direction of Curve	Length of Curve (Feet)		
				Begin Spiral	Curve	End Spiral
1	25.14-25.28	7	R	300	146	300
-	25.28-25.30	0	-	-	-	-
-	25.30-25.42	3	L	240	150	240
2	25.42-25.85	0	-	-	-	-
3	25.85-26.12	2	L	180	1060	210

TABLE 1: TEST SITES FOR WGM STUDY

Test Site	Measurement Point	Location Along Fully Developed Section of Curve (With Respect to the Heavy-Haul Direction)			High Rail	Low Rail	Parameters Measured		
		1/3	1/2	2/3			Wear	L & V Forces	Angle-of-Attack
1	1	X			X		X		
	2	X				X	X		
	3		X		X		X	X	X
	4		X			X	X	X	X
	5			X	X		X		
	6			X		X	X		
2	9		X		-	-	X		
	10		X		-	-	X		
3	15	X			X		X		
	16	X				X	X		
	17		X		X		X	X	X
	18		X			X	X	X	X
	19			X	X		X		
	20			X		X	X		

TABLE 2: WGM STUDY RAIL WEAR MEASUREMENT POINTS

Train No. and Direction	No. of Locomotives and whether robot car is incl. in consist	No. of Cars				Locomotive Tonnage (includes robots and cabs -- tons)	Tare (tons)	Consist (tons)	Tare + Consist (tons)	Average Tonnage/Car			Gross Tonnage (tons)	Replica No.	Action at Measurement Points	
		70-ton		100-ton												
		Full	Empty	Full	Empty					Full (tons)	Empty (tons)	Comb. (tons)			Witness Grooves Inscribed	Replica's Taken
1 , north	5 , yes	0	0	100	0	1,127	2,845	11,182	14,027	129.9	-	129.9	15,154	0	9 & 10	9 & 10
2 , south	2 , no	12	46	0	0	416	1,624	940	2,564	106.3	28.0	44.2	2,980	1	15 → 20	15 → 20
3 , south	4 , yes	0	0	0	100	930	2,850	58	2,908	-	26.9	26.9	3,838	2		
4 , north	2 , no	10	14	0	0	421	672	121	793	40.1	28.0	33.0	1,214	3		
5 , south	4 , yes	0	0	0	100	927	2,856	57	2,913	-	27.0	27.0	3,840	4	1 → 6	1 → 6
6 , south	3 , no	3	21	0	0	618	312	45	357	28.0	13.0	14.9	975	5		
7 , north	4 , yes	0	0	100	0	924	2,845	11,179	14,024	129.9	-	129.9	14,948	6		
8 , north	4 , yes	0	0	100	0	930	2,846	11,182	14,028	129.9	-	129.9	14,958	7		
9 , north	4 , yes	0	0	100	0	930	2,850	11,182	14,032	129.9	-	129.9	14,962	8		
10 , north	2 , no	91	2	0	0	421	2,604	6,520	9,124	99.6	28.0	98.1	9,545	9		
11 , south	4 , yes	0	0	0	100	924	2,844	55	2,899	-	26.8	26.8	3,823	10		
12 , south	4 , yes	0	0	0	100	930	2,848	58	2,906	-	26.9	26.9	3,836	11		
13 , south	4 , no	0	0	0	100	814	2,905	0	2,905	-	26.9	26.9	3,719	12		
14 , north	4 , yes	0	0	100	0	927	2,855	11,181	14,036	130.0	-	130.0	14,963	13		15 → 20
15 , north	1 , no	5	0	0	0	225	140	241	381	95.3	-	95.3	606	14		15 → 20
16 , south	4 , no	0	0	0	100	814	2,930	0	2,930	-	26.9	26.9	3,744	15		
17 , south	2 , no	0	61	0	0	421	1,488	0	1,488	-	24.4	24.4	1,909	16		
18 , south	1 , no	8	23	14	0	225	1,260	1,901	3,161	114.4	28.0	70.2	3,386	17		17 & 18
19 , north	4 , yes	0	0	100	0	924	2,844	11,179	14,023	129.8	-	129.8	14,947	18		
20 , north	4 , yes	0	0	100	0	930	2,848	11,182	14,030	129.9	-	129.9	14,960	19		
21 , south	4 , yes	0	0	0	100	924	2,851	55	2,906	-	26.9	26.9	3,830	20		
21A, north	4 , no	0	0	100	0	814	2,905	11,124	14,029	129.9	-	129.9	14,843	21		
21B, north	2 , no	59	12	0	0	421	1,988	3,973	5,961	95.3	28.0	84.0	6,382	21A		
														21B		

Table 3: Summary of Trains Passing, and Wear Measurements Taken, During Witness Groove Test Program

Train No. and Direction	No. of Locomotives and whether robot car is incl. in consist	No. of Cars				Locomotive Tonnage (includes robots and cabs -- tons)	Tare (tons)	Consist (tons)	Tare + Consist (tons)	Average Tonnage/Car			Gross Tonnage (tons)	Replica No.	Action at Measurement Points	
		70-ton		100-ton												
		Full	Empty	Full	Empty					Full (tons)	Empty (tons)	Comb. (tons)			Witness Grooves Inscribed	Replica's Taken
22 , north	4 , no	0	0	100	0	814	2,930	11,227	14,157	129.9	-	129.9	14,971			
23 , south	4 , no	0	0	0	100	814	2,929	0	2,929	-	26.9	26.9	3,743	22		
24 , north	2 , no	9	23	0	0	421	896	109	1,086	49.0	28.0	33.9	1,506	23		
25 , south	1 , no	11	0	0	0	225	308	457	765	69.5	-	69.5	990	24	1→6	1→6
26 , south	4 , yes	0	0	0	100	924	2,859	56	2,914	-	27.0	27.0	3,838	25		9 & 10, 15→19
27 , north	2 , no	0	0	0	0	207	0	0	0	-	-	-	207	26		
28 , south	4 , yes	0	0	0	100	930	2,846	58	2,904	-	26.9	26.9	3,834	27		
29	- over an approximate 2 hour period, it was incorrectly assumed that 2 trains (here labelled no.'s 28 & 29) had passed over the test sites, and these 2 trains were allowed for in the documentation scheme. It was later discovered that only 1 train (no. 28) passed in this period. Therefore there was no train no. 29, but the documentation method employed (ie. - train and replica numbers) allowed for it.													28 29		17 & 18
30 , north	4 , yes	0	0	100	0	924	2,851	11,179	14,030	129.9	-	129.9	14,954			
31 , north	4 , no	0	0	100	0	814	2,929	11,227	14,156	129.9	-	129.9	14,970	30		
32 , south	4 , no	0	0	0	109	814	2,930	0	2,930	-	27.0	27.0	3,752	31		17 & 18
33 , south	2 , no	30	0	0	0	421	840	758	1,598	53.3	-	53.3	2,019	32		
34 , south	2 , no	3	74	0	0	421	1,848	186	2,034	86.0	24.0	26.4	2,455	33		
35 , north	4 , yes	0	0	100	0	930	2,848	11,182	14,030	129.9	-	129.9	14,960	34		
36 , south	4 , yes	0	0	0	100	930	2,844	58	2,902	-	26.9	26.9	3,832	35		
37 , south	4 , yes	0	0	0	100	928	2,854	57	2,911	-	27.0	27.0	3,839	36		
38 , north	4 , yes	0	0	100	0	958	2,818	11,182	14,000	129.6	-	129.6	14,958	37		1→4
39 , north	4 , yes	0	0	100	0	930	2,844	11,182	14,026	129.9	-	129.9	14,956	38		1→4
40 , south	4 , yes	0	0	0	100	930	2,846	58	2,904	-	26.9	26.9	3,834	39		1→4
41 , north	1 , no	3	10	0	0	225	364	100	544	88.0	28.0	41.8	769	40		
TOTAL	130	244	206	1,620	1,615	30,577	94,682	172,650	267,252	123.0	26.6	70.3	297,829	41		1→4, 9 & 10, 17 & 18

Table 3: Summary of Trains Passing, and Wear Measurements Taken, During Witness Groove Test Program (Cont'd.)

			For All Wheelsets								For Leading Wheelsets of Leading Trucks Only							
			Empty		Loaded		Loaded		Loaded		Empty		Loaded		Loaded		Loaded	
			$\bar{x}$	σ	$\bar{x}$	σ	$\bar{x}$	σ	$\bar{x}$	σ	$\bar{x}$	σ	$\bar{x}$	σ	$\bar{x}$	σ	$\bar{x}$	σ
2° Curve (Test Site 3)	Sanded	γ (min)	29	10	6	9	-	-	-	-	38	6	13	6	-	-	-	-
		T (ksi)	-530	710	-1620	3380	-	-	-	-	-940	600	-4680	2630	-	-	-	-
	Lubricated	γ (min)	-	-	-	-	5	9	2*	7	-	-	-	-	12	7	8*	4
		T (ksi)	-	-	-	-	-630	1690	-230*	1470	-	-	-	-	-1660	1380	-1130*	1290
7° Curve (Test Site 1)	Sanded	γ (min)	-	-	10	14	-	-	-	-	-	-	22	9	-	-	-	-
		T (ksi)	-	-	-2800	3090	-	-	-	-	-	-	-4810	1540	-	-	-	-
	Lubricated	γ (min)	36	20	-	-	8	14	-	-	54	12	-	-	22	8	-	-
		T (ksi)	-820	500	-	-	-1280	1950	-	-	-1010	530	-	-	-2300	1060	-	-

γ : angle-of-attack
T : lateral force on low rail
$\bar{x}$: arithmetic mean
σ : standard deviation (68.2% of events will occur within $\pm 1\sigma$ from mean if distribution is normal)

* Note that this data was obtained for a loaded train passing over lubricated track immediately after the passage of a similar train (whose average lateral force and angle-of-attack data are presented in the column to the left).

TABLE 4: STATISTICAL SUMMARY OF LOW RAIL LATERAL FORCES AND ANGLE-OF-ATTACK VALUES

	Measurement Points	Measurement Locations	Train No.'s	Depth of Wear		Cumulative Depth of Wear	
				mx10^{-6}	inx10^{-3}	mx10^{-6}	inx10^{-3}
Test Site 1, 7° Curve	3 (High Rail)	a	4-24 24-37 37-38 38-39	30.0 5.0 2.5 2.5	1.2 0.2 0.1 0.1	40.0	1.6
		b	4-24 24-37 37-38 38-39	15.0 5.0 2.5 5.0	0.6 0.2 0.1 0.2	27.5	1.1
		c	4-24 24-37 37-38 38-39	15.0 5.0 2.5 5.0	0.6 0.2 0.1 0.2	27.5	1.1
		d	0-39	2.5	0.1	>2.5	>0.1
	4 (Low Rail)	a	24-37 37-38 38-39	7.5 2.5 5.0	0.3 0.1 0.2	15.0	0.6
		b	24-37 37-38 38-39	10.0 2.5 2.5	0.4 0.1 0.1	15.0	0.6
		c	24-37 37-38 38-39	2.5 0.0 0.0	0.1 0.0 0.0	2.5	0.1
		d	0-39	2.5	0.1	>2.5	>0.1
Test Site 2, Tangent Track	9 (Fast Rail)	b	0-25 25-41	12.5 5.0	0.5 0.2	17.5	0.7
		c	0-25 25-41	12.5 7.5	0.5 0.3	20.0	0.8
		d	0-41	2.5	0.1	>2.5	>0.1
	10 (West Rail)	b	1-25 25-41	15.0 5.0	0.6 0.2	20.0	0.8
		c	0-25 25-41	20.0 7.5	0.8 0.3	27.5	1.1
		d	0-41	2.5	0.1	>2.5	>0.1
Test Site 3, 2° Curve	17 (High Rail)	a	1-25 25-41	15.0 5.0	0.6 0.2	20.0	0.8
		b	1-25 25-41	10.0 12.5	0.4 0.5	22.5	0.9
		c	1-25 25-41	15.0 7.5	0.6 0.3	22.5	0.9
		d	1-41	2.5	0.1	>2.5	>0.1
	18 (Low Rail)	a	——grinding marks, no wear——				
		b	1-25 25-41	35.0 15.0	1.4 0.6	50.0	2.0
		c	1-25 25-41	25.0 10.0	1.0 0.4	35.0	1.4
		d	1-41	25.0	1.0	25.0	1.0

TABLE 5: SUMMARY OF WG WEAR MEASUREMENTS

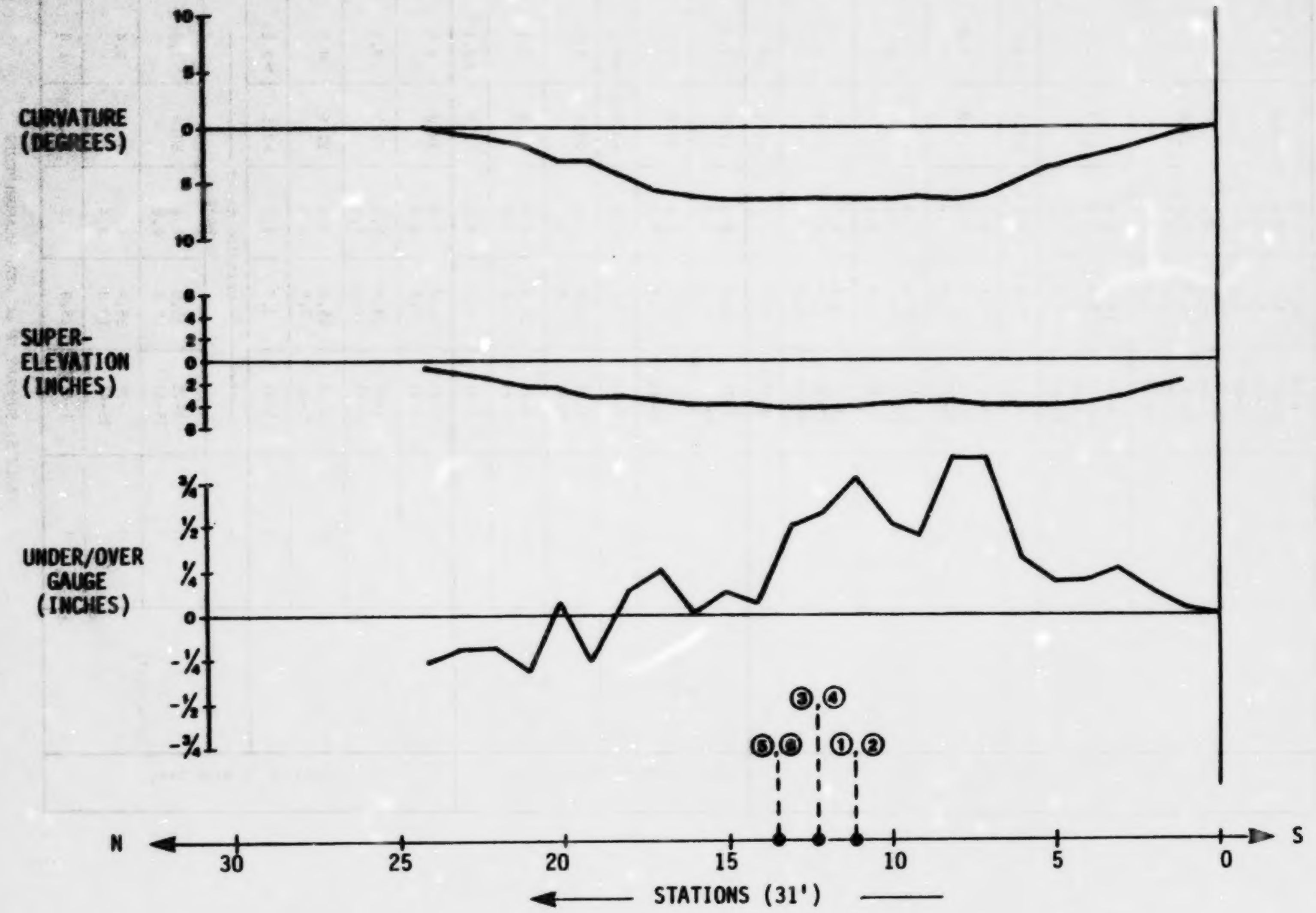

FIGURE 1: TEST SITE #1, 7° CURVE, MP 25.1-25.3, WINDERMERE SUBDIVISION (CIRCLED NUMBERS DESIGNATE WEAR MEASUREMENT POINTS, ANGLE-OF-ATTACK WAS ALSO MEASURED AT POINTS 3 AND 4)

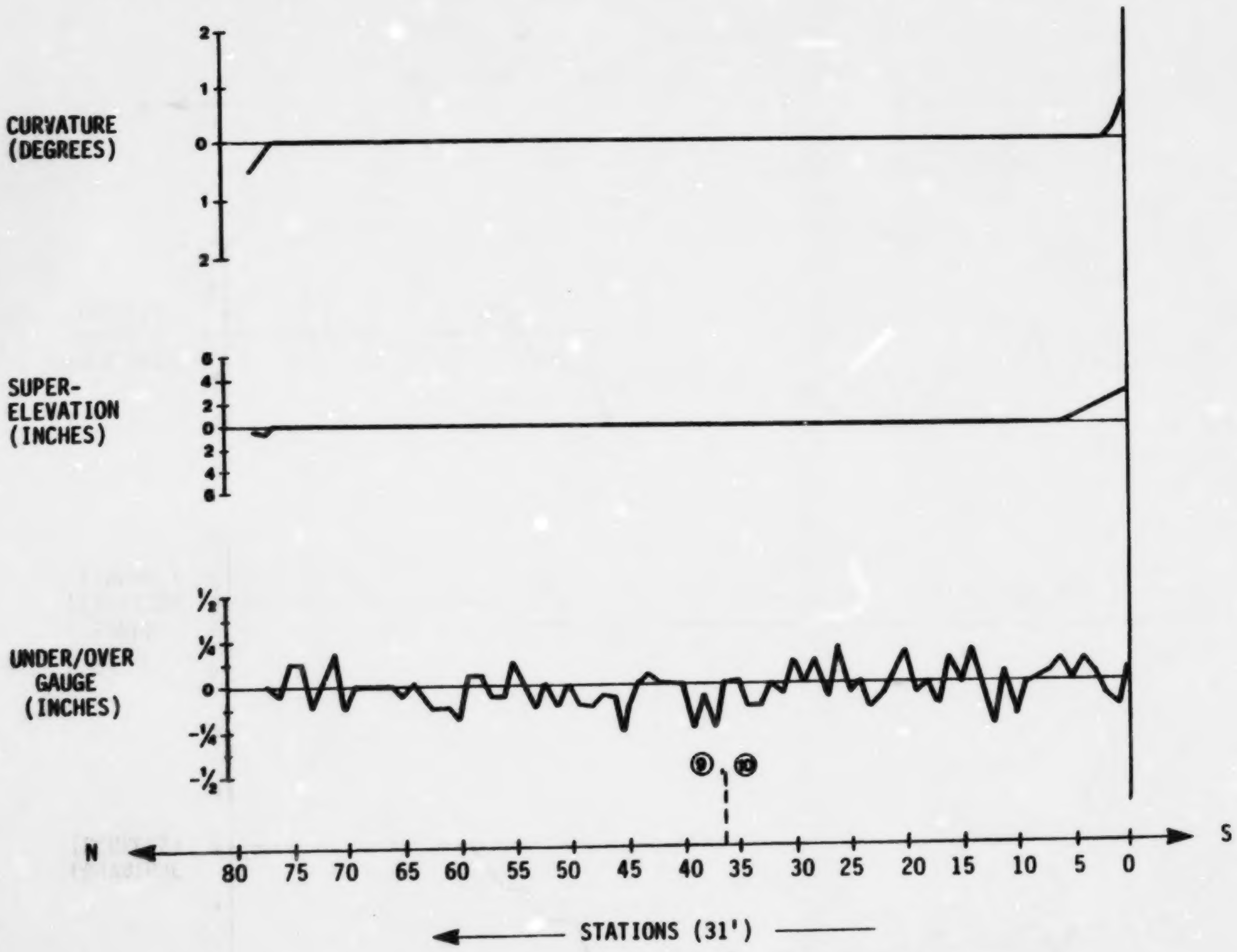

FIGURE 2: TEST SITE #2, TANGENT TRACK, MP 25.4-25.9, WINDERMERE SUBDIVISION (CIRCLED NUMBERS DESIGNATE WEAR MEASUREMENT POINTS, ANGLE-OF-ATTACK WAS NOT MEASURED AT THIS SITE)

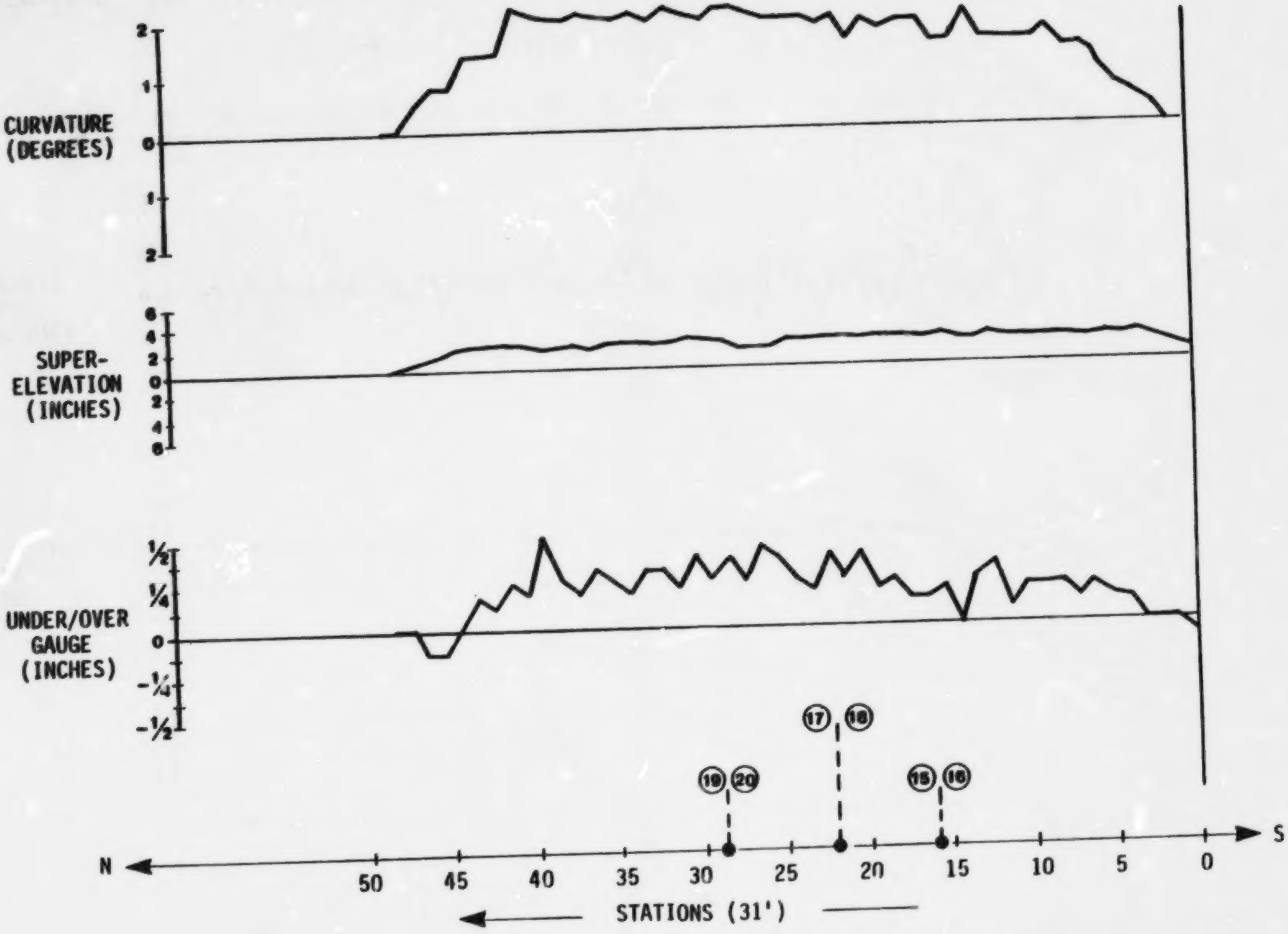

FIGURE 3: TEST SITE #3, 2° CURVE, MP 25.9-26.1, WINDERMERE SUBDIVISION (CIRCLED NUMBERS DESIGNATE WEAR MEASUREMENT POINTS, ANGLE-OF-ATTACK WAS ALSO MEASURED AT POINTS 17 AND 18)

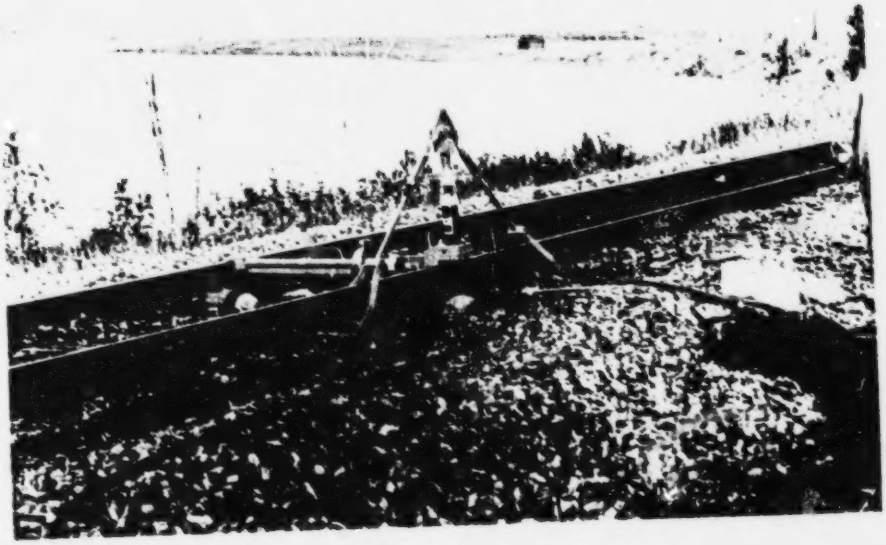

FIGURE 4: HYDRAULIC LOADING DEVICE USED FOR SIMULTANEOUS CALIBRATION OF VERTICAL AND LATERAL LOAD CIRCUITS

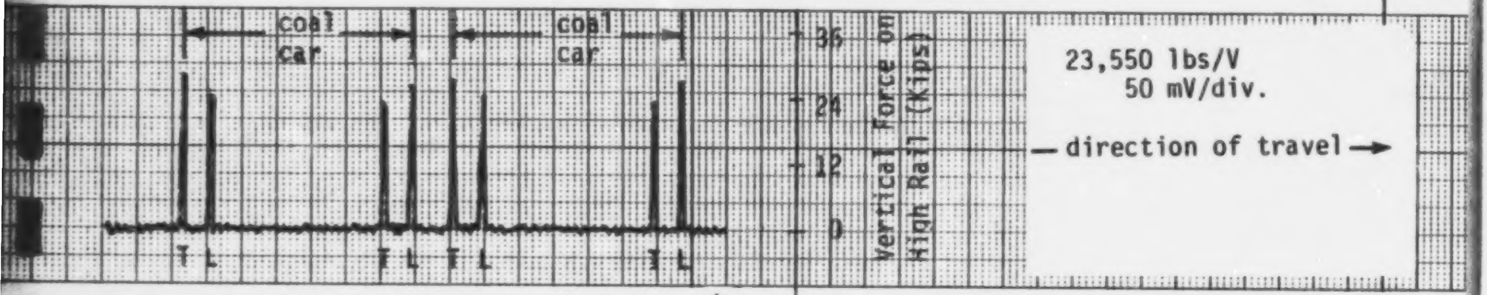

HIGH RAIL VERTICAL FORCE

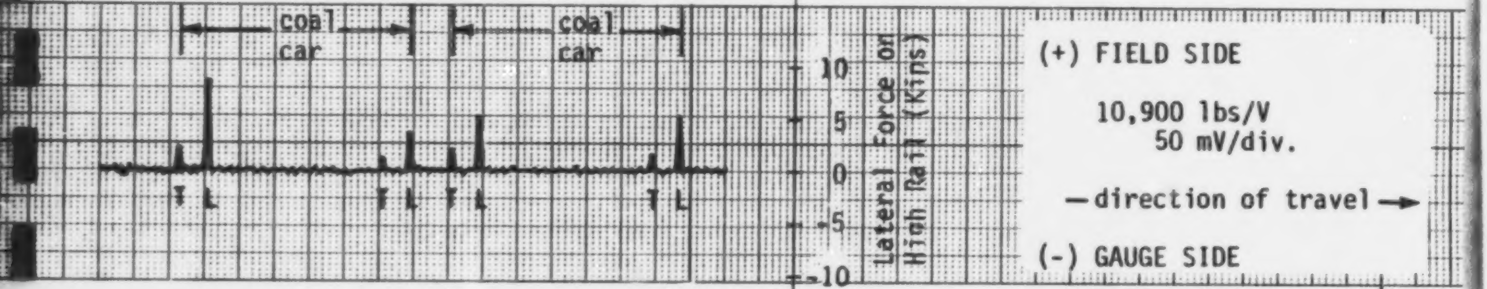

HIGH RAIL LATERAL FORCE

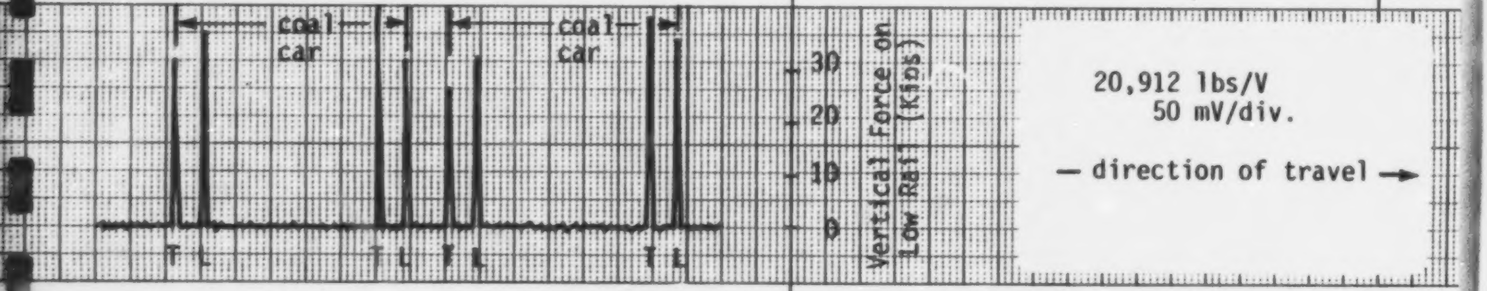

LOW RAIL VERTICAL FORCE

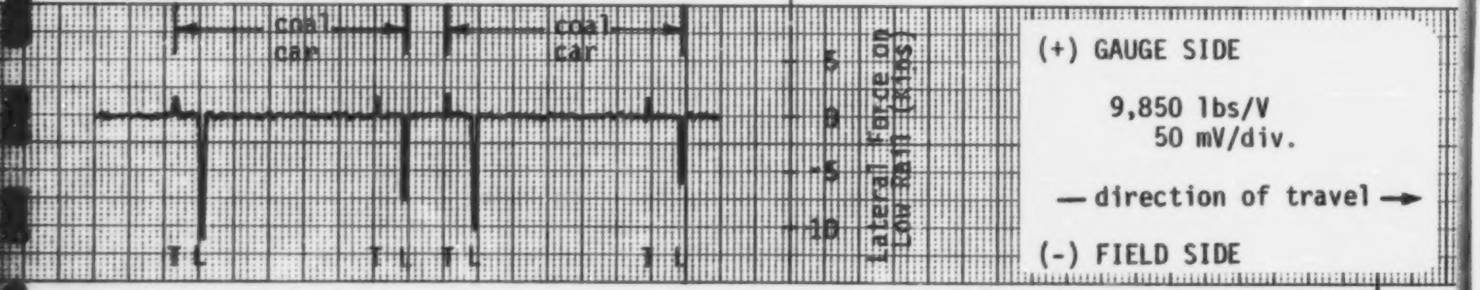

LOW RAIL LATERAL FORCE

FIGURE 5 : SAMPLE OUTPUT FROM BRUSH CHART RECORDER OF WHEEL/RAIL FORCE MEASUREMENT DATA (L AND T DENOTE LEADING AND TRAILING AXLES, RESPECTIVELY)

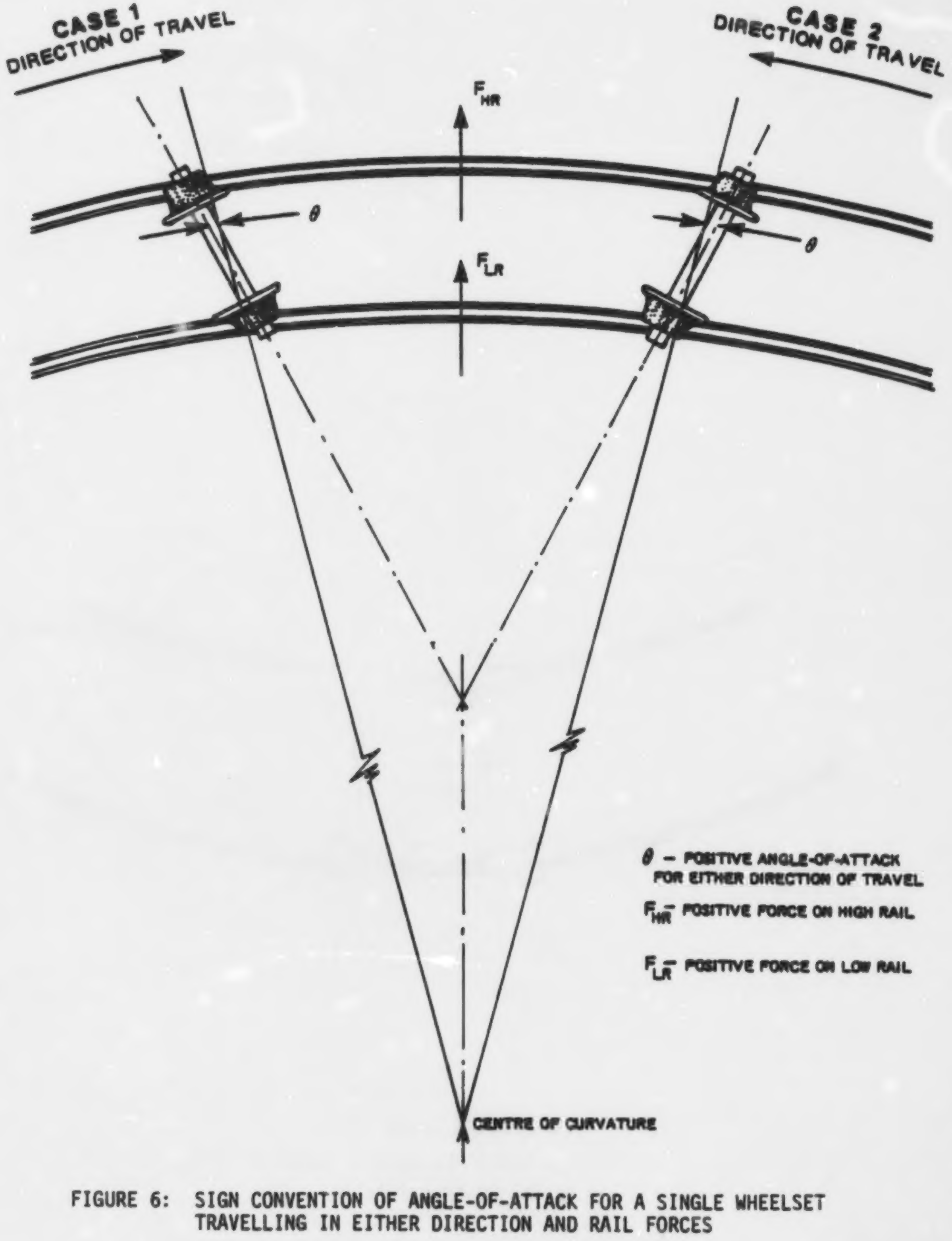
CASE 1
DIRECTION OF TRAVEL
CASE 2
DIRECTION OF TRAVEL
F_{HR}
F_{LR}
θ
θ
θ - POSITIVE ANGLE-OF-ATTACK FOR EITHER DIRECTION OF TRAVEL
F_{HR} - POSITIVE FORCE ON HIGH RAIL
F_{LR} - POSITIVE FORCE ON LOW RAIL
CENTRE OF CURVATURE

FIGURE 6: SIGN CONVENTION OF ANGLE-OF-ATTACK FOR A SINGLE WHEELSET TRAVELLING IN EITHER DIRECTION AND RAIL FORCES

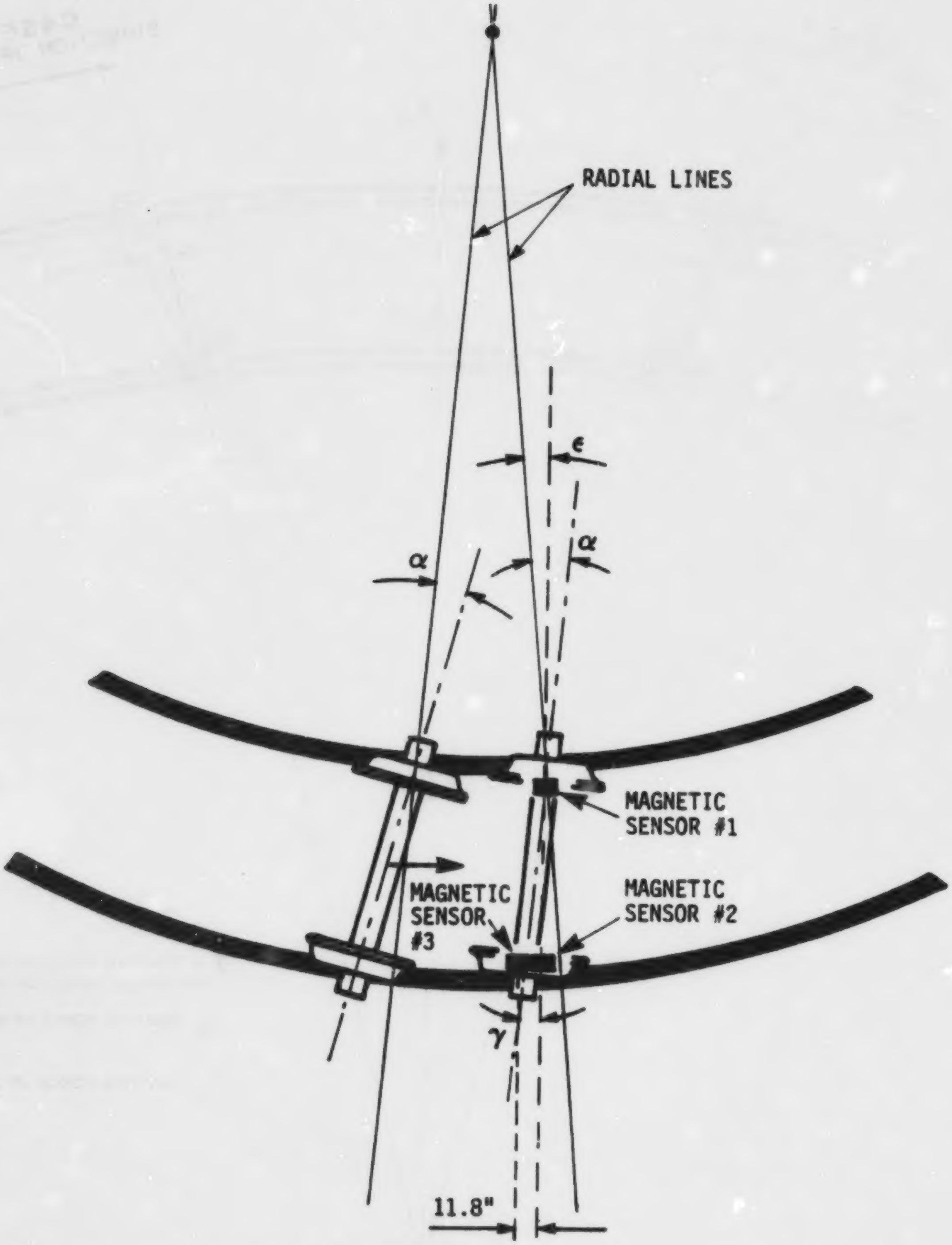
RADIAL LINES
ε
α
α
MAGNETIC SENSOR #1
MAGNETIC SENSOR #2
MAGNETIC SENSOR #3
γ
11.8"

ϵ - OFF-SET ERROR

γ- ANGLE MEASURED BY ANGLE-OF-ATTACK SYSTEM

α- ANGLE-OF-ATTACK

FIGURE 7: ALIGNMENT OF MAGNETIC SENSORS USED IN ANGLE-OF-ATTACK MEASUREMENTS

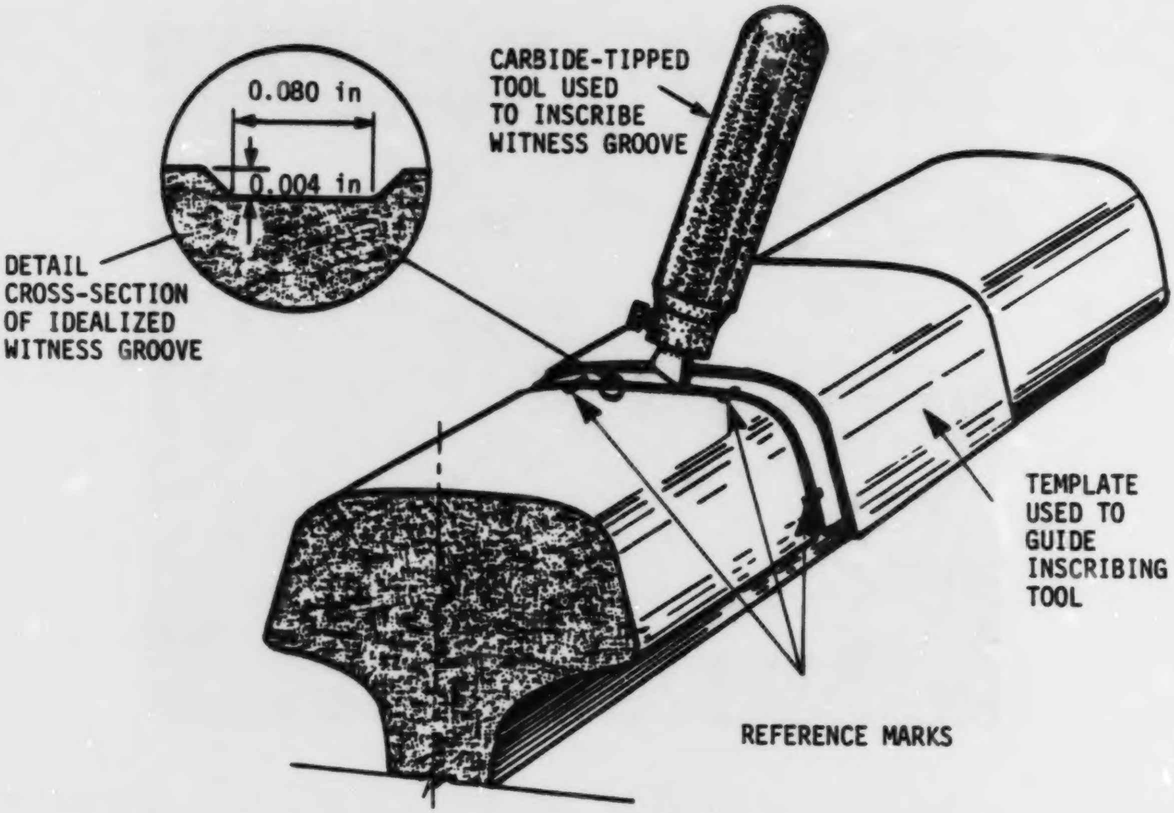
0.080 in
0.004 in
CARBIDE-TIPPED TOOL USED TO INSCRIBE WITNESS GROOVE
DETAIL CROSS-SECTION OF IDEALIZED WITNESS GROOVE
TEMPLATE USED TO GUIDE INSCRIBING TOOL
REFERENCE MARKS

FIGURE 8A: ORIENTATION AND APPROXIMATE DIMENSION OF THE WITNESS GROOVE

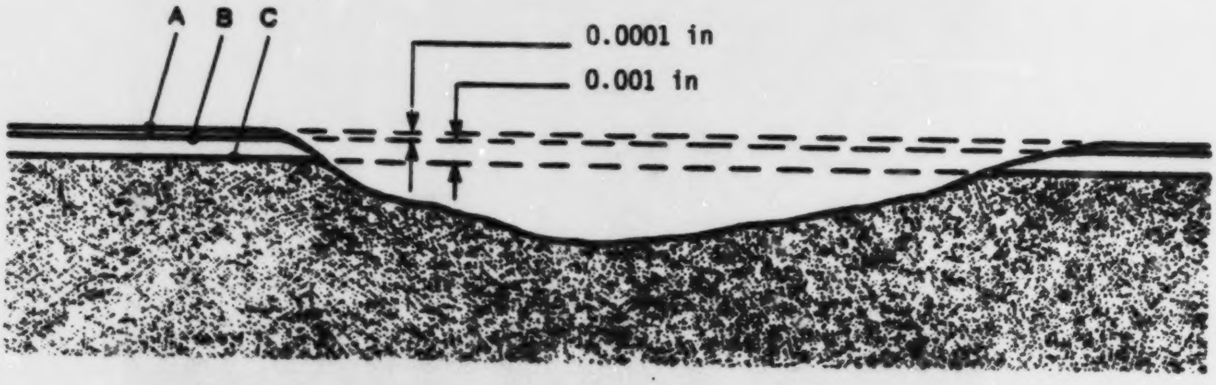
A
B
C
0.0001 in
0.001 in

A - BEFORE TRAINS
B - AFTER ONE LOADED COAL TRAIN
C - AFTER TEN LOADED COAL TRAINS

FIGURE 8B: TRACE OF HYPOTHETICAL WITNESS GROOVE ILLUSTRATING RAIL SURFACE WEAR CAUSED BY THE PASSAGE OF SEVERAL TRAINS

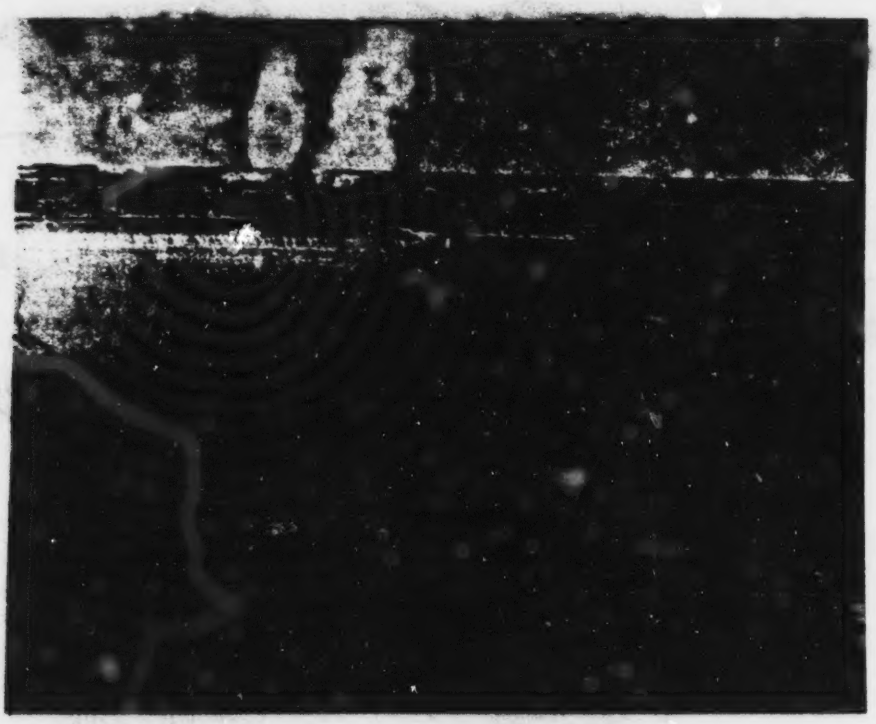

FIGURE 9A: LUBRICANT DEPOSIT ON LOW RAIL IN 7° CURVE IN TEST SITE #1

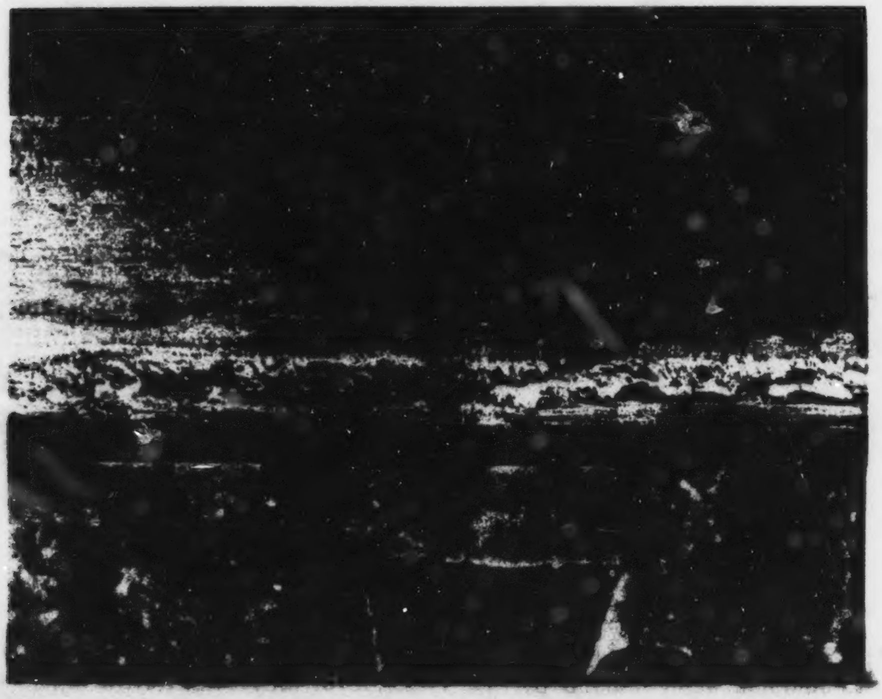

FIGURE 9B: LUBRICANT DEPOSIT ON HIGH RAIL IN 7° CURVE IN TEST SITE #1

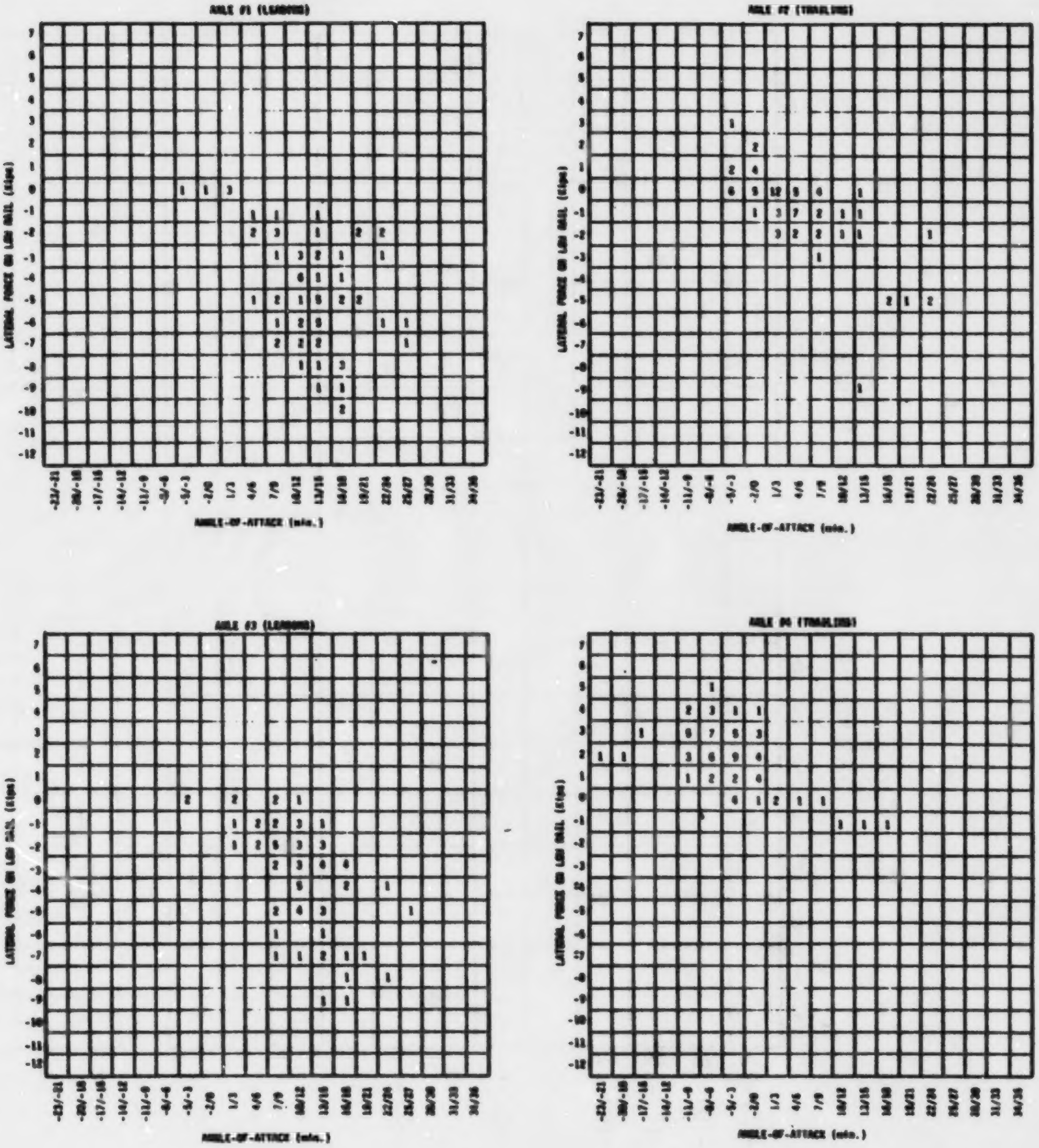

FIGURE 10A: TWO-DIMENSIONAL FREQUENCY DISTRIBUTION OF WHEELSET ORIENTATION AND WHEEL/RAIL FORCE DATA, BY AXLE, COLLECTED IN MIDDLE OF FULLY DEVELOPED SECTION OF 2° CURVE FOR THE PASSAGE OF A LOADED COAL TRAIN (NO. 14) -- RAIL CONDITION IS SANDED

TOTAL TRAIN

LATERAL FORCE ON LOW RAIL (Kips)	-23/-21	-20/-18	-17/-15	-14/-12	-11/-9	-8/-6	-5/-3	-2/0	1/3	4/6	7/9	10/12	13/15	16/18	19/21	22/24	25/27	28/30	31/33	34/36
7																				
6																				
5						1														
4					2	3	1	1												
3			1		5	7	6	3												
2	1	1			3	6	9	6												
1					1	2	4	8												
0							13	7	19	6	7	1	1							
-1								1	4	10	5	5	4	1						
-2									4	6	10	4	5		2	3				
-3											4	6	6	5		1				
-4												11	1	3		1				
-5										1	4	5	8	4	3	2	1			
-6											2	2	6			1	1			
-7											3	3	4	1	1		1			
-8													1	4		1				
-9												1	3	2						
-10														2						
-11																				
-12													1							

ANGLE-OF-ATTACK (min.)

FIGURE 10B: TWO-DIMENSIONAL FREQUENCY DISTRIBUTION OF WHEELSET ORIENTATION AND WHEEL/RAIL FORCE DATA COLLECTED IN MIDDLE OF FULLY DEVELOPED SECTION OF 2° CURVE FOR THE PASSAGE OF A LOADED COAL TRAIN (NO. 14) -- RAIL CONDITION IS SANDED

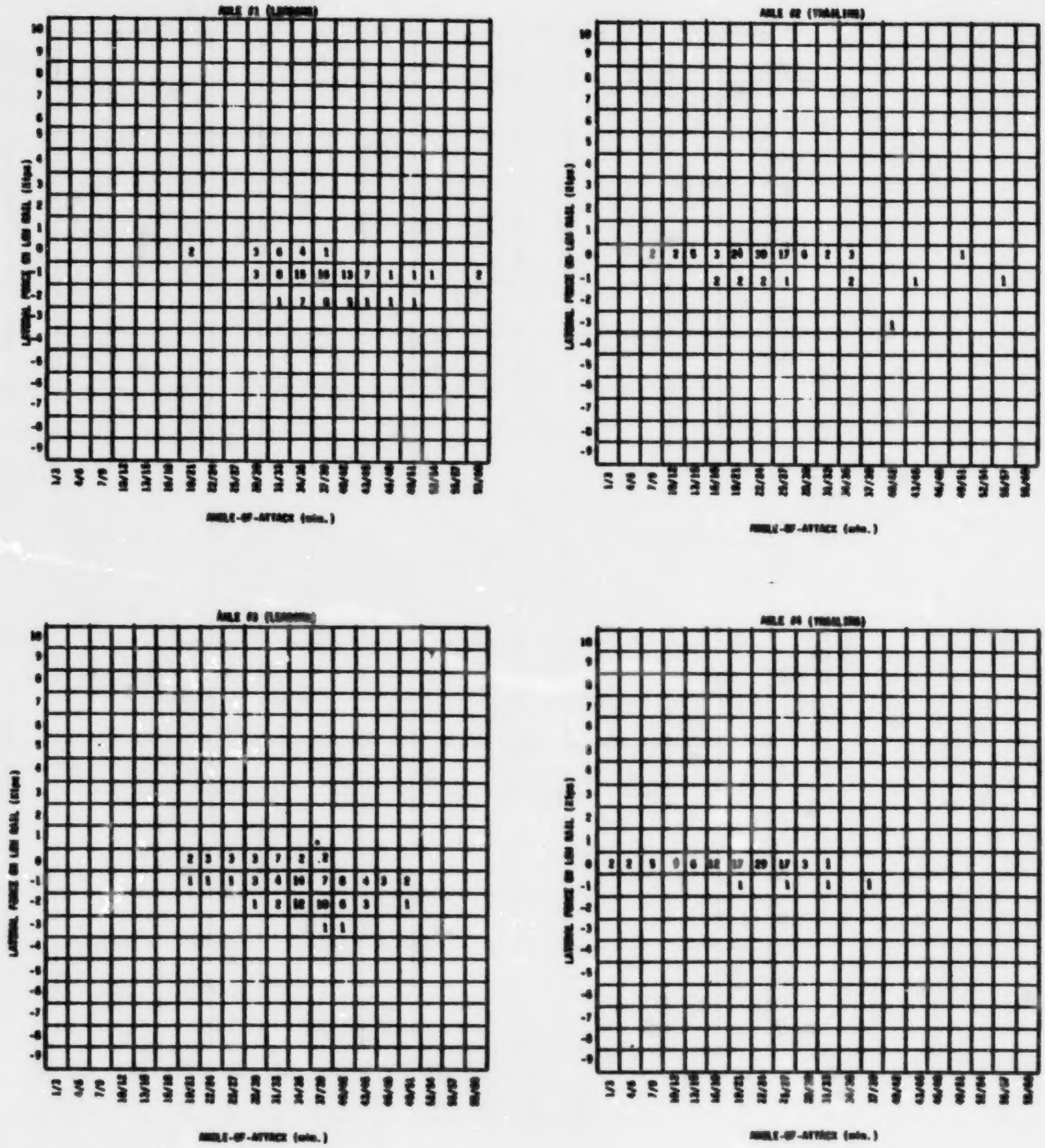

FIGURE 11A: TWO-DIMENSIONAL FREQUENCY DISTRIBUTION OF WHEELSET ORIENTATION AND WHEEL/RAIL FORCE DATA, BY AXLE, COLLECTED IN MIDDLE OF FULLY DEVELOPED SECTION OF 2° CURVE FOR THE PASSAGE OF AN EMPTY COAL TRAIN (NO. 16) -- RAIL CONDITION IS SANDED

TOTAL TRAIN

LATERAL FORCE ON LOW RAIL (Kips)	1/3	4/6	7/9	10/12	13/15	16/18	19/21	22/24	25/27	28/30	31/33	34/36	37/39	40/42	43/45	46/48	49/51	52/54	55/57	58/60
10																				
9																				
8																				
7																				
6																				
5																				
4																				
3																				
2																				
1																				
0	2	2	7	11	11	15	45	62	37	15	16	9	3				1			
-1						2	4	3	3	6	13	31	24	21	12	4	3	1	1	2
-2										1	3	19	18	11	4	1	2			
-3													1	2						
-4																				
-5																				
-6																				
-7																				
-8																				
-9																				

ANGLE-OF-ATTACK (min.)

FIGURE 11B: TWO-DIMENSIONAL FREQUENCY DISTRIBUTION OF WHEELSET ORIENTATION AND WHEEL/RAIL FORCE DATA COLLECTED IN MIDDLE OF FULLY DEVELOPED SECTION OF 2° CURVE FOR THE PASSAGE OF AN EMPTY COAL TRAIN (NO. 16) -- RAIL CONDITION IS SANDED

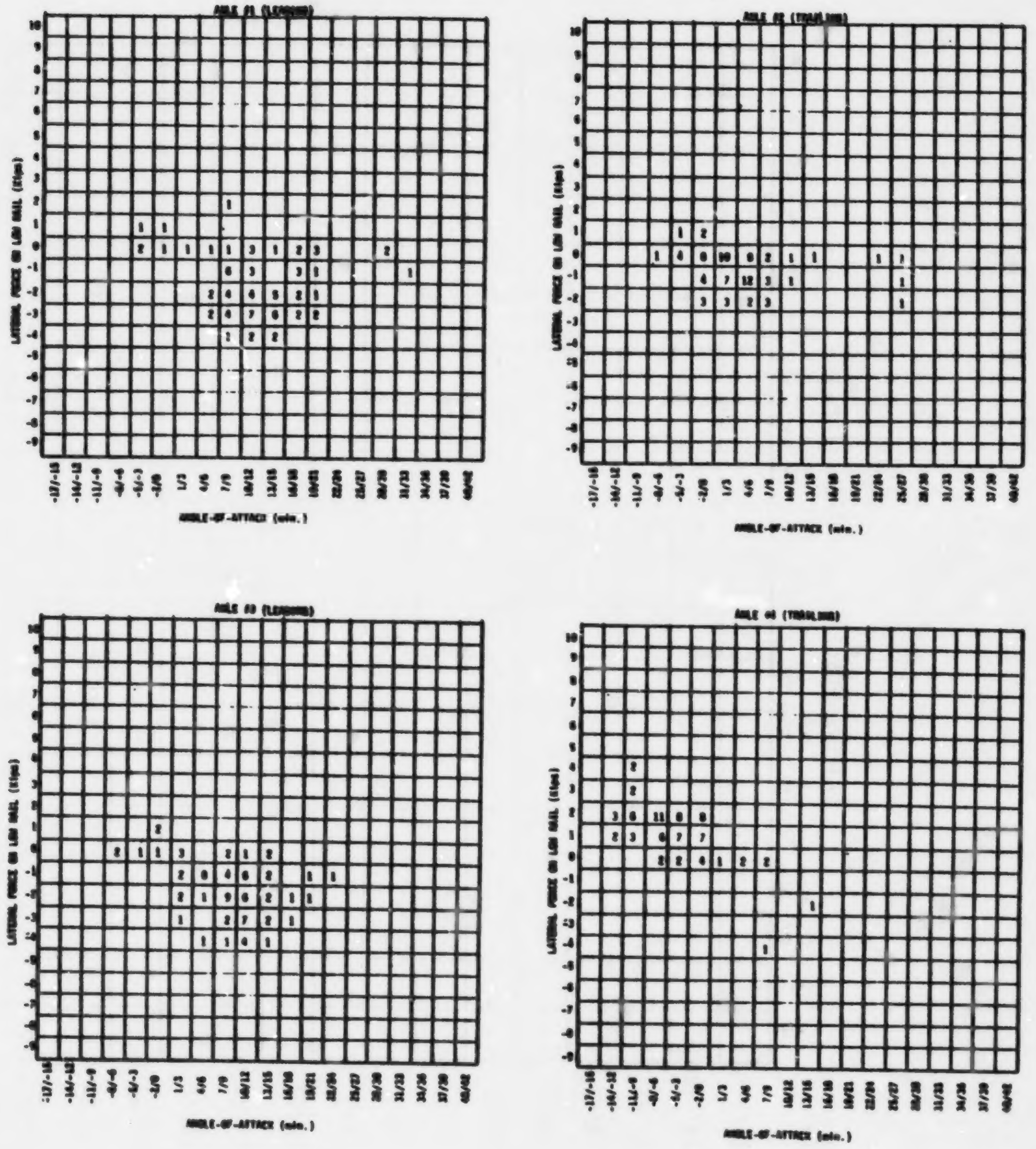

FIGURE 12A: TWO-DIMENSIONAL FREQUENCY DISTRIBUTION OF WHEELSET ORIENTATION AND WHEEL/RAIL FORCE DATA, BY AXLE, COLLECTED IN MIDDLE OF FULLY DEVELOPED SECTION OF 2° CURVE FOR THE PASSAGE OF A LOADED COAL TRAIN (NO. 30) -- RAIL CONDITION IS LUBRICATED

TOTAL TRAIN

LATERAL FORCE ON LOW RAIL (Kips)	-17/-15	-14/-12	-11/-9	-8/-6	-5/-3	-2/0	1/3	4/6	7/9	10/12	13/15	16/18	19/21	22/24	25/27	28/30	31/33	34/36	37/39	40/42
10																				
9																				
8																				
7																				
6																				
5																				
4			2																	
3			2																	
2		3	6	11	8	8			1											
1		2	3	6	9	12														
0				5	9	14	15	11	7	5	4	2	3	1	1	2				
-1						4	9	20	13	10	2	3	2	1	1		1			
-2						3	4	5	16	10	7	4	2		1					
-3							2	2	6	14	8	3	2							
-4								1	3	6	3									
-5																				
-6																				
-7																				
-8																				
-9																				

ANGLE-OF-ATTACK (min.)

FIGURE 12B: TWO-DIMENSIONAL FREQUENCY DISTRIBUTION OF WHEELSET ORIENTATION AND WHEEL/RAIL FORCE DATA COLLECTED IN MIDDLE OF FULLY DEVELOPED SECTION OF 2° CURVE FOR THE PASSAGE OF A LOADED COAL TRAIN (NO. 30) -- RAIL CONDITION IS LUBRICATED

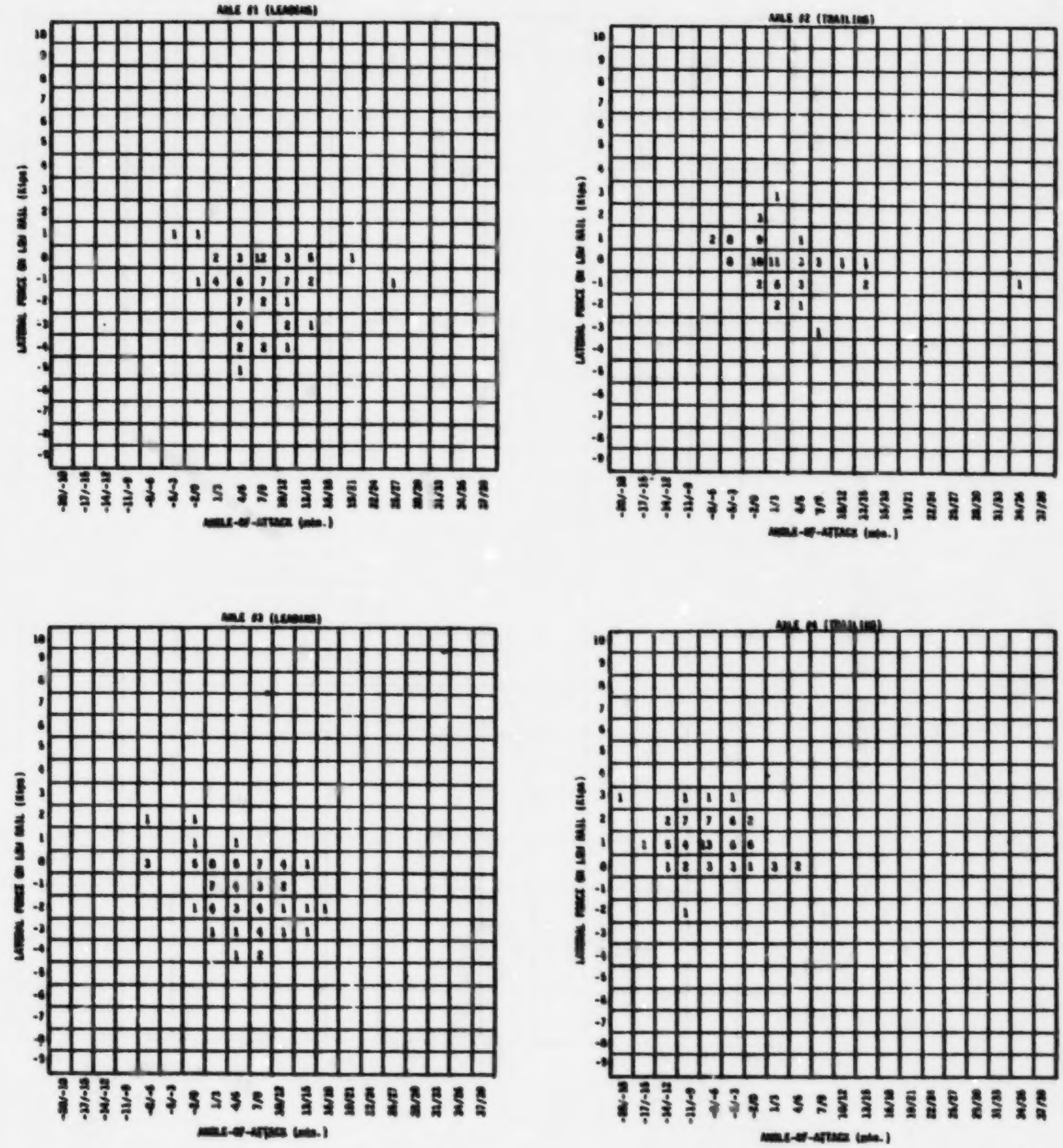

FIGURE 13A: TWO-DIMENSIONAL FREQUENCY DISTRIBUTION OF WHEELSET ORIENTATION AND WHEEL/RAIL FORCE DATA, BY AXLE, COLLECTED IN MIDDLE OF FULLY DEVELOPED SECTION OF 2° CURVE FOR THE PASSAGE OF A LOADED COAL TRAIN (NO. 31) -- RAIL CONDITION IS LUBRICATED

TOTAL TRAIN

LATERAL FORCE ON LOW RAIL (Kips)	-20/-18	-17/-15	-14/-12	-11/-9	-8/-6	-5/-3	-2/0	1/3	4/6	7/9	10/12	13/15	16/18	19/21	22/24	25/27	28/30	31/33	34/36	37/39
10																				
9																				
8																				
7																				
6																				
5																				
4																				
3	1			1	1	1		1												
2			2	7	8	6	6													
1		1	5	4	15	15	17		2											
0			1	2	6	11	16	24	13	21	8	7		1						
-1							3	17	13	10	9	4				1			1	
-2				1			1	6	11	6	2	1	1							
-3								1	5	5	3	2								
-4									4	4	1									
-5									1											
-6																				
-7																				
-8																				
-9																				

ANGLE-OF-ATTACK (min.)

FIGURE 13B: TWO-DIMENSIONAL FREQUENCY DISTRIBUTION OF WHEELSET ORIENTATION AND WHEEL/RAIL FORCE DATA COLLECTED IN MIDDLE OF FULLY DEVELOPED SECTION OF 2° CURVE FOR THE PASSAGE OF A LOADED COAL TRAIN (NO. 31) -- RAIL CONDITION IS LUBRICATED

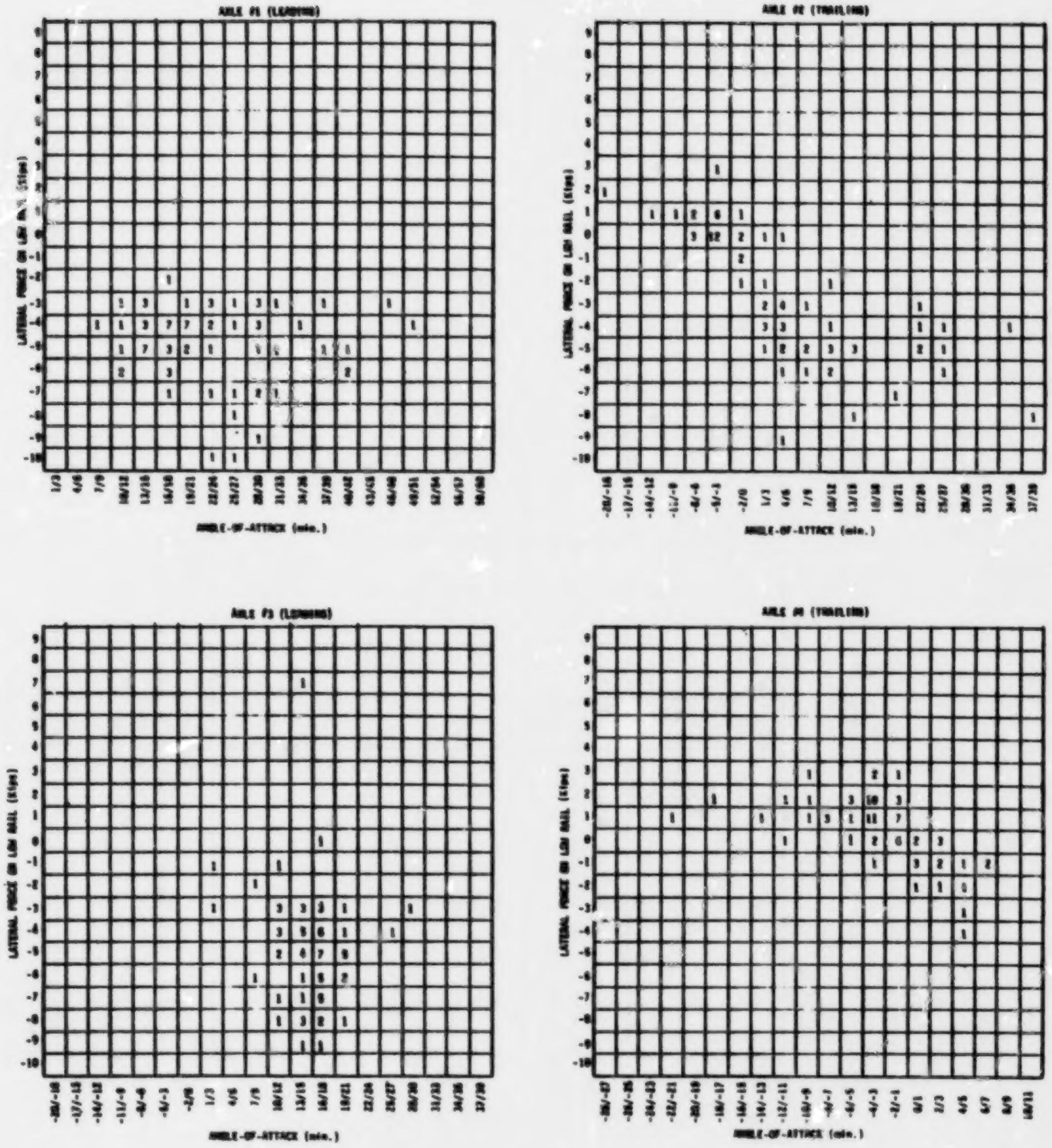

FIGURE 14A: TWO-DIMENSIONAL FREQUENCY DISTRIBUTION OF WHEELSET ORIENTATION AND WHEEL/RAIL FORCE DATA, BY AXLE, COLLECTED IN MIDDLE OF FULLY DEVELOPED SECTION OF 7° CURVE FOR THE PASSAGE OF A LOADED COAL TRAIN (NO. 38) -- RAIL CONDITION IS SANDED

TOTAL TRAIN

LATERAL FORCE ON LOW RAIL (Kips)	-45/-41	-40/-36	-35/-31	-30/-26	-25/-21	-20/-16	-15/-11	-10/-6	-5/-1	0/4	5/9	10/14	15/19	20/24	25/29	30/34	35/39	40/44	45/49	50/54
9																				
8												1								
7																				
6																				
5																				
4																				
3								1	4											
2						2	1	2	15											
1					1		3	7	25											
0		1					1	4	21	8			1							
-1									2	8	2	1								
-2										5	1	1	1							
-3										6	3	8	7	4	5	1	1		1	
-4										4	4	12	15	10	5	1	2			1
-5										2	3	13	19	8	2	1	1	1		
-6											3	4	9	2	1			2		
-7												1	7	1	2	2				
-8												3	4	2	1		1			
-9											1	1	1		1					
-10														1	1					

ANGLE-OF-ATTACK (min.)

FIGURE 14B: TWO-DIMENSIONAL FREQUENCY DISTRIBUTION OF WHEELSET ORIENTATION AND WHEEL/RAIL FORCE DATA COLLECTED IN MIDDLE OF FULLY DEVELOPED SECTION OF 7° CURVE FOR THE PASSAGE OF A LOADED COAL TRAIN (NO. 38) -- RAIL CONDITION IS SANDED

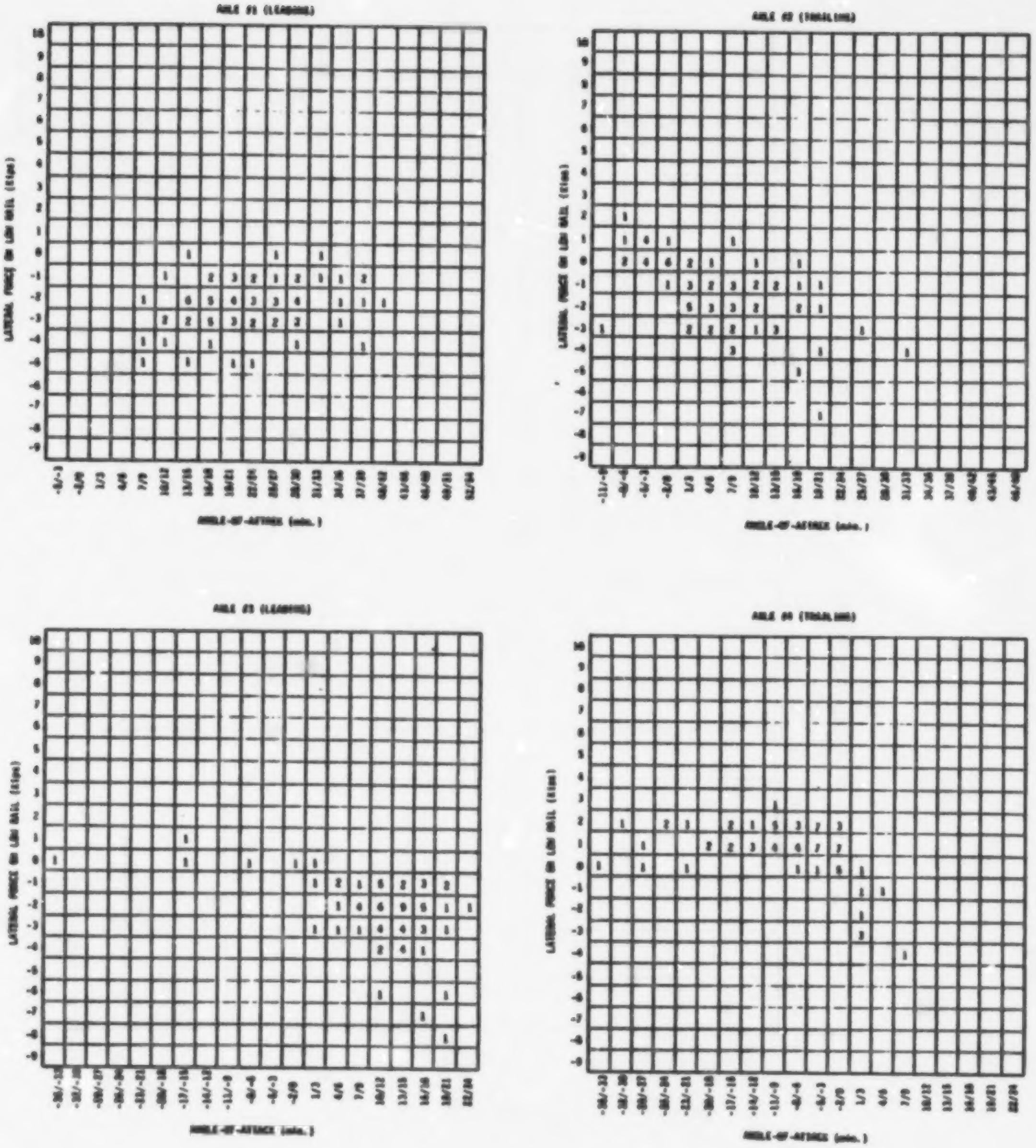

FIGURE 15A: TWO-DIMENSIONAL FREQUENCY DISTRIBUTION OF WHEELSET ORIENTATION AND WHEEL/RAIL FORCE DATA, BY AXLE, COLLECTED IN MIDDLE OF FULLY DEVELOPED SECTION OF 7° CURVE FOR THE PASSAGE OF A LOADED COAL TRAIN (NO. 39) -- RAIL CONDITION IS LUBRICATED

TOTAL TRAIN

LATERAL FORCE ON LOW RAIL (Kips)	-60/-56	-55/-51	-50/-46	-45/-41	-40/-36	-35/-31	-30/-26	-25/-21	-20/-16	-15/-11	-10/-6	-5/-1	0/4	5/9	10/14	15/19	20/24	25/29	30/34	35/39
10																				
9																				
8																				
7																				
6																				
5																				
4																				
3											1									
2						1		3	1	5	6	10								
1	1						1		2	8	7	17	2	1						
0						2	1	1	1		4	16	5	1	1	2		1	1	
-1													8	7	12	9	5	3	1	3
-2													8	10	16	20	9	6	2	2
-3											1		8	4	14	10	6	5	1	
-4														5	5	5		1	1	1
-5														1	1	1	2			
-6															1		1			
-7																1	1			
-8																	1			
-9																				

ANGLE-OF-ATTACK (min.)

FIGURE 15B: TWO-DIMENSIONAL FREQUENCY DISTRIBUTION OF WHEELSET ORIENTATION AND WHEEL/RAIL FORCE DATA COLLECTED IN MIDDLE OF FULLY DEVELOPED SECTION OF 7° CURVE FOR THE PASSAGE OF A LOADED COAL TRAIN (NO. 39) -- RAIL CONDITION IS LUBRICATED

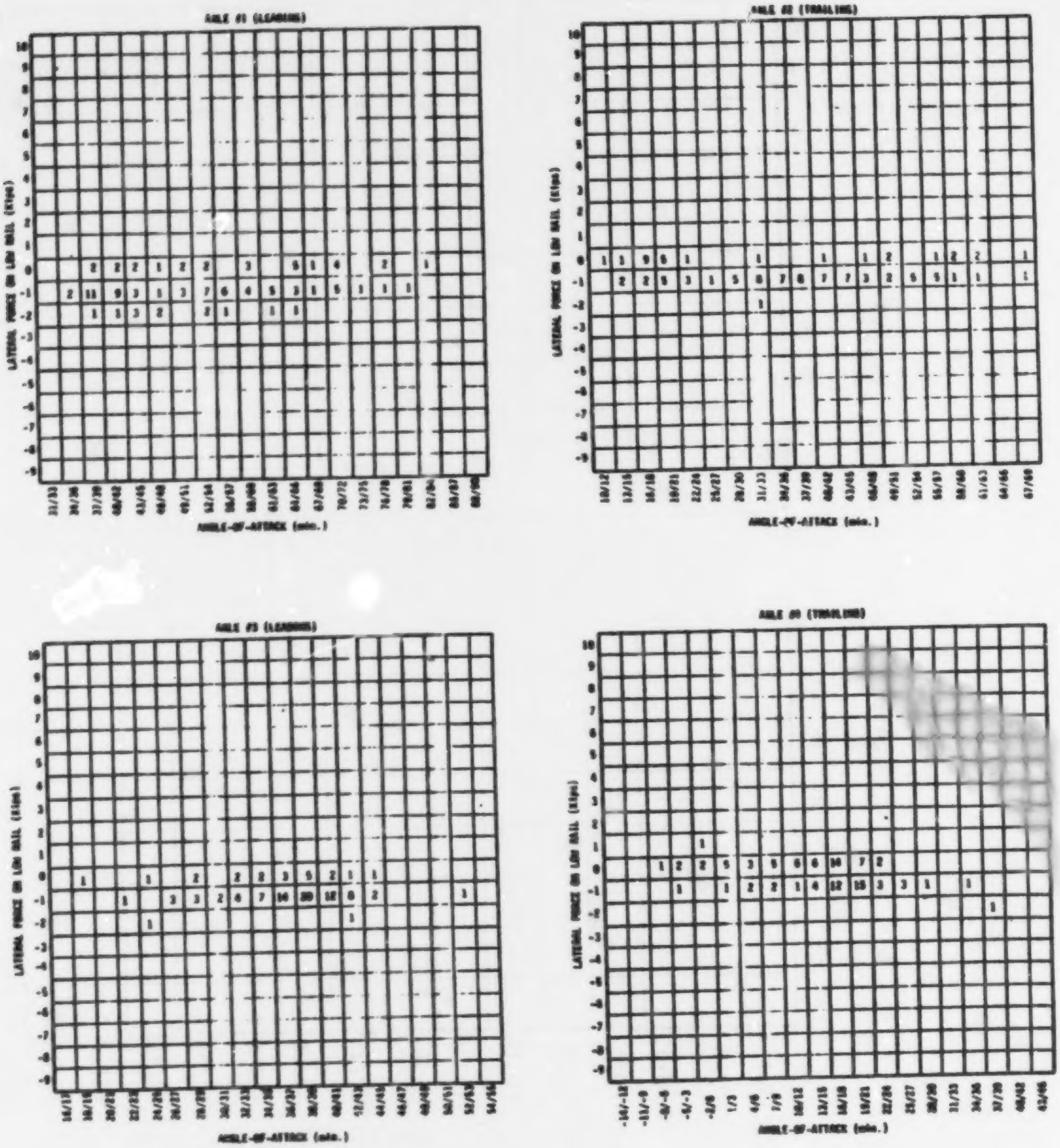

FIGURE 16A: TWO-DIMENSIONAL FREQUENCY DISTRIBUTION OF WHEELSET ORIENTATION AND WHEEL/RAIL FORCE DATA, BY AXLE, COLLECTED IN MIDDLE OF FULLY DEVELOPED SECTION OF 7° CURVE FOR THE PASSAGE OF AN EMPTY COAL TRAIN (NO. 40) -- RAIL CONDITION IS LUBRICATED

TOTAL TRAIN

LATERAL FORCE ON LOW RAIL (Kips)	-15/-11	-10/-6	-5/-1	0/4	5/9	10/14	15/19	20/24	25/29	30/34	35/39	40/44	45/49	50/54	55/59	60/64	65/69	70/74	75/79	80/84
10																				
9																				
8																				
7																				
6																				
5																				
4																				
3																				
2																				
1			1																	
0		1	4	5	8	12	32	9	3	4	11	8	4	5	4	5	6	4	2	1
-1			1	1	4	4	21	23	15	25	60	42	12	16	15	7	5	6	2	
-2									1	1	2	5	2	2	1	1	1			
-3																				
-4																				
-5																				
-6																				
-7																				
-8																				
-9																				

ANGLE-OF-ATTACK (min.)

FIGURE 16B: TWO-DIMENSIONAL FREQUENCY DISTRIBUTION OF WHEELSET ORIENTATION AND WHEEL/RAIL FORCE DATA COLLECTED IN MIDDLE OF FULLY DEVELOPED SECTION OF 7° CURVE FOR THE PASSAGE OF AN EMPTY COAL TRAIN (NO. 40) -- RAIL CONDITION IS LUBRICATED

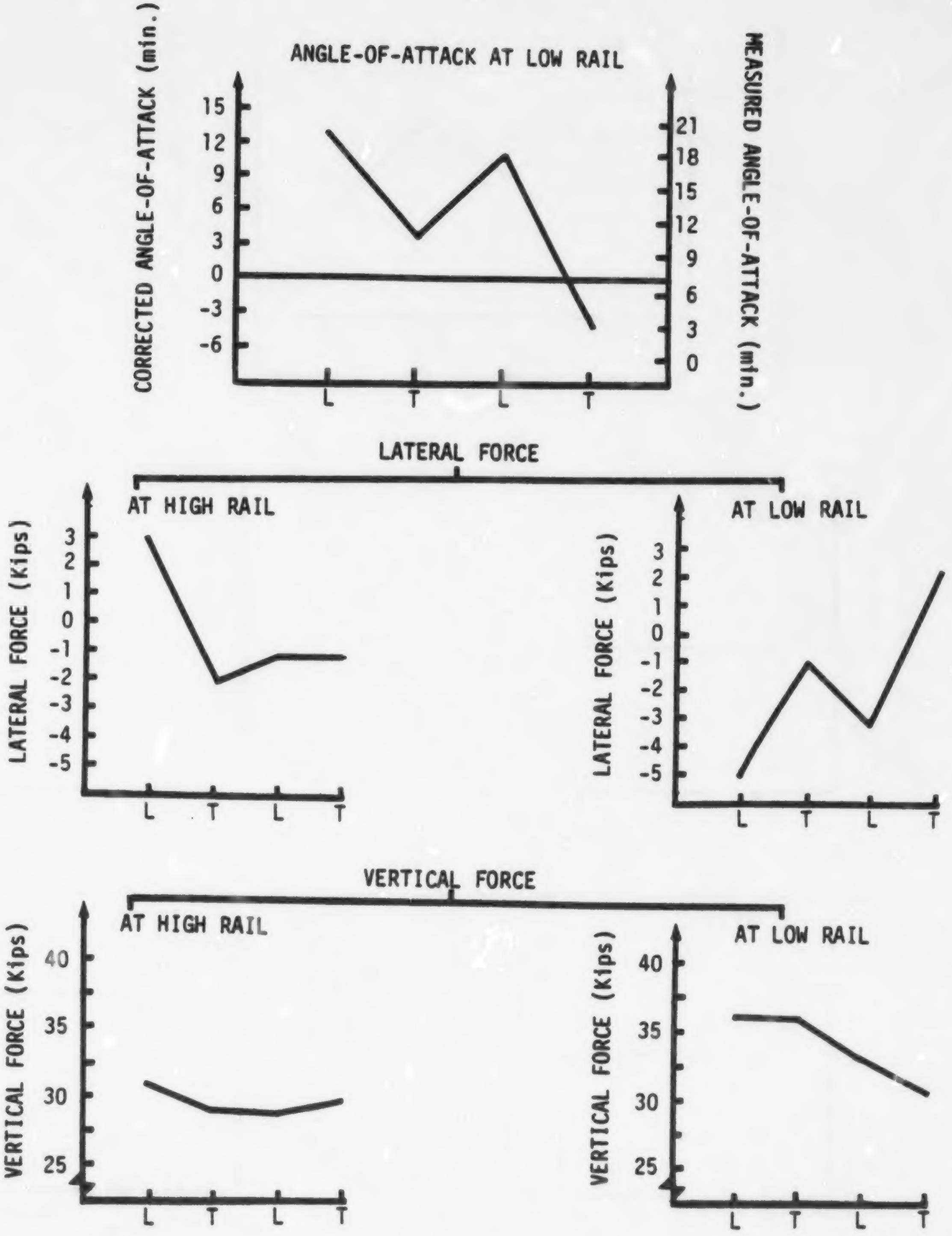

FIGURE 17: AVERAGE WHEELSET ORIENTATION AND WHEEL/RAIL FORCE DATA, BY AXLE, MEASURED IN THE MIDDLE OF THE FULLY DEVELOPED SECTION OF A 2° CURVE DUE TO THE PASSAGE OF A LOADED COAL TRAIN (NO. 14) UNDER SANDED TRACK CONDITIONS

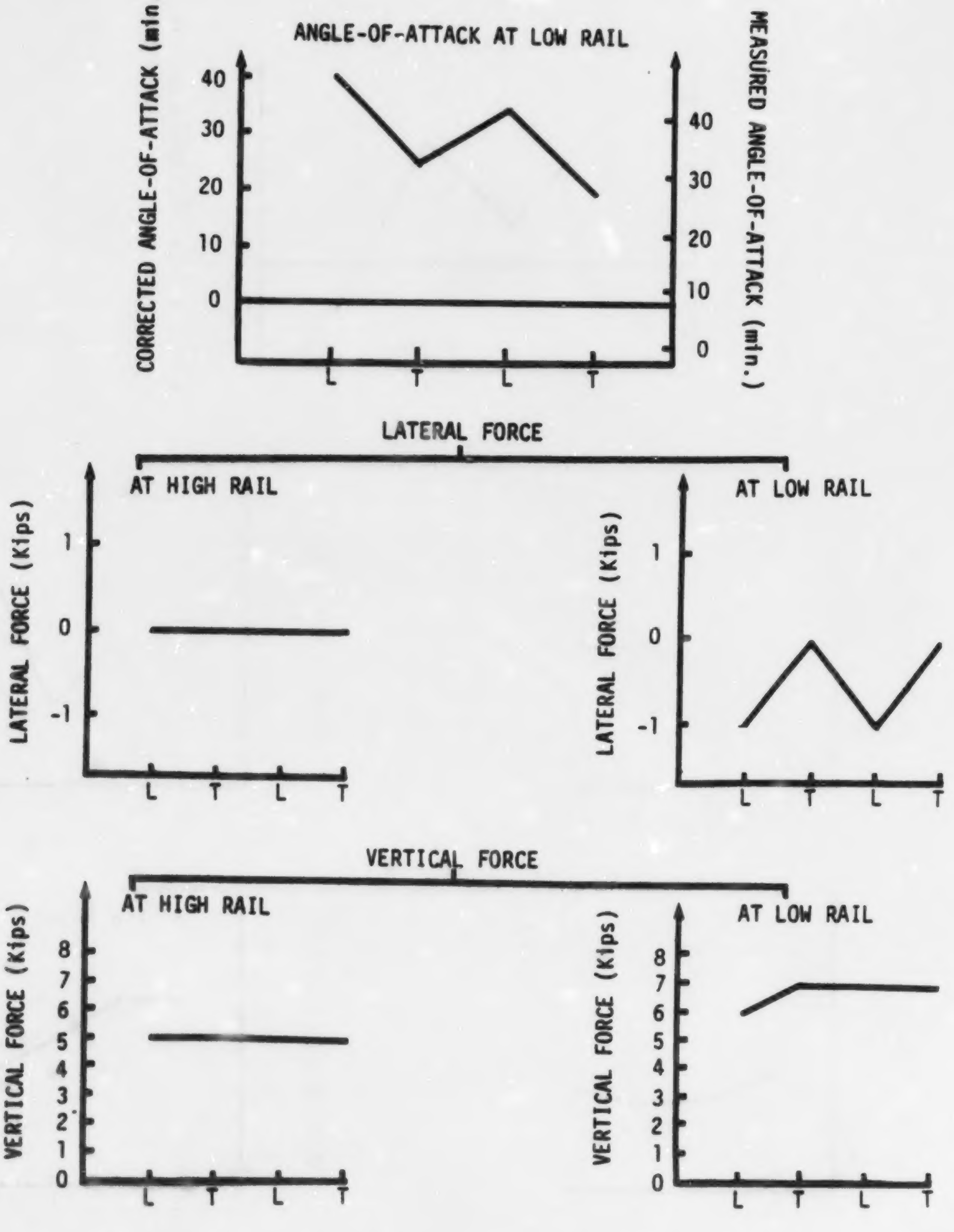

FIGURE 18: AVERAGE WHEELSET ORIENTATION AND WHEEL/RAIL FORCE DATA, BY AXLE, MEASURED IN THE MIDDLE OF THE FULLY DEVELOPED SECTION OF A 2° CURVE DUE TO THE PASSAGE OF AN EMPTY COAL TRAIN (NO. 16) UNDER SANDED TRACK CONDITIONS

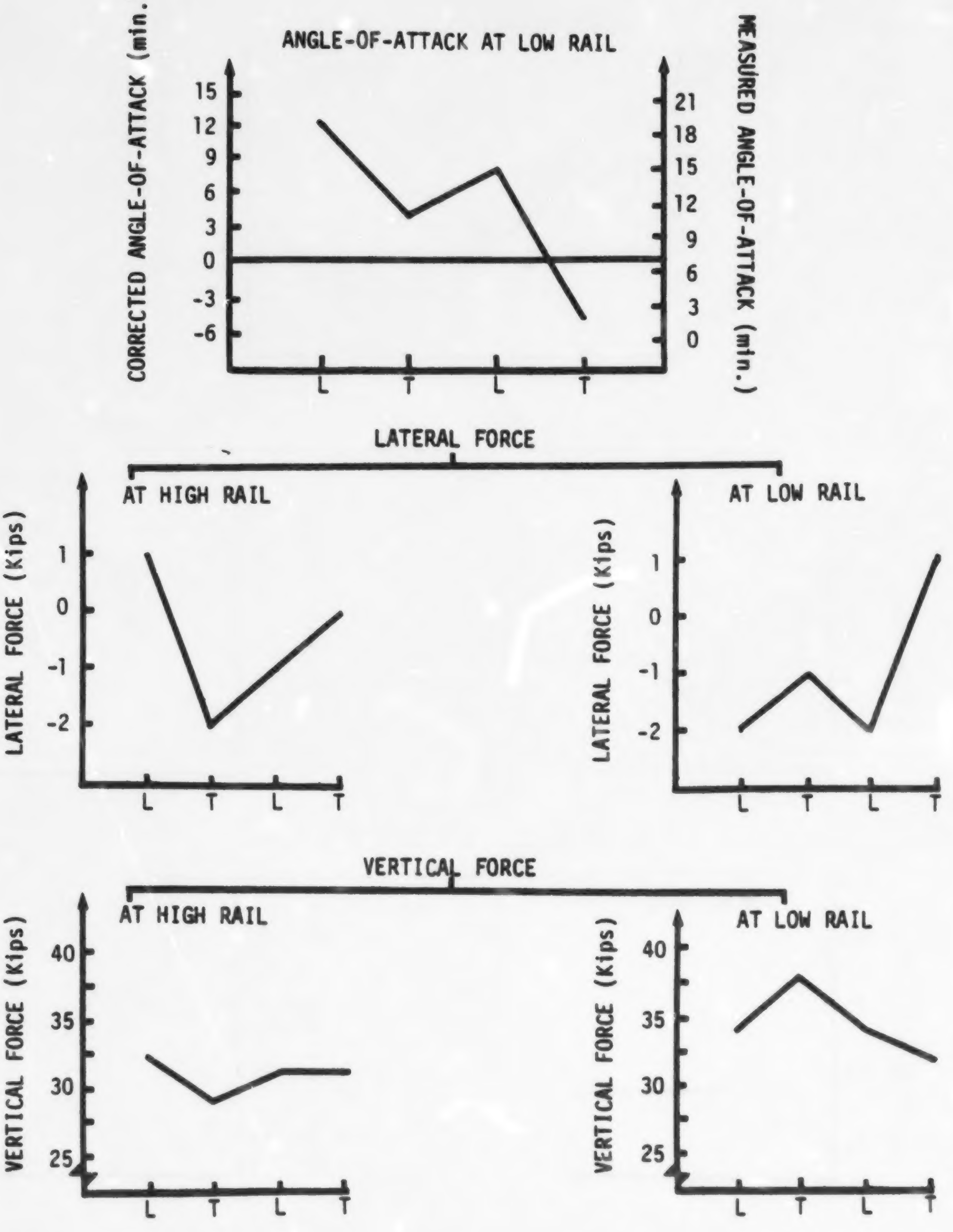

FIGURE 19: AVERAGE WHEELSET ORIENTATION AND WHEEL/RAIL FORCE DATA, BY AXLE, MEASURED IN THE MIDDLE OF THE FULLY DEVELOPED SECTION OF A 2° CURVE DUE TO THE PASSAGE OF A LOADED COAL TRAIN (NO. 30) UNDER LUBRICATED TRACK CONDITIONS

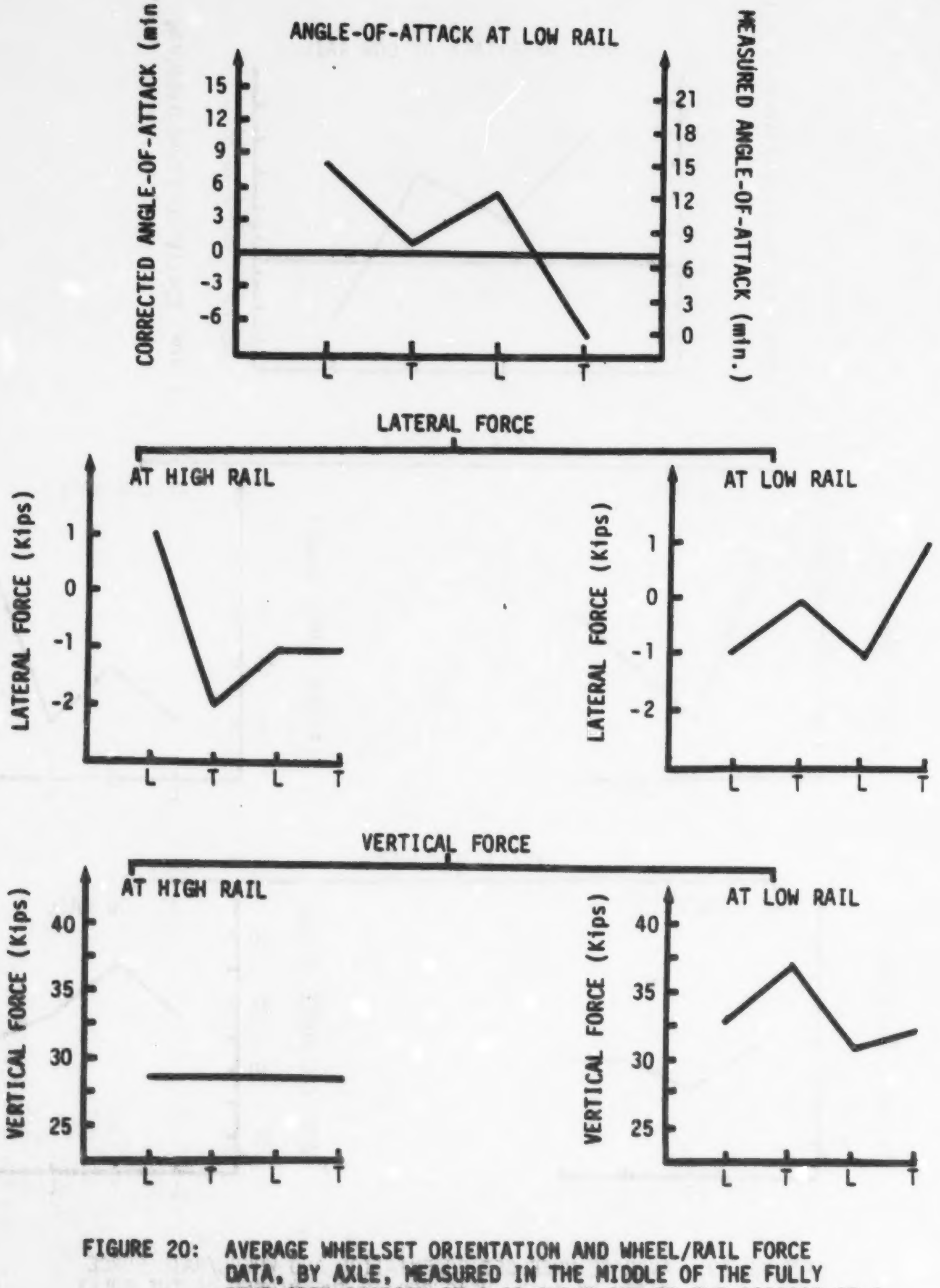

FIGURE 20: AVERAGE WHEELSET ORIENTATION AND WHEEL/RAIL FORCE DATA, BY AXLE, MEASURED IN THE MIDDLE OF THE FULLY DEVELOPED SECTION OF A 2° CURVE DUE TO THE PASSAGE OF A LOADED COAL TRAIN (NO. 31) UNDER LUBRICATED TRACK CONDITIONS

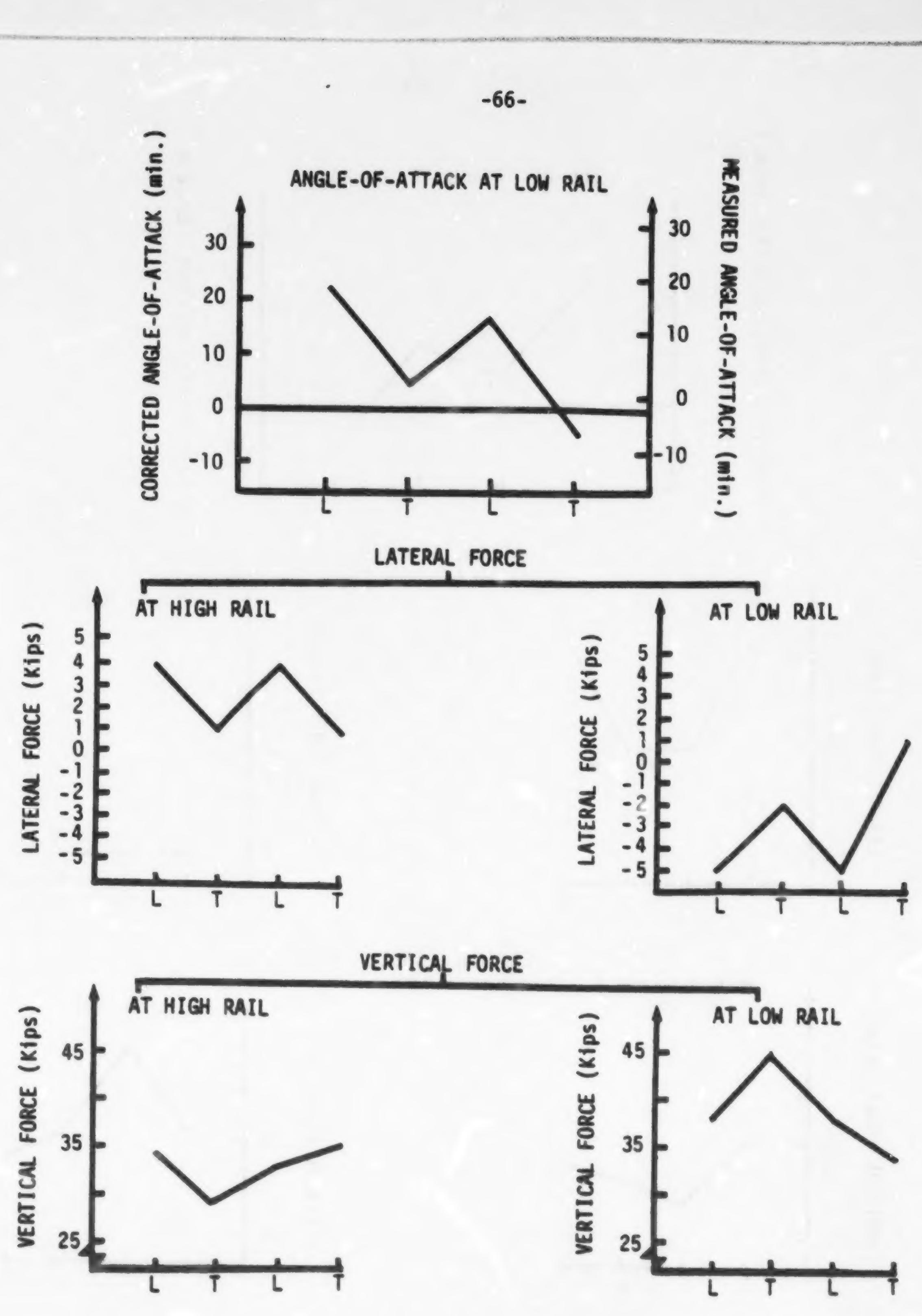

FIGURE 21: AVERAGE WHEELSET ORIENTATION AND WHEEL/RAIL FORCE DATA, BY AXLE, MEASURED IN THE MIDDLE OF THE FULLY DEVELOPED SECTION OF A 7° CURVE DUE TO THE PASSAGE OF A LOADED COAL TRAIN (NO. 38) UNDER SANDED TRACK CONDITIONS

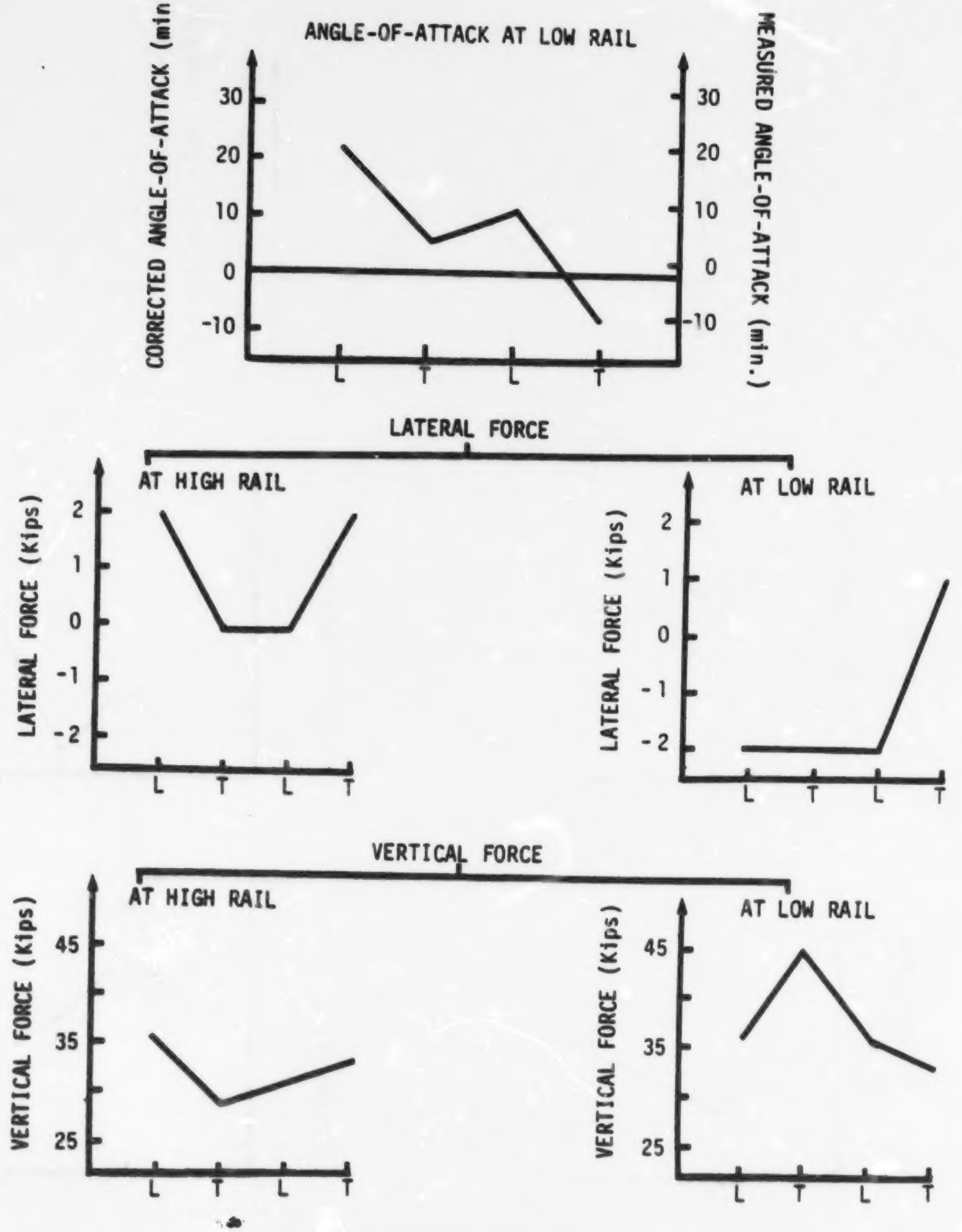

FIGURE 22: AVERAGE WHEELSET ORIENTATION AND WHEEL/RAIL FORCE DATA, BY AXLE, MEASURED IN THE MIDDLE OF THE FULLY DEVELOPED SECTION OF A 7° CURVE DUE TO THE PASSAGE OF A LOADED COAL TRAIN (NO. 39) UNDER LUBRICATED TRACK CONDITIONS

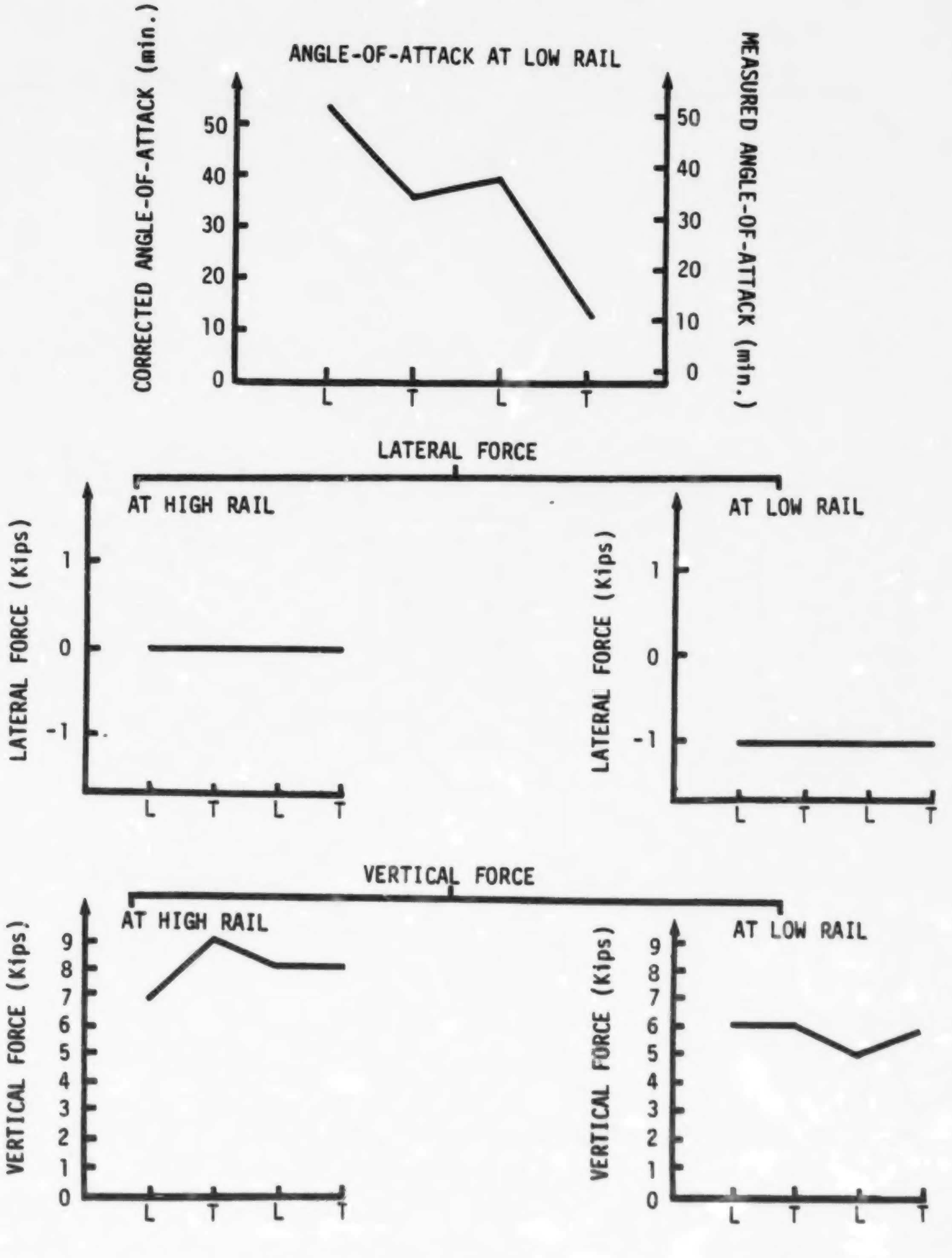

FIGURE 23: AVERAGE WHEELSET ORIENTATION AND WHEEL/RAIL FORCE DATA, BY AXLE, MEASURED IN THE MIDDLE OF THE FULLY DEVELOPED SECTION OF A 7° CURVE DUE TO THE PASSAGE OF AN EMPTY COAL TRAIN (NO. 40) UNDER LUBRICATED TRACK CONDITIONS

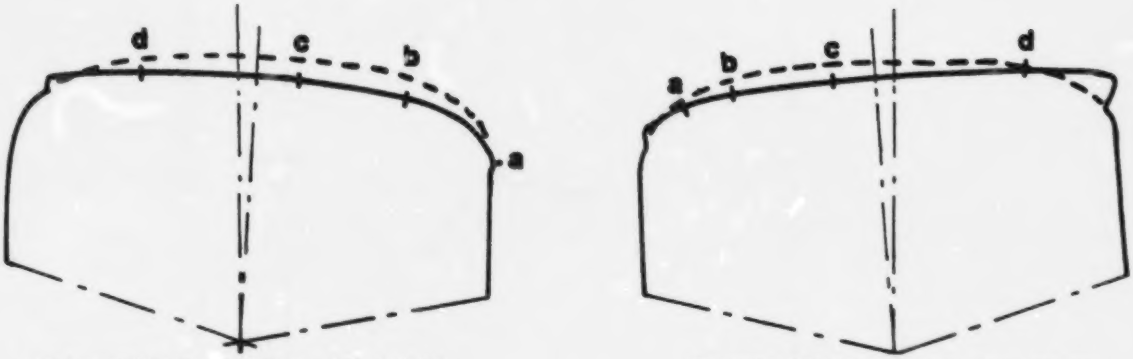

MEASUREMENT POINT 3, 7° CURVE
HIGH RAIL

MEASUREMENT POINT 4, 7° CURVE
LOW RAIL

TEST SITE 1 (CHROMIUM ALLOY RAIL)

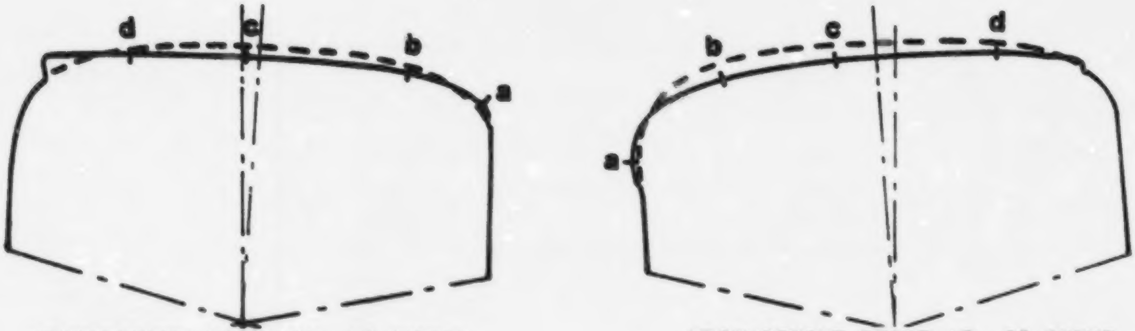

MEASUREMENT POINT 18, 2° CURVE
LOW RAIL

MEASUREMENT POINT 17, 2° CURVE
HIGH RAIL

TEST SITE 3 (CHROMIUM ALLOY RAIL)

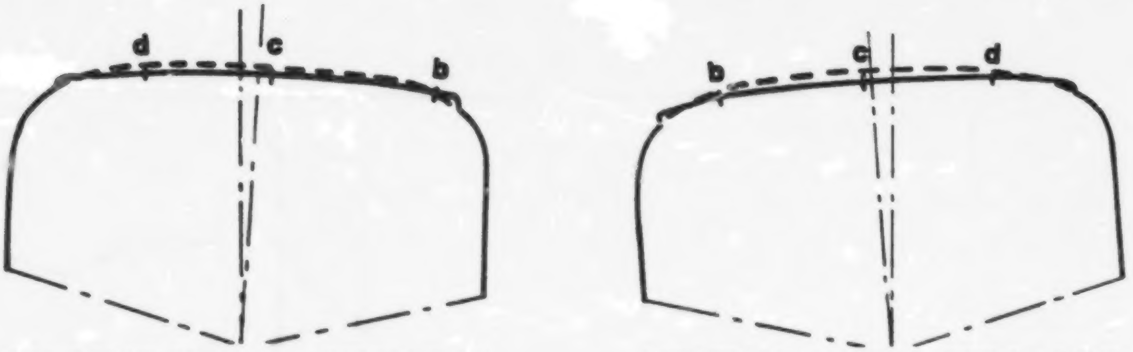

MEASUREMENT POINT 10, TANGENT TRACK

MEASUREMENT POINT 9, TANGENT TRACK

TEST SITE 2 (PLAIN CARBON RAIL)

FIGURE 24: WEAR MEASUREMENT LOCATIONS ABOUT THE RAILHEAD FOR HIGH AND LOW RAILS IN CURVES AND FOR TANGENT TRACK

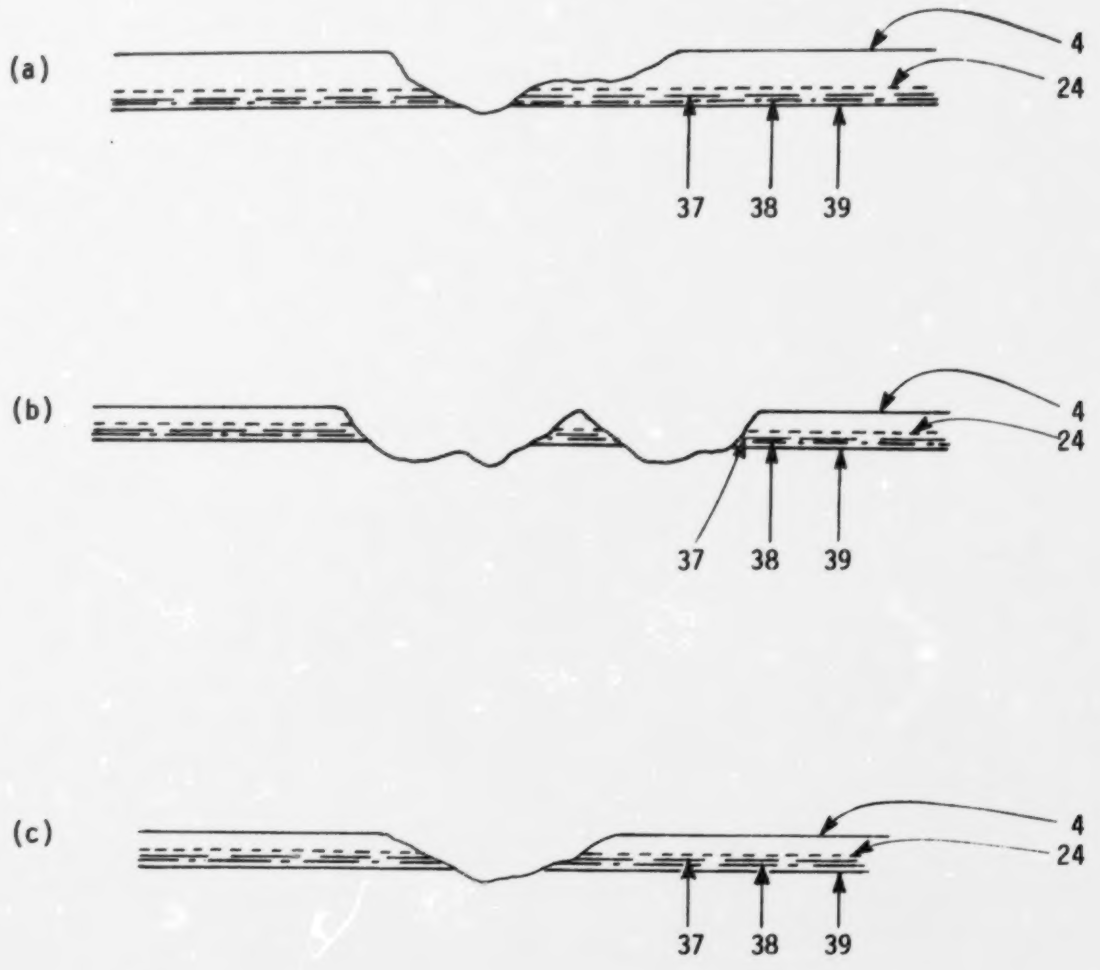

FIGURE 25: TRACE OF WITNESS GROOVE PROFILES ILLUSTRATING PROGRESSIVE RAIL SURFACE WEAR AT MEASUREMENT POINT 3 (HIGH RAIL, MIDDLE OF 7° CURVE, TEST SITE 1) CAUSED BY THE PASSAGE OF SEVERAL TRAINS (VERTICAL AND HORIZONTAL MAGNIFICATIONS ARE 200X AND 50X, RESPECTIVELY. A,B AND C ARE WEAR MEASUREMENT LOCATIONS ABOUT THE RAILHEAD SPECIFIED PREVIOUSLY IN FIGURE 24. NUMBERS IDENTIFY TRAINS AFTER WHICH PROFILES WERE TAKEN).

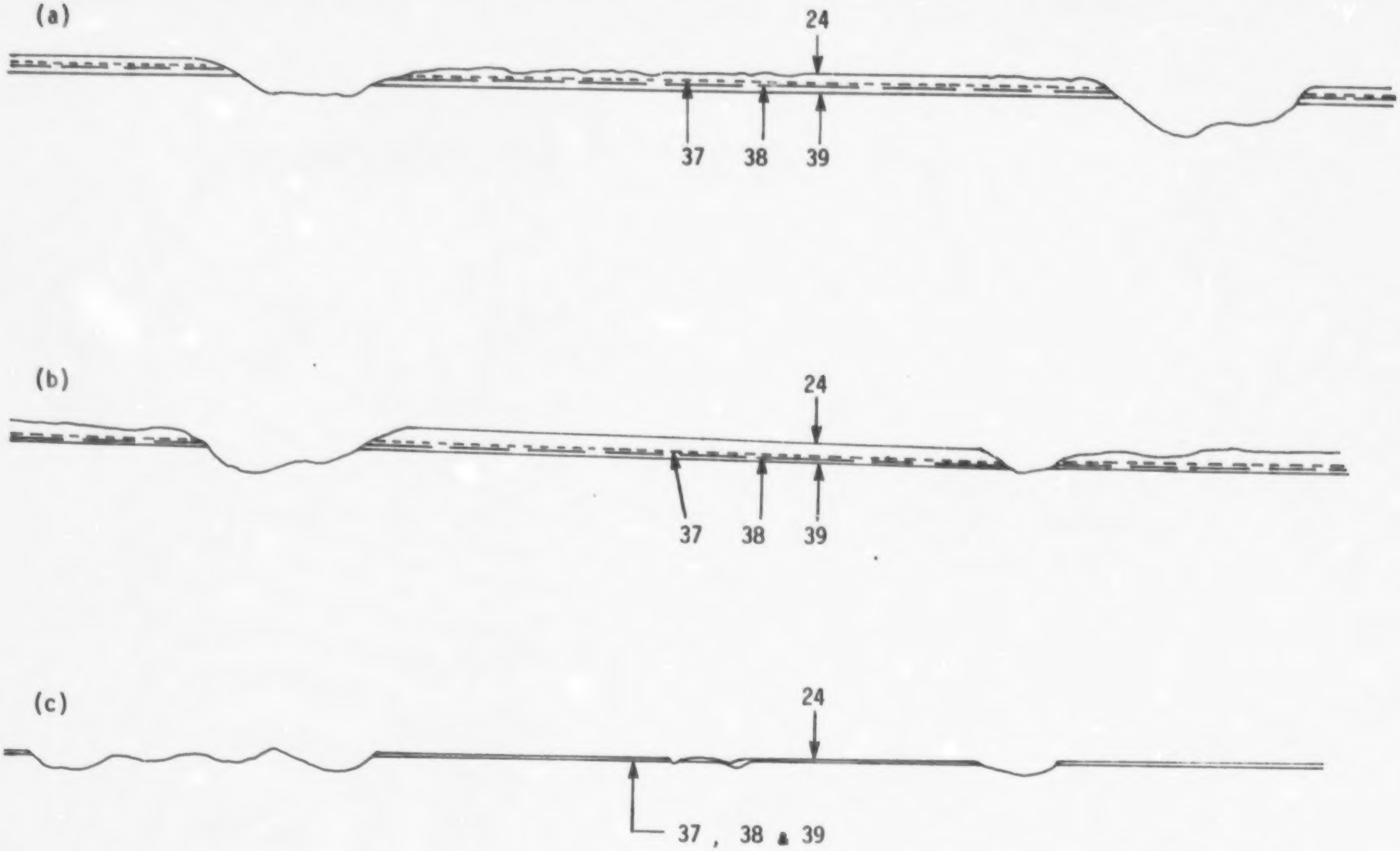

FIGURE 26: TRACE OF WITNESS GROOVE PROFILES ILLUSTRATING PROGRESSIVE RAIL SURFACE WEAR AT MEASUREMENT POINT 4 (LOW RAIL, MIDDLE OF 7° CURVE, TEST SITE 1) CAUSED BY THE PASSAGE OF SEVERAL TRAINS (VERTICAL AND HORIZONTAL MAGNIFICATIONS ARE 200X AND 50X, RESPECTIVELY. A,B AND C ARE WEAR MEASUREMENT LOCATIONS ABOUT THE RAILHEAD SPECIFIED PREVIOUSLY IN FIGURE 24. NUMBERS IDENTIFY TRAINS AFTER WHICH PROFILES WERE TAKEN).

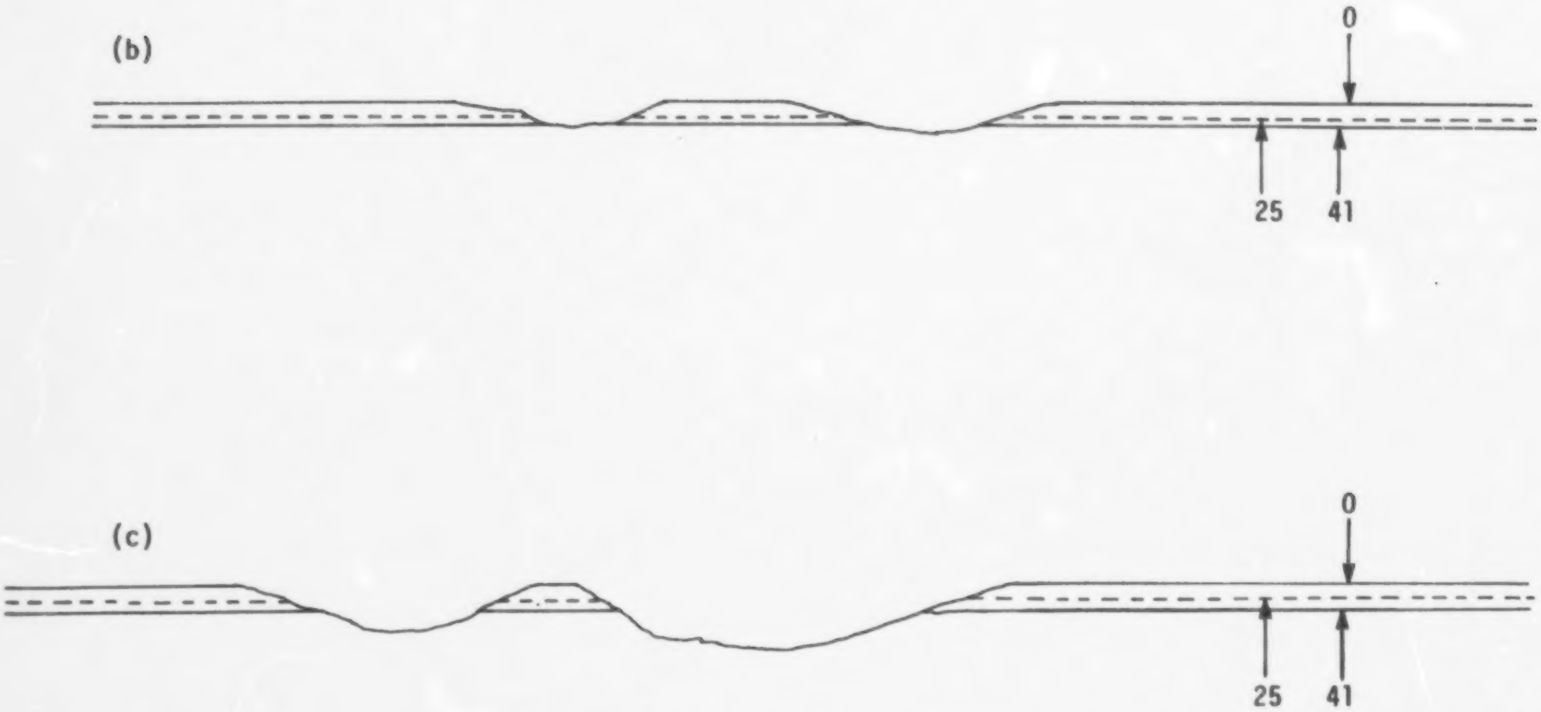

FIGURE 27: TRACE OF WITNESS GROOVE PROFILES ILLUSTRATING PROGRESSIVE RAIL SURFACE WEAR AT MEASUREMENT POINT 9 (TANGENT TRACK, TEST SITE 2) CAUSED BY THE PASSAGE OF SEVERAL TRAINS (VERTICAL AND HORIZONTAL MAGNIFICATIONS ARE 200X AND 50X, RESPECTIVELY. B AND C ARE WEAR MEASUREMENT LOCATIONS ABOUT THE RAILHEAD SPECIFIED PREVIOUSLY IN FIGURE 24. NUMBERS IDENTIFY TRAINS AFTER WHICH PROFILES WERE TAKEN).

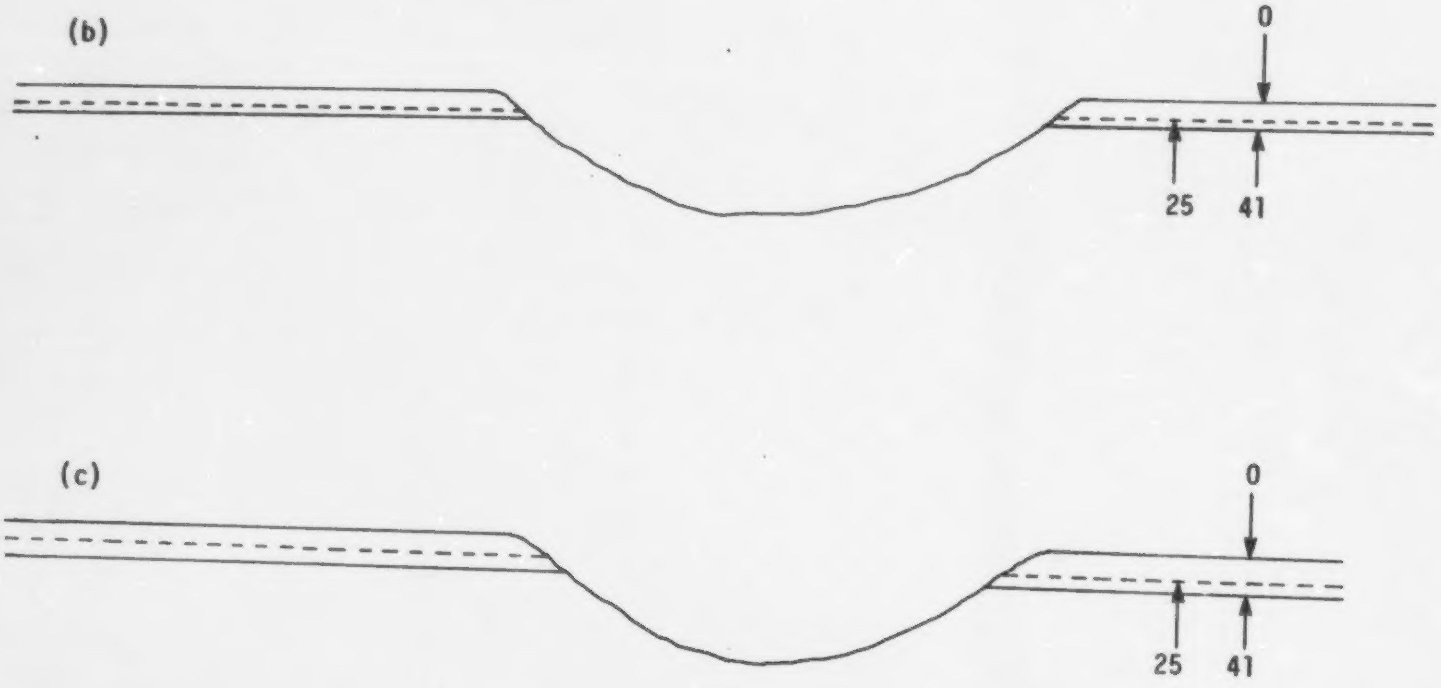

FIGURE 28: TRACE OF WITNESS GROOVE PROFILES ILLUSTRATING PROGRESSIVE RAIL SURFACE WEAR AT MEASUREMENT POINT 10 (TANGENT TRACK, TEST SITE 2) CAUSED BY THE PASSAGE OF SEVERAL TRAINS (VERTICAL AND HORIZONTAL MAGNIFICATIONS ARE 200X AND 50X, RESPECTIVELY. B AND C ARE WEAR MEASUREMENT LOCATIONS ABOUT THE RAILHEAD SPECIFIED PREVIOUSLY IN FIGURE 24. NUMBERS IDENTIFY TRAINS AFTER WHICH PROFILES WERE TAKEN).

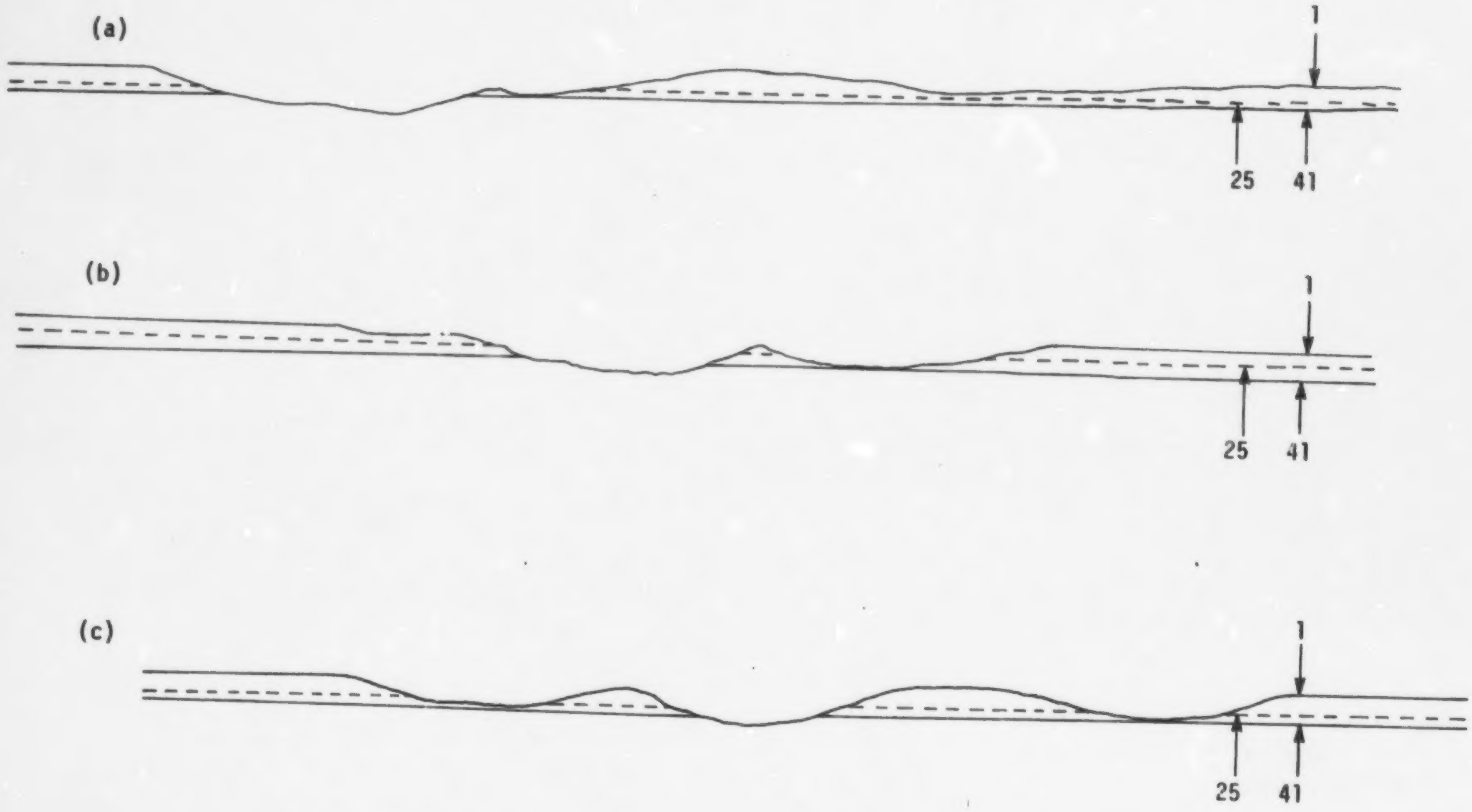

FIGURE 29: TRACE OF WITNESS GROOVE PROFILES ILLUSTRATING PROGRESSIVE RAIL SURFACE WEAR AT MEASUREMENT POINT 17 (HIGH RAIL, MIDDLE OF 2° CURVE, TEST SITE 3) CAUSED BY THE PASSAGE OF SEVERAL TRAINS (VERTICAL AND HORIZONTAL MAGNIFICATIONS ARE 200X AND 50X, RESPECTIVELY. A, B AND C ARE WEAR MEASUREMENT LOCATIONS ABOUT THE RAILHEAD SPECIFIED PREVIOUSLY IN FIGURE 24. NUMBERS IDENTIFY TRAINS AFTER WHICH PROFILES WERE TAKEN).

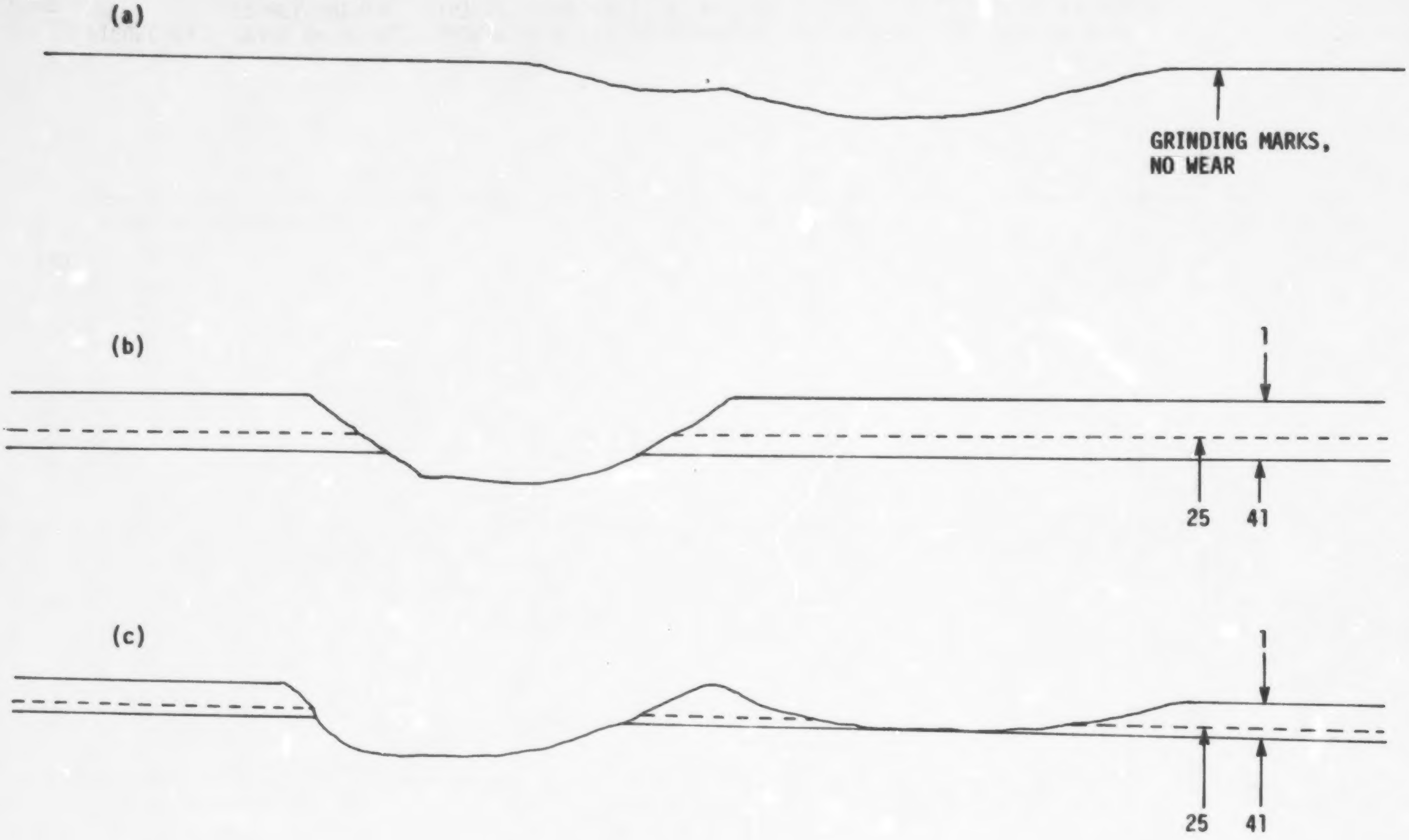

FIGURE 30: TRACE OF WITNESS GROOVE PROFILES ILLUSTRATING PROGRESSIVE RAIL SURFACE WEAR AT MEASUREMENT POINT 18 (LOW RAIL, MIDDLE OF 2° CURVE, TEST SITE 3) CAUSED BY THE PASSAGE OF SEVERAL TRAINS (VERTICAL AND HORIZONTAL MAGNIFICATIONS ARE 200X AND 50X, RESPECTIVELY. A, B AND C ARE WEAR MEASUREMENT LOCATIONS ABOUT THE RAILHEAD SPECIFIED PREVIOUSLY IN FIGURE 24. NUMBERS IDENTIFY TRAINS AFTER WHICH PROFILES WERE TAKEN).

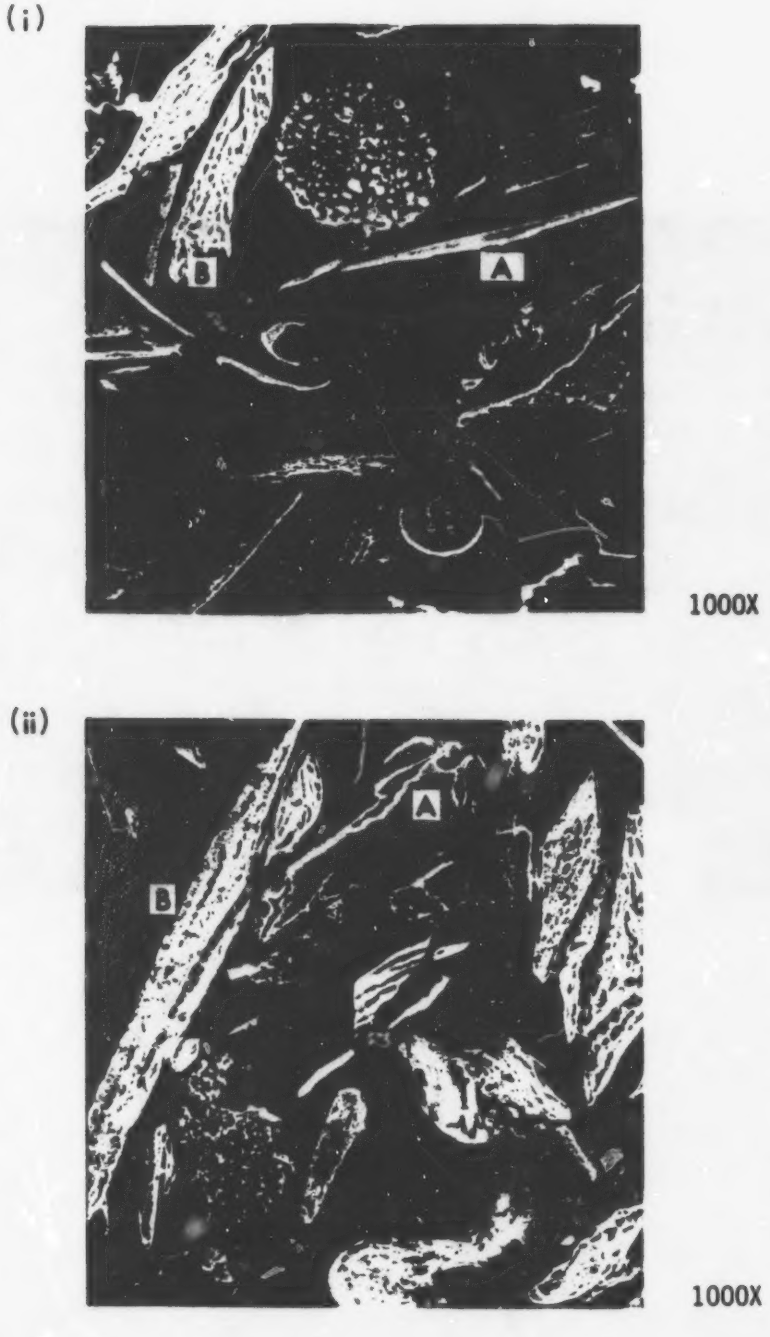
(i)
B
A
1000X
(ii)
A
B
1000X

FIGURE 31: OPTICAL ELECTRON MICROGRAPHS OF WEAR DEBRIS COLLECTED IN 7° CURVE OF TEST SITE 1 (A - WHITE ETCHING LAYER, B - BROKEN DOWN PEARLITE)

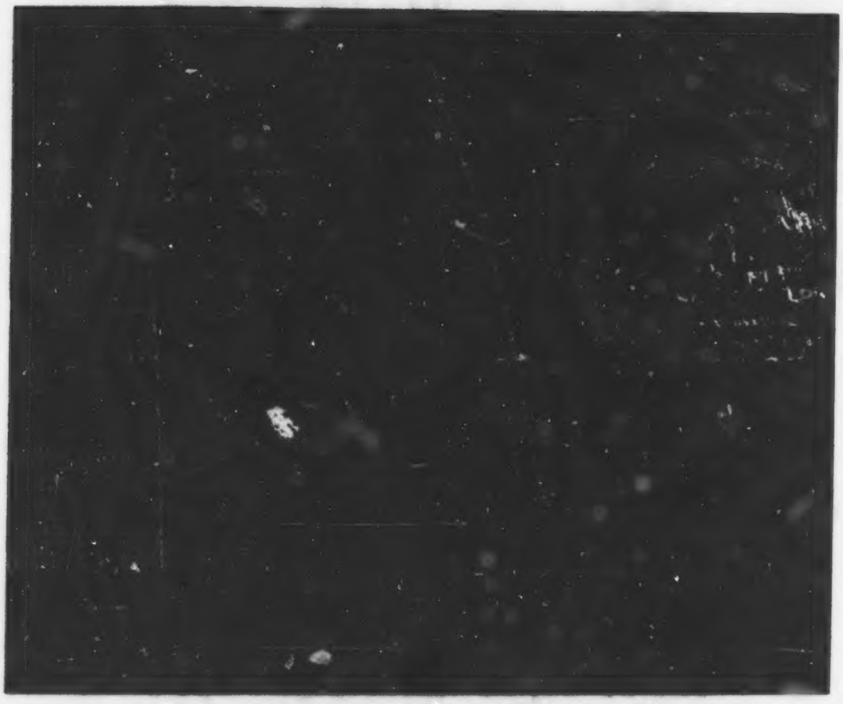

FIGURE 32: SHELLY SURFACE EXHIBITED BY LOW RAIL IN 7° CURVE OF TEST SITE 1

FIELD EVALUATION OF THE WEAR PERFORMANCE OF JAPANESE HEAD-HARDENED ALLOY RAIL -- INTERIM REPORT

K. Griffin
Planning and Research Department
Canadian Pacific Limited
M[illegible]treal

SUMMARY

Head-hardened alloy rail (Superrail) purchased from the Nippon Steel Corporation of Japan was installed, together with Algoma 1% Cr rail, in a series of short sharp reverse curves on the Pacific Region of CP Rail in late-March, 1983. The Planning and Research Department, CP Ltd., is presently evaluating the wear performance of the Superrail, in relation to Algoma 1% Cr rail, using the rail profilometer developed by the department. Qualitative field observations are periodically being made to evaluate the relative susceptibilities of these two rail types to surface defect formation. As of the last measurements taken in September 1984, insufficient tonnage (∿88 MGT) had passed over the test sites to allow for an absolute comparison of these two rails on the basis of either cumulative wear or surface damage -- only initial trends are reported.

For both high and low rail positions in the fully developed sections of curves, Algoma 1% Cr rails have experienced approximately 50-300% more vertical, gauge face and total head wear than similarly located Superrail (based on last measurements collected in September 1984).

Significant shelling damage was first noted on the running surface of Algoma 1% Cr rails on the low rail sections of fully developed curves after approximately 67 MGT. Corresponding Japanese Superrails have yet to experience significant shelling on their top running surface. Japanese Superrails were initially (∿27 MGT) susceptible to slight high rail gauge corner shelling. As of the last measurements in September 1984 (∿88 MGT) these shells had not progressed and are not significant.

For corresponding times in their loading histories, the Japanese Superrail is currently outperforming a previously examined Russian P-65 rail in its resistance to both wear and surface defect formation (of the contact fatigue type) -- in each case performance is measured relative to the standard Algoma 1% Cr rail.

While the data collected to date supports the Japanese Superrail over the Algoma 1% Cr rail (and indirectly over the P-65 rail), more wear measurements for greater tonnage passing levels are required to confidently define the wear patterns of the Japanese and Algoma 1% Cr rails. No attempt was made here to quantitatively predict relative lives of these two rail types on the basis of the cumulative wear measured to date. Further, no absolute comparison of the relative performances of Japanese Superrails and Russian P-65 rails can yet be made.

SOMMAIRE

Le département de planification et de recherche du Canadien Pacifique Ltée évalue la performance d'usure de deux rails, le "Superrail" et le rail de type Algoma 1% Chrome, à l'aide du profilomètre du département. Le "Superrail" est un rail d'alliage au champignon trempé acheté de Nippon Steel Corporation du Japon. Ce rail, et celui de type Algoma 1% Chrome, ont été installés sur une serie de contre-courbes prononcées du réseau CP Rail, région du Pacifique, à la fin mars 1983. Des observations quantitatives de type périodique se font in situ pour déterminer la sensibilité relative des deux types de rail à la formation d'avaries de surface. Etant donné que depuis les dernières mesures (septembre 1984) les tronçons n'ont vu qu'une charge minime de trafic, environ 88 millions de tonnes brutes (MTB), les deux types de rail ne peuvent pas être comparés de façon absolue. Seulement les tendances initiales sont presentées.

Au milieu des courbes, les rails Algoma posés en file exterieur et interieur affichaient de 50 à 300% plus d'usure sur la verticale, le bord interieur, et la totalité du champignon que les "Superrails" dans des positions semblables (calculés d'après les mesures de septembre 1984).

Une détérioration considérable d'écaillage sur la surface de roulement du rail Algoma en file exterieur a été remarquée après le passage d' environ 67 MTB. Les "Superrails" japonais correspondants n'ont pas subi d'écaillage majeur sur la surface de roulement. D'autre part, à environ 27 MTB, les "Superrails" japonais en file exterieur étaient sensibles à un écaillage léger du flanc interieur. D'après les dernières mesures de septembre 1984 (88 MTB) ces écaillages n'ont pas progressé et ne sont pas importants.

Présentement, le "Superrail" japonais se montre supérieur au rail russe P-65 déjà étudié et ce relativement à la formation d'avaries de surface (attribuables à la fatigue sous les efforts de contact), et à l'usure. Dans chaque cas, leurs performances sont mesurées relativement au rail Algoma 1% Cr.

Les données rassemblées avantagent le "Superrail" japonais au rail Algoma 1% Cr et, de façon indirect, le rail P-65. Des mesures seront requises après un passage de trafic plus élevé afin d'évaluer les tendances d'usure des rails Algoma et japonais. Aucune prédiction quantitative n'est faite sur la durabilité des deux rails utilisant les résultats d'usure obtenus. De plus, il est présentement impossible d'évaluer les performances relatives du "Superrail" japonais au rail russe P-65.

ACKNOWLEDGEMENTS

The Planning and Research Department acknowledges the contribution of officers and personnel from the Pacific Region, CP Rail, for their assistance during the course of the test program.

The author would like to thank H. Schrekinger and L. Feiter for their technical support in the collection and processing of the rail profiles.

TABLE OF CONTENTS

	PAGE
SUMMARY	79
ACKNOWLEDGEMENTS	83
LIST OF TABLES	85
LIST OF FIGURES	86
1.0 INTRODUCTION	87
2.0 TEST SITES AND MEASUREMENT POINTS	88
3.0 DATA COLLECTION AND ANALYSIS	92
4.0 RESULTS AND CONCLUSIONS	94
4.1 Wear Analysis	94
4.2 Surface Defects	95
5.0 RECOMMENDATIONS	97
REFERENCES	98

LIST OF TABLES

TABLE NO.	DESCRIPTION	PAGE
1	Comparison of Physical and Metallurgical Properties of Algoma 1% Chrome and Japanese Superrail	88
2	Cumulative Wear Data for Test Site #2	99
3	Cumulative Wear Data for Test Site #3	101

LIST OF FIGURES

FIGURE NO.	DESCRIPTION	PAGE
1	Site #2: Track Layout With Curvatures and Location of Change-Over/Measurement Points	90
2	Site #3: Track Layout With Curvatures and Location of Change-Over/Measurement Points	91
3	Definition of Vertical and Gauge Face Losses	93
4	Profile Comparison, Algoma 1% Cr, Low Rail in Fully Developed Section of 8.5° Curve, Measurement Point 16, Change-Over Point 4, Site 3	103
5	Profile Comparison, Japanese Superrail, High Rail in Fully Developed Section of 8.5° Curve, Measurement Point 13, Change-Over Point 4, Site 3	104
6	Site 3, Change-Over Point 4, Vertical Head Wear Pattern Comparison, for High and Low Rails in the Middle of the Fully Developed Section of an 8.5° Curve, for Algoma 1% Cr and Japanese Superrail	105
7	Site 3, Change-Over Point 4, Gauge Face Wear Pattern Comparison, for High and Low Rails in the Middle of the Fully Developed Section of an 8.5° Curve, for Algoma 1% Cr and Japanese Superrail	106
8	Site 3, Change-Over Point 4, Total Head Wear Pattern Comparison, for High and Low Rails in the Middle of the Fully Developed Section of an 8.5° Curve, for Algoma 1% Cr and Japanese Superrail	107
9	Typical Shelling Damage Exhibited by Algoma 1% Cr Rail Running Surface, for Low Rail in Fully Developed Section of Curve	108

1.0 INTRODUCTION

As part of CP Rail's continuing program for the evaluation of new rail steel metallurgies, head-hardened alloy rail purchased from the Nippon Steel Corporation of Japan was installed in three test sites on the Pacific Region of CP Rail in late March, 1983. This rail, commonly referred to as Japanese Superrail, is 68 Kg/m (136 lb/yd) and combines the two commercially accepted methods for improving the mechanical properties of rail steels -- selective alloying element additions (specifically Cr-Si with trace Nb) and heat treatment (a slack-quenching procedure is employed).

This report presents some preliminary results of in-service comparative wear testing of the Japanese Superrail in relation to Algoma 1% Chrome rail, along with qualitative field observations on the relative susceptibilities of these two rail types to surface defect formation. Descriptions of the test locations and method of data acquisition and analysis are included. General comparisons are also made between the in-service performance of the Superrail, to date, and a previously tested P-65 Russian rail (see Reference 1), each in relation to the standard Algoma 1% Cr rail and for similar tonnage passing levels.

2.0 TEST SITES AND MEASUREMENT POINTS

Details of the rail materials (see Table 1) and track characteristics covered in this study are summarized below:

Table 1

Comparison of Physical and Metallurgical Properties of Algoma 1% Chrome and Japanese Superrail

Characteristic	Algoma 1% Cr(2)	Japanese Superrail(3)
Type	1.15 % Cr alloy	Cr/Si/Nb alloy, head-hardened
Section	AREA 136 RE	AREA 136 RE
Properties:		
0.2% YS (Ksi)	95	130
UTS (Ksi)	150	192
Elongation (%)	9	19
Reduction of Area (%)	17	50
Head Hardness (BHN)	320	380
Steelmaking	BOF, Si-killed	BOF, Si-killed
Microstructure	fully pearlitic	fully pearlitic

Track

Geometry:	High and low rails of fully developed sections of curves ranging in curvature from 3.50 to 9.00 degrees and in length from 250 to 800 ft. Spirals and tangent sections of various lengths, up to 800 ft.
Welding Practice:	Continuously flash-butt welded track. Joint bars connect different rail sections.
Ties:	Wood.
Superelevation:	From 0.00 to 3.75 in. for tangent and spiral sections and 2.25 to 4.50 in. for fully developed sections of curves.
Grade:	-0.68% to +1.30% (westbound).
Lubrication:	Molybdenum disulphide based grease.
Axle Load:	Approximately 32.5 tons maximum.
Track Speed:	10 mph to 30 mph.
Annual Traffic:	Approximately 60 million gross tons (MGT).

The three test sites on the Pacific Region that were initially selected for evaluation of the Japanese Superrail are:

Site #1	Mile 22.9	Cascade Subdivision
Site #2	Mile 102.1	Thompson Subdivision
Site #3	Mile 113.0	Thompson Subdivision

In April 1983, the curvature, superelevation and gauge at these sites were first measured and points of wear measurement selected. In July 1983, the track in test site #1 was significantly altered (i.e. curvature and superelevation reduced, spirals lengthened) and the Research Department discontinued wear measurements on this site. Subsequent track measurements were made in September '83, May '84 and again in September '84 to confirm that there were no significant changes in the remaining test sites 2 and 3 -- shown schematically in Figures 1 and 2, respectively. These remaining test sites experience the same general traffic, approximately 88 MGT up to the end of September 1984. Information on the traffic passing over these sites was supplied by the Engineering Department, CP Rail.

A total of 44 relative wear measurement points were selected on the remaining Japanese Superrail test sites, located in groups of four about the eleven change-over points from one rail type to the other (see Figures 1 and 2). Forty of these measurement points are located on the fully developed sections of curves; the remaining four are on a spiral in test site #3. Possible joint effects required that the measurement points be located several feet from the joint; six feet were allowed for in the present test.

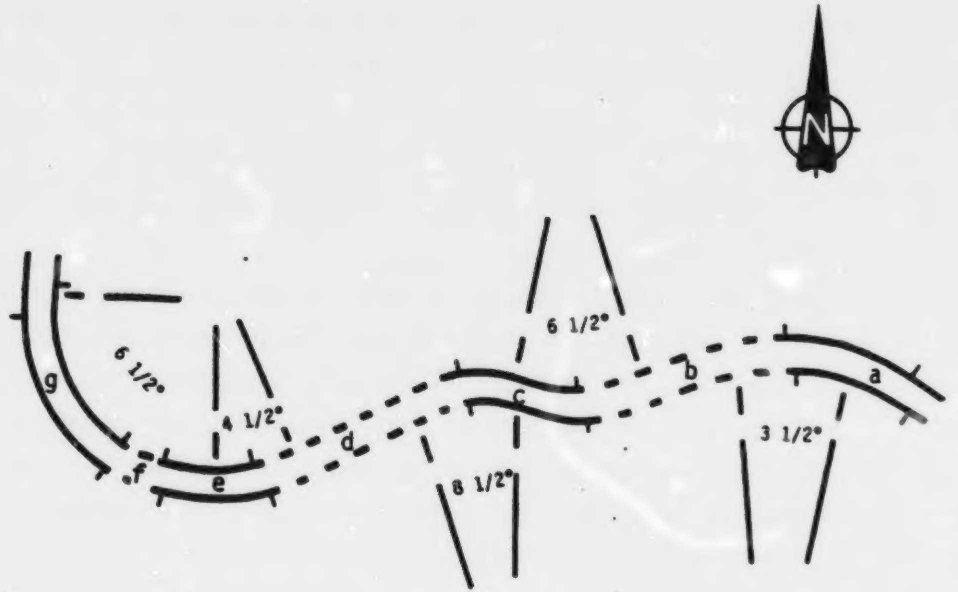

Mile 102.1 to 103.1,
Thompson Subdivision

Lubricators:
north rail - MP 93.3 & 105.1
south rail - MP 102.3

Japanese Superrail ------
Algoma 1% Cr Rail ______

Mark	Jap. Superrail		Algoma Cr		Change-Over and Measurement Pts.
	North	South	North	South	
a			555'	558'	
b	956'	955'			1, 1-4
c			873'	872'	2, 5-8
d	1052'	1053'			3, 9-12
e			1059'	1029'	4, 13-16
f	647'	679'			5, 17-20
g			834'	624'	------

Figure 1: Site #2: Track Layout with Curvatures and Location of Change-Over/Measurement Points

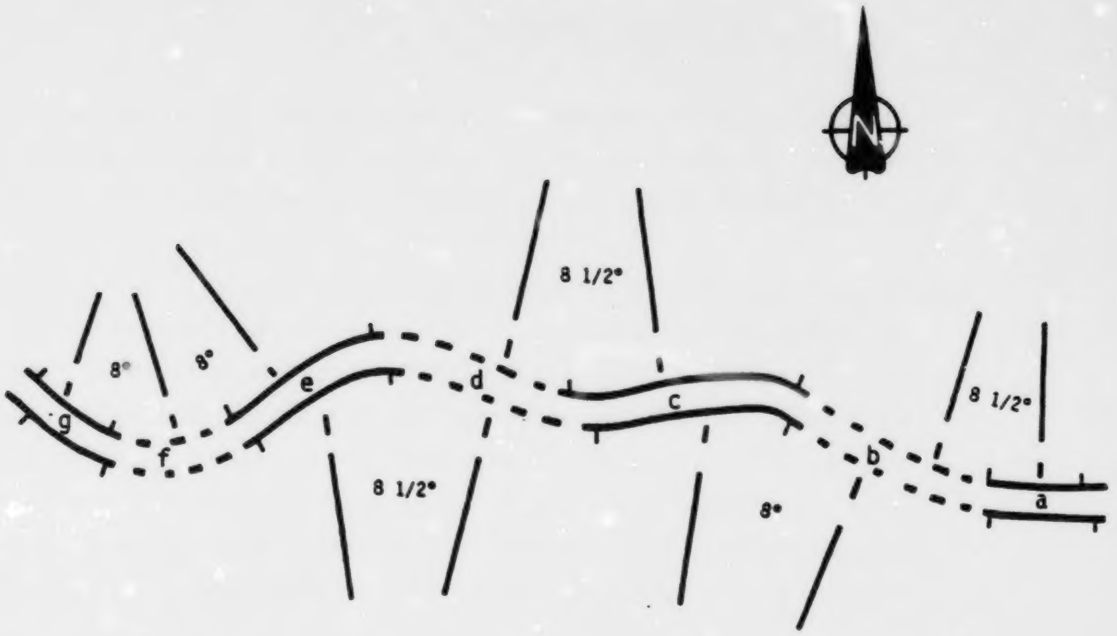

Mile 113.0 to 114.0,
Thompson Subdivision

Lubricators:
north rail - MP 113.3
south rail - MP 113.9

Japanese Superrail ------
Algoma 1% Cr Rail ______

Mark	Jap. Superrail North	South	Algoma Cr north	South	Change-Over and Measurement Pts.
a			286'	294'	
					1, 1-4
b	696'	605'			
					2, 5-8
c			795'	778'	
					3, 9-12
d	924'	925'			
					4, 13-16
e			970'	967'	
					5, 17-20
f	655'	652'			
					6, 21-14
g			333'	340'	

Figure 2: Site #3: Track Layout with Curvatures and Location of Change-Over/Measurement Points

3.0 DATA COLLECTION AND ANALYSIS

All profile/wear data was collected with the rail profilometer (see Reference 4) developed by the Planning and Research Department, CP Ltd., and processed on the microcomputer in the department.

At all three test sites, new profile measurements were first taken at the selected points in April 1983, within several weeks of the installation of the test rail. These new profiles, coupled with future wear measurements, will allow for a relative comparison of the two rail types based on absolute and/or cumulative wear. Subsequent profile measurements were taken at the remaining test sites 2 and 3 in September '83, May '84 and again in September '84. At these times, qualitative field observations of surface defects exhibited by the two rail types were made.

For each profile comparison, three indices of relative wear are reported. These are: vertical head loss, loss at the gauge face and reduction in head area. The vertical and gauge face losses are calculated in accordance with standard practice (see Reference 5), as shown in Figure 3. The area calculations will consider as lost the material which has been removed from the rail head and material which has flowed outside the original profile (eg: - the "lip" often found on rails in tangent track and on the field side of low rails in curves). The resolution limit of the profilometer for vertical and gauge face wear is 0.004 in. (0.1mm) and approximately 0.016 sq. in. (10mm^2) for total head wear. For profile, matching purposes, a difference of 0.008 in. (0.2mm) has been specified as the minimum difference required to constitute significant vertical and/or gauge face wear; 0.031 sq. in. (20mm^2) has been specified for total head wear comparisons.

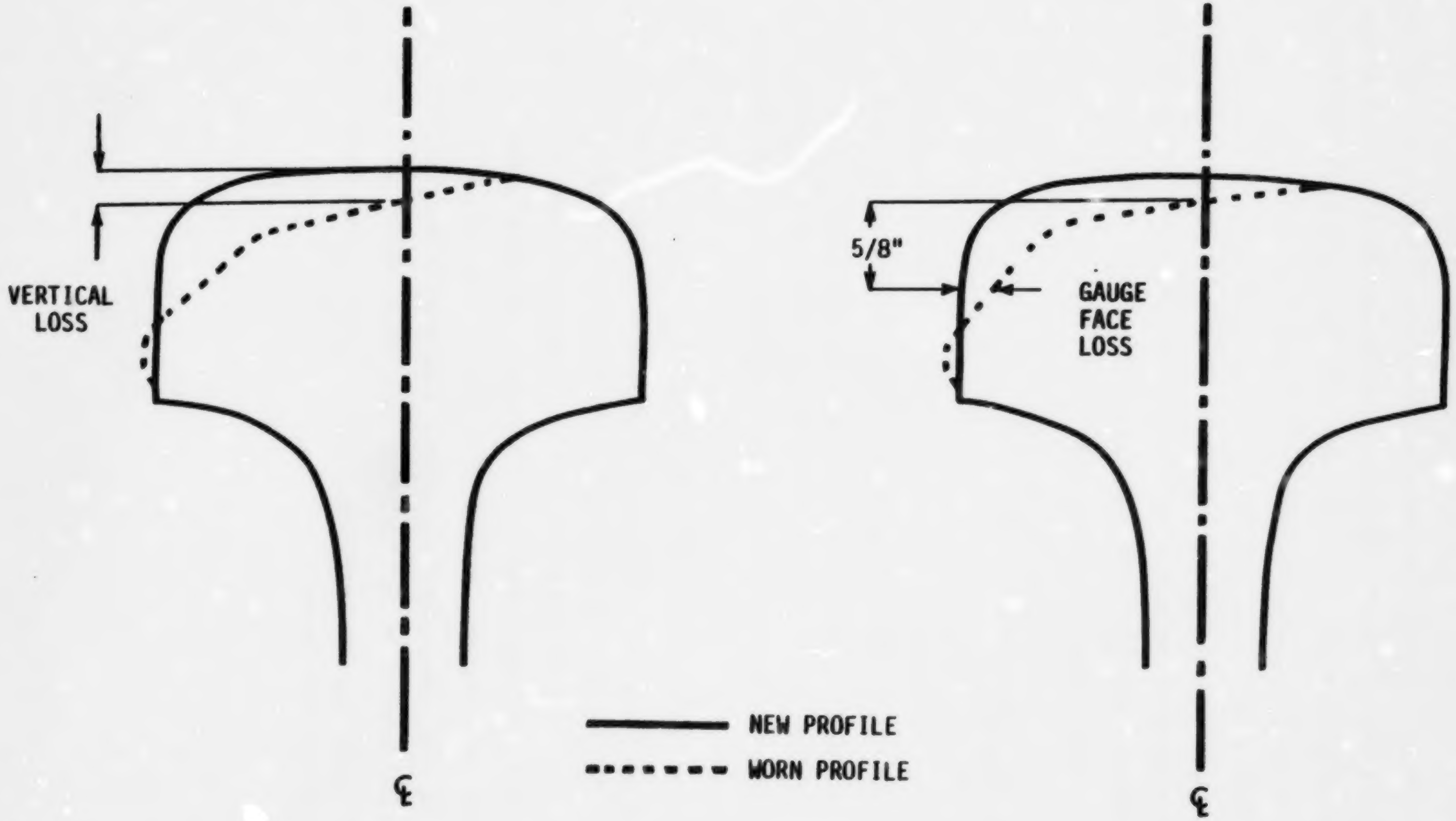
VERTICAL
LOSS
5/8"
GAUGE
FACE
LOSS
NEW PROFILE
WORN PROFILE
℄
℄

Figure 3 : Definition of Vertical and Gauge Face Losses

4.0 RESULTS AND CONCLUSIONS

While both the remaining Japanese Superrail test sites have experienced similar traffic levels, each is uniquely characterized by different track alignment, dynamic loading conditions and lubrication. As such, these test sites differ in the magnitudes of wear and surface damage experienced by similar rail types and rail locations; data collected from different sites have not been compared.

To date, insufficient tonnage has passed over test sites 2 and 3 for any absolute comparison of the two rail types on the basis of susceptibility to cumulative wear and/or surface defect formation. The initial trends have been noted, however, and are reported here.

4.1 Wear Analysis

The wear versus tonnage variations for all of the measurement points in the remaining test sites 2 and 3 are listed in Tables 2 and 3, respectively. A large number of matched profiles and cumulative wear plots were produced to analyze this data. While it is not feasible to include all of these in this report, representative samples are presented (see Figures 4-8).

Algoma 1% Cr rails, for both high and low rail locations in the fully developed sections of curves, have consistently experienced significantly more wear than similarly positioned Japanese Superrails -- ranging from approximately 50-300% more for vertical, gauge face and total head wear, based on the last measurements collected in September 1984. In all cases the Algoma Cr rails are wearing to a flatter running surface profile, similar to that characteristic of new Japanese Superrails. This suggests that the difference in vertical head wear experienced to date by these two rail types may now level out. Future profile measurements will support/refute this trend.

Contrary to the wearing differences noted above, previous testwork has shown that Russian P-65 rails exhibit similar wear resistance to Algoma 1% Cr rails when located in the high rail position in the fully developed section of a curve. In the low rail position, P-65 rails were less resistant to wear than Algoma 1% Cr rails.

While differences in the amount and manner of wear experienced by the Superrail and Cr rails are already noticeable, neither rail type has experienced "substantial" wear (relative to their condemning limits). Further, more wear measurements for greater tonnage passing levels are required to confidently define the wearing pattern for each of these two rail types. For the above reasons, no attempt was made here to quantitatively predict relative lives of these two rail types on the basis of the cumulative wear measured to date. Further, no absolute comparison of the relative performances of Japanese Superrails and Russian P-65 rails can yet be made.

4.2 Surface Defects

Qualitative differences in surface character between the two rail types were first noticeable in May 1984 (after ~67 MGT), have continued to the present, and are consistent for both test sites 2 and 3. The Algoma 1% Cr rails consistently exhibit more evidence of plastic flow than the Japanese Superrails, regardless of rail position. Further, Algoma 1% Cr rails consistently exhibit far more shelling on the low rail running surface (see Figure 9) in fully developed curve sections than do the Japanese Superrails.

Alternately, the Japanese Superrail appears somewhat more susceptible to high rail gauge corner shelling than the Algoma 1% Cr rail -- although the degree of this form of damage is slight for both rail types. This final observation agrees with CN experience (see Reference 6) with a head-hardened carbon steel rail produced by Nippon Steel, and warrants further study. It is presently felt that this shelling does not arise from any weakness in the basic metallurgy of the Superrail; rather, it likely results from the rest of the line being worn, so the wheel flanges had worn to match the worn rail and had a mismatch with the different, new, Superrail profile.

In a similar rail evaluation program completed in mid-1984, Russian P-65 rail experienced far more low rail shelling than did corresponding Algoma 1% Cr rails. Pronounced shelling was observed as early as 65 MGT when qualitative field observations were first made. In that program, neither the P-65 or the Algoma 1% Cr rails exhibited noticeable high rail gauge corner shelling.

5.0 RECOMMENDATIONS

The measurement of profiles of the Japanese Superrail should be continued to confirm the long-term stability of the reported wear versus tonnage patterns.

REFERENCES

1. "Field Evaluation of the Wear Performance of Russian P-65 Rail", K. Griffin, Department of Research, Canadian Pacific Limited, Report No. S799-83, December, 1983.

2. "On the Performance of the Experimental Bainitic Chromium-Molybdenum Rail Steel", H. Ghonem, Dept. of Research, CP Ltd., Report No. S739-82, April, 1982.

3. "Basic Properties of High Strength Rail Steels and New Rail Development", H. Masumoto, Yawata Works, Nippon Steel Corporation, October, 1982.

4. "A Wheel/Rail Profilometer System", G.Izbinsky, H. Shcrekinger and H. Sores, Department of Research, CP Ltd., Report No. T-805-84, February, 1984.

5. "Standard Practice Circulars: Track", CP Rail.

6. "Update on Rail Specifications on CN Rail", A.W. Worth, AREA Bulletin 696, Vol. 85, May 1984, pp. 103-108.

Table 2

Cumulative Wear Data for Test Site #2

Change-Over and Degree	Measurement Point and Description*	Wear Indices	Cumulative Tonnage (MGT) 0(Reference)	27.4	67.1	88.2
1 (3.5°)	1-HCr	Vertical (in.)	0	0.016	0.031	0.028
		Gauge Face (in.)	0	0	0.039	0.074
		Total Area (in.^{2})	0	0.022	0.083	0.120
	2-LCr	Vertical (in.)	0	0.008	0.024	0.035
		Gauge Face (in.)	0	0	0	0
		Total Area (in.^{2})	0	0.016	0.033	0.068
	3-HJ	Vertical (in.)	0	0	0	0.012
		Gauge Face (in.)	0	0	0	0.020
		Total Area (in.^{2})	0	0.007	0.027	0.086
	4-LJ	Vertical (in.)	0	0.016	0.016	0.028
		Gauge Face (in.)	0	0	0	0
		Total Area (in.^{2})	0	0.019	0.024	0.049
2 (6.5°)	5-LJ	Vertical (in.)	0	0.012	0.031	0.039
		Gauge Face (in.)	0	0	0	0
		Total Area (in.^{2})	0	0.031	0.079	0.096
	6-HJ	Vertical (in.)	0	0	0.028	0.024
		Gauge Face (in.)	0	0	0	0
		Total Area (in.^{2})	0	0.011	0.066	0.073
	7-LCr	Vertical (in.)	0	0.028	0.087	0.110
		Gauge Face (in.)	0	0	0	0
		Total Area (in.^{2})	0	0.051	0.170	0.214
	8-HCr	Vertical (in.)	0	0.024	0.039	0.055
		Gauge Face (in.)	0	0.020	0.020	0.039
		Total Area (in.^{2})	0	0.045	0.076	0.124
3 (8.5°)	9-HCr	Vertical (in.)	0	0.024	0.059	0.067
		Gauge Face (in.)	0	0	0.059	0.083
		Total Area (in.^{2})	0	0.049	0.158	0.202
	10-LCr	Vertical (in.)	0	0.039	0.071	0.110
		Gauge Face (in.)	0	0	0	0
		Total Area (in.^{2})	0	0.070	0.139	0.214
	11-HJ	Vertical (in.)	0	0	0.016	0.020
		Gauge Face (in.)	0	0	0	0.028
		Total Area (in.^{2})	0	0.021	0.071	0.104
	12-LJ	Vertical (in.)	0	0.024	0.039	0.043
		Gauge Face (in.)	0	0	0	0
		Total Area (in.^{2})	0	0.045	0.083	0.090

Table 2 (Cont'd.)

Cumulative Wear Data for Test Site #2

Change-Over and Degree	Measurement Point and Description*	Wear Indices		Cumulative Tonnage (MGT)		
			0(Reference)	27.4	67.1	88.2
4 (4.5°)	13-LJ	Vertical (in.)	0	0.008	0.020	0.020
		Gauge Face (in.)	0	0	0	0
		Total Area (in.^{2})	0	0.006	0.030	0.037
	14-HJ	Vertical (in.)	0	0.008	0.012	0.016
		Gauge Face (in.)	0	0	0	0
		Total Area (in.^{2})	0	0.027	0.044	0.065
	15-LCr	Vertical (in.)	0	0.024	0.055	0.063
		Gauge Face (in.)	0	0	0	0
		Total Area (in.^{2})	0	0.082	0.088	0.099
	16-HCr	Vertical (in.)	0	0.008	0.031	0.031
		Gauge Face (in.)	0	0	0	0.020
		Total Area (in.^{2})	0	0.015	0.055	0.073
5 (6.5°)	17-LCr	Vertical (in.)	0	0.028	0.094	0.118
		Gauge Face (in.)	0	0	0	0
		Total Area (in.^{2})	0	0.033	0.160	0.224
	18-HCr	Vertical (in.)	0	0.020	0.047	0.055
		Gauge Face (in.)	0	0.024	0.047	0.083
		Total Area (in.^{2})	0	0.059	0.129	0.171
	19-LJ	Vertical (in.)	0	0.016	0.043	0.047
		Gauge Face (in.)	0	0	0	0
		Total Area (in.^{2})	0	0.018	0.078	0.082
	20-HJ	Vertical (in.)	0	0	0.020	0.055
		Gauge Face (in.)	0	0	0.020	0.055
		Total Area (in.^{2})	0	0.019	0.079	0.126

* The following abbreviations designate the rail position and type particular to each measurement point:

HCr/LCr - Algoma 1% Cr rail on high/low rail of curve.

HJ/LJ - Japanese Superrail on high/low rail of curve.

Table 3

Cumulative Wear Data for Test Site #3

Change-Over and Degree	Measurement Point and Description*	Wear Indices	Cumulative Tonnage (MGT) 0(Reference)	27.4	67.1	88.2
1 (8.5°)	1-LCr	Vertical (in.)	0	0.020	0.083	0.130
		Gauge Face (in.)	0	0	0	0
		Total Area (in.^{2})	0	0.029	0.146	0.234
	2-HCr	Vertical (in.)	0	0.024	0.079	0.110
		Gauge Face (in.)	0	0.024	0.193	0.299
		Total Area (in.^{2})	0	0.050	0.295	0.490
	3-LJ	Vertical (in.)	0	0.016	0.039	0.047
		Gauge Face (in.)	0	0	0	0
		Total Area (in.^{2})	0	0.046	0.068	0.086
	4-HJ	Vertical (in.)	0	0.008	0.028	0.035
		Gauge Face (in.)	0	0.024	0.126	0.165
		Total Area (in.^{2})	0	0.065	0.197	0.249
2 (8°)	5-HJ	Vertical (in.)	0	0.008	0.020	0.028
		Gauge Face (in.)	0	0	0.039	0.071
		Total Area (in.^{2})	0	0.020	0.113	0.163
	6-LJ	Vertical (in.)	0	0.028	0.039	0.043
		Gauge Face (in.)	0	0	0	0
		Total Area (in.^{2})	0	0.043	0.061	0.083
	7-HCr	Vertical (in.)	0	0.031	0.067	0.098
		Gauge Face (in.)	0	0	0.079	0.114
		Total Area (in.^{2})	0	0.052	0.182	0.290
	8-LCr	Vertical (in.)	0	0.024	0.075	0.106
		Gauge Face (in.)	0	0	0	0
		Total Area (in.^{2})	0	0.027	0.112	0.179
3 (8.5°)	9-LCr	Vertical (in.)	0	0.020	0.051	0.075
		Gauge Face (in.)	0	0	0	0
		Total Area (in.^{2})	0	0.023	0.079	0.127
	10-HCr	Vertical (in.)	0	0.024	0.071	0.106
		Gauge Face (in.)	0	0.024	0.193	0.268
		Total Area (in.^{2})	0	0.054	0.290	0.456
	11-LJ	Vertical (in.)	0	0.016	0.039	0.043
		Gauge Face (in.)	0	0	0	0
		Total Area (in.^{2})	0	0.036	0.072	0.083
	12-HJ	Vertical (in.)	0	0.012	0.024	0.035
		Gauge Face (in.)	0	0	0.118	0.193
		Total Area (in.^{2})	0	0.026	0.159	0.261

Table 3 (Cont'd.)

Cumulative Wear Data for Test Site #3

Change-Over and Degree	Measurement Point and Description*	Wear Indices	Cumulative Tonnage (MGT)			
			0(Reference)	27.4	67.1	88.2
4 (8.5°)	13-HJ	Vertical (in.)	0	0.008	0.020	0.035
		Gauge Face (in.)	0	0	0.079	0.130
		Total Area (in.^{2})	0	0.026	0.140	0.219
	14-LJ	Vertical (in.)	0	0.016	0.031	0.043
		Gauge Face (in.)	0	0	0	0
		Total Area (in.^{2})	0	0.018	0.060	0.077
	15-HCr	Vertical (in.)	0	0.020	0.075	0.114
		Gauge Face (in.)	0	0	0.118	0.181
		Total Area (in.^{2})	0	0.042	0.237	0.386
	16-LCr	Vertical (in.)	0	0.031	0.098	0.122
		Gauge Face (in.)	0	0	0	0
		Total Area (in.^{2})	0	0.043	0.158	0.220
5 (8°)	17-LCr	Vertical (in.)	0	0.012	0.047	0.067
		Gauge Face (in.)	0	0	0	0
		Total Area (in.^{2})	0	0.025	0.083	0.127
	18-HCr	Vertical (in.)	0	0.028	0.075	0.098
		Gauge Face (in.)	0	0	0.126	0.142
		Total Area (in.^{2})	0	0.045	0.237	0.298
	19-LJ	Vertical (in.)	0	0.012	0.028	0.024
		Gauge Face (in.)	0	0	0	0
		Total Area (in.^{2})	0	0.024	0.059	0.060
	20-HJ	Vertical (in.)	0	0.012	0.028	0.028
		Gauge Face (in.)	0	0	0.098	0.138
		Total Area (in.^{2})	0	0.025	0.146	0.197
6 (Spiral into 8° Curve)	21-LJ	Vertical (in.)	0	0.008	0.012	0.012
		Gauge Face (in.)	0	0	0	0
		Total Area (in.^{2})	0	0.027	0.036	0.035
	22-HJ	Vertical (in.)	0	0.008	0.012	0.016
		Gauge Face (in.)	0	0	0	0
		Total Area (in.^{2})	0	0.016	0.050	0.067
	23-LCr	Vertical (in.)	0	0.012	0.039	0.043
		Gauge Face (in.)	0	0	0	0
		Total Area (in.^{2})	0	0.012	0.055	0.066
	24-HCr	Vertical (in.)	0	0.016	0.043	0.051
		Gauge Face (in.)	0	0	0.035	0.055
		Total Area (in.^{2})	0	0.017	0.083	0.116

* The following abbreviations designate the rail position and type particular to each measurement point:

HCr/LCr - Algoma 1% Cr rail on high/low rail of curve.
HJ/LJ - Japanese Superrail on high/low rail of curve.

FILE: JR05 ID: 000165
FILE: JR35 ID: 000165

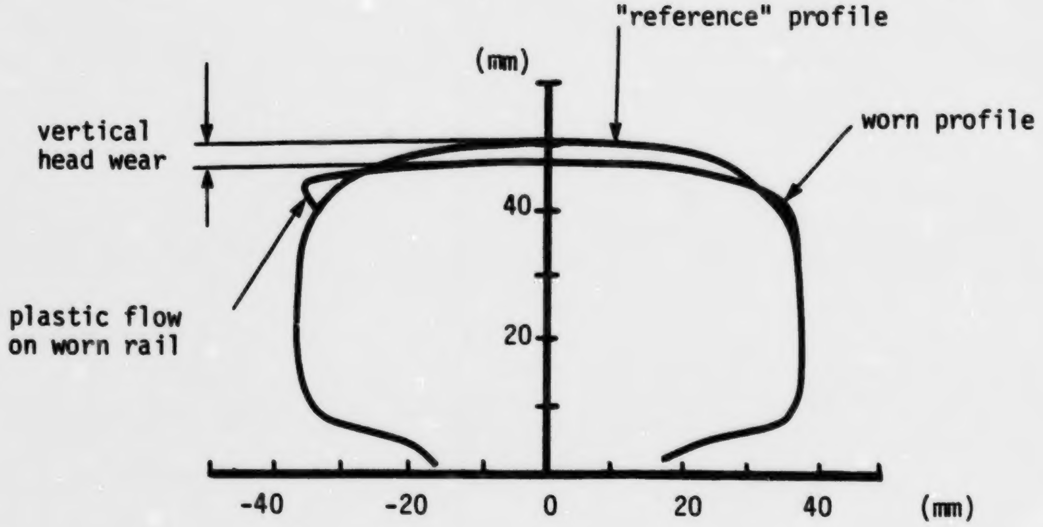
"reference" profile
(mm)
vertical
head wear
worn profile
40
20
plastic flow
on worn rail
-40
-20
0
20
40
(mm)

VERTICAL WEAR : 3.1 mm
GAUGE FACE WEAR : 0.0 mm
AREA OF WEAR : 142.1 sq. mm

Figure 4: Profile Comparison, Algoma 1% Cr, Low Rail in Fully Developed Section of 8.5° Curve, Measurement Point 13, Change-Over Point 4, Site 3.

FILE: JR05 ID: 301135

FILE: JR35 ID: 301135

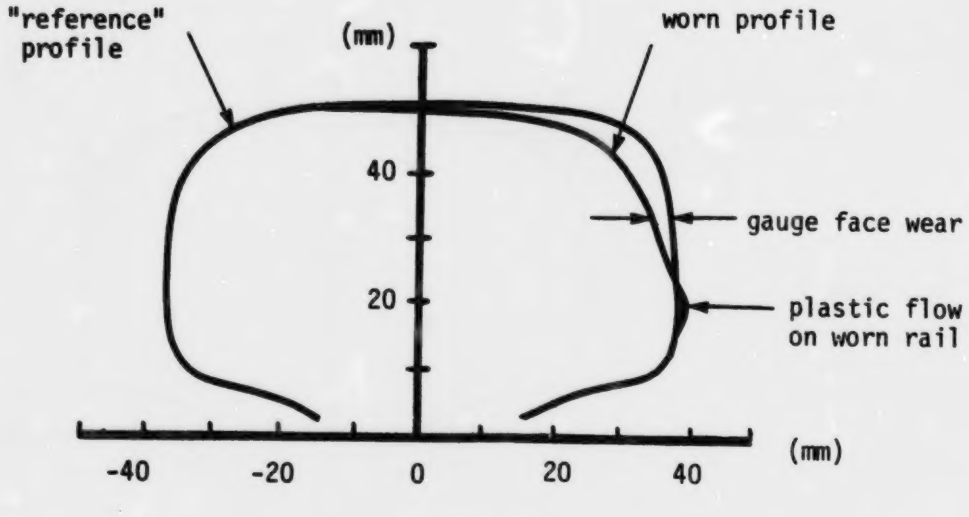

VERTICAL WEAR : 0.9 mm

GAUGE FACE WEAR : 3.3 mm

AREA OF WEAR : 141.3 sq. mm

Figure 5: Profile Comparison, Japanese Superrail, High Rail in Fully Developed Section of 8.5° Curve, Measurement Point 13, Change-Over Point 4, Site 3.

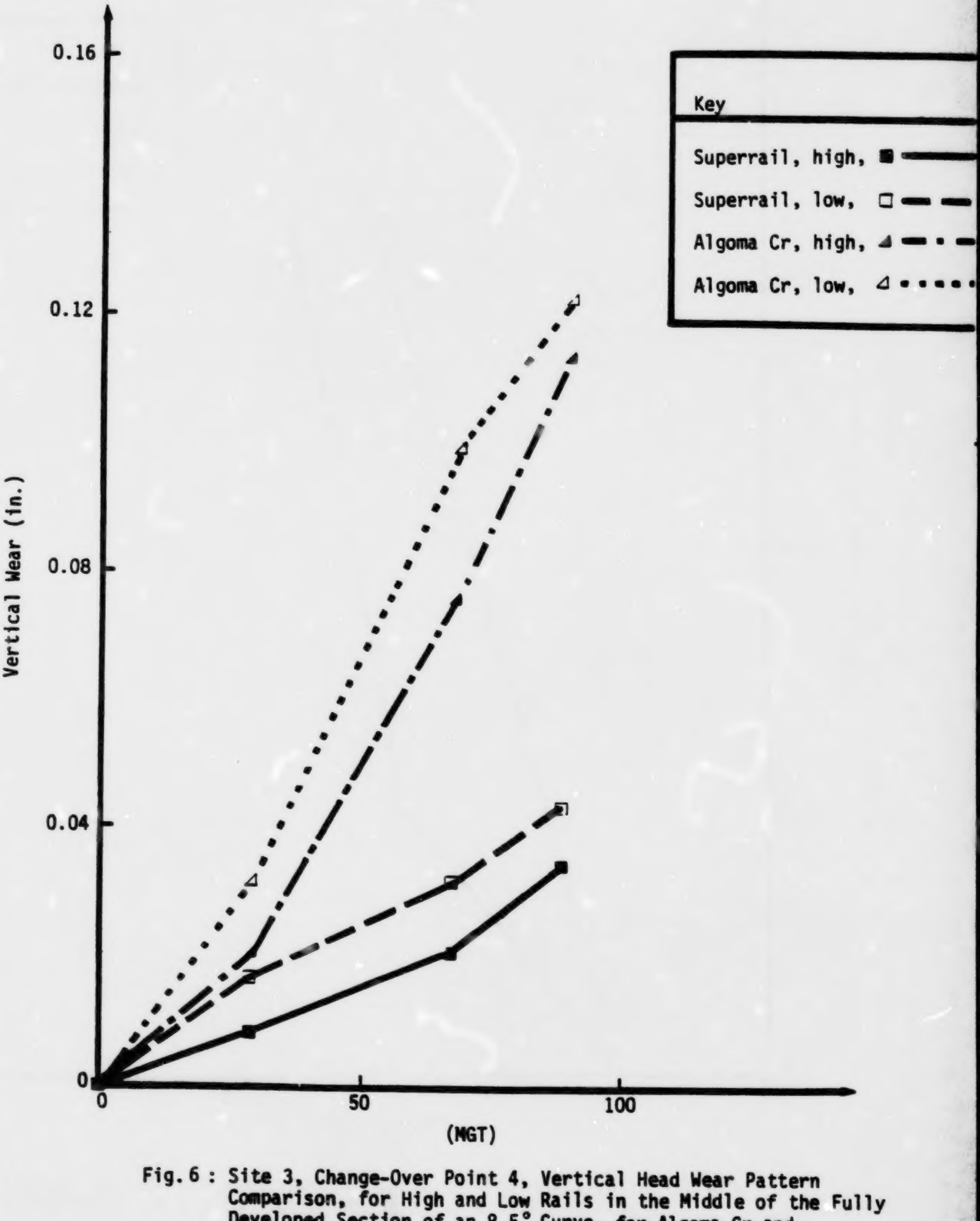

Fig. 6 : Site 3, Change-Over Point 4, Vertical Head Wear Pattern Comparison, for High and Low Rails in the Middle of the Fully Developed Section of an 8.5° Curve, for Algoma Cr and Japanese Superrail

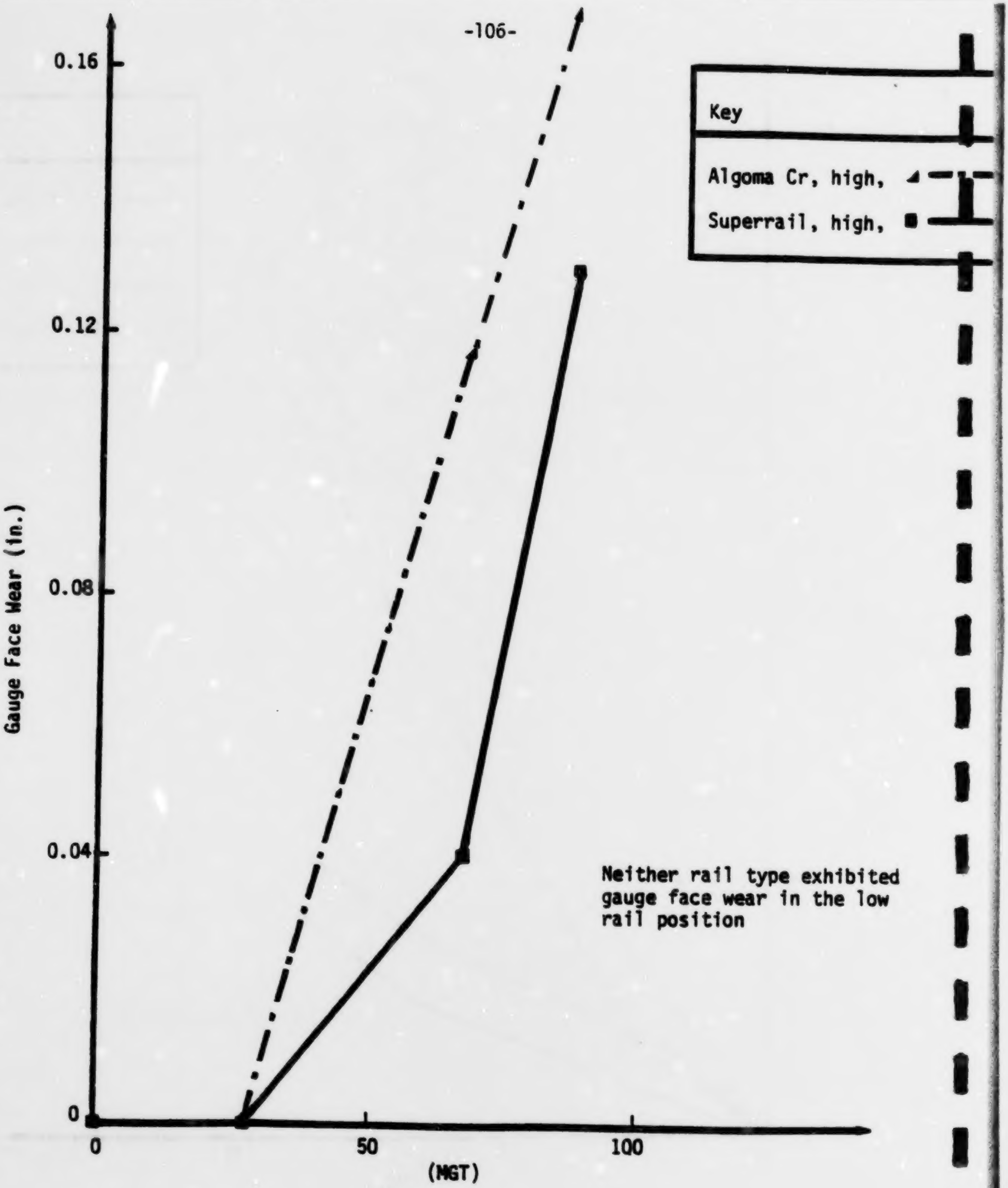

Fig. 7 : Site 3, Change-Over point 4, Gauge Face Wear Pattern Comparison, for High and Low Rails in the Middle of the Fully Developed Section of an 8.5° Curve, for Algoma Cr and Japanese Superrail

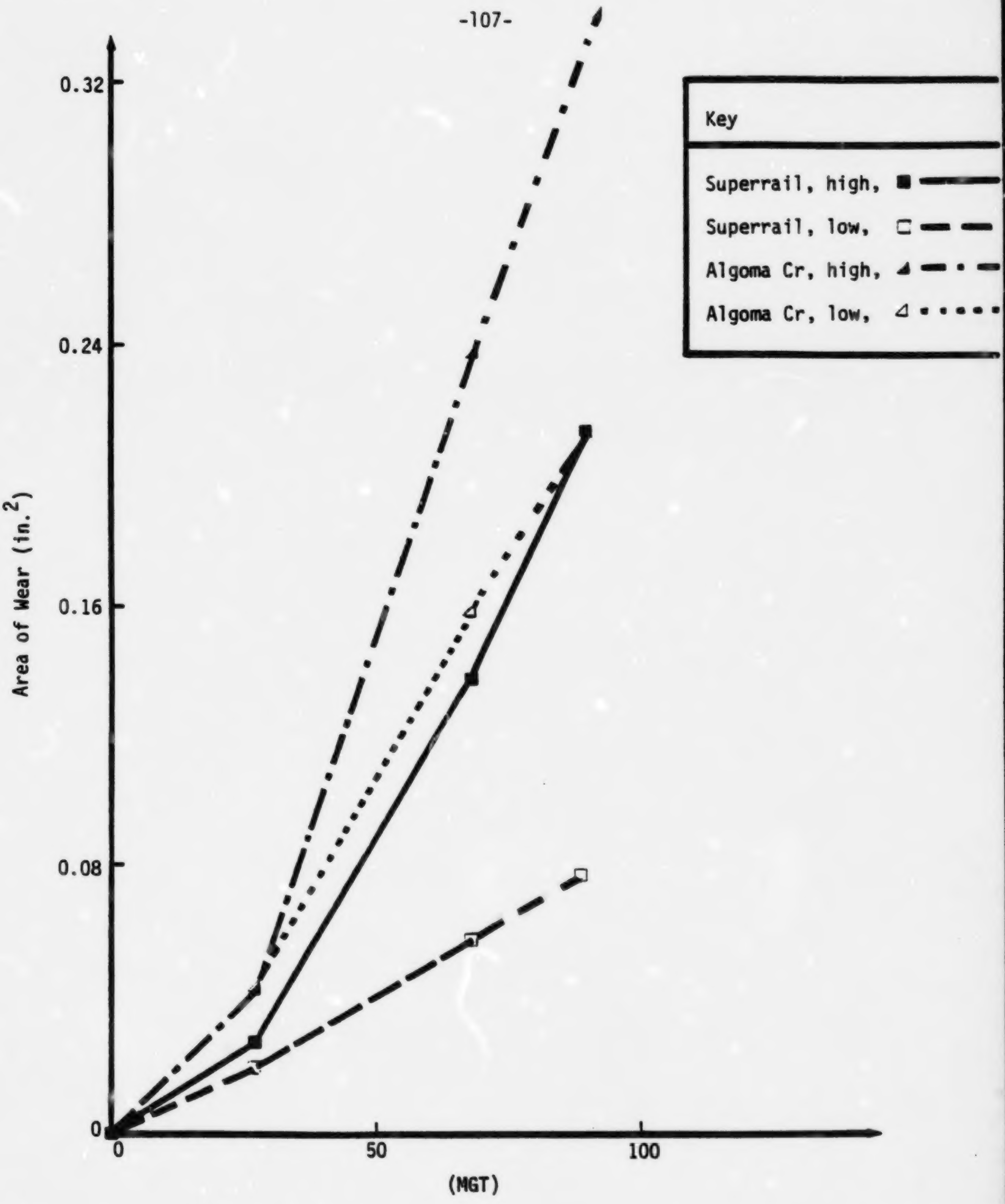

Fig. 8 : Site 3, Change-Over Point 4, Total Head Wear Pattern Comparison, for High and Low Rails in the Middle of the Fully Developed Section of an 8.5° Curve, for Algoma Cr and Japanese Superrail

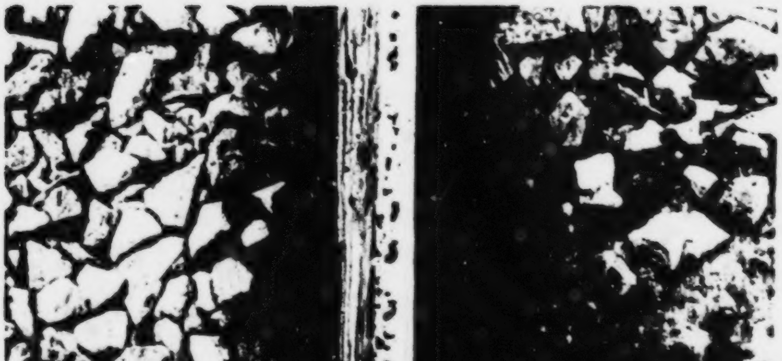

Figure 9: Typical Shelling Damage Exhibited by Algoma 1% Cr Rail Running Surface, for Low Rail in Fully Developed Section of Curve

MODIFICATIONS OF THE ANGLE-OF-ATTACK MEASUREMENT SYSTEM

D. D'Aoust
Planning and Research Department
Canadian Pacific Limited
Montreal

ABSTRACT

This report describes the different transducers, and their arrangements, that were tested for the objective of replacing the lasers and the photodetectors arrangement of the laser based angle-of-attack measurement system. Among the transducers tested were:

- eddy current proximity sensor
- servotrip transducer
- infra-red light emitting diode and photosensor arrangement.

SOMMAIRE

Ce rapport décrit les différents palpeurs, et leurs montages, qui ont été essayés dans le but de remplacer les lasers et les photodétecteurs du système de mesure au laser d'angle d'inscription.

Les palpeurs essayés sont:

- détecteur de proximité à induction
- palpeur "ServoTrip"
- montage diode électroluminescente infra rouge - photodétecteur

ACKNOWLEDGEMENTS

The author would like to thank Mr. Gregory Izbinsky of the Planning and Research Department for the helpful advice and assistance throughout this project. The author would also like to thank Mr. Leo Feiter, of the Planning and Research Department, for his excellent work in producing the printed circuit boards and assembling the various interfaces. Thanks to Mr. Helder Soares, also of the same department, for his assistance during some of the field tests.

TABLE OF CONTENTS

Page

ABSTRACT 110

ACKNOWLEDGEMENTS 112

TABLE OF CONTENTS 113

LIST OF FIGURES 114

LIST OF TABLES 115

1. Laser Based Angle-of-Attack Measurement System 116
    - 1.1 Principle of Operation 116
    - 1.2 The Need For a Different System 117

2. Inductive Proximity Sensor 117

3. Servotrip Transducer 118
    - 3.1 Principle of Operation 118
    - 3.2 Field Tests 119
        - 3.2.1 Field Test 1 119
        - 3.2.2 " " 2 120
        - 3.2.3 " " 3 122

4. Infra-Red Light Emitting Diode Based Angle-of-Attack Measurement System 126
    - 4.1 General Description of IRLED - Photosensor Arrangement 127
    - 4.2 Redundancy Scheme 128
    - 4.3 Photosensor Signal Conditioner 128
    - 4.4 IRLED - Photosensor Mounting Arrangement 128
    - 4.5 Field Test 129
    - 4.6 Conclusions 132
    - 4.7 Recommendations 133

APPENDIX I Servotrip Transducer Interface 134

" II Optical Displacement Transducer 136

" III Line Scan Camera Interface 139

" IV Simulation of Servotrip Transducer 3 140

LIST OF FIGURES

Fig. No.		Page
1	Laser Based AAMS	141
2a	Magnetic Flux ϕ versus Distance D Between Transducer and Wheel	142
2b	Output Voltage Vo versus Distance D Between Transducer and Wheel	142
3	Servotrip Transducers Mounted on Channels	143
4	Field Test 1 Set-up	144
5	Field Test 2 Set-up	145
6	Servotrip Transducer Interface	146
7	Field Test 3 Set-up	147
8	Radiation Pattern of TIL31B	148
9	Photosensor Signal Conditioner	149
10	Mounting Bracket For Support Channel	150
11	IRLED Based AAMS Field Test Set-up	151
12	Line Scan Camera and Target Arrangement	152
13	Line Scan Camera Output Signal When Focused on Target	153
14	Line Scan Camera Interface Output Signals	154
15	Line Scan Camera Interface Circuit Diagram	155

LIST OF TABLES

PAGE

1. Field Test 2, Linear Regression Results 122

2. Field Test 3, 5° Curve Linear Regression Results 124

3. Field Test 4, 10° Curve Linear Regression Results 125

4. Relationship Between Angle-of-Attack Measured With Laser System and IRLED Station #2 130

5. Relationship Between Angle-of-Attack Measured With Laser System and IRLED Station #1 131

6. Pulse Duration of Td For Each Simulated Speed 140

1.0 Laser Based Angle-of-Attack Measurement System

The laser based Angle-of-Attack Measurement System (AAMS) is a wayside device that measures the angle-of-attack of each individual axle of an entire consist at a given point on the track. It is an accurate system that provides precise and repeatable results. Measurements are printed out immediately after the passage of the train.

The laser based AAMS is usually used to evaluate the curving performance of trucks. It has been used in all Canadian Pacific Research projects involving the evaluation of new truck designs, and also in consulting services provided by Canadian Pacific Research to other companies in Canada and the United States.

Because the measurements made with the laser based AAMS have been found to be so repeatable, the laser based AAMS constitute our reference system, to which all of the experimental systems described in this report have been compared.

1.1 Principle of Operation

The laser based AAMS uses three low-power lasers and PIN photodiode detectors configured as shown in Figure 1. When a wheelset passes over the laser detector arrangement, it interrupts the three laser beams generating a rectangular pulse from each photodetector. From the time delays between the midpoint of each pulse, the instantaneous speed and angle-of-attack can be calculated. A microcomputer processes the three detector output signals and prints the angle-of-attack measurement in the field.

The laser-detector arrangements 2 and 3 are spaced 6.35 cm apart.

The microcomputer measures the time delay between the midpoint of the output pulse of detector 2 and 3 to calculate the instantaneous speed. The time delay between the midpoint of the pulses of the detector 1 and 2 in conjunction with the time delay between pulses of detector 2 and 3 are used by the microcomputer to calculate the instantaneous angle-of-attack.

1.2 The Need For a Different System

The laser based AAMS does have severe drawbacks. As can be seen in Figure 1, the photodetectors are positioned between the rails. They are approximately 2 cm above the railhead. Their position makes them very prone to damage from brake hoses, hanging chains and any dragging equipment. Though the lasers are situated on the field side, several of them have been destroyed by passing trains. The system is also difficult and time consuming to install. Hence, a more rugged transducer was sought that could accurately detect the centre of a wheel of a passing car. Several types of transducers were evaluated at the Research Department Laboratory and in field tests, namely:

- eddy current proximity sensor, which is discussed in Section 3
- Servotrip transducer, which is discussed in Section 4
- Infra-red light emitting diode-photosensor arrangement discussed in Section 5.

2.0 Inductive Proximity Sensor

An inductive proximity sensor consists of an oscillator connected to a coil which generates a magnetic field. Eddy currents are induced in any metallic target entering the sensing field. The result is a lower load impedance as seen by the oscillator which in turn will require a larger supply current. Hence, the supply current indicates if the sensor is detecting a metallic object or not.

The sensor tested was a N150-SR-90YO manufactured by Turck Inc. It is hermetically sealed, compact, and extremely rugged. It has a nominal sensing distance of 50 mm.

The sensor was tested in the Research Department Laboratory using test fixtures designed to verify its static and dynamic behaviour.

In the dynamic test, a metallic plate (10 cm x 10 cm) passed over the sensor at different heights above it and at a constant speed. When the target passed at a height of 1 cm above the sensor, the centre of the output pulse of the sensor corresponded to the centre of the target. However, at a height of 2 cm, the centre of the pulse corresponds to a point on the target approximately 2 cm from its centre. If the sensor was used to measure angle-of-attack and the distance between the sensor and the wheel flange changed by only 1 cm, an error in excess of 80 minutes would be induced. The actual distance between the sensor and the wheel flange can vary considerably more than 1 cm. For this reason, the inductive proximity sensor was rejected, and this type of sensor is no longer considered.

3.0 ServoTrip Transducer

The ServoTrip transducer, manufactured by the Servo Corporation of America, is specifically designed to detect the presence of train wheels. They are used to trigger hot-box detectors, count the number of wheels of a passing train, etc.

The transducer consists of a U-shaped permanent magnet and a sensing coil wound on to it. The magnet and coil are hermetically sealed in an epoxy case which is virtually indestructible.

Three field tests were made to evaluate the transducer.

3.1 Principle of Operation

When a wheel passes over the magnet, it shunts the poles of the magnet, thereby reducing the magnetic reluctance between them. This results in an increase in the magnetic flux ϕ, flowing through the magnet. The magnetic flux ϕ will increase to a maximum value when the flange of the wheel is at a minimum distance from the two poles. This condition corresponds to the centre of the wheel being directly above the poles of the magnet. The magnetic flux ϕ will then decrease to its quiescent value as the wheel moves away from the transducer.

Figure 2a shows a graph of the magnetic flux ϕ versus the distance D between the centre of a wheel and the ServoTrip transducer.

The voltage V_o at the terminals of the sensing coil is:

$$V_o = -n \frac{d\phi}{dt}$$

A graph of the voltage V_o of the sensing coil versus the distance D between the centre of the wheel and the ServoTrip transducer is shown in Figure 2b. As can be seen, the zero crossing of the waveform corresponds to the centre of the wheel being directly over the magnet.

An angle-of-attack measurement system based on this type of transducer possessed all the characteristics required of an easy-to-install test system that would be extremely rugged.

3.2 Field Tests

The ServoTrip transducer is designed to be attached directly to the rail. For our application, however, we initially mounted the transducers on aluminium channels that were supported by fence posts (see Figure 3). This was done because the longitudinal rail movement created by a passing train would induce an offset angle that could vary within the passage of a train. This offset angle can be evaluated by measuring the longitudinal rail displacement, but it is much simpler to mount the transducers on channels. This technique was used for the first two field tests.

3.2.1 Field Test 1

Because the ServoTrip transducers are mounted on aluminium channels, they are positioned further away from the wheel flange of a passing car than if they had been attached directly to the rail. A reduced output signal was thus expected. The first objective of this test was to characterize the output signal of the ServoTrip transducer under actual operating conditions. Parameters of interest included: peak amplitude of the output waveform, noise level, spurious signals, etc. The field test was made on a tangent track near Beaconsfield station in Montreal on June 29th, 1983.

The second objective of this test was to verify that an arrangement of two ServoTrip transducers separated by a known distance could be used to measure the instantaneous speed of a passing car. The two transducers were mounted 30 cm apart, as shown on Figure 4. The laser based AAMS was used as a reference. The signals (2 ServoTrip transducers, 2 photodetectors) were recorded on a FM tape recorder and subsequently played back onto a strip chart recorder.

The output signal amplitude of the ServoTrip transducer was between 0.5 and 2.5 volt peak. The measured signals did not contain any spurious pulses and the noise produced by the ServoTrip transducers was below the residual noise level of the tape recorder-strip chart recorder combination. The lasers are separated by 6.35 cm, while the ServoTrip transducers are 30 cm apart. The time delay between the zero crossing of the two ServoTrip transducers should be 4.72 times greater than that of the time delay between the midpoint of the pulses of the photodetectors. The actual coefficient was found to be 4.7, the resolution being limited by the strip-chart recorder.

3.2.2 Field Test 2

The purpose of this field test was to evaluate a ServoTrip based AAMS. The laser based AAMS was used as the reference system. The instrumentation set-up is shown in Figure 5. The field test was conducted on a 10° curve near Calgary in September 1983.

A test consist totalling 26 axles passed through the test zone at two different speeds (25, 37, mph) three times each, in both directions. The train was then wyed and the process repeated.

An interface was designed and assembled that transforms the output signals of the ServoTrip transducers into a format that is compatible with the microcomputer of the laser based AAMS. The circuit diagram of the interface is shown in Figure 6. Essentially the interface produces a fixed length pulse whose midpoint is at a precise time interval from the zero crossing point of the ServoTrip transducer output waveform. A complete description of the interface is given in Appendix I.

The output of the ServoTrip transducers were recorded via the interface on an FM tape recorder, to be subsequently analysed by the microcomputer. The microcomputer software assumes a distance of 6.35 cm (2.5") between laser 2 and laser 3. However, ServoTrip transducer 2 and 3 are separated by approximately 30 cm. Hence, the instantaneous speed and the angle-of-attack of each axle of the passing train should be multiplied by a constant, normally 4.72.

The average ratio of $\frac{V_L}{V_m}$ where V_L : speed measured by laser, V_m : speed measured by ServoTrip transducer was 4.71. The average was taken over several runs at 25 and 37 mph.

We expect a linear relationship between the angle-of-attack as seen by the laser based system, γ_L, and the angle-of-attack as seen by the ServoTrip based system γ_s of the form

$$\gamma_L = a\,\gamma_s + b \qquad (1)$$

where a : 4.71

b: proportional to the angle between the laser based system and the ServoTrip based system.

A linear regression between the two sets of data was made for the 25 and 37 mph runs for each direction of travel. The results are tabulated in Table 1.

As can be seen, the coefficient a of equation 1 above varies between 2.30 and 2.75 depending on speed and direction. The value of b (of equation 1) is practically independent of direction, but changes by about 16 minutes from 25 mph and 37 mph.

We cannot propose a suitable explanation for the unexpected behaviour of the ServoTrip transducers.

TABLE 1

Field Test 2, Linear Regression Results

DIRECTION	2- 3	3- 2
SPEED	25 mph	25 mph
	$\gamma_L = 2.75 \gamma_S - 58.7$	$\gamma_L = 2.69 + 59.1$
	$r^2 = 0.96$	$r^2 = 0.97$
DIRECTION	2- 3	3- 2
SPEED	37 mph	37 mph
	$\gamma_L = 2.39 \gamma_S - 42.5$	$\gamma_L = 2.30 \gamma_S + 43.2$
	$r^2 = 0.92$	$r^2 = 0.88$

3.2.3 Field Test 3

For this test, the ServoTrip transducers were attached directly to the rail. By doing so, the wheel flange passes closer to the poles of the magnet. This will increase the transducer's output signal and provide a "cleaner" zero crossing (which is indicative of the passage of the wheel centre).

Four transducers were deployed as shown in Figure 7. With this configuration, two axles of a truck can be measured simultaneously. The test was conducted in March 1984 at FAST, Pueblo Colorado. Measurements were made on a 5° and a 10° curve.

To measure the longitudinal movement of the rail, optical transducers were used. A description of the transducer and the interface circuit associated with them is given in Appendix II.

The output signals of the four ServoTrip transducers along with the two optical transducers and the three photodetector outputs of the laser based AAMS we recorded on an FM tape recorder.

The test consist passed through the test zone at three different speeds in both directions. The consists was then wyed and the process repeated.

Each station consists of 2 transducers contrary to the usual 3. To enable the computation of the angle-of-attack with the microcomputer, the output signal of transducer 2 was delayed by a fixed time period Td and then connected to the microcomputer channel 3. The speed measurement was thus simulated. The modifications to the ServoTrip interface circuit to simulate transducer 3 are discussed in Appendix 3. The angle-of-attack measurements were corrected with the following equation:

$$\gamma_{cs} = \gamma_s \times \frac{V_L}{V_{sim}}$$

γ_{cs} : speed corrected angle-of-attack as seen by ServoTrip

γ_s = angle-of-attack as seen by ServoTrip

V_L = instantaneous speed as measured by laser based AAMS

V_{sim} = simulated speed

We expected a linear relationship between the speed corrected angle-of-attack measurement γ_{cs}, as seen by the ServoTrip based AAMS and the angle-of-attack γ_L as seen by the laser based AAMS, of the form

$$\gamma_L = a\,\gamma_{cs} + b \qquad (2)$$

where a: should be equal to 1

b: angle between laser system and the ServoTrip based system

A linear regression was performed between the data produced by the ServoTrip based AAMS and the laser based AAMS. The results are shown in Table 2 for the 5° curve and in Table 3 for the 10° curve.

The data of station #2 of the 5° curve was lost due to a tape recorder malfunction.

TABLE 2

Field Test 3, 5° Curve
Linear Regression Results

	2- 3		3- 2	
15 mph	$\gamma_L = 0.59\,\gamma_s + 3.1$	$r^2 = .91$	$\gamma_L = 0.67\,\gamma_s - 11.4$	$r^2 = .95$
25 mph	$\gamma_L = 0.67\,\gamma_s + 4.1$	$r^2 = .94$	$\gamma_L = 0.67\,\gamma_s - 11.3$	$r^2 = .94$
30 mph	$\gamma_L = 0.66\,\gamma_s + 3.5$	$r^2 = .95$	$\gamma_L = 0.71\,\gamma_s - 12.9$	$r^2 = .95$
Overall	$\gamma_L = 0.63\,\gamma_s + 3.5$	$r^2 = .92$	$\gamma_L = 0.68\,\gamma_s - 11.4$	$r^2 = .94$

TABLE 3

Field Test 4, 10° Curve Linear Regression Results

Station 1

Direction	2- 3		3- 2	
Speed				
10 mph	$\gamma_L = 1.1\ \gamma_s + 13.4$	$r^2 = 0.60$	$\gamma_L = 1.76\ \gamma_s - 66.5$	$r^2 = 0.12$
15 mph	$\gamma_L = .77\ \gamma_s + 19.2$	$r^2 = 0.71$	$\gamma_L = 1.94\ \gamma_s - 68.6$	$r^2 = 0.15$
20 mph	$\gamma_L = .84\ \gamma_s + 18.2$	$r^2 = 0.84$	$\gamma_L = 1.48\ \gamma_s - 53.7$	$r^2 = 0.38$
Overall	$\gamma_L = .90\ \gamma_s + 17.0$	$r^2 = 0.69$	$\gamma_L = 1.73\ \gamma_s - 63.0$	$r^2 = 0.17$

Station 2

10 mph	$\gamma_L = 0.80\ \gamma_s - 8.5$	$r^2 = .8$	$\gamma_L = .37\ \gamma_s + 3.7$	$r^2 = .66$
15 mph	$\gamma_L = 0.73\ \gamma_s - 2.6$	$r^2 = .96$	$\gamma_L = .58\ \gamma_s + 7.2$	$r^2 = .83$
20 mph	$\gamma_L = 1.36\ \gamma_s - 33.8$	$r^2 = .80$	$\gamma_L = .38\ \gamma_s + 0.1$	$r^2 = .56$
Overall	$\gamma_L = 0.89\ \gamma_s - 11.6$	$r^2 = .81$	$\gamma_L = .43\ \gamma_s + 3.3$	$r^2 = .60$

The test consist was an electrically powered 3 truck (6 axles) mass transit vehicle. On the 5° curve, the car was pulled by a locomotive. On the 10° curve, the car was self-propelled. The rails were used as a conductor to supply electrical power to the car. Because of the large transient currents in close proximity to the ServoTrip transducers, noise was induced in their output signal. This noise could not be filtered out without drastically altering the signal of the transducers. Hence, the r^2 factor value for the 10° curve is generally less than that of the 5° curve.

From Tables 2 and 3, we see that the value of the variable a (of equation 2) is not equal to 1 as expected, but was between 0.55 and 0.71, depending on the speed and the direction of the passing train. The average value of variable b is 3.5' for direction 2- 3 and -11.7 minutes for direction 3- 2. This implies that the physical angle between the laser system and the ServoTrip based system changes with direction.

The exact physical process that would explain the behaviour of the ServoTrip based AAMS still eludes us. Therefore, because of its unpredictability, we no longer consider the ServoTrip transducer based AAMS as a suitable replacement to the laser based system.

4.0 Infra-Red Light Emitting Diode Based Angle-of-Attack Measurement System

The basic principle of operation of the Infra-Red Light Emitting Diode (IRLED) based AAMS is the same as the laser based system in that the train wheels interrupt light beams which are detected by photosensors. The general arrangement of the IRLED based AAMS is shown in Figure 11.

The main differences between the IRLED system and the laser system are the following:

- the lasers have been replaced with infra-red light emitting diodes

- the central photodetector assembly of the laser system has been replaced by two assemblies that are mounted closer to the rails, making them less prone to being damaged by air brake hoses and dragging equipment.

- the mounting scheme has been modified to simplify its installation and alignment.

4.1 General Description of IRLED-Photosensor Arrangement

IRLED's have many advantages over lasers: they are small (0.1 cm^3 versus 15.4 cm^3 for a laser tube), consume less power, and they are inexpensive (IRLED costs less than $300. A laser tube and power supply costs about $800).

Because the IRLED and photosensors are so small, they can be mounted in small enclosures which have less chance of being hit by dragging equipment, and contrary to the laser tubes, they are rugged enough to widthstand a large impact, should it occur.

The IRLED's used for the IRLED based AAMS are TIL31B. Each IRLED is connected in series with a current limiting resistor and then to a direct current power supply. The power supply output voltage is adjusted so the average current flowing through each IRLED is 160 mA.

The radiation pattern of the TIL31B is shown in Figure 8. As can be seen, it is not a "pencil beam" like the lasers, but a narrow lobe with half intensity angle of 10°. Because direct current is used to bias the IRLED, the photosensor output signal can be saturated by direct sunlight. To avoid interference from the sunlight, the field of view of the photosensor was restricted by attaching an opague plexiglass bloc, one inch thick, with a 1/16" diameter hole aligned with the photosensor.

The beam diameter, as seen by the photosensor, was measured in the following way. An opaque plate attached to a micrometer was moved across the beam perpendicular to it. The plate crossed the beam at equal distance between the IRLED and the photosensor, as this is where the wheel flange of a passing train would cross the beam.

The output signal of the photosensor was measured. For a change of 0.1 to 0.9 of the maximum photosensor signal output, the plate moved 0.9 mm (.035").

4.2 Redundancy Scheme

The IRLED based system has four emitter-photosensor pairs compared to the three laser-photosensor pair. The additional pair enables the user to measure speed on either the low or high rail, and to measure angle-of-attack on two "lines", i.e. 1-2 or 3-4. This redundancy is useful in the event of a failure of one of the emitter-photosensor pairs, or in verifying the repeatability of the measurements.

4.3 Photosensor Signal Conditioner

Only a fraction of the emitted radiant power falls on the photosensor, which is a TIL78. Signal conditioners are used to amplify and make the output signal of the photosensors compatible with the AAMS microcomputer.

The photosensor signal conditioner circuit diagram is shown in Figure 9. The output of the photosensor is applied to an inverting amplifier formed by U1 (LF353) which has a gain of 100 V/V. The output of the amplifier is then applied to a comparator (U2, LM311). When 160 mA flows through the IRLED, and the beam is not interrupted, the output voltage of U1 is approximately -9 volts. When the beam is interrupted, it goes to 0 volts. The threshold voltage of U2 is adjusted with R5 to 4 volts. R8 provides hysterisis of approximately 300 mV. (Note that R5 and R8 are defined in Figure 9.)

The output of the comparator (U2, pin 7) is connected to the AAMS microcomputer. Two signal conditioner circuits were implemented per printed circuit board. Each printed circuit board is housed in the box used to mount the photosensors.

4.4 IRLED-Photosensor Mounting Arrangement

The small enclosures, in which the IRLED and photosensors are mounted, are attached to mounts which are themselves attached to a supporting channel. The mounts and supporting channel are precision machined. Each component that makes up a mount is kept aligned with dowel pins. Once the mounts are bolted to the support channel, the system need only be aligned to the true radial line of the curve. This task has also been simplified.

Figure 10 shows a close-up view of the bracket used to attach the support channel to the support rods. When the top retainer plate is unbolted, the support channel can be easily moved so the axis formed by emitter 1 and emitter 2 coincides with the true radial line of the curve.

Because the radiation emitted from the IRLED is invisible to the human eye, a taught string attached between emitter 1 and emitter 2 is used to visually indicate their axis. The channel is moved so the string (indicating the axis of emitter 1 and emitter 2) coincides with markings on the rails indicating the true radial line of the curve. Once this is done, the retainer plates are bolted down and the string is removed. The alignment procedure is then complete.

4.5 Field Test

A field test of the IRLED based AAMS was conducted in September 1984, on a 10° curve near Calgary. Two IRLED based AAMS stations were built at the Research Department laboratory for this test. One of the IRLED station was mounted on the support channel of the reference laser based system, so the distance between the axis of laser 1 and laser 2 and the axis of emitter 1 and 2 of the IRLED based system is only 10.16 cm (4"). The other IRLED station was set up so the distance between the two IRLED stations is approximately equal to the wheelbase of a truck. The two axles of a passing truck were thus measured simultaneously. Figure 11 shows the general arrangement of the test site.

We expect a relationship between the measurements produced by the laser based system and the IRLED based system of the form:

$$\gamma_L = a\,\gamma_S + b \qquad (3)$$

where γ_L : angle-of-attack as measured by laser based AAMS

γ_S : angle-of-attack as measured by IRLED based AAMS

a : should be equal to 1

b : angle between laser and IRLED systems.

The data produced by the IRLED system was compared to the data produced by the laser based system using the linear regression technique as discussed in Section 3.2.3. The results are tabulated in Table 4 and Table 5. The IRLED system mounted in the support channel of the laser system is labelled system #2. The other IRLED based system is labelled system #1.

TABLE 4

Relationship Between Angle-of-Attack Measured With Laser System and IRLED Station #2

Direction: 2 to 3

Speed

25 mph $\gamma_L = 0.98\,\gamma 2 + 15.1 \quad r^2 = 0.99$

37 mph $\gamma_L = 0.97\,\gamma 2 + 15.8 \quad r^2 = 0.99$

45 mph $\gamma_L = 1.00\,\gamma 2 + 15.4 \quad r^2 = 0.99$

Direction: 3 to 2

Speed

25 mph $\gamma_L = 1.02\,\gamma 2 - 14.0 \quad r^2 = 0.99$

37 mph $\gamma_L = 1.04\,\gamma 2 - 15.3 \quad r^2 = 0.99$

45 mph $\gamma_L = 0.99\,\gamma 2 - 12.1 \quad r^2 = 0.98$

γ_L : angle-of-attack measured with laser based AAMS

$\gamma 2$: angle-of-attack measured with IRLED based AAMS station #2

TABLE 5

Relationship Between Angle-of-Attack Measured With Laser System and IRLED Station #1

Direction: 2 to 3

Speed

25 mph $\gamma_L = 0.99\ \gamma 1 + 1.3 \quad r^2 = 0.96$

37 mph $\gamma_L = 1.10\ \gamma 1 + 1.4 \quad r^2 = 0.98$

45 mph $\gamma_L = 1.04\ \gamma 1 + 1.8 \quad r^2 = 0.97$

Direction: 3 to 2

Speed

25 mph $\gamma_L = 1.07\ \gamma 1 - 1.4 \quad r^2 = 0.96$

37 mph $\gamma_L = 1.06\ \gamma 1 - 1.3 \quad r^2 = 0.96$

45 mph $\gamma_L = 1.04\ \gamma 1 - 1.2 \quad r^2 = 0.93$

γ_L : angle-of-attack measured with laser based AAMS

$\gamma 1$: angle-of-attack measured with IRLED based AAMS station #1

As can be seen from Tables 4 and 5, the value of the constant "a" of equation 3 is indeed very close to unity. The angle "b" of Table 4 (which is indicative of the angle formed between the axis of laser 1 and 2, and the axis of IRLED 1 and 2 of station #2) does not change significantly with speed on direction. The same can be said of the angle "b" of Table 5.

Further analysis was performed with the data produced by the laser based system and the IRLED system #2. We assume that the relationship between the angle-of-attack γ_L measured with the laser system and the angle-of-attack $\gamma 2$ measured with the IRLED system 2 is of the form:

$$\gamma_L = \gamma 2 + \varepsilon \qquad (4)$$

where ε is the angle formed between the axis of laser 1 and 2, and the axis of IRLED 1 and 2 of station #2.

The mean $\overline{\varepsilon}$ and the standard deviation σ are evaluated using the following equations:

$$\overline{\varepsilon} = \frac{1}{N} \sum_{i-1}^{n} \frac{\varepsilon i}{N}$$

$$\sigma^2 = \sum_{i=1}^{n} \frac{(\varepsilon i - \overline{\varepsilon})^2}{N}$$

For N = 180, (30 axles x three speeds, 25, 37, 45 mph x two directions)

$$\overline{\varepsilon} = 14.5$$
$$\sigma = 1.3$$

Hence, our assumption that the laser based system measurements and the IRLED based system measurements can be related with equation (4) is valid for our purposes.

4.6 Conclusion

For our purposes, the IRLED based AAMS can be used to measure angle-of-attack of general traffic trains without being damaged. When measuring the angle-of-attack of locomotive axles however, the measurement can be distorted by the sand pipes if they are low enough to cut through the light beams.

4.7 Recommendations

The circuitry associated with the IRLED and photosensors should be modified to make the system insensitive to ambient light. The mounting scheme of the IRLED and photosensors should be modified to facilitate their servicing.

To eliminate distortions created by locomotive sand pipes, a reflective type of photoscanner can be used to detect the presence of train wheels. The accuracy of an AAMS based on such a transducer should be investigated.

APPENDIX I

ServoTrip Transducer Interface

The interface circuit diagram is shown in Figure 6 . Each channel consists essentially of a zero crossing detector followed by a monostable multivibrator. Referring to Figure 6, U1-B is an operational amplifier (TL084) configured as a comparator. When the signal V_i at the positive input (i.e. the output signal of the ServoTrip transducer) of the comparator (U1-B) is zero, the output of the comparator V_o is low and the reference voltage V_R at the negative input of U1-B is equal to:

$$V_R = \left(\frac{-R6}{R4+R14} * -4.7 \right) - \frac{R6}{R5} * 0 \quad , V_o = \text{low} \qquad (1)$$

$$V_R = \frac{R6}{R4+R14} * 4.7 \quad , \quad V_o = \text{low} \qquad (2)$$

For the component values shown in Figure ,

$$V_R = 240 \text{ mV} \quad , \quad V_o = \text{low}$$

When the signal V_i at the positive input of U1-B reaches 240 mV, the output V_o of U1-B goes high, V_R is then equal to:

$$V_R = \left(\frac{R6}{R4+R14} * 4.7 \right) - \frac{R6}{R5} * 4.7$$

R14 is adjusted so that:

$$R4 + R14 = R5$$

For that condition,

$$V_R = 0 \text{ volts}$$

When the input signal V_i crosses the zero level, which indicates the centre of the wheel is directly above the transducer, the output V_o of U1-B goes low, the falling edge triggering the monostable multivibrator U2A (4538B).

Hence, if the input signal V_i is less than the threshold voltage V_t (240 mV), it is disregarded.

The pulse duration of the three monostable multivibrator were adjusted to 74 ms ± 10 μs.

The output of the monostable goes through a buffer (4050B) which makes the signal TTL (Transistor Transistor Logic) compatible. The 3 output signals are then connected to the inputs of the laser based AAMS microcomputer.

The input section of each channel has a transient voltage suppressor (V22ZA3) and back to back zener diodes (D1, D2, IN5228B) which limits the input signal V_i to a maximum of ± 10V. Potentiometer R3 scales the output voltage of the ServoTrip transducer which effectively increases the threshold voltage Vt.

To test the interface, the input of channels 1 and 2 and 3 were connected to a triangle wave generator. Because there is no time delay between signal 1 and 2, the angle-of-attack calculated by the microcomputer should be zero.

The output of channel 3 was delayed as to simulate a speed of less than 95 mph which is required by the microcomputer software. The angle-of-attack as seen by the microcomputer did not exceed 0.1 minute.

APPENDIX II

Optical Displacement Transducer

Each optical transducer used to measure the longitudinal rail displacement consists of a line scan camera (SUNX, IS-NC5L) and a target. The image sensor of the line scan camera is a linear array of 512 light sensitive elements. For a field of view of 100 mm, the resolution is 0.2 mm. The target consists of two white bars, on a black background, whose midpoints are separated by 7.62 mm (0.3"). The target is attached to the rail while the camera is positioned on the channel used to mount the lasers and photodetector mounts of the laser based AAMS (see Figure 12).

The output signal of the camera, when it is focussed on the target, is shown in Figure 13. When the rail moves longitudinally, the two positive pulses representing the two white bars of the target will move with respect to the synchronization pulses (negative pulses).

The time delay between the midpoint of the two positive pulses is labelled Tpp. The time delay between the rising edge of the synchronization pulse and the midpoint of the first positive pulse is Tsp. When the cameras and targets are installed, the two camera output signals are sampled. Any subsequent rail displacement is evaluated by sampling the two camera output signals, and using the following equation:

$$d = 7.62 \times \frac{Tsp' - Tsp}{Tpp} \text{ mm} \qquad (1)$$

where:

d: displacement of target in mm

Tsp: time delay between rising edge of synchronization pulse and the midpoint of the first positive pulse, when system is initially installed

Tsp': time delay Tsp at subsequent sample

Tpp: time delay between the midpoint of the two positive pulses

The advantage of this measurement technique is that the camera output signal does not need to be calibrated each time the camera target arrangement is installed at a different site. The calibration information is contained in each scan of the target.

Equation (1) above can be written as:

$$d = 7.62 \times \frac{Tsp'}{Tpp} - 7.62 * \frac{Tsp}{Tpp}$$

Once the camera target arrangement is installed, Tsp and Tpp are constant. Hence,

$$d = 7.62 * \frac{Tsp'}{Tpp} - K \qquad (2)$$

$$\text{where } K = 7.62 * \frac{Tsp}{Tpp}$$

The laser based AAMS microcomputer calculates the angle-of-attack from the output of the three photodetector signals, with the following equation:

$$\alpha = A * \frac{D12}{D23} \pm \varepsilon \qquad (3)$$

where:

α : angle-of-attack

A : time to angle constant

D12 : time delay between the midpoint of the pulses from detector 1 and detector 2

D23 : time delay between the midpoint of the pulses from detector 2 and detector 3

ε : offset angle. It is the angle between the axis of each laser 1 and 2 and the true radial line of the curve. It is added or subtracted depending on the direction of travel of the passing train.

Because of the similarity of equations 2 and 3 above, we could use the AAMS microcomputer to perform the time delay measurements and required arithmeric operations to obtain the displacement measurement.

The interface circuit diagram is shown in Figure 15. The external trigger signal enables the circuit to produce a set of three pulses which can be analyzed by the AAMS microcomputer. A ServoTrip transducer is used to trigger the interface so that the position of the rail (and hence the ServoTrip sensor itself) is measured each time a wheel passes over it.

APPENDIX III

Line Scan Camera Interface

The purpose of the camera interface is to transform the camera output signal into three signals, as shown in Figure 14 that are compatible with the AAMS microcomputer hardware and software.

APPENDIX IV

Simulation of ServoTrip Transducer 3

To simulate the output signal of ServoTrip transducer 3, the ServoTrip interface was modified. Referring to Figure 6, the zero crossing detector of Channel 3 (U3-A, U3-B) was disabled by removing U3 and R34. The signal at pin 11 of U2-B was applied to a monostable multivibrator whose pulse duration is Td. The output pulse of the monostable multivibrator triggered U4-A to produce an output pulse delayed by Td seconds after the output pulse of Channel 2.

The pulse duration of Td was adjusted according to Table 6 below:

TABLE 6

Pulse Duration of Td For Each Simulated Speed

Desired Speed, mph	Pulse duration of Td, ms
10	14.2
15	9.46
20	7.10
25	5.68
30	4.74

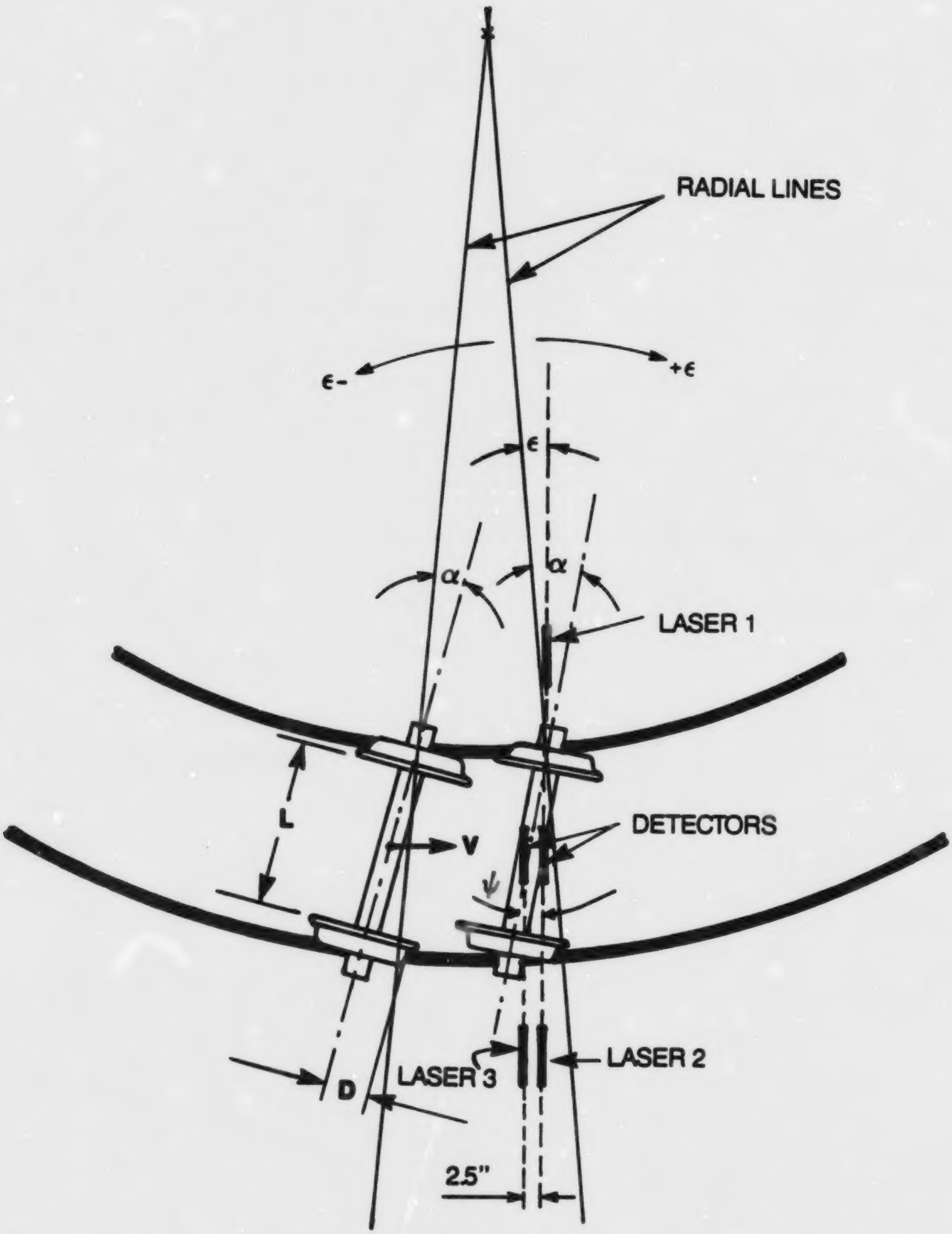
RADIAL LINES
ϵ-
+ϵ
ϵ
α
α
LASER 1
L
V
DETECTORS
ψ
LASER 3
LASER 2
D
2.5"

ϵ - LASER SET-UP ERROR
ψ - ANGLE MEASURED BY ANGLE-OF-ATTACK SYSTEM
α - ANGLE-OF-ATTACK

ALIGNMENT OF LASERS AND DETECTORS USED FOR ANGLE-OF-ATTACK MEASUREMENTS
FIGURE 1

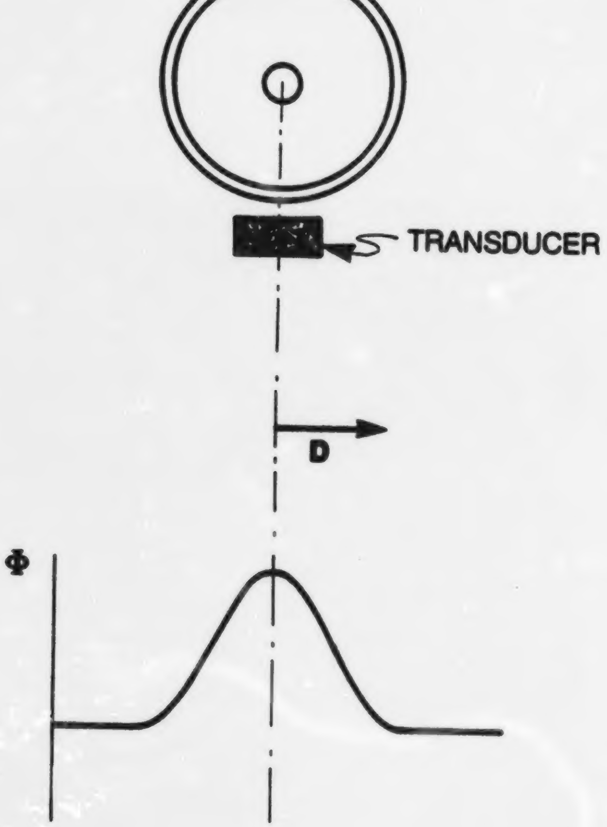

A) MAGNETIC FLUX Φ VERSUS DISTANCE "D" BETWEEN TRANSDUCER AND WHEEL

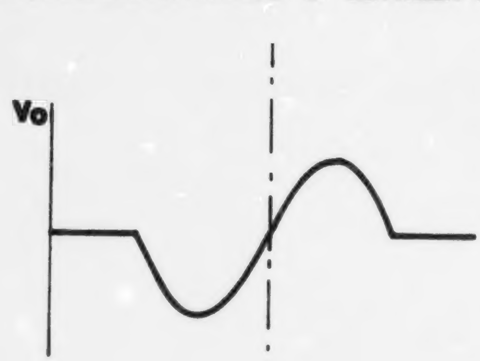

B) OUTPUT VOLTAGE Vo VERSUS DISTANCE BETWEEN TRANDSDUCER AND WHEEL

FIGURE 2

SERVOTRIP TRANSDUCER MOUNTED ON CHANNELS

FIGURE 3

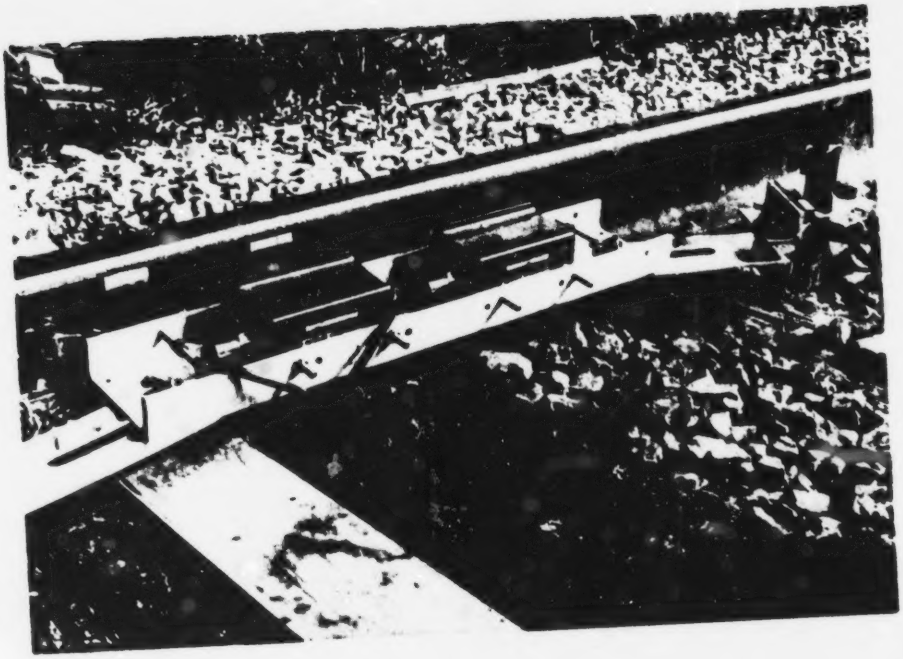

FIELD TEST 1 SET-UP

FIGURE 4

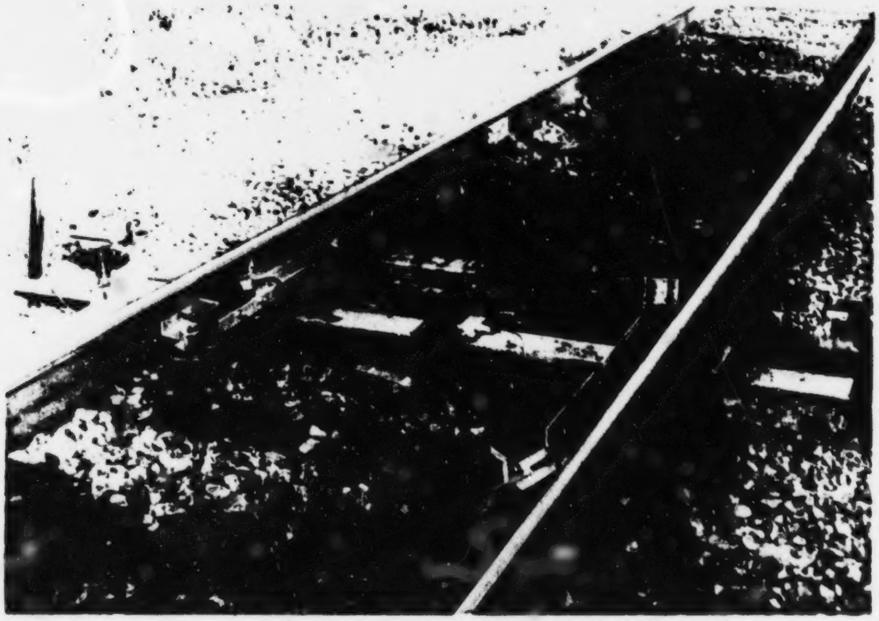

FIELD TEST 2 SET-UP

FIGURE 5

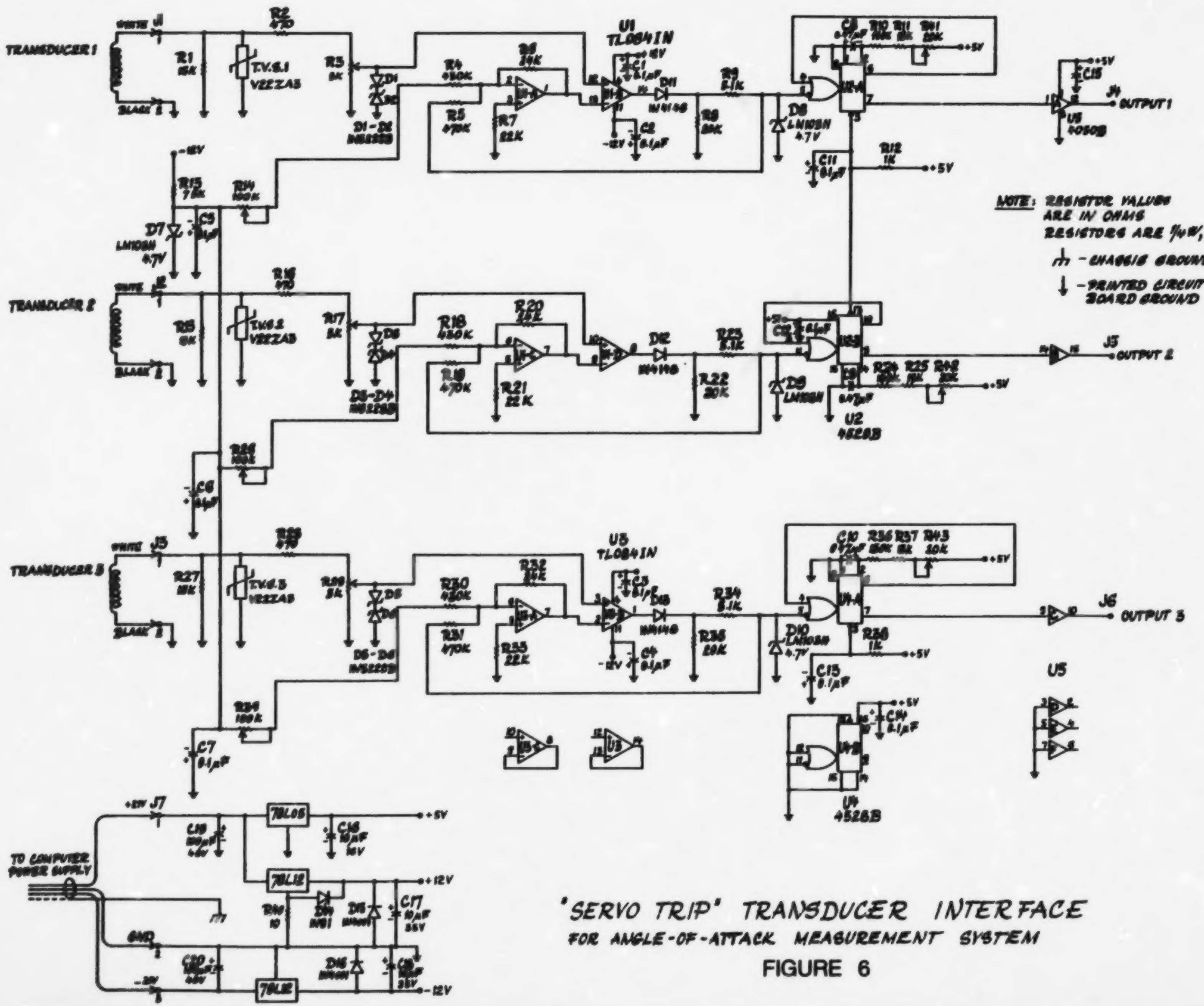
TRANSDUCER 1
TRANSDUCER 2
TRANSDUCER 3
WHITE
BLACK
J1
J2
J3
J4
J5
J6
J7
R1 15K
R2 470
R3 5K
T.V.S.1 V22ZA3
T.V.S.2 V22ZA3
T.V.S.3 V22ZA3
D1-D2 1N5225B
D3-D4 1N5225B
D5-D6 1N5225B
R4 430K
R5 470K
R6 24K
R7 22K
U1 TL084IN
C1 0.1µF
C2 0.1µF
D11 1N4148
R8 20K
R9 5.1K
D8 LM103H 4.7V
U2 4528B
U4 4528B
U5 4050B
R12 1K
C11 0.1µF
+5V
-12V
+12V
R15 7.5K
R14 100K
D7 LM103H 4.7V
C5 0.1µF
R16 470
R17 5K
R18 430K
R19 470K
R20 24K
R21 22K
D12 1N4148
R23 5.1K
R22 20K
D9 LM103H
R26
C6 0.1µF
R28 470
R27 15K
R29 5K
R30 430K
R31 470K
R32 24K
R33 22K
U3 TL084IN
C3 0.1µF
C4 0.1µF
D13 1N4148
R34 5.1K
R35 20K
D10 LM103H 4.7V
C10 0.47µF
R36 150K
R37 5K
R43 20K
R38 1K
C13 0.1µF
C14 0.1µF
R39 100K
C7 0.1µF
C15
OUTPUT 1
OUTPUT 2
OUTPUT 3
NOTE: RESISTOR VALUES ARE IN OHMS
RESISTORS ARE ¼W, 5%
- CHASSIS GROUND
- PRINTED CIRCUIT BOARD GROUND
TO COMPUTER POWER SUPPLY
+15V
GND
-15V
78L05
78L12
79L12
C16 10µF 16V
C17 10µF 35V
C19 100µF 40V
C20 100µF 40V
R40 10
D14 1N914
D15
D16

'SERVO TRIP' TRANSDUCER INTERFACE
FOR ANGLE-OF-ATTACK MEASUREMENT SYSTEM
FIGURE 6

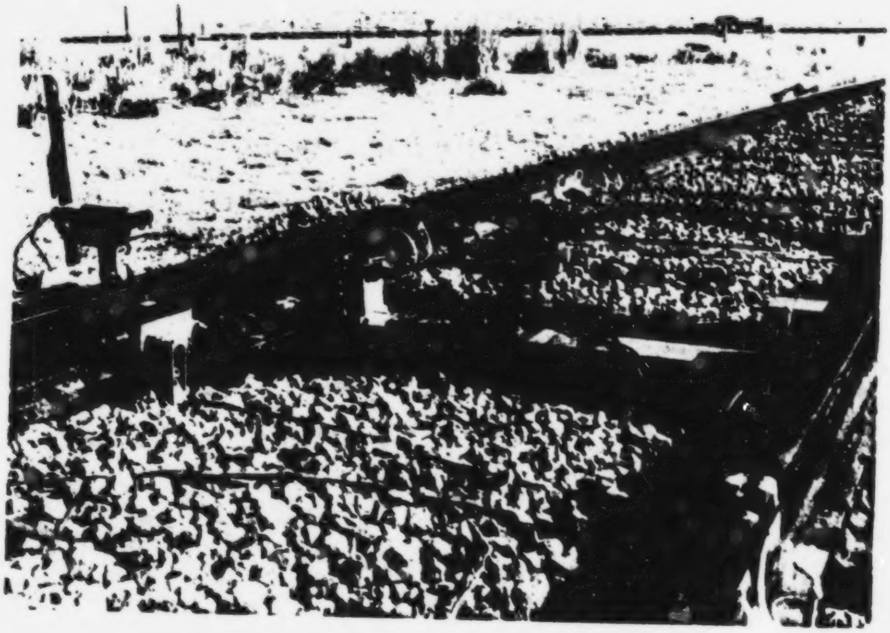

FIELD TEST 3 SET-UP

FIGURE 7

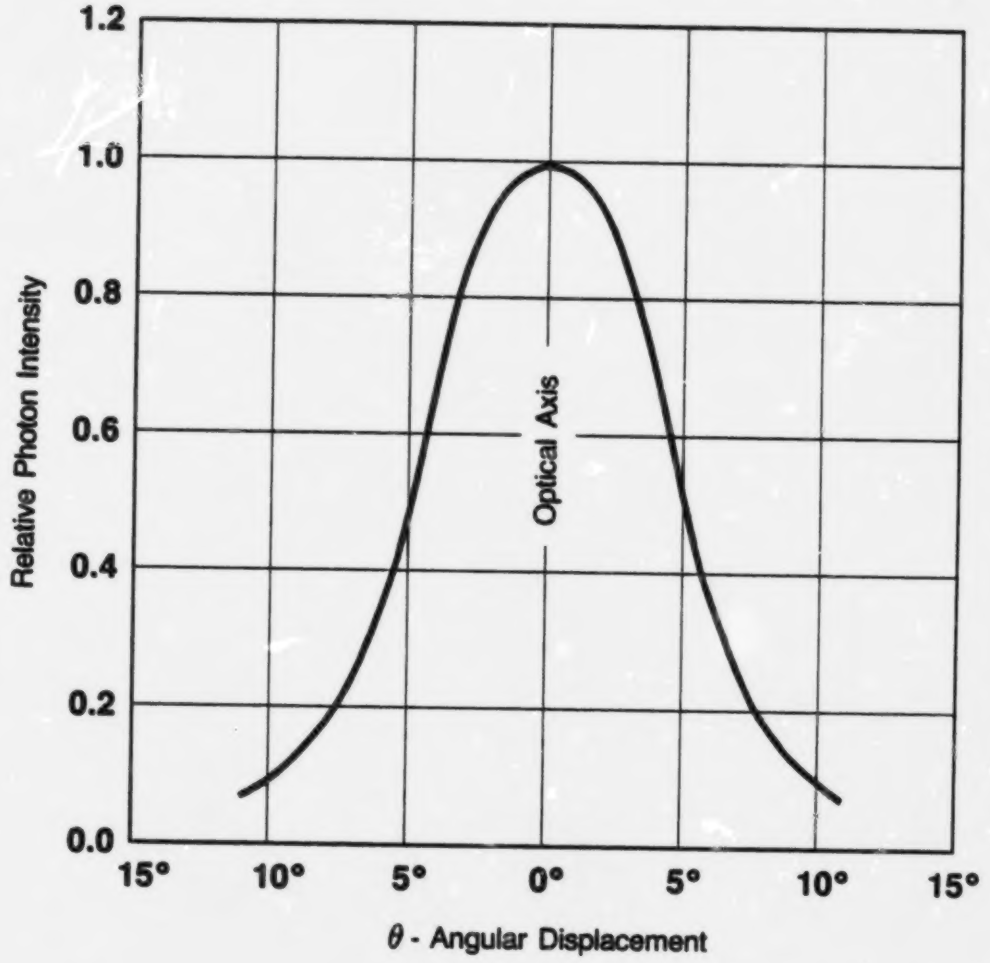

RELATIVE RADIANT INTENSITY
VS
ANGULAR DISPLACEMENT

FIGURE 8

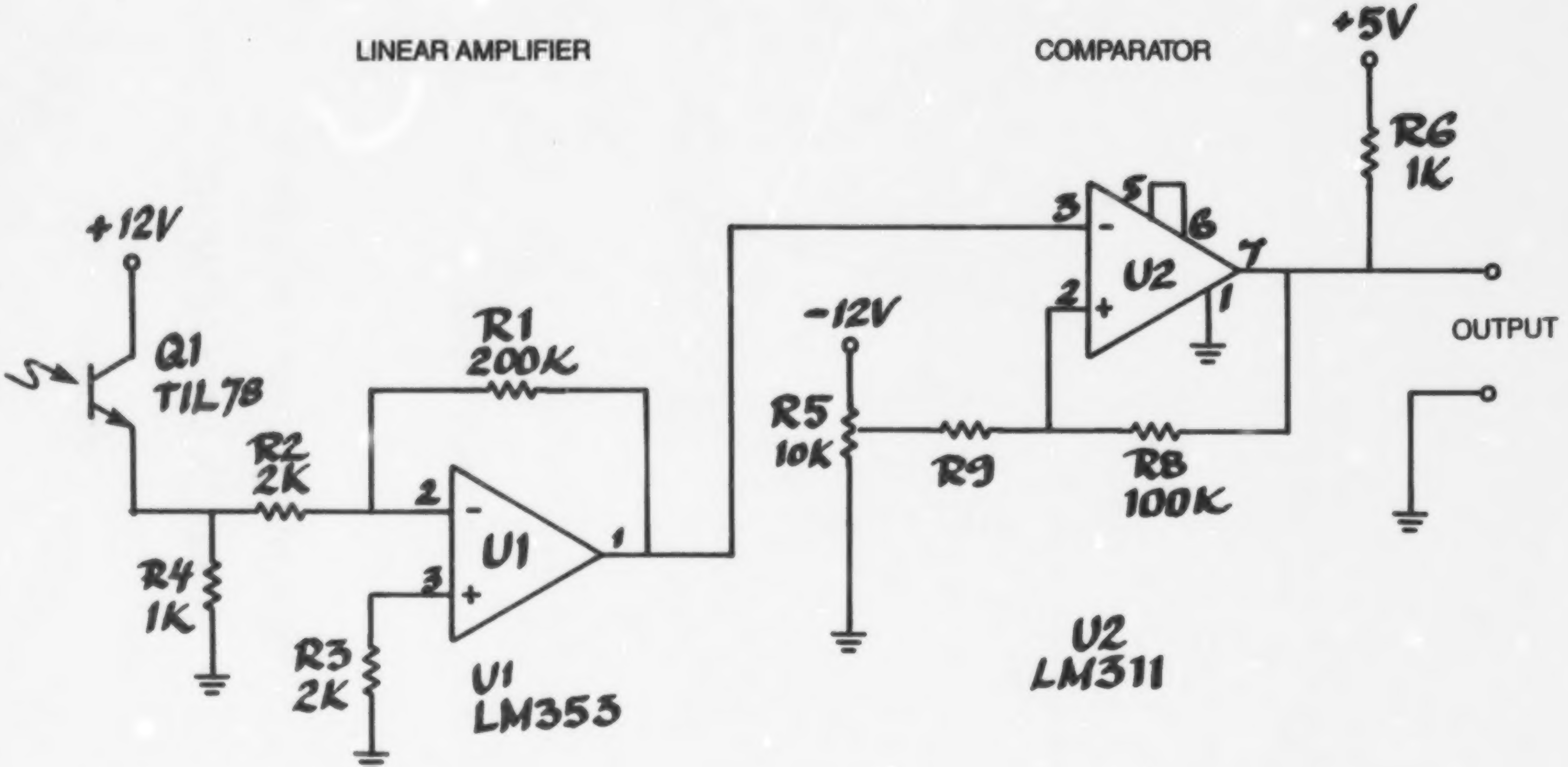
LINEAR AMPLIFIER
COMPARATOR
+12V
Q1
TIL78
R4
1K
R2
2K
R3
2K
R1
200K
2
3
1
U1
U1
LM353
-12V
R5
10K
R9
R8
100K
3
5
6
7
2
1
U2
U2
LM311
+5V
R6
1K
OUTPUT

PHOTOSENSOR SIGNAL CONDITIONER
FIGURE 9

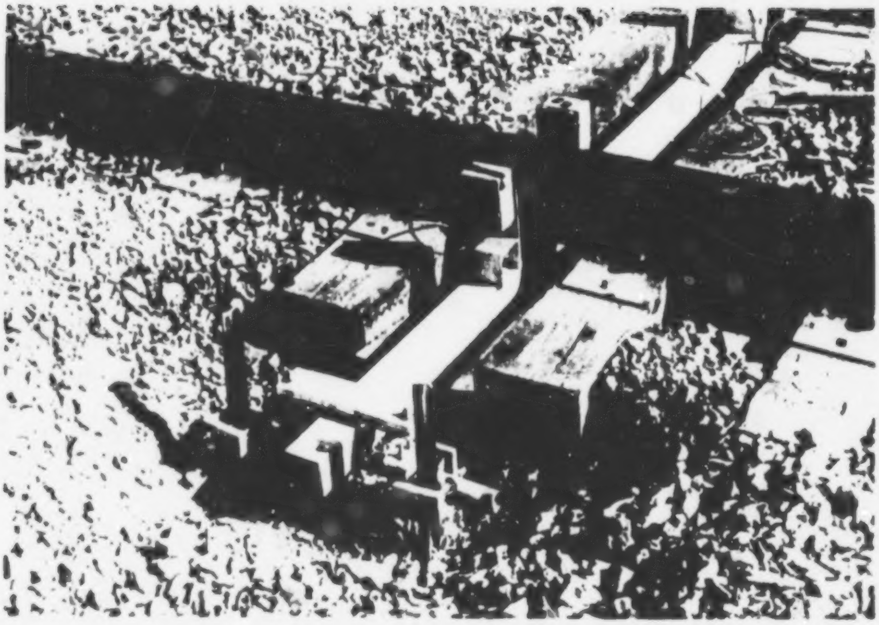

MOUNTING BRACKET FOR SUPPORT CHANNEL

FIGURE 10

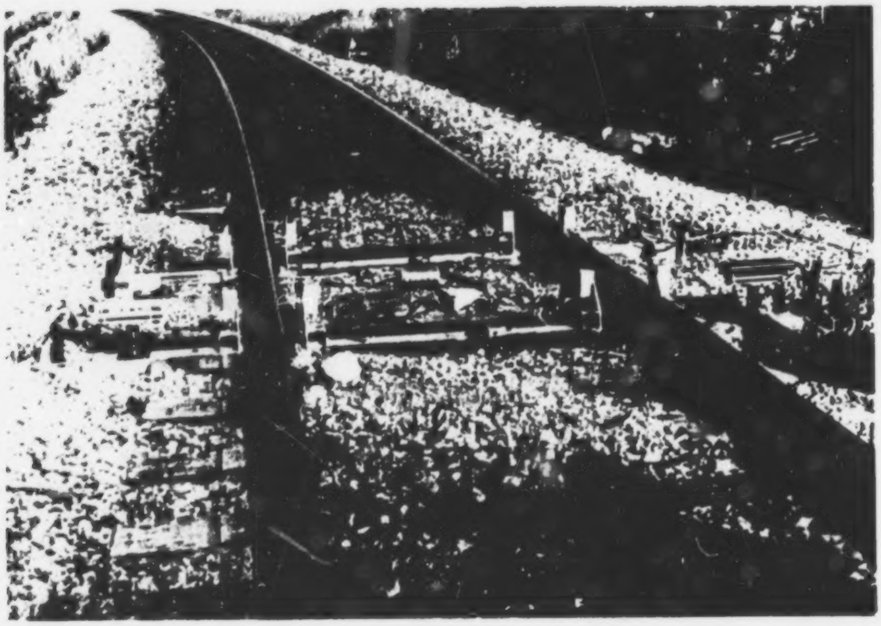

IRLED BASED AAMS FIELD TEST SET-UP

FIGURE 11

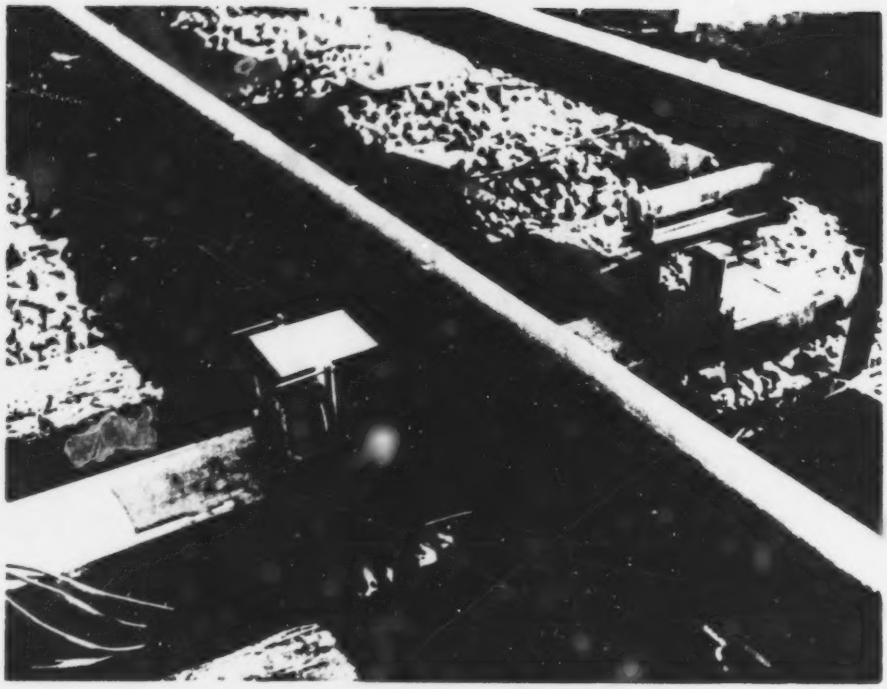

LINE SCAN CAMERA AND TARGET ARRANGEMENT

FIGURE 12

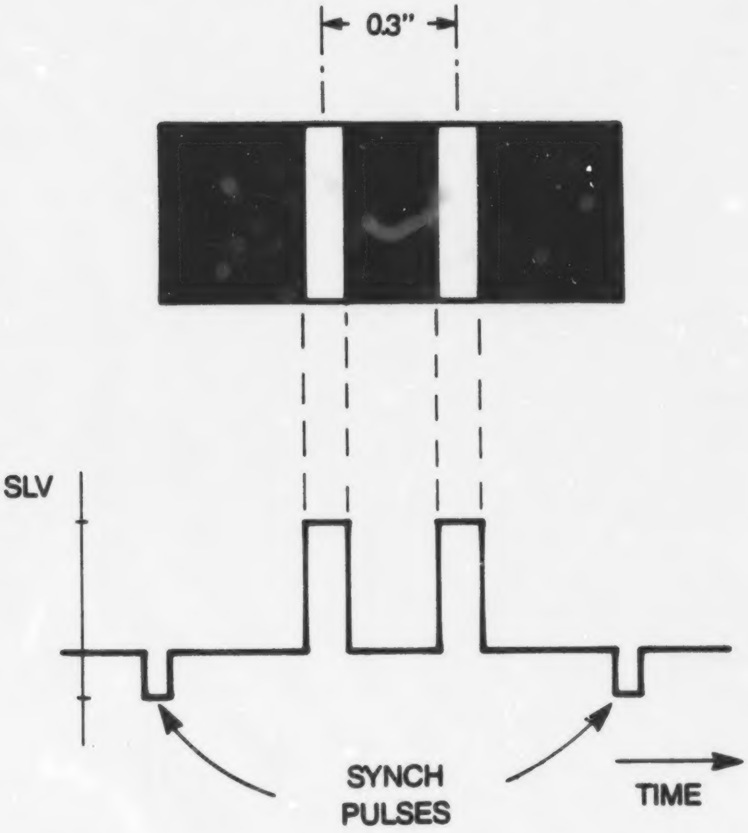
0.3"
SLV
SYNCH
PULSES
TIME

LINE SCAN CAMERA OUTPUT SIGNAL
WHEN FOCUSED ON TARGET
FIGURE 13

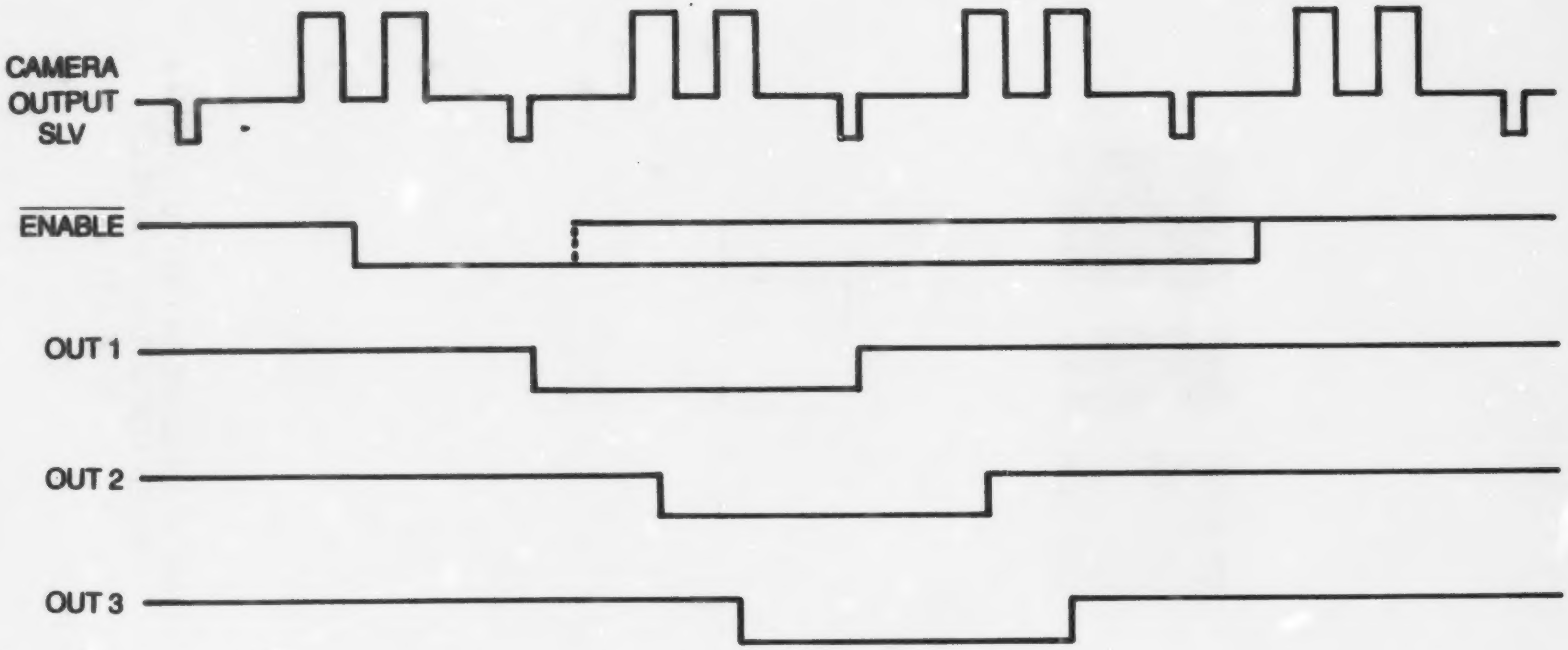
CAMERA
OUTPUT
SLV
ENABLE
OUT 1
OUT 2
OUT 3

LINE SCAN CAMERA INTERFACE OUTPUT SIGNALS

FIGURE 14

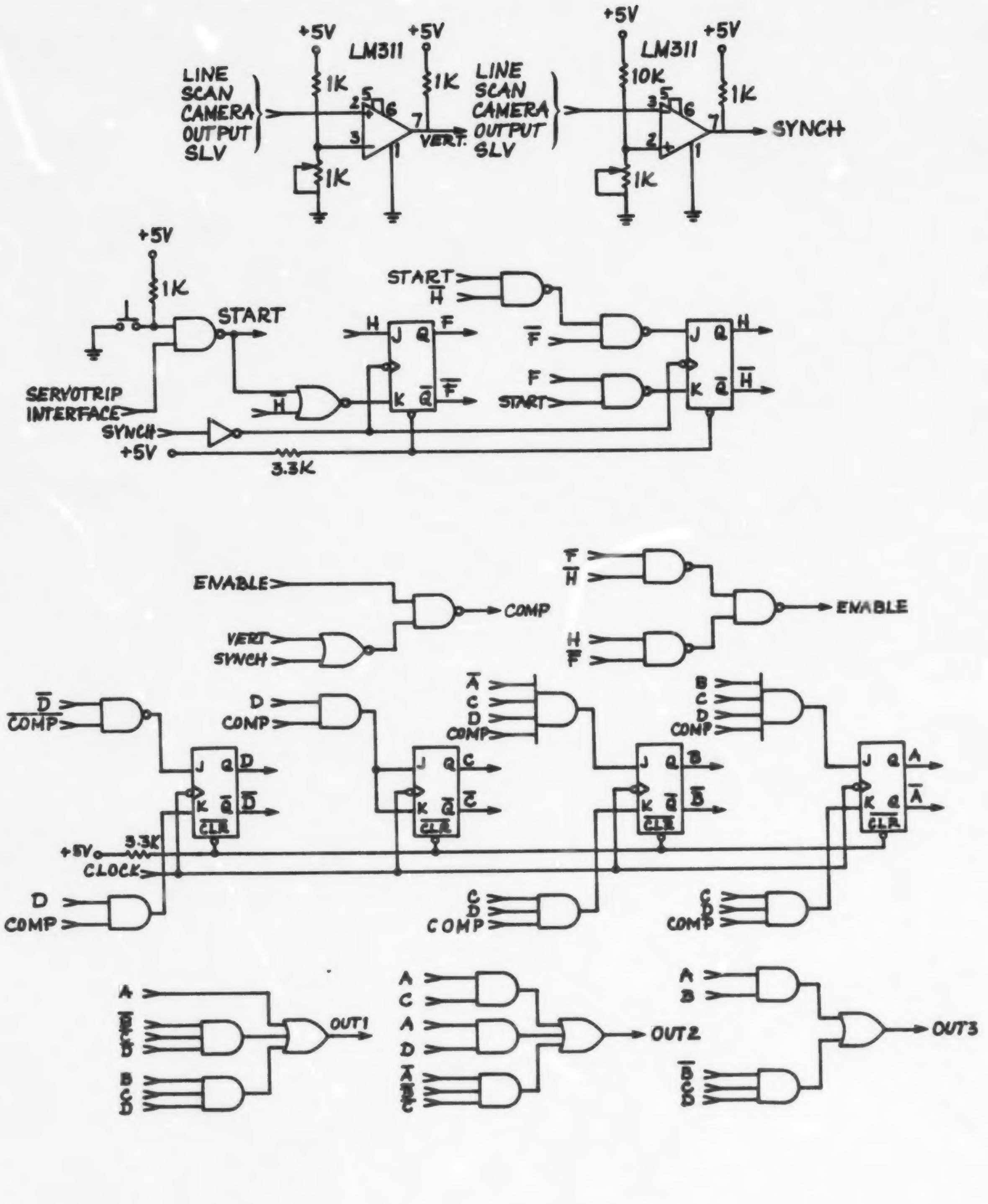
+5V
LM311
1K
LINE SCAN CAMERA OUTPUT SLV
VERT.
10K
SYNCH
+5V
1K
START
SERVOTRIP INTERFACE
SYNCH
+5V
3.3K
H
J Q F
K Q̄ F̄
START
H̄
F̄
F
J Q H
K Q̄ H̄
ENABLE
VERT
SYNCH
COMP
F
H̄
H
F̄
ENABLE
D̄
COMP
D
COMP
Ā
C
D
COMP
B
C
D
COMP
J Q D
K Q̄ D̄
CLR
J Q C
K Q̄ C̄
J Q B
K Q̄ B̄
J Q A
K Q̄ Ā
+5V
3.3K
CLOCK
D
COMP
C
D
COMP
C
D
COMP
A
B̄
C
D
B
C
D
OUT1
A
C
A
D
Ā
B̄
C̄
OUT2
A
B
B̄
C
D
OUT3

LINE SCAN CAMERA INTERFACE
FIGURE 15

RAIL STRESSES DEVELOPED DUE TO LIVE LOADS -- PRELIMINARY RESULTS

M. Shaw
P.C. Ireland
Planning and Research Department
Canadian Pacific Limited
Montreal

SUMMARY

Strain gauges are routinely attached to rails by the Planning and Research Department to measure the vertical and lateral wheel/rail forces of passing vehicles. The existing gauge orientations and locations and signal processing circuitry are adequate for some cases, but not for others. Two particular problems are the cross-talk, or interdependence, of the lateral and vertical signals, and the inability to accurately detect high speed signals due, for example, to wheelflat impacts.

As a first step in developing an alternate, more reliable load measuring circuit, strain gauge rosettes were attached to a rail on the Vaudreuil Subdivision in October, 1984. A locomotive passed over the strain gauged section of rail at speeds ranging from 1 to 40 mph, while the strain signals were recorded on a tape recorder.

An analysis of the data, considered in conjunction with the output from a finite element program, yielded a potential circuit which may be capable of measuring high speed vertical loads. The influence of lateral loads were not dealt with in this report. Additional work, both experimental and theoretical, is required.

SOMMAIRE

Au cours des essais normaux, le bureau de planification et de recherche utilise parfois des jauges d'extensometrie pour mesurer les forces roue-rail dues au passage de véhicules. Les positions des jauges ainsi que le circuit électrique de traitement de signaux dont on se sert ne sont pas adéquats ou suffisants pour toutes les mesures désirées. Deux problèmes particuliers sont: la sensibilité transversale des signaux verticaux et latéraux, et la détection impossible des signaux rapides causés par l'impact de méplats de roue.

Le point de départ fut le dévelopement d'un circuit électrique composé de rosettes. Celles-ci furent posées au mois d'octobre 1984 sur un rail dans la subdivision Vaudreuil. Par la suite, les signaux de déformation furent enregistrés sur magnétophone pendant qu'une locomotive passait à une vitesse de 1 à 40 mi/h sur la section du rail où se trouvaient les jauges.

Un circuit prometteur pour la mesure de forces verticales rapides a été obtenu suite à l'analyse des données de l'essai et des résultats d'une étude d'éléments finis. Cependant, l'influence des charges latérales sur le circuit n'a pas été considerée dans ce rapport. Des travaux théoriques et expérimentaux supplémentaires sont requis.

TABLE OF CONTENTS

Page

SUMMARY 157

LIST OF FIGURES 160

LIST OF TABLES 161

1.0 INTRODUCTION 162

2.0 TEST PREPARATION AND SITE 162

3.0 TEST RESULTS 165

4.0 CONCLUSION 173

REFERENCES 175

LIST OF FIGURES

Figure		Page
1	Location of Rosettes Within the Tested Rail Crib	164
2	Output Traces for Rosette #2 at Test Speed 1 mph (Eastbound)	167
3	Sum of Gauges 4 and 6 for Test Speed 18 mph (Eastbound)	172
4	Sum of Gauges 4, 6, 10, and 12 for Test Speed 18 mph (Eastbound)	172

LIST OF TABLES

Table		Page
1	Principal Rail Stresses Developed at Rosette #2 for Test Speed = 1 mph	169
2	Principal Rail Stresses Developed at Rosette #2 for Test Speed = 30 mph	170

1.0 INTRODUCTION

The stresses developed within a rail due to passing loads have been investigated for some time. Their importance was realized by the Office of Research and Experiments of the International Union of Railways (O.R.E.) in 1969 while investigating ballast stresses resulting from traffic loads. Since then O.R.E., the National Research Council of Canada, and Batelle-Columbus have actively investigated these stresses. A result of these studies has been the base-chevron strain gauge patterns which are used extensively by our department in field tests where rail force measurements are necessary.

CP Research conducted a series of field tests during the mornings of October 15 and 16, 1984 to examine the stresses developed within a rail. The purpose of these tests was twofold:

i) to obtain strain gauge circuits having less crosstalk errors between vertical and lateral circuits, and also displaying more recording consistencies,

ii) to obtain potential strain gauge configurations for recording dynamic phenomena such as wheelflat impacts.

2.0 TEST PREPARATION AND SITE

Testing was conducted on the Vaudreuil Subdivision near mileage 18.9 in proximity to the Dorion passenger train station. The actual testing took place in the yard adjacent to this station. A total of four stacked rosettes, Micro-Measurements type WA-06-120WR-350, each made up of three 350 ohms strain gauges with active gauge lengths of 0.12 inches were bonded to the underside of a rail head. This instrumented section of rail was located within a crib having similar support conditions at either end, i.e. the surrounding ties and rail east and west of the crib appeared to be in good condition. The rosette configuration and their locations are shown in Figure 1.

The rosette configuration in Figure 1 shows the orientation of the three strain gauges which make up a stacked rosette. The numbering convention employed to identify the strain gauges is typified by rosette #1. Each rosette's gauges are numbered sequentially west to east and from one rosette to another. Following this logic, the i-th rosette is comprised of gauges numbered ((3*i)-2), ((3*i)-1), and (3*i). Following this convention, rosette #1 in Figure 1 consists of strain gauges G1, G2, and G3.

The locations along the rail were selected from the results of a finite element study. Summarily, the study was composed of varying the position of a statically applied vertical load on the head of a rail section located within a crib. Output from the stress analysis program was then used to plot stress isoclines along the crib length with changes in the location of the applied load. It could be seen from these graphs that the rail head underside was characterized by near-constant isoclines, even as the load was moved longitudinally. The sensitivity of this region to

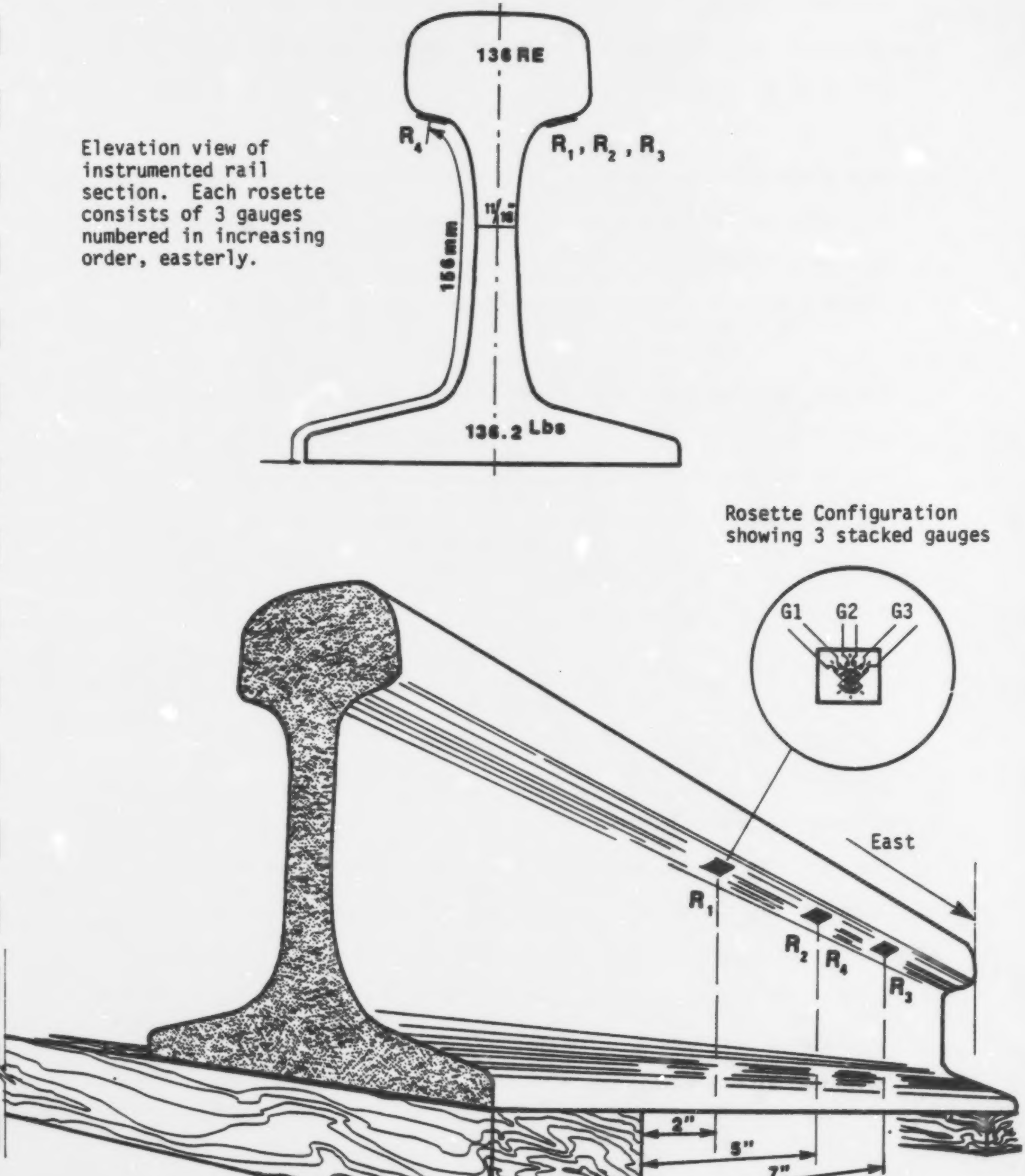
136 RE
R_4
R_1, R_2, R_3
11/16"
156mm
136.2 Lbs
G1
G2
G3
East
R_1
R_2
R_4
R_3
2"
5"
7"
℄

Elevation view of instrumented rail section. Each rosette consists of 3 gauges numbered in increasing order, easterly.

Rosette Configuration showing 3 stacked gauges

Figure 1

Location of Rosettes Within the Tested Rail Crib changes in the lateral location of the load could not be investigated with the model used. This stress ridge thus outlined the area for potential strain gauge sites.

Each gauge of the rosettes formed quarter bridges which were conditioned and amplified by Vishay 2100 Signal Conditioners. The twelve bridge outputs were recorded on a 14-channel Racal FM tape recorder and subsequently played out onto a Dash II strip chart recorder for analysis.

Loading tests were conducted on October 16. Static and dynamic loads were applied using the locomotive of the Cornwall Express, CP 4025. At the time of testing the locomotive had an average axle load of 67,900 pounds. Test runs were conducted at approximately <1, 5, 10, 15, 20, 30, and 40 mph in both eastward and westward directions. The test run of less than 1 mph is considered static for the purpose of comparing circuit outputs in the presence or absence of dynamic effects.

3.0 TEST RESULTS

A number of test objectives were thwarted during on-site preparation for the test. This resulted from the poor quality of rosettes which were unusually dry and brittle; gauges numbered 7 and 11 cracked during installation, gauge 2 failed to function properly prior to testing, and gauge 12 subsequently failed possibly due to breakage from rapid flexure at elevated test speeds. Consequently, no study of the stress fields developed along the rail could be done as this required calculating the principal stresses at several rosettes having three functional gauges — this eliminated rosettes 1, 3, and 4 which had each lost at least one strain gauge.

It has been observed however, that the strains recorded with the gauges of rosette #2 are similar to functional gauges of the other rosettes where the gauges have the same orientation with respect to the rail's longitudinal axis. The strains recorded with the 3 gauges of rosette #2 for the case of 1 mph are shown in Figure 2. The similarity just mentioned which exists between the traces of gauges of different rosettes indicates that a gauge's proximity to an end support does not significantly alter the stresses near a railhead. Since the rosettes are located far from the foot of the rail the influence of the reaction forces at the tie plates on the stress field in the rail head is minimal. Therefore, the choice of gauge sites is insensitive to support conditions. This is considered a key quality needed of strain gauge circuits for rail force evaluations.

The form of the traces of Figure 2 may be explained by visualizing the influences of the wheelset positions on the flexure of the rail. Initially, when wheelsets are near but not within the instrumented rail crib, the rail head experiences tensile bending stresses which result primarily from rail flexure. Eventually, these stresses give way to compressive bending stresses and localized contact stresses as the wheelset enters the crib area containing the gauges. The combination of these flexural and contact stresses result in erratic and rapidly fluctuating strains which are difficult to interpret.

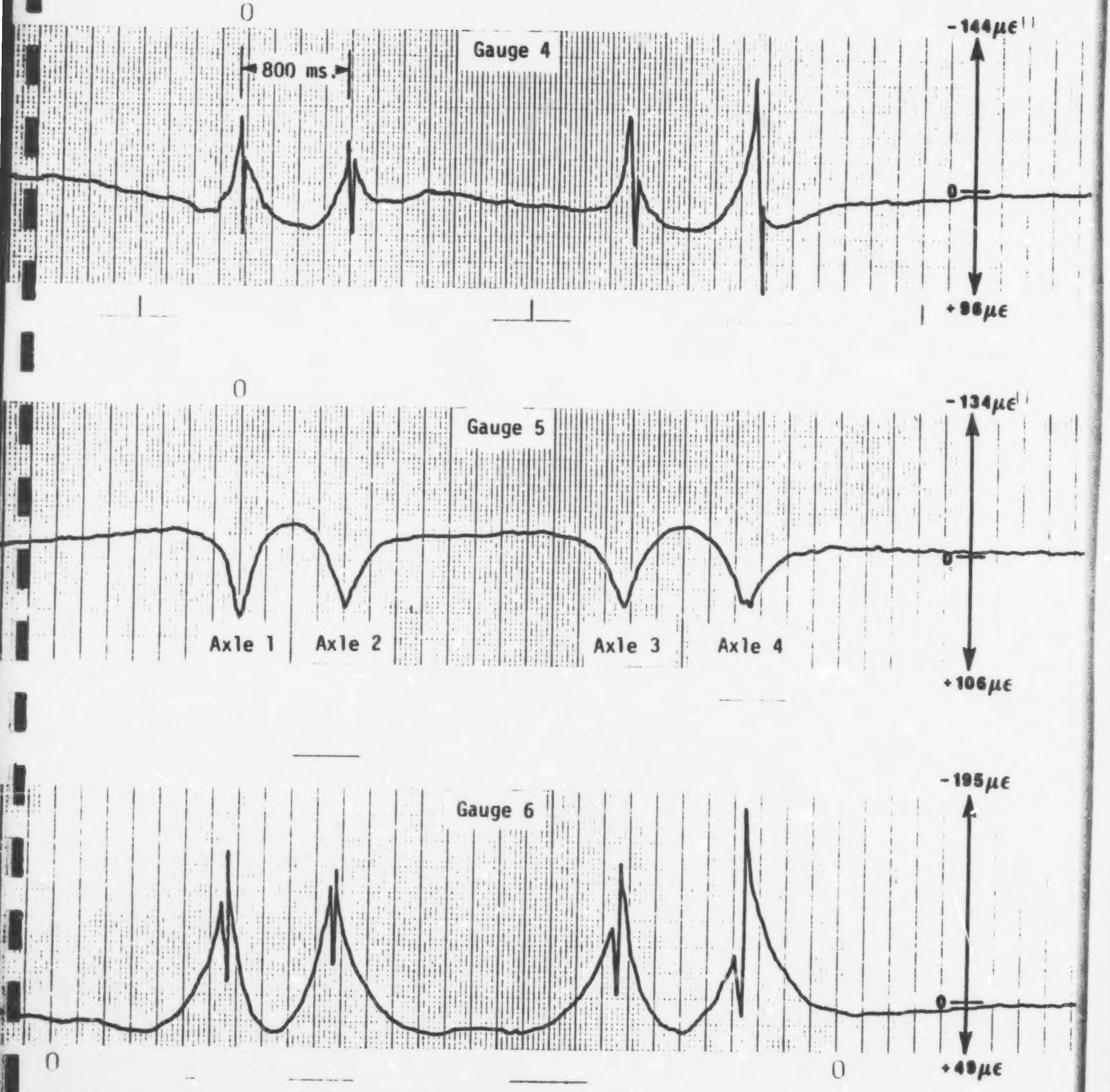

Figure 2
Output Traces for Rosette #2
at Test Speed 1 mph (eastbound)

If, for example, the stresses developed were simply flexural the expected traces would be inversely symmetrical about the origin and easier to analyze. The additional contact stresses introduce, unfortunately, an extra factor contributing to the stress field. Several different computer programs exist which can estimate these stresses.(2) From these programs it may be seen that the maximum subsurface shear stresses can easily exceed 100 ksi. These maximum values occur just below the surface of the rail head at depths of less than 0.03 inches. Unfortunately, the study of contact stresses concerns itself primarily with a small volume of the rail immediate to the contact patch not extending beyond a depth of 0.2 inches. Also, the underlying theories applied to calculating the contact stresses assume limited contact patch geometries, and approximate the rail by a semi-infinite plane. The latter assumption restricts any contact stress analysis to the region just below the rail head surface. It would be possible to calculate these stresses using a finite element program and a finely meshed model with numerous nodal points but the associated costs of such a study would be quite high. It has been noted however by British Rail Research(1) that railhead stresses are acutely dynamic with rise times and fluctuations between tensile and compressive stresses similar to those observed here.

To obtain a quantitative idea of the stresses developed, the traces of runs at 1 and 30 mph were digitized and evaluated using the output of gauges 4, 5, and 6. The data obtained is presented in Tables 1 and 2, respectively. The principal stresses occasionally exceed 6 or 7 ksi. It is worth noting that the finite element study done as preparation for this test calculated stresses in the order of 5 ksi. The agreement between

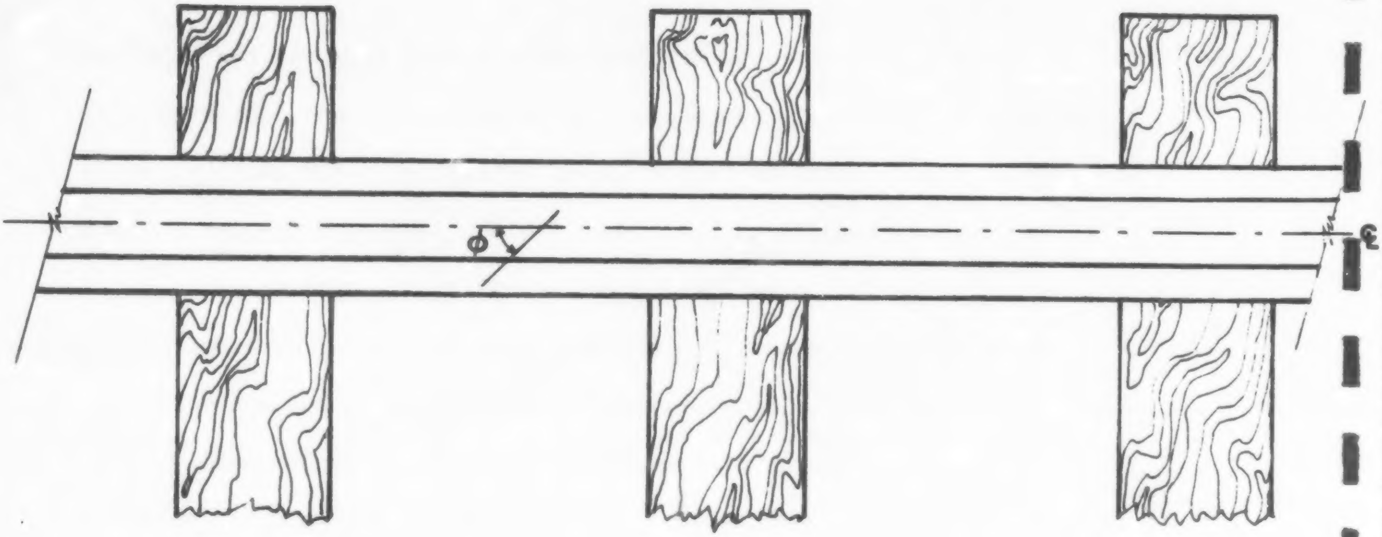

Table 1

(Test speed = 1 mph)

Time (ms)	Normal Stresses (psi)		ϕ (deg)[1]	Shear Stress (psi)
	maximum	minimum		maximum
-66	219.	-1157.	79.	688.
-43	308.	-2488.	83.	1398.
-20	235.	-4789.	85.	2512.
-13	257.	-5630.	89.	2944.
-8	71.	-6361.	49.	3216.
-6	114.	-6189.	56.	3151.
-5	140.	-5904.	52.	3022.
-4	371.	-5203.	53.	2787.
-1	1488.	-1069.	38.	1278.
0	2007.	391.	85.	807.
2	2817.	197.	59.	1310.
3	2584.	-1132.	61.	1858.
7	890.	-6731.	69.	3811.
8	751.	-7217.	70.	3984.
9	655.	-7433.	71.	4044.
12	544.	-7320.	73.	3932.
17	602.	-6648.	75.	3625.
22	577.	-5893.	76.	3235.
37	410.	-4996.	75.	2703.
52	684.	-3917.	73.	2301.
66	343.	-3471.	74.	1907.

(1) Angle ϕ represents the direction of maximum shear stress.

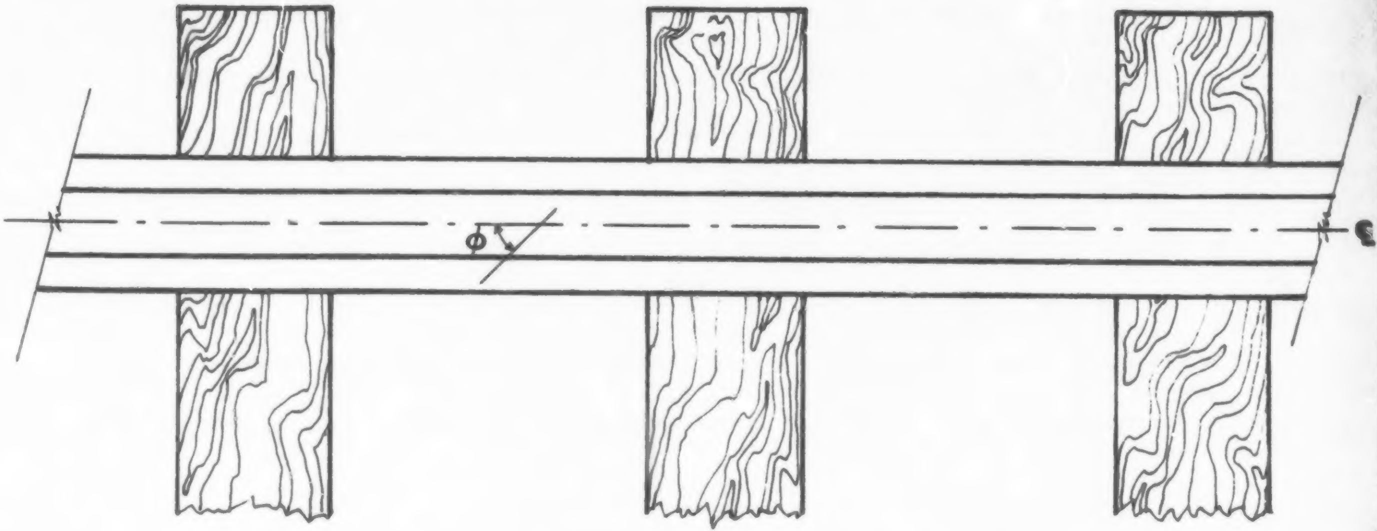

Table 2

(Test speed = 30 mph)

Time (ms)	Normal Stresses (psi) maximum	 minimum	φ (deg)(1)	Shear Stress (psi) maximum
-100	702.	26.	13.	337.
-90	819.	12.	27.	403.
-80	670	-46.	26.	358.
-70	598.	-287.	36.	442.
-60	610.	-404.	42.	507.
-50	756.	-655.	48.	705.
-40	716.	-1344.	59.	1030.
-30	645.	-1795.	61.	1220.
-20	463.	-2550.	65.	1506.
-10	1226.	-2898.	65.	2062.
0	-353.	-5744.	89.	2695.
10	153.	-3657.	5.	1905.
20	179.	-1829.	4.	1004.
30	143.	-560.	80.	352.
40	683.	44.	27.	319.
50	1275.	-27.	16.	651.
60	1873.	1.	9.	936.
70	2212.	-23.	7.	1117.
80	2361.	37.	5.	1161.
90	2569.	38.	4.	1265.
100	2569.	38.	4.	1265.

(1) Angle φ represents the direction of maximum shear stress.

the two values is surprisingly good considering the coarseness of the model used. Also notice that the principal stresses are not symmetric about the passage of the wheelset. This is due to the asymmetrical tractive forces applied to the rail by the locomotive traction motors as well as the flexural strains attributed to the influence of the leading and trailing axle loads. The stresses also appear quite different between the quasi-static 1 mph run and the 30 mph run. At elevated speeds the dynamic loading seems to greatly affect the principal stresses developed.

Given the loss of strain gauges prior to testing little can be said of the stress fields developed due to live loads. A positive result from the tests however are the traces obtained post-testing when several gauge outputs were summed. These traces have proven to be consistent over the range of test speeds and are void of the rapidly changing peaks and valleys obtained with individual gauge outputs.

Figure 3 shows a trace obtained by summing gauges 4 and 6. These gauges are analogous to gauges 1 and 3 at rosette #1 but are located at rosette #2. This trace was produced using data from the 18 mph test speed and is representative of the traces for the range of test speeds. By comparison, Figure 4 is the sum of gauges 4, 6, 10, and 12 for the same 18 mph test speed. Once again the traces of this summation for other test speeds are similar.

These two traces are notably cleaner and smoother than the traces of Figure 2. Figures 3 and 4 are also symmetric about the valleys which represent the point in time when the wheelset is immediately above the

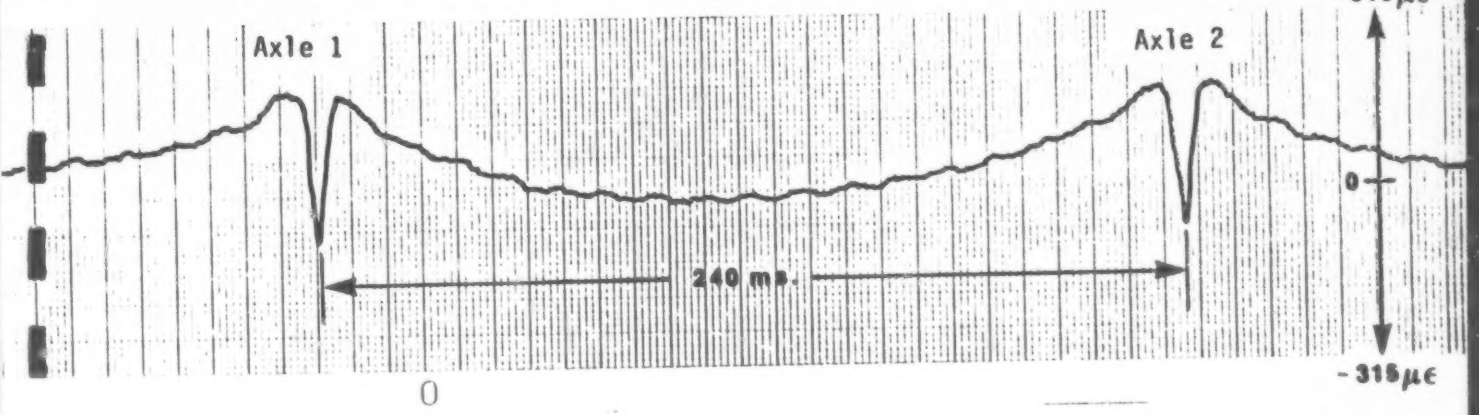

Figure 3
Sum of Gauges 4 and 6 for 18 mph (eastbound)

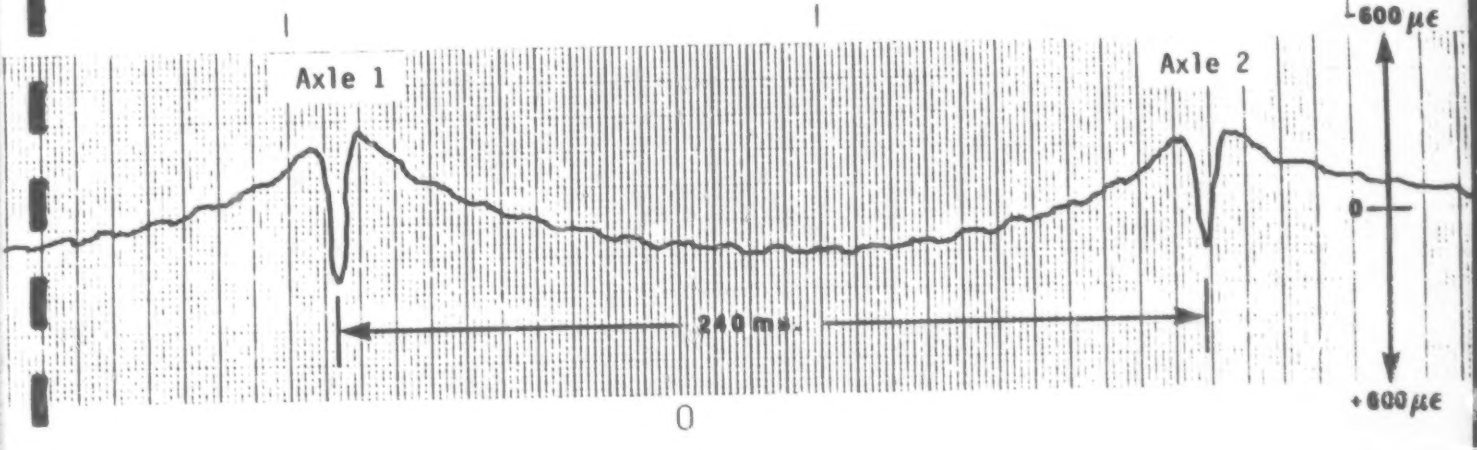

Figure 4
Sum of Gauges 4,6,10 and 12
for 18 mph (eastbound)

rosettes. The outputs of gauges 4, 5, and 6 lack this symmetry. Notice however that the full scale value of Figure 4 is not twice that of Figure 3, 1200 microstrain as compared to 660 microstrain. This slight difference may be explained by the strain contributions due to lateral rail flexure. Referring to Figures 1 and 3 it can be seen that the sum of gauges 4 and 6 located at rosette 2 would result in an output produced by vertical and lateral rail flexures. The lateral rail flexure creates tensile strains in the gauges. A similar observation can be made with respect to Figure 4 showing the sum of gauges 4, 6, 10, and 12. Notice however that gauge pairs 4, 6 and 10, 12 each belong to rosettes which are located on opposite sides of the rail (Ref. rosettes 2 and 4 in Figure 1). While lateral rail flexure continues to create tensile strains in gauges 4 and 6 it also produces compressive strains in gauges 10 and 12. Summing these four gauges thus produces an output potentially void of lateral influences having a somewhat lower signal than twice the output of gauge 4 added to gauge 6.

4.0 CONCLUSIONS

The investigative nature of this study has lead to several interesting points.

Firstly, the circuit created post-testing by summing gauges 4, 6, 10, and 12 has significant potential for future field tests. Further testing must be done, however, to analyze its characteristics vis-a-vis linearity to applied loads, and sensitivity to cross-talk. Also, it is hypothesized that since gauges of different rosettes yet having similar orientations produced similar traces, the circuit's output is independent of the gauges' longitudinal position within the rail crib provided the gauges act on a common vertical plane through the rail.

Secondly, it has been shown in another study (1) that impact loads such as those due to wheelflats may be detected and quantified using strain gauge positions similar to those employed in this test. Another potential application could be detecting skidding wheels which result from stuck brakes, or hand brakes left applied. This could lead to potential wayside systems to record such conditions.

Lastly, the strains recorded are highly localized due to the positioning of the rosettes. Future studies to chart the stress fields along a rail must consist of rosettes and/or strain gauges in a number of different locations along the rail's profile and towards the ties to plot a more global picture of stress propogation through a rail.

REFERENCES

1. Cannon, D.F., and Sharpe, K.A., "Wheel Flats and Rail Fracture", Paper presented at British Rail/A.A.R. Organized Seminar, Nottingham University, September, 1981.

2. Pak, W., "Manual for Three Dimensional Sub-Surface Contact Stress Analysis Program for Wheel/Rail Interaction", CP Report No. S-659-80, October, 1980.

A BATTERY POWERED DATA LOGGER AND ACQUISITION SYSTEM FOR RAIL/WHEEL PROFILE MEASUREMENTS

H. Soares
H. Schrekinger
L. Feiter
Planning and Research Department
Canadian Pacific Limited
Montreal

EXECUTIVE SUMMARY

The Planning and Research Department has been involved with several studies requiring accurate measurements of rail and wheel profiles. In 1981, a microprocessor based rail/wheel profilometer system was developed. After extensive field testing, this profilometer proved to be an accurate and reliable method of obtaining data.

In the case of rail measurements it was necessary to carry a generator to each test site in order to supply power to the unit. This required more track time, as well as manpower. Also, under conditions of direct sunlight, the display was difficult to read. With wheel measurements, profiles were usually taken at shop tracks where AC power was readily available.

As a result of the success of this device in the field and a foreseeable increase of its use in future studies, it was decided that a portable battery-powered data acquisition and logger should be developed so as to optimize the process of rail measurements.

It was decided to base the system on the standard STD bus architecture. The STD bus is an 8-bit microprocessor bus standard for modular card approaches in system configurations. The data logger will be implemented using only low-powered CMOS (complementary metal-oxide semiconductor) technology.

The computer implements the CMOS Z-80 microprocessor for two main reasons. The first reason is that the existing software is based on the Z-80 micro and therefore the new system would require less software overhead; secondly, the Z-80 offers the Mode 2 interrupt feature which other processors do not.

A more detailed description of both hardware and software is available with the Planning and Research Department.

SOMMAIRE

Le Bureau de planification et de recherche du Canadien Pacifique Ltée a entrepris plusieurs études nécessitant des mesures précises de profils de rails et de roues. Un profilomètre utilisant la technologie de microprocesseur fut développé en 1981. Des essais in situ approfondis de profilomètre ont demontré que ce système est précis et fiable.

Dans le cas de mesure de rails, il est nécessaire de transporter une géneratrice à chaque point de mesure afin d'alimenter le système. Ceci exige plus de main-d'oeuvre et un intervalle de circulation plus long. L'affichage numérique de l'enregistreur/totalisateur est difficile à lire lorsqu'il est directement éclairé par le soleil. Les profils de roues sont généralement mesurés aux ateliers où le courant alternatif 120 V est disponible.

A cause de son succès et d'une utilisation accrue prévue pour ce système, il a été décidé qu'un enregistreur/totalisateur portatif fonctionnant sur piles soit développé afin d'optimiser le procédé de mesure de profil de rail.

Il a été décidé de baser le système sur l'architecture bus STD. Ce bus est conçu pour des systèmes modulaires basés sur des microprocesseurs 8 bits. L'enregistreur/totalisateur utilisera uniquement des circuits intégrés CMOS afin de réduire la consommation de courant.

Le microprocesseur choisi est le Z-80. Il fut selectionné pour deux raisons. Premièrement, le logiciel actuel est écrit pour le Z-80,

donc le nouveau logiciel nécessitera moins de modifications. Deuxièment, seulement le Z-80 est capable d'interruption en mode 2.

Une description détaillée des circuits électroniques et du logiciel est disponible au Bureau de planification et de recherche.

TABLE OF CONTENTS

PAGE

EXECUTIVE SUMMARY 177

LIST OF FIGURES 184

1.0 INTRODUCTION 186

2.0 SCOPE 188

3.0 SPECIFICATIONS OF BATTERY POWERED DATA ACQUISITION AND LOGGER 189

4.0 MICROPROCESSOR BOARD 192

5.0 DATA ACQUISITION 195

- 5.1 Purpose of the Analog-to-Digital Converter Board 195
- 5.2 Features of the A/D Board 195
- 5.3 Channel Assignment of the A/D Board 197

6.0 DATA LOGGING 199

- 6.1 Purpose of the Cassette Transport Interface Board 199
- 6.2 Functional Description of the Cassette Controller 201
- 6.3 Manchester Phase Encoder 201
- 6.4 Adaptive Decoder 205
- 6.5 Cassette Transport Control and Monitoring 210
- 6.6 Cassette Transport 210
- 6.7 Record Formatting 211
- 6.8 Programming the Cassette Controller Board 212

7.0 PERIPHERAL INTERFACING 214

- 7.1 Purpose of the Input-Output Interface Board 214
- 7.2 Features of the I/O Board 214
- 7.3 Functional Description of Parallel I/O 216
- 7.4 Functional Description of Serial I/O 217
- 7.5 Programming the Peripheral I/O Board 220

8.0 KEYPAD AND DISPLAY INTERFACING 221

- 8.1 Purpose of the Keypad and Display Board 221
- 8.2 Functional Description of the Keypad and Display Board 221
- 8.3 The LCD Module 223
- 8.4 Programming the Keypad/Display Board 223

TABLE OF CONTENTS (Contd.)

PAGE

9.0 COUNTER-TIMER AND BUS EXTENDER BOARD 226

- 9.1 Purpose of the Counter/Timer Board 226
- 9.2 Features of the Counter/Timer Board 226
- 9.3 Programming the C/T Board 228

10.0 VIDEO INTERFACE MODULE 229

- 10.1 Purpose of the Video Interface Module 229
- 10.2 Video Board 229
- 10.3 Interface Circuitry 231

11.0 POWER SUPPLY AND BATTERY CHARGER 232

- 11.1 Features of the Power Supply 232
- 11.2 Specifications 233
- 11.3 Power Requirements of System 234
- 11.4 Functional Description 236

12.0 WIRING LAYOUT/RELAY INTERFACE MODULE 238

13.0 SOFTWARE DESCRIPTION 239

- 13.1 Keyboard Assignments 239
- 13.2 Monitors 241
  - 13.2.1 E-Mode Monitor 241
  - 13.2.2 A-Mode Monitor 244
  - 13.2.3 B-Mode Monitor 248
  - 13.2.4 D-Mode Monitor 250
- 13.3 Allocation of Data in RAM Memory 256
- 13.4 Storage of Data on Tape 257
- 13.5 Transmission of Data 258

14.0 CONCLUSION 259

REFERENCES/BIBLIOGRAPHY 261

TABLE OF CONTENTS (Contd.)

PAGE

APPENDICES

1. STD BUS AND INTERRUPT PRIORITY DAISY CHAINING 262
2. Z-80 PROCESSOR CARD 266
3. A/D CONVERTER CARD 270
4. CASSETTE CONTROLLER BORAD AND TRANSPORT 272
5. INPUT-OUTPUT PERIPHERAL BOARD 277
6. KEYPAD/DISPLAY BOARD 285
7. COUNTER/TIMER BOARD 288
8. VIDEO GRAPHICS MODULE 294
9. POWER SUPPLY 298
10. WIRING LAYOUT/RELAY MODULE 301

LIST OF FIGURES

FIGURE NO.	DESCRIPTION	PAGE
1	Block Diagram of Battery Powered Data Acquisition and Logger	187
2	Block Diagram of CMOS Z-80 Processor Card	193
3	Jumper Functions of Processor Card	194
4	Block Diagram of the A/D Board	196
5	Channel Assignment of the A/D Converter	197
6	Addressing of the A/D Board	198
7	Block Diagram of Data Flow for Cassette Transport System	200
8	Block Diagram of Cassette Controller Board	202
9	Manchester Phase Encoding Using ANSI Rules	203
10	Manchester Phase Encoder Circuit	204
11	Timing Diagram for Phase Encoding Circuit	206
12	Adaptive Decoder	208
13	Timing Diagram of Adaptive Decoder	209
14	Addressing Scheme of the Cassette Controller Board	212
15	Programming the Cassette Control Port Operation	213
16	Reading the Cassette Control Port Status	213
17	Block Diagram of Input-Output Peripheral Board	215
18	Port Assignment of the PIO Device	216
19	RS-232C Transmitter and Receiver	218
20	RS-232C Pin Assignment for the I/O Board	219
21	Addressing Scheme of the I/O Board	220

LIST OF FIGURES (Contd.)

FIGURE NO.	DESCRIPTION	PAGE
22	Block Diagram of Keypad/Display Board	222
23	Addressing Scheme of Display Module	224
24	Instruction Table for LCD Module	225
25	Block Diagram of Counter-Timer Board	227
26	Addressing of the Counter-Timer Board	228
27	Block Diagram of Video Interface Module	230
28	Timing Control Logic of STD to S-100 Bus	231
29	Breakdown of Current Requirements of Battery Data Logger	235
30	Breakdown of Current Consumption of Power Supply/Charger	236
31	Power Supply/Charger Block Diagram	237
32	Keyboard Assignments	240
33	E-Mode Logic	245
34	A-Mode Logic	247
35	B-Mode Logic	251
36	D-Mode Logic	252
37	Allocation of Data in RAM Memory	253

1.0 INTRODUCTION

The battery-powered data acquisition and logging system is a microprocessor based instrument which monitors and records in a digital format, the X-Y displacement of a probe along a wheel or rail surface profile. In order to accomplish this process, analog signals from dc potentiometers must be first digitized through an analog-to-digital converter and then recorded in a digitally encoded format on to a mini cassette.

In general, this instrument is responsible for three basic functions: data acquisition, data logging, and monitoring of operations. Figure 1 is a block diagram which illustrates the system architecture. The battery data acquisition and logger consists basically of six boards, a power supply, a tape transport, and a video module. The operator has access to the system by means of a keypad and dedicated switches and can monitor the process of data acquisition and logging by means of a sunlight readable liquid crystal alphanumeric display.

After retrieval of data, analysis can be accomplished by means of a development system. All the data acquired during field work can be downloaded automatically from the battery data logger into the development system via an RS-232 communication link.

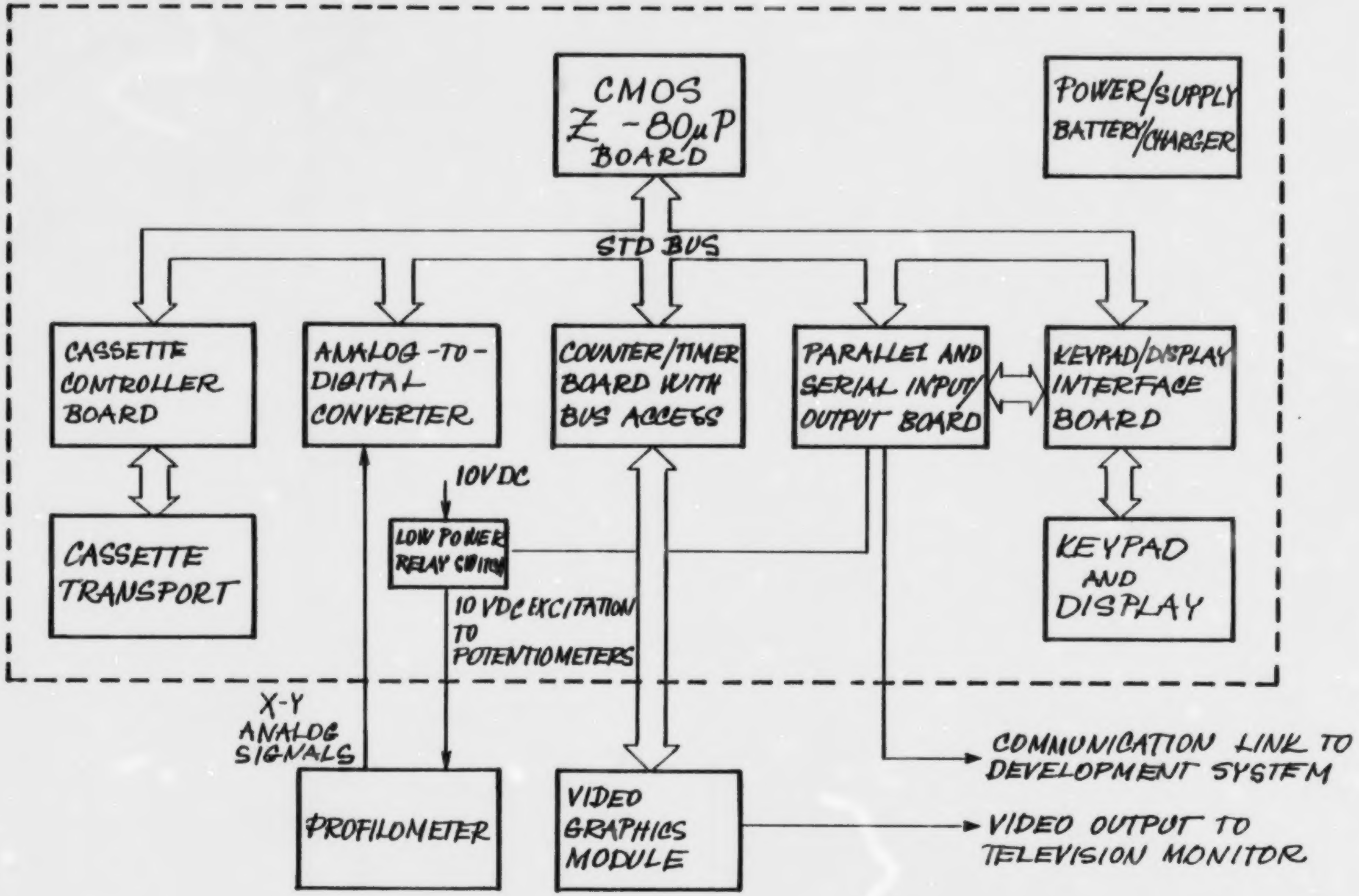
CMOS
Z-80µP
BOARD
POWER/SUPPLY
BATTERY/CHARGER
STD BUS
CASSETTE CONTROLLER BOARD
ANALOG-TO-DIGITAL CONVERTER
COUNTER/TIMER BOARD WITH BUS ACCESS
PARALLEL AND SERIAL INPUT/OUTPUT BOARD
KEYPAD/DISPLAY INTERFACE BOARD
CASSETTE TRANSPORT
10VDC
LOW POWER RELAY SWITCH
10 VDC EXCITATION TO POTENTIOMETERS
KEYPAD AND DISPLAY
X-Y ANALOG SIGNALS
PROFILOMETER
VIDEO GRAPHICS MODULE
COMMUNICATION LINK TO DEVELOPMENT SYSTEM
VIDEO OUTPUT TO TELEVISION MONITOR

Figure 1: **BLOCK DIAGRAM OF BATTERY POWERED DATA ACQUISITION AND LOGGER**

2.0 SCOPE

This report describes a battery data logger and acquisition system. This unit is functional, in most respects, to a unit developed by the Planning and Research Department in the 1981/1982 period. There are four basic improvements featured with this unit - battery-powered, smaller size, readability of display in direct sunlight and operator-prompted messages.

It was decided that this unit should be low-powered CMOS, Z-80 microprocessor based and be compatible with any STD bus system. The STD bus was chosen because of its small board size and because of a multitude of support boards available on the market. Appendix 1 provides a description of the STD bus structure and pin assignment. Those boards which were application specific to the battery data logger were developed in-house; all others were purchased from manufacturing sources.

3.0 SPECIFICATIONS OF BATTERY POWERED DATA ACQUISITION AND LOGGER

Features

- rail/wheel profile measurements and logging unit
- enclosed in carry case
- low power battery operation (provision for 2 batteries, 12 hours operation)
- battery charging capability with LED indicator
- STD Bus modular card system
- Z-80 processor based
- 12-bit analog-to-digital conversions in 70 microseconds
- 16 digital input-output ports + handshaking lines
- serial communications port to printer or other computer
- counter/timer on-board
- display and keypad interfacing

- tape controller and transport
- liquid crystal display (LCD)
- video display output of unprocessed data on a regular television or monitor

Physical and Environmental Specifications

dimensions: 17"W x 11 1/2"D x 7 1/2"H
weight: approx. 15 lbs. (one battery)
operating temp.: 10 degrees Celsius to 45 degrees Celsius (limits on tape transport media)
storage temp.: -20 degrees to 60 degrees Celsius (limits on LCD)
operating rel. humidity: 20% to 80% (limits on tape transport media)
storage rel. humidity: 0% to 90% (limits on tape transport media)

Electrical Specifications

operating voltage: 100-170 VAC, 60 Hz
battery operation: 12 volts (1 battery at 5AH for 6 hours operation)
power supply: +5VDC + .2% up to 5 amps
+12VDC + .2% up to +40mA
+10VDC +2mV, 0.01% regulation, 15mA output 25 degrees celsius

power requirements: 0.3 amps max during standby (3.6 watts)
0.4 amps max during measurements (4.8 watts)
1.1 amps max during rewind of tape (13.2 watts)
battery charging: 1.2 amps (1 battery, 5AH)
2.2 amps (2 batteries, 5AH ea.)
charging time: approx. 10 hrs. for fully discharged battery

Data Storage

medium: mini cassette tapes
length: 50-foot length tapes
capacity: 90K bytes both sides
40 wheel profiles total
52 rail profiles total

Operator Interaction

display: 2 lines x 16 characters liquid crystal sunlight readable
keyboard: 16 keys + 7 dedicated function keys

Measurement Time

wheel: approx. 8 minutes per profile (3 sides)
rail: approx. 2 minutes per profile (3 sides)

4.0 MICROPROCESSOR BOARD

The microprocessor board is a PRO-LOG Z-80 based CPU card implemented entirely in high-speed CMOS technology. The CPU board contains four 28 pin sockets which can accept either all 2K byte or all 8K byte RAM's or EPROM's. There are provisions on board to expand the memory beyond 64K bytes.

Some of the features of the board which are discussed in more detail in Appendix 2 are:

- Fully CMOS: high noise immunity, low power consumption, wide temperature range.
- Implemented in high-speed CMOS.
- 2.5 MHz CMOS Z-80 processor (400ns clock).
- Four sockets for 2 or 8K byte-wide RAM's or EPROM's (32K bytes total).
- MEMEX and segment memory expansion control.
- Power-on reset with Vcc sensing.
- Single +5V operation.

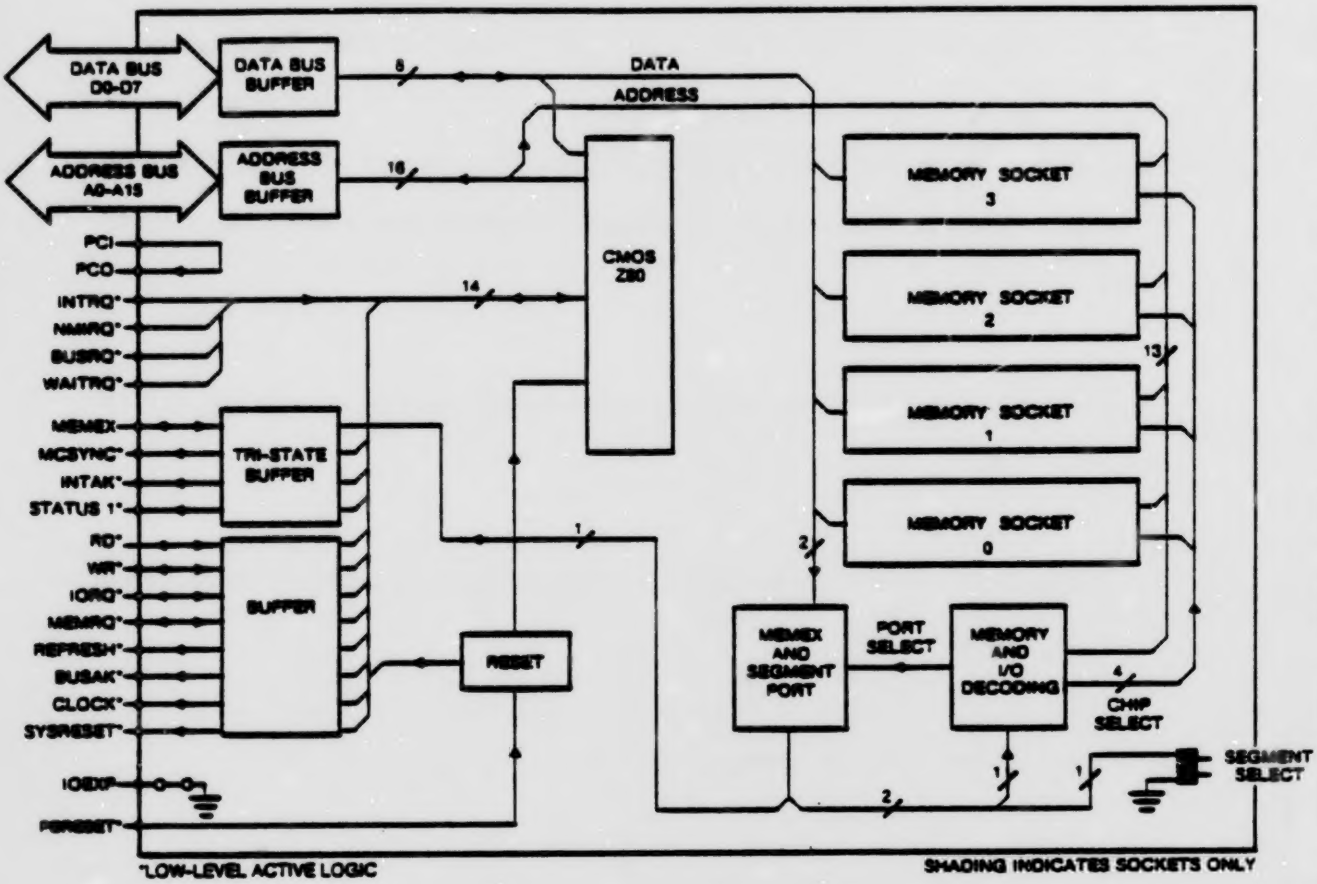
DATA BUS
D0-D7
ADDRESS BUS
A0-A15
DATA BUS BUFFER
ADDRESS BUS BUFFER
8
16
DATA
ADDRESS
CMOS Z80
MEMORY SOCKET 3
MEMORY SOCKET 2
MEMORY SOCKET 1
MEMORY SOCKET 0
13
PCI
PCO
INTRQ*
NMIRQ*
BUSRQ*
WAITRQ*
14
MEMEX
MCSYNC*
INTAK*
STATUS 1*
TRI-STATE BUFFER
RD*
WR*
IORQ*
MEMRQ*
REFRESH*
BUSAK*
CLOCK*
SYSRESET*
BUFFER
RESET
1
2
MEMEX AND SEGMENT PORT
PORT SELECT
MEMORY AND I/O DECODING
4
CHIP SELECT
1
1
2
SEGMENT SELECT
IOEXP
PBRESET*
*LOW-LEVEL ACTIVE LOGIC
SHADING INDICATES SOCKETS ONLY

Figure 2: Block Diagram of CMOS Z-80 Processor Card

A block diagram extracted from Pro-Log Corporation 78C13 CMOS Z-80 Processor Card User's Manual is shown in Figure 2. Figure 3 shown below describes the jumper configuration of the CPU board used with the battery data logger.

Jumper	Description	Configuration
W4	8KX8 memory devices	9-10
		11-12
		13-14
		15-16
W11	Selects RAM or ROM for	1-2
W12	MEM3 to MEM0 respect	1-2
W13	for 8KX8 devices	3-4
W14	1-2 (RAM); 3-4 (ROM)	3-4
W15	Configure MEM0 to MEM3	3-4
W16	Respec. for RAM/ROM, 2K/8K	3-4
W17	Memory sockets	3-4
W18	1-2 (memory socket 2KX8 ROM)	3-4
	3-4 (memory socket 8KX8)	
	5-6 (memory socket 2KX8 RAM)	

Figure 3: Jumper Functions of Processor Card

5.0 DATA ACQUISITION

5.1 Purpose of the Analog-to-Digital Converter Board

The analog-to-digital converter board provides all the necessary analog conversions of the data logger. The three types of analog conversions that the A/D board is responsible for are:

1. monitor the X-Y displacement of the DC potentiometers,

2. monitor the voltage status of the battery,

3. monitor reference voltages on power supply (+10V and 0V).

5.2 Features of the Analog-to-Digital Converter

The A/D board (see figure 4) consists of only CMOS devices. It contains an on-board DC/DC voltage converter to supply the necessary voltages to the amplifiers. The A/D board can do fast (70 micro seconds) and precise (12-bit resolutions) conversions. The board can handle up to 16 single-ended channels or 8-channel differential inputs. Other features of this board are:

- Z-80 interrupt handling

- input voltage -10V to +10V in four ranges

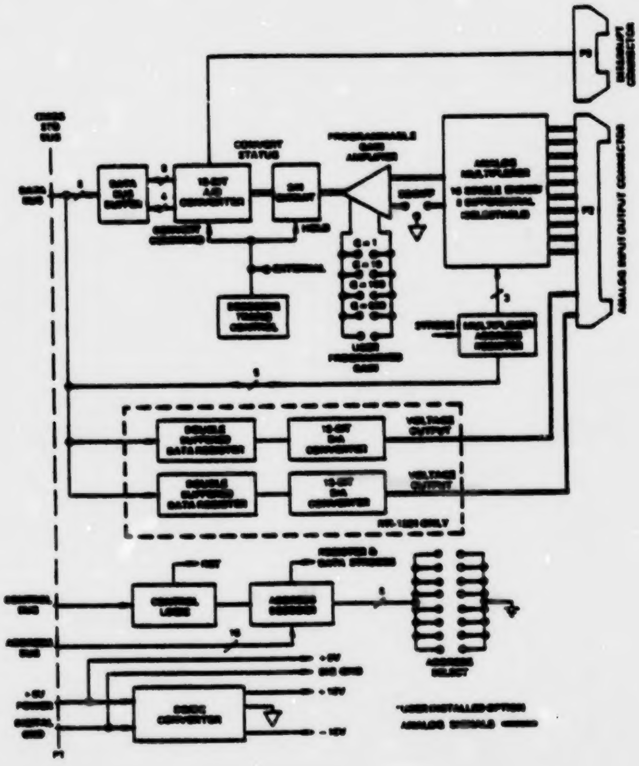
CONVERT STATUS
HOLD
G = 1
VOLTAGE OUTPUT
VOLTAGE OUTPUT
+5V

Figure 4: Block Diagram of the A/D Board

- input protection for overrange
- consumes less than 120 mA at 5 volts.

5.3 Channel Assignment of the A/D Board

Nine single-ended channels are required for analog conversion by the A/D board. Figure 5 shows the channel assignment configured for the battery data logger. Figure 6 illustrates the addressing of the A/D board.

Channel	Assignment
0	X1
1	Y1
2	X2
3	Y2
4	X3
5	Y3
6	GND reference
7	+10V reference
8	Battery status

Figure 5: Channel Assignment of the A/D Converter

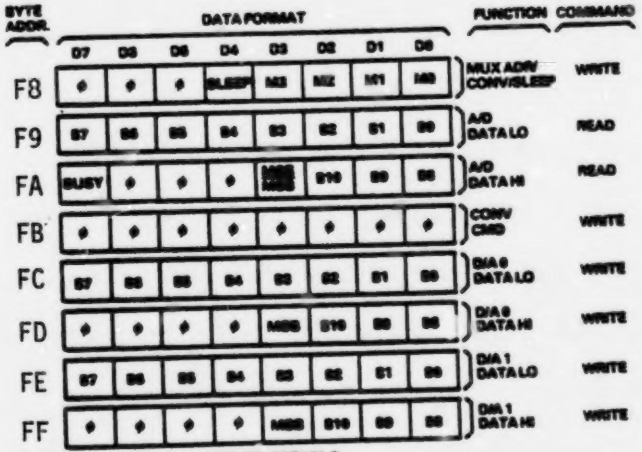

BYTE ADDR.	DATA FORMAT								FUNCTION	COMMAND
	D7	D6	D5	D4	D3	D2	D1	D0		
F8	ϕ	ϕ	ϕ	SLEEP	M3	M2	M1	M0	MUX ADR/ CONV/SLEEP	WRITE
F9	B7	B6	B5	B4	B3	B2	B1	B0	A/D DATA LO	READ
FA	BUSY	ϕ	ϕ	ϕ	MSB MSB	B10	B9	B8	A/D DATA HI	READ
FB	ϕ	ϕ	ϕ	ϕ	ϕ	ϕ	ϕ	ϕ	CONV CMD	WRITE
FC	B7	B6	B5	B4	B3	B2	B1	B0	D/A 0 DATA LO	WRITE
FD	ϕ	ϕ	ϕ	ϕ	MSB	B10	B9	B8	D/A 0 DATA HI	WRITE
FE	B7	B6	B5	B4	B3	B2	B1	B0	D/A 1 DATA LO	WRITE
FF	ϕ	ϕ	ϕ	ϕ	MSB	B10	B9	B8	D/A 1 DATA HI	WRITE

NOTES: 1. X AND Y ARE USER SELECTABLE.

2. BITS SHOWN AS ⊟ HAVE THE UPPER VALUE FOR UNIPOLAR CODES AND LOWER VALUE FOR 2's COMPLEMENT.

3. THE SYMBOL ϕ MEANS THE BIT IS IGNORED.

4. BUSY BIT EQUALS "1" DURING CONVERSIONS AND "0" WHEN DONE.

Figure 6: Addressing of the A/D Board

6.0 DATA LOGGING

6.1 Purpose of the Cassette Transport Interface Board

The data acquired from wheel or rail profile measurements is stored digitally on a Braemar CM-600 mini cassette transport on a 50-foot standard length tape. The data path from the cassette deck to the microprocessor is shown in Figure 7.

It can be noted from Figure 7 that parallel and serial conversions must take place through the cassette interface board. This would be the only interfacing required if the system was tolerant to varying tape speeds. Since read and write speeds are not always constant, one must encode the data in a manner such that the encoded data can generate its own timing clock to be used in the decoding process. For optimum reliability, the decoder must be adaptive to varying parameters so as to produce error-free results. Some of the varying parameters may be: speed differences between read and write, speed differences from one transport to another, and tape jitter.

In general, the cassette interface board must accomplish five tasks:

1. board selection,

2. data formatting since all data must be read and written in a serial fashion,

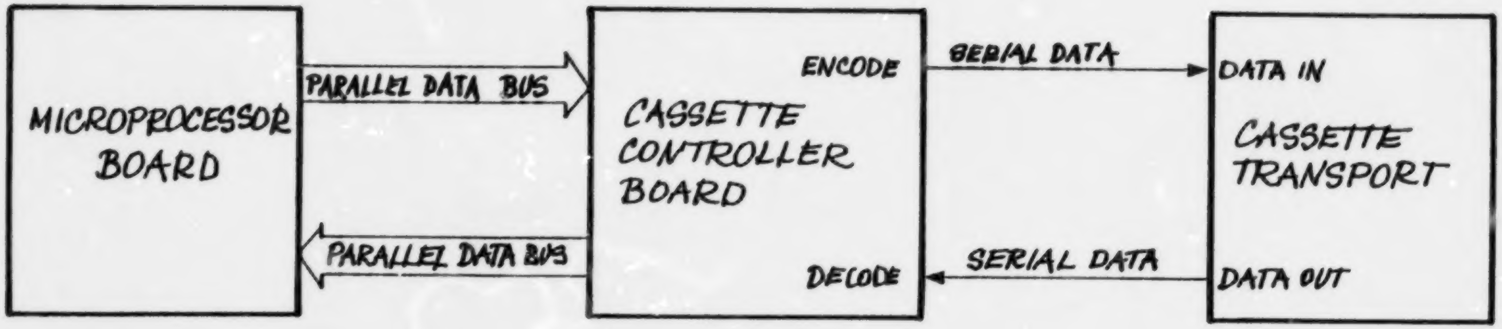
MICROPROCESSOR BOARD
PARALLEL DATA BUS
PARALLEL DATA BUS
CASSETTE CONTROLLER BOARD
ENCODE
DECODE
SERIAL DATA
SERIAL DATA
DATA IN
CASSETTE TRANSPORT
DATA OUT

Figure 7: **BLOCK DIAGRAM OF DATA FLOW FOR CASSETTE TRANSPORT SYSTEM**

3. data must be encoded when written on tape,

4. data must be decoded when read from tape,

5. controlling operations of the cassette transport.

6.2 Functional Description of the Cassette Controller

The cassette interface board consists basically of four blocks - bus interface, decoder, encoder, and cassette controller/status ports. A block diagram of the cassette interface board is shown in Figure 8. Appendix 4 contains a more detailed description of the hardware configuration.

The cassette controller board is implemented in low power CMOS technology compatible with STD bus systems. The serial communications device performs the data formatting (serial/parallel) and is used with the read strobe from the adaptive decoder to clock in only the valid transitions of the encoded data. The cassette controller board provides Z-80 Mode 2 interrupt capabilities if ever necessary to implement. All encoding and decoding of data is performed on this board and will be described in more detail in a later section.

6.3 Manchester Phase Encoder

Due to the fact that speeds vary from transport to transport, an encoding and decoding scheme is compulsory. A highly recommended decoding scheme

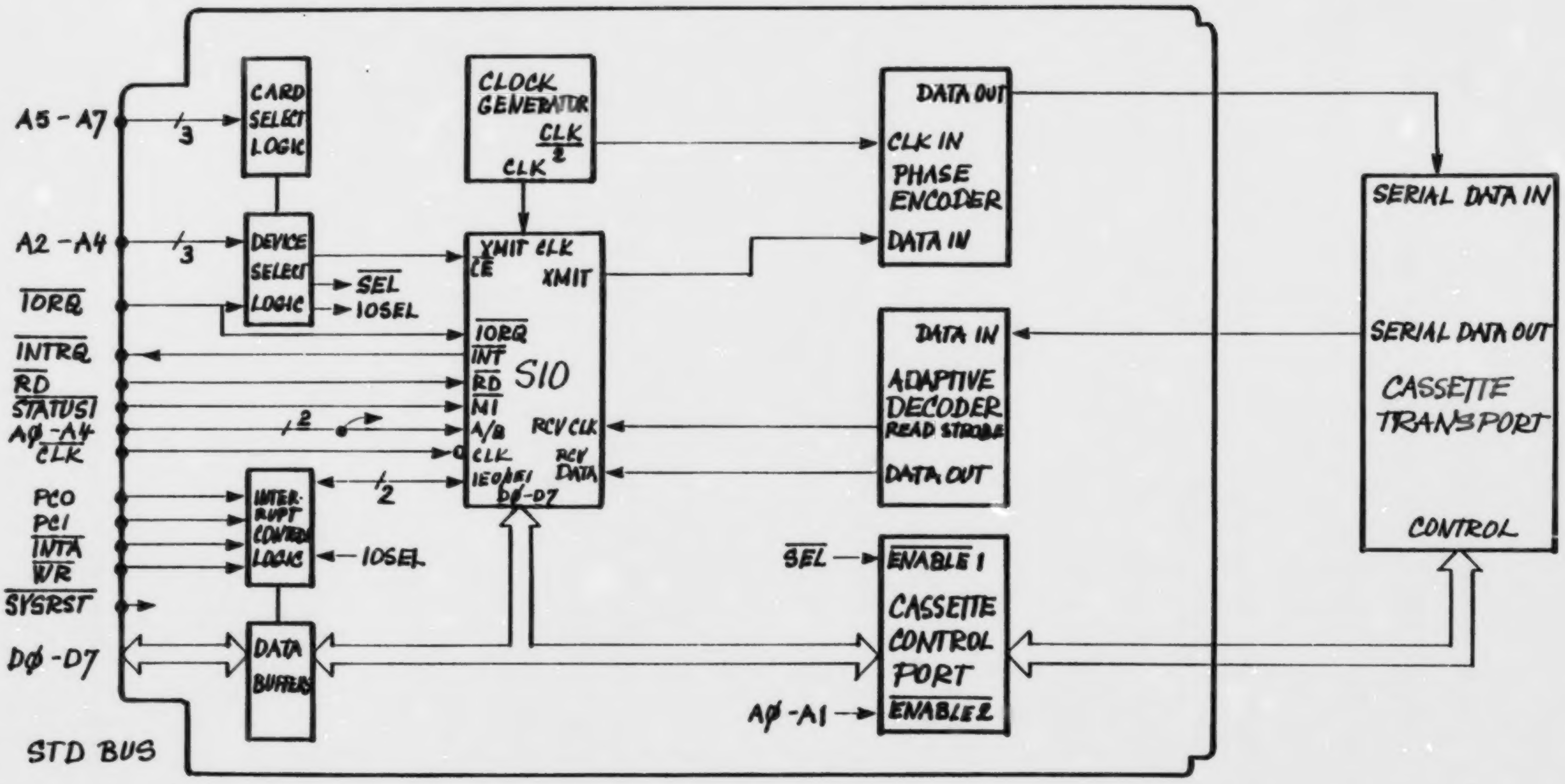
A5 - A7
A2 - A4
IORQ
INTRQ
RD
STATUS1
A0 - A4
CLK
PCO
PCI
INTA
WR
SYSRST
D0 - D7
STD BUS
/3
/3
/2
/2
CARD SELECT LOGIC
DEVICE SELECT LOGIC
SEL
IOSEL
INTER-RUPT CONTROL LOGIC
IOSEL
DATA BUFFERS
CLOCK GENERATOR
CLK/2
CLK
XMIT CLK
CE
XMIT
IORQ
INT
RD
M1
A/B
CLK
IEO/IEI
D0-D7
S10
RCV CLK
RCV DATA
DATA OUT
CLK IN
PHASE ENCODER
DATA IN
DATA IN
ADAPTIVE DECODER
READ STROBE
DATA OUT
SEL
ENABLE 1
CASSETTE CONTROL PORT
A0 - A1
ENABLE 2
SERIAL DATA IN
SERIAL DATA OUT
CASSETTE TRANSPORT
CONTROL

Figure 8: **BLOCK DIAGRAM OF CASSETTE CONTROLLER BOARD**

is the variable three-quarter cell timer. The encoding method used is the Manchester Phase Encoder. Both these methods were implemented in the tape controller board.

Manchester Phase Encoding is a technique defined by the ANSI standards. This method of encoding is sensitive only to data transitions. A change in data level and the direction of this transition can then be manipulated to generate proper timing.

By definition (as set by ANSI), 1) the data transition occurs at the beginning of the data cell, 2) the data transition from a logic low to high is encoded as a "one", and 3) a transition from a high to a low is encoded as a "zero". An example of data encoding using the above rules is shown below in Figure 9.

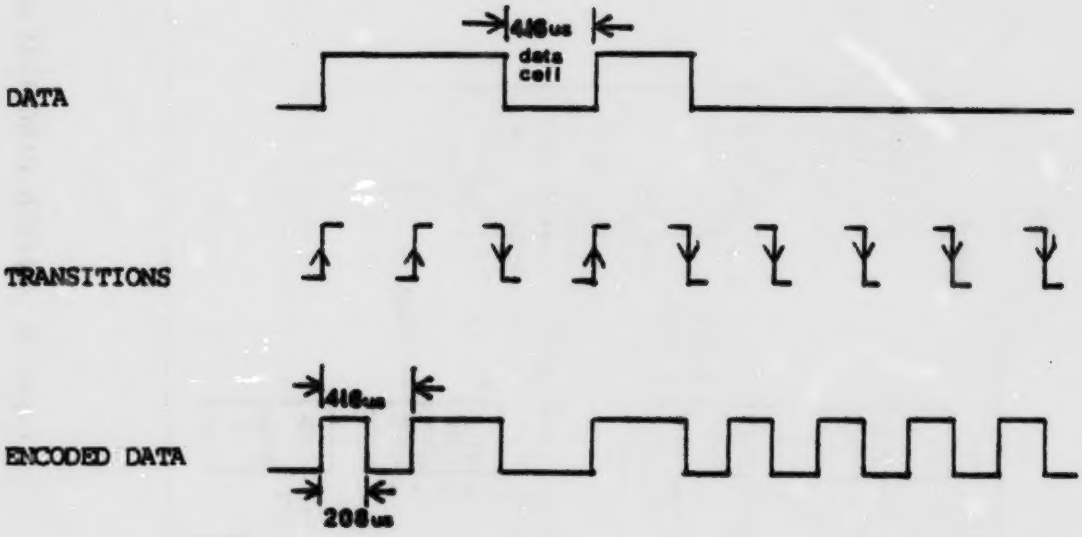

Figure 9: Manchester Phase Encoding Using ANSI Rules

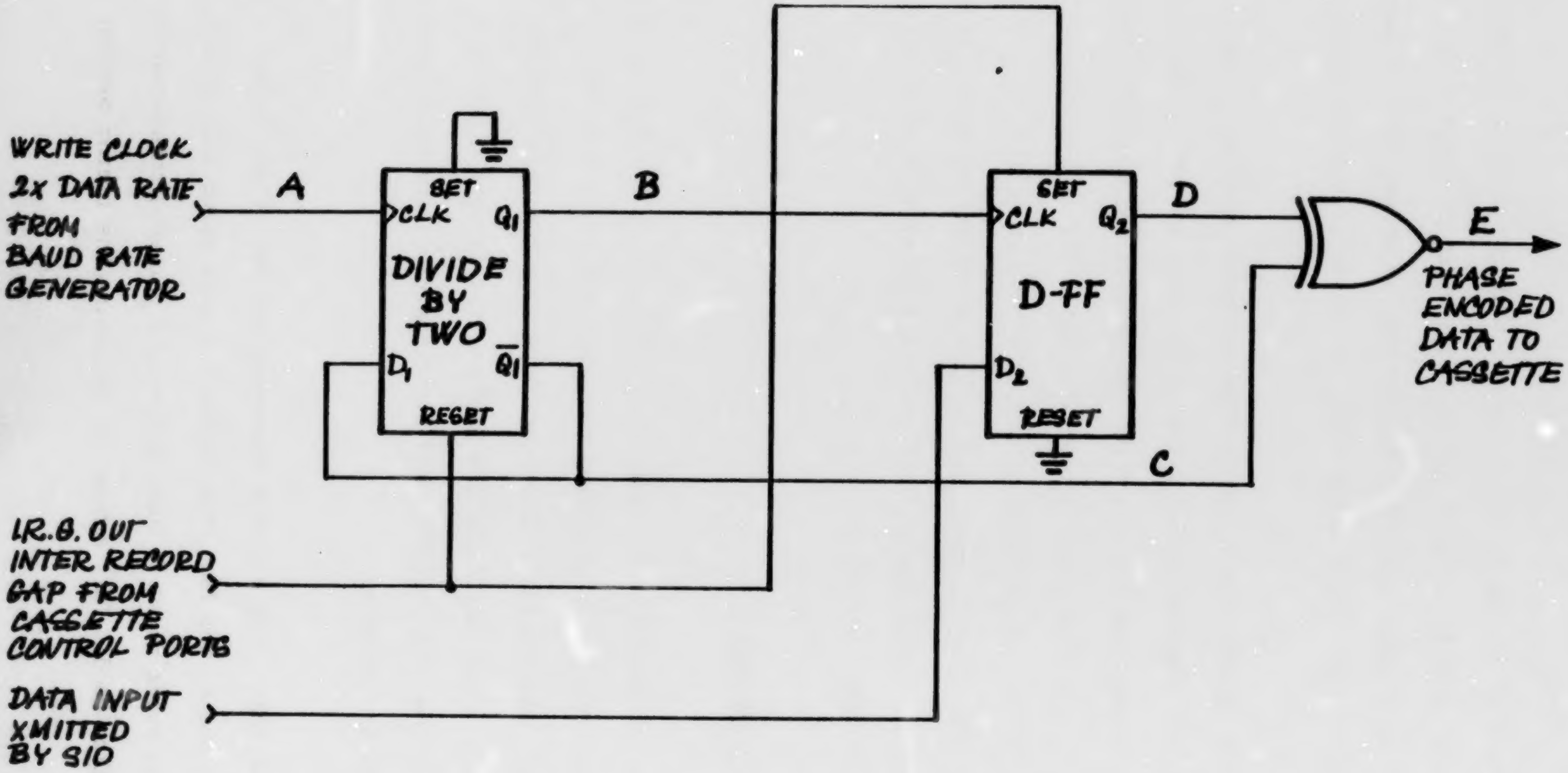
WRITE CLOCK
2x DATA RATE
FROM
BAUD RATE
GENERATOR
A
SET
CLK
Q_1
DIVIDE
BY
TWO
D_1
$\overline{Q_1}$
RESET
B
SET
CLK
Q_2
D-FF
D_2
RESET
D
C
E
PHASE
ENCODED
DATA TO
CASSETTE
I.R.G. OUT
INTER RECORD
GAP FROM
CASSETTE
CONTROL PORTS
DATA INPUT
XMITTED
BY SIO

Figure 10: **MANCHESTER PHASE ENCODER CIRCUIT**

In the example of Figure 9, it is assumed that the data is transmitted at 2400 bits per second with each bit having a width of 416μs. It can be noted from the encoded data that transitions sometimes occur midway between data cells. These transitions are known as mid bit transitions.

The hardware implementation for Manchester Phase Encoding is shown in Figure 10. It consists of two D-type flip-flops and an exclusive NOR gate. If the data and the clock are 180 degrees out of phase, the output E is a logic low. The first D-type flip-flop acts as a divide-by-two circuit which ensures an accurate output clock, as well as a synchronous operation. The clock is then used to strobe the serial data. Figure 11 illustrates the timing diagram for the phase encoding circuit using the example discussed previously.

6.4 Adaptive Decoder

The decoder circuit must be capable of interpreting the encoded data transitions properly by rejecting those which are mid-bit transitions. The approach used to reconstruct serial data is the three-quarter cell timer method. The reason for the name is that for the first three quarters of the data cell, the mid-bit transitions are masked and data transitions are accepted.

It is known that using a simple three-quarter cell timer is not always sufficient due to the fact that changes in tape speed will introduce errors. In order to avoid such problems, a variable three-quarter cell timer must be used. This scheme can determine the timing between

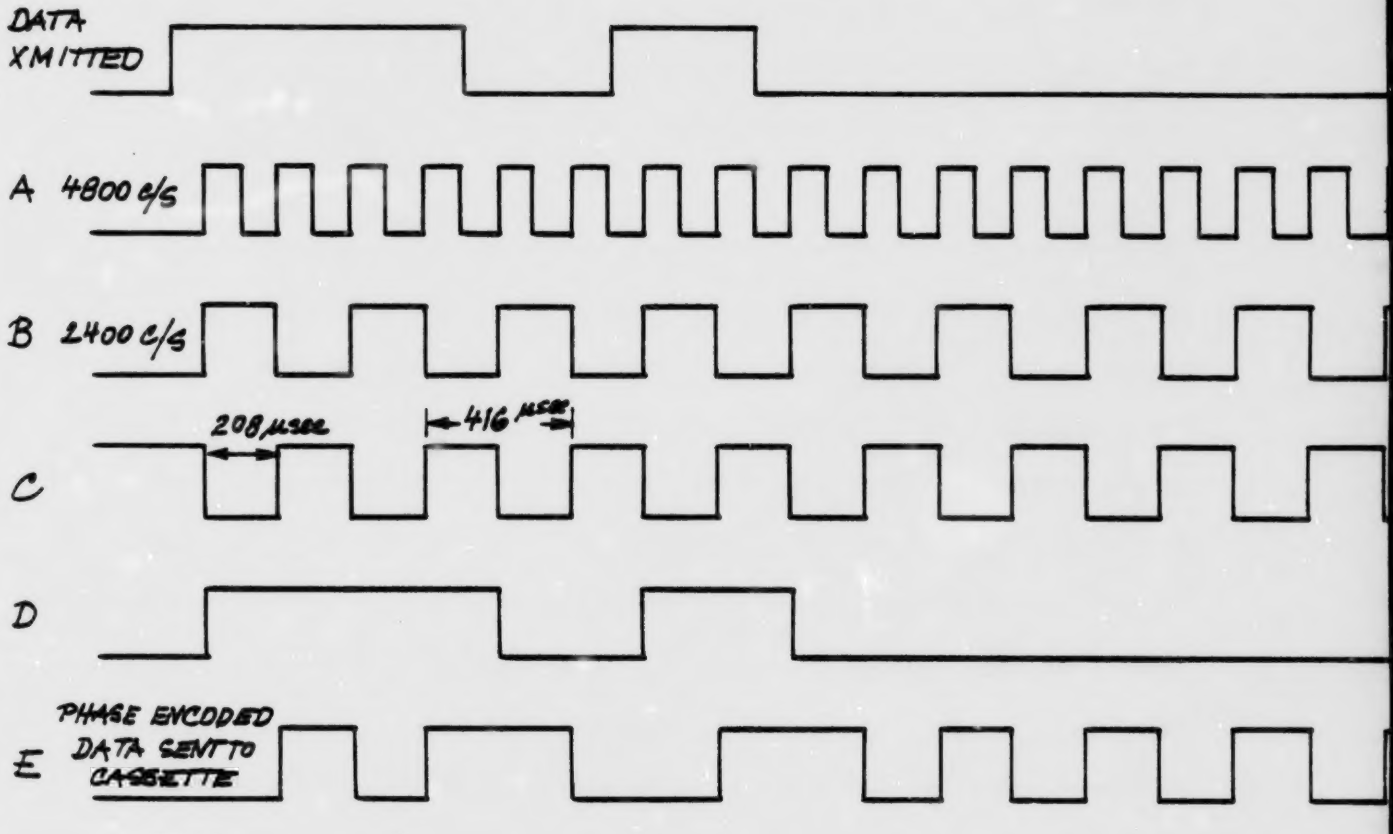
DATA XMITTED
A 4800 c/s
B 2400 c/s
208 µsec
416 µsec
C
D
E
PHASE ENCODED DATA SENT TO CASSETTE

Figure 11: **TIMING DIAGRAM FOR PHASE ENCODING CIRCUIT**

transitions and predict the occurrence of the next transition; it is, therefore, an adaptive technique.

An adaptive decoder circuit is shown in Figure 12. It is based on the standard Braemar wide range decoding approach. The objective of this decoder circuit is to produce a read strobe which contains both the timing and window which accepts data transitions and ignores mid-bit transitions. Figure 13 demonstrates the timing for this circuit.

The one-shot circuit shown on the left of Figure 12 is responsible for producing the read strobe. By choosing proper component values, the window length can be varied. For example, a baud rate of 2400 bits/sec has a data spacing of 416μs. In a three-quarter cell timer, the window length of the read strobe will be 208μs or 3/4 of the data cell. The interesting feature of the decoder circuit shown in Figure 12 is that it is adaptive, that is, the window length is varied according to the average spacing of the previous transitions. In lab tests it was verified that by selecting the proper component values, the circuit was capable of tracking tape speeds over a wide range of 1200 baud to 4800 baud without losing stability.

The decoder circuit can be divided into three parts - edge detector, mid-bit mask out, and gap detector. The edge detector puts out a single pulse for every level change in the encoded data including mid-cell transitions. The one-shot circuit which is responsible for mid-bit mask out will then produce the desired read strobe. For varying baud rates, the amplifier circuit will take the average of previous transition spacings

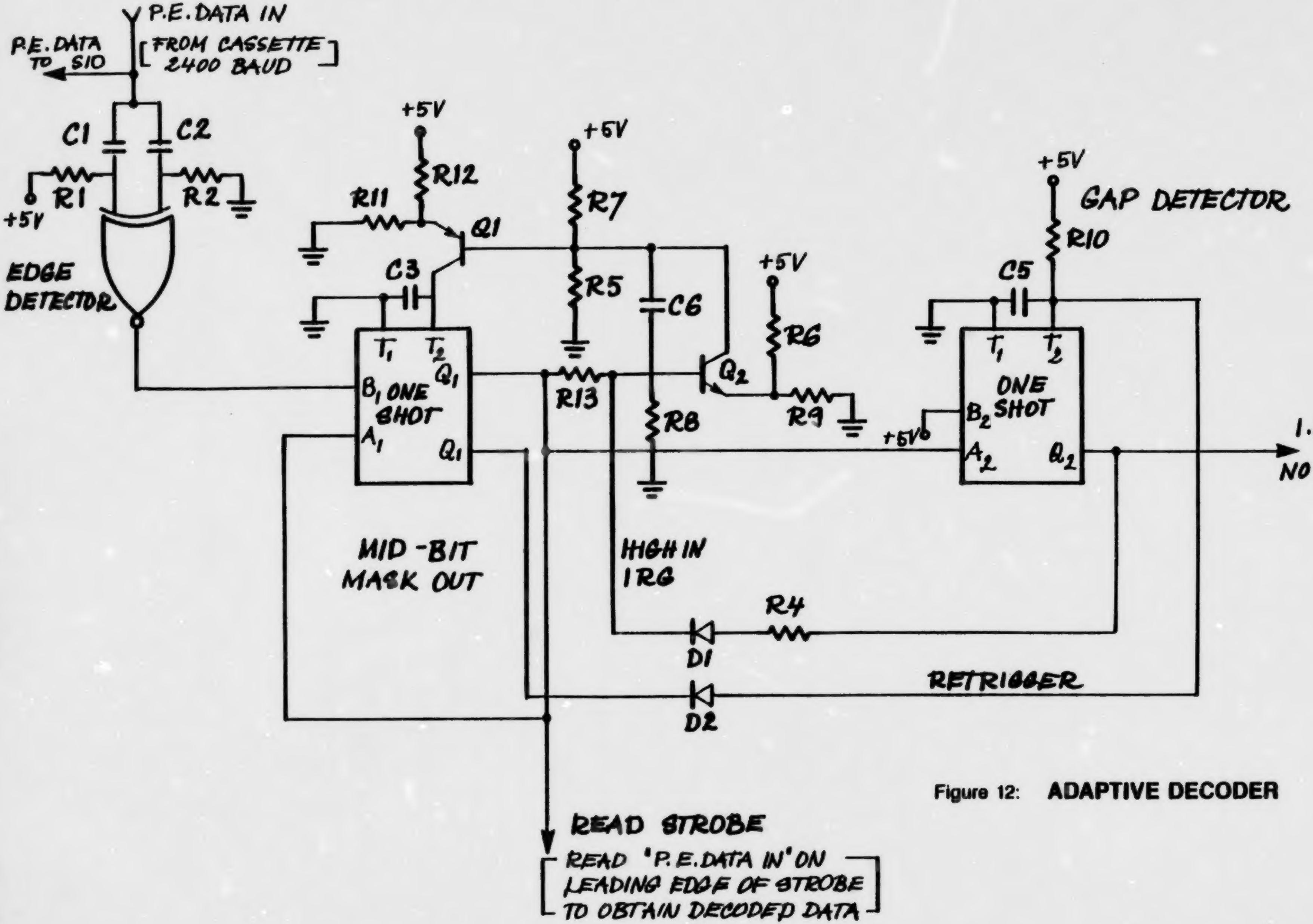
P.E. DATA IN
[FROM CASSETTE 2400 BAUD]
P.E. DATA TO SIO
C1
C2
R1
R2
+5V
EDGE DETECTOR
+5V
R12
R11
Q1
C3
T1
T2
Q1
B1 ONE SHOT
A1
Q1
MID-BIT MASK OUT
+5V
R7
R5
C6
R13
R8
Q2
+5V
R6
R9
HIGH IN IRG
R4
D1
D2
RETRIGGER
+5V
GAP DETECTOR
R10
C5
T1
T2
ONE SHOT
B2
+5V
A2
Q2
I.R.G.
NO DATA
READ STROBE
[READ 'P.E. DATA IN' ON LEADING EDGE OF STROBE TO OBTAIN DECODED DATA]

Figure 12: **ADAPTIVE DECODER**

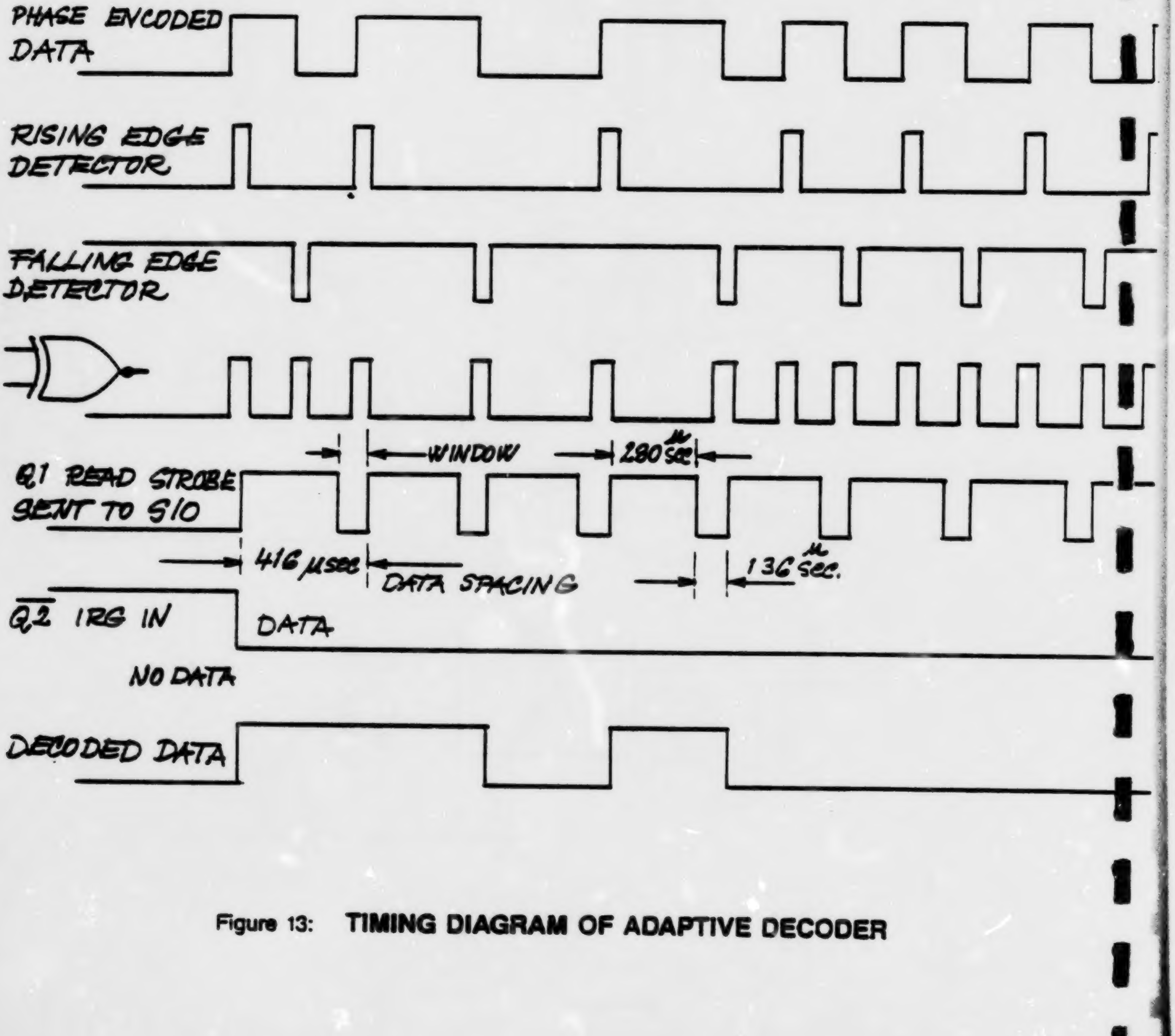
PHASE ENCODED DATA
RISING EDGE DETECTOR
FALLING EDGE DETECTOR
WINDOW
280 μsec
Q1 READ STROBE SENT TO S/O
416 μsec
DATA SPACING
136 μsec.
$\overline{Q2}$ IRG IN
DATA
NO DATA
DECODED DATA

Figure 13: **TIMING DIAGRAM OF ADAPTIVE DECODER**

and vary the window length of the read strobe accordingly. The gap detector is an additional one-shot circuit which goes low on the first data transition of the read strobe indicating valid data, as shown in Figure 13. The read strobe along with the encoded data is sent to the serial (SIO) chip. The leading edge of the read strobe will clock the data at the input of the SIO into a buffer.

6.5 Cassette Transport Control and Monitoring

The last block of the cassette interface board is the cassette controller/status port. In order to select a particular operation (read, write, tape direction, tape speed, tape motion), the microprocessor clocks the appropriate control data into a latch. This latch acts as a control port to the tape transport.

The status of the tape transport can also be monitored. The microprocessor can read from the input buffer states such as: cassette presence, clear leader, cassette side, and file protect.

6.6 Cassette Transport

As described earlier, data retrieved by the data acquisition system is stored by the Braemar CM-600 digital mini cassette transport on a 50-foot standard length tape. The data handling density of the tape is 800 BPI at a data rate of 2400 baud. The data capacity for both sides of a 50-foot tape is 90K bytes.

Electrically, the tape transport needs only a supply voltage of 5VDC and contains its own interface board with all the read/write amplifiers, direction and motioncontrol circuits, and cassette status controls. Typically, the mini cassette transport consumes 1 watt in the read/write mode, however, during a rewind the consumption may be as high as 3.5 watts. Environmentally, the cassette transport imposes a stringent operating temperature of 50 to 113 degrees farenheit. For more detailed specifications and schematics see Appendix 4.

6.7 Record Formatting

To remain within industry ANSI standards, a convention was employed for formatting a data record on tape. A single data record measurement will consist of the following format:

1. gap (beginning of tape)

2. IRG (inter-record gap always logic high)

3. preamble (alternating ones and zeros)

4. data

5. CRC (cyclical redundancy check)

6. postamble (alternating ones and zeros)

The last record will end before detection of end-of-tape marker.

6.8 Programming the Cassette Controller Board

The cassette controller board is addressed as eight contiguous I/O port locations. The board addressing can be varied via on-board jumpers. The address selection for the cassette interface board is given below in Figure 14.

Hex Address	Description
0014H	Data Register Channel A SIO
0015H	Data Register Channel B SIO
0016H	Control Register Channel A SIO
0017H	Control Register Channel B SIO
0018H	Disable Read/Write; Select In-Out Cassette Control Status Ports
0019H-001BH	Disable SIO and Control Ports

Figure 14: Addressing Scheme of the Cassette Controller Board

All formatting of data is accomplished through the serial input/output controller. This device must first be initialized for a selected mode of operation. With the cassette controller board, the SIO is initialized for the asynchronous mode. The following are particulars concerning the actual programming of this device for Channel A:

1. disable interrupts
2. 8 bits per character
3. 2 stop bits/character; no parity bit
4. X1 clock mode

The status information of the SIO such as character available and buffer empty can be read from the data registers. With this, all parallel data from the microprocessor can be formatted into serial data which is then encoded and transferred to tape and vice versa.

Before writing or reading from the tape, the proper operation of the transport must be slected. In order to do this the data must be latched into the control port of the cassette board. Figure 15 shows the data necessary to program the cassette control port:

Data Bit	Function	Operation
0	Read/Write	L = Read, H = Write
1	Tape Direction	L = Forward, H = Rewind
2	Tape Speed	L = Fast, H = Slow
3	Tape Motion	L = Go, H = Stop
4	Inter Record Gap	H = Write IRG

Figure 15: Programming the Cassette Control Port

The microprocessor can also determine the status of the tape transport by reading the status port. Figure 16 shows the bit assignment of the status port.

Data Bit	Function	Status
0	Cassette Side	L = Side A In
1	Cassette Present	L = Present
2	File Protect	L = Tab Removed
3	Clear Leader	L = Tape Present, H = Clear Leader
4	Read IRG	H = IRG Present

Figure 16: Reading the Cassette Control Port Status

7.0 PERIPHERAL INTERFACING

7.1 Purpose of the Input-Output Interface Board

The purpose of the STD bus based peripheral board is twofold. First, the parallel ports provide the interface necessary to monitor the decoded and debounced key pad entries, as well as control relay switching of the d.c. voltage source to the profilometer. Secondly, the serial communication between the host development system and the data logger occurs via this board. A block diagram of the peripheral board is shown in Figure 17.

7.2 Features of the I/O Board

Some of the features provided by the peripheral interface board are the following:

- all low-powered CMOS design
- optoisolated RS-232C interface
- jumper programmable baud rate (up to 9600 baud)
- DCE/DTE jumper programmable with handshaking
- 16 bidirectional input-output ports with four handshaking lines
- mode 2 Z-80 interrupt capabilities for the PIO device
- three edge connectors provided

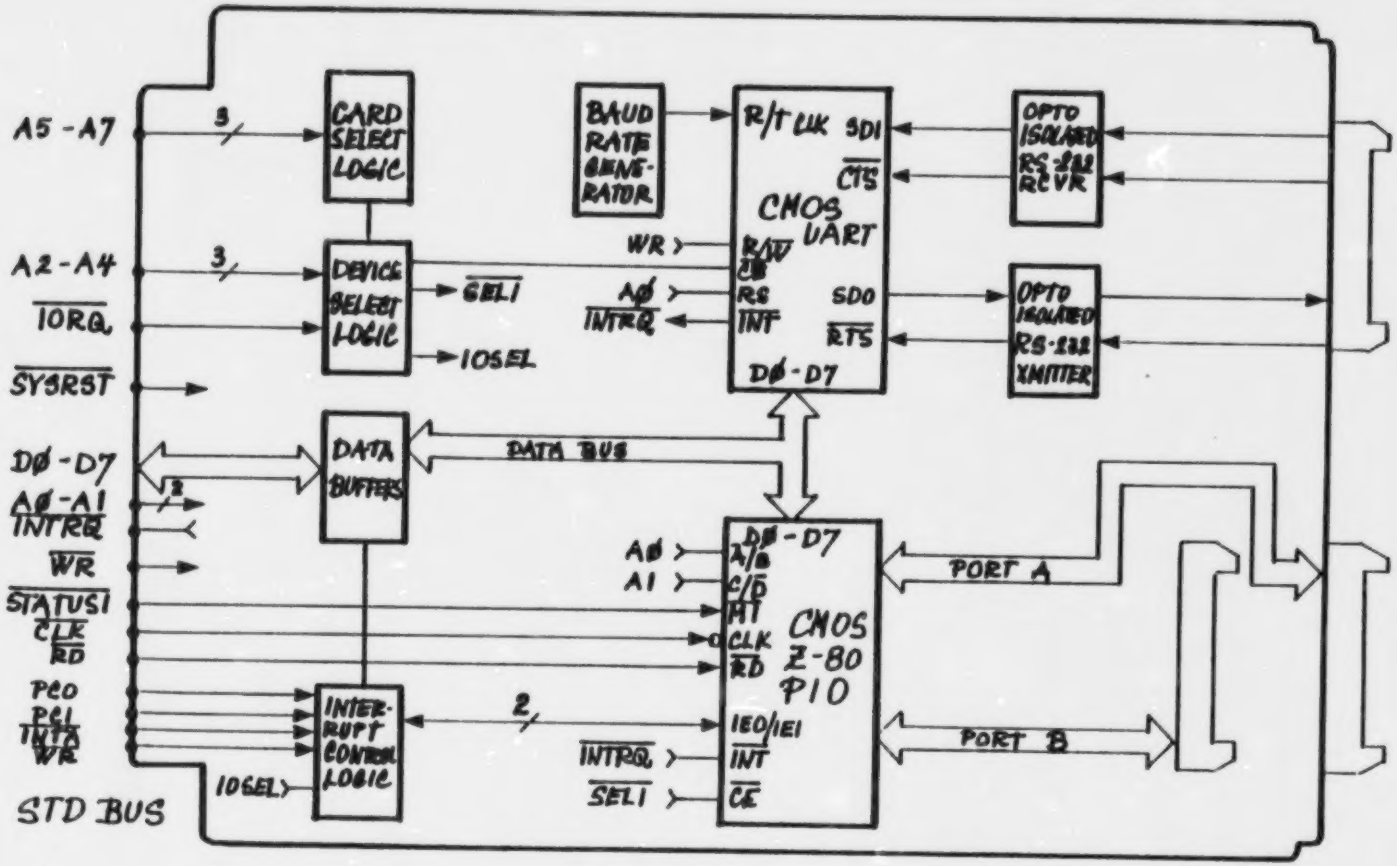
A5 - A7
A2 - A4
IORQ
SYSRST
DØ - D7
AØ - A1
INTRQ
WR
STATUS1
CLK
RD
PCO
PCI
INTA
WR
STD BUS
3
3
2
CARD SELECT LOGIC
DEVICE SELECT LOGIC
SEL1
IOSEL
DATA BUFFERS
INTER-RUPT CONTROL LOGIC
IOSEL
BAUD RATE GENERATOR
R/T CLK
SDI
CTS
CMOS UART
R/W
CE
RS
INT
SDO
RTS
DØ - D7
WR
AØ
INTRQ
DATA BUS
OPTO ISOLATED RS-232 RCVR
OPTO ISOLATED RS-232 XMITTER
DØ - D7
A/B
C/D
M1
CLK
RD
CMOS Z-80 PIO
IEO/IEI
INT
CE
AØ
A1
INTRQ
SEL1
2
PORT A
PORT B

Figure 17: **BLOCK DIAGRAM OF INPUT-OUTPUT PERIPHERAL BOARD**

7.3 Functional Description of the Parallel Input-Output Section

The parallel input-output section consists of a Z-80 PIO device which provides the interfacing to the keypad. The PIO contains two programmable bidirectional ports, as well as capabilities for mode 2 type interrupts. Port A of the PIO is used to switch one of three relays which provides +10VDC to the corresponding side of profilometer. Port A is also used to verify whether the measurements being taken are rail or wheel type.

The PIO is the Toshiba CMOS version of the Zilog Z-80 PIO and consumes only 2 MA. The interrupt control circuit for the parallel I/O is configured so that it is compatible with the STD bus daisy-chain interrupt structure. Electrical specifications of this device are provided in Appendix 5.

The assignment of Port B with respect to the keypad interface is shown in Figure 18.

PIO	Assignment
Port A, bit0	monitor rail(low)/wheel(high)
Port A, bit1	+10V relay switch to side 1 profilometer
Port A, bit2	+10V relay switch to side 2 profilometer
Port A, bit3	+10V relay switch to side 3 profilometer
Port B, bit0	data output, keypad data bit A
Port B, bit1	data output, keypad data bit B
Port B, bit2	data output, keypad data bit C
Port B, bit3	data output, keypad data bit D
Port B, bit4	data output, keypad data bit E
Port B, bit5	data output, latched data available
Port B, bit6	data input, clear data available

Figure 18: Port Assignment of the PIO Device

7.4 Functional Description of the Serial I/O Section

The serial input-output circuit consists of three sections - the SIO device, the baud rate generator, and the optoisolated RS-232C interface. The serial input-output device is the RCA CDP1854A programmable universal asynchronous receiver/transmitter (UART). The SIO is a CMOS device which consumes only 1.5 ma of current. This device provides the means for serial transmission of data from the battery logger to the development system.

The SIO device could operate in the full or half duplex mode. In the full duplex mode, the SIO is capable of converting serial data to parallel at the same time that it converts parallel data to a serial format. The SIO device could also be programmed with variable word lengths, stop bits, and parity.

The baud rate generator is the low-powered Fairchild 4702 clock generator. The 4702 contains an external crystal and is jumper programmable for baud rates of 50 to 9600. Specifics for this baud rate generator were given in Appendix 4.

The RS-232C interface circuitry provides an optoisolated and low-power standby means of serial data transfer to the SIO device. The RS-232C section employs the use of the high speed low-power 6N139 optoisolators and the low-power TL062 JFET input operational amplifiers. The +12VDC from the DC-DC converter is switched on only during RS-232C serial operation; in this way power consumption is minimized during field operation.

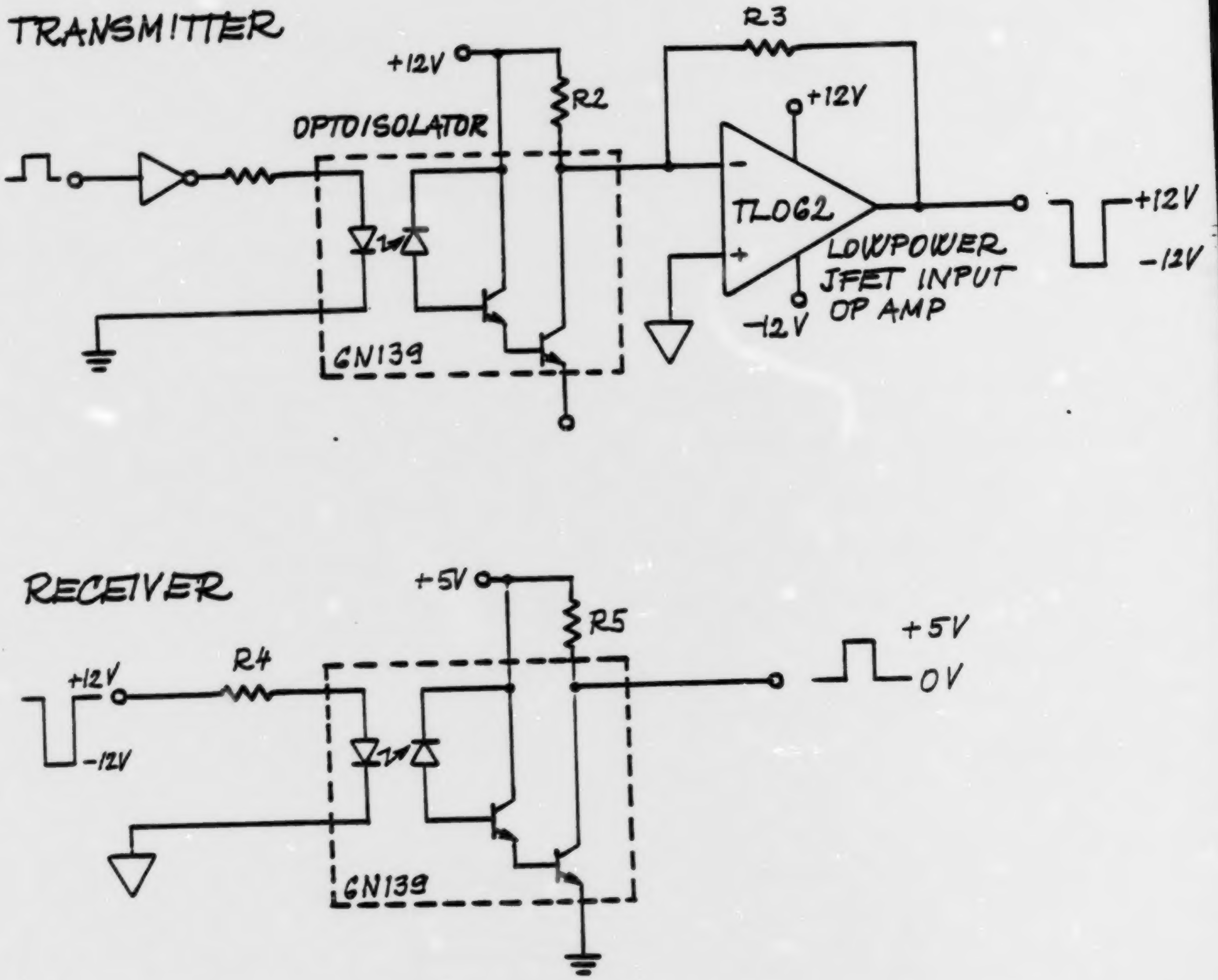
TRANSMITTER
+12V
R3
R2
+12V
OPTOISOLATOR
-
+
TL062
+12V
-12V
LOWPOWER
JFET INPUT
OP AMP
-12V
6N139
RECEIVER
+5V
R5
+5V
0V
R4
+12V
-12V
6N139

Figure 19: **RS-232C TRANSMITTER AND RECEIVER**

The RS-232C transmitter circuit is shown in Figure 19. The TL062 provides line driving and short-circuit protection. During standby, the serial data and request to send output lines of the SIO are logic high. In order to minimize the power consumption, these signals are inverted so as to turn off the optoisolator. In this way, the current consumption is reduced to less than 0.5 ma during standby.

The RS-232C receiver circuit is also given in Figure 19. This circuit also provides complete isolation between the battery powered data logger and a host system. During standby the power consumption is negligible.

The serial communications section provides a subset of the full RS-232C signals at an edge connector. Two of the signals are used for peripheral handshaking. The serial data communications channel could be configured for DTE (data terminal equipment) or DCE (data communications equipment) applications via on-board jumpers. For the case of the battery data logger, the serial port of the I/O board is hardwired for DTE applications. The RS-232C pin assignment for the I/O board is given in Figure 20.

RS-232C Signal	DTE Pin	DCE Pin
transmitted data	2	3
received data	3	2
request to send	4	5
clear to send	5	4
signal ground	7	7

Figure 20: RS-232C Pin Assignment for the I/O Board

7.5 Programming the Peripheral I/O Board

The peripheral I/O board is addressed as two blocks of I/O port locations with jumper selectable base addresses. Four I/O addresses control the serial port and another four addresses control parallel ports. The default addresses and their assignment are given in Figure 21.

HEX Address	Assignment
0008H (or 000AH)	Transmit/Receive data register of SIO
0009H (or 000BH)	Control/Status register of SIO
000CH	PIO Port A, data word register
000DH	PIO Port B, data word register
000EH	PIO Port A, control word register
000FH	PIO Port B, control word register

Figure 21: Addressing Scheme of the I/O Board

The details for programming the CDP1854 UART device is given in Appendix 5. In the case of the battery data logger, the control register was programmed in mode 1 for 8 data bits and 2 stop bits with parity and interrupt disabled. The status register of the UART was read by the microprocessor for the following flags: transmitter holding register empty, transmitter shift register empty, external status (CTS), and data available.

The PIO was programmed for mode 3 using only Port B to scan the keypad. Mode 3 permits each bit to be defined as either input or output signals. For the process of scanning the keypad, the PIO interrupts were disabled. For details concerning mode 3 operation and programming, see Appendix 5 on the Z-80 PIO parallel input/output controller.

8.0 KEYPAD AND DISPLAY INTERFACING

8.1 Purpose of the Keypad and Display Board

The keypad and display board provides two independent purposes. The first function of the board is to provide the necessary interfacing and timing requirements of the Daystar liquid crystal display to the STD bus. The second function of the board is to provide the debouncing of all keypad and switch entries and to indicate that a valid entry has occurred and has been encoded. A block diagram of the board is shown in Figure 22.

8.2 Functional Description of Keypad/Display Board

The keypad encoder is the 74C923 CMOS device which incorporates all the necessary debounce circuitry and encoding logic for two-key rollover. This device also contains a register which latches the encoded data of the last key depressed even after the key is released.

The data available flag of the encoder is active only as long as the entered key is depressed. For this reason an external flip-flop is used to latch this flag and reset it only after the microprocessor acknowledges a key entry. The keypad encoded data is available at an edge connector which is monitored by the PIO of the peripheral board.

Interfacing the Daystar liquid crystal display to the STD bus is shown in the block diagram of Figure 22. Since the display is microprocessor oriented, only minimal hardware is necessary. The timing control circuit

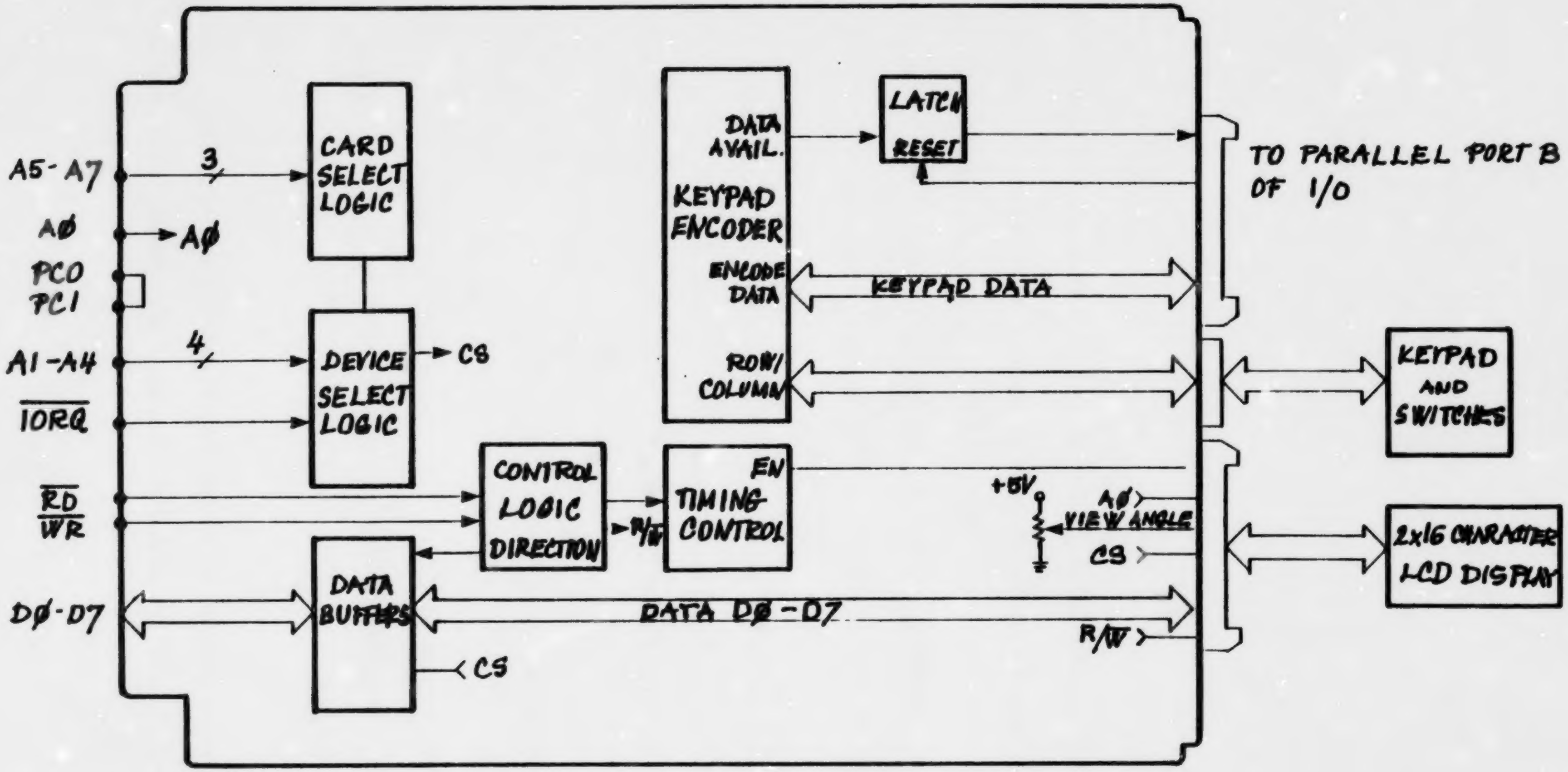
A5-A7
3
A0
PC0
PC1
A1-A4
4
$\overline{IORQ}$
$\overline{RD}$
$\overline{WR}$
D0-D7
CARD SELECT LOGIC
DEVICE SELECT LOGIC
CS
CONTROL LOGIC DIRECTION
R/W
DATA BUFFERS
CS
DATA AVAIL.
KEYPAD ENCODER
ENCODE DATA
ROW/ COLUMN
LATCH
RESET
KEYPAD DATA
EN
TIMING CONTROL
DATA D0-D7
+5V
A0
VIEW ANGLE
CS
R/W
TO PARALLEL PORT B OF I/O
KEYPAD AND SWITCHES
2x16 CHARACTER LCD DISPLAY

Figure 22: **BLOCK DIAGRAM OF KEYPAD/DISPLAY BOARD**

is basically a pulse stretcher and delay which ensures that the enable pulse is high for 450nsec and delayed for 140nsec with respect to the R/W signal. The potentiometer adjustment for the display view angle is also available on the board.

8.3 The LCD Module

A 2 line by 16 character liquid crystal display was implemented with the data logger to meet the requirements of low power and sunlight readability. The IEE Daystar module was chosen because of its compact size and because it contains an on-board CMOS VLSI microprocessor controller which handles character generation and other functions.

The LCD provides a parallel ASCII data bus and microprocessor control signals which facilitates the task of interfacing to the STD bus. The LCD module requires only +5VDC and has a current consumption of 1 MA.

8.4 Programming the Keypad/Display Board

Programming the PIO port B of the peripheral board is necessary in order to read a keypad encoded entry. The programming for this was discussed in Section 7.3.

The display module is addressed as two jumper variable I/O base addresses. The two default addresses and their functions are shown in Figure 23.

Address	Function
0004H	write control information to display
0005H	write alphanumeric data to display

Figure 23: Addressing Scheme of Display Module

In order to obtain the maximum character loading rate, the 'busy flag' (data bit 7) should be read to determine when the module is ready to accept the next character. See Figure 24 for instruction table and Appendix 6 for particulars concerning the display module.

Figure 24: Instruction Table for LCD Module

Function			Read/Write	Address	Code							
					DB7	DB6	DB5	DB4	DB3	DB2	DB1	DB0
Display Clear			Write	0004H	0	0	0	0	0	0	0	1
Cursor Return			Write	0004H	0	0	0	0	0	0	1	0
Cursor On			Write	0004H	0	0	0	0	0	1	0	0
Cursor Off			Write	0004H	0	0	0	0	0	1	0	1
Set Cursor at	1 Line		Write	0004H	1			(N-1)B				
Nth Digit	2 Lines	1st	Write	0004H	1	0		(N-1)B				
		2nd	Write	0004H	1	1		(N-1)B				
Display Character			Write	0005H		Character Code						
Read Busy Flag	Busy		Read	X	1	X	X	X	X	X	X	X
	Ready		Read	X	0	X	X	X	X	X	X	X

9.0 COUNTER-TIMER AND BUS EXTENDER BOARD

9.1 Purpose of the Counter-Timer Board

The counter-timer board contains a CMOS Z-80 counter-timer circuit with all the Z-80 interrupt features compatible with the STD bus daisy chain interrupt structure. The counter-timer board also provides a subset of STD bus signals at an edgeboard connector. These signals will be used to interface an S-100 bus video graphics board with the data logger. A block diagram of the counter-timer board is shown in Figure 25.

9.2 Features of the Counter-Timer Board

Some of the features of the counter board are:

- subset of STD bus signals at an edge connector
- CMOS low-power Z-80 counter-timer circuit
- four independent 8-bit counter-timer channels
- cascading of counters is possible
- three zero count/timeout outputs available at a connector

The counter-timer board provides the logic necessary to handle the mode 2 daisy chain interrupt structure of the STD bus like most of the other boards described thus far. For a detailed schematic see Appendix 7.

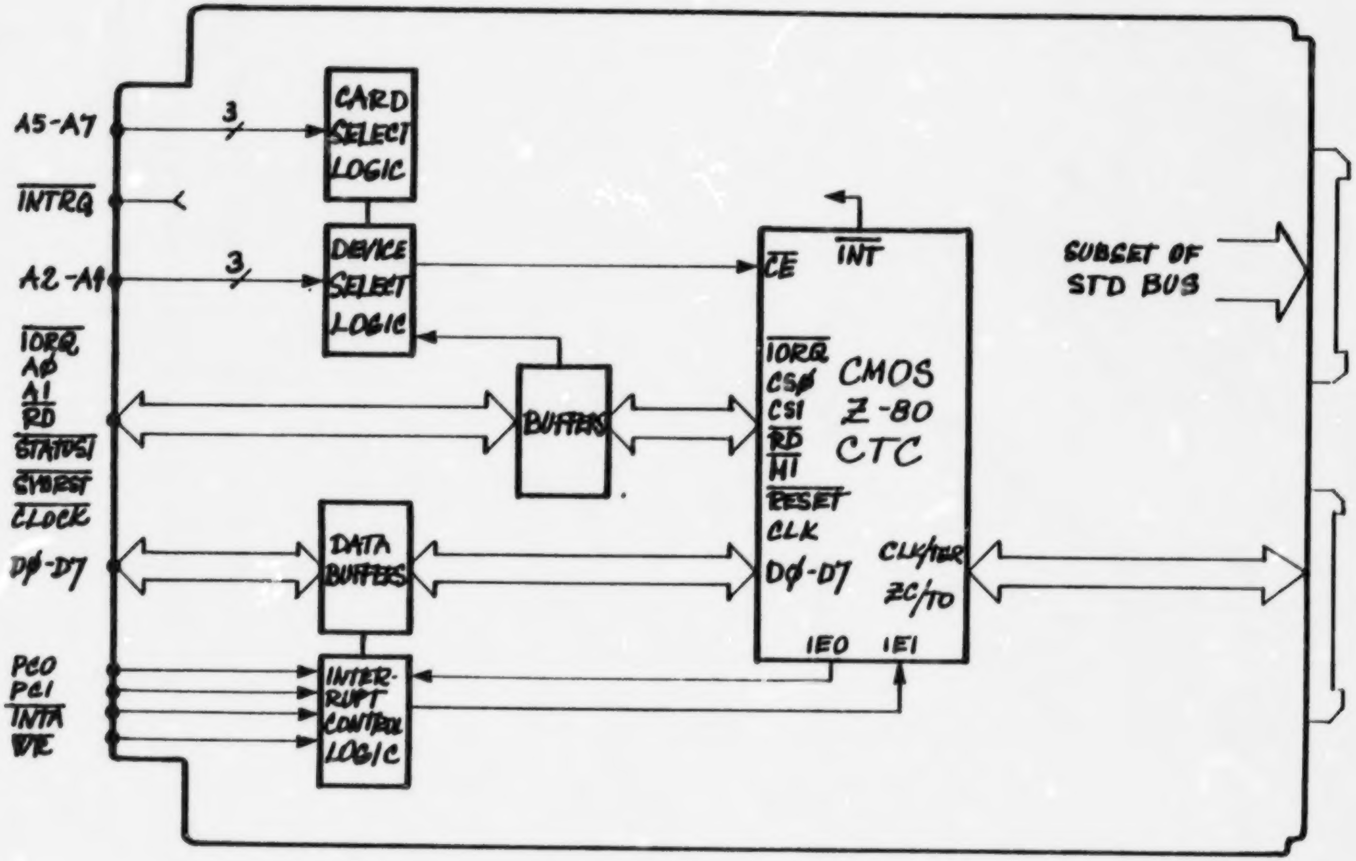
A5-A7
INTRQ
A2-A4
IORQ
AØ
A1
RD
STATUS1
SYSRST
CLOCK
DØ-D7
PCO
PCI
INTA
WE
3
3
CARD SELECT LOGIC
DEVICE SELECT LOGIC
BUFFERS
DATA BUFFERS
INTER-RUPT CONTROL LOGIC
CE
INT
IORQ
CSØ
CS1
RD
M1
RESET
CLK
DØ-D7
CMOS Z-80 CTC
CLK/TRG
ZC/TO
IEO
IEI
SUBSET OF STD BUS

Figure 25: **BLOCK DIAGRAM OF COUNTER-TIMER BOARD**

9.3 Programming the Counter-Timer Board

The counter-timer device is addressed as four jumper variable I/O base addresses. The default addresses and their corresponding counter/timer channel designation is shown in Figure 26.

Address	Function
0010H	select channel 0
0011H	select channel 1
0012H	select channel 2
0013H	select channel 3

Figure 26: Addressing of the Counter-Timer Board

When programming the counter as an interrupt timer, three control words must be written to the applicable counter/timer channel - channel control word, time constant, and interrupt vector word. Programming the control word for the corresponding I/O port is explained in the Zilog Product Specification sheet listed in Appendix 7. The counter/timer device is programmed so as to provide an interrupt to the CPU at specified time intervals. During the interrupt handling routine, the CPU will monitor (through the A/D board) the battery condition and alert the operator if the battery status is unacceptable.

10.0 VIDEO INTERFACE MODULE

The operator has the option of displaying the unprocessed profile sides on a regular television using a high resolution graphics board. All field measurement data which has been logged on tape can be verified using the video interface module. By examining the video display, any error made during a profile measurement can be easily detected.

10.1 Purpose of the Video Interface Module

It was decided to use the existing graphics board from the former data logging system. Because the former data logger is based on the S-100 bus, an interface is necessary to accommodate the two different bus sytems.

The graphics board itself consumes over 1 amp and is not necessary during field measurement. For these reasons a separate module is used to house all interfacing, power supplies, modulator, and graphics board.

10.2 Video Board

All video graphics are displayed by the MicroAngelo MA520 graphics board. It is a high resolution graphics board with 512 pixels horizontal by 480 pixels vertical. It is a Z-80 microprocessor based S-100 board which contains on-board firmware that handles all graphics control commands. Literature on the graphics board and its interfacing to other systems is listed in Appendix 8.

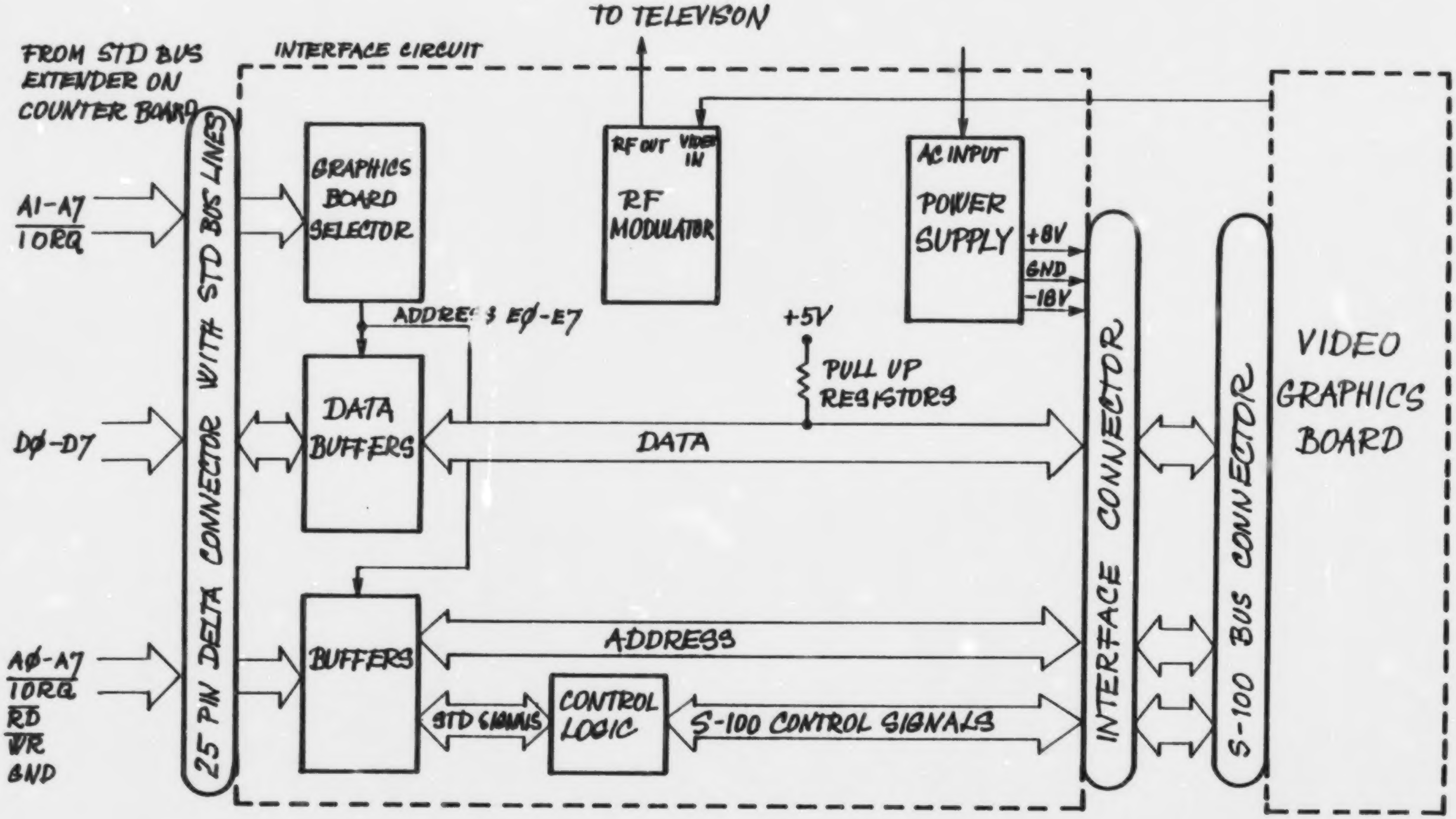
TO TELEVISON
FROM STD BUS EXTENDER ON COUNTER BOARD
INTERFACE CIRCUIT
A1-A7
IORQ
DØ-D7
AØ-A7
IORQ
RD
WR
GND
25 PIN DELTA CONNECTOR WITH STD BUS LINES
GRAPHICS BOARD SELECTOR
ADDRESS EØ-E7
DATA BUFFERS
BUFFERS
STD SIGNALS
CONTROL LOGIC
RF OUT
VIDEO IN
RF MODULATOR
AC INPUT
POWER SUPPLY
+8V
GND
-18V
+5V
PULL UP RESISTORS
DATA
ADDRESS
S-100 CONTROL SIGNALS
INTERFACE CONNECTOR
S-100 BUS CONNECTOR
VIDEO GRAPHICS BOARD

Figure 27: **BLOCK DIAGRAM OF VIDEO INTERFACE MODULE**

10.3 Interface Circuitry

The interface logic and associated hardware is illustrated in the block diagram of Figure 27. The interface logic is enabled only when the video graphics board is addressed. The interface between the STD bus signals and the S-100 is not complicated because of the parallel port configuration of the graphics board and the fact that both systems are Z-80 based.

The timing logic necessary to interface the STD bus control signals and those of the S-100 bus is given in Figure 28.

S-100 Control Signal	STD Bus Equivalent
PDBIN	IORQ.RD
SINP	IORQ.RD
SOUT	IORQ.WR
$\overline{\text{PWR}}$	$\overline{\text{IORQ.WR}}$

Figure 28: Timing Control Logic of STD to S-100 Bus

The data bus lines are also pulled high with 10KOhm resistors because the 'HC' (high speed CMOS) logic levels of the data logger's STD bus cards are not directly compatible with the graphics board 'LS' (low power Schottky) logic levels.

The RF modulator is a self-contained module which interfaces the RS-170 composite video output standard of the graphics board to a regular RF input television set on channel 3 or 4. The specification sheets for this modulator are contained in Appendix 8.

11.0 POWER SUPPLY/CHARGER BOARD

The battery data logger system required a precision +10VDC voltage source, as well as ±12VDC and +5VDC. The power supply required also had to have the capability of re-charging two 5AH batteries and be as small in size as possible. It was decided to develop a unit in-house since there was no power supply/charger unit readily available to meet these requirements.

11.1 Features of the Power Supply/Charger

The power supply/charger provides four separate regulated outputs on either an A.C. line source or batteries. There are two dc-to-dc converters on the board. One provides +12VDC and -12VDC with an isolated ground for serial communications with peripheral devices or other computers. The other converter maintains a sufficient voltage to a precision regulator when the battery gets discharged.

Other features are as follows:

- +12VDC
- +10.000 VDC
- delivers up to 5 amps at 5 volts for TTL/CMOS boards
- crowbar overvoltage protection on +5VDC output

- fuse protection

- continuous operation in the event of A.C. power failure

- cycle-charging for extended battery life

- charger on only when main power switch is off so as to prevent voltage spikes during measurements

- current limit on charger

- charger "on" indicator

- one or two 12-volt batteries of 5AHR each can be used simultaneously

- will provide with single battery (12V at 5AH), 6 hours of continuous measurements at 0.6 amps average current consumption expected

- 4"W x 9"L x 1.5"H

11.2 Specifications of Power Supply/Charger

The electrical specifications for the power supply/charger board are as follows:

- 100-170 VAC operation

- +5VDC +.2% at 5 amps output

- +12VDC +.2% voltage regulation at +40mA output

- +10.000 VDC +2mV maximum with a load regulation of .01% with 15mA available at 25 degrees celsius

11.3 Power Requirements of Battery Data Logger

The worst case voltage and current requirements for the battery data logger are as follows:

- +5VDC +.2% at 1.1 amps max
- +12VDC +.25% at +25mA
- +10VDC +2mV at 4mA

A breakdown of the current requirements of the battery data logger is given in Figures 29 and 30.

Figure 29: Breakdown of Current Requirements of Battery Data Logger

Description	Max Current (mA)
Power supply board	45
Power supply board with serial link on standby and transducers on	170
CPU board	63
Display/keypad board with display on	13
Serial/parallel board	11
Serial/parallel board with link	61
Cassette board with cassette drive on standby	31
Cassette board with cassette drive on read/write	161
Cassette board with cassette drive on rewind	661
Counter-timer board	21
Analog-to-digital converter board	120
Total Standby Current	304
Total Current During Tape Read/Write	559
Total Current During Tape Rewind	1059
Total Current During Measurements	429

Figure 30: Breakdown of Current Consumption of Power Supply/Charger

Description	Max Current
With batteries and potentiometer load	45
With batteries and serial link on (normally off)	135 ma
On A.C. power with potentiometer load and trickle charging	80 ma
On A.C. power with serial link on and trickle charging	170 ma
Battery charging (1 battery 12V, 5AH)	up to 1.2 A
(2 batteries 12V, 5AH)	up to 2.2 A

11.4 Functional Description of Power Supply/Charger

The main function of the power supply/charger board is to charge the batteries and provide power to the various circuits of the data logger. A block diagram of the power supply is shown in Figure 31 and the actual circuit is given in Appendix 9.

Charging is done in accordance with battery specifications where the charge current is limited to 1 amp at a maximum voltage of 14.7 volts for a 12-volt battery. When this voltage is reached the charger is turned off and a "float" voltage of 14 volts with a trickle current is left on. If this current is insufficient and the potential across the battery terminals drops below 13.4 volts, the charger is turned on again and the cycle repeats until the battery settles at a current sufficient to maintain itself in a fully charged condition.

Other sections of the power supply board convert the battery voltage to the appropriate levels required by a computer system. One DC-to-DC converter provides +12VDC required for computer communications. Another converter maintains sufficient voltage to power a precision regulator used for dc excitation to the transducers. A high current regulator powers the logic circuits and the over-voltage circuitry protects the computer from high voltages.

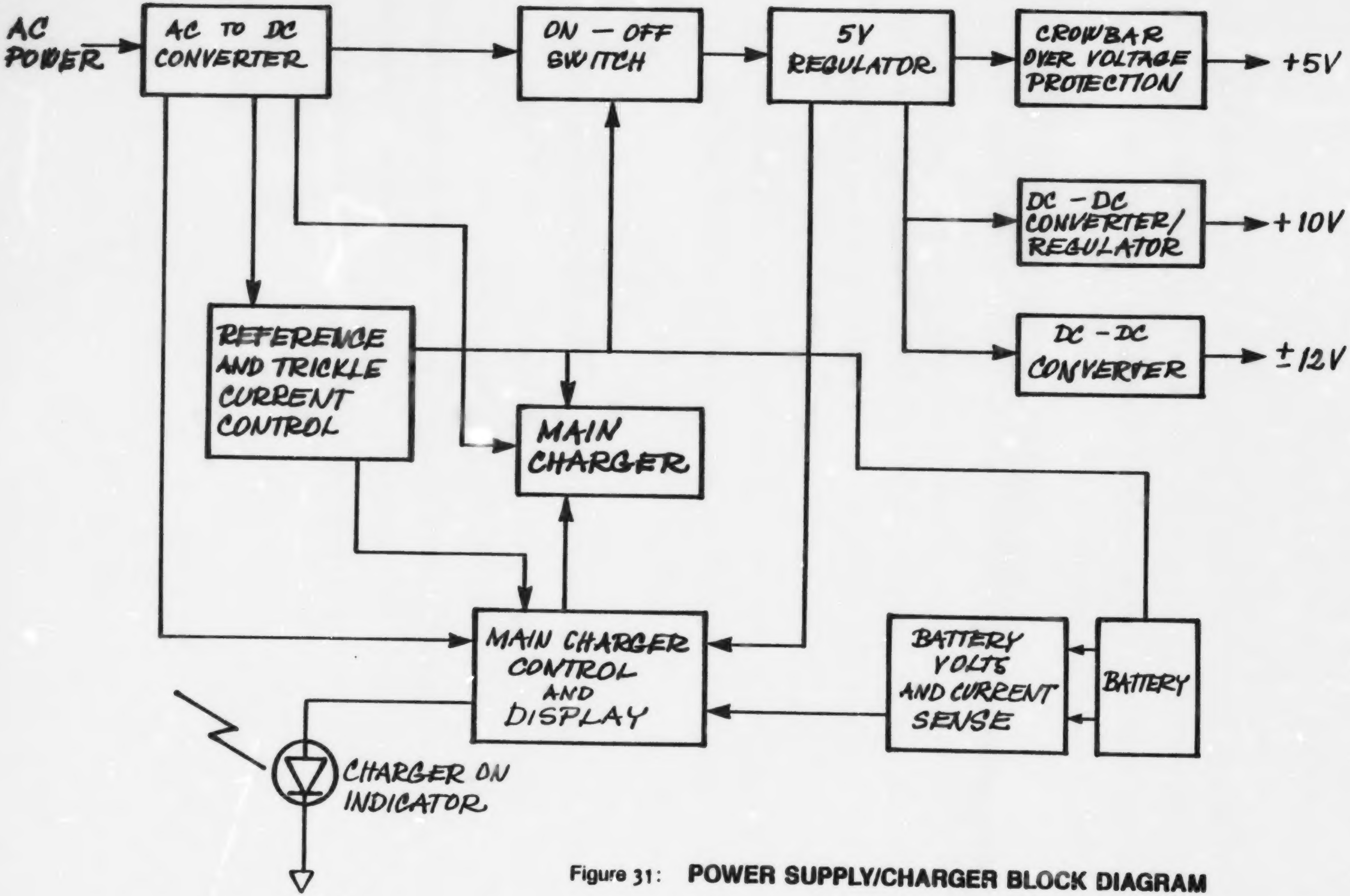
AC POWER
AC TO DC CONVERTER
ON — OFF SWITCH
5V REGULATOR
CROWBAR OVER VOLTAGE PROTECTION
+5V
DC – DC CONVERTER/ REGULATOR
+10V
DC – DC CONVERTER
±12V
REFERENCE AND TRICKLE CURRENT CONTROL
MAIN CHARGER
MAIN CHARGER CONTROL AND DISPLAY
BATTERY VOLTS AND CURRENT SENSE
BATTERY
CHARGER ON INDICATOR

Figure 31: **POWER SUPPLY/CHARGER BLOCK DIAGRAM**

12.0 WIRING LAYOUT/RELAY INTERFACE MODULE

The interconnection of the battery data logger to the profilometer head is given in Appendix 10. A 16-pin connector mounted on the front panel provides the electrical connection to the profilometer head via a 16-conductor cable. At the other end of the cable is a 24-pin connector configured with jumpers which in turn mates with a corresponding receptacle which is located on the profilometer head.

The jumpers on the 24-pin connector of the cable provide a method of wiring X and Y potentiometers in parallel. The 24-pin receptacle on the profilometer head contains a jumper which is hardwired as either rail (ground) or wheel (+5V) so that the computer can recognize what type of measurements are to take place on power-up.

The relay module provides a method of automatically switching the precision 10VDC to the appropriate potentiometer side that measurements are being taken. By using low power reed relays, power consumption can be decreased by not having to provide power to all potentiometers at once. Reed relay control has the advantage over other methods of switching, such as a manual rotary switch, because it is completely sealed in epoxy, has negligible contact resistance, less contact degradation, and can be automatically controlled by the computer. The circuit for the relay module is given in Appendix 10.

13.0 SOFTWARE DESCRIPTION

The following sections contain a general description of the software routines contained in UV EPROM (ultraviolet erasable programmable read only memory). These routines are responsible for the process of collecting and storing data, monitoring the tape transport, voltage conditions, and interacting with the operator via keyboard and display.

The hardware driver routines which are also contained in EPROM were discussed previously along with the associated board. A more detailed software description and listing is available by the Planning and Research Department.

The software responsible for processing and analyzing the data which is transferred from the data logger to the development system is discussed in another report (see Reference 6) produced by the Planning and Research Department.

13.1 Keyboard Assignments

The operator has access, via the keyboard and dedicated switches, to tape operations such as recording, positioning, and reading. The operator can also monitor voltages across the potentiometers by displaying them on the LCD. Entry of measurement identification labels can also be done through the keyboard. There are eleven modes which can be accessed by the keyboard or dedicated function keys. These are listed in Figure 32.

Key Entry	Function	Extended Key Entry	Function
A	Scan the tape and display the number of records	E	Exit from scan tape mode
B	Display voltage for X and Y channels	E F	Exit to system monitor Display next channel
C	Cancel error condition		
D	Read a record and display the contents on a television or video monitor	E F	Exit to system monitor Display next record
Measure	Enter a measurement	E	Exit to system monitor
Store	Record measurement on tape		
Label	Enter identification of record	E F	Exit from label mode carriage return which locks in I.D. parameter being changed
Position	Position tape to nth record	C E F	Clear entry Exit without moving tape Carriage return after entry of digits (tape is positioned and returns)
Start	Commence measurement		
Stop	Halt measurement		
Finish	End of measurement of profile side		

Figure 32: Keyboard Assignment

13.2 Monitors

The software controlling the Rail and Wheel Profile Data Acquisition system is divided into four logical units called monitors. Each monitor is capable of communicating with the user via the keyboard and LCD display and is designed to perform a specific set of functions. Whenever one of the monitors is invoked by the user, it indicates its control of the system by writing a message on the display.

13.2.1 E-Mode Monitor

The E-Mode monitor takes control of the system on power-up and performs the following four tasks:

1. System Initialization

- initializes the buffer which is to contain the rail/wheel profile identification parameters.

- initializes the UART used in communicating with an external computer.

- initializes the appropriate flags and variables used by the B-Mode monitor.

- initializes the keypad/switches.

- initializes the display with a 6-digit ID mark, the number of last record written, and displays the "ready" message as shown below:

READY	ID	REC
(R/W)	XXXXXX	XXX

2. Scanning

- scans keypad for entry of data.

- scans UART for communication from external computer.

- checks the ground voltage, the voltage of the power supply used to excite the potentiometers, the A/D converter reference voltage, and battery low condition.

3. Action

- transfers control to A-Mode, B-Mode, or D-Mode monitors upon receipt of command via keyboard.

- upon receipt of "start of communication" character from external computer, the monitor will get command line from external computer, set system flag indicating that a dialogue with external computer is in progress, and transfer control to B-Mode monitor.

- displays appropriate error message on LCD if monitored voltages are out of range.

4. Error Status Display Conditions

- battery low.
- voltage out of range (power supply voltage too low, too high and/or ground not zero volts).
- tape not positioned after power-up (clear leader).
- end of tape, cassette door open, tape not present, tape is write protected.
- ID label not changed after power-up.
- ID mark not changed after complete profile recorded.
- unable to write record (after four attempts).
- unable to read record (after four attempts).
- entering B-Mode twice without first entering D-Mode (attempting to write the same record twice.)

- record missing (only two sides of a profile were recorded and a new profile was measured.)

All error conditions will prevent the recording of a record on tape unless the operator clears the error condition or cancels the error condition by pressing the "C" key. See flowchart of E-Mode in Figure 33.

13.2.2 A-Mode Monitor

The A-Mode monitor is given control of the system only by the E-Mode monitor. Its task is to enable the user to attach an identification label to each measurement made with the profilometer. The identification label consists of an 8-bit field. One digit defines the distance (in MM) the X-sensor must move before the coordinates of a point on the surface of the profile are stored. One digit defines the coordinate system in which the current measurement is made. Six digits uniquely identify each profile measured.

The A-Mode monitor performs four tasks in the following order:

1. Scanning

- keyboard scanning occurs until a digit entry from the keyboard has been received or a character requesting exit from the monitor.

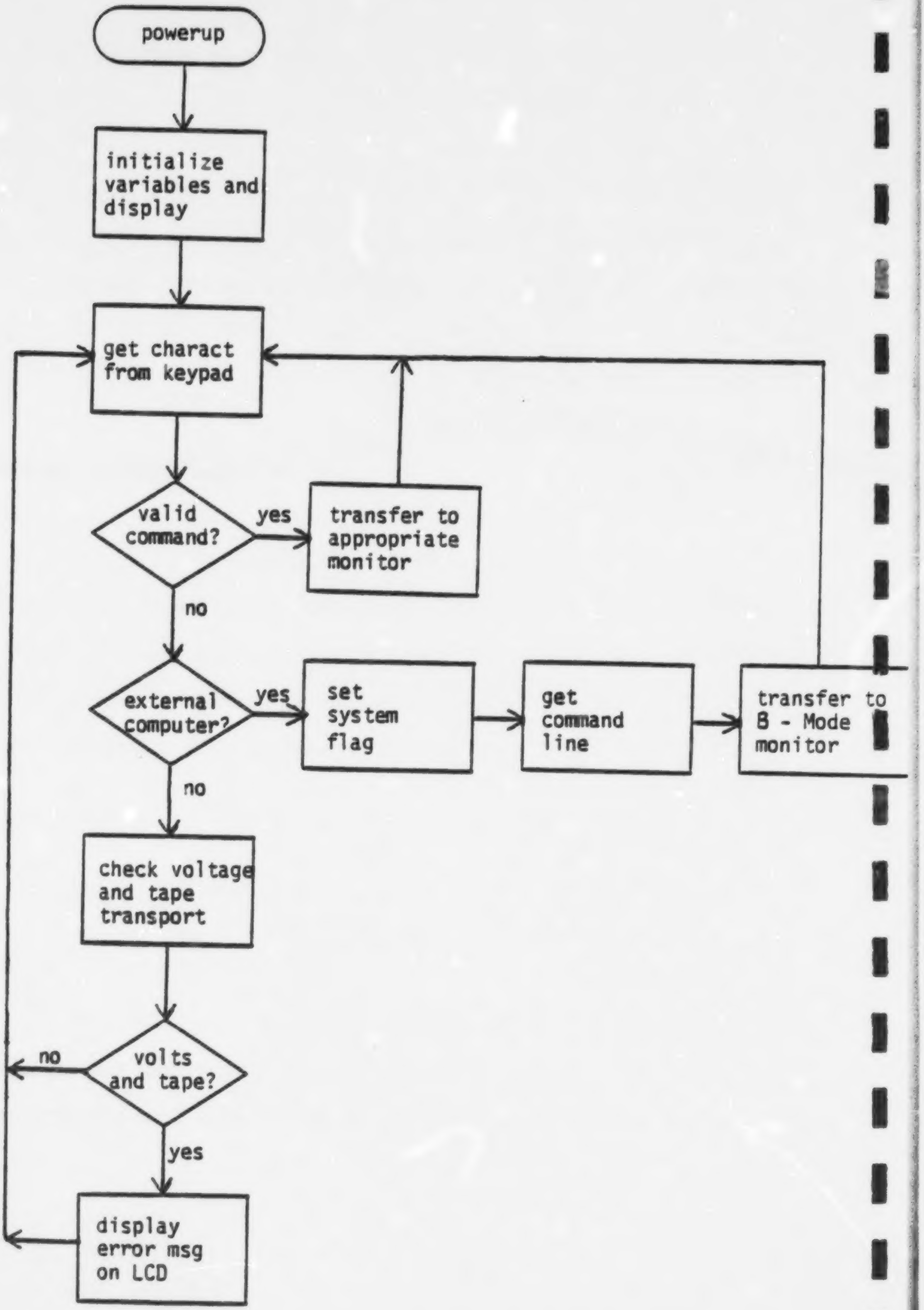
powerup
initialize variables and display
get charact from keypad
valid command?
yes
transfer to appropriate monitor
no
external computer?
yes
set system flag
get command line
transfer to B - Mode monitor
no
check voltage and tape transport
volts and tape?
no
yes
display error msg on LCD

Figure 33: E - Mode Logic

2. Action

- the monitor will indicate that a particular parameter may be modified by turning on the cursor underneath the corresponding digit on the display.

- returns control to the E-Mode monitor.

3. Scanning

- the keyboard is scanned until a digit is received from the keyboard or a character indicating that the user has modified the desired identification parameter.

4. Action

- displays the digit entered from the keyboard on the LCD display and stores it in RAM.

- indicates that the desired identification parameter has been modified by turning the cursor off.

See Figure 34 for a flowchart description of the A-Mode.

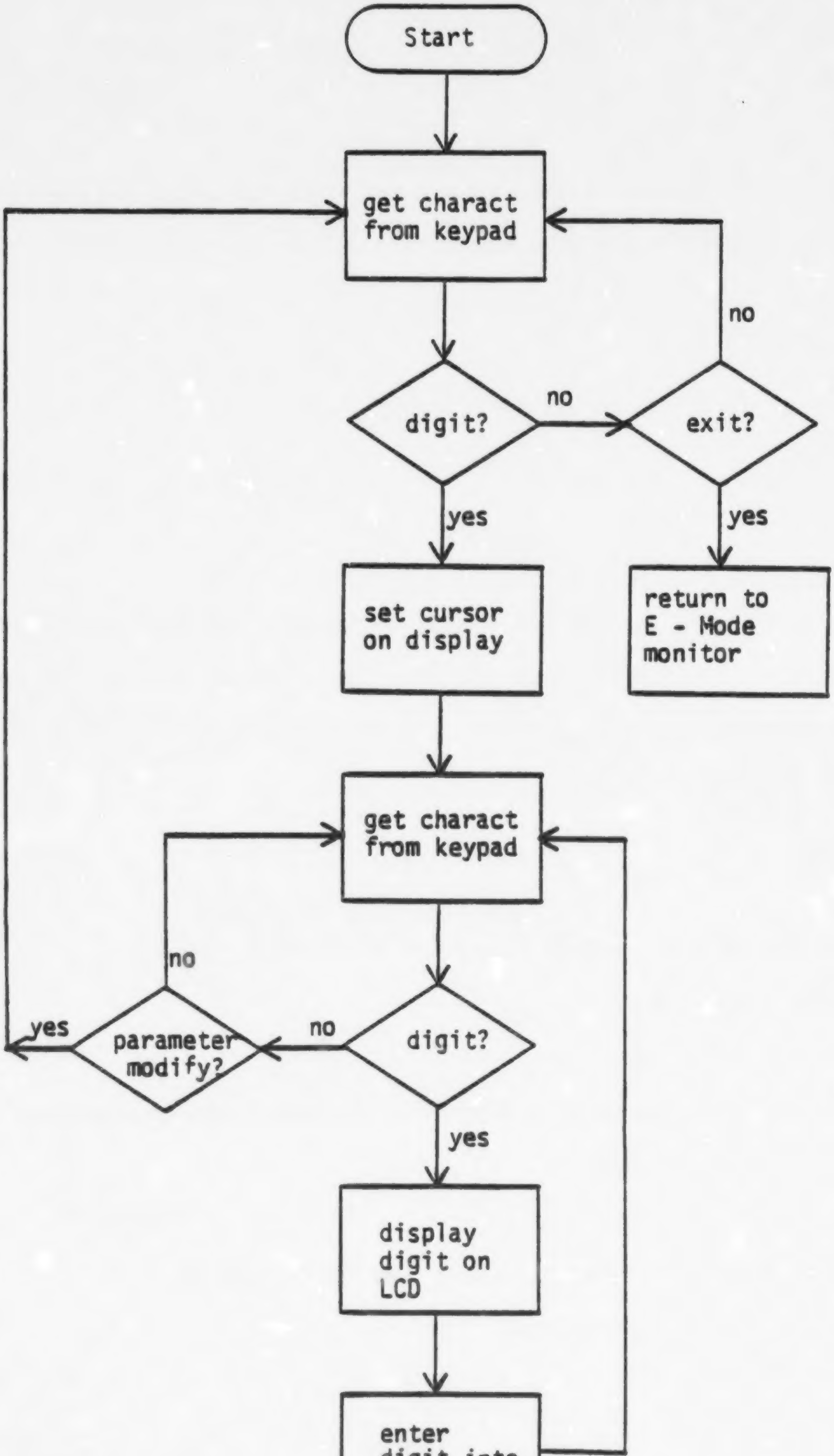
Start
get charact from keypad
digit?
no
exit?
no
yes
yes
set cursor on display
return to E - Mode monitor
get charact from keypad
no
yes
parameter modify?
no
digit?
yes
display digit on LCD
enter digit into buffer

Figure 34: A - Mode Logic

13.2.3 The B-Mode Monitor

The B-Mode monitor acquires control of the system only from the E-Mode monitor. It performs the following tasks:

1. Scanning

- checks the flag indicating whether a dialogue with an external computer is in progress.

- scans the keyboard for entry of a valid function selection.

- scans the keyboard for entry of parameter if a selected function requires one.

2. Action

- echos keyboard entries on LCD.

- extracts the function and parameters from a special buffer whenever a dialogue with an external computer is in progress.

3. Position Tape to Nth Record

- displays "position tape to" message on first line of display.

- displays "record #" message on second line of display.

- prompts operator for entry of digits from keyboard by turning cursor on at the position following "record #" on display.

- gets record number and scans "F", "E", and "C" function key commands.

- before positioning tape, the monitor will display "advancing tape" on line 1 and "to record XXX" on line 2.

- exit to system monitor directly after positioning tape.

4. Storing Data on Tape

- displays "writing record" message on line 1.

- displays "number XXX" message on line 2.

- writes record to tape.

- exits to system monitor.

5. Scanning Tape for Number of Records Written

- displays "scanning tape" message.

- displays "tape contains" message on line 1 and "XXX records" on line 2.

- waits for operator to press "E" key and exits to system monitor while ignoring all other keypad entries.

6. Display Data on Video Monitor

- displays ID mark on LCD display.

- displays profile side on video.

- looks for "F" and "E" function key commands from operator.

See Figure 35 for a flowchart representation of the B-Mode monitor.

13.2.4 The D-Mode Monitor

The D-Mode monitor acquires control of the system only from the E-Mode monitor. Its task is to get the coordinates of the profile and to store them in RAM. The flowchart description is shown in Figure 36. The D-Mode monitor accomplishes its tasks as follows:

1. Initialization

- determines which side of profile is to be measured first.

- from a table, determines the voltage (in A to D counts) corresponding to the user-specified X-sensor movement of 0.5, 1 or 2 millimeter

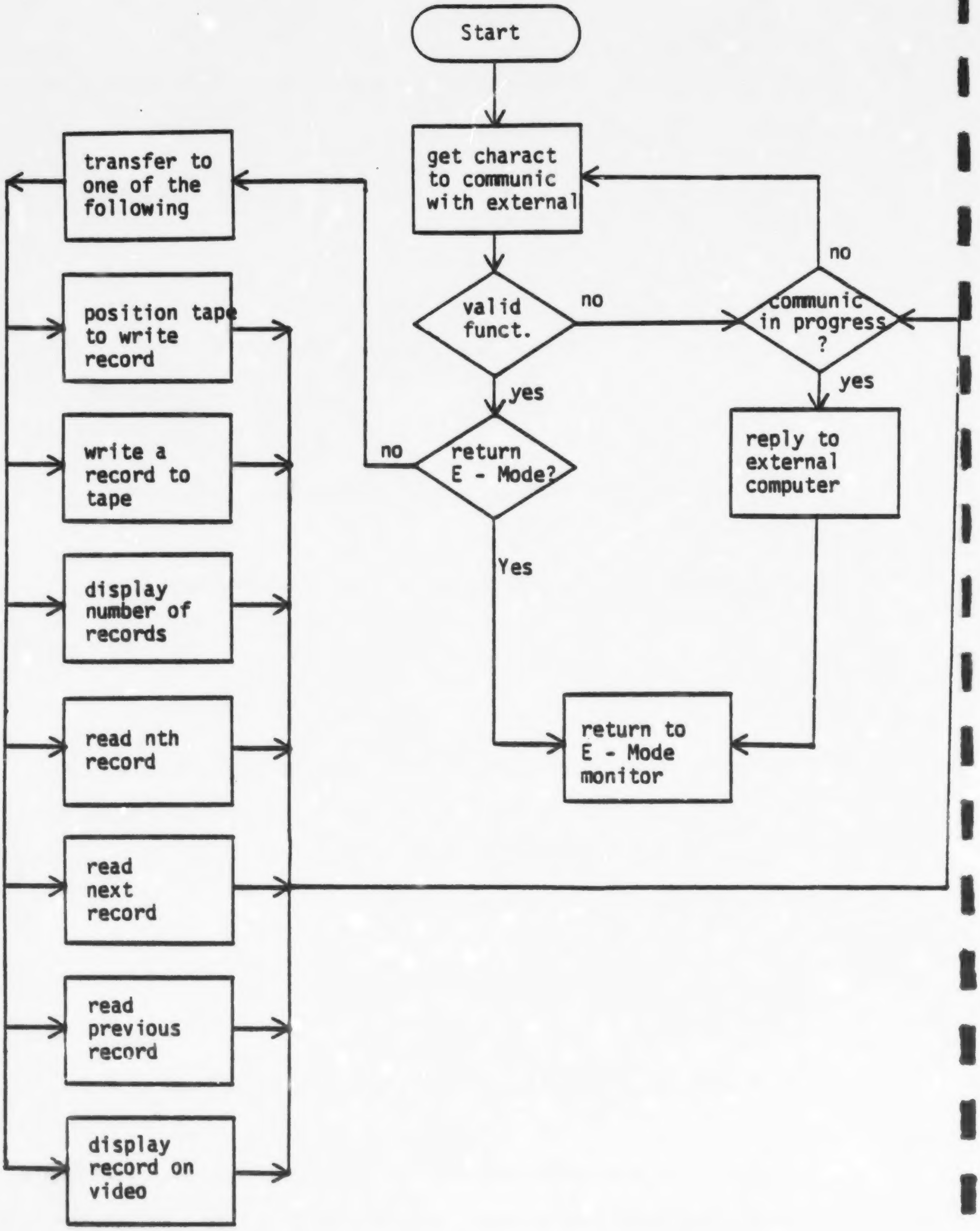
Start
get charact to communic with external
valid funct.
no
yes
communic in progress ?
no
yes
reply to external computer
return E - Mode?
no
Yes
return to E - Mode monitor
transfer to one of the following
position tape to write record
write a record to tape
display number of records
read nth record
read next record
read previous record
display record on video

Figure 35: B - Mode Logic

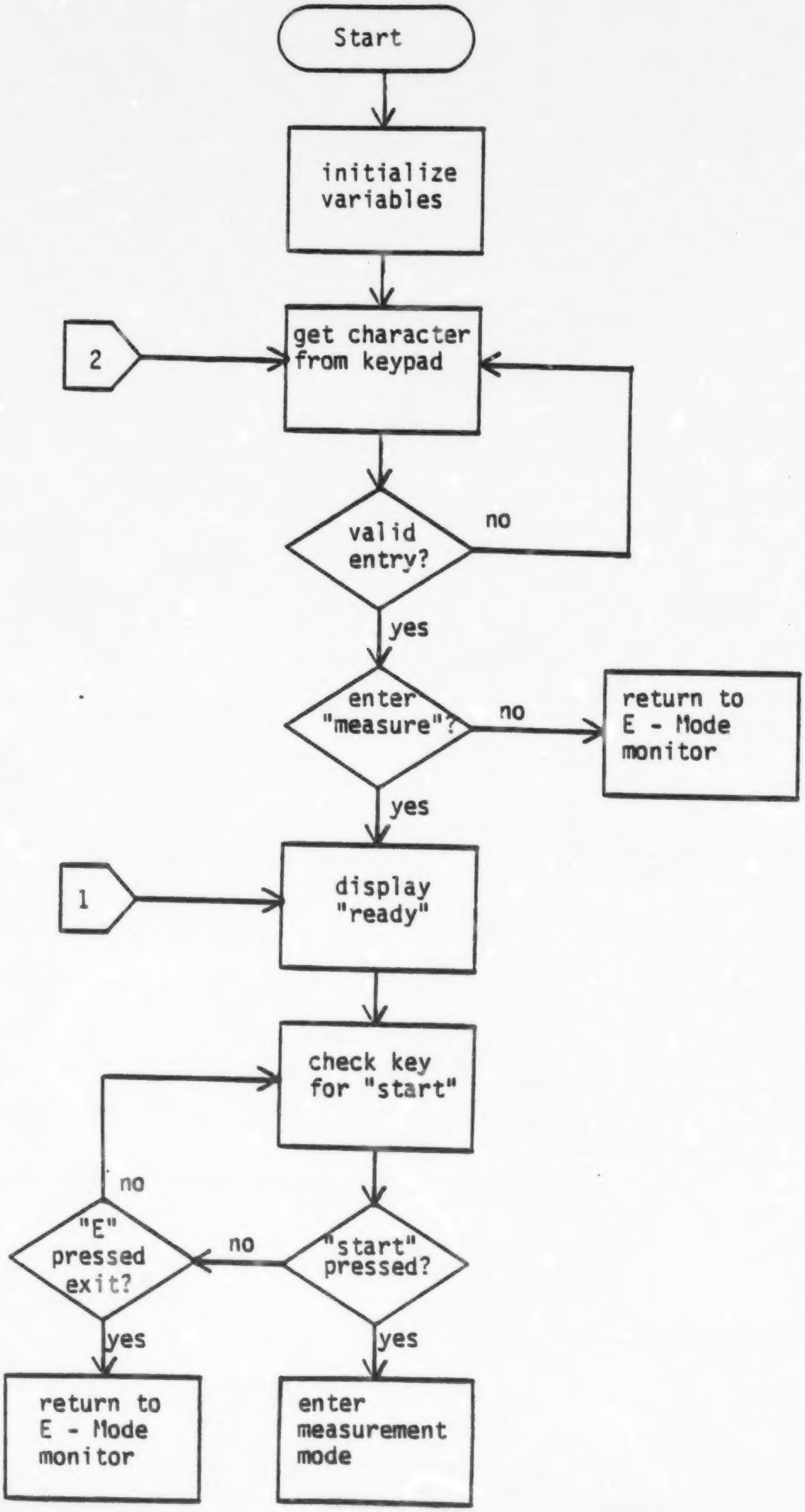
Start
initialize variables
get character from keypad
2
valid entry?
no
yes
enter "measure"?
no
return to E - Mode monitor
yes
1
display "ready"
check key for "start"
no
"E" pressed exit?
no
"start" pressed?
yes
yes
return to E - Mode monitor
enter measurement mode

Figure 36: D - Mode Logic

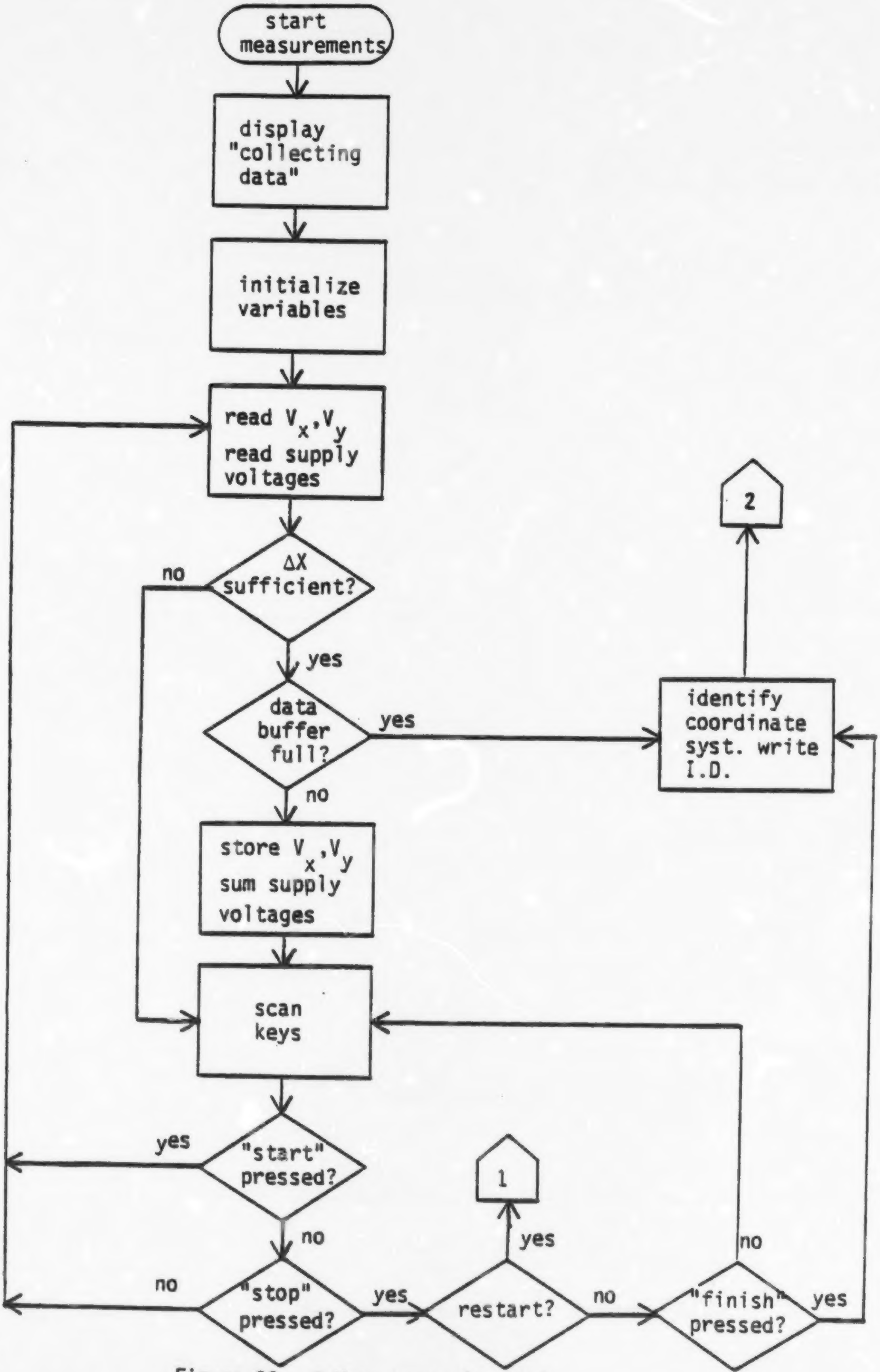
start measurements
display "collecting data"
initialize variables
read V_x,V_y read supply voltages
ΔX sufficient?
no
yes
data buffer full?
yes
no
identify coordinate syst. write I.D.
2
store V_x,V_y sum supply voltages
scan keys
yes
"start" pressed?
no
1
yes
no
no
"stop" pressed?
yes
restart?
no
"finish" pressed?
yes

Figure 36: D-Mode Logic (Cont'd)

steps and sets the appropriate variable to the value found in the table.

- sets to zero the four-byte variable which is to contain the sum of the voltage readings.

- sets to zero the variable which is to contain the number of coordinates measured.

2. Scanning

- the keyboard is scanned until the command to start measurements or exit ("E") from the D-Mode monitor is entered by the user.

- the "start", "stop", and "finish" switches are scanned.

3. Action

- depending on the command entered from the keyboard, control is returned to the E-Mode monitor or measurements are begun.

- on entry of "measure" condition, a "ready" message will be displayed on the LCD.

- the user starts measurement by entering "start", which in turn displays the "collecting data" message on the LCD.

- data storage will occur when the difference between the current and the previous measurement of the X-sensor voltage indicates that the X-sensor has moved a distance greater than or equal to the user-selected distance of 0.5, 1, or 2 mm.

4. Data Storage

- the buffer which is to contain the measurement data is checked for overflow.

- the voltage (in A/D counts) measured on the X-sensor channel is stored as a 2-byte integer in RAM.

- the voltage (in A/D counts) measured on the Y-sensor channel is stored as a 2-byte integer in RAM.

- the voltage (in A/D counts) measured on the channel connected to the X and Y sensor power supply is added into a 4-byte variable.

- the one-byte variable containing the number of points measured is incremented.

5. Scanning

- next the keyboard will be scanned for "stop", "finish", and "E" key entries.

- with "finish", the monitor will display "XXXX points" on line 1 and "side Y" on line 2 so as to indicate to the operator the number of measurements that were made.

- on exit from measurement mode, by pressing "E", the coordinate system used in making the measurements is identified and this information is stored in the appropriate position of the profile identification label.

- the side number of the measurement ID buffer is incremented after the record is written to tape which enables an entry into D-Mode to cancel a bad measurement.

13.3 Allocation of Data in RAM Memory

Upon exit from D-Mode, the rail/wheel profile measurement data exists in a 1024-byte buffer in RAM. The data has the format shown in Figure 37.

Byte			Description
Least Signif.		Most Signif.	
1	-	2	total number of bytes making up the data including bytes 1 and 2
3	-	8	rail/wheel profile identification field
9			I.D. of coordinate system in which measurements were made (1, 2, or 3)
10			distance between points along X-axis 1 = 0.5mm, 2 = 1mm, 3 = 2mm
11			number of points measured
12	-	15	sum of power supply voltage measurements

Byte			Description
Least Signif.		Most Signif.	
16	-	17	X coordinate (bit 15 = "1")
18	-	19	Y coordinate (bit 15 = "0")
20	-	1024	X and Y coordinates

Figure 37: Allocation of Data in RAM Memory

13.4 Storage of Data on Tape

The actual format used to store a record on tape was discussed in Section 6.7. The software control routine used to write data to tape includes the following steps:

1. the tape is positioned to write the record.

2. the record is written.

3. the tape is rewound to the beginning of the record just written.

4. the record is read and compared byte for byte with its image in RAM.

5. four attempts at rewriting the record are made before an error condition is indicated.

13.5 Transmission of Data

Additions to the data are made in order to ensure that there is no modification of the data during storage/retrieval to and from tape. Also during transmission to an external document, the same procedure is used.

It is necessary to ensure that the integrity of the data is not lost at any time. In order to do this, the data is modified as follows:

- the first field contained in bytes 1 and 2 is incremented twice.
- the entire record, starting from byte 1 and ending with the last Y-coordinate measured is divided by the 16-bit cyclical redundancy check polynominal (CRC check).
- the 16-bit remainder of the division is appended to the record following the Y-coordinate of the last point measured.
- the entire record, including the remainder is written to tape or transmitted to the external computer.

In order to verify that the data has remained unchanged, it is only necessary to divide the record by the same CRC. A remainder of zero ensures that no changes in data have occurred.

14.0 CONCLUSION

A battery powered data logger and data acquisition system was described. This unit presented an improvement on an earlier-developed system used to measure wheel and rail profiles.

The versatility of the data logger and data acquisition system has also been demonstrated. It was proposed to temporarily use the battery data logger for locomotive adhesion tests. Using basically the same hardware, the software was modified to handle two separate tests. The first test was the GE locomotive and the SD40-2 locomotive adhesion test. The second test was the 4744 AC locomotive and SD40-2 comparative adhesion test.

The battery data logger was configured to measure and calculate the following parameters:

1. power
2. drawbar pull
3. speed
4. wheel creep

The high performance A/D board described in Section 5 has not yet been tested. This results from delays in production and delivery from the manufacturer. Instead, a bus compatible version of the board was used temporarily for the locomotive adhesion tests.

The battery data logger proved both successful in bench tests and field tests and showed its immunity to electrical noise and vibrations inherent in railroad environments.

A more detailed description of the software package for the battery data logger is available from the Planning and Research Department. The software used for the actual analysis of the data is also available from the Planning and Research Department, as well as processed plots of both wheel and rail profiles.

REFERENCES/BIBLIOGRAPHY

1. STD Bus Technical Manual, Monterey CA: Pro-Log Corporation, 1982: pps 1-1 to 3-4.

2. Toshiba CMOS Z-80 8 Bit Microprocessor Data Book, Tokyo, Japan: Toshiba Corporation, 1984-11-30.

3. 1984 Z-80 Family Product Specification Handbook, Campbell, CA: Zilog Corporation, 1984: pp 1-86.

4. J.C. Rooks, "Interface Information as Applied to CM600-MiniDek", Application Note Spec. 0072, Braemar Computer Devices.

5. J.C. Rooks, "Manchester Phase Encoding as Applied to Digital Cassette Tape Transports", Application Note Spec 0070, Braemar Computer Devices.

6. G. Izbinsky, H. Schrekinger, H. Soares, "A Wheel/Rail Profilometer System", Report No. T-805-84, Department of Research, Canadian Pacific Ltd., Feb. 1984.

7. G. Izbinsky, G. Warshaw, "Concept of a Profilometer for Rail Wear Determination", Report No. S655-81, Department of Research, Canadian Pacific Ltd., Dec. 1981.

APPENDIX 1

STD BUS AND INTERRUPT PRIORITY DAISY CHAINING

SECTION 1
STD BUS Specification

Introduction

The STD BUS standardizes the physical and electrical aspects of modular 8-bit microprocessor card systems. It provides a dedicated and orderly interconnection scheme (Fig. 1-1). The standardized pinout and 56-pin connector lend themselves to a bussed motherboard that permits any card to work in any slot.

The STD BUS is dedicated to internal communications. All other interconnections are made via suitable connectors at the I/O interface card edge. The concept gives an orderly signal flow across the cards. Peripheral and I/O devices can be connected to the system, according to their own unique connector and cabling requirements.

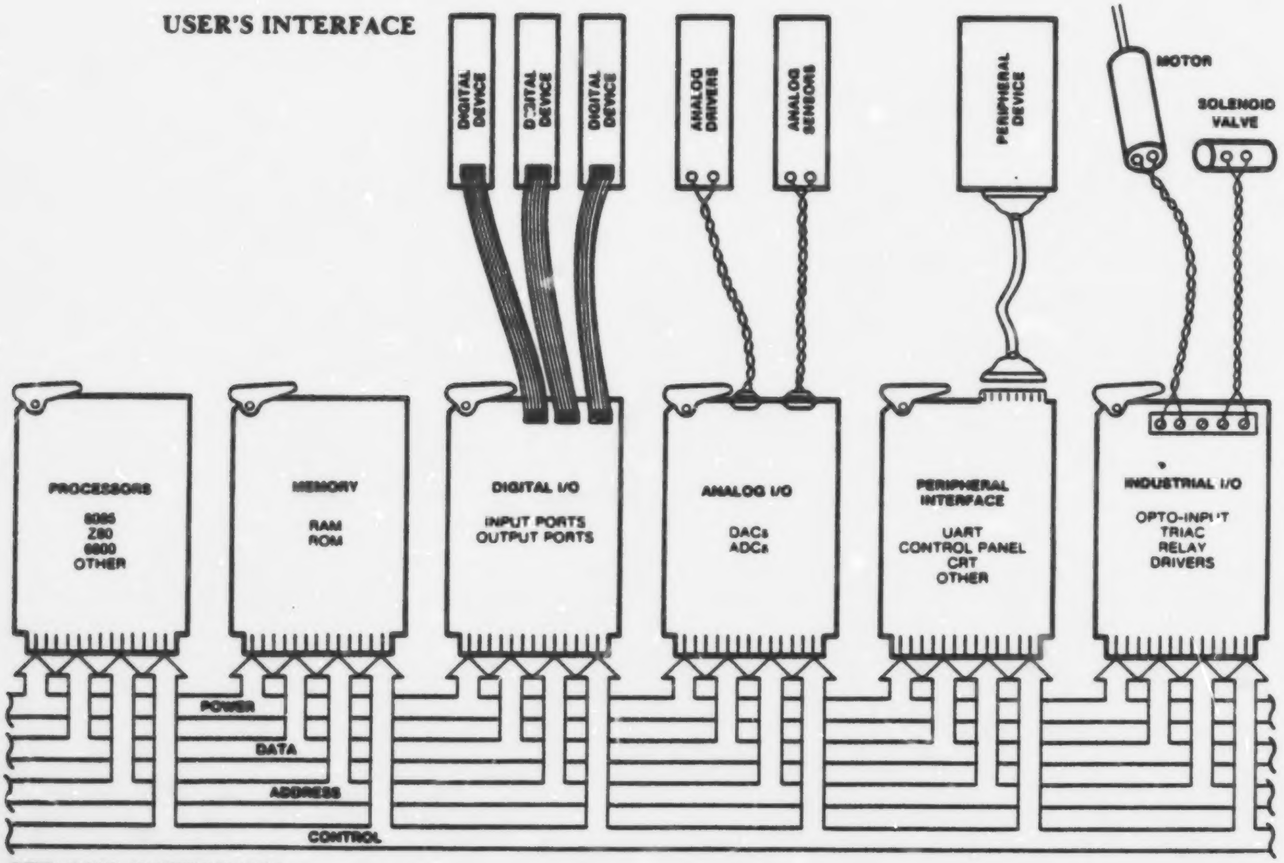
USER'S INTERFACE
DIGITAL DEVICE
DIGITAL DEVICE
DIGITAL DEVICE
ANALOG DRIVERS
ANALOG SENSORS
PERIPHERAL DEVICE
MOTOR
SOLENOID VALVE
PROCESSORS
8085
Z80
6800
OTHER
MEMORY
RAM
ROM
DIGITAL I/O
INPUT PORTS
OUTPUT PORTS
ANALOG I/O
DACs
ADCs
PERIPHERAL INTERFACE
UART
CONTROL PANEL
CRT
OTHER
INDUSTRIAL I/O
OPTO-INPUT
TRIAC
RELAY
DRIVERS
POWER
DATA
ADDRESS
CONTROL
STD BUS INTERFACE

Figure 1-1. STD BUS Implementation.

Organization and Functional Specifications (with pin definitions)

The STD BUS pinout is organized into four functional groups:

• Dual Power Busses:	Pins 1-6 and 53-56
• Data Bus:	Pins 7-14
• Address Bus:	Pins 15-30
• Control Bus:	Pins 31-52

The organization and pinouts are shown in Table 1-1. This table lists the mnemonic function and signal flow direction (referenced to the processor card in control of the BUS) for each pin of the STD BUS. The STD BUS is further defined as requiring a 56-pin (dual 28) card edge connector, with 0.125-in. pin centers. Connectors are on a spacing interval of 0.5-in. centers minimum, and they accept the standard 4.5 x 6.5 x 0.062-in. card.

Table 1-1. STD BUS Pinouts with Signal Flow Referenced to the Processor Card.

	COMPONENT SIDE				CIRCUIT SIDE			
	PIN	MNEMONIC	SIGNAL FLOW	DESCRIPTION	PIN	MNEMONIC	SIGNAL FLOW	DESCRIPTION
LOGIC POWER BUS	1	+5VDC	In	Logic Power (bussed)	2	+5VDC	In	Logic Power (bussed)
	3	GND	In	Logic Ground (bussed)	4	GND	In	Logic Ground (bussed)
	5	VBB #1	In	Logic Bias #1 (-5V)	6	VBB #2	In	Logic Bias #2 (-5V)
DATA BUS	7	D3	In/Out	Low-Order Data Bus	8	D7	In/Out	High-Order Data Bus
	9	D2	In/Out	Low-Order Data Bus	10	D6	In/Out	High-Order Data Bus
	11	D1	In/Out	Low-Order Data Bus	12	D5	In/Out	High-Order Data Bus
	13	D0	In/Out	Low-Order Data Bus	14	D4	In/Out	High-Order Data Bus
ADDRESS BUS	15	A7	Out	Low-Order Address Bus	16	A15	Out	High-Order Address Bus
	17	A6	Out	Low-Order Address Bus	18	A14	Out	High-Order Address Bus
	19	A5	Out	Low-Order Address Bus	20	A13	Out	High-Order Address Bus
	21	A4	Out	Low-Order Address Bus	22	A12	Out	High-Order Address Bus
	23	A3	Out	Low-Order Address Bus	24	A11	Out	High-Order Address Bus
	25	A2	Out	Low-Order Address Bus	26	A10	Out	High-Order Address Bus
	27	A1	Out	Low-Order Address Bus	28	A9	Out	High-Order Address Bus
	29	A0	Out	Low-Order Address Bus	30	A8	Out	High-Order Address Bus
CONTROL BUS	31	WR*	Out	Write to Memory or I/O	32	RD*	Out	Read Memory or I/O
	33	IORQ*	Out	I/O Address Select	34	MEMRQ*	Out	Memory Address Select
	35	IOEXP	In/Out	I/O Expansion	36	MEMEX	In/Out	Memory Expansion
	37	REFRESH*	Out	Refresh Timing	38	MCSYNC*	Out	CPU Machine Cycle Sync.
	39	STATUS 1*	Out	CPU Status	40	STATUS 0*	Out	CPU Status
	41	BUSAK*	Out	Bus Acknowledge	42	BUSRQ*	In	Bus Request
	43	INTAK*	Out	Interrupt Acknowledge	44	INTRQ*	In	Interrupt Request
	45	WAITRQ*	In	Wait Request	46	NMIRQ*	In	Nonmaskable Interrupt
	47	SYSRESET*	Out	System Reset	48	PBRESET*	In	Push-Button Reset
	49	CLOCK*	Out	Clock from Processor	50	CNTRL*	In	AUX Timing
	51	PCO	Out	Priority Chain Out	52	PCI	In	Priority Chain In
AUXILIARY POWER BUS	53	AUX GND	In	AUX Ground (bussed)	54	AUXGND	In	AUX Ground (bussed)
	55	AUX +V	In	AUX Positive (+12V DC)	56	AUX -V	In	AUX Negative (-12V DC)

*Low-level active indicator

SECTION 2

STD BUS Practice

The industry-based STD Manufacturers Group meets regularly to review concerns regarding the STD BUS. It has resolved the following recommended practice for the design of STD BUS cards. The STD Practice is supplemental to the STD Specification and is to be applied at the discretion of the user. The current STD Practice relates to:

- Compatibility designation
- Bus timing
- Parallel priority interrupt
- Card keying for polarity
- Open collector bus signals

Compatibility Designation

STD BUS cards that use peripheral chips usually depend on specific timing signals from the processor. This dependency prevents peripheral cards from being used interchangeably with cards from other families.

The STD Practice for designating compatibility is to label cards that are processor-timing-dependent, with reference to the CPU device: STD-Z80, STD-8085, STD-6800, etc.

Bus Timing

Card designers require bus timing definitions to insure compatibility. The recommended STD Practice for cards that source the bus control signals is for each card to specify the waveforms and timing information. Bus timing is further defined in the STD-Z80 and STD-8085 specifications.

Parallel Priority Interrupt

The STD BUS provides signal lines for interrupt requests and bus requests. In systems with only a single interrupting device or a single alternate controller, these lines are sufficient to allow direct implementation. But in systems with multiple interrupting devices or multiple bus controllers, a priority scheme is necessary. The STD BUS is designed to handle either serial priority or parallel priority schemes.

Serial Priority. The STD BUS includes a priority-chain bus signal for serial priority schemes. Serial priority, using PCI and PCO signals, requires that each peripheral needing priority must have logic on the card to service the request, as shown in Figure 2-1. This scheme is practical with peripheral devices designed to service a serial priority chain such as the Z80 family of devices.

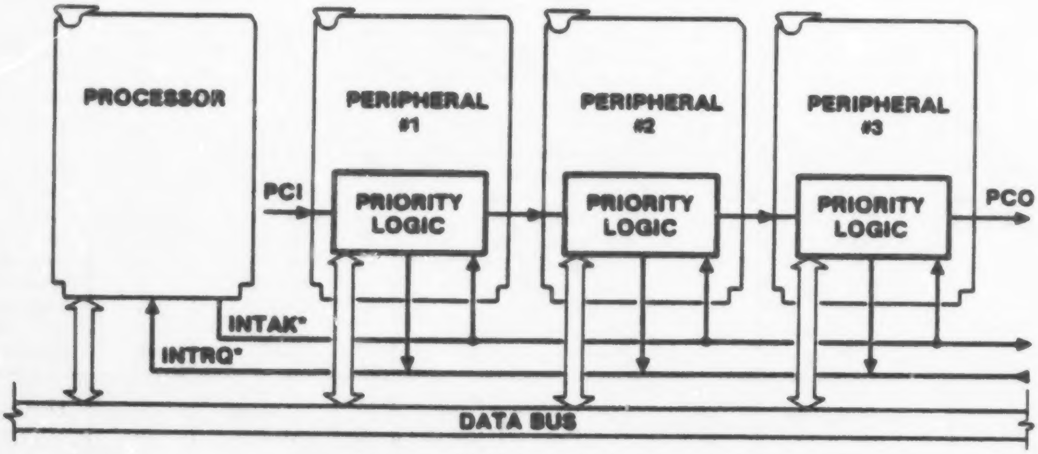

Figure 2-1. Serial Priority Interrupt Scheme.

APPENDIX 2

Z-80 PROCESSOR CARD

PRO-LOG®
CORPORATION

STD 7000

78C13 CMOS Z80 Processor Card

USER'S MANUAL

5/84

SECTION 1
Purpose and Main Features

PURPOSE

The 78C13 combines the advantages of CMOS logic and a CMOS CPU with onboard memory and memory expansion controls.

The memory consists of four JEDEC standard 28-pin sockets, which can be configured for 8K x 8 or 2K x 8 static CMOS RAM, PROM, or EPROM. Address, data, and control buses are bidirectional which allows external access to on-card memory.

Onboard I/O ports control MEMEX and Segment, so that the 78C13 can control expanded memory schemes.

Fully implemented in high speed CMOS, the 78C13 offers high noise immunity, low power consumption, and a wide temperature range. It is designed to be used with other CMOS cards on the STD BUS.

FEATURES

- **Fully CMOS: high noise immunity, low power consumption, wide temperature range**
- **CMOS Z80 processor**
- **32K byte capacity with four 8K x 8 memory devices or 8K byte capacity with four 2K x 8 memory devices**
- **DMA to onboard memory sockets**
- **2.5 MHz crystal**
- **Dynamic RAM refresh control**
- **Power-on reset with Vcc sensing**
- **MEMEX and Segment memory expansion control**
- **Single +5V operation**

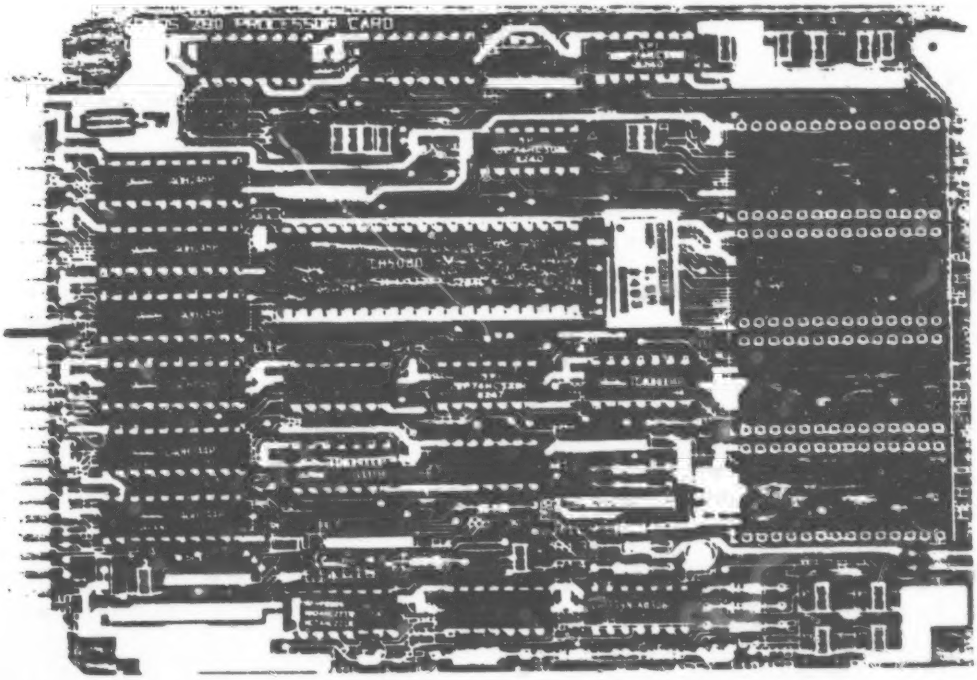

Figure 1-1. 78C13 CMOS Z80 Processor Card

FUNCTIONAL DESCRIPTION

This portion of section 1 describes the function of each block of circuitry shown in the Functional Block Diagram of figure 1-2.

CMOS Z80 CPU

The CMOS Z80 CPU is a CMOS version of the industry standard Z80. All the functions, features, and capabilities of a Z80 are coupled with the advantages of CMOS technology; high noise immunity, low power consumption, and wide temperature range. The result is a CPU with proven features that can use existing software and that can be used under extreme conditions. Note that the part number for the CMOS Z80 may not include "Z80."

Onboard Memory

The onboard memory capability consists of four 28-pin sockets. This memory can be 32K bytes consisting of a combination of four 8K x 8 RAMs or ROMs, or it can be 8K bytes consisting of a combination of four 2K x 8 RAMs or ROMs. The 2K parts cannot be mixed with the 8K parts.

Memory Decode

The memory decode consists of both an 8K x 8 and a 2K x 8 memory decoder. This circuitry decodes the memory address lines into 8K and 2K blocks to select the addressed memory socket. For more information, see section 2, **Installation and Specifications**.

I/O Decode

The I/O decode section selects the onboard port and decodes the address lines only during an I/O write cycle. MEMEX and Segment can be written through the onboard port.

Reset

The reset circuit resets the CPU during power-up or during a pushbutton reset. During power-up, the circuit keeps the CPU in a reset state until the power supply reaches a voltage in the proper operating range. This delay ensures that the CPU has a valid power supply when it leaves reset, which prevents latch-up. The pushbutton reset circuit debounces the pushbutton input and then shortens the pulse width and synchronizes it with the M1* signal to avoid interference with refresh of any dynamic RAM.

MEMEX and Segment Port

Both the STD BUS memory expansion line, MEMEX, and the user card edge memory expansion line, Segment, are controlled by the on-card port of the 78C13. Both signals provide control to expand memory for large systems. See section 3, Operation and Programming, for more detail.

APPENDIX 3

A/D CONVERTER CARD

BARADINE®

CMOS 12-bit
A/D Converter

CMOS-ADC12

Preliminary Data January, 1984

FEATURES

- Fully CMOS design
- Single +5 volt, 120 mA or triple 5V/15mA, +/-15V/+/-20mA
- Operation -40°C to +85°C
- Z80, 8085, 6800 compatibility
- Interrupts for Z80 and 8085
- TTL/CMOS compatible BUS
- 16 channel single-ended or 8 channel differential inputs
- Input voltage -10V to +10V in four ranges
- Input protection for overrange
- 12-bit conversion at 70 microseconds
- Sample and Hold Amplifier
- Programmable Gain Amplifier
- DC/DC converter software controllable

DESCRIPTION

The CMOS-ADC12 provides a 16 channel 12-bit A/D Converter for fast, precise analog conversion on a single STD card. Eight channel differential input operation is also provided. The card features a programmable gain amplifier and sample and hold amplifier providing extra flexibility in various applications, Input voltage range varies from -10 volts to + 10 volts in four ranges. Protection for overvoltaged inputs is also included. An on-board dc/dc converter can provide the +/- 15 volts required for the analog front end, thus allowing single +5 volt operation if required. For lowest power consumption, the dc/dc converter can be turned on and off via software. Programmable interrupt logic supports both vectored and restart responses for Z80 or 8085-based systems.

The CMOS-ADC12 provides heretofore unprecedented performance in terms of a low power yet fast precision A/D Converter. Operating from a single supply, it consumes less than 120mA at 5 volts by virtue of the 75% efficient on-board dc/dc converter. Two versions of the CMOS-ADC12 card are available: a TTL BUS compatible version for operation on the regular STD BUS with a drive capability of 25 LSTTL loads, and a CMOS BUS compatible version for operation on the CMOS STD BUS.

APPENDIX 4

CASSETTE CONTROLLER BOARD AND TRANSPORT

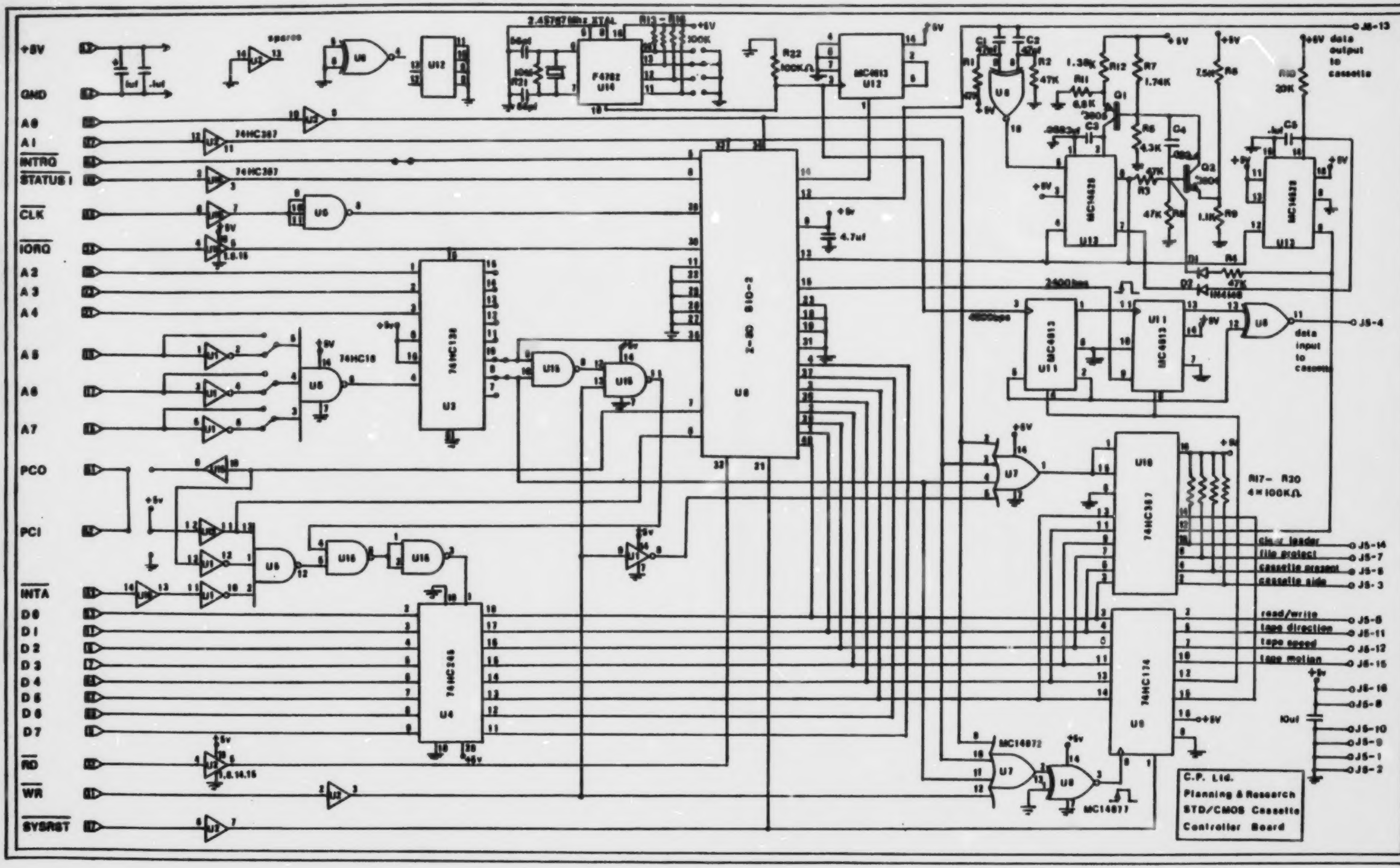
C.P. Ltd.
Planning & Research
STD/CMOS Cassette
Controller Board
+5V
GND
A0
A1
INTRQ
STATUS I
CLK
IORQ
A2
A3
A4
A5
A6
A7
PCO
PCI
INTA
D0
D1
D2
D3
D4
D5
D6
D7
RD
WR
SYSRST
spares
74HC367
74HC10
74HC138
74HC245
Z-80 SIO-2
F6782
U14
2.4576MHz XTAL
R13 - R16
100K
R22
100KΩ
MC4013
4.7uf
MC14528
MC4013
2400bps
4800bps
data input to cassette
+5V data output to cassette
74HC367
74HC174
R17 - R20
4×100KΩ
MC14072
MC14077
clear leader
file protect
cassette present
cassette side
read/write
tape direction
tape speed
tape motion
10uf
J5-13
J5-4
J5-14
J5-7
J5-5
J5-3
J5-6
J5-11
J5-12
J5-15
J5-16
J5-8
J5-10
J5-9
J5-1
J5-2
1N4148
47K
1.1K
7.5K
20K
1.74K
4.3K
6.8K
1.36K

BRAEMAR

CM-600 DIGITAL MINI CASSETTE TRANSPORT

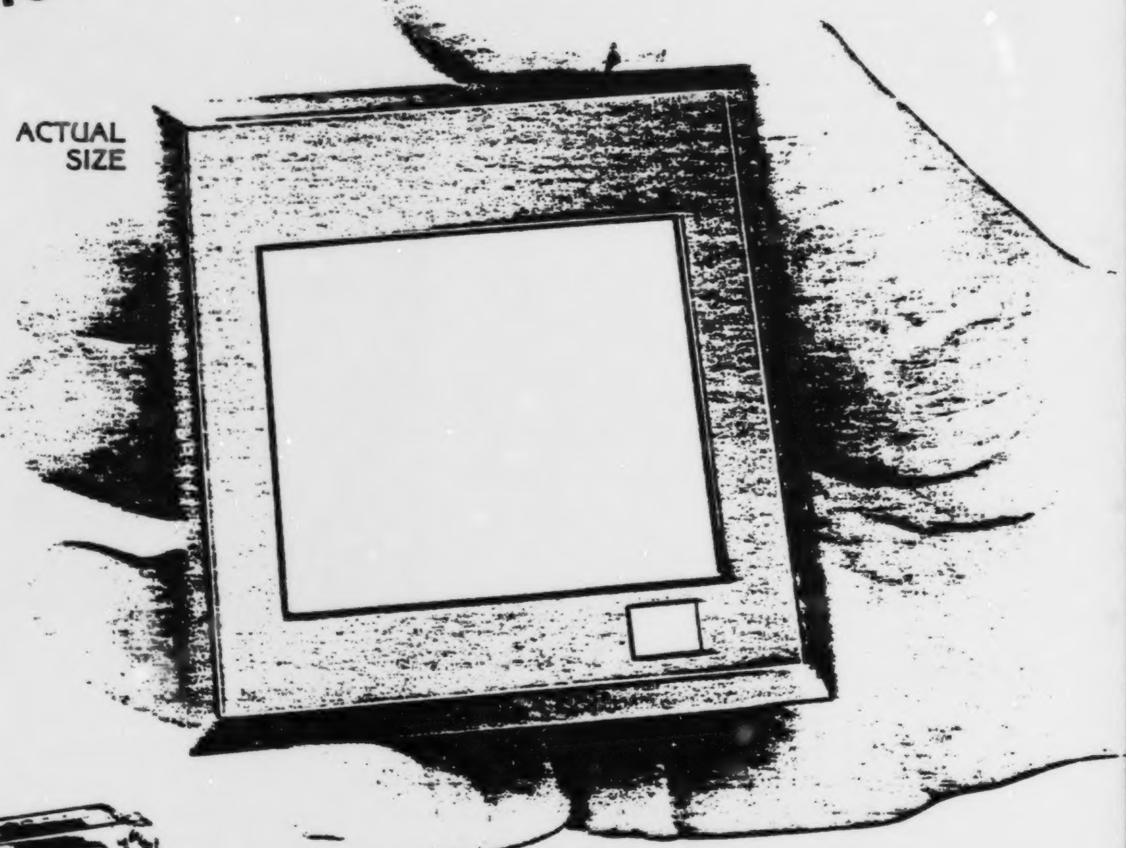

MINI-DEK®

- Very Small
- +5 Volt Supply
- Less than a Watt
- Includes Read-Write Amplifiers
- Read-After-Write Optional

CM 600 MINI CASSETTE TRANSPORT

SPECIFICATIONS

FUNCTIONAL

Media	Certified Digital Mini Cassette
Number of Heads	One
Tracks on Tape	Two
Channels in Head	One
Operating Modes	Read/Write Forward, Search Forward, Rewind
Motor Drive Transport	Reel to Reel Drive with constant reel speed (Varying Tape Speed)

PERFORMANCE

Read/Write Speed	3 IPS (BOT) (Consult Factory for Alternate Speeds & Data Rates)
Read/Write Time (50' Cassette)	2 Min. 40 Sec.
Read/Write Time (80' Cassette)	4 Min.
Start Time, Read/Write	150 MS
Stop Time, Read/Write	150 MS
Start Distance, Read/Write	.19 to .3 Inch
Stop Distance, Read/Write	.21 to .35 Inch
Search Forward Speed	5 IPS Average
Search Forward Time (50' Cassette)	1 Min. 30 Sec.
Search Forward Time (80' Cassette)	2 Min. 30 Sec.
Rewind Speed	15 IPS
Rewind Time (50' Cassette)	45 Sec.
Rewind Time (80' Cassette)	60 Sec.
Hub Speed (No Load)	± 2%
Jitter	± 5%

PHYSICAL AND ENVIRONMENTAL

Dimensions	3 x 3 x 2.5 (HWD)
Bezel	3.5 x 3.5
Weight	Less than 1/2 lb.
Operating Position	Horizontal to Vertical
Operating Temperature	50° F to 113° F (Media Limits)
Storage Temperature	−40° F to + 160° F
Operating Relative Humidity (Non-Condensing)	20% to 80% (Media Limits)
Storage Relative Humidity (Non-Condensing)	0% to 90%

ELECTRICAL

Supply Voltage	+ 5 VDC (+ .5, −0 VDC)
Supply Current	200 MA Max in Read/Write, 700 MA in Rewind
Power Consumption	1 Watt in Read/Write

MTBF—1000 hrs. **MTTR**—20 min.

DATA HANDLING

Density	800 BPI Max
Data Rate	2400 Baud
Data Capacity (Both Sides) (50' Cassette)	90 K Bytes (8 Bit)
Data Capacity (Both Sides) (80' Cassette)	145 K Bytes (8 Bit)

INPUT/OUTPUT

- TTL Levels
- Go/Stop
- Fast/Slow
- Forward/ Rewind
- Select Read/Write
- Write Data Input
- Read Data Output
- End of Tape Sensor
- Cassette Presence

OPTIONS

- Cassette Side Switch
- File Protect Switch
- 4800 Baud (2 x Search & Rewind Speeds)
- Tape Viewing Window
- Shielded Tape Head
- 2 Channel Tape Head
- Read-After-Write (Model CM-600 B)

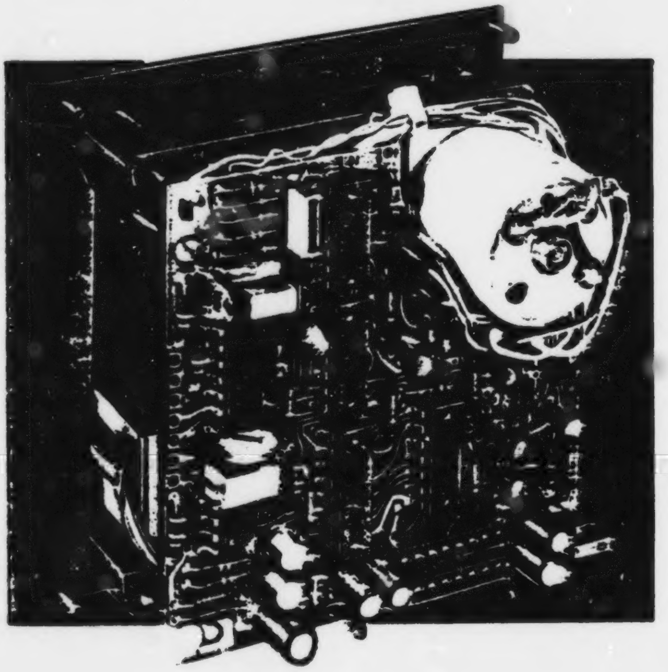

BLOCK DIAGRAM

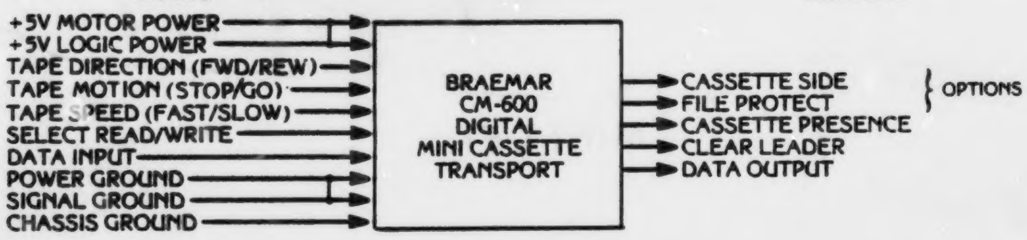
INPUTS
+5V MOTOR POWER
+5V LOGIC POWER
TAPE DIRECTION (FWD/REW)
TAPE MOTION (STOP/GO)
TAPE SPEED (FAST/SLOW)
SELECT READ/WRITE
DATA INPUT
POWER GROUND
SIGNAL GROUND
CHASSIS GROUND
BRAEMAR
CM-600
DIGITAL
MINI CASSETTE
TRANSPORT
OUTPUTS
CASSETTE SIDE
FILE PROTECT
OPTIONS
CASSETTE PRESENCE
CLEAR LEADER
DATA OUTPUT

BRAEMAR, THE DIGITAL CASSETTE PEOPLE
—APPROX. 50,000 IN THE FIELD—

BRAEMAR
COMPUTER
DEVICES, INC.
11950 TWELFTH AVENUE SOUTH • BURNSVILLE, MINNESOTA 55337 • AREA (612) 890-5135

FORM 178-8-79

ALL SPECIFICATIONS SUBJECT TO CHANGE WITHOUT NOTICE

PRINTED IN U S A

4702
(FAIRCHILD)

BIT-RATE GENERATOR

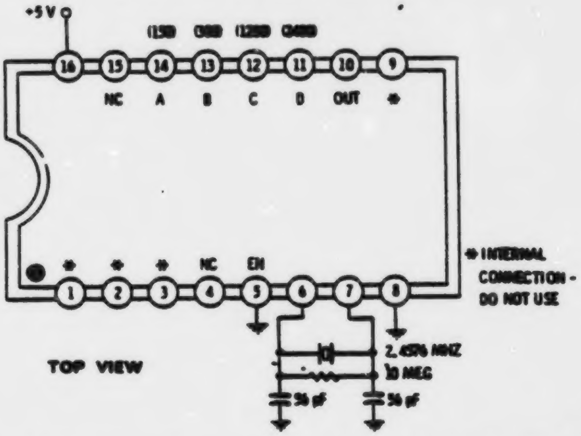
+5 V
(150)
(300)
(1200)
(2400)
16
15
14
13
12
11
10
9
NC
A
B
C
D
OUT
*
*
*
*
NC
EN
1
2
3
4
5
6
7
8
* INTERNAL CONNECTION - DO NOT USE
2.4576 MHZ
10 MEG
56 pF
56 pF
TOP VIEW

This special-purpose package synthesizes frequencies often used in serial data communications, particularly with UARTs.

In normal operation, pin 5 is grounded. If pins 11 through 14 are *not* grounded, an output frequency of 1760 hertz results. This is sixteen times the 110-baud rate used on serial teletypes.

Grounding only pin A generates sixteen times 150 baud. Grounding only pin B produces 16× 300 baud. Pin C generates 16× 1200 baud, and pin D generates 16× 2400 baud. The output can drive one regular TTL load.

Operating current varies with loading. Five milliamperes from a 5-volt supply is typical.

APPENDIX 5

INPUT-OUTPUT PERIPHERAL BOARD

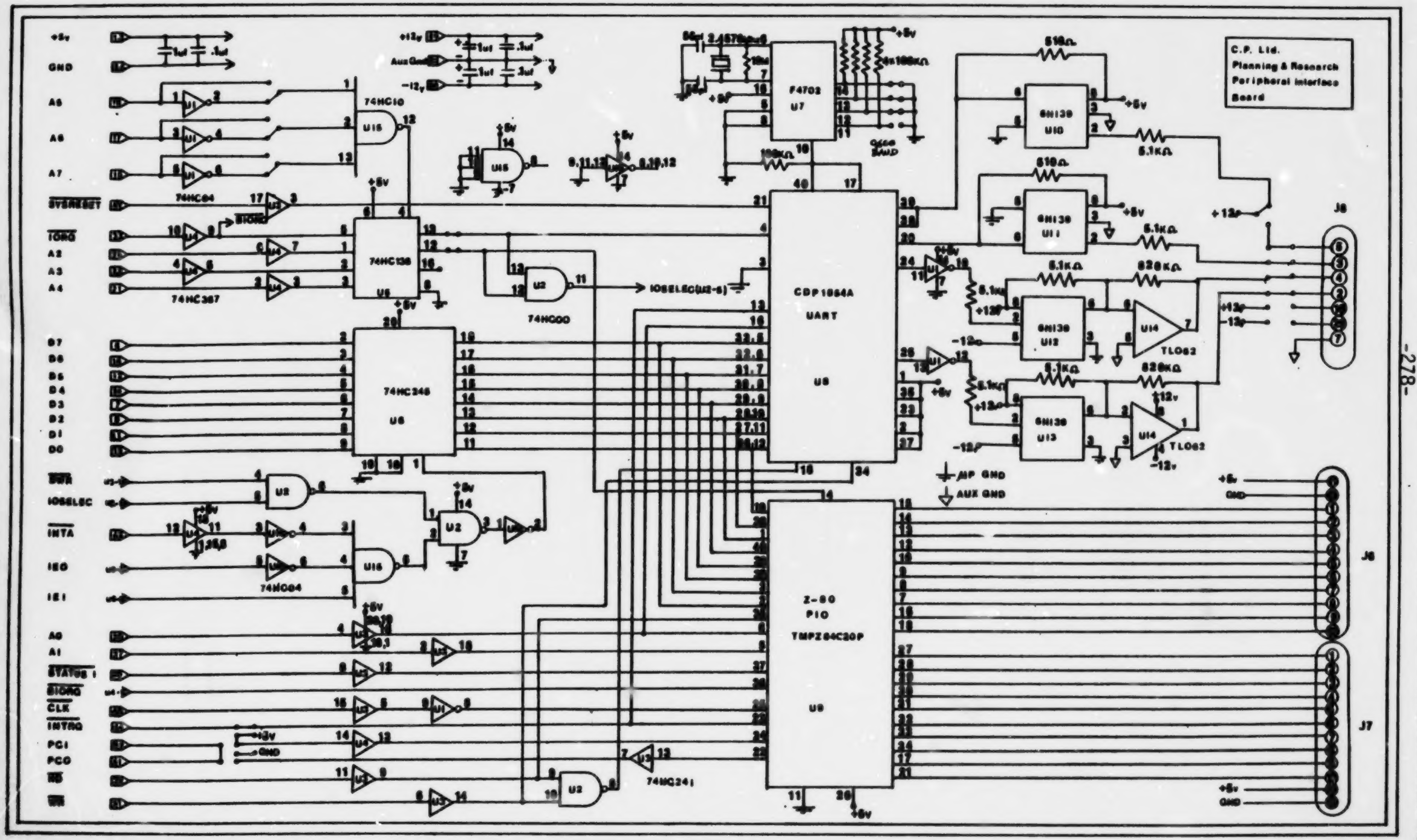
C.P. Ltd.
Planning & Research
Peripheral Interface
Board
+5v
GND
A5
A6
A7
SYSRESET
IORQ
A2
A3
A4
B7
B6
B5
D4
D3
D2
D1
D0
SWR
IOSELEC
INTA
IEO
IEI
A0
A1
STATUS 1
BIORQ
CLK
INTRQ
PC1
PC0
RD
WR
74HC04
74HC10
74HC367
74HC138
74HC245
74HC00
74HC241
IOSELEC(U2-6)
F4702
U7
CDP1854A
UART
U8
Z-80
PIO
TMPZ84C20P
U9
6N139
U10
U11
U12
U13
U14
TL062
510Ω
5.1KΩ
820KΩ
100KΩ
4x100KΩ
2.4576MHz
Open BAUD
+12v
-12v
AuxGnd
μP GND
AUX GND
J6
J7
J8

TOSHIBA
INTEGRATED CIRCUIT
TECHNICAL DATA

TOSHIBA MOS TYPE DIGITAL INTEGRATED CIRCUIT
TMPZ84C20P
SILICON MONOLITHIC
CMOS SILICON GATE

PRELIMINARY

CMOS Z80® PIO: Parallel Inout/Output Controller

GENERAL DESCRIPTION

The TMPZ84C20P (from here on referred to as PIO), is CMOS version of Z80 PIO and have been designed to provide low power operation. The PIO is a programmable, dual-port device that provides a direct interface between Z80 microcomputer systems and peripheral devices. Also all logic necessary to implement a fully nested interrupt structure is included in the PIO.

The device is fabricated with Toshiba's CMOS Silicon Gate Technology.

FEATURES

- Z80 Compatible PIO
- DC to 4 MHz Operation
- Single 5V Power Supply
  4 MHz @ 5V ± 10%
- Four Programmable Operation Modes
  - Byte Input
  - Byte Output
  - Byte Input/Output (Port A Only)
  - Bit Input/Output
- Low Power Consumption
  2mA Typ. @ 4 MHz @ 5V
  Less than 10μA @ 5V (Power down)
- Extended Operating Temperature
  - 40°C to 85°C
- Two Independent 8-bit Bidirectional ports
- Interrupt-driven Handshake for Fast Response
- Eight Outputs of Port B Capable of Driving Darlington Transistors
- Z80 Compatible Daisy-chain Interrupt Structure

Z80® is a trademark of Zilog Inc.

Z8420
Z80® PIO Parallel Input/Output Controller

Zilog

Product Specification

September 1983

Features

- Provides a direct interface between Z-80 microcomputer systems and peripheral devices.
- Both ports have interrupt-driven handshake for fast response.
- Four programmable operating modes: byte input, byte output, byte input/output (Port A only), and bit input/output.
- Programmable interrupts on peripheral status conditions.
- Standard Z-80 Family bus-request and prioritized interrupt-request daisy chains implemented without external logic.
- The eight Port B outputs can drive Darlington transistors (1.5 mA at 1.5 V).

General Description

The Z-80 PIO Parallel I/O Circuit is a programmable, dual-port device that provides a TTL-compatible interface between peripheral devices and the Z-80 CPU. The CPU configures the Z-80 PIO to interface with a wide range of peripheral devices with no other external logic. Typical peripheral devices that are compatible with the Z-80 PIO include most keyboards, paper tape readers and punches, printers, PROM programmers, etc.

One characteristic of the Z-80 peripheral controllers that separates them from other interface controllers is that all data transfer between the peripheral device and the CPU is accomplished under interrupt control. Thus, the interrupt logic of the PIO permits full use of the efficient interrupt capabilities of the Z-80 CPU during I/O transfers. All logic necessary to implement a fully nested interrupt structure is included in the PIO.

Another feature of the PIO is the ability to interrupt the CPU upon occurrence of specified status conditions in the peripheral device. For example, the PIO can be programmed to interrupt if any specified peripheral alarm conditions should occur. This interrupt capability reduces the time the processor must spend in polling peripheral status.

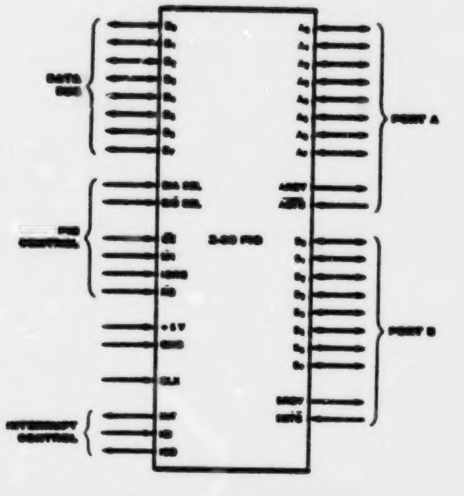

Figure 1. Pin Functions

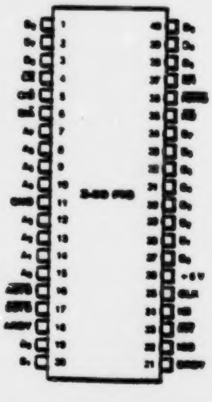

Figure 2. Pin Assignments

General Description (Continued)

The Z-80 PIO interfaces to peripherals via two independent general-purpose I/O ports, designated Port A and Port B. Each port has eight data bits and two handshake signals, Ready and Strobe, which control data transfer. The Ready output indicates to the peripheral that the port is ready for a data transfer. Strobe is an input from the peripheral that indicates when a data transfer has occurred.

Operating Modes. The Z-80 PIO ports can be programmed to operate in four modes: byte output (Mode 0), byte input (Mode 1), byte input/output (Mode 2) and bit input/output (Mode 3).

In Mode 0, either Port A or Port B can be programmed to output data. Both ports have output registers that are individually addressed by the CPU; data can be written to either port at any time. When data is written to a port, an active Ready output indicates to the external device that data is available at the associated port and is ready for transfer to the external device. After the data transfer, the external device responds with an active Strobe input, which generates an interrupt, if enabled.

In Mode 1, either Port A or Port B can be configured in the input mode. Each port has an input register addressed by the CPU. When the CPU reads data from a port, the PIO sets the Ready signal, which is detected by the external device. The external device then places data on the I/O lines and strobes the I/O port, which latches the data into the Port Input Register, resets Ready, and triggers the Interrupt Request, if enabled. The CPU can read the input data at any time, which again sets Ready.

Mode 2 is bidirectional and uses Port A, plus the interrupts and handshake signals from both ports. Port B must be set to Mode 3 and masked off. In operation, Port A is used for both data input and output. Output operation is similar to Mode 0 except that data is allowed out onto the Port A bus only when $\overline{ASTB}$ is Low. For input, operation is similar to Mode 1, except that the data input uses the Port B handshake signals and the Port B interrupt (if enabled).

Both ports can be used in Mode 3. In this mode, the individual bits are defined as either input or output bits. This provides up to eight separate, individually defined bits for each port. During operation, Ready and Strobe are not used. Instead, an interrupt is generated if the condition of one input changes, or if all inputs change. The requirements for generating an interrupt are defined during the programming operation; the active level is specified as either High or Low, and the logic condition is specified as either one input active (OR) or all inputs active (AND). For example, if the port is programmed for active Low inputs and the logic function is AND, then all inputs at the specified port must go Low to generate an interrupt.

Data outputs are controlled by the CPU and can be written or changed at any time.

- Individual bits can be masked off.
- The handshake signals are not used in Mode 3; Ready is held Low, and Strobe is disabled.
- When using the Z-80 PIO interrupts, the Z-80 CPU interrupt mode must be set to Mode 2.

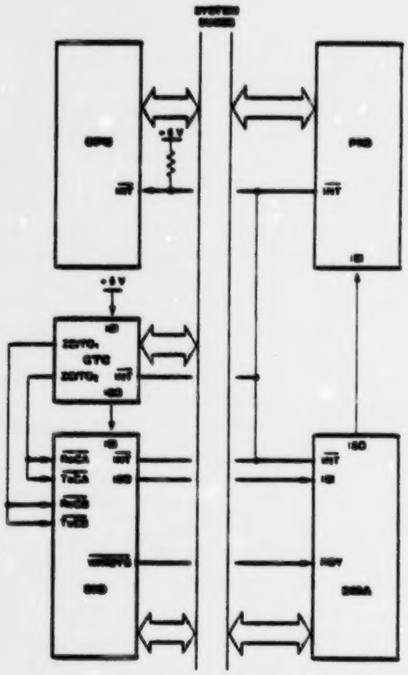

Figure 2. PIO in a Typical Z80 Family Environment

Programming **Mode 0, 1, or 2.** *(Byte Input, Output, or Bidirectional).* Programming a port for Mode 0, 1, or 2 requires two words per port. These words are:

A Mode Control Word. Selects the port operating mode (Figure 6). This word may be written any time.

An Interrupt Vector. The Z-80 PIO is designed for use with the Z-80 CPU in interrupt Mode 2 (Figure 7). When interrupts are enabled, the PIO must provide an interrupt vector.

Mode 3. *(Bit Input/Output).* Programming a port for Mode 3 operation requires a control word, a vector (if interrupts are enabled), and three additional words, described as follows:

I/O Register Control. When Mode 3 is selected, the mode control word must be followed by another control word that sets the I/O control register, which in turn defines which port lines are inputs and which are outputs (Figure 8).

Interrupt Control Word. In Mode 3, handshake is not used. Interrupts are generated as a logic function of the input signal levels. The interrupt control word sets the logic conditions and the logic levels required for generating an interrupt. Two logic conditions or functions are available: AND (if all input bits change to the active level, an interrupt is triggered), and OR (if any one of the input bits changes to the active level, an interrupt is triggered). Bit D_6 sets the logic function, as shown in Figure 9. The active level of the input bits can be set either High or Low. The active level is controlled by Bit D_5.

Mask Control Word. This word sets the mask control register, allowing any unused bits to be masked off. If any bits are to be masked, then D_4 must be set. When D_4 is set, the next word written to the port must be a mask control word (Figure 10).

Interrupt Disable. There is one other control word which can be used to enable or disable a port interrupt. It can be used without changing the rest of the interrupt control word (Figure 11).

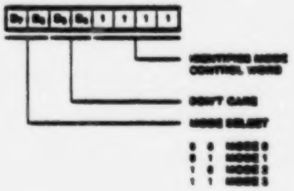
D7 D6 D5 D4 1 1 1 1
IDENTIFIES MODE CONTROL WORD
DON'T CARE
MODE SELECT
0 0 MODE 0
0 1 MODE 1
1 0 MODE 2
1 1 MODE 3

Figure 6. Mode Control Word

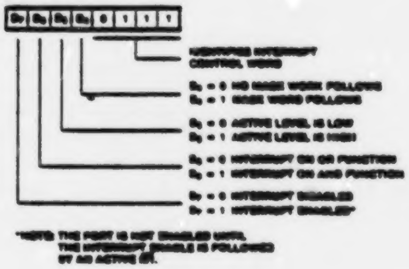
D7 D6 D5 D4 0 1 1 1
IDENTIFIES INTERRUPT CONTROL WORD
D4 = 0 NO MASK WORD FOLLOWS
D4 = 1 MASK WORD FOLLOWS
D5 = 0 ACTIVE LEVEL IS LOW
D5 = 1 ACTIVE LEVEL IS HIGH
D6 = 0 INTERRUPT ON OR FUNCTION
D6 = 1 INTERRUPT ON AND FUNCTION
D7 = 0 INTERRUPT DISABLED
D7 = 1 INTERRUPT ENABLED*
*NOTE: THE PORT IS NOT ENABLED UNTIL THE INTERRUPT ENABLE IS FOLLOWED BY AN ACTIVE M1.

Figure 9. Interrupt Control Word

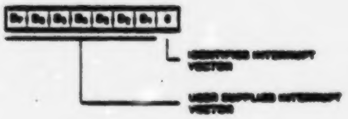
V7 V6 V5 V4 V3 V2 V1 0
IDENTIFIES INTERRUPT VECTOR
USER SUPPLIED INTERRUPT VECTOR

Figure 7. Interrupt Vector Word

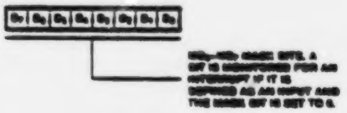
MB7 MB6 MB5 MB4 MB3 MB2 MB1 MB0
MB0–MB7 MASK BITS. A BIT IS MONITORED FOR AN INTERRUPT IF IT IS DEFINED AS AN INPUT AND THE MASK BIT IS SET TO 0.

Figure 10. Mask Control Word

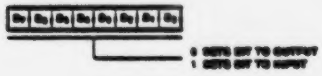
IO7 IO6 IO5 IO4 IO3 IO2 IO1 IO0
0 SETS BIT TO OUTPUT
1 SETS BIT TO INPUT

Figure 8. I/O Register Control Word

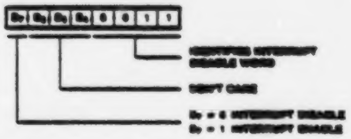
D7 X X X 0 0 1 1
IDENTIFIES INTERRUPT DISABLE WORD
DON'T CARE
D7 = 0 INTERRUPT DISABLE
D7 = 1 INTERRUPT ENABLE

Figure 11. Interrupt Disable Word

CDP1854A, CDP1854AC Types

COS/MOS Programmable Universal Asynchronous Receiver/Transmitter (UART)

Features:

- Static silicon-gate CMOS circuitry— CD4000 Series compatible
- Two operating modes:
  - Mode 0—functionally compatible with industry standard types such as the TR1602A
  - Mode 1—interfaces directly with the CDP1802 and CDP1804 microprocessors without additional components
- Full- or half-duplex operation
- Baud rate — DC to 250K bits/sec. (typ.) @ V_{DD} = 5 V
  DC to 500K bits/sec. (typ.) @ V_{DD} = 10 V
- Fully programmable with externally selectable word length (5-8 bits), parity inhibit, even/odd parity, and 1, 1½, or 2 stop bits
- False start bit detection
- Parity, framing, and overrun error detection
- Low quiescent and operating power
- Single-voltage supply
- Wide operating-voltage range
- Operating-temperature range: −55 to +125°C (CDP1854AD, CDP1854ACD) −40 to +85°C (CDP1854AE, CDP1854ACE)

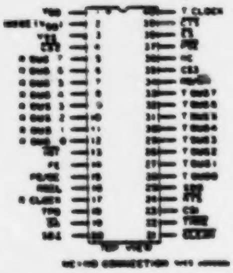

MODE 1
Terminal Assignment

The CDP1854A and CDP1854AC are silicon-gate COS/MOS Universal Asynchronous Receiver/Transmitter (UART) circuits. They are designed to provide the necessary formatting and control for interfacing between serial and parallel data. For example, it can be used to interface between a peripheral or terminal with serial I/O ports and the 8-bit CDP1802 or CDP1804 parallel data bus system. The CDP1854A is capable of full duplex operation, i.e., simultaneous conversion of serial input data to parallel output data and parallel input data to serial output data.

The CDP1854A UART can be programmed to operate in one of two modes by using the mode control input. When the mode input is high (MODE = 1), the CDP1854A is directly compatible with the CDP1802 and CDP1804 microprocessor system without additional interface circuitry.

When the mode input is low (MODE = 0), the device is functionally compatible with in-

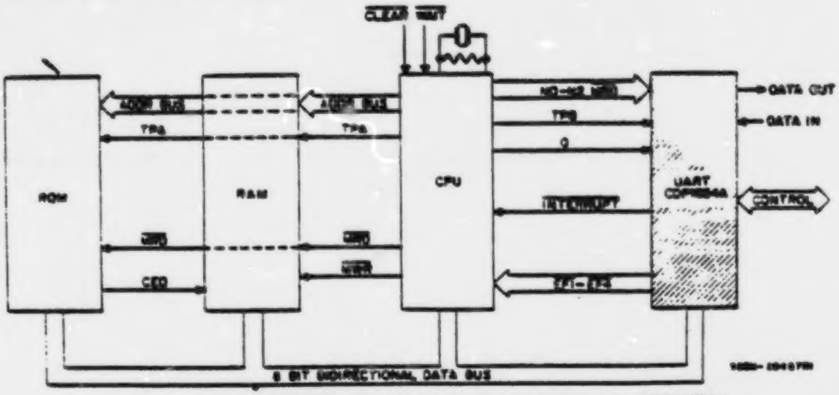

Fig. 1 – Typical CDP1800-series microprocessor system using the CDP1854A.

CDP1854A, CDP1854AC Types

dustry standard UART's such as the TR-1602A. It is also pin compatible with these types, except that pin 2 is used for the mode control input instead of a V_{GG} = −12 V supply connection.

The CDP1854A and the CDP1854AC are functionally identical. The CDP1854A has a recommended operating-voltage range of 4—10.5 volts, and the CDP1854AC has a recommended operating-voltage range of 4—6.5 volts.

The CDP1854A and CDP1854AC are supplied in hermetic 40-lead dual-in-line ceramic packages (D suffix) and in 40-lead dual-in-line plastic packages (E suffix).

MAXIMUM RATINGS, ***Absolute-Maximum Values:***

DC SUPPLY-VOLTAGE RANGE, (V_{DD})
(Voltage referenced to V_{SS} Terminal)
CDP1854A . . . . −0.5 to +11 V
CDP1854AC . . . . −0.5 to +7 V
INPUT VOLTAGE RANGE, ALL INPUTS . . . . −0.5 to V_{DD} +0.5 V
DC INPUT CURRENT, ANY ONE INPUT . . . . ±10 mA
POWER DISSIPATION PER PACKAGE (P_D):
For T_A = −40 to +60°C (PACKAGE TYPE E) . . . . 500 mW
For T_A = +60 to +85°C (PACKAGE TYPE E) . . . . . . Derate Linearly at 12 mW/°C to 200 mW
For T_A = −55 to 100°C (PACKAGE TYPE D) . . . . 500 mW
For T_A = +100 to +125°C (PACKAGE TYPE D) . . . . . Derate Linearly at 12 mW/°C to 200 mW
DEVICE DISSIPATION PER OUTPUT TRANSISTOR
FOR T_A = FULL PACKAGE-TEMPERATURE RANGE (All Package Types) . . . . 100 mW
OPERATING-TEMPERATURE RANGE (T_A):
PACKAGE TYPE D. . . . . −55 to +125°C
PACKAGE TYPE E . . . . −40 to +85°C
STORAGE TEMPERATURE RANGE (T_{stg}) . . . . −65 to +150°C
LEAD TEMPERATURE (DURING SOLDERING):
At distance 1/16 ± 1/32 inch (1.59 ± 0.79 mm) from case for 10 s max. . . . . +265°C

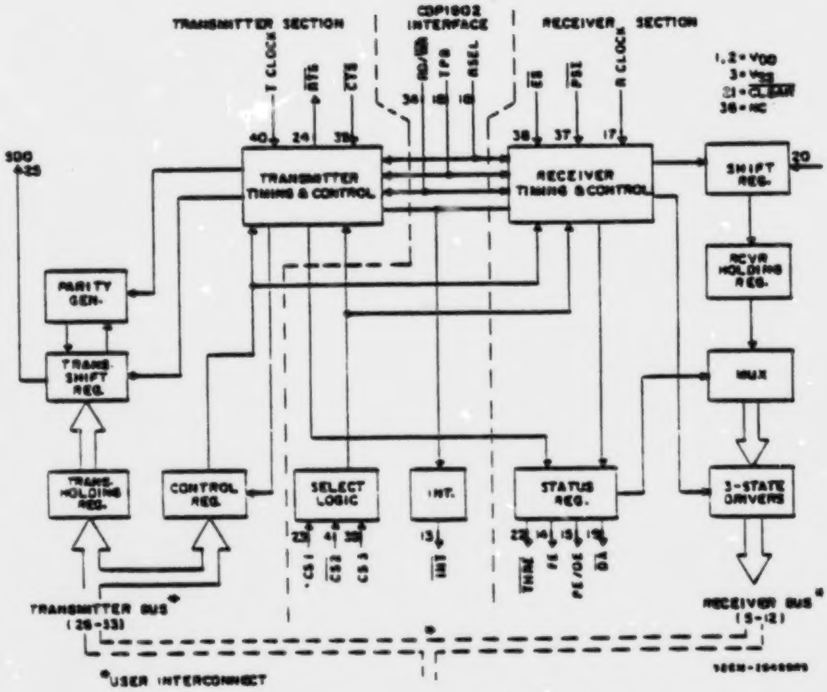
TRANSMITTER SECTION
CDP1802 INTERFACE
RECEIVER SECTION
T CLOCK
RTS
CTS
RD/WR
TPB
RSEL
ES
PSI
R CLOCK
1, 2 = VDD
3 = VSS
21 = CLEAR
36 = NC
40
24
39
34
18
16
38
37
17
SDO
25
TRANSMITTER TIMING & CONTROL
RECEIVER TIMING & CONTROL
SHIFT REG.
20
SDI
RCVR HOLDING REG.
PARITY GEN.
TRANS. SHIFT REG.
MUX
TRANS. HOLDING REG.
CONTROL REG.
SELECT LOGIC
INT.
STATUS REG.
3-STATE DRIVERS
23
4
35
CS1
CS2
CS3
13
INT
22
14
15
19
THRE
FE
PE/OE
DA
TRANSMITTER BUS* (26-33)
RECEIVER BUS* (5-12)
*USER INTERCONNECT
92CM-29489R5

Fig. 2 – MODE 1 block diagram (CDP1802 and CDP1804 compatible).

APPENDIX 6

KEYPAD-DISPLAY BOARD

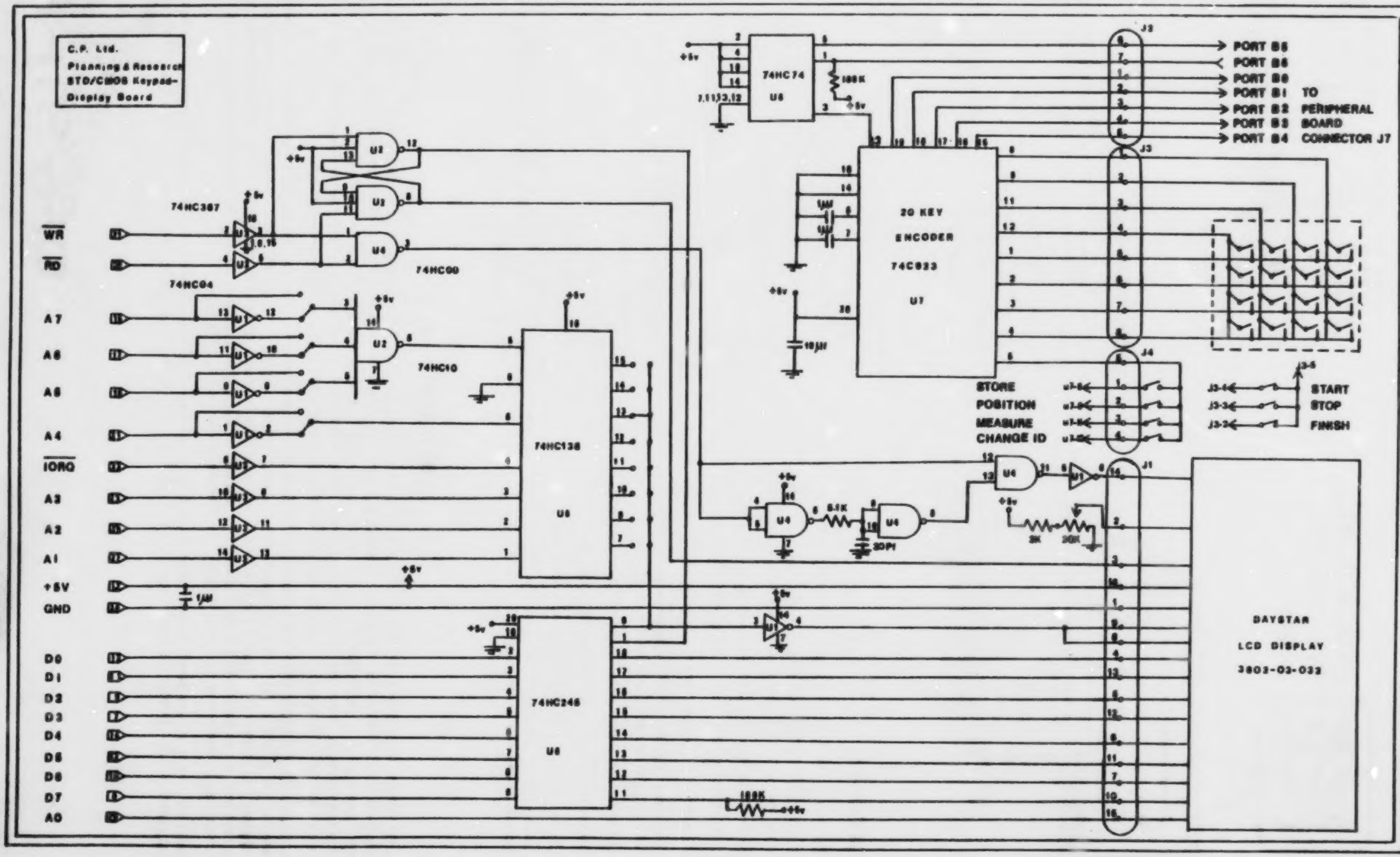
C.P. Ltd.
Planning & Research
STD/CMOS Keypad-
Display Board
WR
RD
A7
A6
A5
A4
IORQ
A3
A2
A1
+5V
GND
D0
D1
D2
D3
D4
D5
D6
D7
A0
74HC367
74HC04
74HC00
74HC10
74HC138
U5
74HC245
U6
74HC74
U8
180K
20 KEY
ENCODER
74C923
U7
1µf
10µf
+5v
PORT B5
PORT B6
PORT B0
PORT B1
PORT B2
PORT B3
PORT B4
TO
PERIPHERAL
BOARD
CONNECTOR J7
J2
J3
J4
J1
STORE
POSITION
MEASURE
CHANGE ID
START
STOP
FINISH
5.1K
30Pf
2K
20K
180K
DAYSTAR
LCD DISPLAY
3803-03-032

IEE® **INDUSTRIAL PRODUCTS DIVISION**

DAYSTAR™ ASCII MODULE LIQUID CRYSTAL DISPLAYS
3802-02-016 3802-03-032

John G. Weiss Co. Ltée Ltd

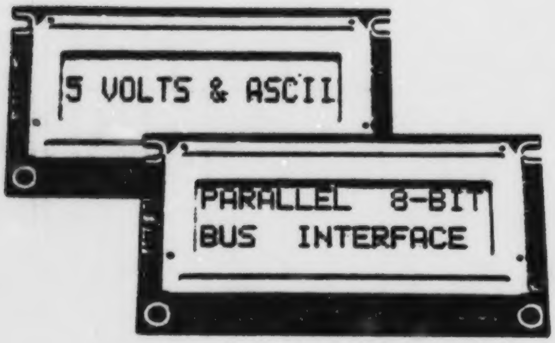

FEATURES

- On-board CMOS VLSI microprocessor-controller
- Parallel TTL ASCII data bus requires minimum hardware to interface to most popular microprocessors
- Requires only +5VDC power supply
- .2 in. (5mm) characters for clear, easy-to-read display
- Viewing angle adjustment allows optimum readability
- Low power consumption (typically < 25mW) for battery-powered applications
- Compact and lightweight for portable equipment
- Excellent contrast and readability in sunlight
- Up to 10,000 characters per second data rate
- Low cost in a premium, full logic, dot matrix alphanumeric display module

APPLICATIONS

DAYSTAR Alphanumeric Displays can be used in a wide variety of applications including (but not limited to):

- Portable test equipment
- Portable data terminals
- Hand held computers
- Medical equipment
- Text editing devices (e.g. word-processors and typesetters)
- TTY Terminals for the deaf
- Pollution monitors (industrial and automotive)
- Telephone test sets
- Telephone interconnect equipment
- Seismographic and oil exploration devices
- Copiers
- Automated scales and labeling equipment
- Alarms
- Energy management systems
- Portable simulators
- Process controllers
- Development aids

Small size, low cost, low power and sunlight readability make DAYSTAR Products ideal for most portable and/or outdoor applications.

DESCRIPTION

The DAYSTAR 3802-02-016 and DAYSTAR 3802-03-032 are Liquid Crystal Alphanumeric Display Modules arranged as 1 line of 16 characters and 2 lines of 16 characters respectively. The characters are formed using a 5x7 dot matrix which allows upper and lower case alphabet, numerals and punctuation, along with the Japanese Katakana character set. The use of liquid crystal technology makes these modules an excellent choice when low power and sunlight readability are required as in such applications as oil exploration equipment, portable data loggers and communication equipment.

The Series 3802 display modules include a CMOS VLSI microprocessor controller which supplies character memory RAM, character generator ROM and all refresh, control, and timing signals, and an on-board voltage converter provides all the necessary multiplexing voltages so that the engineer need only provide +5VDC and parallel TTL level ASCII to display data. The 8-bit bus interfaces easily with most popular microprocessors with a minimum of additional hardware, and allows such control functions as cursor home or cursor location to be easily implemented.

Small size, low cost, low power and sunlight readability plus ease of interface make DAYSTAR ASCII Display Modules ideal for most portable and outdoor display needs. "DAYSTAR" from IEE — your first choice in displays for more than 30 years.

DAYSTAR

APPENDIX 7

COUNTER-TIMER BOARD

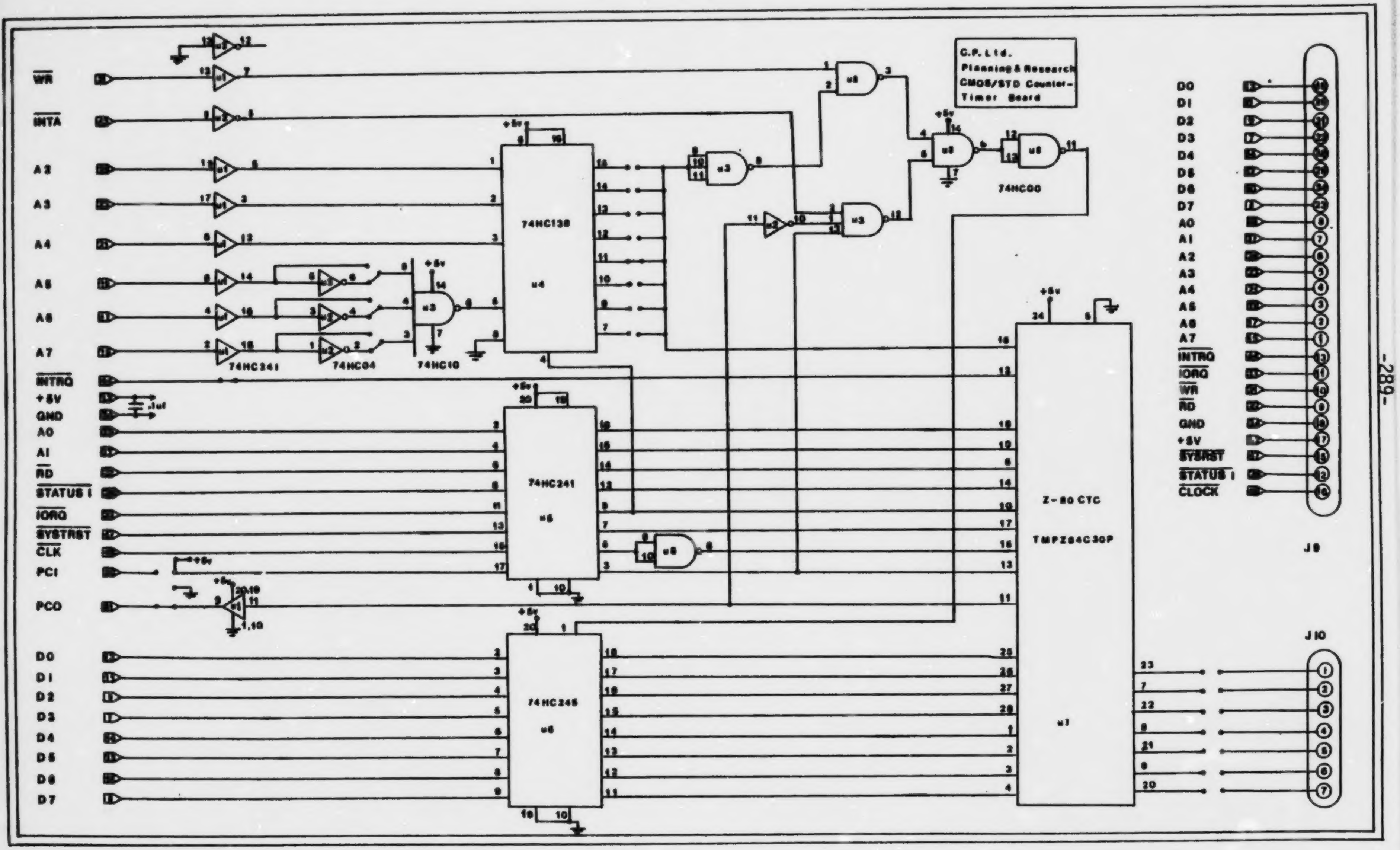
C.P. Ltd.
Planning & Research
CMOS/STD Counter-
Timer Board
WR
INTA
A2
A3
A4
A5
A6
A7
INTRQ
+5V
GND
A0
A1
RD
STATUS 1
IORQ
SYSTRST
CLK
PCI
PCO
D0
D1
D2
D3
D4
D5
D6
D7
74HC241
74HC04
74HC10
74HC138
u4
74HC241
u5
74HC245
u6
74HC00
Z-80 CTC
TMPZ84C30P
u7
+5v
.1uf
J9
J10
D0
D1
D2
D3
D4
D5
D6
D7
A0
A1
A2
A3
A4
A5
A6
A7
INTRQ
IORQ
WR
RD
GND
+5V
SYSRST
STATUS 1
CLOCK

TOSHIBA
INTEGRATED CIRCUIT
TECHNICAL DATA

TOSHIBA MOS TYPE DIGITAL INTEGRATED CIRCUIT
TMPZ84C30P
SILICON MONOLITHIC
CMOS SILICON GATE

PRELIMINARY

CMOS Z80® CTC : COUNTER/TIMER CIRCUIT

GENERAL DESCRIPTION

The TMPZ84C30P, (from here on referred to as CTC), is CMOS version of Z80 CTC (Counter/Timer circuit) that provides low power operation. The CTC has four independent counter/timer channels, each with a readable downcounter and a selectable 16 or 256 prescaler. Also standard Z80 family daisy-chain interrupt structure is provided. The device is fabricated with Toshiba's C^{2}MOS Silicon Gate Technology.

FEATURES

- Z80 Compatible CTC
- DC to 4 MHz Operation
- Single 5 V Power Supply
  4 MHz @ 5 V ±10%
- Low Power Consumption
  3mA Typ. @5V @4MHz
  Less than 10μA @ 5V (Power down)
- Extended Operating Temperature
  -40°C to 85°C
- Four Independent 8-bit Counter/Timer Channels
- More than One Counter Can be Cascaded for Counts greater than 256.
- Selectable in either Counter Mode or Timer Mode for Each Channel.
- Selectable Positive or Negative Trigger Operation
- Three Zero Count/Timeout Outputs Capable of Driving Darlington Transistors
- Z80 Compatible Daisy-chain Interrupt Structure

® Z80 is a trademark of Zilog Inc..

Z8430
Z80® CTC Counter/ Timer Circuit

Zilog

Product Specification

September 1983

Features

- Four independently programmable counter/timer channels, each with a readable downcounter and a selectable 16 or 256 prescaler. Downcounters are reloaded automatically at zero count.
- Three channels have Zero Count/Timeout outputs capable of driving Darlington transistors.
- Selectable positive or negative trigger initiates timer operation.
- Standard Z-80 Family daisy-chain interrupt structure provides fully vectored, prioritized interrupts without external logic. The CTC may also be used as an interrupt controller.
- Interfaces directly to the Z-80 CPU or—for baud rate generation—to the Z-80 SIO.

General Description

The Z-80 CTC four-channel counter/timer can be programmed by system software for a broad range of counting and timing applications. The four independently programmable channels of the Z-80 CTC satisfy common microcomputer system requirements for event counting, interrupt and interval timing, and general clock rate generation.

System design is simplified because the CTC connects directly to both the Z-80 CPU and the Z-80 SIO with no additional logic. In larger systems, address decoders and buffers may be required.

Programming the CTC is straightforward: each channel is programmed with two bytes; a third is necessary when interrupts are enabled. Once started, the CTC counts down, reloads its time constant automatically, and resumes counting. Software timing loops are completely eliminated. Interrupt processing is simplified because only one vector need be specified; the CTC internally generates a unique vector for each channel.

The Z-80 CTC requires a single +5 V power supply and the standard Z-80 single-phase system clock. It is fabricated with n-channel silicon-gate depletion-load technology, and packaged in a 28-pin plastic or ceramic DIP.

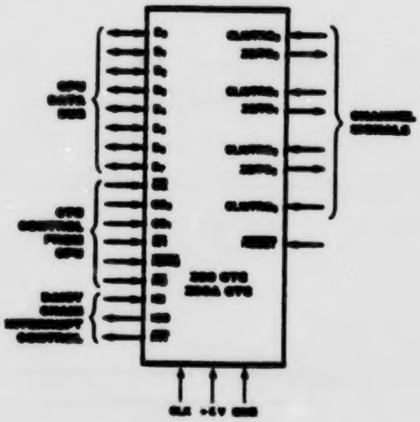

Figure 1. Pin Functions

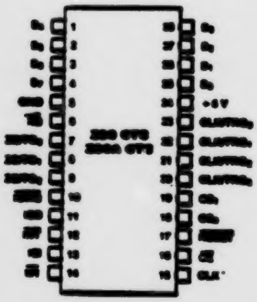

Figure 2. Pin Assignments

amming Each Z-80 CTC channel must be programmed prior to operation. Programming consists of writing two words to the I/O port that corresponds to the desired channel. The first word is a control word that selects the operating mode and other parameters; the second word is a time constant, which is a binary data word with a value from 1 to 256. A time constant word must be preceded by a channel control word.

After initialization, channels may be reprogrammed at any time. If updated control and time constant words are written to a channel during the count operation, the count continues to zero before the new time constant is loaded into the counter.

If the interrupt on any Z-80 CTC channel is enabled, the programming procedure should also include an interrupt vector. Only one vector is required for all four channels, because the interrupt logic automatically modifies the vector for the channel requesting service.

A control word is identified by a 1 in bit 0. A 1 in bit 2 indicates a time constant word is to follow. Interrupt vectors are always addressed to Channel 0, and identified by a 0 in bit 0.

Addressing. During programming, channels are addressed with the channel select pins CS_1 and CS_2. A 2-bit binary code selects the appropriate channel as shown in the following table.

Channel	CS_1	CS_0
0	0	0
1	0	1
2	1	0
3	1	1

Reset. The CTC has both hardware and software resets. The hardware reset terminates all down-counts and disables all CTC interrupts by resetting the interrupt bits in the control registers. In addition, the ZC/TO and Interrupt outputs go inactive, IEO reflects IEI, and D_0–D_7 go to the high-impedance state. All channels must be completely reprogrammed after a hardware reset.

The software reset is controlled by bit 1 in the channel control word. When a channel receives a software reset, it stops counting. When a software reset is used, the other bits in the control word also change the contents of the channel control register. After a software reset a new time constant word must be written to the same channel.

If the channel control word has both bits D_1 and D_2 set to 1, the addressed channel stops operating, pending a new time constant word. The channel is ready to resume after the new constant is programmed. In timer mode, if $D_3 = 0$, operation is triggered automatically when the time constant word is loaded.

Channel Control Word Programming. The channel control word is shown in Figure 5. It sets the modes and parameters described below.

Interrupt Enable. D_7 enables the interrupt, so that an interrupt output ($\overline{INT}$) is generated at zero count. Interrupts may be programmed in either mode and may be enabled or disabled at any time.

Operating Mode. D_6 selects either timer or counter mode.

Prescaler Factor. (Timer Mode Only). D_5 selects factor—either 16 or 256.

Trigger Slope. D_4 selects the active edge or slope of the CLK/TRG input pulses. Note that reprogramming the CLK/TRG slope during operation is equivalent to issuing an active edge. If the trigger slope is changed by a control word update while a channel is pending operation in timer mode, the result is the same as a CLK/TRG pulse and the timer starts. Similarly, if the channel is in counter mode, the counter decrements.

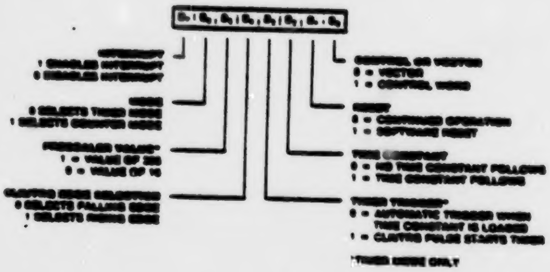

Figure 5. Channel Control Word

Programming (Continued)

Trigger Mode (Timer Mode Only). D_3 selects the trigger mode for timer operation. When D_3 is reset to 0, the timer is triggered automatically. The time constant word is programmed during an I/O write operation, which takes one machine cycle. At the end of the write operation there is a setup delay of one clock period. The timer starts automatically (decrements) on the rising edge of the second clock pulse (T_2) of the machine cycle following the write operation. Once started, the timer runs continuously. At zerp count the timer reloads automatically and continues counting without interruption or delay, until stopped by a reset.

When D_3 is set to 1, the timer is triggered externally through the CLK/TRG input. The time constant word is programmed during an I/O write operation, which takes one machine cycle. The timer is ready for operation on the rising edge of the second clock pulse (T_2) of the following machine cycle. Note that the first timer decrement follows the active edge of the CLK/TRG pulse by a delay time of one clock cycle if a minimum setup time to the rising edge of clock is met. If this minimum is not met, the delay is extended by another clock period. Consequently, for immediate triggering, the CLK/TRG input must precede T_2 by one clock cycle plus its minimum setup time. If the minimum time is not met, the timer will start on the third clock cycle (T_3).

Once started the timer operates continuously, without interruption or delay, until stopped by a reset.

Time Constant to Follow. A 1 in D_2 indicates that the next word addressed to the selected channel is a time constant data word for the time constant register. The time constant word may be written at any time.

A 0 in D_2 indicates no time constant word is to follow. This is ordinarily used when the channel is already in operation and the new channel control word is an update. A channel will not operate without a time constant value. The only way to write a time constant value is to write a control word with D_2 set.

Software Reset. Setting D_1 to 1 causes a software reset, which is described in the Reset section.

Control Word. Setting D_0 to 1 identifies the word as a control word.

Time Constant Programming. Before a channel can start counting it must receive a time constant word from the CPU. During programming or reprogramming, a channel control word in which bit 2 is set must precede the time constant word to indicate that the next word is a time constant. The time constant word can be any value from 1 to 256 (Figure 6). Note that 00_{16} is interpreted as 256.

In timer mode, the time interval is controlled by three factors:

- The system clock period (ϕ)
- The prescaler factor (P), which multiplies the interval by either 16 or 256
- The time constant (T), which is programmed into the time constant register

Consequently, the time interval is the product of $\phi \times P \times T$. The minimum timer resolution is $16 \times \phi$ (4 µs with a 4 MHz clock). The maximum timer interval is $256 \times \phi \times 256$ (16.4 ms with a 4 MHz clock). For longer intervals timers may be cascaded.

Interrupt Vector Programming. If the Z-80 CTC has one or more interrupts enabled, it can supply interrupt vectors to the Z-80 CPU. To do so, the Z-80 CTC must be pre-programmed with the most-significant five bits of the interrupt vector. Programming consists of writing a vector word to the I/O port corresponding to the Z-80 CTC Channel 0. Note that D_0 of the vector word is always zero, to distinguish the vector from a channel control word. D_1 and D_2 are not used in programming the vector word. These bits are supplied by the interrupt logic to identify the channel requesting interrupt service with a unique interrupt vector (Figure 7). Channel 0 has the highest priority.

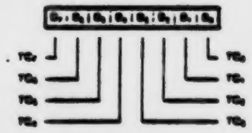

Figure 6. Time Constant Word

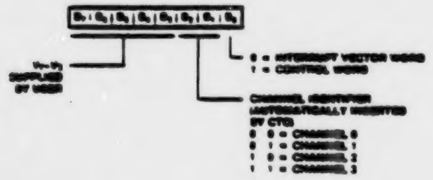

Figure 7. Interrupt Vector Word

APPENDIX 8

VIDEO GRAPHICS MODULE

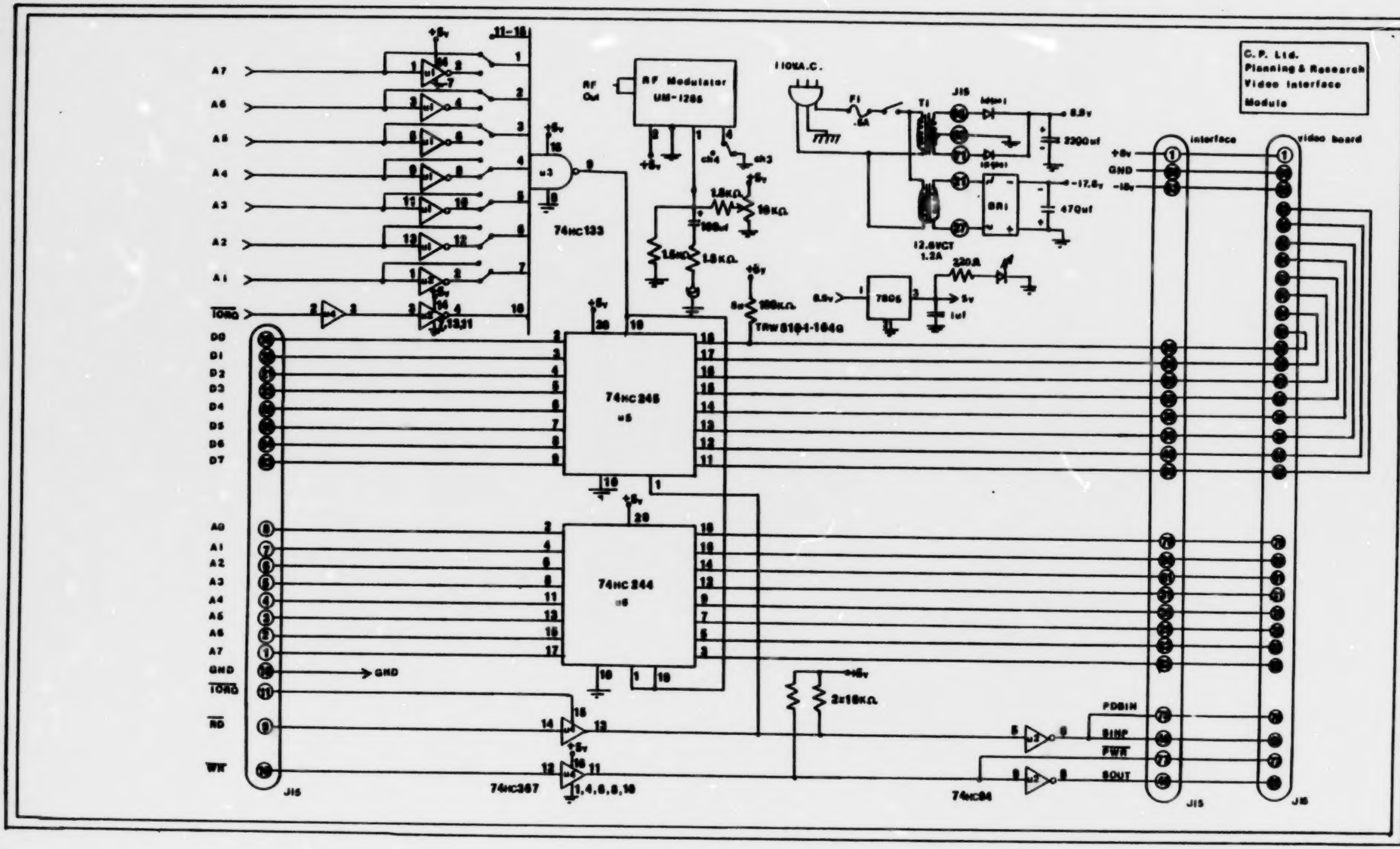
C. P. Ltd.
Planning & Research
Video Interface
Module
A7
A6
A5
A4
A3
A2
A1
IORQ
D0
D1
D2
D3
D4
D5
D6
D7
A0
A1
A2
A3
A4
A5
A6
A7
GND
IORQ
RD
WR
J15
→ GND
11-18
74HC133
u3
RF Out
RF Modulator
UM-1285
ch4
ch3
1.8KΩ
10KΩ
100uf
1.8KΩ
1.8KΩ
+5v
100KΩ
TRW 8101-104G
74HC245
u5
74HC244
u6
74HC367
1,4,6,8,10
2x10KΩ
74HC04
110VA.C.
F1
.5A
T1
J15
12.6VCT
1.2A
8.8v
2200uf
-17.8v
470uf
BR1
8.5v
7805
5v
1uf
220Ω
+5v
GND
-15v
interface
video board
PDBIN
SINP
PWR
SOUT
J15
J16

SCION

if the image is important.

MICROANGELO MA520 GRAPHICS COMPUTER Technical Data

- Low Cost. Single Board Graphics Computer
- 512 x 480 Resolution
- Video Refresh Plus User Utility Memory
- ScreenWare Plots Graphics. Manages Text Display
- Easy-To-Integrate S-100 and Multibus Versions

Multibus is a trademark of Intel Corporation

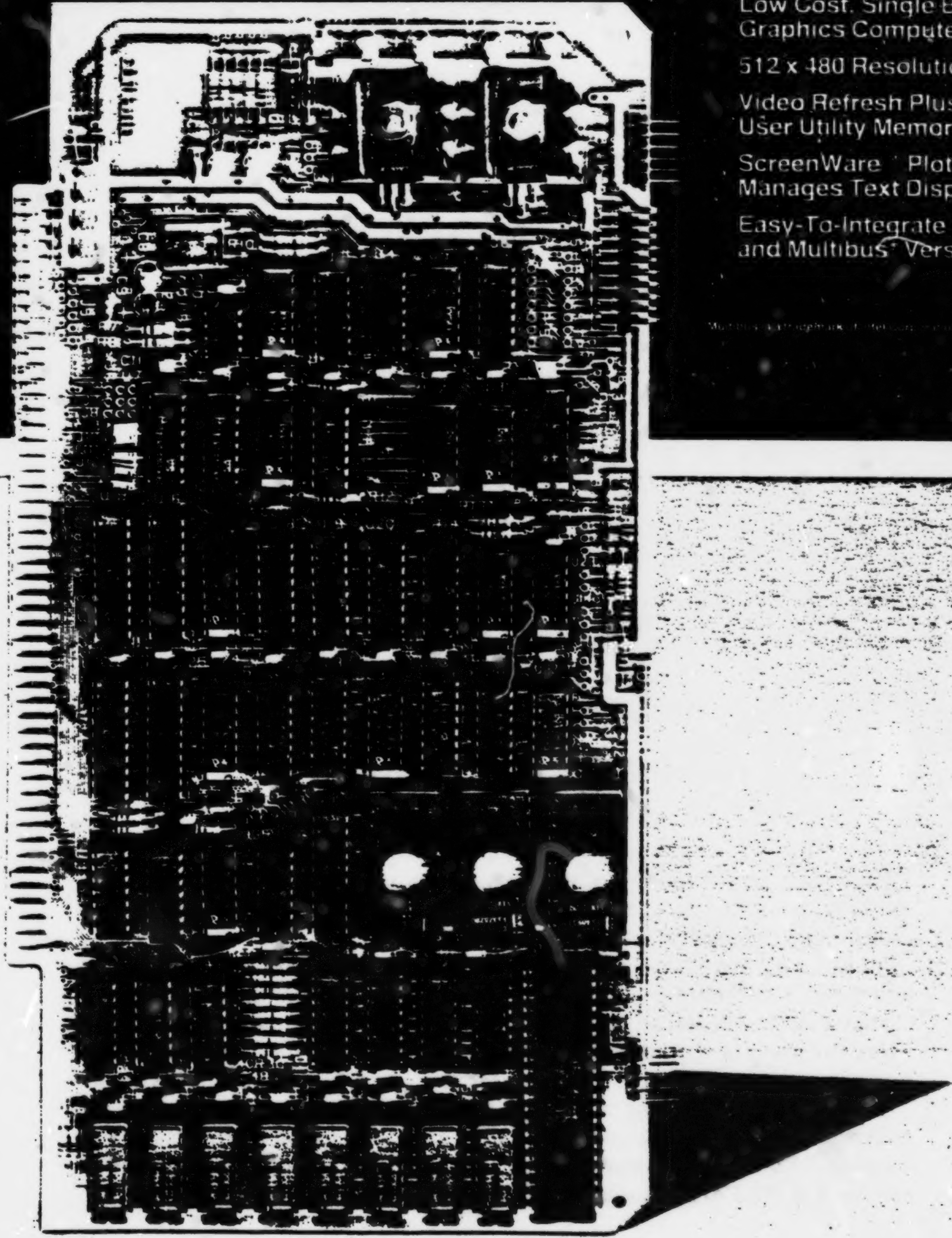

SCION
if the image is important.

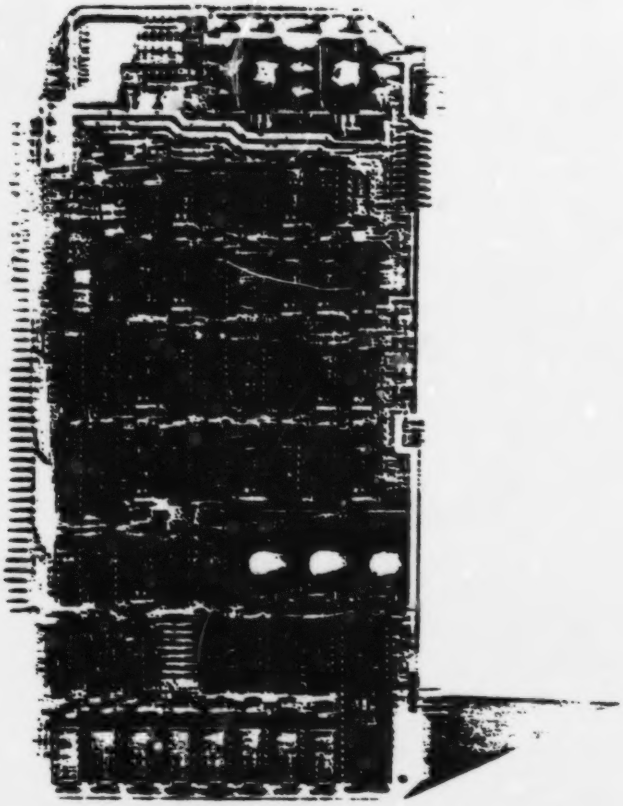

SYSTEM OVERVIEW

MicroAngelo MA520 is a single board monochrome graphics computer with a Z80 microprocessor. It displays graphics with sharp, 512 x 480 pixel resolution. 30K bytes of RAM memory buffers the display and takes all the raster-scan refresh burden off the host system. The additional RAM memory you may use as you wish. ROM firmware contains ScreenWare, a graphics control package that manages the graphics and text on display and performs the hundreds of calculations needed to draw graphics elements. Text controls in ScreenWare recognize 128 ASCII text and control characters and produce an 85 character, 40 line text display. MA520 drives a TTL or composite video monitor. There is a lightpen interface on the board. S-100 and Multibus versions of MA520 are simple to integrate into any standard system.

APPENDIX 9

POWER SUPPLY

CP RESEARCH

POWER SUPPLY/CHARGER BOARD

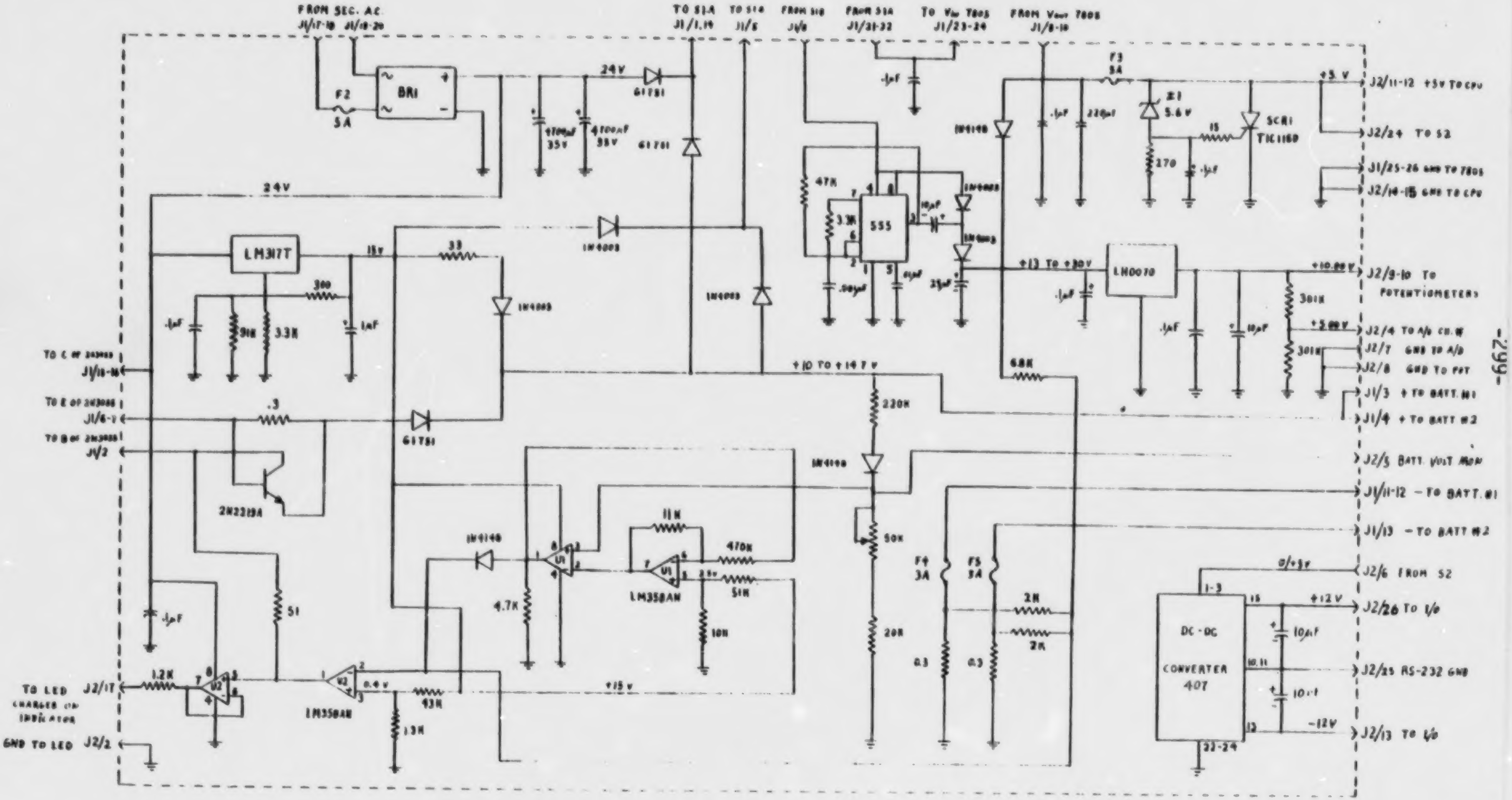
FROM SEC. AC
J1/17-18
J1/19-20
F2
5A
BR1
24V
G1781
4700μF
35V
TO S1A
J1/1,19
TO S1A
J1/5
FROM S1B
J1/6
FROM S1A
J1/21-22
TO V_in 7805
J1/23-24
FROM V_out 7805
J1/8-10
.1μF
F3
3A
1N4148
220μF
Z1
5.6V
270
15
SCR1
TIC116D
+5 V
J2/11-12 +5V TO CPU
J2/24 TO S2
J1/25-26 GND TO 7805
J2/14-15 GND TO CPU
24V
LM317T
11V
33
1N4003
300
91K
3.3K
1μF
47K
3.3K
555
.01μF
.001μF
10μF
25μF
+13 TO +30V
LH0070
+10.00V
J2/9-10 TO POTENTIOMETERS
301K
+5.00V
J2/4 TO A/D CH. 0
J2/7 GND TO A/D
J2/8 GND TO POT
J1/3 + TO BATT. #1
J1/4 + TO BATT #2
J2/5 BATT. VOLT MON
J1/11-12 − TO BATT. #1
J1/13 − TO BATT #2
J2/6 FROM S2
0/+5V
+12V
J2/26 TO I/O
J2/25 RS-232 GND
−12V
J2/13 TO I/O
DC-DC
CONVERTER
407
1-3
15
10,11
12
22-24
10μF
TO C OF 2N3055
J1/15-16
TO E OF 2N3055
J1/6-7
TO B OF 2N3055
J1/2
.3
2N2219A
G1781
+10 TO +14.7 V
220K
68K
1N4148
50K
20K
F4
3A
F5
3A
0.3
2K
11K
470K
51K
10K
2.5V
LM358AN
U1
4.7K
U2
0.4V
43K
13K
+15V
51
1.2K
TO LED
J2/17
CHARGER ON INDICATOR
GND TO LED
J2/2

CP RESEARCH

POWER SUPPLY/CHARGER
SCHEMATIC DIAGRAM

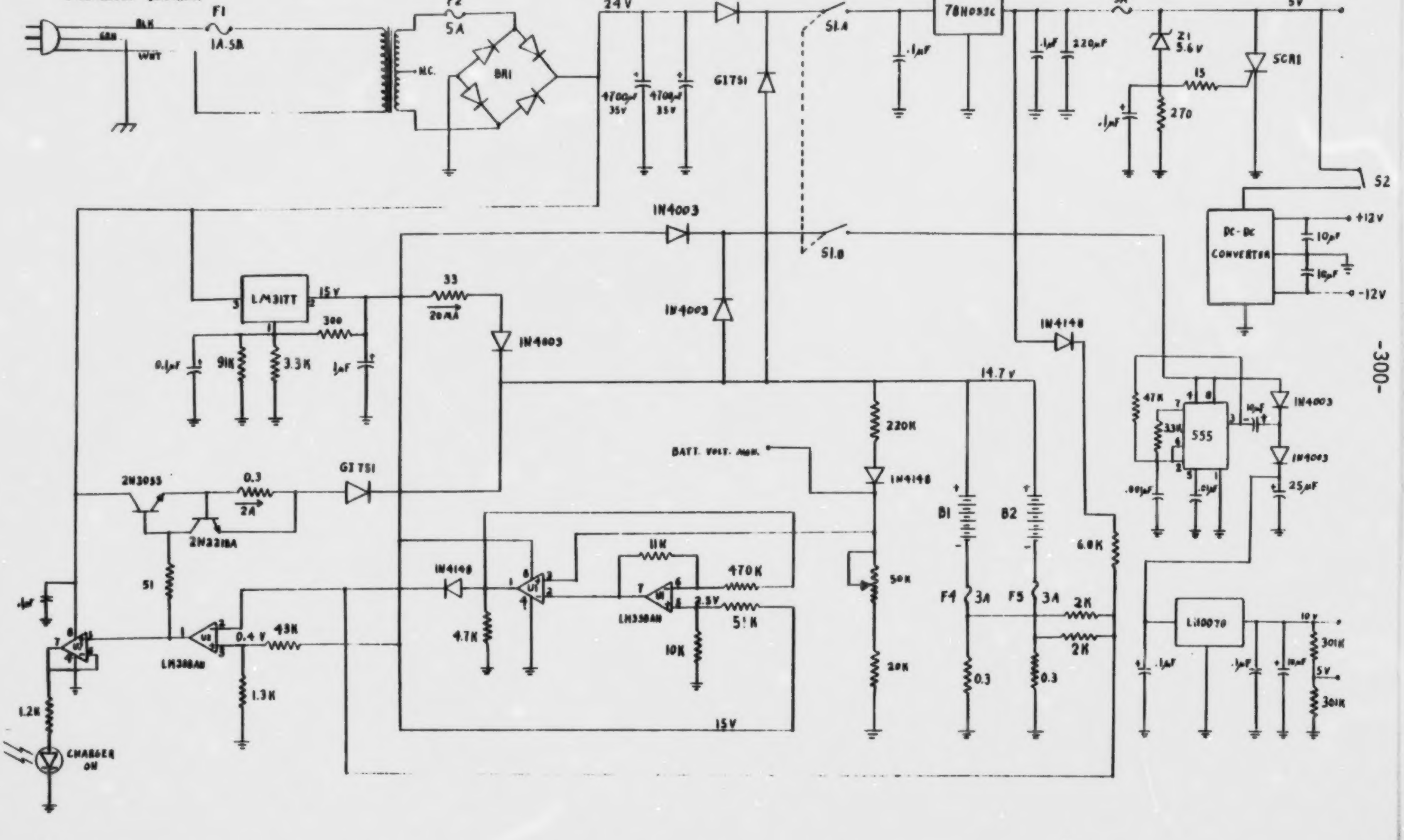
BLK
GRN
WHT
F1
1A.SB
N.C.
F2
5A
BR1
24V
4700µF 35V
4700µF 35V
G1751
G1751
S1.A
S1.B
78H05SC
.1µF
.1µF
220µF
F3
5A
Z1
5.6V
15
270
.1µF
SCR1
5V
S2
DC-DC CONVERTER
10µF
10µF
+12V
-12V
1N4003
1N4003
1N4003
LM317T
15V
33
20MA
300
0.1µF
91K
3.3K
1µF
1N4148
14.7V
220K
1N4148
BATT. VOLT. MON.
50K
20K
B1
B2
F4
3A
F5
3A
0.3
0.3
2K
2K
6.8K
47K
33K
555
.001µF
.01µF
10µF
1N4003
1N4003
25µF
LH0070
.1µF
.1µF
10µF
10V
301K
5V
301K
2N3055
0.3
2A
2N3218A
G1751
51
U2
LM388AN
0.4V
43K
1.3K
U1
1N4148
4.7K
11K
470K
2.5V
51K
10K
LM388AN
15V
.1µF
1.2K
CHARGER ON

APPENDIX 10

WIRING LAYOUT/RELAY MODULE

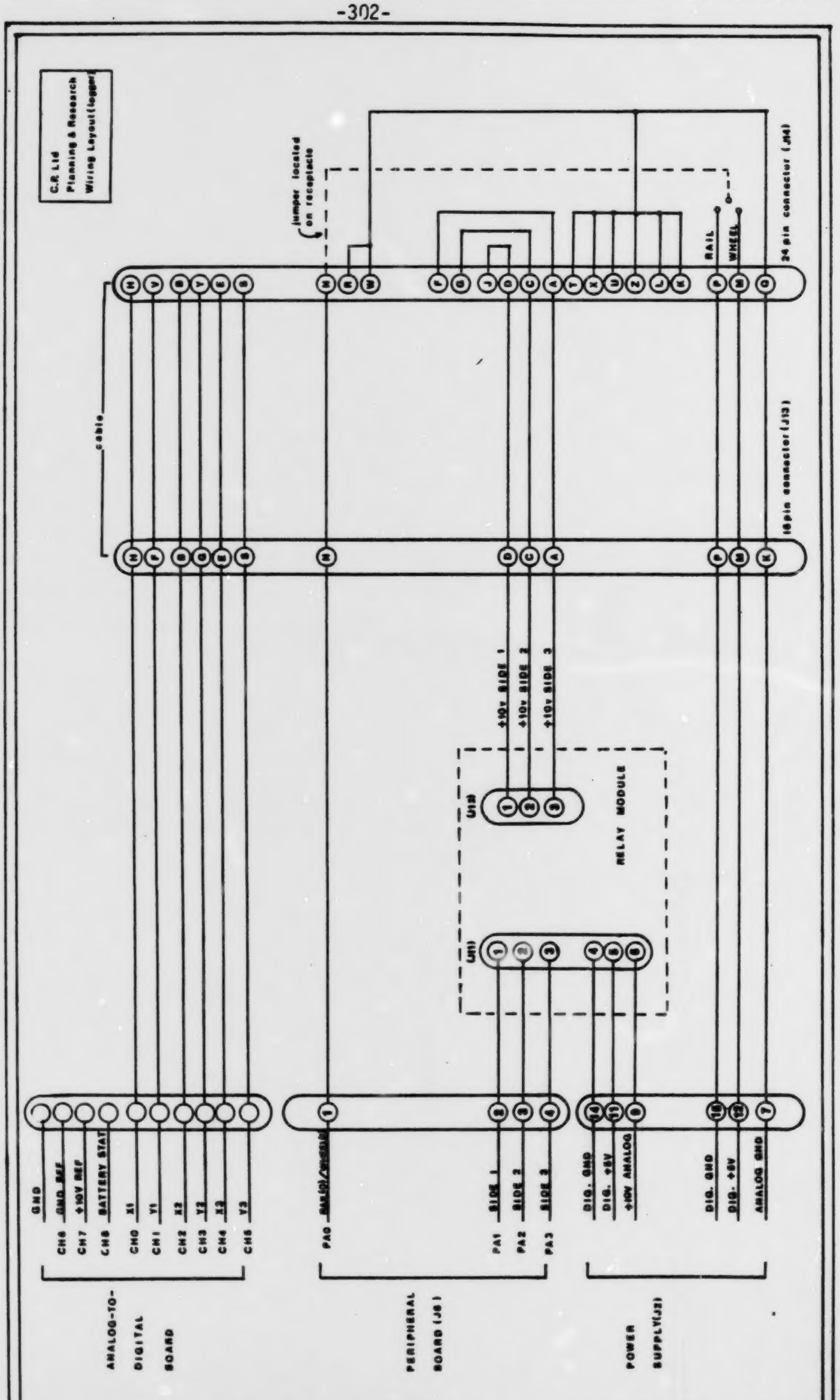
C.R. Ltd
Planning & Research
Wiring Layout (logger)
jumper located on receptacle
24 pin connector (J14)
RAIL
WHEEL
cable
16pin connector (J13)
+10v SIDE 1
+10v SIDE 2
+10v SIDE 3
U10
U11
RELAY MODULE
GND
CH6 GND REF
CH7 +10V REF
CH8 BATTERY STAT
CH0 X1
CH1 Y1
CH2 X2
CH3 Y2
CH4 X3
CH5 Y3
PA0
PA1 SIDE 1
PA2 SIDE 2
PA3 SIDE 3
DIG. GND
DIG. +5V
+10V ANALOG
DIG. GND
DIG. +5V
ANALOG GND
ANALOG-TO-DIGITAL BOARD
PERIPHERAL BOARD (J6)
POWER SUPPLY (J2)

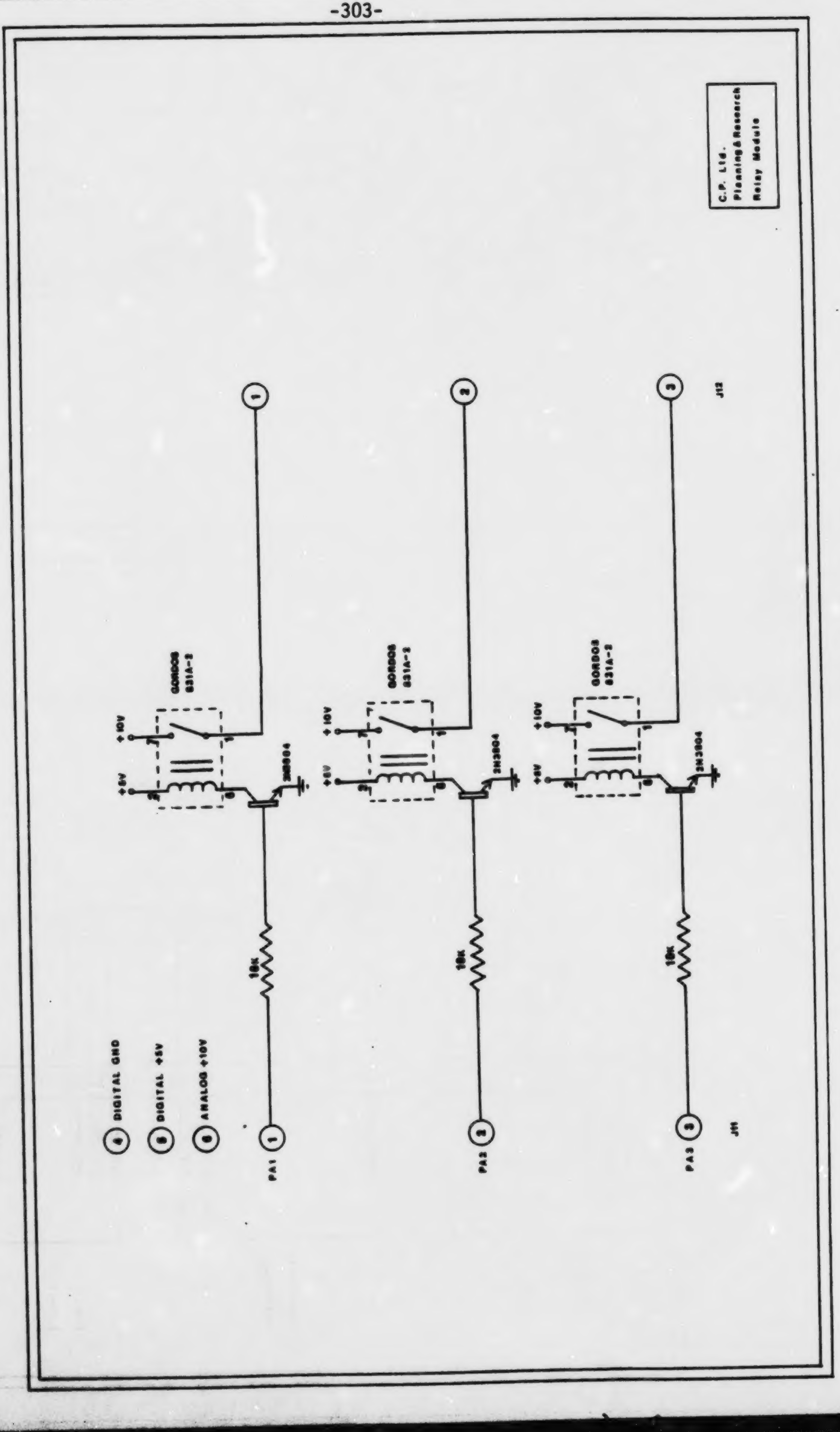
C.P. Ltd.
Planning&Research
Relay Module
④ DIGITAL GND
⑤ DIGITAL +5V
⑥ ANALOG +10V
PA1
PA2
PA3
J11
J12
10K
2N3904
GORDOS
831A-2
+5V
+10V
2
6
7
1
①
②
③

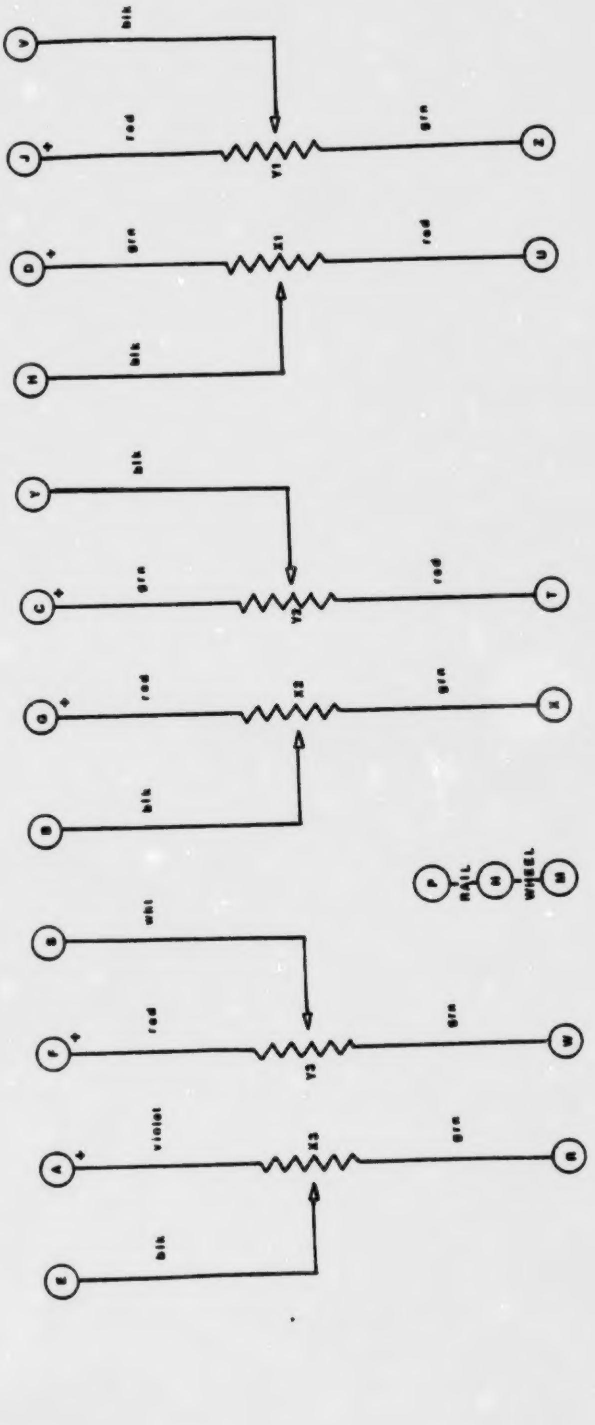
V
blk
J
+
red
Y1
grn
Z
D
+
grn
X1
red
U
H
blk
Y
blk
C
+
grn
Y2
red
T
G
+
red
X2
grn
X
B
blk
S
wht
F
+
red
Y3
grn
W
A
+
violet
X3
grn
R
E
blk
P
RAIL
N
WHEEL
M

C.P. Ltd
Planning & Research
Profilometer Wiring
24-Pin Connector

- · red wire in middle eyelet of potentiometers
- · connector on profilometer head

TESTING OF PACT SLAB, MILE 106.1
MOUNTAIN SUBDIVISION (ALBERT CANYON)

P.C. Ireland
D. Knez
Planning and Research Department
Canadian Pacific Limited
Montreal

SUMMARY

The PACT (Paved Concrete Track) at Mile 106.1 on the Mountain Subdivision is a test installation constructed to evaluate the suitability of the PACT system for C.P. Rail's conditions of climate and loading. The site is close to the Rogers Pass tunnel location and was selected to resemble as closely as possible the conditions in and around these tunnels, which would be the primary location for use of this track system.

Various measurements and observations need to be made to allow proper evaluation of the PACT system's performance.

These include:

- measurement of rail levels, alignment and gauge
- inspection for cracks in slab, and separation of track and base slabs
- measurement of vertical deflection of the track slab under live load
- inspection of rails for wear and defects
- measurement of longitudinal rail creep
- measurement of rail pad compression under live load
- inspection of pads, clips, insulators and shoulders for any developing problems

These measurements will allow the slab designers to evaluate the appropriateness of the design for local conditions and operating personnel to examine the system's effect on maintenance of track geometry and on wear and damage of track hardware.

The first set of measurements was obtained in November, 1984. Measurements will be conducted in February, 1985. A schedule for further testing will be dependent on those and subsequent results; it is anticipated that the test program will last two years.

Following each test an addendum to this report will be issued. For information on the performance of the slab, the reader is referred to the conclusions contained within each addendum.

SOMMAIRE

Le PACT (Plate-forme ferroviaire en béton) au millage 106.1 dans la subdivision Mountain, est un prototype construit dans le but d'évaluer l'aptitude du système PACT aux conditions de climat, et de chargement du CP Rail. Le site est proche du tunnel du Roger's Pass, où sera installé le premier système PACT, et a été choisi pour présenter le mieux possible les conditions existantes à l'intérieur et aux environs de ce tunnel.

Il faut effectuer plusieurs mesures et observations pour être en mesure d'évaluer correctement la performance du système PACT. Cela comprend:

- mesure du niveau, de l'alignement et de l'écartement des rails
- inspection de la dalle pour les fissures et la séparation entre la dalle de voie et la dalle de base
- mesure de la déflexion verticale de la dalle de voie due à la charge vive
- inspection des rails pour des défauts et des fissures
- mesure du cheminement longitudinal des rails
- mesure de la compression des semelles élastiques due à la charge vive
- inspection des semelles élastiques, des attaches, des isolateurs et des épaulements d'attache.

Ces mesures vont permettre aux concepteurs de plates-formes en béton d'évaluer la crédibilité de la conception pour les conditions locales.

Ces mesures aideront aussi les personnes concernées par l'entretien de la voie d'examiner l'effet du système sur le maintien de la géometrie de la voie ainsi que l'usure et les dégâts du système de fixation des rails.

Le premier ensemble de mesures a été obtenu en novembre 1984. D'autres mesures auront lieu en février 1985. Une cédule pour des essais supplémentaires dépendra des résultats actuels et futurs; il est prévu que le programme d'essai durera deux ans.

A la suite de chaque essai un addenda à ce rapport sera émis. Concernant la performance de la dalle le lecteur doit se référer aux conclusions de chaque addenda.

TABLE OF CONTENTS

PAGE

SUMMARY 306

LIST OF TABLES 311

LIST OF ILLUSTRATIONS 312

1.0 INTRODUCTION 313

2.0 TESTS IN NOVEMBER/DECEMBER 1984 (TEST 1) 313

- 2.1 Introduction 313
- 2.2 Test Description 317
- 2.3 Instrumentation 317
- 2.4 Test Results and Observations 321
- 2.5 Conclusions 325

LIST OF TABLES

TABLE NO.	DESCRIPTION	PAGE
1	Maximum Rail Pad Compression and Slab Vertical Deflections (Test 1).	322

LIST OF FIGURES

FIGURE NO.	DESCRIPTION	PAGE
1	East end of slab showing concrete ties on approach. The objects lying between rails are concrete test cylinders curing in the same environment as the slab itself.	314
2	View from beginning of rock cut looking west.	314
3	View from middle of slab looking west.	315
4	West end of slab.	315
5	View of site from east end at time of testing.	316
6	View of site from west end at time of testing.	316
7	Optron mounted on rock face. The control unit is slung below the support bracket.	318
8	Rail side instrumentation. At extreme left is the Optron target, near centre are the LVDTs.	318
9	Same set up as photo #8, viewed from above.	319
10	Same instrumentation setup at end of slab. Note lead from LVDT on gauge side of rail passes under rail at the end of the slab.	319
11	Recording equipment in portable shed. Generator in background.	320
12	General view of test installation. Rail side instrumentation is out of picture to the right.	320
13	Optron Trace - Train #6054, Clip #0, Low Rail.	323
14	LVDT Traces - Train #6054, Clip #0, Low Rail.	324

1.0 INTRODUCTION

The PACT (Paved Concrete Track) test site is located in a rock cut in Albert Canyon, approximately 24 kilometers east of Revelstoke. The slab begins on a spiral to a 6 degree curve left and ends within the curve. Construction work was completed at the end of September 1984. Photos #1 to #4 give an overview of the test site.

The PACT system consists of a base slab reinforced by two layers of mat reinforcement, and a top slab (reinforced with one layer of mat reinforcement) which carries the track and its fastening system. The base slab was supposed to have been founded on bedrock, but the jointed nature of the rock and its tendency to fracture resulted in about 1.5 metres of overexcavation upon the completion of cleanup operations. The site was then backfilled to the required grade with carefully compacted fill from a local source.

The rails are C.W.R. of 136 lb. RE section in 1% Chromium alloy manufactured by Algoma. They are fastened to the slab using Pandrol shoulders and clips at 300mm center to center. The clips on the high rail side are numbered with the numbers ascending from west to east. The rails are supported on the concrete surface by rail pads throughout the length of the slab. Two types of rail pads were used so their performance could be compared. These are Walker rubber bonded cork pads on the western half of the slab and Avon grooved rubber pads on the eastern half.

2.0 TESTS IN NOVEMBER/DECEMBER 1984

2.1 Introduction

The PACT system was instrumented at several locations along its length at both rails in order to determine the deflection of the slab with respect to a fixed reference and the compression of the pads between the rail and the concrete. The heads of the rails were inspected for surface defects and wear. Other proposed measurements were deferred because of difficulties generated by the presence of ice and snow at the site. Photos #5 and #6 show the site conditions at the time of testing.

Photo #1. East end of slab showing concrete ties on approach. The objects lying between the rails are concrete test cylinders curing in the same environment as the slab itself.

Photo #2. View from beginning of rock cut looking west.

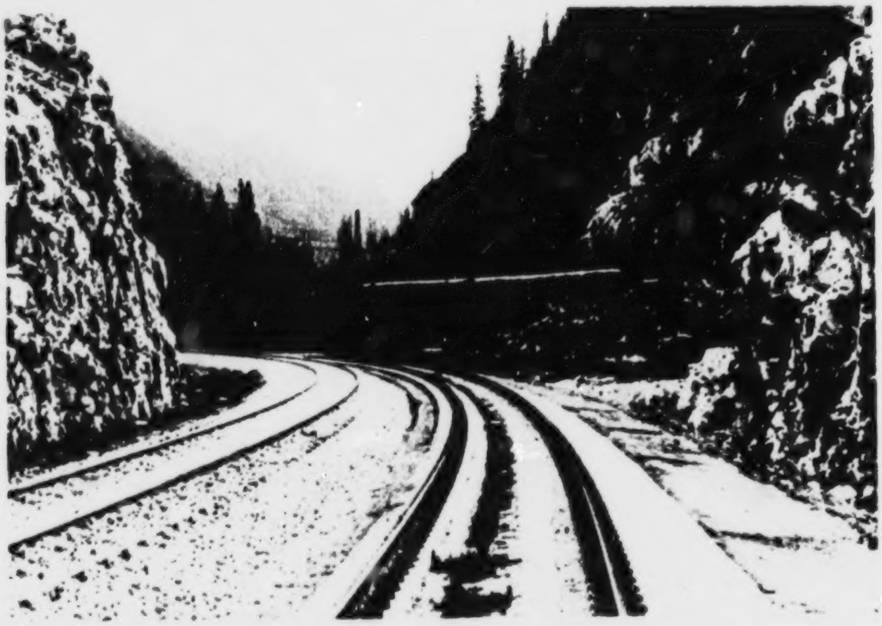

Photo #3. View from middle of slab looking west.

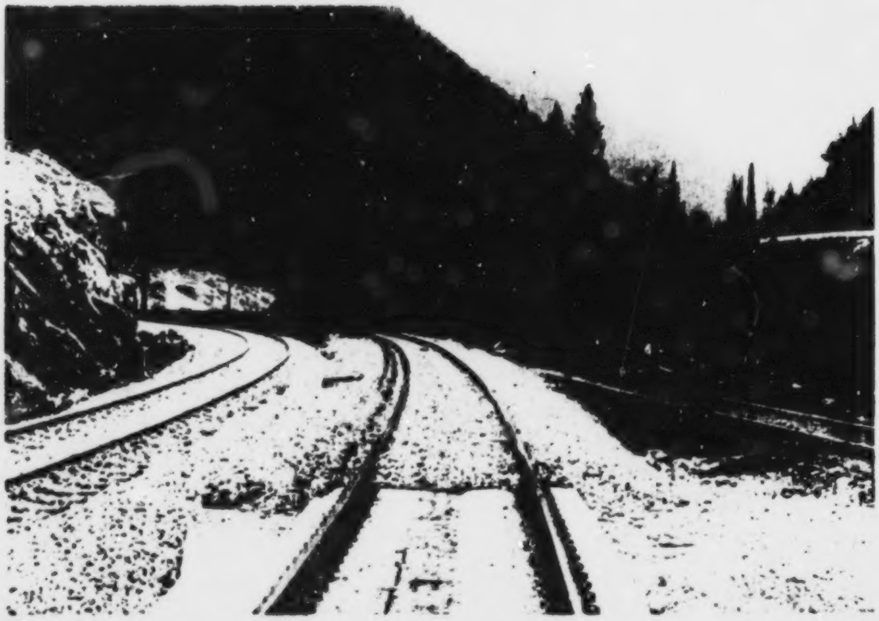

Photo #4. West end of slab.

Photo #5. View of site from east end at time of testing.

Photo #6. View of site from west end at time of testing.

2.2 Test Description

Instrument readings were taken at eight locations under live load from loaded freight trains, which were travelling at speeds between 19 and 26 miles per hour. Readings were taken until at least one heavy unit train was recorded at each location. During testing the temperature hovered around 0 degrees C.

2.3 Instrumentation

Slab deflection was measured using an optical displacement following device known as the "Optron"* The Optron target was mounted on the slab adjacent to the field side of the rail using screws set into the concrete with lead anchor plugs. The target mount included micrometer adjustments for both horizontal and vertical translation, which were used to calibrate the Optron readings (see photo #8). The Optron itself was mounted via a custom manufactured bracket to the rock face of the cut for five sets of readings, to utility poles for two sets of readings, and to a boulder for one set (see photo #7).

Pad compression was measured using two DC-powered linear variable differential transformers (LVDT's) mounted on the flange of the rail with magnetic clamps. Contact with the concrete slab was maintained by spring loading the plunger of each LVDT - see photos #8 to #10.

The Optron target was positioned at each end of the slab as well as between clips 469/470 and 450/451, with the LVDTs in close proximity. Setups on the low rail side were performed as close as possible to directly opposite those on the high rail side.

---

* For a description of this system, see: "Strain and Displacement Measurement on Bridge 0.7 QCR Connection", Planning and Research Department, Report No. S724-82, April 1982.

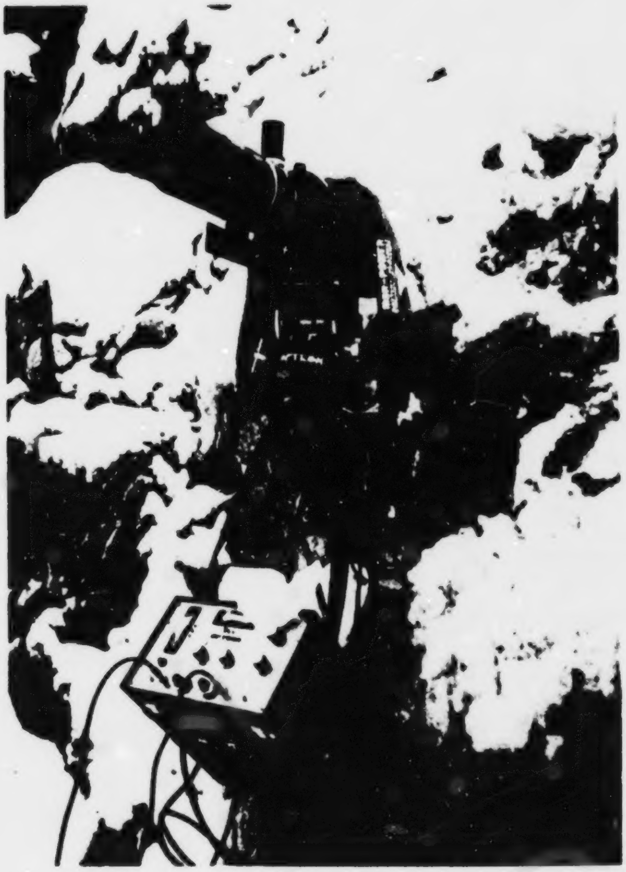

Photo #7. Optron mounted on rock face. The control unit is slung below the support bracket.

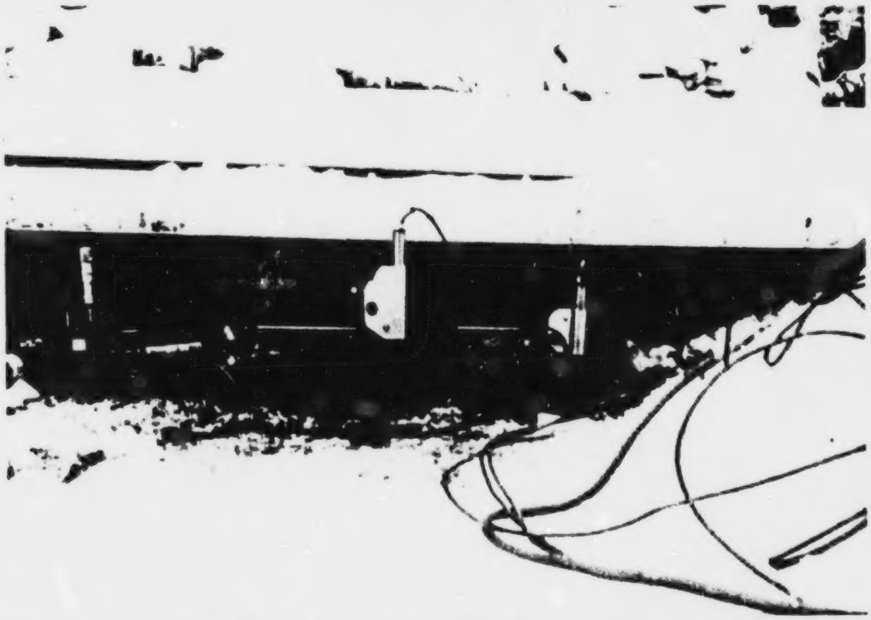

Photo #8. Railside instrumentation. At extreme left is the Optron target, near center are the LVDT's.

Photo #9. Same set up as photo #8, viewed from above.

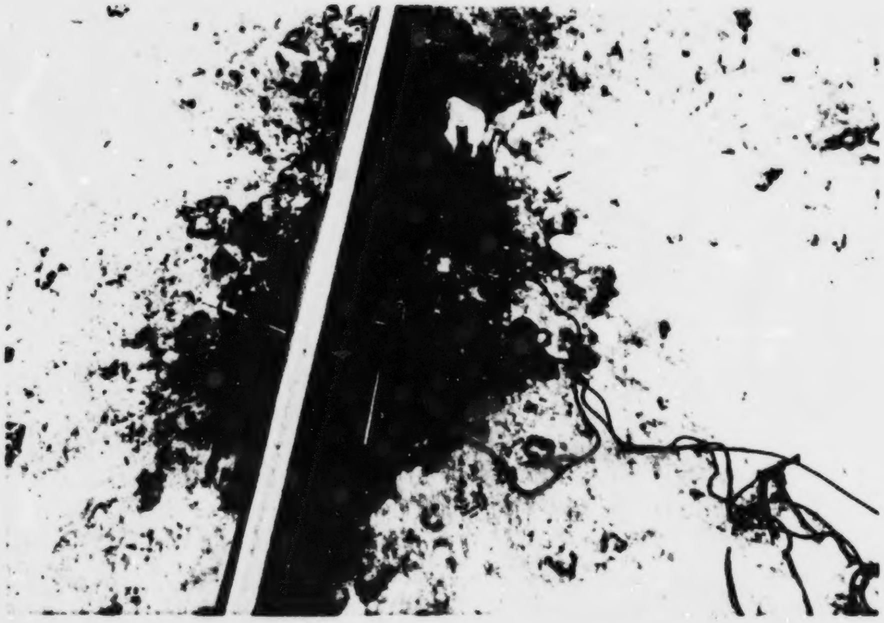

Photo #10. Same instrumentation set up at end of slab. Note lead from LVDT on gauge side of rail passes under rail at the end of the slab.

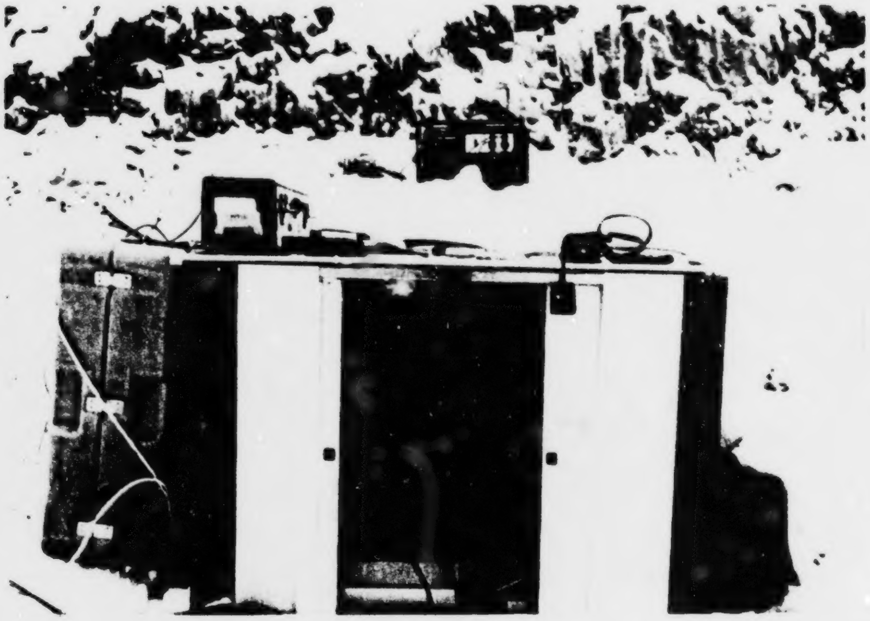

Photo #11. Recording equipment in portable shed. Generator in background.

Photo #12. General view of a test installation. Railside instrumentation is out of the picture to the right.

Unfortunately, cold temperatures made soldering of instrument leads extremely difficult, therefore it was decided not to take the LVDT leads apart so they could be threaded through the joints between individual rail pads at the interior of the slab. Thus both LVDTs were on the same side of the rail as the Optron target at these locations. To correct this problem in future tests, connectors slender enough to fit through the pad joints will be used to avoid soldering in the field. At the ends of the slab one LVDT was placed on each side of the rail, with the leads passing through the ballast under the rail off the end of the slab. Measuring pad compression on both sides of the rail allows for determination of the extent of rail roll-over.

Data generated by these measurement devices was recorded on a 14-channel FM magnetic tape recorder for later playback and analysis. A two-channel strip chart recorder was used to check the functioning of the Optron and LVDTs at each test installation.

2.4 Test Results and Observations

The recordings of Optron and LVDT output were played back on a strip-chart recorder, and the maximum values of movement were extracted from these traces. The quality of Optron recordings was good with the Optron mounted on the rock face, but very poor at the other setups due to ground vibrations moving the instrument. The data obtained for the various loaded unit trains passing over the PACT are presented, in their processed form, in Table 1; sample Optron and LVDT traces for a representative unit train are shown in Figures 13 and 14. Please note that at clips #0 and #922, LVDT#1 was on the gauge side of the rail, with LVDT#2 on the field side of the rail, whereas at clips #450 and #470 both LVDTs were on the field side. The Optron readings with poor traces are indicated by asterisks.

The slab is located on the north track of a double tracked section. Generally, all westbound traffic is routed across it. A high percentage of this traffic consists of loaded unit trains. At the time of testing, this section of track had been in service for 2 months and had experienced approximately 8.3 MGT.

Table 1 - Maximum Rail Pad Compression and Slab Vertical Deflections (Test 1)

Location	Train Speed mph	Readings in millimetres		
		LVDT #1	LVDT #2	Optron V
clip # 0 - high side	22	0.31	0.50	0.83 *
- low side	23	0.19	0.27	1.36
- low side	26	0.15	0.22	1.74
clip #450 - high side	21	0.50	0.59	1.09
- low side	20	0.36	0.59	2.20
clip #470 - high side	24	0.69	0.71	1.14
- high side	20	0.77	0.77	1.50
- low side	25	0.77	0.82	0.95
- low side	-	1.00	1.06	----
clip #922 - high side	24	0.38	0.59	1.11 *
- high side	25	0.38	0.71	0.95 *
- high side	19	0.69	0.94	----
- low side	23	----	0.59	1.19 *

* Optron readings with poor strip chart traces due to ground vibrations.

Figure 13. Optron Trace

Train #6054, clip #0, low rail

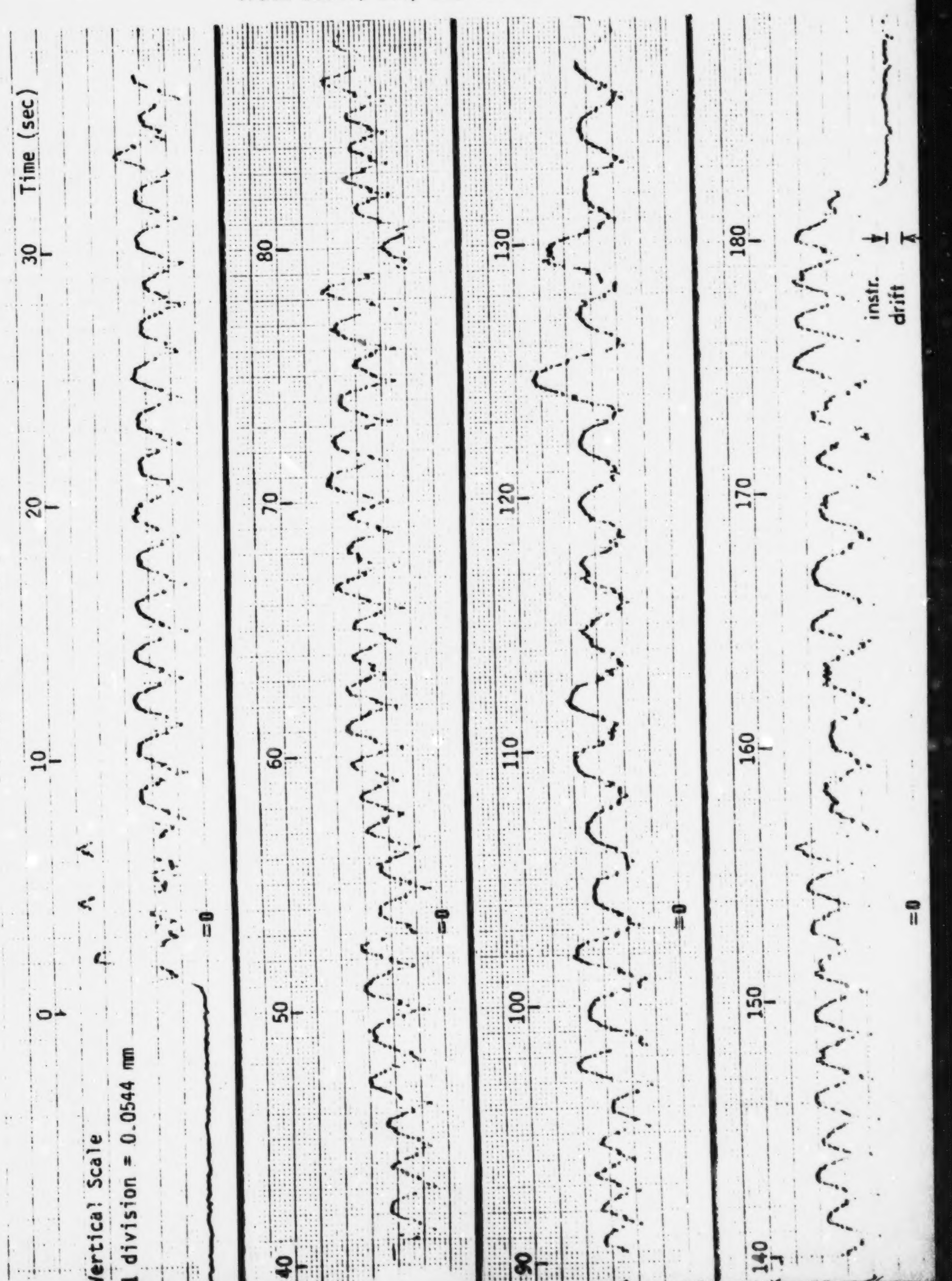

Figure 14. LVDT Traces

Train #6054, clip #0, low rail

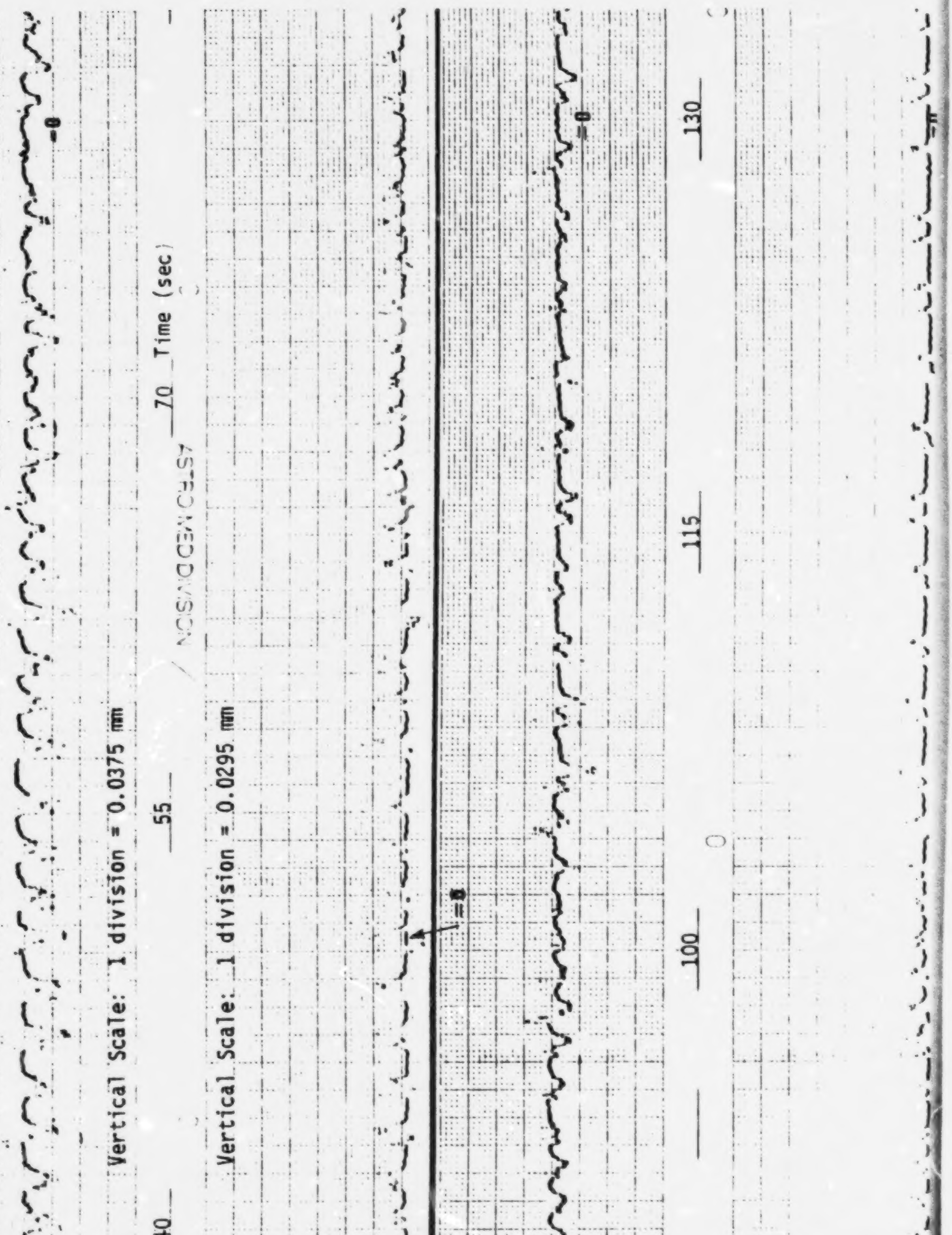

High and low rail running surfaces have experienced limited wear and plastic flow. As well, the high rail has not experienced significant gauge face wear. These observations are consistent with the limited tonnage over the PACT to date.

2.5 Conclusions

The PACT and rail pads were designed for an axle load of 80 kips with a 3.5 dynamic overload factor. Under these conditions the slab was to deflect no more than 1.1 mm.* Testing to date indicates that slab deflection generally exceeds this value and in one case, even reached 2.20 mm (See Table 1).

Rail pad deflection under design loading was specified to have a maximum deflection of 1.2 mm at a temperature of 32°C. The test results show that the deflection is generally lower. The reason for this might be attributed to lower axle loads, pre-compression of the rail pad, and the lower temperature (measurements were taken at 0°C).

In the spring, when the PACT will be clear of snow, the location and extent of cracks in the slab will be noted. If areas of significant cracking exist, they will be measured for vertical slab deflections.

Measurements will continue to be taken at 3 month intervals. The second test is tentatively scheduled for the end of February 1985.

* For reference see "Slab Track-Rogers Pass Tunnels", E.H. Talyor, Office of the Chief Engineer, July 1983.

TESTING OF BRIDGE 24.0 WINCHESTER SUBDIVISION - CONCRETE BRIDGE TIES

P.C. Ireland
D. Knez
Planning and Research Department
Canadian Pacific Limited
Montreal

SUMMARY

Bridge 24.0, located on tangent track on the Winchester Subdivision, Smiths Falls Division, is a 33 foot deck plate girder span. The wooden ties on this span were recently replaced with prestressed concrete ties. In response to a request from the Engineering Department, CP Rail, selected ties of the span were instrumented and an initial test was conducted October 29, 1984.

Three ties in the centre of the span and three ties at the west entry of the span were instrumented with strain gauges. The strain gauges were oriented so as to record maximum bending strains in order to experimentally determine the distribution of axle loads amongst ties. This information would allow for comparison with expected values to aid in the design of prestressed concrete ties. Of specific interest were dynamic loading effects.

Analysis of the data from the first test showed that two of the instrumented ties were taking little or no load. Subsequent examination of the deck system revealed that these ties were not seated solidly on the girders. This phenomenon is caused by a series of ties having non-uniform distances between the rail seat and the base of the tie/girder pad. When stiff rails are installed on the rail seats, it is possible for the tie to be physically lifted from the girder. This 'lack of fit' between adjacent ties results in the lifted tie receiving none of the load. After meeting with representatives of the Bridge Section, CP Rail, it was decided to bring all rail seat elevations to the same level by the use of metal shims. A second test was conducted November 21, 1984.

The results from the second test indicate that the load taken by ties previously 'free floating' increased and therefore reduced on adjacent ties. It is anticipated that a modification in the procedure used for shimming would result in a further improvement in load distribution. The results from this second test also indicated that the entry tie experiences the greatest axle load - 24.76 Kips at 60 mph. This load is relatively constant with increasing speed. However, in test one, a centrally

located tie adjacent to a 'free floating' tie experienced an axle load of 26.69 Kips at 60 mph - a 25% increase from the load at 40 mph. Lack of fit between adjacent ties can have a large effect on the load carried by the ties. It is a major consideration to be dealt with in future installations.

It is proposed to conduct a third test in the summer of 1985. This would involve recording strains during the passage of regular traffic to obtain a statistical distribution of in-service loading. A follow-up report will be issued following this test.

SOMMAIRE

Le pont DPG (pont à poutres pleines à tablier supérieur) au milage 24.0, situé le long d'une voie en alignement droit dans la subdivision Winchester, Division de Smiths Falls, est constitué d'une travée de 33 pieds. Récemment, les traverses de bois de ce pont ont été remplacées par des traverses en béton précontraint. Suite à la demande faite par le département d'ingénierie de CP Rail, un choix de traverses a été fait pour l'installation d'instruments de mesures et un essai initial a été effectué le 29 octobre 1984.

A l'aide de jauges électriques d'extensométrie des mesures de déformations ont été prises sur les trois traverses centrales ainsi que les trois traverses de l'entrée ouest. Les jauges d'extensométrie étaient orientées de sorte à mesurer les déformations maximales dues à la flexion dans le but de déterminer expérimentalement la distribution, dans les traverses, de charges provenant des essieux. Cela permettra de comparer l'information obtenue avec les valeurs calculées pour aider dans la conception future de traverses en béton précontraint. Un intérêt particulier était porté sur l'effet des charges dynamiques.

A la suite du premier essai l'analyse des résultats montra que deux des traverses reprenaient peu ou pas de charges. Une examination ultérieure du système de tablier démontra que ces traverses n'étaient pas solidement installées sur les poutres maîtresses. Ce phénomène est dû au fait que plusieurs traverses n'ont pas une distance uniforme entre la table de sabotage et la base de la semelle élastique qui se trouve entre la traverse et la poutre maîtresse. Lorsque des rails rigides sont installés il est physiquement possible que la traverse soit soulevée de la poutre maîtresse. De cette non-conformité de l'appui parmi des traverses adjacentes résulte une poutre soulevée qui ne reçoit aucune charge. A la suite d'une rencontre avec les représentants de la section des Ponts de CP Rail, il a été decidé de porter toutes les tables de sabotage de traverses à la même élévation en utilisant des cales métalliques de nivellement. Un deuxième essai a eu lieu le 21 novembre 1984.

Les résultats du deuxième essai montre que la charge reprise par les traverses initialement soulevées a augmenté et a donc diminué dans les traverses adjacentes. Il est prévu qu'une amélioration dans la procédure de nivellement par calage résulterait en une meilleure distribution des charges. D'aprés les valeurs obtenues du second essai la première traverse subit la plus grande charge d'essieu - 24.76 kips à 60 mi/h. Cette charge reste relativement constante avec une vitesse croissante. Cependant, durant le premier essai, une traverse centrale et adjacente à une traverse soulevée a repris une charge d'essieu de 26.69 kips à 60 mi/h, ce qui correspond à une augmentation de 25% de la charge reprise à 40 mi/h. Cet appui inadéquat parmi des traverses adjacentes peut avoir un effet considérable sur la charge reprise par les traverses. Ceci est une préocupation majeure dont it faut tenir compte dans les installations futures.

Il a été proposé d'exécuter un troisième essai durant l'été 1985. Ce dernier consisterait à enregistrer des déformations dues à une circulation régulière dans le but d'obtenir une distribution statistique des charges de services. Un rapport ultérieur sera émis à la suite de cet essai.

TABLE OF CONTENTS

		PAGE
SUMMARY		327
LIST OF FIGURES		332
1.0 INTRODUCTION		333
2.0 TEST DESCRIPTION		333
3.0 INSTRUMENTATION		334
4.0 TEST RESULTS AND OBSERVATIONS		337
5.0 CONCLUSIONS AND RECOMMENDATIONS		341
REFERENCES		344
APPENDICES		
I	TIE PAD OBSERVATIONS	345
II	CALCULATION OF LOAD FROM MEASURED STRAINS	348

LIST OF FIGURES

PAGE

1. Elevation View of Bridge 24.0/Winchester Subdivision 335

2. Location of Strain Gauges: Tie Number 14 336

3. Load Versus Speed for Instrumented Ties (Test 2) 339

4. (a) Load Versus Speed for Test 1 - Before Shimming 340
   (b) Load Versus Speed for Test 2 - After Shimming 340

1.0 INTRODUCTION

Bridge 24.0, located on tangent track on the Winchester Subdivision, is a 33 foot deck plate girder span. The wooden ties on this span were recently replaced with prestressed concrete ties. These ties are precast and pre-tensioned with forty-four 0.196 inch OD wires (with an effective stress per wire of 129 Ksi). The ties are spaced at 13 1/2 inch centres and are affixed to the span by means of two hook bolts. EVA (ethyl vinyl acetate) rail pads of thickness 5 mm are situated between the 115 RE running rails and the ties. The rails are fastened to the ties by Pandrol rail clips (PR 600 AV). Neoprene pads of thickness 0.75 inch have been placed between the ties and girders. This span also has 100 RE-HF Jordan guard rails.

Six ties, three in the centre and three at the west end, were instrumented with strain gauges to experimentally determine the load being taken by the concrete ties. Of specific interest were dynamic loading effects.

2.0 TEST DESCRIPTION

Testing was initially conducted on October 29, 1984. The test procedure involved recording the strains during the passage of a locomotive, CP 8800, with a gross weight of 134 tons and a caboose, CP 434661. Test runs were conducted at speeds varying from 1 mph to 60 mph (in increments of 10 mph), in both directions.

Analysis of the data from this test (hereafter referred to as Test 1) indicated that some ties were not seated properly. After meeting with representatives of the Bridge Section, CP Rail, it was decided to correct this situation by placing metal shims between the rails and the ties where required, to bring all rail seat elevations to the same level.

A second test (Test 2) was conducted on November 21, 1984. The same test procedure as used in the first test was followed using locomotive CP 8796, with a gross weight of 134 tons and caboose CP 434343.

3.0 INSTRUMENTATION

On October 22 and 23, 1984, 24 metal foil strain gauges were attached to the concrete ties. These gauges were 350 ohm single element gauges with active gauge lengths of one inch. The manufacturer's (William T. Bean, Inc.) designation was BAE-06-10CFF-350. A complete description of the materials used and the method followed in attaching the gauges to the concrete surface are detailed in a previous report (see Reference 1).

The gauges were applied to tie numbers 1, 2, 3, 14, 15 and 16 at the centre of the tie, top and bottom (see Figure 1). This allowed for the recording of maximum bending strain. In addition, tie number 14 was instrumented with additional gauges as shown in Figure 2. This was to verify that the strain distribution within the tie does in fact remain linear.

Ten of the bridge circuits used were of the single active arm type with 350 ohm dummy resistors. The remaining four bridge circuits (used for Gauges 3 + 3', 4 + 4', 8 + 8', 9 + 9' — see Figure 2) were of the double active arm type also with 350 ohm dummy resistors. Lead wire compensation was employed for all strain gauges, but temperature compensation was not, due to the short time interval over which measurements were taken.

The bridge circuitry was contained in a 14 channel Vishay 2100 Signal Conditioner/Amplifier. The output was recorded on a 14 channel Racal Magnetic Tape Recorder for future analysis.

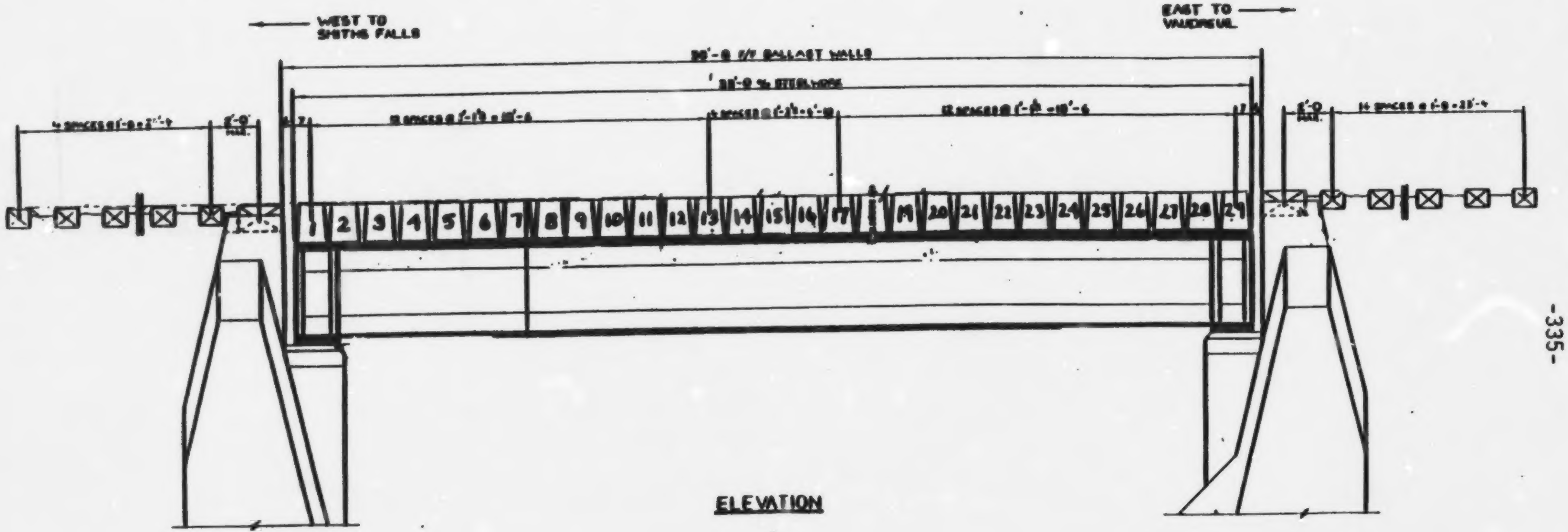
WEST TO SMITHS FALLS
EAST TO VAUDREUIL
1 2 3 4 5 6 7 8 9 10 11 12 13 14 15 16 17
19 20 21 22 23 24 25 26 27 28 29
ELEVATION

FIGURE 1: ELEVATION VIEW OF BRIDGE 24.0/WINCHESTER SUBDIVISION

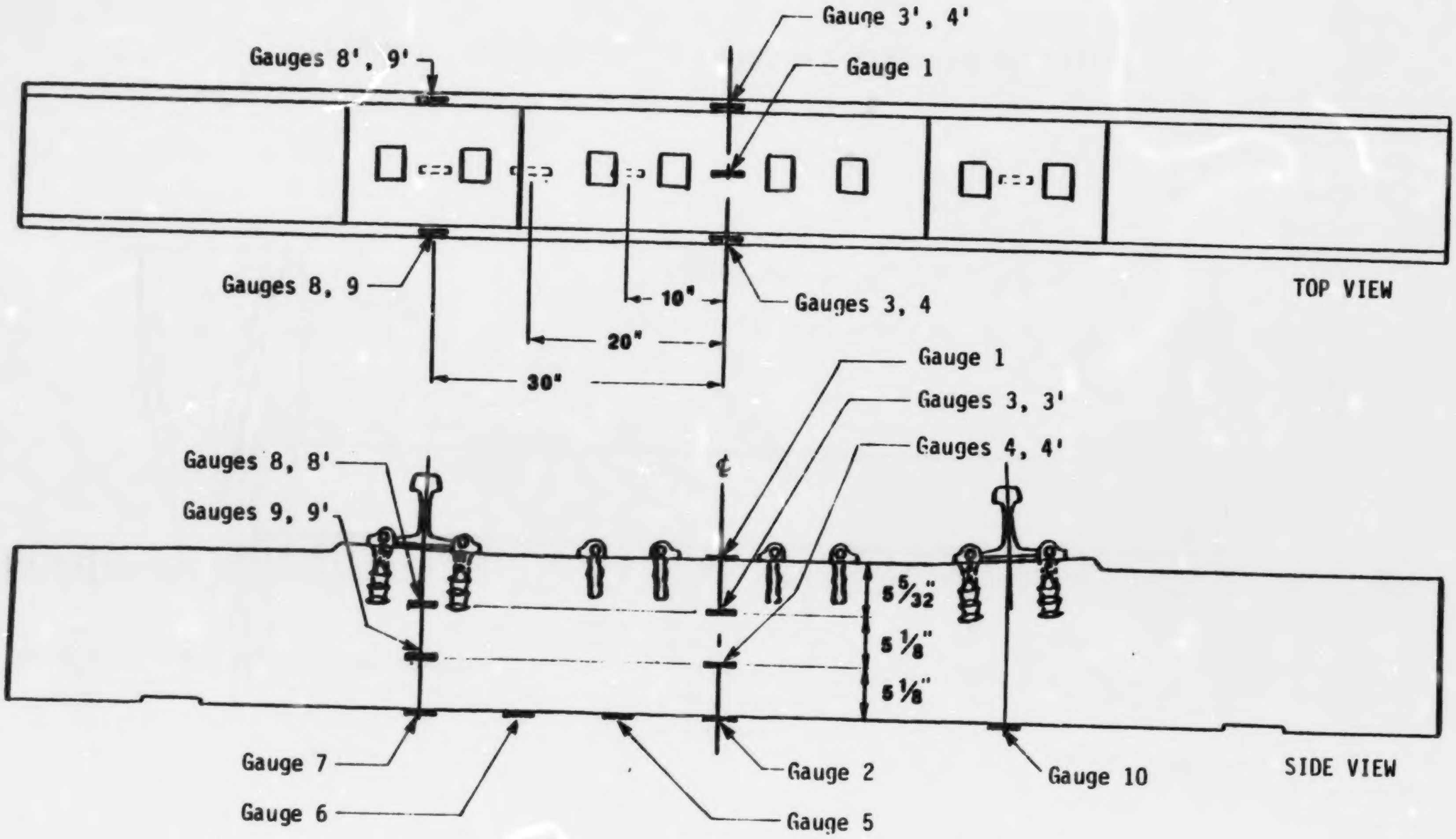
Gauges 8', 9'
Gauge 3', 4'
Gauge 1
Gauges 8, 9
10"
20"
30"
Gauges 3, 4
TOP VIEW
Gauge 1
Gauges 3, 3'
Gauges 8, 8'
Gauges 4, 4'
Gauges 9, 9'
℄
5 5/32"
5 1/8"
5 1/8"
Gauge 7
Gauge 6
Gauge 2
Gauge 5
Gauge 10
SIDE VIEW

FIGURE 2: LOCATION OF STRAIN GAUGES - TIE 14

4.0 TEST RESULTS AND OBSERVATIONS

Analysis of the data from the first test conducted on Bridge 24.0 showed that two of the instrumented ties (Numbers 2 and 14 - see Figure 1) were taking little or no load. Subsequent examination of the deck system showed lack of fit in many locations, as detailed in Appendix 1. From this examination, it was noted that ties not carrying significant loads were those which were not properly supported on the girder. Observation under traffic revealed that some of these gaps did not completely close even with an axle directly over the ill-fitting tie.

The following observations were made:

1. The maximum load taken by the end tie is independent of the direction of train travel.

2. The size of the loads would appear in certain instances to be independent of train speed. However, ties adjacent to free floating ties do experience a rapid increase in load with increasing speed.

3. There is very little reverse bending when the wheelset leaves the tie.

Tie 14, which was instrumented with additional strain gauges yielded no useful data as, unfortunately, it was a free floating tie.

The gaps between the ties and the girder are caused by differential elevation among the ties. This phenomenon was noted by Queen's and McGill Universities in their reports (References 2 and 3). It is caused by a series of ties having different distances between the rail seat and the base of the tie girder pad. When stiff rails are installed on the rail seats, it is possible for the tie to be physically lifted from the girder. This results in the lifted tie receiving none of the load. This condition is aggravated by small spacing between adjacent ties and by the Jordan guardrail.

Measurements taken on three spare ties showed that there can be substantial variation in the elevation measurement between the rail seat and base of the girder pad (which is glued to the tie) as detailed below.

	Left side	Right side
Tie A	15 45/64"	15 42/64"
Tie B	15 33/64"	15 51/64"
Tie C	15 34/64"	15 49/64"

As a result of discussions with members of the Bridge Section, CP Rail, it was decided to try to correct the lack of fit problem by placing metal shims between the rail and the tie. This was done by removing the Pandrol clips, allowing the ties to sit fully on the girder, measuring the gap between the rail and tie, and installing an appropriate thickness of shim.

A subsequent test was performed on Bridge 24.0 to determine if there had been any change in the response of the bridge ties. The load taken by ties previously 'free floating' increased and therefore reduced on adjacent ties. Figure 3 is a presentation of load carried by the ties as a function of speed (Test 2). Figure 4(a) shows the load carried by ties 3, 15 and 16 versus speed (Test 1). These ties were adjacent to free floating ties, that is ties number 2 and 14. Figure 4(b) shows the load carried by the same ties after shimming (Test 2). The reduction in load and the improved uniformity of load on different ties is quite evident. See Appendix II for an example of how the load carried by a tie was calculated from the measured strains.

As can be noted from Figures 3 and 4, the shimming has had a significant effect on load distribution, but there is still a large variation in tie loads. This is partly due to the procedure which was used to determine shim thickness. The deficiency arose because the gap between the rail and tie could only be measured at an edge of the rail seat, with feeler gauges. A better procedure for correcting lack of fit problems would

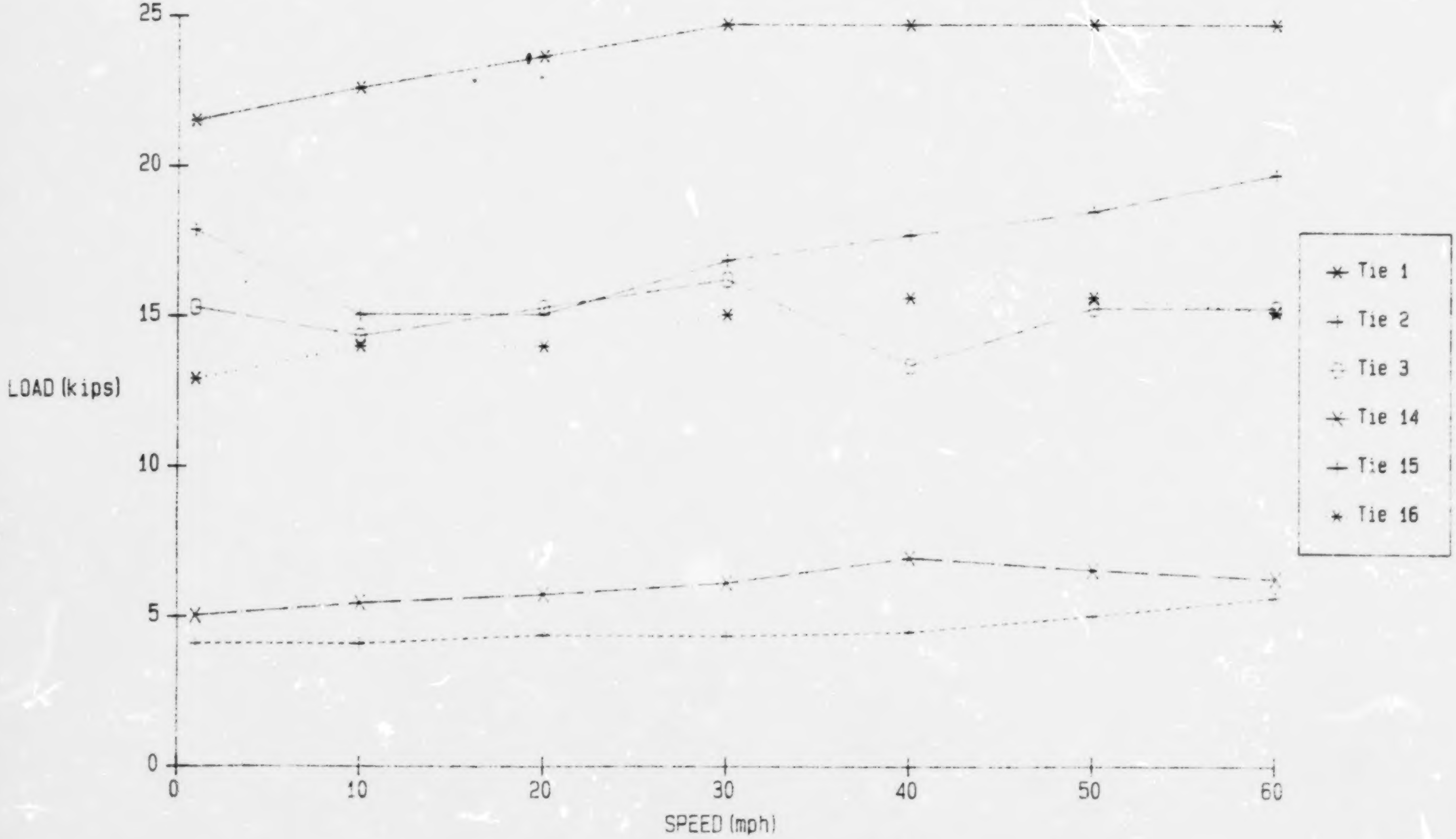

FIGURE 3: LOAD VS. SPEED FOR INSTRUMENTED TIES (TEST 2)

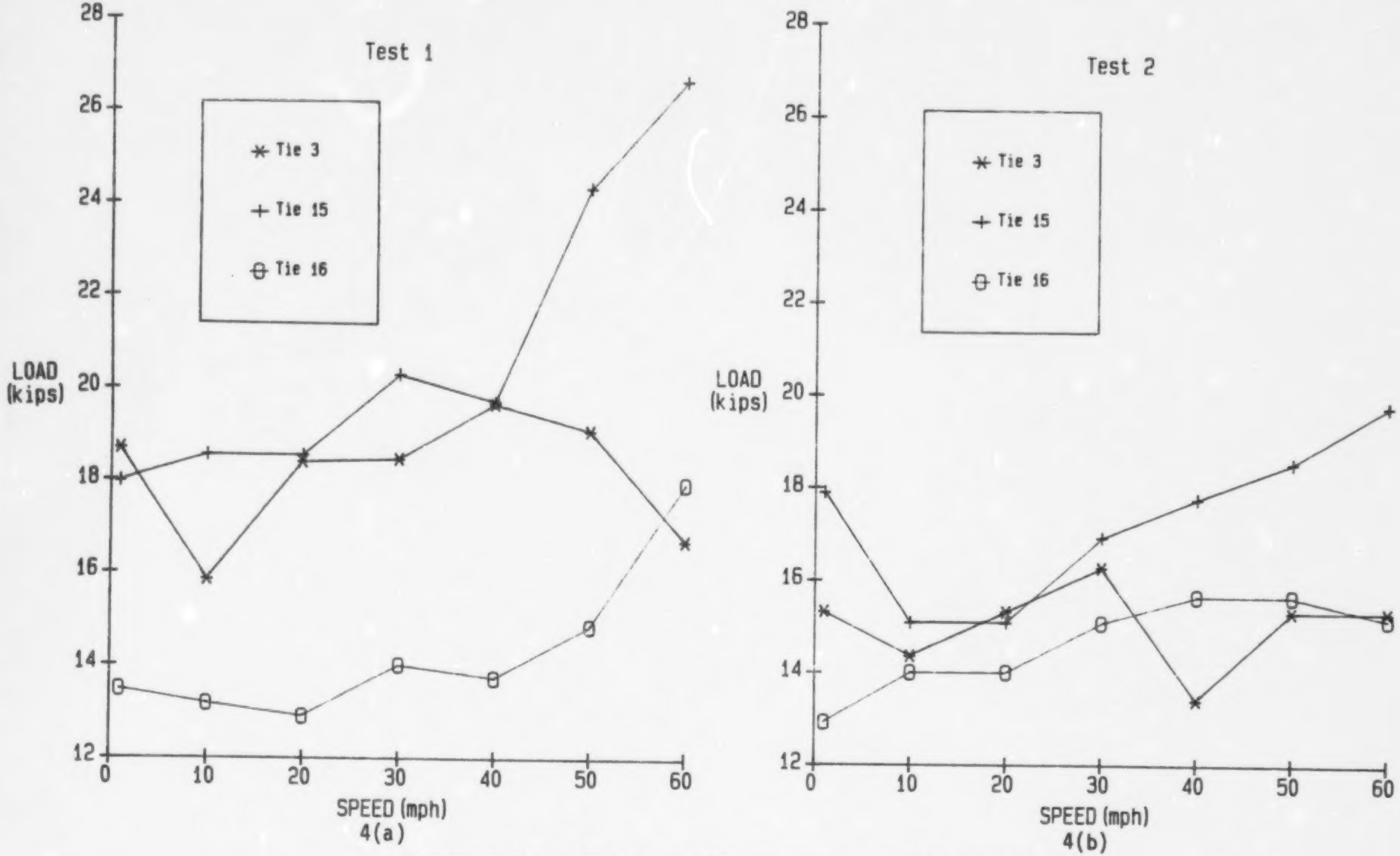

4(a)

4(b)

FIGURE 4 (a) LOAD VS. SPEED FOR TEST 1 - BEFORE SHIMMING
(b) LOAD VS. SPEED FOR TEST 2 - AFTER SHIMMING

involve seating the concrete ties on the girder, then measuring the height of the centres of the rail seat elevations with a surveyor's level, installing appropriate thicknesses of metal shims where needed to bring all rail seat elevations to the same level and then installing rail/tie pads and rails. It is anticipated that this procedure would result in a further improvement in load distribution.

As a result of work done by Queen's and McGill University, it is known that the variation of load with tie spacing can be approximated by an equation of the form

$$P = A + BS$$

where for 115 RE rail and tie girder pad stiffness of 288 K/in., $A = 9$ and $B = 1.27$. In this equation, S is the tie spacing in inches and P is the percentage of wheel load on the bridge tie. Solving for P using $S = 14.5$ in. (as is the case in the central portion of Bridge 24.0) and using an axle load of 67 Kips (as was the case in our tests) the load carried by a tie should be in the order of 18.4 Kips assuming no impact.

All the measured loads in Test 2 are less for all ties except for tie number one up to a speed of 50 mph - even with the lack of fit problem. Therefore each tie is taking less load than predicted.

If the ties were to be spaced at 18 in. centres, an axle load of 85 Kips (standard CP Rail design value for bridge spans under 45 feet) would, by the above equation, cause the load carried by a tie to reach 27.1 Kips. Even considering 150% impact (as used in the original design), the maximum load would be 67.8 Kips. As the present tie design load is 69 Kips it should be safe to respace interior ties to 18 in. centres. Once the system is tested under regular traffic, the assumption of 150% impact can be verified. Testing so far indicates this value is conservative.

5.0 CONCLUSIONS AND RECOMMENDATIONS

As a result of tests conducted on Bridge 24.0 the following conclusions can be drawn about concrete ties.

1. The entry tie (tie Number 1) experienced an axle load of 24.76 Kips at 60 mph. This result was the same even when tie Number 2 was floating, i.e., not taking any load. However, in Test 1, tie Number 15 (adjacent to a 'free floating' tie) experienced an axle load of 26.69 Kips at 60 mph - a 25% increase from the load at 40 mph.

2. The maximum load taken by the end tie and central ties appears to be independent of the direction of train travel.

3. The variation in the load carried by an individual tie with increasing speed is very dependent on the degree of lack of fit. Where uniformity in rail seat elevations exist, the load would appear to be independent of train speed.

4. The top fibres of the concrete tie have a design prestress of 75 psi compressive. Reverse bending when a wheelset leaves a tie causes a reduction in this pre-compression of maximum value 30 psi. Therefore, the net top fibre stress with reverse bending is 45 psi compression. The cracking stress for 6000 psi concrete is 581 psi tension, and hence reverse bending does not appear to be a problem.

5. The load taken by central ties can be affected by whether an adjacent tie is 'floating' or solidly seated. Lack of fit in an actual installation of concrete ties is a major consideration.

The following course of action is now recommended.

1. Strain gauges should be applied to several ties, and measurements obtained during the passage of regular traffic. A statistical distribution of in-service loading will be obtained.

2. The influence of tie spacing should be further investigated. Either on this bridge, or another where wood ties are to be replaced with concrete ties, the spacing should be increased and the rail seat elevations accurately set. Testing similar to that described in this report would then be conducted.

REFERENCES

1. G. Rosval, "Strain and Displacement Measurements on Bridge 0.7 Q.C.R. Connection", Research Department, Report No. S724-82, April, 1982.

2. "Precast Prestressed Concrete Railway Bridge Ties", Queen's University, Project P-8202, February, 1984.

3. M.S. Mirza et al, "Experimental-Analytical Study of Load Distribution Characteristics of an Open Deck Bridge System With Precast Prestressed Ties", McGill University, Project P-8203, February, 1984.

4. C. Wang and C. Salmon, "Reinforced Concrete Design," International Textbook Company, New York, 1973.

APPENDIX I: TIE PAD OBSERVATIONS

Refer to Figure 1 of this report for Tie No. location.

Tie No.	South Girder	North Girder
1	seated solidly	intermittent gaps between steel shims and girder
2	about 1/16" wide gap between neoprene pad and steel shim	about 1/16" gap between neoprene pad and steel shim
3	gaps between steel shims and girder at edges	gaps between steel shims and girder at edges - also gap at west end between neoprene and steel shim
4	intermittent gaps between steel shims and girder	gap between steel shims and girder at west end
5	1 1/2" long gap between steel shims and girder	seated solidly
6	seated solidly	seated solidly
7	gap between steel shims and girder	gap between steel shims and girder
8	seated solidly	seated solidly
9	seated solidly	seated solidly
10	seated solidly	3/4's of neoprene pad is off steel shim - only east end touching
11	seated solidly	gap at east edge of tie between steel shim and girder

Tie No.	South Girder	North Girder
12	seated solidly	intermittent gaps between steel shim and girder
13	intermittent gaps between steel shim and girder	intermittent gaps between steel shim and girder
14	gap at west edge between steel shim and girder	1/16" wide gap between neoprene pad and steel shim
15	seated solidly	seated solidly
16	seated solidly	at west end small gap between steel shim and girder
17	gap at west edge between	intermittent gaps between steel shim and girder end of tie very badly spalled - 7 prestressing wires exposed
18	gaps at east edge between steel shims and girder	gaps between steel shim and and girder
19	seated solidly	seated solidly
20	gap between steel shim and girder at central portion	seated solidly
21	seated solidly	neoprene pad off steel shim - less than 1/16" wide gap
22	seated solidly	seated solidly
23	intermittent gaps between steel shim and girder	seated solidly
24	gaps between steel shim and girder at several spots	2" long gap between steel shim and girder
25	intermittent gaps between steel shim and girder	intermittent gaps between steel shim and girder
26	west end of tie - gap between steel shim and girder	east end of tie - gap between steel shim and girder
27	seated solidly	a few intermittent gaps between steel shim and girder

Tie No.	South Girder	North Girder
28	seated solidly	east end of tie - gap between steel shim and girder
29	seated solidly	seated solidly

APPENDIX II: CALCULATION OF LOAD CARRIED BY TIE FROM MEASURED STRAINS

The modulus of elasticity of concrete may be approximated by (Reference 4).

$$E = 33w^{1.5} f_c^{0.5}$$

where, w = weight of concrete per cubic foot

f_c = compressive strength of concrete

The load P carried by a tie is given by

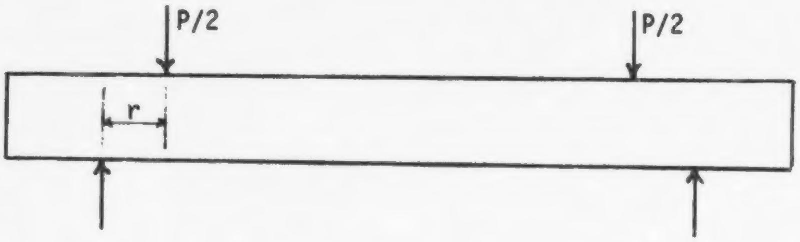

$$P = 2M/r$$

where 'M' is the moment and 'r' is the moment arm. The value of M is given by the expression

$$M = \sigma Z$$

where, σ = stress = εE

Z = section modulus

Substituting, the following expression is obtained.

$$P = \frac{2\varepsilon E Z}{r}$$

For the purposes of this test, the following values were used.

$E = 4.463 \times 10^6$ psi

$r = 12$ in.

$Z_t = 410$ in.^{3}

$Z_B = 449$ in.^{3}

The section moduli were calculated using the equivalent area method to take account of the presence of prestressing wire. By substituting 'ε', the measured strain in the above expressions, the load P carried by the tie is known.

WHEEL SHELLING -- METALLURGICAL ANALYSIS

K. Griffin
Planning and Research Department
Canadian Pacific Limited
Montreal

SUMMARY

In November 1983, seven wheelsets were selected from the CP Yard in Revelstoke, B.C. One of these wheelsets was new, three were condemned for excessive wear and the remaining three were condemned for shelling. A comparative metallurgical examination was performed on these wheels to determine, and identify, the most likely manufacturing and/or operational factors responsible for shelling, as experienced in 100-ton unit-coal-train service on the Pacific Region of CP Rail. The analysis was done in three parts:

i) residual stress analysis,
ii) macroscopic examination, and
iii) microscopic examination

There is no obvious critical residual stress distribution uniquely associated with wheel shelling. A comparison of shelled and non-shelled wheels indicates a general trend of increasing compressive residual stress values with increasing mileage. Shelling is not due to manufacturing/operational factors that alter residual stresses over the entire wheel circumference.

Macroscopic material defects arising during wheel manufacture were not observed and, therefore, cannot be related to shelling. The active failure mechanism in the shelled test wheels is fatigue, with localized fractures originating on the tread surface.

Shelled and non-shelled wheels are uniformly dirty, consistently exhibiting an ASTM microcleanliness rating for light globular oxide-type inclusions of 3-4 and a heavy rating of 1-2. These well-dispersed inclusions arise during manufacture and facilitate shelling, but do not account for the preferential shelling of some wheels. Shelling cracks noted during the microcleanliness evaluations typically contain high-temperature oxides -- indicative of local temperatures having reached in excess of 1000°F.

The test wheels exhibit consistent hardness values/gradients which reflect the mechanical/thermal loading characteristic of the Pacific Region, except in specific areas of shelling. In-and-around shells, surface hardnesses are very high ($\sim$60 R_c) -- evidence of severe thermal or mechanical loading in these areas. The treads of wheels from non-shelled wheelsets exhibit pearlitic microstructures while those of shelled wheelsets are characterized by martensitic surface structures. Further, these martensitic structures are uniformly tempered about the wheel circumference, except in those highly localized regions of shelling. Both the hardness and microstructural data indicate that severe, local, thermal loads are associated with shelling.

Because of the evidence of highly specific thermal loading, shelling appears to be fundamentally associated with sliding wheels. It is recommended that short-term test work be devised to specifically investigate the role, and causes, of severe thermal loading (sliding wheels) on wheel shelling.

SOMMAIRE

Sept essieux ont été choisis du triage CP à Revelstoke en novembre 1983. Un essieu était neuf, trois étaient condamnés dû à l'usure excessive et les trois autres dû à l'écaillage. Une éxamination comparative métallurgique a été effectuée sur les roues pour déterminer et identifier les causes prédominantes de l'écaillage tel que remarqué dans le service des trains-blocs charbonniers de 100 tonnes dans le réseau Pacifique du CP Rail. L'analyse a été faite en trois parties:

i) analyses des contraintes résiduelles
ii) examen macroscopique, et
iii) examen microscopique

Il n 'y a aucune distribution critique de contraintes résiduelles reliée uniquement à l'écaillage de roues. La comparaison de roues écaillées et non-écaillées indique une tendance à une augmentation de contraintes résiduelles compressives avec le millage. L'écaillage n'est pas dû aux variables de fabrication ni d'exploitation qui modifient les contraintes résiduelles sur toute la circonférence de la roue.

Des défauts macroscopiques de matériaux dûs à la fabrication n'ont pas été observés et donc ne peuvent être reliés à l'écaillage. L'écaillage des roues d'essai est attribuable à la fatigue mécanique caracterisée par des fractures locales à la surface de roulement de la roue.

Les roues écaillées et non-écaillées sont uniformément impures. Elles possédent aussi un classement consistant sur l'échelle ASTM de propreté microscopique pour inclusions globulaires de type oxyde, de 3 à 4 et de 1 à 2 pour les inclusions légères et lourdes, respectivement. Ces inclusions proviennent de la manufacture et facilitent l'écaillage (cependant, ceci n'explique pas l'écaillage préférentiel de quelques roues). Des fissures d'écaillage (remarquées dans l'évaluation de

propreté microscopique) contiennent des oxydes à haute-température indiquant que les températures ambiantes ont depassé 1000^{o} F.

Excepté dans des regions specifiques d'écaillage, les roues d'essai exhibent des valeurs/gradients consistants de dureté qui reflètent les caractéristiques de chargement mécanique ou thermique, représentatifs de la region du Pacifique. A l'intérieur et autour des écailles la dureté de la surface est très elevée (~60 Rc), ce qui indique la présence de charges thermiques ou mécaniques sévères. Les surfaces de roulement des essieux non-écaillés et écaillés ont des structures microscopiques perlitiques et martensitiques, respectivement. De plus, les structures martensitiques sont trempées de façon uniforme sur toute la circonférence de la roue, excluant les régions d'écaillage. Les données de dureté et de structure microscopique indiquent que les charges qui sont thermiques, locales, et sévères sont reliées à l'écaillage.

Dû à la présence de charges thermiques spécifiques élevées on estime que l'écaillage est associé au glissement de roues. On suggère q'un travail d'essai à court terme soit réalisé afin d'étudier le rôle et les causes de charges thermiques sévères (glissement de roues) sur l'écaillage de roues.

ACKNOWLEDGEMENTS

The Department of Planning and Research acknowledges the personnel of Angus Shops, in particular Mr. A.G.K. Wylie and Mr. G. Doyle of the Tests Department, for their support throughout the course of this test program.

TABLE OF CONTENTS

	PAGE
SUMMARY	351
ACKNOWLEDGEMENTS	355
LIST OF TABLES	357
LIST OF FIGURES	358
1.0 INTRODUCTION	361
2.0 TEST GROUP	363
3.0 TEST PROCEDURE	365
3.1 Residual Stress Analysis	366
3.2 Macroscopic Examination	367
3.3 Microscopic Examination	369
3.3.1 Microcleanliness Evaluations	369
3.3.2 Hardness Gradients	370
3.3.3 Microstructural Examination	370
4.0 RESULTS AND CONCLUSIONS	371
4.1 Residual Stress Analysis	371
4.2 Macroscopic Examination	373
4.3 Microscopic Examination	374
4.3.1 Microcleanliness Testing Results	374
4.3.2 Hardness Testing Results	376
4.3.3 Microstructural Examination Results	379
5.0 RECOMMENDATIONS	392
REFERENCES	393
APPENDIX A PRINCIPLE OF THE BLIND-HOLE-DRILLING METHOD	394
APPENDIX B CALIBRATION PROCEDURE EMPLOYED FOR RESIDUAL STRESS MEASUREMENT TESTWORK	397
APPENDIX C DETERMINING INCLUSION CONTENT OF STEEL	399
APPENDIX D TEST WHEELSETS COMPARISON -- WEAR	400
APPENDIX E PHOTOMICROGRAPHS OF REPRESENTATIVE NON-METALLICS PRESENT IN STUDIED WHEEL STEELS	402
APPENDIX F COMPOSITE HARDNESS GRADIENT PLOTS	404

LIST OF TABLES

TABLE NO.	DESCRIPTION	PAGE
1	Test Wheelsets Used for Wheel Shelling Investigation	364
2	Residual Stress Measurement Testwork Summary	371
3	Average Residual Stress Values	372
B1	Measured Strains from Residual Stress Calibration Procedure	398

LIST OF FIGURES

FIGURE NO.	DESCRIPTION	PAGE
1	Top View of Wheel Tread Exhibiting Shell Defect	361
2	Top View of Wheel Tread with Strain Gauge Rosette Arrangement for Determining Residual Stresses	366
3	Depiction of Acetylene Torch Cutting Borders Employed with Each Test Wheel to Maintain Integrity of Wheel Steel	368
4	Typical Fracture Surface in Shelling Failure, Exhibiting Progression Rings Characteristic of Fatigue	374
5	Typical Shelling Crack with High-Temperature Oxide Formation	376
6	Composite Hardness Gradients Characteristic of Microscopic Wheel Steel Sample Sets	376
7	Running Surface of New Wheel -- Tempered Martensite Structure (100X)	380
8	Running Surface of New Wheel -- Tempered Martensite Structure (1000X)	380
9	Fine Pearlitic Structure Approx. 1/8" Below Running Surface of New Wheel (100X)	381
10	Fine Pearlitic Structure Approx. 1/8" Below Running Surface of New Wheel (1000X)	381
11	Pearlitic Structure Immediately Below Deformed Surface Layer of Non-Shelled Wheel (Designation 7A) Taken From Wheelset Condemned for Excessive Wear (100X)	382
12	Pearlitic Structure Immediately Below Deformed Surface Layer of Non-Shelled Wheel (Designation 7A) Taken From Wheelset Condemned for Excessive Wear (1000X)	383
13	Fine Pearlitic Structure Approx. 1/8" Below Running Surface of Non-Shelled Wheel (Designation 7A) Taken From Wheelset Condemned for Excessive Wear (100X)	383
14	Fine Pearlitic Structure Approx. 1/8" Below Running Surface of Non-Shelled Wheel (Designation 7A) Taken From Wheelset Condemned for Excessive Wear (1000X)	384

LIST OF FIGURES (Cont'd.)

FIGURE NO.	DESCRIPTION	PAGE
15	Tempered Martensite Structure Immediately Below Deformed Surface Layer of Non-Shelled Wheel (Designation 2A) Taken From Shelled Wheelset (100X)	385
16	Tempered Martensite Structure Immediately Below Deformed Surface Layer of Non-Shelled Wheel (Designation 2A) Taken From Shelled Wheelset (1000X)	385
17	Slack-Quenched Structure Approx. 1/8" Below Running Surface of Non-Shelled Wheel (Designation 2A) Taken From Shelled Wheelset (100X)	386
18	Slack-Quenched Structure Approx. 1/8" Below Running Surface of Non-Shelled Wheel (Designation 2A) Taken from Shelled Wheelset (1000X)	336
19	Untempered Martensite Structure Immediately Below Deformed Surface Layer in Shelled Region on Shelled Wheel (Designation 2B) -- 100X	387
20	Untempered Martensite Structure Immediately Below Deformed Surface Layer in Shelled Region on Shelled Wheel (Designation 2B) -- 1000X	388
21	Slack-Quenched Structure Approx. 1/8" Below Running Surface of Shelled Region on Shelled Wheel (Designation 2B) -- 100X	388
22	Slack-Quenched Structure Approx. 1/8" Below Running Surface of Shelled Region on Shelled Wheel (Designation 2B) -- 1000X	389
A1	Strain Relaxation at Point P After Introduction of Hole	394
A2	Strain Gauge Rosette Arrangement for Determining Residual Stresses	395
B1	RS-200 Milling Guide, as Set-Up for Residual Stress Measurement Calibration Procedure	397
C1	The Jernkontoret Inclusion Chart for the Estimation of Slag Inclusions in Steel	399
D1	Variation in Flange Wear Versus Tread Wear (Each Expressed as Percentage of its Respective Condemning Limit) for Wheels Studied in Wheel Shelling Test Program	401

LIST OF FIGURES (Cont'd.)

FIGURE NO.	DESCRIPTION	PAGE
E1	Cluster of Small, Irregular-Shaped, Silicate Inclusions Surrounded by Small Globular Oxide-Type Inclusions	402
E2	Aluminia-Type Inclusion	402
E3	Sulphide/Silicate-Type Inclusions	403
F1	Composite Hardness Gradient for New Wheel (Designation 1A)	405
F2	Composite Hardness Gradients Exhibited at Various Areas on Both Wheels Comprising Wheelset #2	406
F3	Composite Hardness Gradients Exhibited at Various Areas on Both Wheels Comprising Wheelset #3	408
F4	Composite Hardness Gradients Exhibited at Various Areas on Both Wheels Comprising Wheelset #4	410
F5	Composite Hardness Gradient For Severely Worn, Non-Shelled, Wheel (Designation 5A)	412
F6	Composite Hardness Gradient For Severely Worn, Non-Shelled, Wheel (Designation 6A)	413
F7	Composite Hardness Gradient For Severely Worn, Non-Shelled, Wheel (Designation 7A)	414

1.0 INTRODUCTION

A railway wheel performs the dual function of serving as both a brake drum and a load bearing member responsible for maintaining rolling contact with the rail. It is subjected to both wheel/rail contact stresses and thermal stresses due to such factors as braking and sliding. It is generally recognized that these stresses can cause tread defects, such as the wheel shell depicted in Figure 1 below, to arise in service.

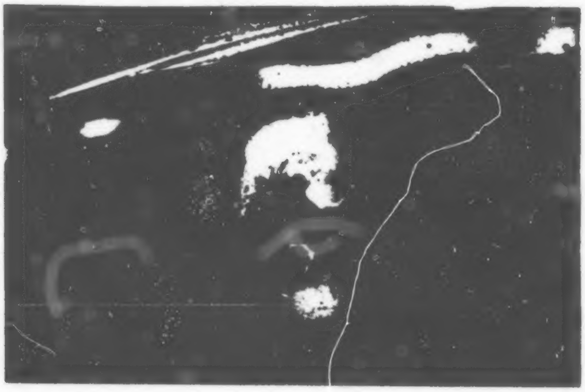

Figure 1: Top View of Wheel Tread Exhibiting Shell Defect

In practice, it is common to call any non-wear type of deterioration of the tread surface as shelling. More correctly, shelling is a fatigue failure of the tread due to repeated mechanical overstressing by heavy wheel loads. Examination of tread damaged wheels from 100-ton unit-train service usually shows the damage is thermally related; either in-whole or in-part (Reference 1).

The incidence of wheel removal due to shelling (general surface defects) is apparently higher on CP Rail than other similar operations. At the request of the Mechanical Department of CP Rail, CP Research formulated a test plan to investigate wheel shelling. The program is specifically aimed at 100-ton unit-coal-train service on the Pacific Region of CP Rail. The test program consists of two phases, the objectives of which are:

A. To determine the most likely operating conditions and/or manufacturing factors responsible for shelling from a metallurgical analysis of new and worn, shelled wheels and non-shelled wheels, with varying mileages traversed. The analysis consists of three parts:

   (i) residual stress analysis,
   (ii) macroscopic examination, and
   (iii) microscopic examination

B. To devise, and carry out, tests to closely examine specific factors brought forth above, and make recommendations to reduce the severity of the wheel shelling problem.

To date phase (A) has been completed and is reported here, and work is to be initiated on phase (B).

The objectives of the residual stress analysis portion of the test program are to determine whether there is a critical residual stress distribution associated with wheel shelling, whether this distribution is consistent and distinguishable between wheels that shell and do not shell, and how this distribution arises.

The objectives of the comparative examination of the macro/microstructures of shelled and non-shelled wheels are to determine whether material features are uniquely associated with shelled and/or non-shelled regions, how these specific material features may arise, and whether they arise in production or in service.

This report documents the results of a partial metallurgical investigation of numerous heavy-duty, heat-treated wheels, some of which contain shelling defects that originate and/or develop in service. The most likely operating and/or metallurgical condition(s) responsible for this shelling, as defined and experienced by CP Rail, is cited. Also included are descriptions of the test wheel group, the methods employed for stress measurement and structural examination, and recommendations for the orientation of future test work.

2.0 TEST GROUP

The test group consists of 10 wheels taken from 7 wheelsets removed from unit-coal-train service:

a) 1 new wheelset,

b) 3 wheelsets exhibiting various states of wear, each consisting of 1 shelled and 1 non-shelled wheel, and

c) 3 wheelsets exhibiting severe wear, each comprised of 2 non-shelled wheels

All wheels are cast, class "C" (CJ-36 design), two-wear wheels produced by the Griffin Wheel Company. Each of the shelled wheels exhibits shells at similar locations on the tread, as measured in the axial direction from the front rim face, and at various points about the wheel circumference. Table 1 contains a specific description of each wheel examined in the present investigation.

Table 1

Test Wheelsets Used For Wheel Shelling Investigation

Wheelset No.	Wheel Designation	Condition of Wheel			Flange Wear (% C.L.)**	Tread Wear (% C.L.)**	Comments On Tread Surface
		New	Worn	Shelled			
1	1A	X			0	0	-thin surface oxide layer
	1B*	X			-	-	
2	2A		X		34	21	-no apparent crack network or grooving
	2B		X	X	38	16	-slight grooving, crack network in both shelled & non-shelled regions
3	3A		X		29	36	-no apparent crack network or grooving
	3B		X	X	30	40	-crack network only in shelled region
4	4A		X		38	24	-no apparent crack network or grooving
	4B		X	X	24	16	-slight grooving, visible crack network in both shelled and non-shelled regions
5	5A		X		97	28	-slight grooving
	5B*		X		-	-	
6	6A		X		83	100	-slight grooving, unusually high amount of tread wear
	6B*		X		-	-	
7	7A		X		84	32	-slight grooving
	7B*		X		-	-	

* - Wheel sample is redundant and was not tested

** - (C.L.) - Condemning Limit

3.0 TEST PROCEDURE

In November 1983, six wheelsets were selected from a group of condemned wheelsets stored in the CP Yard in Revelstoke, B.C. Three of these wheelsets were identified as having been removed from service for excessive wear (thin flange), the other three for shelling. Together with a new wheelset taken from the same Yard, these seven wheelsets comprise the test group for the Wheel Shelling Study (see Table 1). These test wheelsets were sent to Angus Shops in Montreal, Quebec where all the wheels were stored prior to testing.

At this point it is important to recognize the difference between shelling as absolutely defined in the technical literature and as employed by field personnel. Strictly speaking, pure shelling is a mechanical fatigue failure of the tread surface which does not involve severe thermal effects from braking and/or sliding. In practice, it is very difficult to distinguish true shelling from other tread defects, such as spalling, with only a cursory visual examination. The test wheelsets are a representative grouping of wheelsets removed from service because of excessive wear and/or shelling, as designated by CP Rail field personnel.

For the new wheelset (#1) and the three wheelsets condemned for excessive wear (#'s 5, 6 and 7), testwork was performed on only one of the wheels comprising each wheelset (5A, 6A and 7A). The mates of these wheels (5B, 6B and 7B) were considered redundant, and were not examined to minimize time required for sample preparation and testwork. For the three test wheelsets removed for shelling (#'s 2, 3 and 4), both wheels in each wheelset were examined. Three different categories of wheels were thereby distinguished, and examined, in these tests:

(i) - those that shelled (2B, 3B and 4B)

(ii) - those that did not shell, but were mated to a shelled wheel (2A, 3A and 4A), and

(iii) - those that belonged to a wheelset that did not shell (1A, 5A, 6A and 7A)

An initial visual examination was performed on each wheel of interest to locate and identify obvious areas of shelling and other tread defects. The actual testwork was done in three parts:

1. Residual Stress Analysis
2. Macroscopic Examination
3. Microscopic Examination

3.1 Residual Stress Analysis

The Blind-Hole-Drilling method (ASTM Designation E837-81) was employed in the determination of all residual stresses. For each measurement performed, a strain rosette was installed on the wheel tread, as shown in Figure 2 below, in that location (ie. distance from front rim face) previously identified as having most consistently experienced shelling.

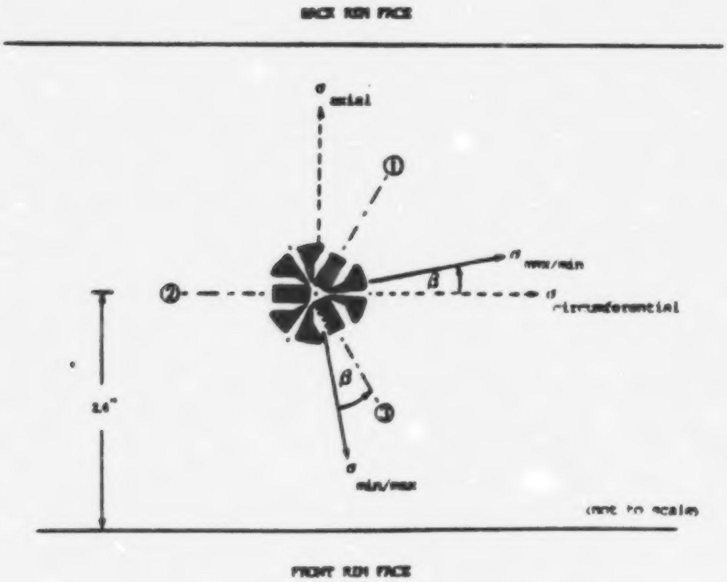
BACK RIM FACE
σ_{axial}
①
②
③
$\sigma_{max/min}$
β
$\sigma_{circumferential}$
β
2.4"
$\sigma_{min/max}$
(not to scale)
FRONT RIM FACE

Figure 2: Top View of Wheel Tread With Strain Gauge Rosette Arrangement for Determining Residual Stresses

For each of the three shelled wheels in the test group, a single residual stress measurement was taken from a non-shelled region on the tread (for a total of three measurements). Single residual stress measurements were taken on those non-shelled wheels which were either mated to a shelled wheel (three) or that belonged to a wheelset that did not shell (four). A total of ten residual stress measurements were thus performed on the test group.

Using the RS-200 milling guide (see Reference 2), a very accurate hole was drilled through the center of each rosette into the wheel surface. Each hole was 1/8" in diameter and 1/8" deep (consecutive 1/16" depth increments were employed). After drilling, the residual stresses in the immediate vicinity of the hole are relaxed, and the metal strains according to well documented principles (see Appendix A and Reference 2). These changes in strain were measured by the strain rosettes and recorded by a strain indicator. The residual stresses were calculated from this data. It was recognized that the drilling process itself induced stresses into the metal; these stresses were measured in a calibration procedure (see Appendix B) and are accounted for in the final results.

3.2 Macroscopic Examination

Railway wheel shelling is essentially a surface or shallow sub-surface phenomena; therefore, a formal macroscopic examination of material features more than 1/2" below the wheel running surface was not done. The macroscopic examination which was performed was actually an intermediate step which availed itself during dissection of the test wheels prior to the production of the microscopic examination samples (see Section 3.3).

Each wheel of interest first had to be cut into a more manageable size. Using an acetylene torch, two full radial-axial sections were taken from each shelled wheel; one intersecting a region of shelling, the other not. For those test wheels of interest which had not shelled, one full radial-axial section was removed from each. A total of thirteen wheel sections were thus generated; ten of these sections contained that portion of the tread where the residual stress measurements had been performed previously. Being consistent with the testing locations ensures the comparability of the different types of data generated during the test program.

Care was exercised during torch cutting to maintain the structural integrity of the wheel metal in the areas to be further investigated on a microscopic scale. This was accomplished by employing cutting borders, as depicted in Figure 3, about each of the specific areas of interest.

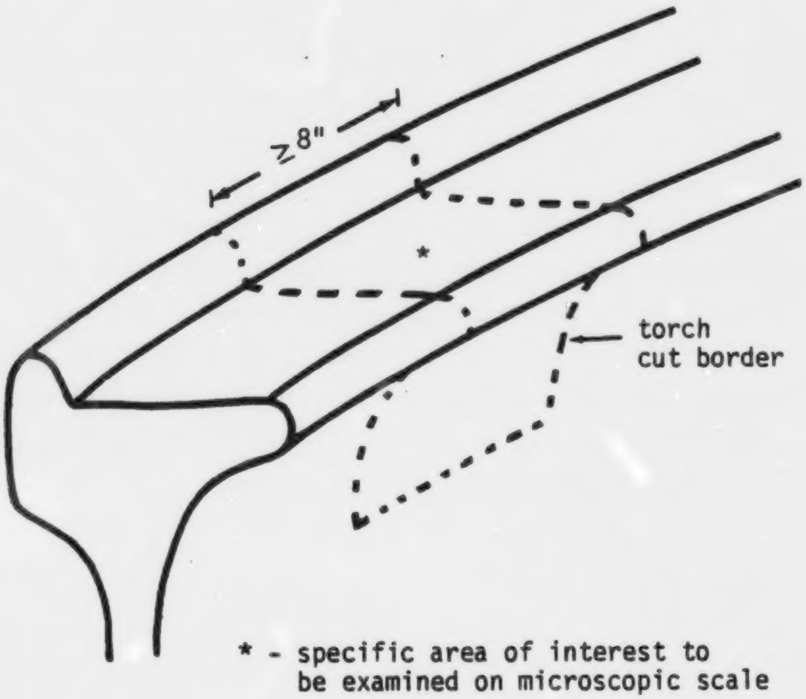
≥8"
*
torch
cut border
* - specific area of interest to
be examined on microscopic scale

Figure 3: Depiction of Acetylene Torch Cutting Borders Employed With Each Test Wheel to Maintain Integrity of Wheel Steel

Each radial-axial surface thus generated was examined for large inclusions, shatter cracks and other macroscopic material defects. As well, several cracks contained within shelled regions were opened to examine their fracture surfaces and determine the active failure mechanism in these shelling failures.

Upon completion of this intermediate step, the thirteen wheel sections were ready for further dissection -- as required for the preparation of microscopic examination samples.

3.3 Microscopic Examination

One set (2 samples) of standard metallographic samples was taken from each of the two sections removed from each shelled wheel -- one set from the shelled section, the other set from the non-shelled section. Another sample set was taken from each wheel section removed from a non-shelled wheel.

One sample from each set was polished using standard metallographic techniques so that its plane of polish was perpendicular to the wheel rolling surface; the plane of polish of the other wheel sample in each set was parallel to the wheel rolling surface. All such samples (a total of 26) were taken from the free tread surface, down to a depth of approximately 1/2" -- and examined for variations and/or gradients in microcleanliness, hardness and microstructure. It was sought to determine whether these differences categorized shelled and non-shelled areas/wheels.

3.3.1 Microcleanliness Evaluations

Microcleanliness ratings were conducted using the ASTM Practice E-45, Method A. For each specimen, worst inclusion fields were isolated and then evaluated for type and number of each type of inclusion (alumina, silicate, sulphide or oxide) within a 2-3/4" square area, for comparison with the ASTM standard inclusion rating chart (see Appendix C and Reference 3). In some cases, the particular inclusion types were very heavy; a distinction was generally made between light and heavy inclusions, again based on the ASTM standard inclusion rating chart.

3.3.2 Hardness Gradients

Each of the sample sets mentioned in Section 3.3 consists of two samples whose planes of polish are parallel and perpendicular to a given wheels running surface, respectively. Composite Rockwell C hardness gradients were established (for a depth of approximately 1/3-1/2" below the wheel running surface) for each sample set by conducting hardness surveys over each surface of interest in each sample set. Hardness measurements were made at intervals of approximately 1/16", allowing for good definition of localized hardness trends.

3.3.3 Microstructural Examination

The wheel sample sets used in Sections 3.3.1 and 3.3.2 were etched in a 3% nital solution. A standard metallographic microscope was used to determine whether the sample sets exhibited variations and/or gradients in microstructure, and whether these differences uniquely categorized shelled and non-shelled areas/wheels.

4.0 RESULTS AND CONCLUSIONS

4.1 Residual Stress Analysis

A total of 10 residual stress measurements were performed on the test wheel group; the results of which are shown below in Tables 2 and 3. Reported stress values are resolved in the axial and circumferential directions (see Figure 2) to facilitate stress comparisons between the various wheels in the test group.

Table 2

Residual Stress Measurement Testwork Summary

Wheel-set No.	Wheel Designation	Cond. of Wheel on Which Measurements Performed			Flange Wear (%CL)*	Tread Wear (%CL)*	Stresses**			
		New	Worn	Shelled			Principal min. (Ksi)	Principal max. (Ksi)	Axial σ_a (Ksi)	Circum. σ_c (Ksi)
1	1A	X			0	0	-35.5	-37.7	-37.7	-35.5
2	2A		X		34	21	-22.2	-39.6	-39.6	-22.2
	2B		X	X	38	16	-15.5	-37.6	-37.1	-16.0
3	3A		X		29	36	-50.5	-61.3	-61.1	-50.7
	3B		X	X	30	40	-54.6	-61.1	-59.9	-55.8
4	4A		X		38	24	-39.6	-50.9	-49.7	-49.8
	4B		X	X	24	16	-37.3	-40.4	-38.1	-39.6
5	5A		X		97	28	-68.5	-87.3	-86.8	-68.9
6	6A		X		83	100	+26.0	-50.9	-35.9	+11.0
7	7A		X		84	32	-48.2	-63.8	-63.8	-48.2

* (C.L.) - Condemning Limit.

**As is the normal convention, positive and negative residual stress values indicate tensile and compressive stresses, respectively.

Referring to Table 2 and Figure 2, the magnitude and orientation of the recorded principal stresses generally coincide with the axial and circumferential stresses; the single exception is wheel 6A.

Table 3

Average Residual Stress Values

Average Stress (Ksi)	New Wheel	Shelled Wheelset		Non-Shelled Wheel, Severely Worn**
		Shelled Wheel	Non-Shelled Wheel	
σ_a	-38	-45	-50	-75
σ_c	-36	-37	-38	-59
σ_{max}	-38	-46	-51	-76
σ_{min}	-36	-36	-37	-58

** - excluding wheelset No. 6

The new wheel exhibits stresses of comparable sign and magnitude to those reported for new wheels in the technical literature (see References 1 and 4) and by the various manufacturers.

One wheel only of each of the wheelsets numbered 2, 3 and 4 (specifically 2B, 3B and 4B) is shelled. The residual stresses in these wheels at locations away from a shell are similar (on average, slightly less compressive) to the residual stresses on the non-shelled wheels from the same wheelsets.

A comparison of all wheels, except those from wheelset No. 6, indicates a general trend of increasing compressive residual stress values with accumulated mileage (as reflected by increasing amounts of wear, see Appendix D), although the data is somewhat scattered and a larger sample size is required to form a definite conclusion. Wheels from wheelset No. 6, which are condemnable for tread wear (a rather uncommon reason for removal on CP Rail's Pacific Region -- usually wheel removal is for shelling or thin flange), have drastically different residual stresses, being in fact tensile in the circumferential direction.

The consistently compressive nature of the residual stresses for both shelled and non-shelled wheels suggests that severe circumferential thermal loading (which can act to lower an existing compressive stress or increase a tensile stress) is not, in itself, solely responsible for the observed shelling. Such thermal loading can account however, for the existing stress state in the tread of wheels from wheelset No. 6.

There is no obvious critical residual stress distribution associated with shelling, nor are there significant differences in the residual stresses values exhibited by non-shelled areas on shelled wheels and non-shelled mates of shelled wheels. This strongly suggests that the observed shelling is not due to any specific manufacturing and/or operational processes that undesirably alter residual stresses over the entire circumference of the wheel.

4.2 Macroscopic Examination

Macroscopic material features arising during wheel manufacture were not observed and, therefore, cannot be related to shelling. Examination of radial-axial wheel segments produced during dissection of the test group wheels failed to reveal a single case of any large inclusions, shatter cracks or any other macro-defects. This further supports the view (see Section 4.1) that specific operational practices/conditions acting in a localized manner on the wheel tread, and not material flaws, are responsible for the majority of incidences of shelling.

Several cracks, found within shelled regions, which did not progress to failure in-service were opened to examine their fracture surfaces to:

(i) identify the active failure mechanism(s) in shelling, and
(ii) determine the consistency of this failure mode.

Many of the crack surfaces are severely oxidized which prevents any failure mechanism determinations. Several surfaces are relatively undamaged; however, and a typical fracture surface is shown in Figure 4.

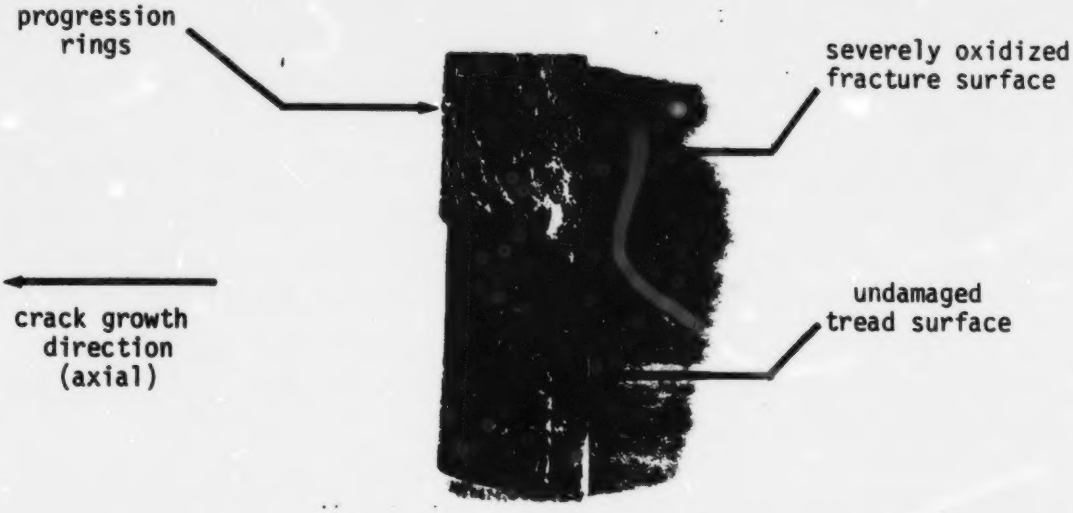
progression rings
severely oxidized fracture surface
crack growth direction (axial)
undamaged tread surface

Figure 4: Typical Fracture Surface in Shelling Failure, Exhibiting Progression Rings Characteristic of Fatigue (X200)

The fracture surface is characterized by the progression rings (ie - ring-shaped markings on the fracture surface which are concentric with the origin of fracture and make possible its determination) typical of fatigue failures. Further, both the orientation of these progression rings and the shape of the fracture surface indicate that the cracks start at finite points on the tread surface, possibly at thermal cracks (ie - cracks resulting from tensile stresses induced by thermal expansion of all or part of the rim). As illustrated in Figure 4, these cracks typically progress in an axial direction. The nature of these shelling regions and cracks is more closely examined in Section 4.3, but the mechanism of fatigue failure appears consistent.

4.3 Microscopic Examination

4.3.1 Microcleanliness Testing Results

Non-metallic inclusions arise in railway wheels during their manufacture and can have a harmful effect on wheel steel fatigue strength. In general, small inclusions which are uniformly dispersed throughout the surface are not markedly detrimental. However, long stringer-type inclusions oriented at right angles to the principal stress direction, or inclusions running into some other stress raiser, can severely reduce the fatigue life of a wheel steel by serving as fatigue crack nuclei (Reference 3).

Corresponding areas on all unetched microscopic samples contain only isolated alumina-, sulphide- and/or silicate-type inclusions. The wheel specimens taken from the test group consistently exhibit an ASTM rating for light globular oxide-type inclusions of 3-4 and a heavy rating of 1-2. No microcleanliness gradients are apparent; the globular oxide-type inclusions are uniformly dispersed through the depths of the samples. Representative micrographs depicting the various types of microstructural inhomogenities found in the examined wheel steels are presented in Appendix E.

The wheel steels are consistently quite dirty metallurgically, but exhibit no gross differences between shelled and non-shelled areas. Further, there is no evidence of shelling cracks being precipitated by these inclusions. There are, however, many instances where the progression of shelling cracks is faciliated by passing through these inclusions. A cleaner wheel steel (eg. vacuum-degassed steel) will very likely exhibit greater fatigue strength and resistance to shelling-type failures, but microcleanliness differences do not exist to account for why certain wheels in the test group shelled while others did not shell.

The above further suggests that shelling generally occurs due to too-severe operational practices/conditions acting locally on the tread. Further to the above, Figure 5 below is a micrograph of a typical shelling crack noted during the microcleanliness evaluation -- note the presence of a high-temperature oxide formation inside the crack cavity. Theoretical analysis and laboratory experiments suggest that such oxide formations occur rapidly at temperatures of 1000°F, and above (see Reference 1). The heat required to locally produce such temperatures can be generated by severe sliding.

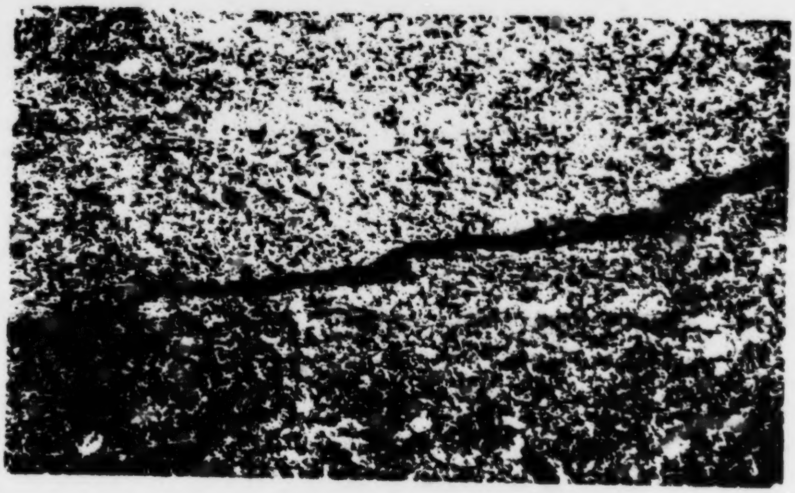

Figure 5: Typical Shelling Crack With High Temperature Oxide Formation (200X)

4.3.2 Hardness Testing Results

Composite hardness versus depth plots for each of the microscopic sample sets examined during the test program are contained in Appendix F. While each sample set exhibits its own unique hardness values and gradients, two general gradient patterns consistently arise and are illustrated in Figure 6 below.

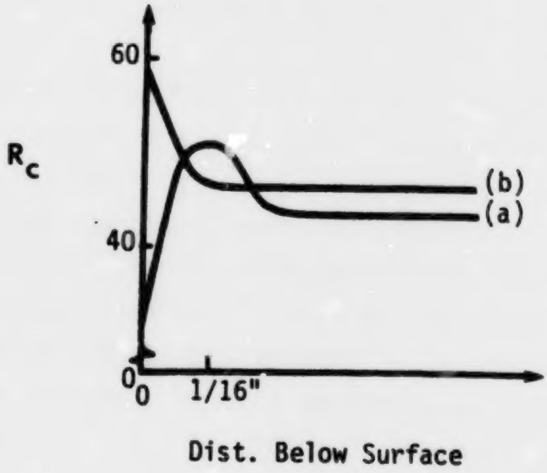

Figure 6: Composite Hardness Gradients Characteristic of Microscopic Wheel Steel Sample Sets

The most striking observations from the hardness testing are:

(1) samples from new wheels exhibit surface hardnesses of approximately 34 R_c, consistent with manufacturers specifications for a class "C" wheel. These samples exhibit the lowest hardness values, irrespective of depth (for approx. 1/2" below the tread surface), of all samples tested. These samples also exhibit a positive hardness gradient just below the surface, as illustrated by (a) in Figure 6.

(2) samples from wheels that did not themselves shell but which were mated to a shelled wheel (specimens 2A, 3A and 4A), as well as samples taken from shelled wheels (specimens 2B, 3B and 4B) but from areas well removed from the shelling, also exhibit positive sub-surface hardness gradients; however, these wheels have consistently 5-10 R_c higher through-depth hardnesses.

(3) samples from, and directly adjacent to, shelled areas on shelled wheels (specimens 2B, 3B and 4B) exhibit hardness gradients similar to (b) in Figure 6. Surface hardnesses here (approximately 60 R_c) are characteristic of untempered martensite, and are 10-20 R_c higher than those for non-shelled areas and/or wheels. For depths greater than approximately 1/16" below the wheel running surface; however, hardness values are only marginally higher than for corresponding non-shelled areas and wheels.

(4) samples from wheels which did not shell, but which were condemned for severe wear (specimens 5A, 6A and 7A) exhibit hardness values and gradients very similar to (2).

Because in-service mechanical/thermal loading can be sufficiently severe to cause mechanical property changes in the metal near the tread surface, an indication of the specific operating conditions different wheels have been subjected to may be made by comparing their mechanical properties to those of new wheels. Surface hardness is, perhaps, the most common and easily measured of these properties.

Railway wheels are subjected to two opposing types of in-service loading. Mechanical loading promotes cold working and an increase in surface, and sub-surface, hardness for that part of the wheel tread in contact with the rail. Repeated thermal loading due to normal low-energy-braking, or sliding, will partially offset the hardening effect of mechanical loading. The effect of both modes of loading on the mechanical properties of the wheel steel is greatest at the tread surface and decreases with depth. (As the severity of each loading mode increases, so too does the surface effect and depth of metal affected. The effects of normal thermal loading on the mechanical properties of railway wheels are commonly detectable to a depth of approximately 1/16" -- see Reference 4). Thermal loading can increase material hardness only through phase changes. Such phase changes require very high energies and energy dissipation rates, and are detectable through metallographic examination (see Section 4.3.3).

Increasing hardness values, and the positive sub-surface hardness gradients generally exhibited by the test wheels, are expected under normal operating conditions. The severe mechanical loading associated with unit-coal-train service significantly increases hardness all about the tread, this effect increasing with increasing mileage/wear; this is observed. The positive sub-surface hardness gradients result from the shallow surface softening associated with normal, low-energy-dissipation, braking practice. Further, the depth of the affected layer here agrees with that reported in the technical literature (see Reference 4).

These observations are noted all about the test wheel circumferences, except in those highly localized regions which shelled. This local difference is due to severe operating conditions acting on local tread regions, and may be related to local shelling susceptibility. It remains to determine whether thermal or mechanical loading is specifically responsible for this local failure; this is determined in Section 4.3.3.

4.3.3 Microstructural Examination Results

Using the approach adopted in the previous section, the microstructures of the different categories of wheels comprising the test group are examined to determine the specific operating conditions responsible for shelling. Four different sets of metallographs are presented to distinguish the different types of wheel samples investigated.

New Wheels

Samples from new wheels exhibit a shallow (approx. 1/16" deep) surface layer of relatively soft, tempered martensite (see Figures 7 and 8) over a fine pearlite base (see Figures 9 and 10). Small amounts of proeutectoid ferrite are visible at the pearlite grain boundaries. It is noted that the wear resistance of tempered martensite, for a given hardness, is significantly less than for a fine pearlite. The existing surface layer of tempered martensite is, therefore, very likely removed early in service.

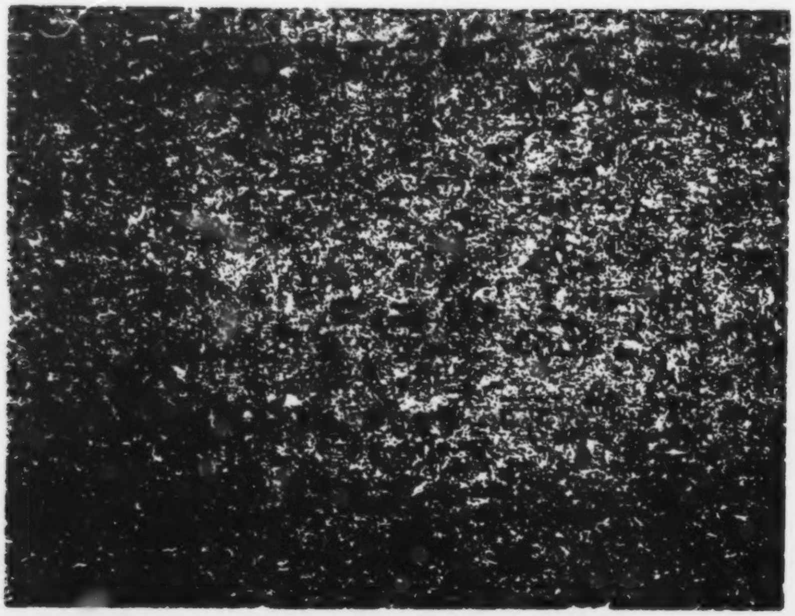

Figure 7: Running Surface of New Wheel--Tempered Martensite Structure (100X)

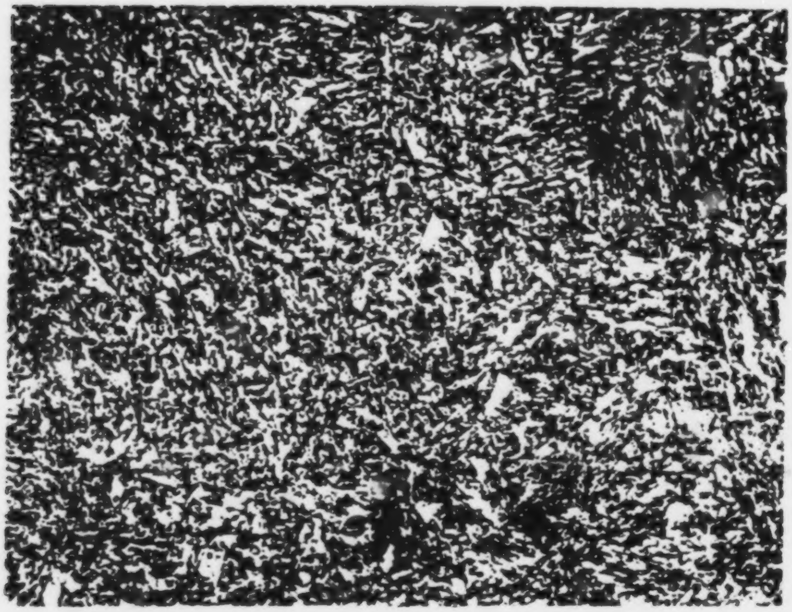

Figure 8: Running Surface of New Wheel--Tempered Martensite Structure (1000X)

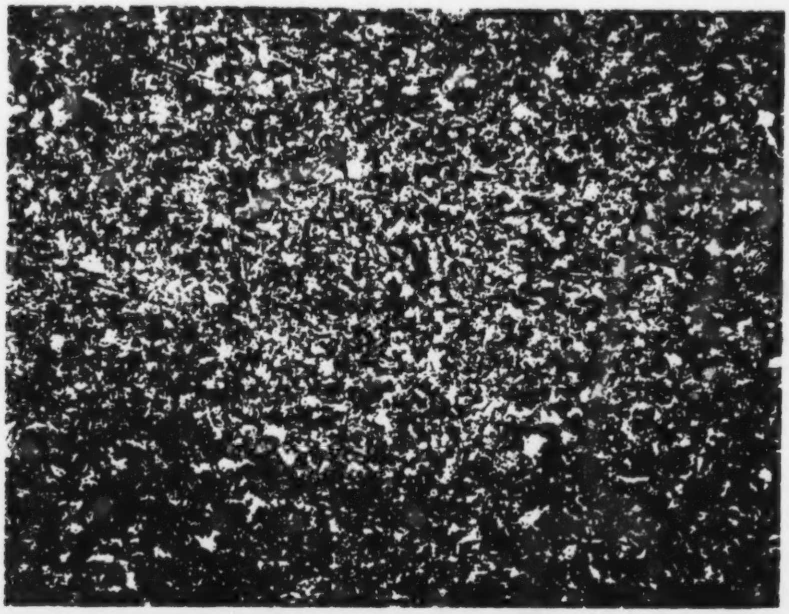

Figure 9: Fine Pearlitic Structure Approx. 1/8" Below Running Surface of New Wheel (100X)

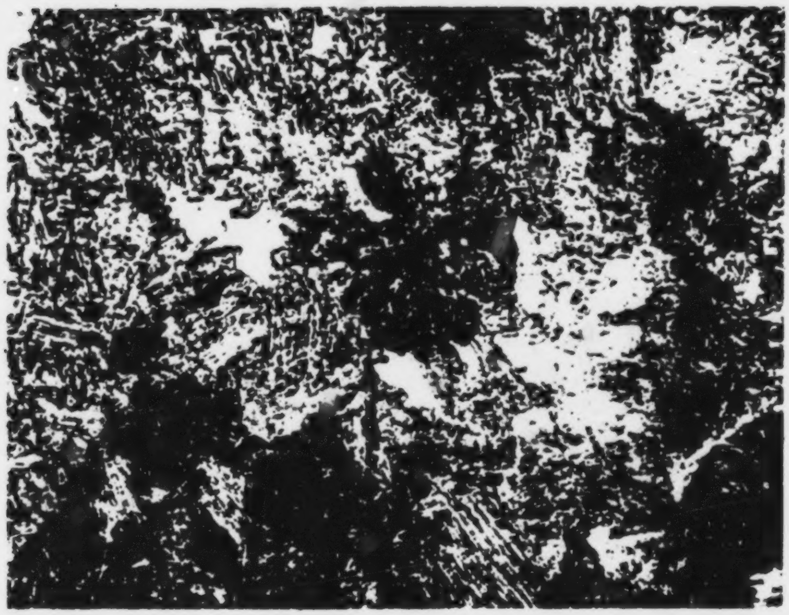

Figure 10: Fine Pearlitic Structure Approx. 1/8" Below Running Surface of New Wheel (1000X)

Worn Wheels, From Non-Shelled Wheelsets

Samples from wheels condemned for excessive wear (thin flange), not shelling, consistently exhibit a severely deformed surface layer approximately 0.02" deep. The deformed layer structure cannot be resolved at 2000X, but is likely deformed cementite lamellae in pearlite (see Reference 5). The remaining structure is essentially pearlitic, with no apparent heat-affected-layer (microstructural gradient). The pearlite grain size is somewhat larger (ASTM grain size No. 7) 1/8" below the wheel running surface than immediately beneath the deformed layer (ASTM grain size No. 8). Figures 11 & 12 and 13 & 14 depict the microstructures of these wheel types immediately below their deformed surface layer approx. 1/8" below the tread, respectively.

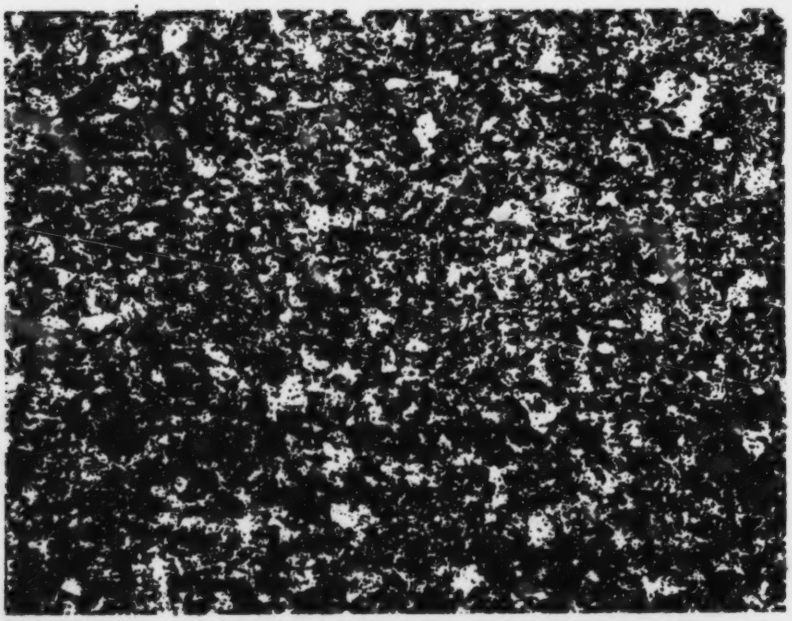

Figure 11: Pearlitic Structure Immediately Below Deformed Surface Layer of Non-Shelled Wheel (Designation 7A) Taken From Wheelset Condemned for Excessive Wear (100X)

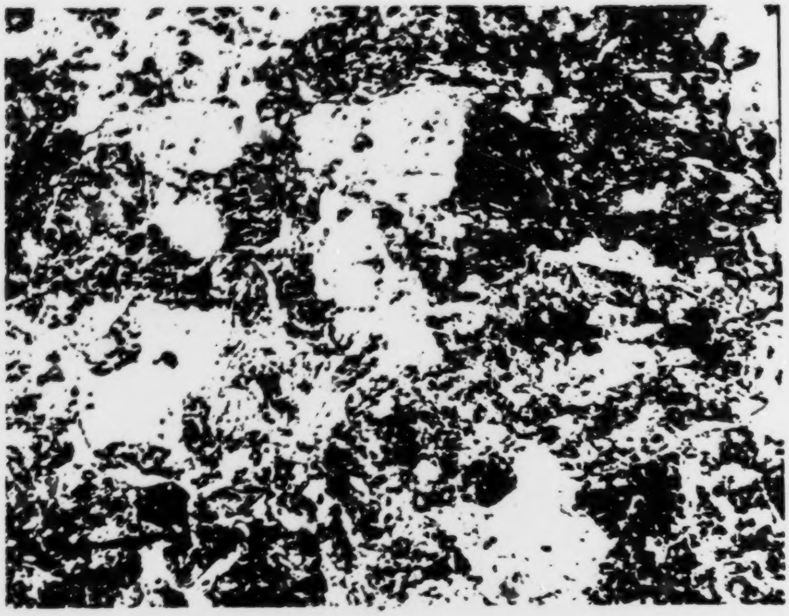

Figure 12: Pearlitic Structure Immediately Below Deformed Surface Layer of Non-Shelled Wheel (Designation 7A) Taken From Wheelset Condemned for Excessive Wear (1000X)

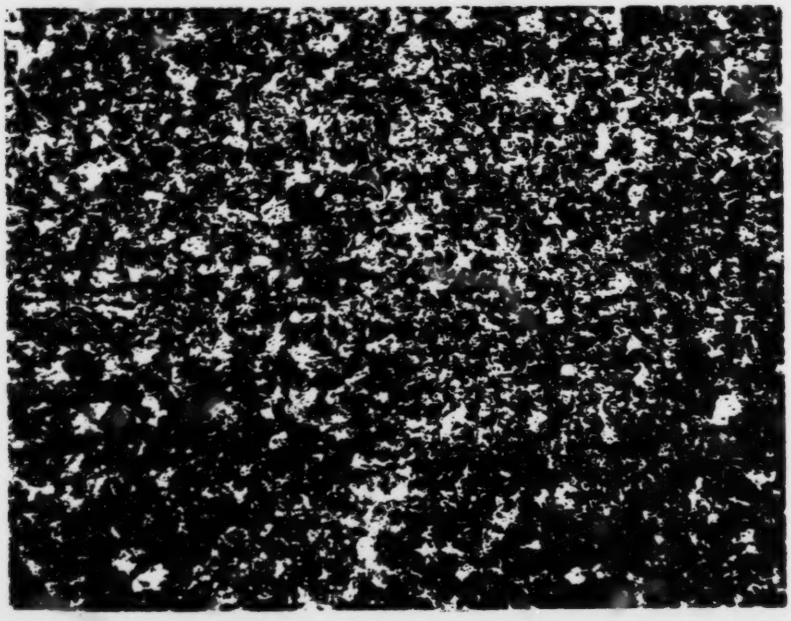

Figure 13: Fine Pearlite Structure Approx. 1/8" Below Running Surface of Non-Shelled Wheel (Designation 7A) taken from Wheelset Condemned for Excessive Wear (100X)

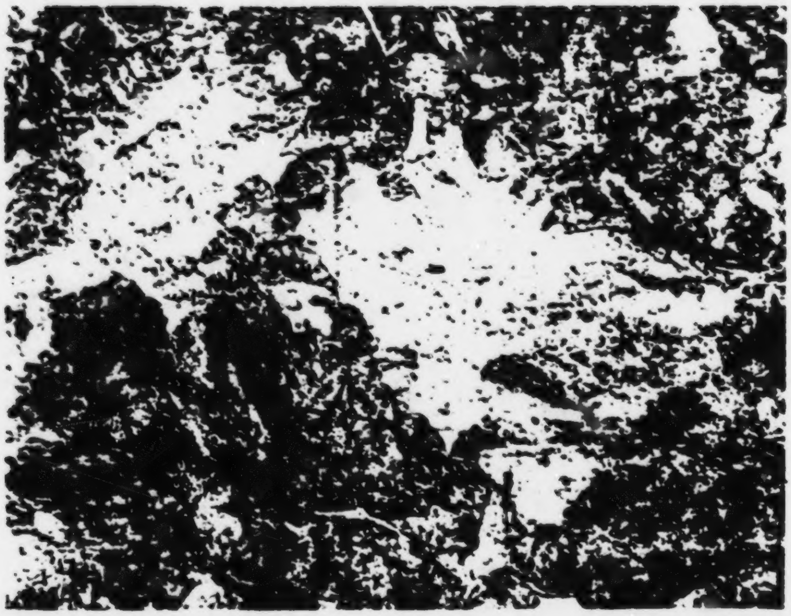

Figure 14: Fine Pearlite Structure Approx. 1/8" Below Running Surface of Non-Shelled Wheel (Designation 7A) Taken from Wheelset Condemned for Excessive Wear (1000X)

Non-Shelled Wheels/Areas, from Shelled Wheelsets

Samples from wheels that did not themselves shell but which were mated to shelled wheels, as well as samples taken from shelled wheels but well away from the region of shelling, exhibit a similar deformed surface layer (approx. 0.02" deep) as described earlier. The structure immediately below the deformed layer is tempered martensite (see Figures 15 and 16), while a slack-quenched structure of tempered martensite and pearlite exists approx. 1/8" below the wheel running surface (see Figures 17 and 18). This heat-affected-layer is found to a depth of approx. 0.2", below which the structure is as-produced pearlitic.

Figure 15: Tempered Martensite Structure Immediately Below Deformed Surface Layer of Non-Shelled Wheel (Designation 2A) Taken From Shelled Wheelset (100X)

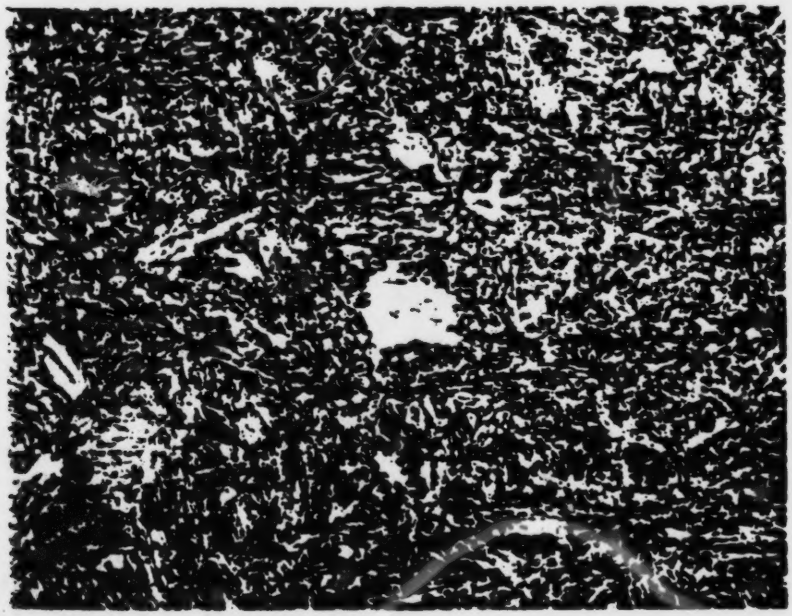

Figure 16: Tempered Martensite Structure Immediately Below Deformed Surface Layer of Non-Shelled Wheel (Designation 2A) Taken From Shelled Wheelset (1000X)

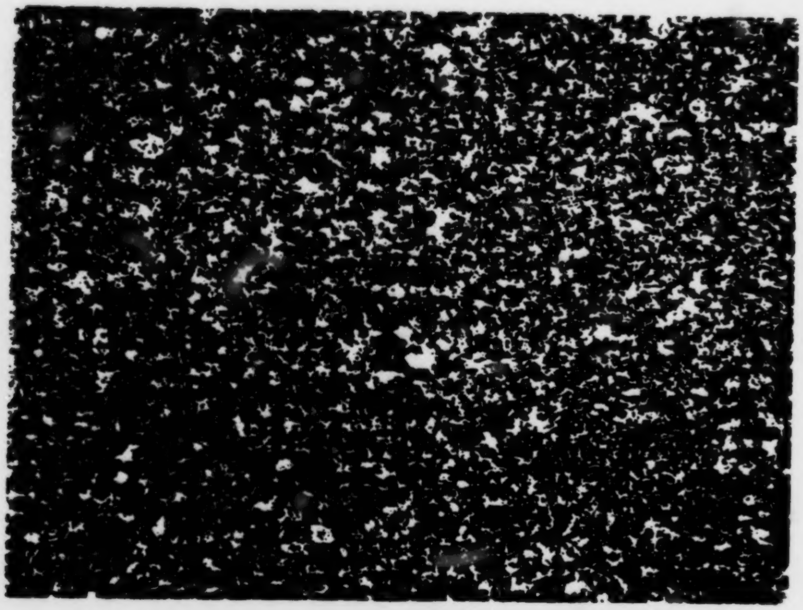

Figure 17: Slack-Quenched Structure Approx. 1/8" Below Running Surface of Non-Shelled Wheel (Designation 2A) Taken From Shelled Wheelset (100X)

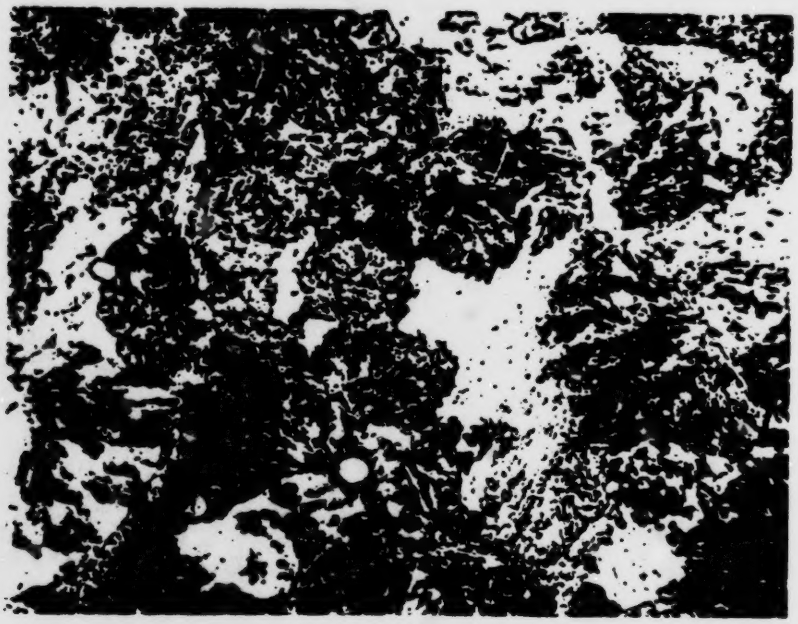

Figure 18: Slack-Quenched Structure Approx. 1/8" Below Running Surface of Non-Shelled Wheel (Designation 2A) Taken From Shelled Wheelset (1000X)

Shelled Areas on Shelled Wheels

Samples from shelled areas on shelled wheels exhibit the approx. 0.02" deep, heavily-deformed, surface layer common to the other sample types. The consistent presence of this deformed layer in all of the test wheels which saw service is evidence that these wheels were subjected to similar mechanical loading, and that the deformation preceded any shelling crack formation. The structure immediately below this deformed layer is untempered martensite (see Figures 19 and 20). This changes to a slack-quenched structure comprised of martensite, tempered martensite, bainite, various incompletely hardened structures and pearlite approx. 1/8" below the tread surface (see Figures 21 and 22). As above, this heat affected layer is found to a depth of approx. 0.2", below which the structure is as-produced pearlitic.

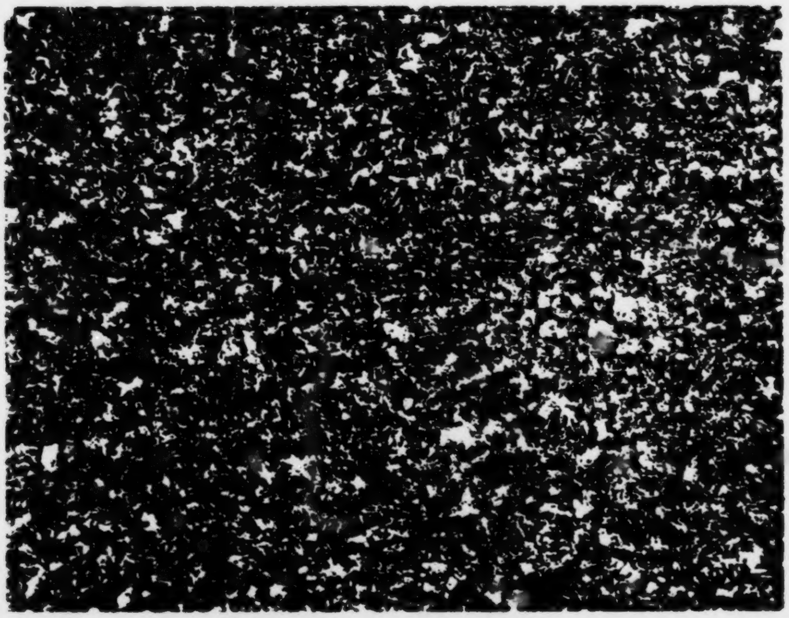

Figure 19: Untempered Martensite Structure Immediately Below Deformed Surface Layer in Shelled Region on Shelled Wheel (Designation 2B) -- 100X

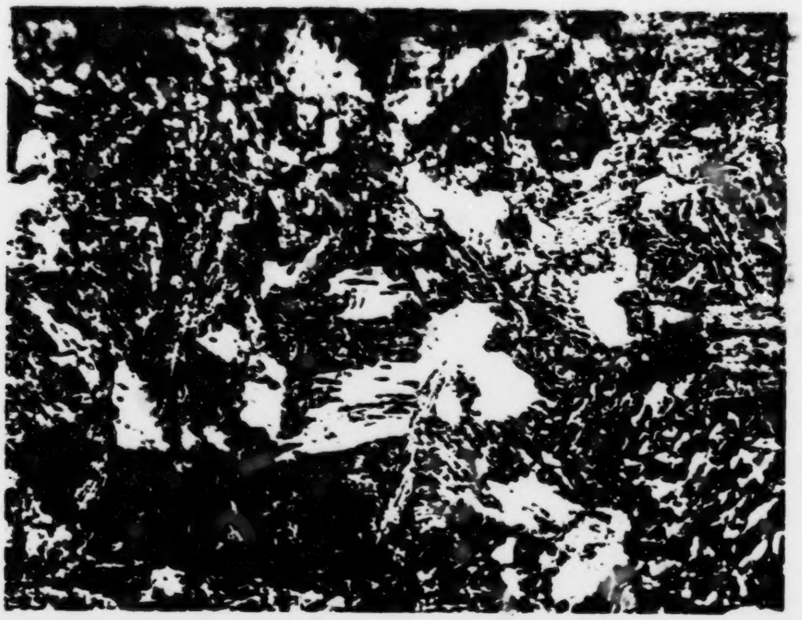

Figure 20: Untempered Martensite Structure Immediately Below Deformed Surface Layer in Shelled Region on Shelled Wheel (Designation 2B) -- 1000X

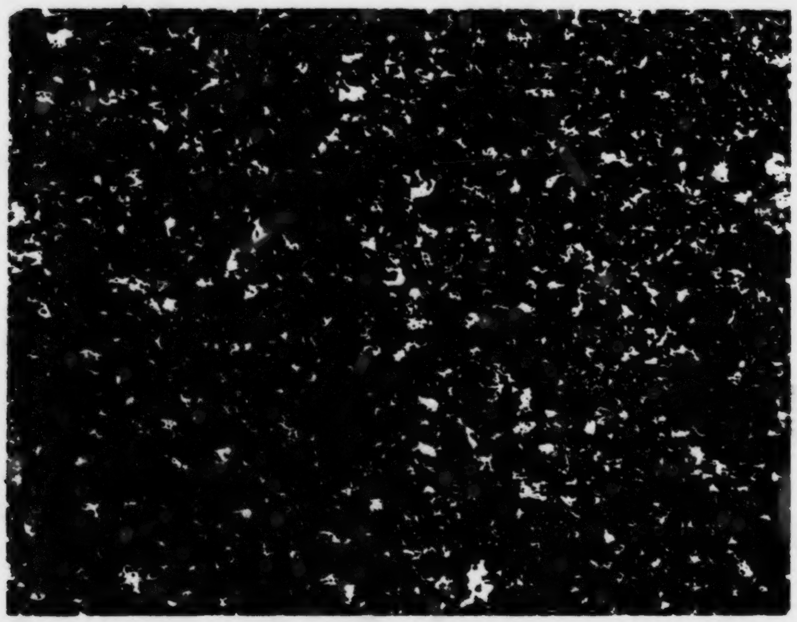

Figure 21: Slack-Quenched Structure Approx. 1/8" Below Running Surface of Shelled Region on Shelled Wheel (Designation 2B) -- (100X)

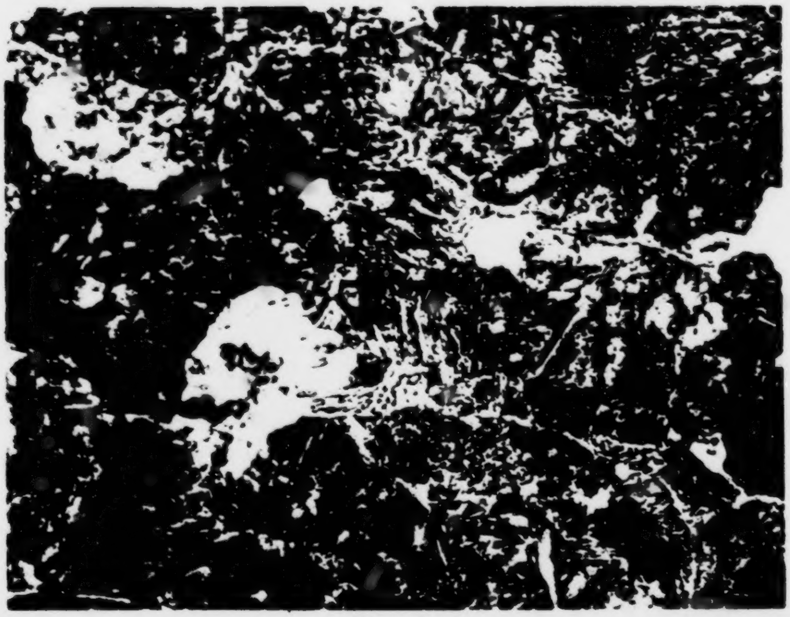

Figure 22: Slack-Quenched Structure Approx. 1/8" Below Running Surface of Shelled Region on Shelled Wheel (Designation 2B) -- (1000X)

The two most distinguishing microstructural differences between test group wheels/wheelsets are:

i) new wheels, along with worn wheels taken from non-shelled wheelsets, exhibit a wholly pearlitic structure about the wheel circumference. There is a logical structural progression from these new-to-worn wheels, with no physical suggestion of abnormal mechanical/thermal loading. Wheels taken from shelled wheelsets have a martensitic surface structure about the tread. This martensitic structure changes gradually with depth (approx. 1/8") to the base pearlite structure described above, and is evidence of relatively severe thermal loading.

ii) the martensitic surface structure found about the tread of wheels taken from shelled wheelsets is uniformly tempered (ie. softened), except in those highly localized areas which shell.

Martensite forms when local temperatures exceed 1325°F and are accompanied by rapid cooling; its formation appears to be fundamental to the majority of shelling failures. With the high axle loads and low operational speeds characteristic of unit-coal-train service, the most likely cause of martensite formation is sliding wheels (see Reference 6). Under certain conditions, sliding wheels generate sufficient heat to locally exceed 1325°F and also allow for relatively cool wheel metal surrounding this region to provide rapid cooling. Very severe braking conditions can provide for sufficiently high temperatures, but the required rapid cooling is unlikely since the entire wheel tread surface is heated.

The collected physical/mechanical data indicates that, for the seven wheelsets constituting the test group, damage:

- is not due to material defects or stress maldistributions arising during manufacture,
- is due to severe operating conditions (some critical combination of thermal and mechanical loading for each case),
- involves a fatigue failure mechanism, with failure originating at the tread surface and developing in-service,
- is thermally related, either entirely or in-part, as evidenced by the unique presence of martensitic structures about the treads of wheels from shelled wheelsets,
- occurs in localized tread regions which experience thermal loading different than is experienced in non-shelled regions, as evidenced by the unique presence of untempered martensite within areas of shelling. (The presence of martensite about the wheels taken from shelled wheelsets, along with high temperature oxides in shelling

cracks, suggest: (1) circumferential martensite formation precedes shelling, and (2) shelling damage results after specific thermal loads are applied to those areas which subsequently shell).

- appears to be fundamentally associated with sliding wheels.

5.0 RECOMMENDATIONS

Short-term testwork should be devised to further investigate the role, and causes, of severe thermal loading on wheel shelling.

Heat is produced, and directed into the wheel tread, by two sources: (i) the brake shoe/wheel tread interface and (ii) the rail/wheel tread interface. Given that severe thermal loading appears fundamental to the majority of shelling instances; there are two approaches (discounting an entirely new braking system) which will reduce shelling:

A) - utilize wheel steel that is more resistant to thermal loading, and

B) - reduce the number, severity and non-uniformity of in-service thermal loads

A lower carbon (and cleaner) wheel steel has greater tolerance to the severe thermal inputs occurring in-service, but also has lower wear resistance and tensile strength. These problems can be overcome by increasing the diameter of the wheel, but extensive equipment modifications would be involved.

In the present test work a logical correlation was established between wheel shelling - thermal loading (specifically wheel sliding) - and martensite formation. It is recommended that a test program be initiated in which a number of operational factors/conditions (eg. braking ratios, empty/load ratios, wheels having skid flats, etc.) are manipulated in-service or using a test consist, to determine their effect on the uniformity, frequency and severity of thermal loads (and shelling) imposed about the wheel tread. It is relatively straightforward to identify martensite in the field (chemical etching, scratch method, etc.); the presence/absence of this phase can be used to monitor a test program as described in general terms above.

REFERENCES

1. "A Review of Thermal Damage in Railroad Wheels", N.A. Berg and Wm. J. Kucera, Griffin Wheel Company, for presentation at The Air Brake Association Annual Meeting, Chicago, September 15, 1970.

2. "Measurement of Residual Stresses by the Blind-Hole-Drilling Method", Measurements Group, Inc., Tech Note TN-503.

3. "Metals Engineering Design", ASME Handbook, edited by O.J. Horger, 2nd edition, McGraw-Hill Book Company, 1965.

4. "Thermal Checking of Wrought-Steel Railway-Wheel Material", H.R. Wetenkamp, Trans. ASME, Vol. 76, 1954, pp. 649-654.

5. "The Metallographic Observation of the Tread of Wheels Subjected to Various Service Conditions", T. Kunikake et al., Trans. ISIJ, Vol. 10, 1970, pp. 476-489.

6. "Tread Braking Versus the Wheel", N.A. Berg and R.H. Alber, Griffin Wheel Company, for presentation at The Air Brake Association Annual Meeting, Chicago, September 18, 1972.

APPENDIX A

PRINCIPLE OF THE BLIND-HOLE-DRILLING METHOD

The introduction of a hole into a residually stressed specimen relaxes the stresses at that location since the stress normal to any free surface (ie. the hole surface) is zero. Further, the stresses in the immediate area of the hole are altered and local surface strains change accordingly. Measuring these changes in strains permits calculation of the original residual stress state at the hole location.

When a small diameter hole (see Figure A1) is drilled in a residually stressed region, the strains relieved at any point P are functions of the local principal stresses σ_p and σ_q, and of the geometric relationships between the point and the hole, and the point and the principal axes.

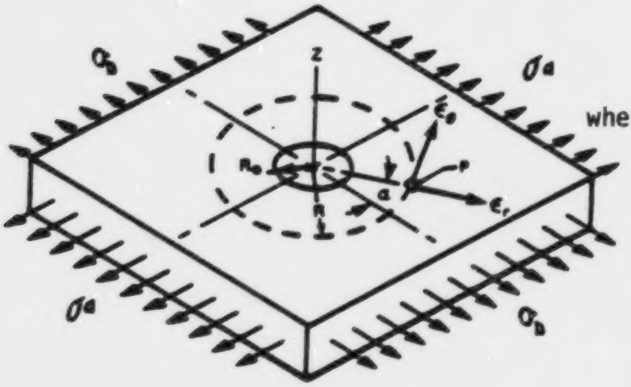

where:

$\varepsilon_r, \varepsilon_\theta$ = radial and tangential normal strains relieved, respectively, at point P

R_o = radius of drilled hole

R = distance from hole center to point P

α = angle defining orientation of P to principal axes.

Figure A1: Strain Relation at Point P After Introduction of Hole

Three independent strain measurements are required to determine the magnitude and orientation of the principal residual stresses at the surface of a body, with respect to any reference axes. The most common procedure for measuring these strains is to mount a strain rosette around the site of the hole prior to drilling (see Figure A2).

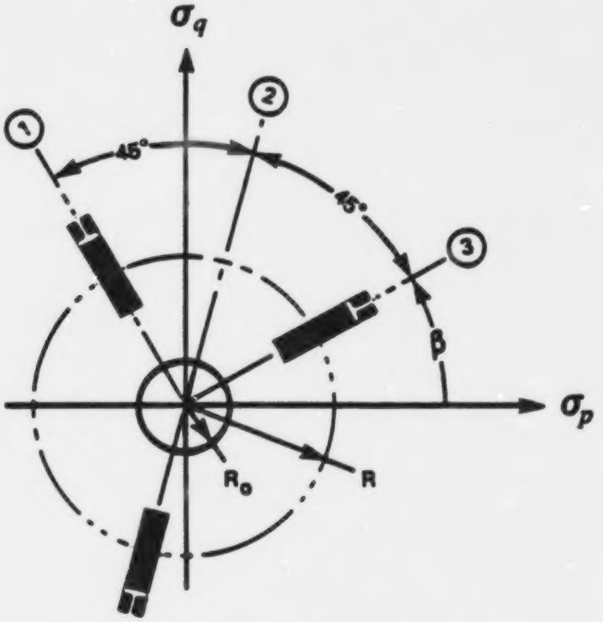

Figure A2: Strain Gauge Rosette Arrangement For Determining Residual Stresses

The development of the strain rosette relationships listed below will not be undertaken here (see Reference 2). Substituting the measured strains ε_1, ε_2 and ε_3 into the given relationships yields the principal stresses σ_p and σ_q, and their orientation with respect to the established reference axes. It is assumed that the stresses in the immediate vicinity of the hole are fully relieved when the hole depth approaches one hole diameter

$$\sigma_p = \frac{M}{4\bar{A}} + \frac{N}{4\bar{B}\cos 2\beta}$$

$$\sigma_q = \frac{M}{4\bar{A}} - \frac{N}{4\bar{B}\cos 2\beta}$$

$$\tan 2\beta = \frac{M-2\varepsilon_2}{N}$$

where: $M = \varepsilon_3 + \varepsilon_1$

$N = \varepsilon_3 - \varepsilon_1$

$$A = -\frac{(1+\nu)}{2E}\left(\frac{1}{r^2}\right)$$

$$B = -\frac{(1+\nu)}{2E}\left\{\left(\frac{4}{1+\nu}\right)\frac{1}{r^2} - \frac{3}{r^4}\right\}$$

ν = Poisson's ratio for wheel steel
(0.29 for steel casting)

E = elastic modulus
(30×10^6 psi for steel casting)

r = R/R_o
(established by drilling and
strain rosette employed)

β = is determined arbitrarily

APPENDIX B

CALIBRATION PROCEDURE EMPLOYED FOR RESIDUAL STRESS MEASUREMENT TESTWORK

A 6 x 2 x 2" section was cut from the tread of a new wheel (Designation 1A) and subjected to a RECOVERY ANNEAL (two hours in annealing furnace with neutral atmosphere at 1100°F, and furnace cooled) to remove most of the stresses locked in the section. Trace residual stresses will remain indefinitely, but this is acceptable for calibration purposes.

As in the actual test program, the Blind-Hole-Drilling method (see Figure B1 for test set-up) was used to measure the residual stresses in the calibration specimen. Since these residual stresses are appxoximately zero, the stresses measured here are actually those induced by the measurement procedure, and normally incorporated with the actual residual stress values recorded during each test run. Table B1 lists the "residual" strains relieved during the calibration run.

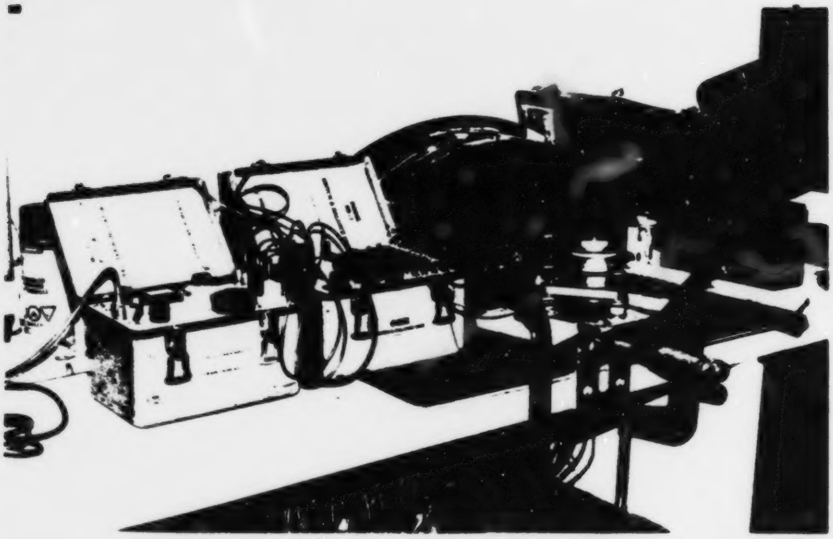

Figure B1: RS-200 Milling Gide, as Set-Up for Residual Stress Measurement Calibration Procedure

Table B1

Measured Strains from Residual Stress Calibration Procedure

Hole Depth (inches)	Hole Diameter (inches)	Measured Strains		
		ε_1	ε_2	ε_3
0	0	0	0	0
0.070	0.130	-40	-38	-35
0.140	0.130	-56	-52	-50

The values listed in Table B1 are measures of the errors induced by the testing process, and must be subtracted from the test measurements to provide calibrated strain data. Using the procedure detailed in Appendix A, these "new" values of ε_1, ε_2 and ε_3 provide calibrated residual stress values (magnitude and orientation) for each specimen examined.

APPENDIX C

DETERMINING INCLUSION CONTENT OF STEEL

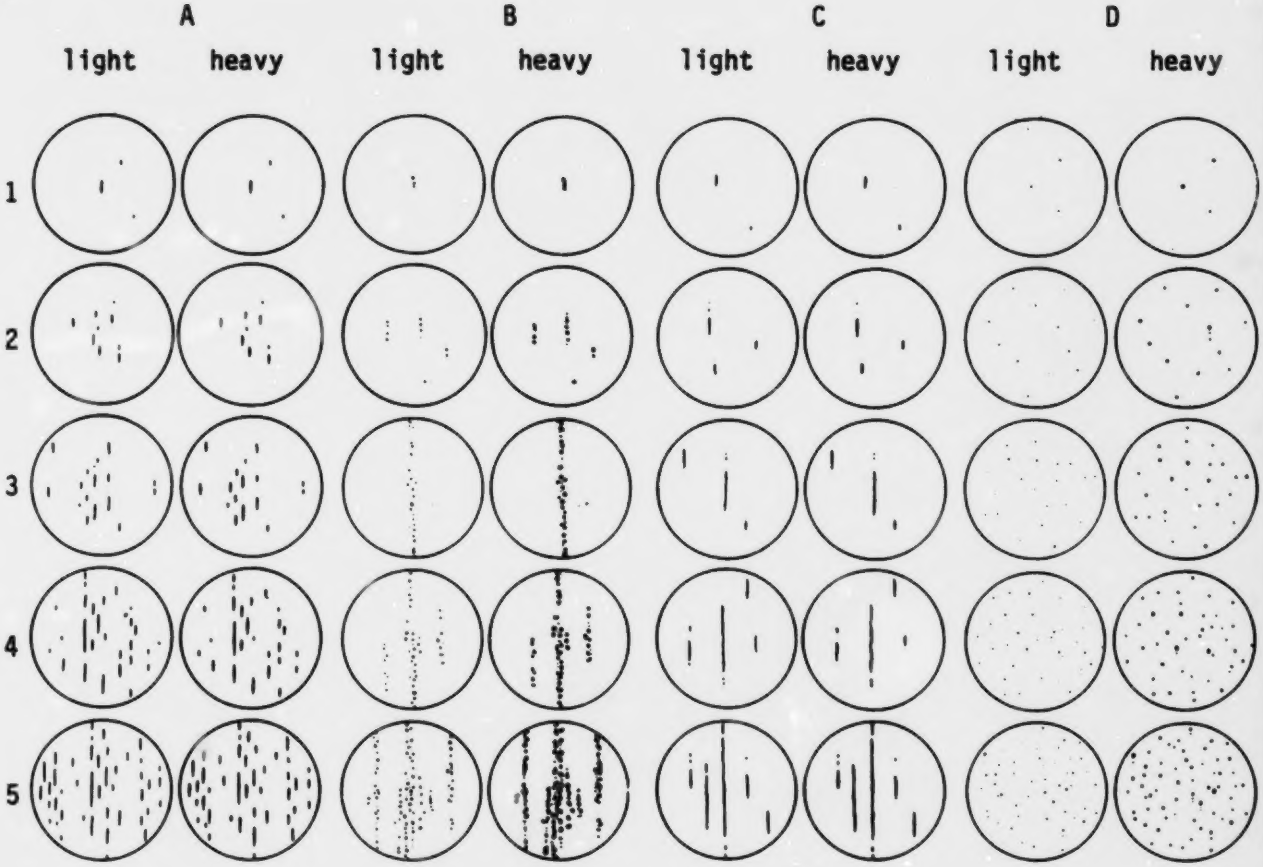
A
B
C
D
light
heavy
light
heavy
light
heavy
light
heavy
1
2
3
4
5

where:
A. Sulphide Type
B. Aluminia Type
C. Silicate Type
D. Globular Oxide Type

Figure C1: The Jernkontoret Inclusion Chart for the Estimation of Slag Inclusions in Steel

APPENDIX D

TEST WHEELSETS COMPARISON -- WEAR

Figure D1 characterizes each wheel examined in the present study on the basis of the amount of tread wear and flange wear (each expressed as a percentage of the wheels condemning limit) experienced prior to removal.

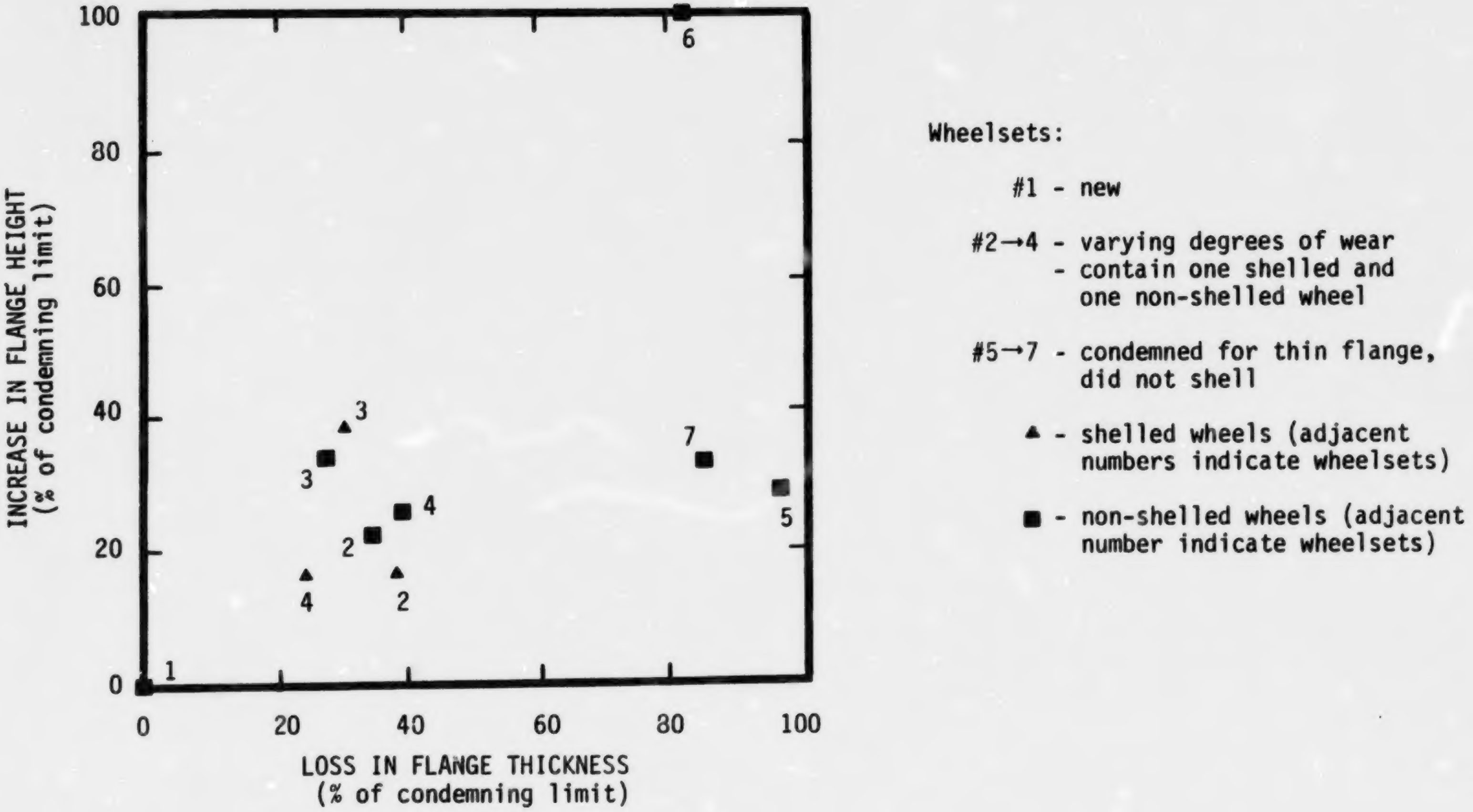

Figure D1: Variation in Flange Wear Versus Tread Wear (Each Expressed as Percentage of its Respective Condemning Limit) for Wheels Studied in Wheel Shelling Test Program

APPENDIX E

PHOTOMICROGRAPHS OF REPRESENTATIVE NON-METALLICS PRESENT IN STUDIED WHEEL STEELS

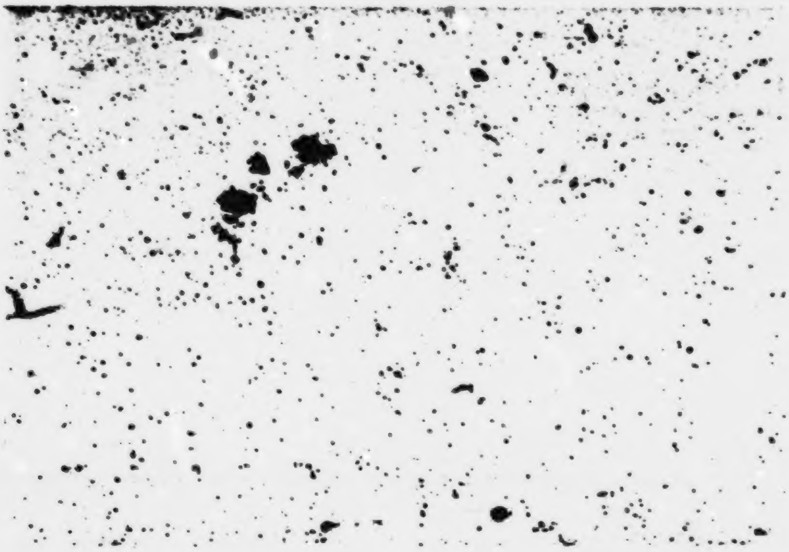

Figure E1: Cluster of Small, Irregular-Shaped, Silicate Inclusions Surrounded by Small Globular Oxide-Type Inclusions (100X, no filter, unetched)

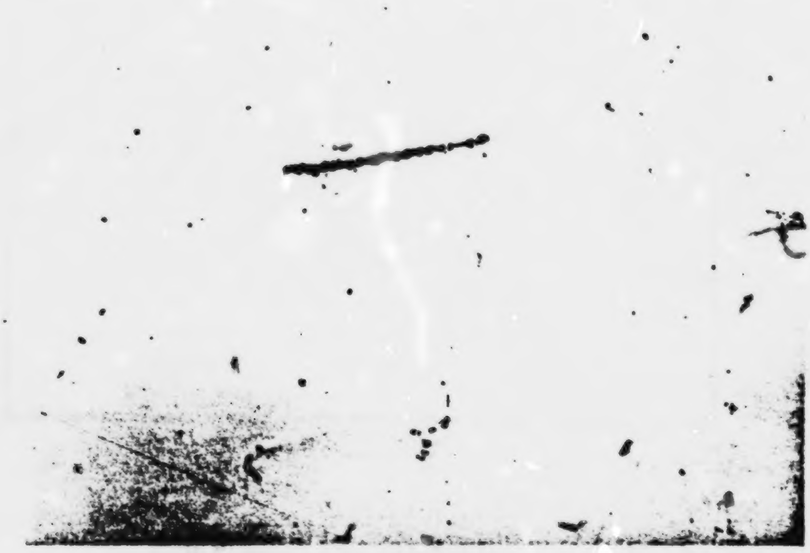

Figure E2: Aluminia-Type Inclusion (100x, no filter, unetched)

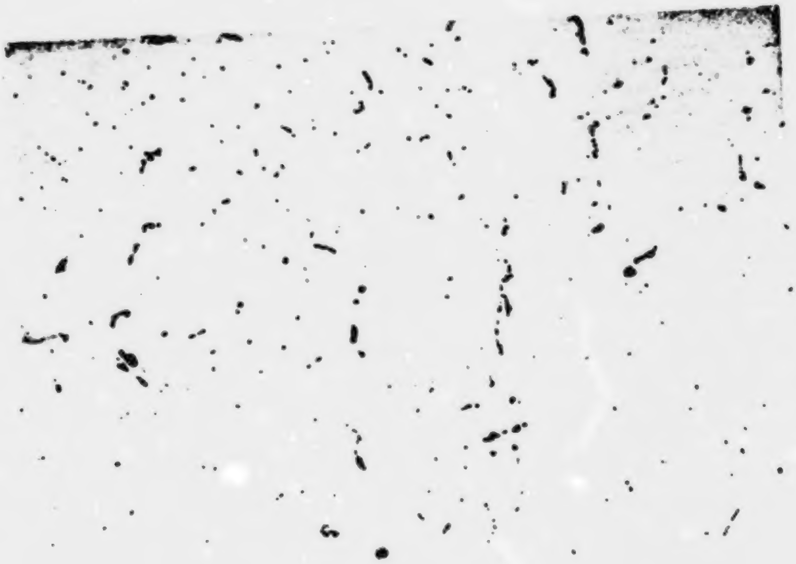

Figure E3: Sulphide/Silicate-Type Inclusions
(100X, no filter, unetched)

APPENDIX F

COMPOSITE HARDNESS GRADIENT PLOTS

Composite hardness gradients, corresponding to various shelled and non-shelled regions, determined from each of the 10 wheels examined in the test program are presented here. All hardness measurements were performed with a portable Rockwell C steel hardness tester (the accuracy of this device was confirmed before each usage with a 50 R_c calibration block).

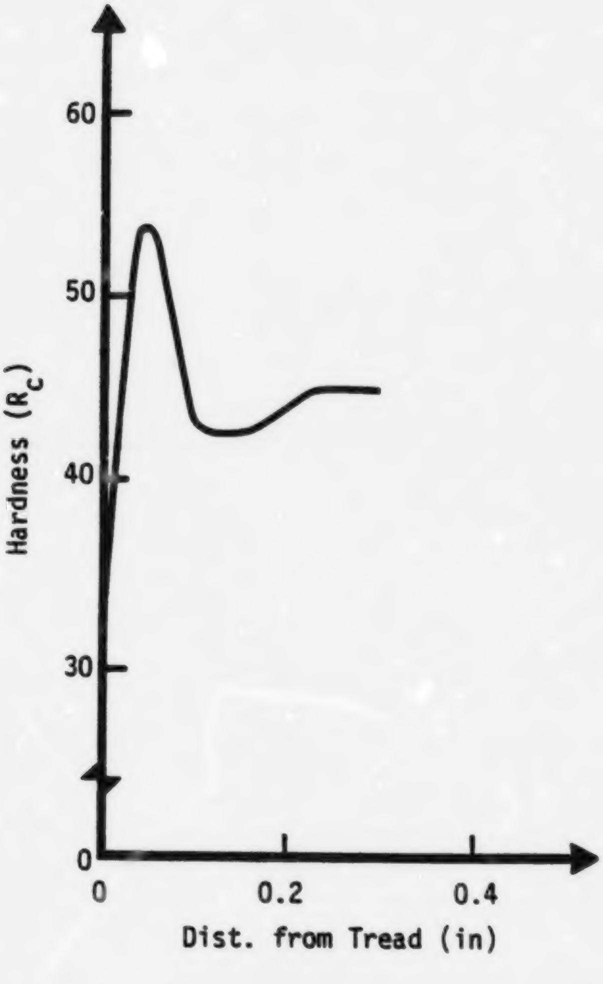

Figure F1: Composite Hardness Gradient for New Wheel (Designation 1A)

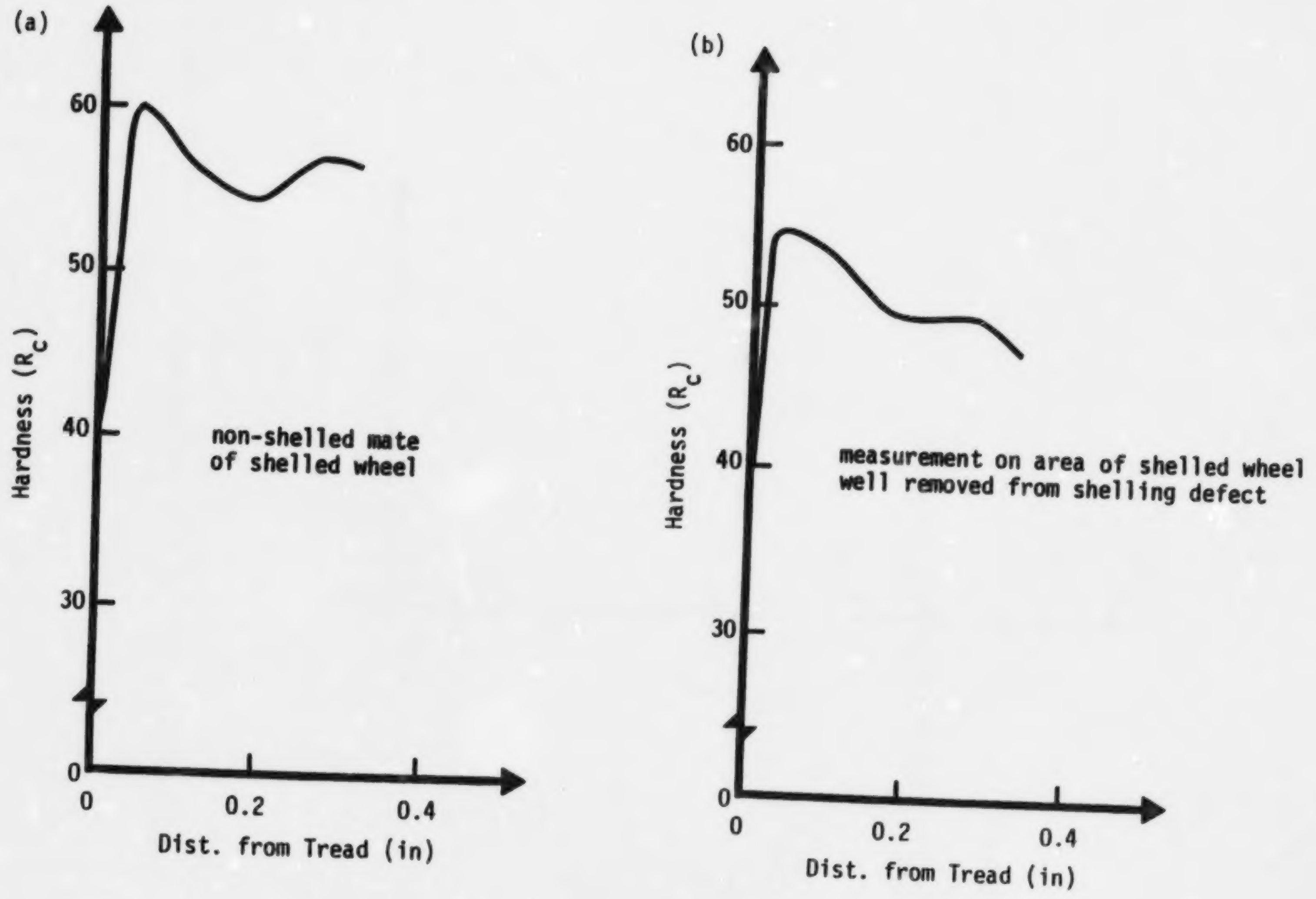

Figure F2: Composite Hardness Gradients Exhibited at Various Areas on Both Wheels Comprising Wheelset #2

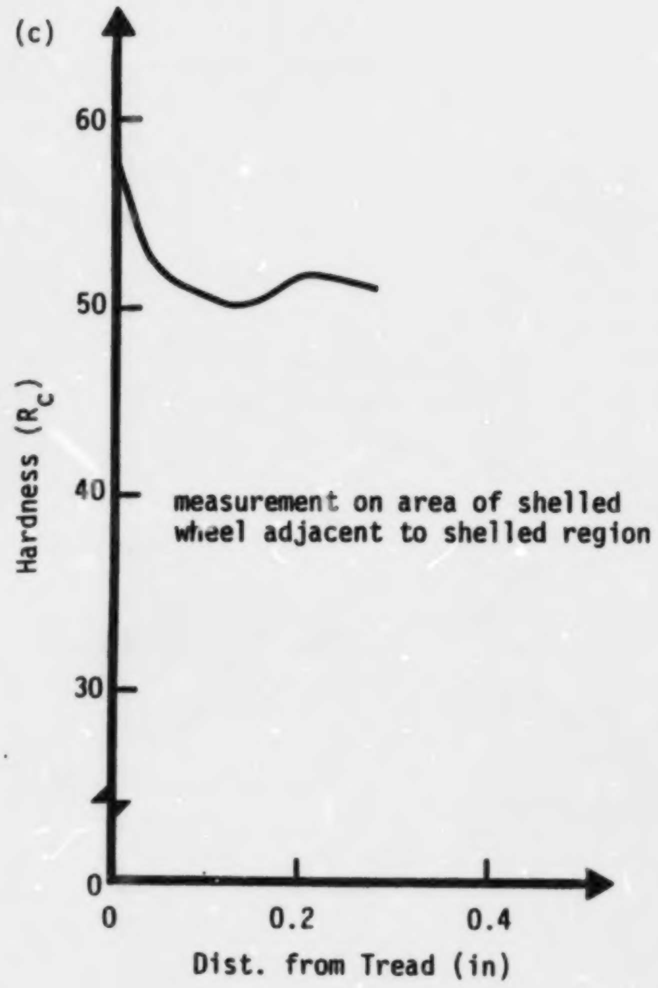
(c)
Hardness (R_c)
60
50
40
30
0
0
0.2
0.4
Dist. from Tread (in)
measurement on area of shelled wheel adjacent to shelled region

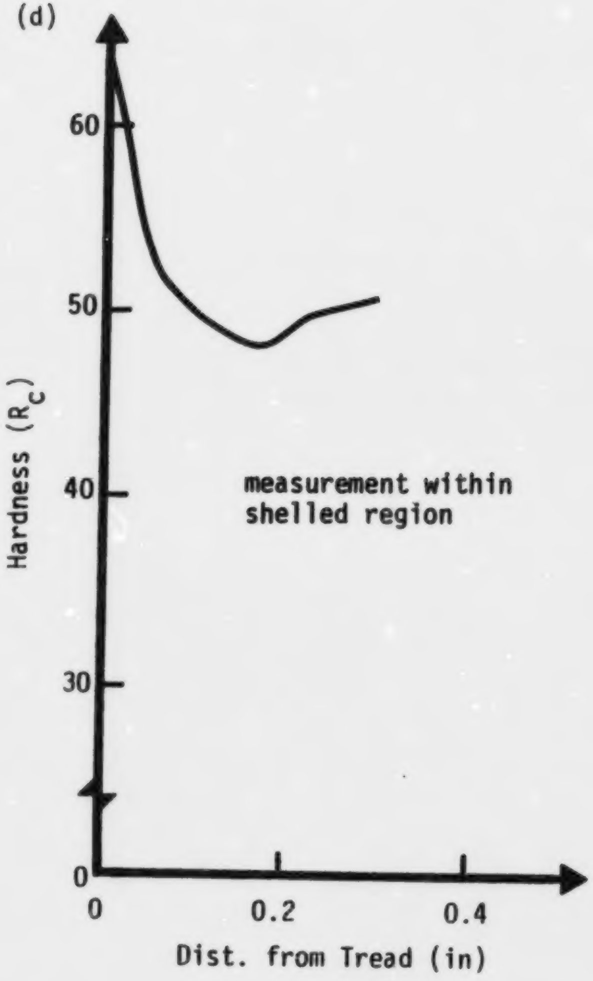
(d)
Hardness (R_c)
60
50
40
30
0
0
0.2
0.4
Dist. from Tread (in)
measurement within shelled region

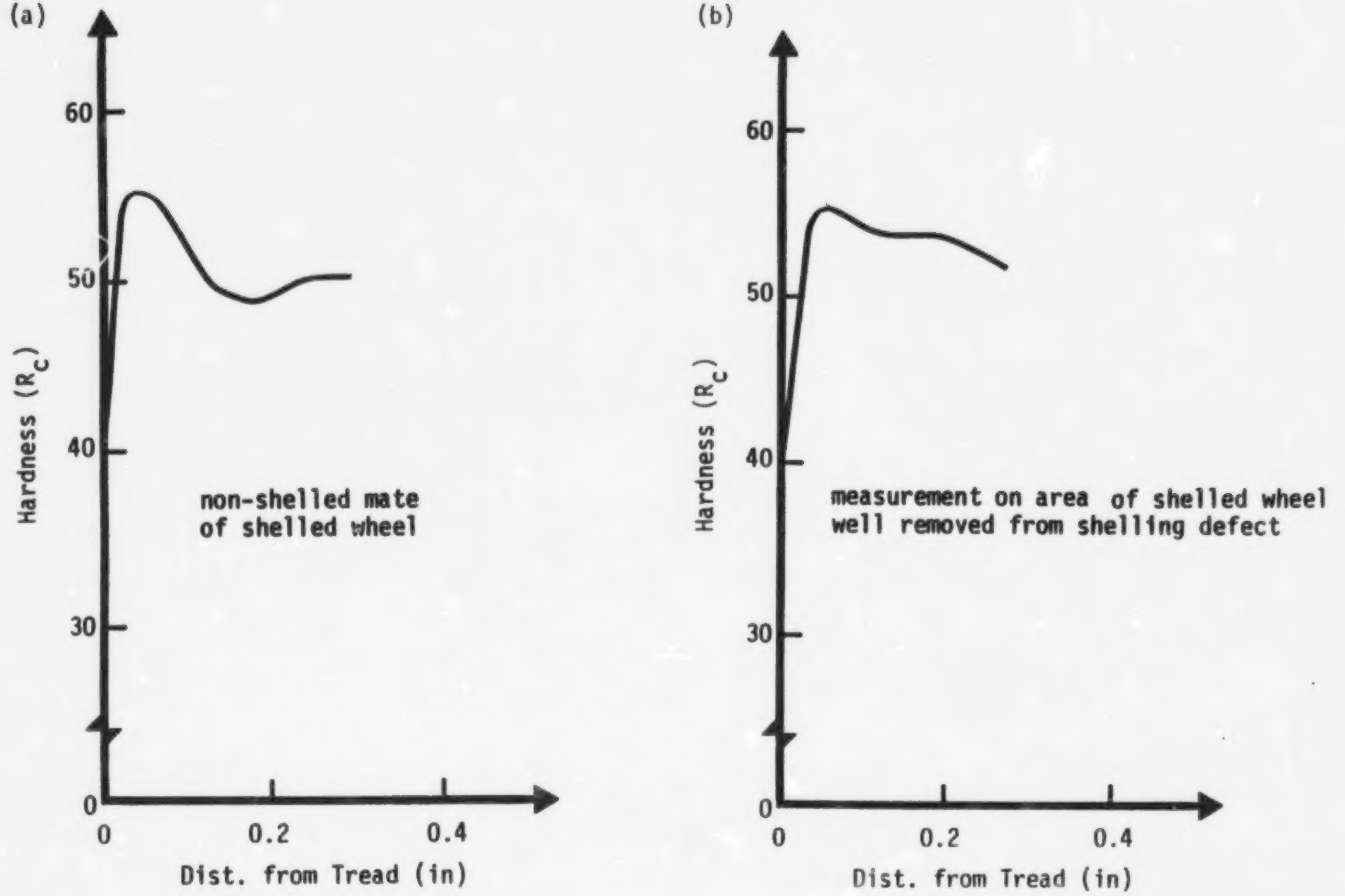

Figure F3: Composite Hardness Gradients Exhibited at Various Areas on Both Wheels Comprising Wheelset #3

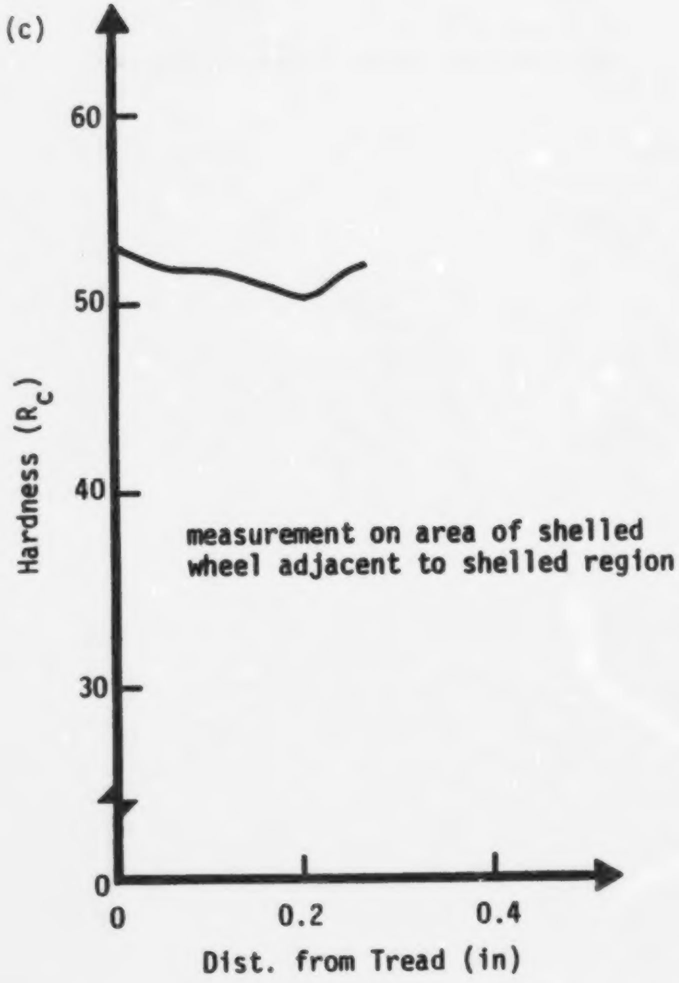
(c)
Hardness (R_c)
60
50
40
30
0
0
0.2
0.4
Dist. from Tread (in)
measurement on area of shelled
wheel adjacent to shelled region

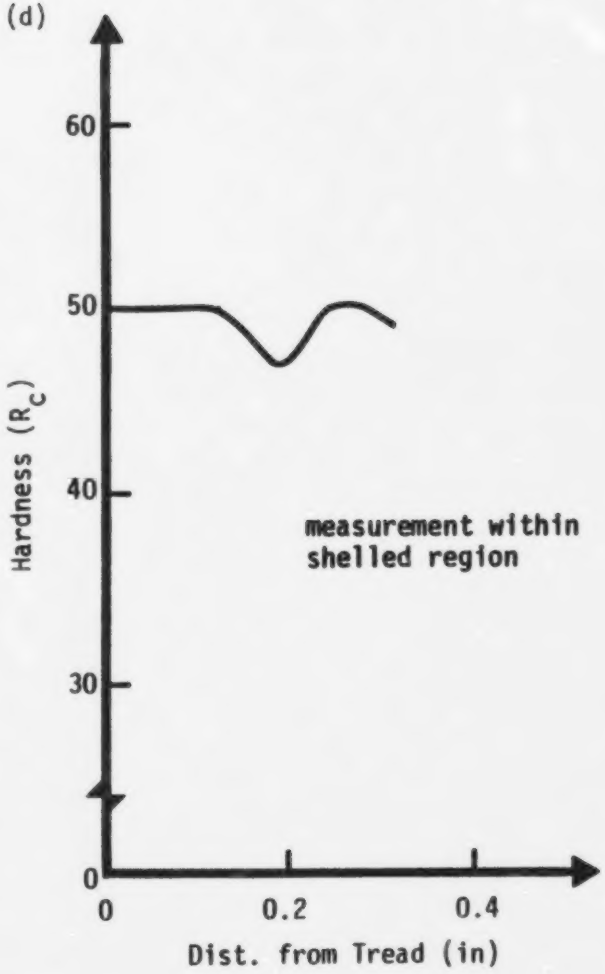
(d)
Hardness (R_c)
60
50
40
30
0
0
0.2
0.4
Dist. from Tread (in)
measurement within
shelled region

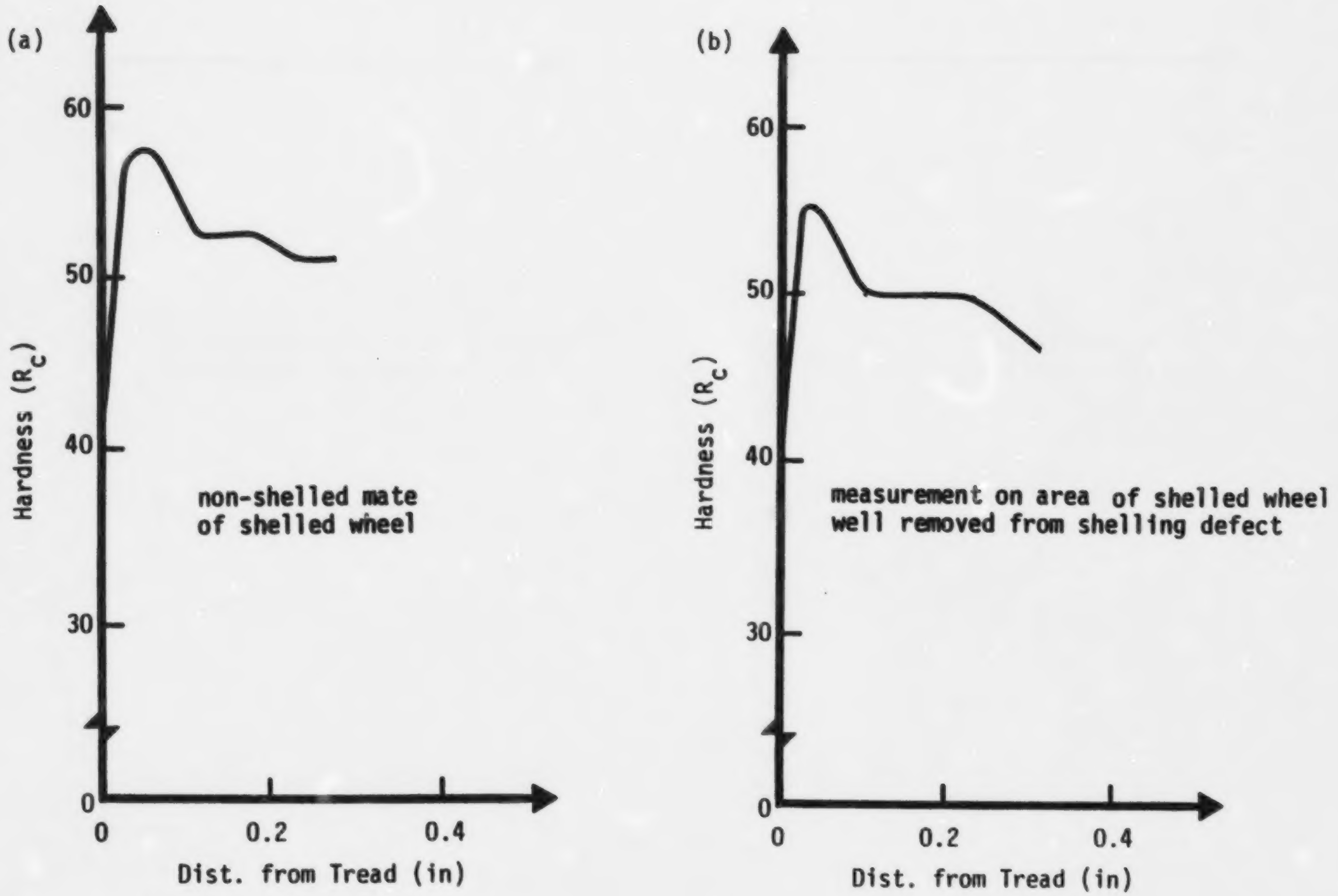

Figure F4: Composite Hardness Gradients Exhibited at Varous Areas on Both Wheels Comprising Wheelset #4

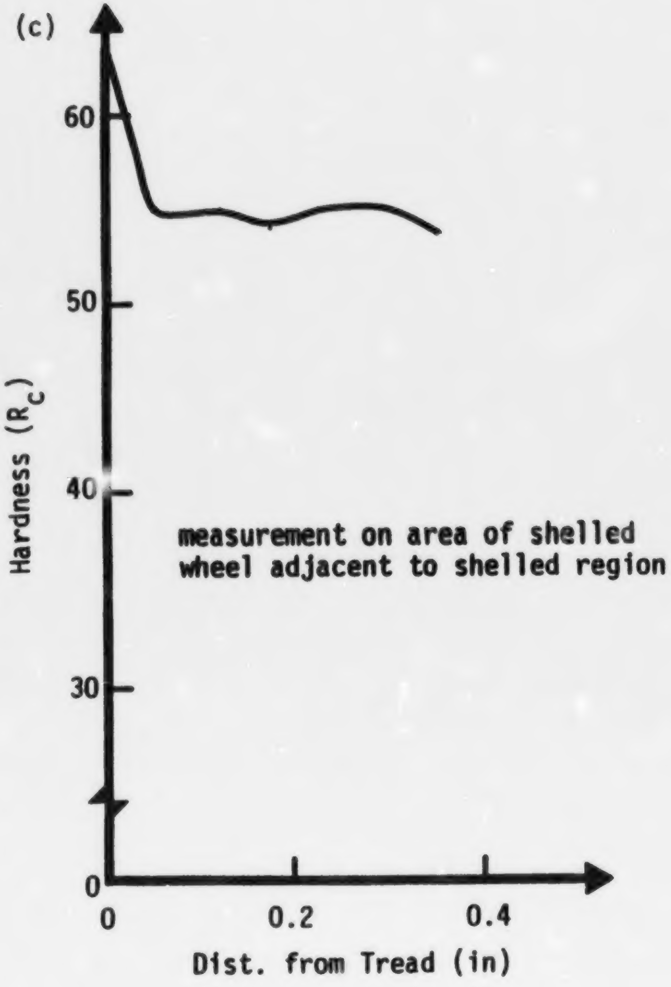
(c)
60
50
40
30
0
Hardness (R_c)
measurement on area of shelled
wheel adjacent to shelled region
0
0.2
0.4
Dist. from Tread (in)

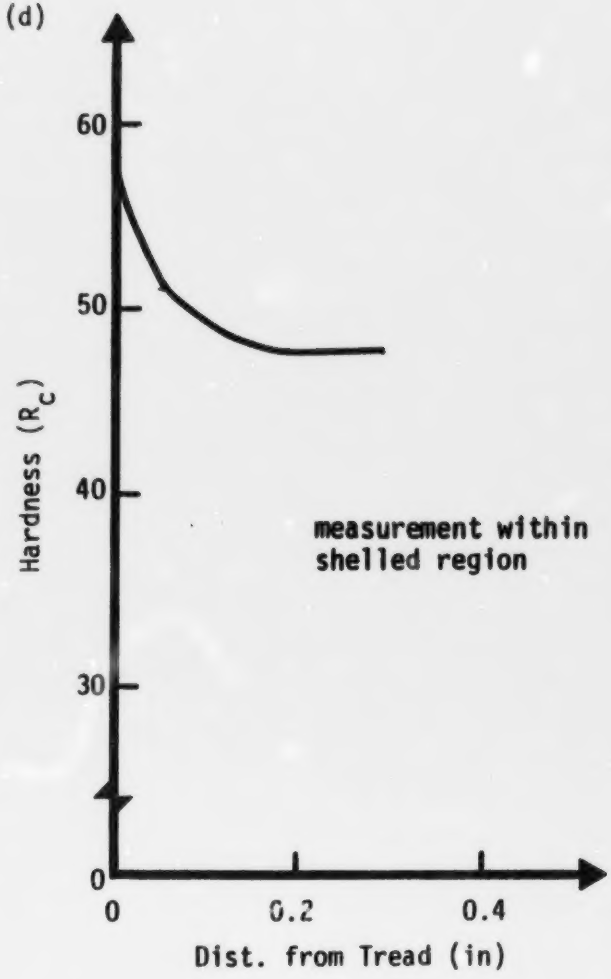
(d)
60
50
40
30
0
Hardness (R_c)
measurement within
shelled region
0
0.2
0.4
Dist. from Tread (in)

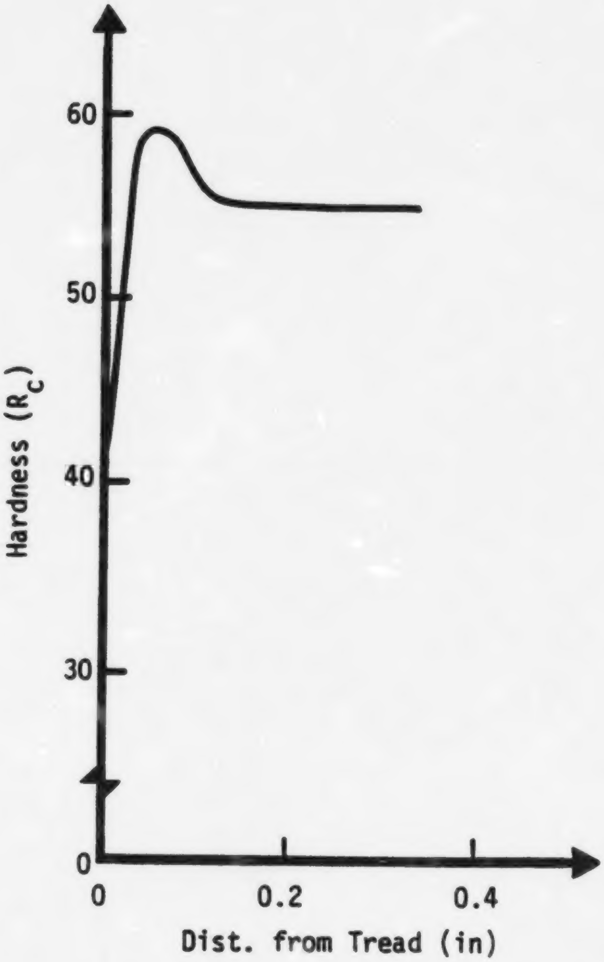

Figure F5: Composite Hardness Gradient For Severely Worn, Non-Shelled, Wheel (Designation 5A)

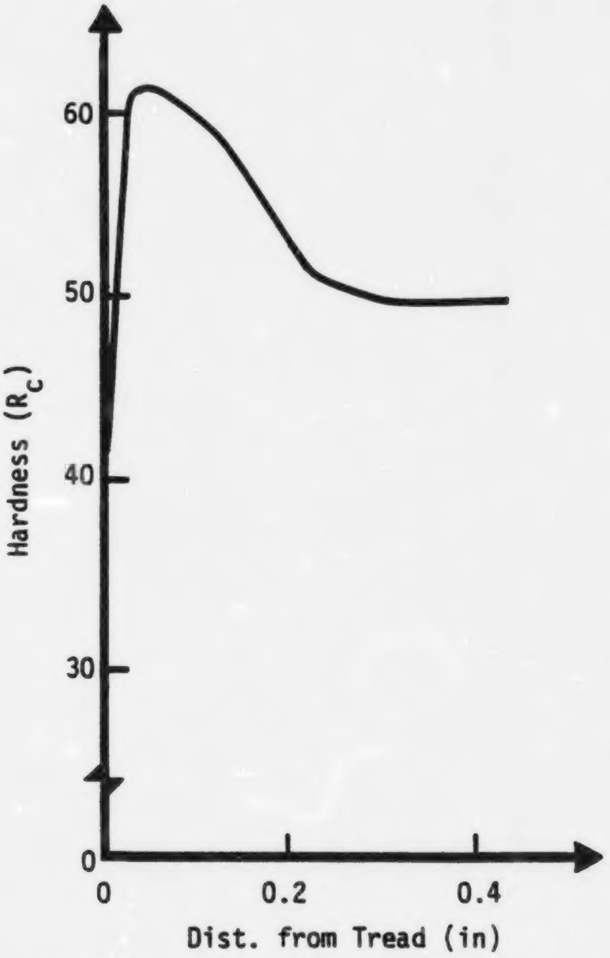

Figure F6: Composite Hardness Gradient For Severely Worn, Non-Shelled Wheel (Designation 6A)

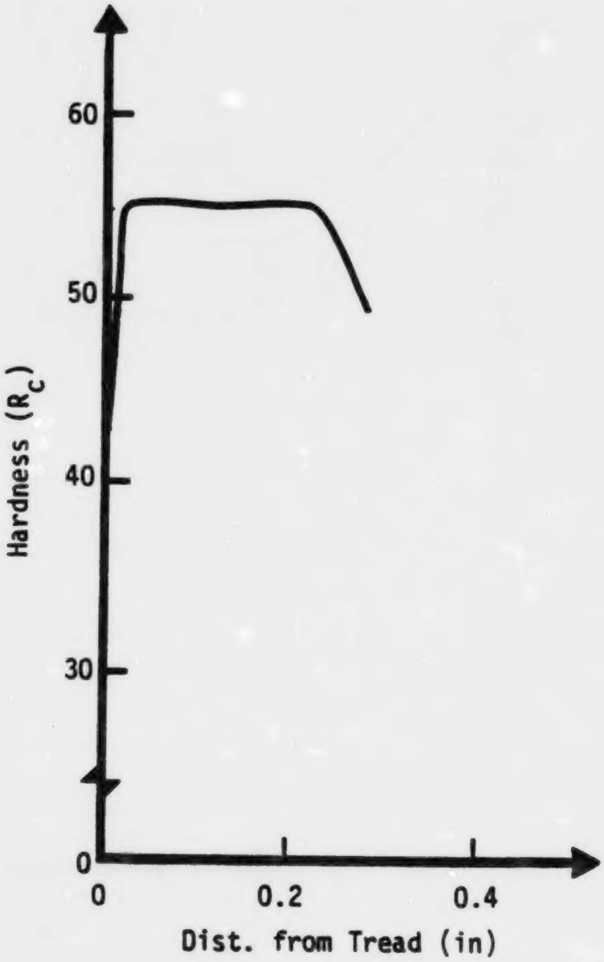

Figure F7: Composite Hardness Gradient For Severely Worn, Non-Shelled Wheel (Designation 7A)

A DYNAMIC RAIL VEHICLE MODEL

M. Shaw
Planning and Research Department
Canadian Pacific Limited
Montreal

EXECUTIVE SUMMARY

A dynamic truck model has been developed by CP Research to gain greater foresight and hindsight in areas concerned with track/train dynamics.

This model is a nonlinear seventeen degree-of-freedom time-based simulation which considers such nonlinearities as creep-force laws, physical limits of travel between truck components and wheel/rail flanging. The theoretical framework used to obtain the equations of motion provides enough flexibility to simulate a variety of scenarios. Resultingly, the model may be used for tangent or curved track studies. Several aspects of tangent truck hunting are presented as an initial step to the model's validation.

Parametric studies related to freight truck hunting are compared to previous work and, when possible, to test data obtained first hand through various departmental tests. In general, the model output has provided reasonable critical speeds for studies on suspension alterations, effective wheel conicities, and centerplate friction levels. No studies were performed on the gravitational or primary torsional stiffness -- it is felt that the measurement or approximation of these values is too questionable for discussion purposes.

All analyses of parametric influences on critical hunting speeds are presented in graphical form. Future studies dealing with steady-state and dynamic curving simulations will form complimentary reports on the model's potential uses.

SOMMAIRE

Le département de recherche du Canadien Pacifique a developpé un modèle du comportement dynamique d'un bogie visant à obtenir une meilleure compréhension sur les interactions dynamiques roue-rail.

Le modèle est une simulation itérative à 17 degrés de liberté basée sur le temps. Ce programme informatique est composé de variables non-linéaires tels que les forces de glissement, les limites physiques de mouvement entre les éléments du bogie, et les interactions roue-rail quand le boudin s'appuit sur le rail. De plus, la théorie de base donne des équations flexibles de mouvement et permet des études de voies en alignement droit ou en courbe. Comme première étape pour valider ce modèle on présente les résultats d'études sur le comportement de bogie sur voie en alignement droit.

Ces études du comportement du bogie sont comparées aux travaux précedents de recherche et aux résultats d'essais de chantier du département. En génèral, les vitesses critiques de lacet du véhicule sont des valeurs raisonnables pour des études de changements de rigidité des ressorts, du niveau de friction à la crapaudine, et de la conicité effective de l'essieu. Aucune étude n'a été faite de l'influence de la rigidité de suspension torsionelle primaire ou de la rigidité gravitationnelle sur les vitesses de lacet. La quantification de ces rigidités est doutable et ne peut être presentée comme sujet de discours.

Toutes les analyses des influences paramétriques sur les vitesses critiques de lacet sont présentées en forme graphique. Les études sur le comportement d'un bogie sur une voie en courbe formeront des rapports complémentaires pour valider le modèle.

ACKNOWLEDGEMENTS

The author wishes to express his sincere thanks and appreciation to:

- Members of CP Technical and Operations Research Department, and in particular Mr. Greg Rosval, for their support and aid throughout the development of this dynamic model.
- Transportation Development Centre, Transport Canada for financial support under Contract #OSD83-00193.

TABLE OF CONTENTS

PAGE

EXECUTIVE SUMMARY 416

ACKNOWLEDGEMENTS 419

LIST OF FIGURES 421

1.0 INTRODUCTION 422

2.0 THEORETICAL FRAMEWORK 424

- 2.1 System Description 424
- 2.2 Database Description 426

3.0 MODEL NONLINEARITIES 428

- 3.1 Wheel/Rail Creepages and Creep Forces 428
- 3.2 Suspension Nonlinearities 430

4.0 TRUCK HUNTING PARAMETRIC STUDIES 432

- 4.1 The Influences of Suspension Stiffness on Critical Speed 432
- 4.2 Effective Wheel Conicity Study 436
- 4.3 Effects of Centerplate Friction on Truck Yaw Hunting 436

5.0 CONCLUSIONS 441

REFERENCES 442

APPENDICES

- A. Description of Generalized Coordinates 444
- B. Base Truck Characteristics 449

LIST OF FIGURES

FIGURE	DESCRIPTION	PAGE
1.	Location of Bolster's Center of Mass for an Arbitrary Truck Orientation	425
2.	Body Fixed Coordinate Systems for a Conventional Three-Piece Truck	425
3.	Arbitrary Wheelset Position Along A Tangent Track	429
4a.	Deadband Spring Characteristic	430
4b.	Hardening Spring Characteristic	430
5.	Primary Stiffness Influence on Critical Hunting Speed	433
6.	Secondary Yaw Stiffness Influence on Critical Hunting Speed	435
7.	Effective Wheelset Conicity Influence on Critical Hunting Speed	437
8.	Large Centerplate Yaw Stiffness Effects on Bolster Yaw Hunting	439
9.	Small Centerplate Yaw Stiffness Effects on Bolster Yaw Hunting	440
A-1	Description of Generalized Coordinates	446
A-2	Description of Generalized Coordinates	447
A-3	Description of Generalized Coordinates	448
A-4	Description of Generalized Coordinates	448

1.0 INTRODUCTION

Assessing the dynamic behaviour of trucks and carbodies as well as evaluating the track structure's influence on this behaviour is an on-going concern of all railroads. Studying such behaviour can result in improvements in equipment with considerable savings through reduced component wear, reductions in track maintenance, fuel savings, and so on. CP Research has been actively involved in field tests to perform such studies for a number of years. As an extension to this work the Research Department has developed several theoretical models. The department's most recent undertaking has been a dynamic truck model.

Many theoretical truck models deal with one specific area of track/train dynamics such as steady-state curving or hunting. Most of the models also apply straight forwardly a Newtonian approach to solving the problem in obtaining its equations of motion. Other common methods of solution used are describing functions or statistical linearization techniques(1). CP Research's dynamic truck model, on the other hand, has been developed using generalized coordinates and Lagrangian Dynamics(2,3).

The choice of dealing with generalized coordinates stems from the simplified description of a three-piece truck which results with a judicious choice of coordinates(4). Also, the use of generalized coordinates leads indirectly to a model which may be applied to a variety of scenarios (Section 2).

The generalized coordinates are complemented by a database made up of track geometries, truck suspension and inertia values, and contact patch geometries. The combination of these data and the generalized coordinates provides enough flexibility to simulate tangent track or fully developed curve negotiations, each of which have characteristic contact patch and track geometry data. Eventually track structures such as spirals may be investigated.

Hunting studies were completed as a first step in validating the dynamic model. This report presents the results of these tests performed to date. Findings of other researchers or other model predictions are used for comparative purposes. Sections 2 and 3 describe the dynamic model's theoretical framework with the latter section concentrating on creep force laws and those used in this model. Section 4 presents the results obtained from the hunting simulations. Lastly, Section 5 reports the conclusions and potential modifications to the model based on experience gained through the model's development.

2.0 THEORETICAL FRAMEWORK

This section presents a global overview of the simulation, its underlying theories and method of solution, and the necessary data considered. A more detailed explanation of the governing simplifications of the model are reported in reference 4.

2.1 System Description

Generalized coordinates are carefully chosen coordinates which fully describe the mechanical system while at the same time reducing the system's number of degrees of freedom. The coordinates selected relate the centers of mass of the various truck components to one another or to the track centerline and define the components' orientations.* In addition, the truck components are located by a combination of coordinate systems:

i) A translational set of axes which locates a vertical plane, perpendicular to the track tangent line at a given location, through which the bolster's center of mass may be found (Figure 1),

ii) Body fixed axes (Figure 2) which locate the translational and rotational positions of each principal mass of the truck to the translational frame of reference noted in i),

---

* A description of these coordinates is presented in Appendix A.

iii) An inertial frame of reference.

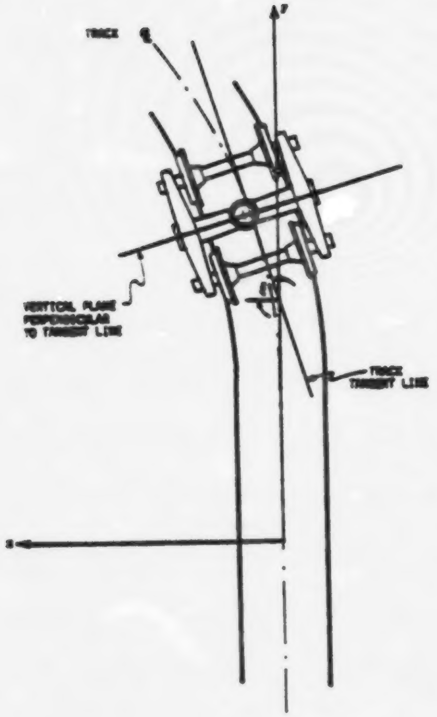
TRACK ℄
y
VERTICAL PLANE PERPENDICULAR TO TANGENT LINE
TRACK TANGENT LINE
x

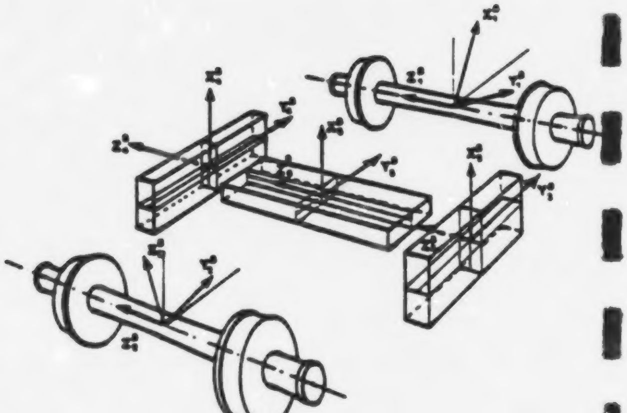

Figure 1

Location of Bolster's Center of Mass for an Arbitrary Truck Orientation

Figure 2

Body Fixed Coordinate Systems for A Conventional Three-Piece Truck

With these sets of axes and the seventeen degrees of freedom chosen(4) Langrangian dynamics theory is applied to obtain a set of seventeen equations of motion, each being functions of these degrees of freedom. This set of equations is then equated to a generalized force vector and solved in terms of generalized accelerations using Gaussian elimination.

The simulation proceeds by assuming that the acceleration vector of the i-th iteration may be integrated numerically twice to obtain velocity and displacement vectors for the (i+1)th iteration. These vectors help generate a new set of equations and forces and consequently accelerations, which are used to perpetuate the numeric scheme until completion of the simulation.

2.2 Database Description

To support the dynamic model much emphasis was placed on the realism of the database used within the simulation. Accordingly, most data used is obtained firsthand and not through mathematical approximations.

A major portion of the database is comprised of:

i) track geometry data,
ii) contact patch geometries,
iii) truck characteristics.

Track geometry data include such details as track superelevations, curvatures, and rates of change of curvature. These values are expressed as cubic polynomials on a station to station basis at 62 foot intervals. With this data the simulation can iteratively advance along a track section and record changes in track structure or geometry e.g. gauge variations which alter the truck orientation.

Contact patch geometries included in the simulation are generated by a supporting contact geometry program(5). This program uses field data obtained with CP Research's rail and wheel profilometers(6). These profilometers permit any arbitrary new and/or worn wheel or rail profiles to be accurately portrayed digitally. Using these reproductions the contact patch program generates information such as contact ellipse dimensions, spatial locations of the contact patch with respect to the wheelset's center of mass, contact angles, and rolling radii for a number of wheelset displacements and yaw angles. The wheel and rail used by this program are assumed rigid therefore the effects of rail roll or gauge widening on the contact patch data are neglected. They may, however, be considered at a later date.

The truck characteristics consist of physical dimensions, component masses and inertia, suspension values, and friction wedge angles. The suspension values form two (1 x 17) stiffness and damping vectors used to describe the suspensions. In addition, the truck-related data includes dimensional restrictions between truck components in order to simulate new or used truck conditions and mechanical stops.

3.0 MODEL NONLINEARITIES

Freight trucks are highly nonlinear mechanical systems consisting of physical stops, coulomb friction, and other nonlinear mechanisms. Several of these physical systems have been included in the model.

3.1 Wheel/Rail Creepages and Creep Forces

Linear profiles of wheel and rail are frequently used for modelling wheel/rail interactions. Similarly creep force laws governing the wheel/rail force calculations are sometimes taken to be linear. Both are adequate for linear models and/or small wheelset displacements which avoid high contact angles.

This approach, however, has not been considered. Rather, nonlinear wheel/rail profiles and creep theories have been incorporated into the model. These nonlinearities thus account for changes in rolling radii or contact angles with lateral displacements, creepage saturation, flange contact geometries, and other nonlinearities occuring at the wheel/rail interface.

The definitions for lateral and longitudinal creep reported by Brann(7) are employed. A single wheelset having an arbitrary yaw angle and/or lateral displacement may have associated velocities in the longitudinal, lateral, and yaw directions. Figure 3 illustrates such an orientation.

The associated normalized creepages are therefore given by

$$U_1 = U_2 = \frac{\dot{Y}}{V_{hub}} - \theta$$

$$V_1 = \frac{V_{hub} - \dot{\Omega} r_1 - b\dot{\theta}}{V_{hub}}$$

$$V_2 = \frac{V_{hub} - \dot{\Omega} r_2 + b\dot{\theta}}{V_{hub}}$$

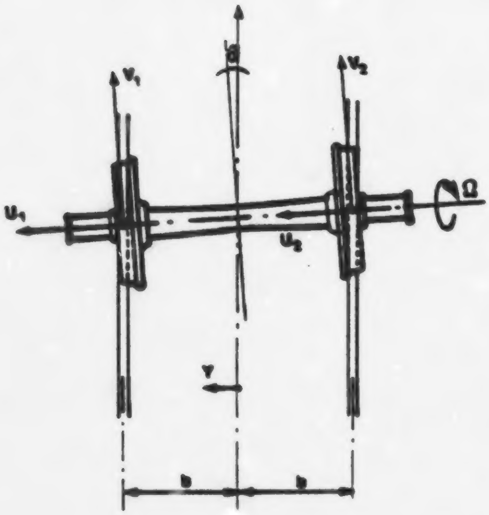

Figure 3

Arbitrary Wheelset Position
Along a Tangent Track

Creep forces may be calculated using a number of creep force laws. The theory of Vermuelen-Johnson(8) is considered sufficient for a hunting analysis and is also advantageous in its ability to limit the creep forces to the available friction force at the wheel-rail interface. (Johnson and Vermuelen use a cubic saturation law which reduces the creep forces to the nonlinear values which follow the common creep saturation curve.)

3.2 Suspension Nonlinearities

Primary and secondary suspension may be modelled by three different displacement-force relationships. For a linear analysis the suspension points are modelled using linear spring constants. Non-linear analyses employ deadband or hardening springs according to the suspension interface being modelled. The nonlinear suspension models are shown in Figure 4.

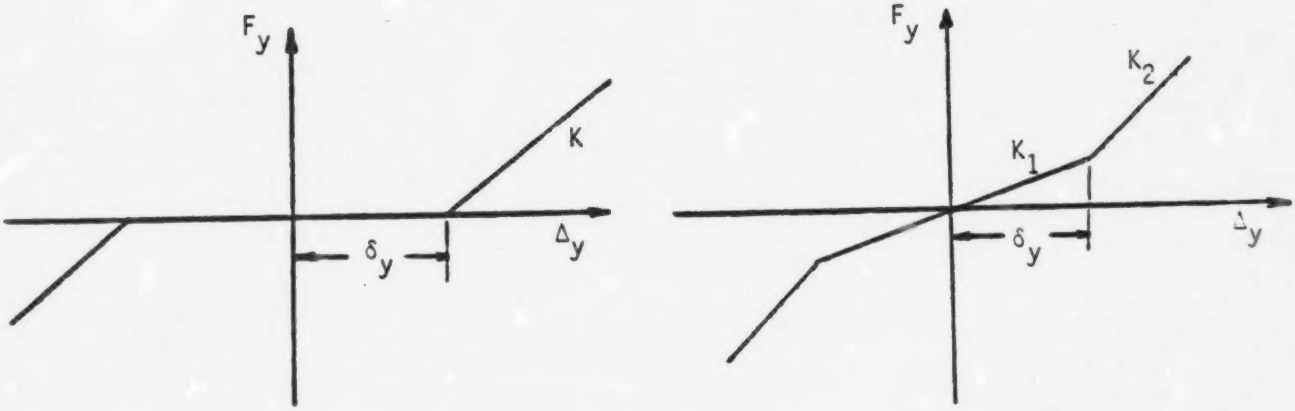

Figure 4

(a) Deadband Spring Characteristic (b) Hardening Spring Characteristic

Each suspension description is also governed by physical limits which restrict the relative motions between adjoining truck components to the new or worn tolerance limits.

4.0 TRUCK HUNTING PARAMETRIC STUDIES

As previously mentioned, the model presented may be used to study truck hunting for various truck configurations. Only bogie, or secondary, hunting shall be dealt with since carbody dynamics have not been incorporated into the model. Also, the results presented shall be compared to other research papers or field tests to illustrate the model's sensitivity to those factors which influence truck hunting behaviour.

Throughout the parametric study all comparisons will be with respect to a Barber S2-C truck fitted with elastomeric shear pads. Appendix B details the truck parameters used in this base configuration. This base truck configuration was selected because of the attention it has received from several researchers. Also, the presence of linear springs at the sideframe-wheelset primary suspension allows comparisons to be made between this model's output and linear models.

4.1 The Influences of Suspension Stiffnesses on Critical Speeds

The small amounts of damping possessed by freight truck suspensions have no significant effect on a truck's hunting performance(10). Consequently, the analysis of suspension stiffnesses versus critical speeds include only minimal damping coefficients for all spring values used.

Figure 5 shows a damping ratio versus speed plot for different primary longitudinal and lateral stiffnesses in which the critical speed is defined as the speed at which the damping ratio is equal to zero. At speeds

Figure 5: Primary Stiffness Influence on Critical Hunting Speed

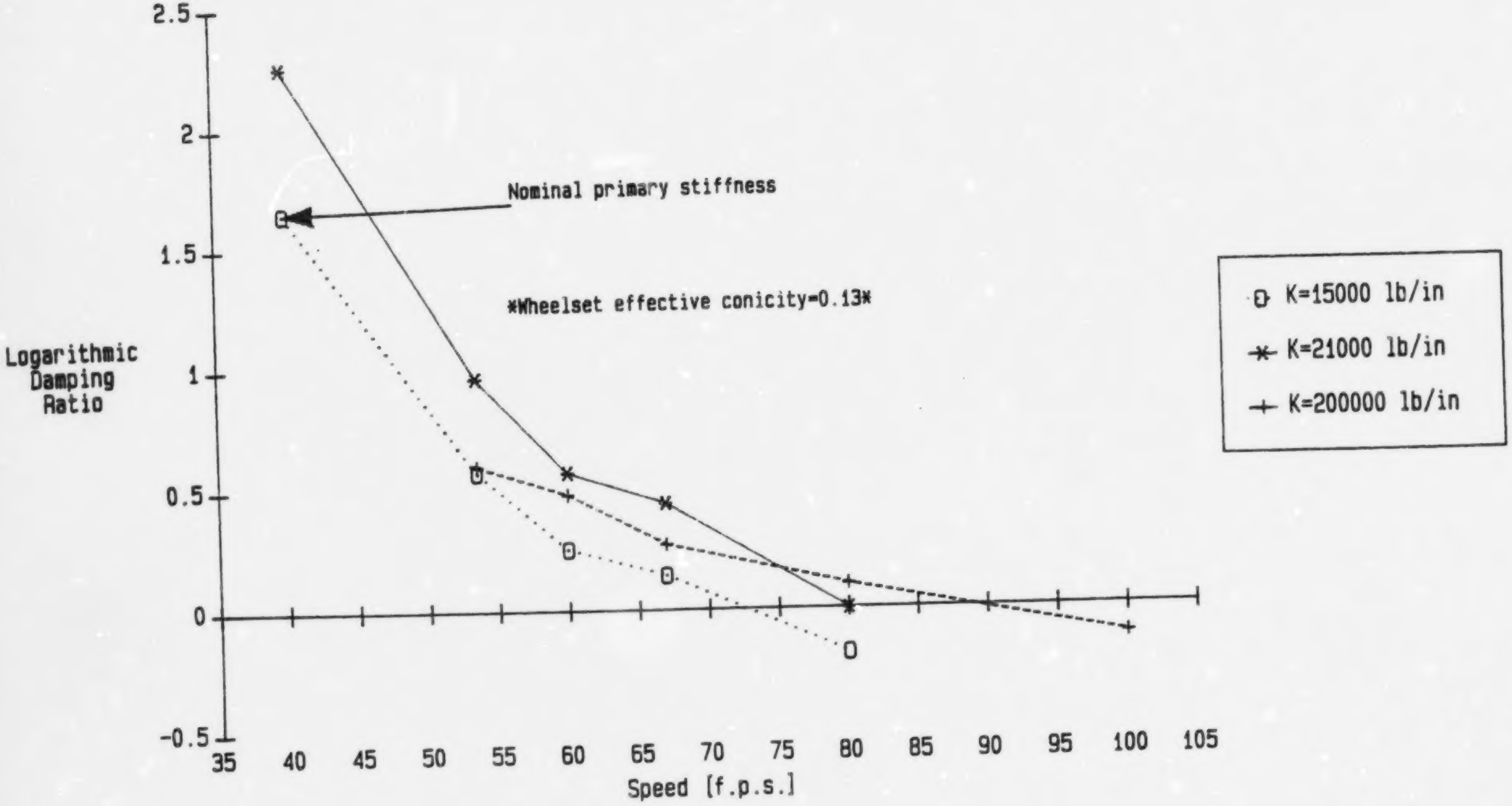

greater than this the damping ratio is negative and lateral wheelset oscillations continually increase in amplitude. The graph illustrates that the truck's critical hunting speed decreases proportionally with reductions in primary spring stiffnesses. Dukkipati(9) has shown that the change in critical speeds plateaus with elevated spring stiffnesses. Other researchers(11,12) have reported similar findings. This trend is apparent from figure 5 given the small increase in critical speed despite an almost ten-fold increase in the stiffness from 21000 lbf/in. to 200000 lbf/in.

Secondary yaw stiffnesses have an equally important influence on truck hunting. Figure 6 illustrates the trend. The value of 450000 ft-lb/rad per spring nest is the nominal torsional spring constant for all simulation runs. This stiffness is reported by Schwam(12) as being that of a typical three-piece truck for small yaw angles between bolster and sideframe.

Schwam also states that the warp stiffness of a truck is drastically reduced when the yaw angle between bolster and sideframe is increased past the value over which static friction has been overcome. This reduction in warp stiffness i.e. secondary yaw stiffness, and its effect on the critical hunting speed is plotted in the figure. Continually reducing the yaw stiffness of the spring nests would eventually reach a limit below which further reductions would not affect the hunting speed.

At the other end of the scale i.e. infinite torsional stiffness, tests have been conducted by the Research Department on rigidized truck frames. It has been reported(13,14) that hunting was observed when these trucks were equipped with 15000 and 21000 lbf/in. shear pads. With 30000 lbf/in. shear

Figure 6: Secondary Yaw Stiffness Influence on Critical Hunting Speed

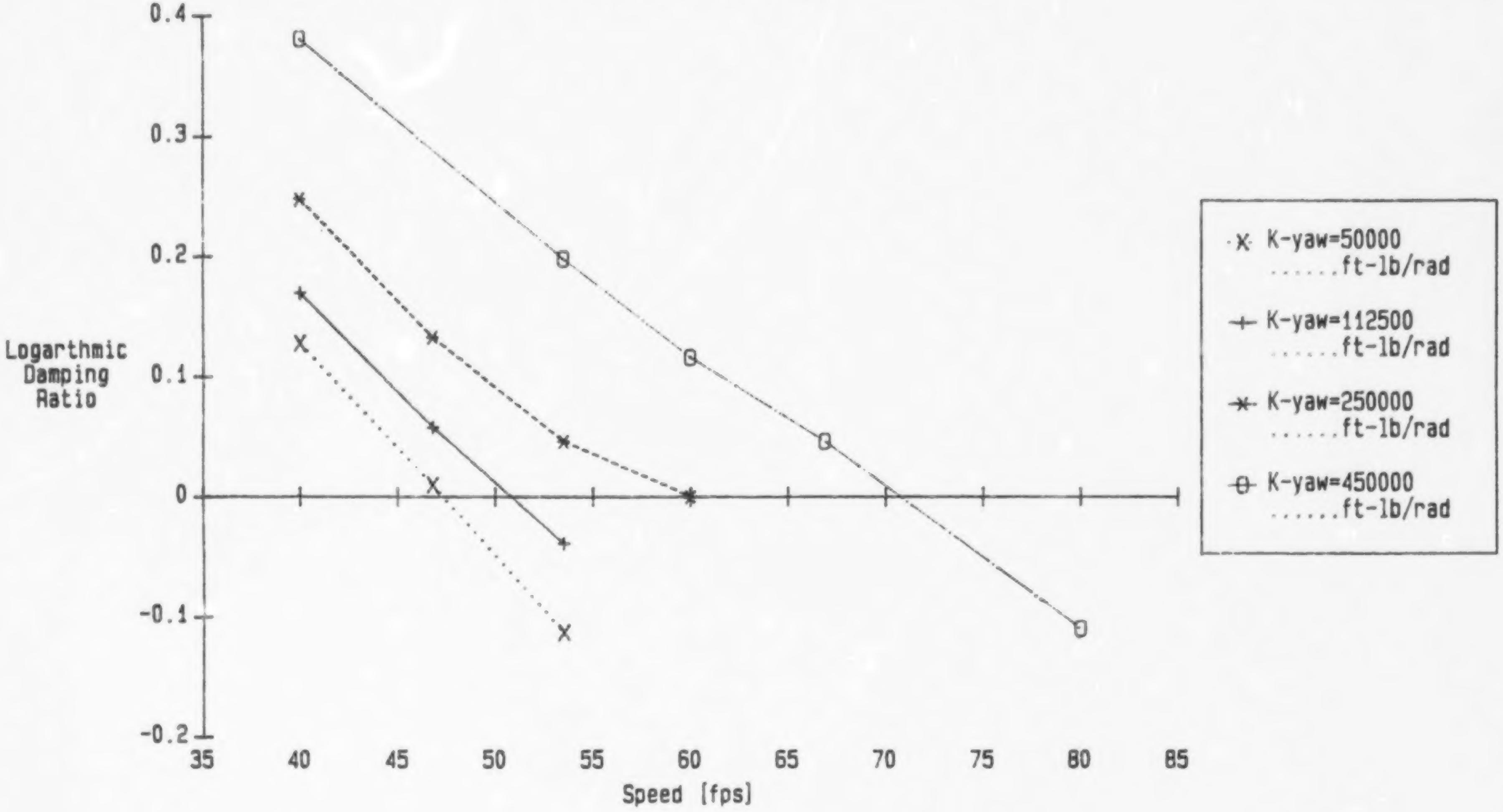

pads truck stability was reported up to 65 mph, the maximum test speed. A partial simulation of these rigidized truck tests was made and indicated that the truck equipped with 30000 lbf/in. shear pads was far more stable than either truck equipped with 15000 or 21000 lbf/in. pads. No critical speeds were obtained.

4.2 Effective Wheel Conicity Study

The critical hunting speed of a bogie is approximately inversely proportional to the square root of the effective conicity. Consequently, lowering the conicity significantly increases the critical speed as seen in Figure 7. With a conicity of 0.2 the simulation output approximately represents worn wheel conditions. Field tests done by CP Research in the fall of 1984(14) involving the same truck configuration as the one presented herein revealed that its critical speed was below 40 mph, the lowest test speed. The simulation estimates this speed at roughly 36 mph (Figure 7).

4.3 Effects of Centerplate Friction on Truck Yaw Hunting

When operating above critical speed truck yaw hunting depends on the magnitudes of the restoring spring forces and the initial disburbances. If these spring forces are large and the disturbances small the yaw amplitudes will remain constant or decay. However, when the forces are great enough to promote friction breakaway at the centerplate yaw hunting will increase till wheel/rail flanging occurs regardless of the yaw stiffness values.

Figure 7: Effective Wheelset Conicity Influence on Critical Hunting Speed

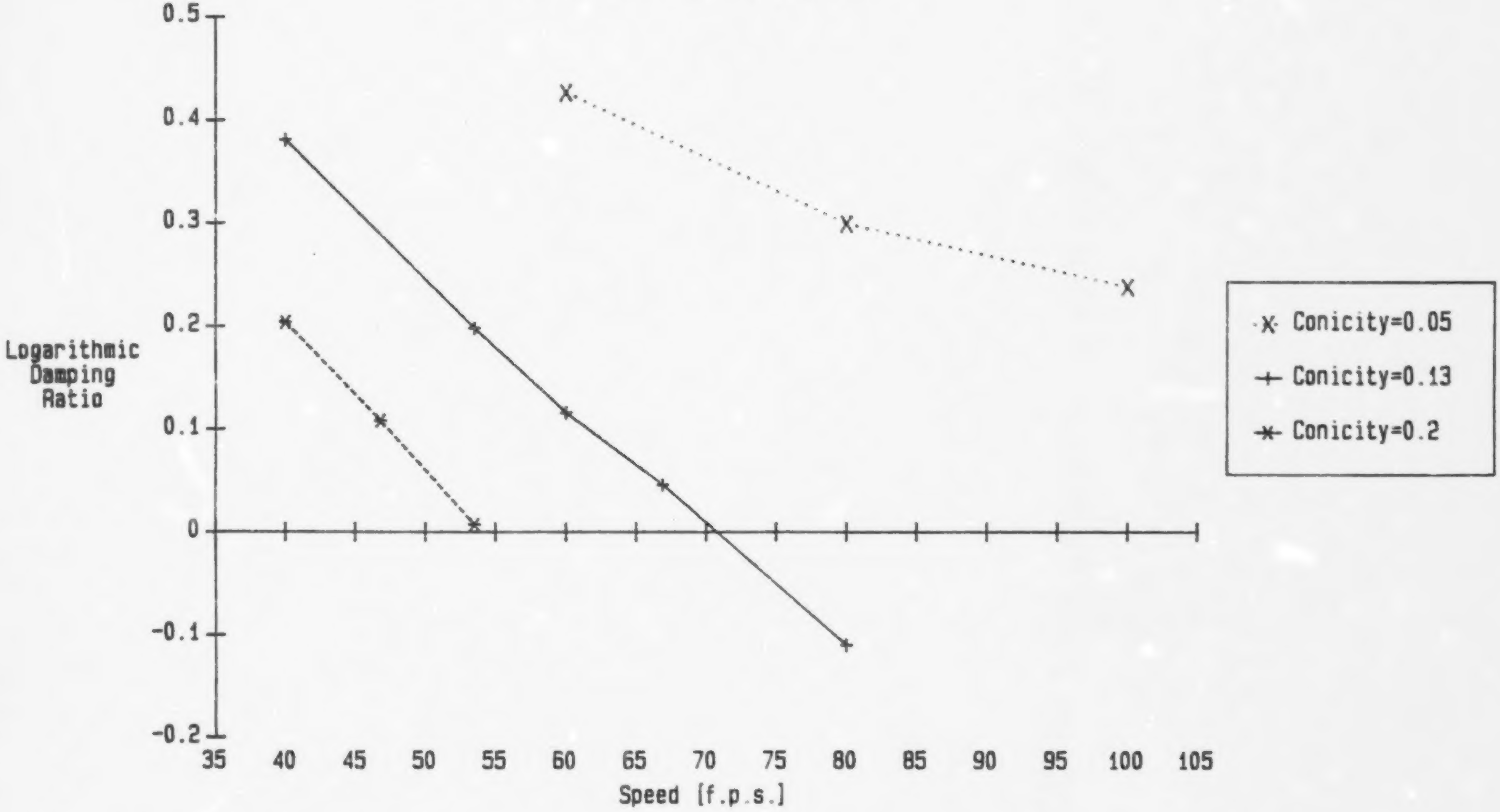

Small centerplate yaw stiffnesses may lead to sustained hunting even if only small displacements are examined.

Woytowich(15) has shown for locomotives that the truck bolster yaw angle increases gradually from the initial displacement when that displacement is "large" regardless of whether the centerplate is modelled by a Coulomb friction pivot or a free pivot provided the truck is travelling above critical speed. Similar yaw hunting behaviour has been observed in freight trucks.

Benefits from centerplate friction may be noticed by significantly increasing or decreasing the effective centerplate yaw stiffness. Doing so results in the yaw amplitude traces of Figures 8 and 9, respectively. Figure 8, the large yaw stiffness, shows that despite a large initial disturbance the yaw amplitudes will decay thus preventing the onset of hunting. For the truck configuration with low centerplate yaw stiffness Figure 9 illustrates yaw amplitude growth due to insufficient restraining forces. This growth occurs despite the small initial disturbance.

Figures 8 and 9 show the affect centerplate or bolster yaw stiffness has on the hunting phenomena and, as reported by Matsudaira(17) and others, is a major stabilizing force in truck hunting behaviour.

Figure 8: Large Centerplate Yaw Stiffness Effects on Bolster Yaw Hunting

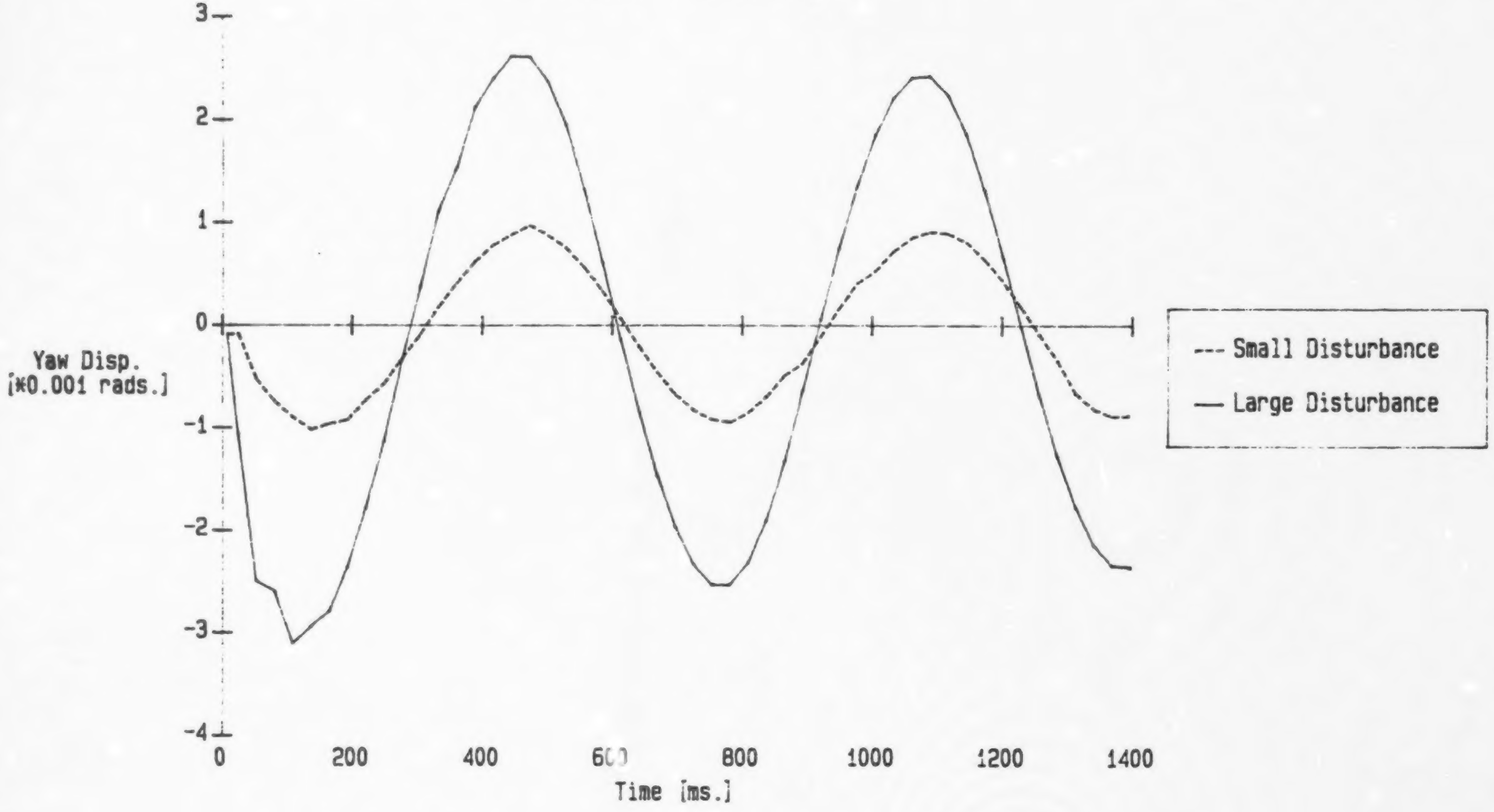

Figure 9: Small Centerplate Yaw Stiffness Effects on Bolster Yaw Hunting

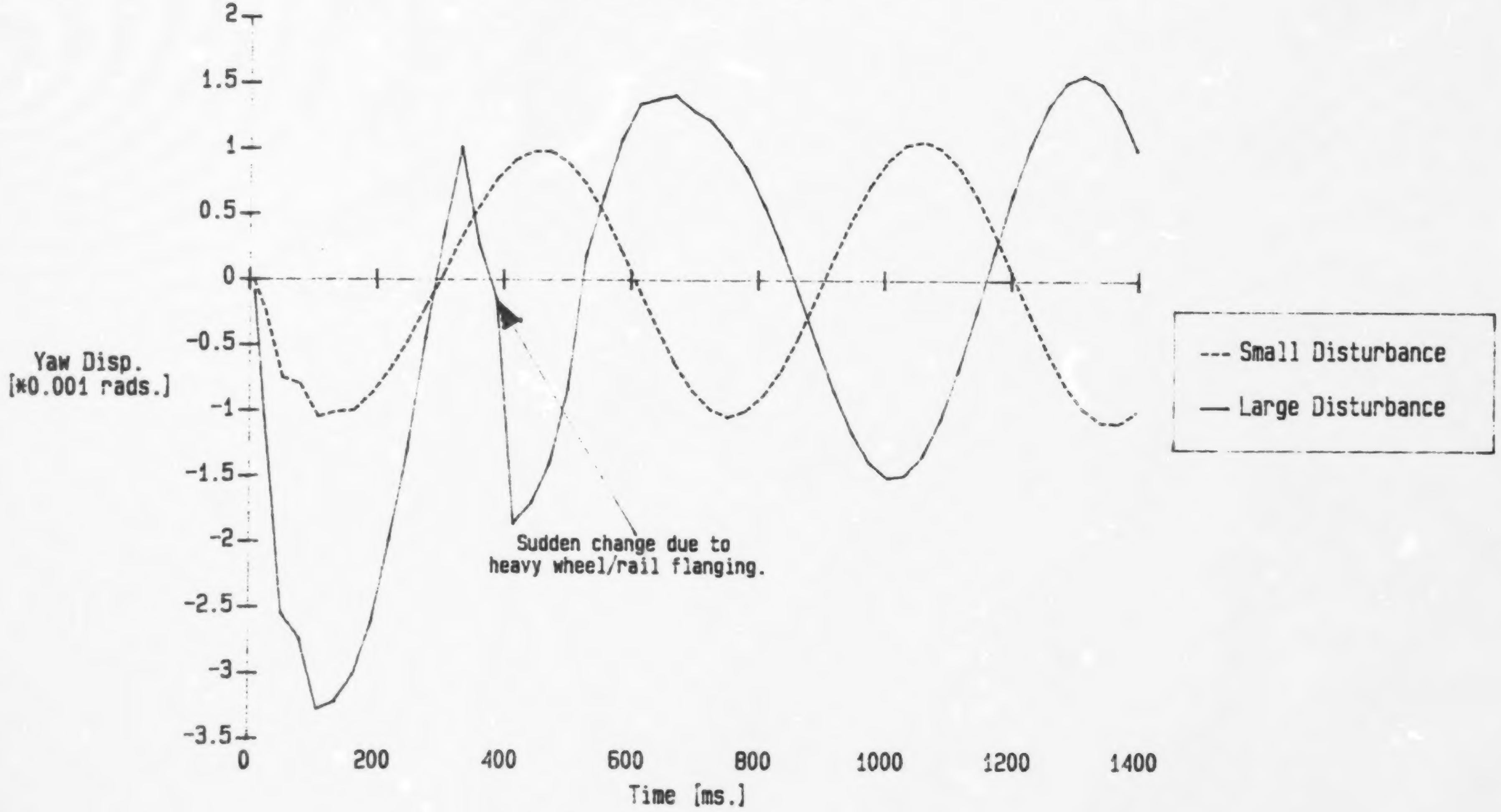
Sudden change due to heavy wheel/rail flanging.

5.0 CONCLUSIONS

1) Simulation outputs have provided trends comparable to other model predictions and field test results. Data from future tangent track tests measuring wheel/rail forces and angles-of-attack may also be used. These data would provide another basis for comparisons and validation by simulating the traffic for which the forces were measured and correlating the field test results with model predictions.

2) Primary and secondary stiffnesses play equally important roles in truck stability. However, their relative contributions to this stability are not one-to-one and attempts to increase suspension stiffnesses at one interface such as the wheelset-sideframe connection will not significantly alter the critical hunting speed if the bolster-sideframe stiffnesses are less predictable/controllable.

3) The use of Vermuelen-Johnson's theory for creep force calculations is sufficiently accurate but requires more computer time than would Kalker's Exact theory. Kalker's Exact theory with the cubic saturation law of Vermuelen-Johnson would provide quick, accurate solutions comparable to DUVOROL or FASTSIM(16) and warrants its future inclusion in the model.

REFERENCES

1. Hedrick, J.K., Arslan, A.V., "Nonlinear Analysis of Rail Vehicle Forced Lateral Response and Stability," Journal of Dynamic Systems, Measurement, and Control, ASME Trans., Vol.101, September 1979, pp. 230-237.

2. Wells, D.A., Lagrangian Dynamics. New York: McGraw-Hill Book Co., 1967.

3. Langhaar, H.L., Energy Methods in Applied Mechanics. New York: John Wiley and Sons, Inc., 1962.

4. Rosval, G., Shaw, M., Dynamic Truck Model: General Description, Department of Research, CP Ltd., Report No. T-813-84, March 1984.

5. Shaw, M., Henderson, C., Contact Geometry Program, Department of Research, CP Ltd., March 1984.

6. Izbinsky, G., Schrekinger, H., Soares, H., A Wheel/Rail Profilometer System, Department of Research, CP Ltd., February 1984.

7. Brann, R.P., "Some Aspects of the Hunting of a Railway Axle," Journal of Sound Vibration, Vol.4, October 1965, pp. 18-32.

8. Vermuelen, P.J., Johnson, K.L., "Contact of Nonspherical Elastic Bodies Transmitting Tangential Forces," Journal of Applied Mechanics, ASME Trans., pp.338-440, June 1964.

9. Dukkipati, R.V., Elasto-Cushion Truck Parametric Study, N.R.C.C., LTR-R-462, July, 1982.

10. Wickens, A.H., "The Dynamics of Railway Vehicles on Straight Track: Fundamental Considerations of Lateral Stability," Proc. Instn. Mech. Engrs., Vol. 180, Pt.3F, 1965-66.

11. Wickens, A.H., "General Aspects of the Lateral Dynamics of Railway Vehicles," Journal of Engineering for Industry, ASME Trans., August 1969, pp.869-878.

12. Schwam, S.A., "Truck Hunting in the Three-Piece Freight Car Truck," Proc. The Economics and Performance of Freight Car Trucks, October 1983, pp.119-133.

13. Gonsalves, R., Izbinsky, G., Soares, H., Hunting and Curving Performance of Rigidized Elasto-Cushion Trucks, Department of Research, CP Ltd., Report No. T-820-84, May 1984.

14. Gonsalves, R., Izbinsky, G., D'Aoust, D., UTDC Frame Braced, Rigidized Elasto-Cushion and Elasto-Cushion Truck Tests, Department of Research, CP Ltd., Report No. T-864-85, March 1985.

15. Woytowich, P.E., Effects of Centerplate Friction on Truck Yaw Hunting and Carbody Lateral Stability, ASME, January 1981.

16. Shen, Z.Y., Hedrick, J.K., Elkins, J.A., "A Comparison of Alternative Creep Force Models for Rail Vehicle Dynamic Analysis," The Dynamics of Vehicles on Roads and on Railway Tracks, Proc. 8th IAVSD-Symposium, August 1983, pp.591-605.

17. Matsudaira, T., "Hunting Problem of High-Speed Railway Vehicles with Special Reference to Bogie Design for the New Tokaido Line", Proc. Instn. Mech. Engrs., Vol. 180, Pt 3F, 1965-66.

Appendix A

Description of Generalized Coordinates

Description of Generalized Coordinates

Coordinate Number	Description	Reference Figure
1	Vertical distance - left sideframe to bolster	A-1
2	Vertical distance - right sideframe to bolster	A-1
3	Yaw angle - left sideframe w.r.t. bolster	A-1
4	Yaw angle - right sideframe w.r.t. bolster	A-1
5,8	Perpendicular distance - leading, trailing wheelset center of mass, resp., to right sideframe C. of M.	A-2
6,9	Parallel distance - leading, trailing wheelset C. of M., resp., to right sideframe C. of M.	A-2
7,10	Yaw angle - leading, trailing wheelset, resp., w.r.t. sideframe longitudinal centerline	A-2
11	Vertical distance - leading right wheel to right sideframe datum line	A-3
12	Vertical distance - trailing right wheel to right sideframe datum line	A-3
13	Vertical distance - leading left wheel to left sideframe datum line	A-3
14	Perpendicular lateral distance of lead wheelset C. of M. to track tangent line	A-4
15	Yaw angle of lead wheelset w.r.t. track tangent line	A-4
16	Angular rotation - lead wheelset	A-2
17	Angular rotation - trail wheelset	A-2

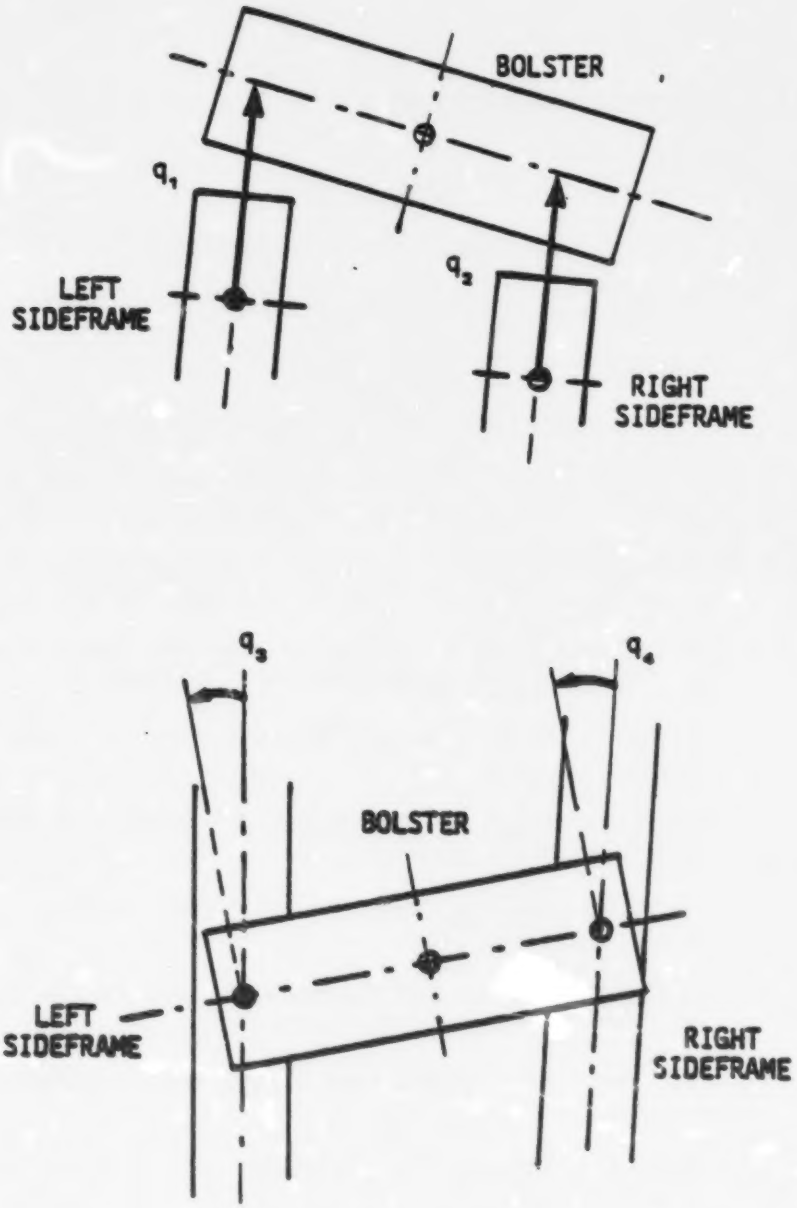
BOLSTER
q1
LEFT SIDEFRAME
q2
RIGHT SIDEFRAME
q3
q4
BOLSTER
LEFT SIDEFRAME
RIGHT SIDEFRAME

Figure A-1

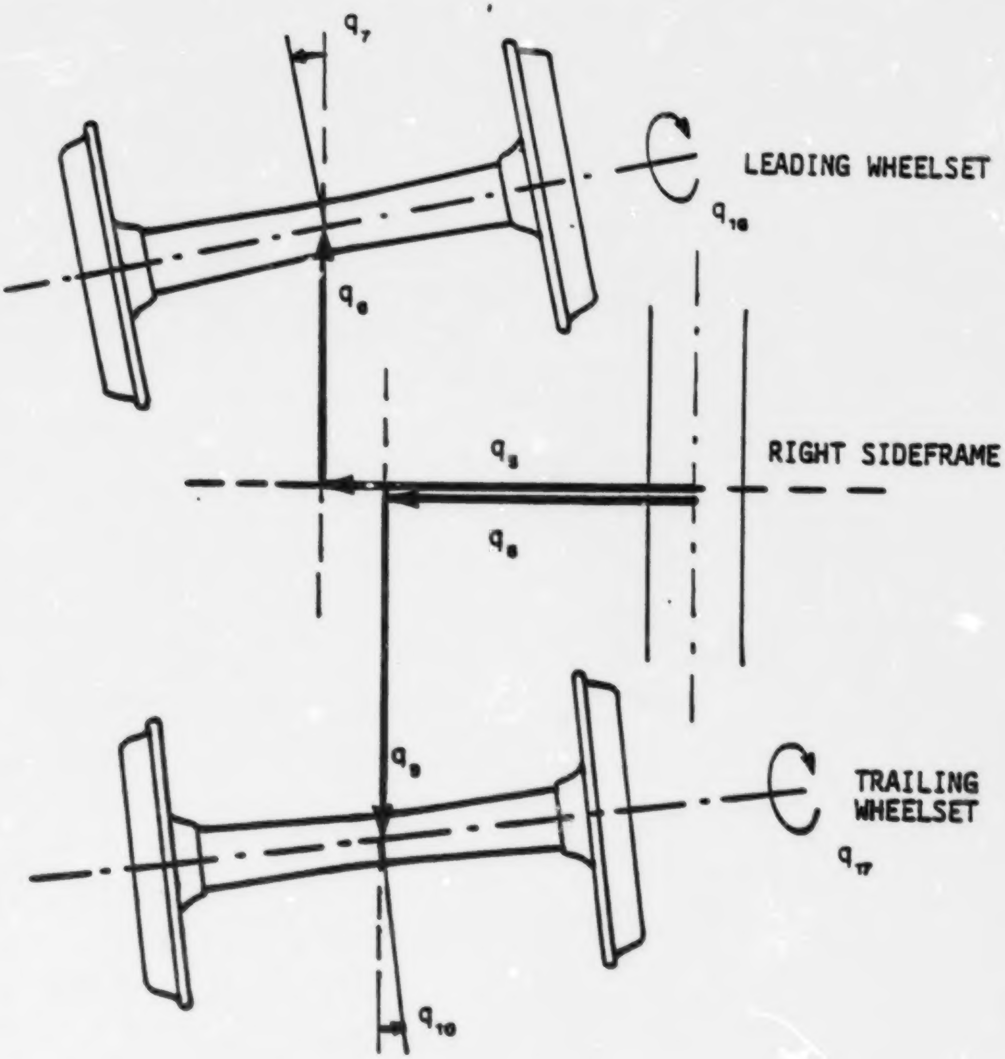
q_7
LEADING WHEELSET
q_{16}
q_6
RIGHT SIDEFRAME
q_5
q_8
q_9
TRAILING WHEELSET
q_{17}
q_{10}

Figure A-2

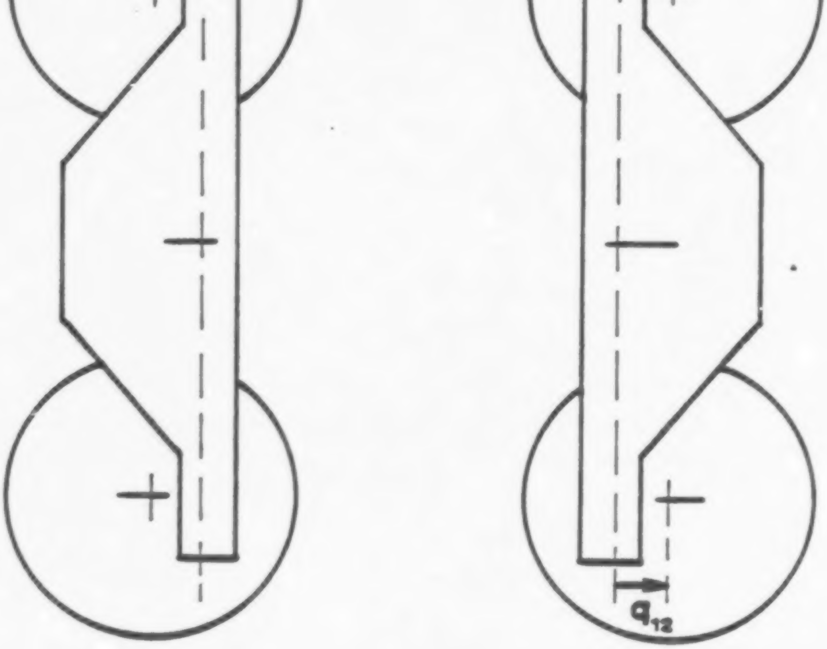

Figure A-3

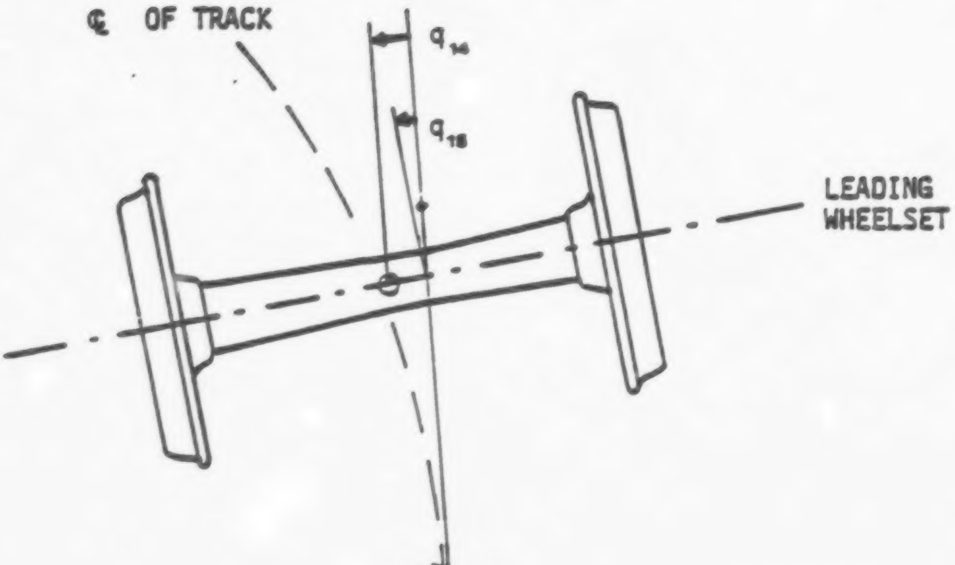
℄ OF TRACK
q_{14}
q_{15}
LEADING
WHEELSET
ξ

Figure A-4

Appendix B

Base Truck Characteristics

Base Truck Characteristics

Mass		
Wheelset		86.956 slugs
Sideframe		34.161 "
Bolster		46.739 "
Inertia		
Wheelset	- yaw	550. slug-ft^2
	- pitch	100. " "
Sideframe	- yaw	80. slug-ft^2
	- pitch	132. " "
Bolster	- yaw	185. slug-ft^2
	- pitch	185. " "
	- roll	185. " "
Suspension Stiffness		
Lateral primary		15000 lb/in
Longitudinal primary		15000 lb/in
Torsional primary		19200 lb-in/rad
Vertical primary		250000 lb/in
Lateral secondary		10000 lb/in
Longitudinal secondary		N/A*
Torsional secondary		5400000 lb-in/rad
Vertical secondary		28645 lb/in
Suspension Damping		
Lateral primary		150 lb-s/in
Longitudinal primary		150 "
Torsional primary		0 "
Vertical primary		0 "
Lateral secondary		300 lb-s/in
Longitudinal secondary		N/A*
Torsional secondary		0 lb-s/ft
Vertical secondary		1500 lb-s/in
Wheelbase		78 in.
Wheel diameter, measured at tapeline		32 in.

* An initial assumption in the development of the model was that no longitudinal motion occurred between the bolster and sideframe. Consequently, no suspension values are necessary for longitudinal secondary stiffness.

IN-SERVICE EVALUATION OF PIGGYBACK CAR TRUCK STABILIZING DEVICES -- INTERIM REPORT

V. Khatchadourian
Planning and Research Department
Canadian Pacific Limited
Montreal

EXECUTIVE SUMMARY

At the request of the Mechanical Department of CP Rail the Planning and Research Department initiated a program to monitor wheel wear performance of piggyback cars equipped with various types of truck stabilizing devices.

A total of 40 piggyback cars were equipped with four types of devices and introduced to revenue service testing. All were equipped with new 33 inch AAR profile wheels at test commencement and new wheel profiles were recorded.

Three groups of piggyback test cars were equipped with Miner and Stucki constant contact side bearings and RDI split wedges (each group of 10 cars with a different type of device). A reference group was equipped with conventional roller type side bearings.

Two major inspections, one after 55,000 miles and another after approximately 110,000 miles were made by CP Research and Mechanical Department personnel. Representatives of Miner and Stucki companies were present during the inspections.

The measurements of wheel wear, obtained by use of a calibrated AAR finger gauge, show that with respect to flange wear rates, a significant reduction in wear rate occurred on all groups of cars between 55,000 and 110,000 miles. In terms of tread wear, all test groups with the exception of RDI split wedges have had a reduction in the rate of tread wear between 55,000 and 110,000 miles. The RDI cars exhibited an increase in the tread wear rate of 21% in the mileage interval 55,000 to 110,000 miles. A possible reason for the decreasing performance of RDI trucks at higher mileages may be loss of "squareness", or reduced warp stiffness. This will be further investigated during a truck tear down test planned to be carried out in the fall of 1985.

With respect to piggyback cars equipped with constant contact side bearings it was observed that the Stucki cars exhibited lower tread wear rates as compared to the Miner cars in the mileage interval between 55,000 and 110,000 miles. Flange wear on both types of devices was comparable.

With respect to total amount of tread wear, both Miner and Stucki constant contact side bearings did not provide any appreciable improvement compared to conventional cars equipped with roller type side bearings. Also both Stucki and Miner cars exhibited the largest variation in wheel performance within the same group i.e. higher incidence of bad performers as compared to conventional cars. RDI split wedges equipped cars also showed substantial variations in wheel wear performance of test cars.

Good and bad performers from each group of cars being tested will be subjected to a tear down inspection this fall to determine the influence of wear of other truck components and truck assembly practices on truck performance.

SOMMAIRE

A la demande des services mécaniques du CP Rail, le bureau de planification et de recherche a entrepris un programme d'observation de l'usure des roues de wagons plats porte remorque équipés de divers types de dispositifs de stabilisation.

Quarante wagons plats porte remorque ont été équipés avec quatre dispositifs de stabilisation et introduits dans le trafic commercial. Au début de l'essai, les wagons furent tous équipés de nouvelles roues de 33 pouces dotées du profil AAR, et de nouveaux profils furent mesurés.

Trois groupes de wagons plats porte remorque d'essais furent équipés de glissoires de traverses danseuses à contact constant des compagnies Miner et Stucki et de cales modifiées de RDI (chaque groupe de 10 wagons ayant été équipé d'un dispositif différent) et un groupe référence fut équipé de palier à roulement conventionnel.

Le personnel du bureau de recherche et des services mécaniques du CP a fait deux inspections approfondies, la première après 55,000 milles, et la deuxième après approximativement 110,000 milles. Des représentants des compagnies Miner et Stucki étaient présents lors des inspections.

Les mesures de l'usure des roues, obtenues avec la jauge AAR de roues indiquent une réduction appréciable de taux d'usure des boudins sur tous les groupes de wagons entre 55,000 et 110,000 milles. Pour l'usure de la surface de roulement, tous les groupes, sauf ceux équipés de cales modifiées RDI, ont eu une diminution de taux d'usure de la surface de roulement entre 55,000 et 110,000 milles. Les wagons RDI ont démontré une augmentation de taux d'usure de la surface de roulement de 21% dans l'intervalle de 55,000 à 118,000 milles. La

détérioration de la performance de bogie RDI, à kilométrage élevé, peut être attribuée à la perte de son équerrage, ou à une diminution de sa rigidité de voilement. Ceci sera examiner lors de l'inspection générale prévue pour l'automne 1985.

En ce qui concerne les wagons plats porte remorque équipés de glissoires de traverses danseuses à contact constant, le taux d'usure de la surface de roulement était moindre pour les wagons Stucki que les wagons Miner, dans l'intervalle de 55,000 à 110,000 milles. L'usure de boudins des deux types de wagons était comparable.

Les wagons équipés de glissoires de traverses danseuses à contact constant de Miner et Stucki n'ont pas produit une amélioration appréciable de l'usure totale de la surface de roulement lorsqu'ils sont comparés aux wagons équipés de paliers à roulement conventionnel. De plus, les wagons Stucki et Miner ont démontré la plus grande variation dans la performance de roues d'un même groupe, c'est à dire, une existance plus fréquente de "mauvaises roues" lorsqu'ils sont comparés aux wagons conventionnels. Les wagons équipés de cales modifiées RDI ont aussi démontré des variations substentielles de l'usure des roues des wagons d'essais.

Des candidats de chaque groupe (bons et mauvais) des wagons d'essais seront soumis à une inspection générale en automne '85 afin de déterminer l'influence de l'usure des autres composantes et des pratiques d'assemblage des bogies sur la performance des bogies.

TABLE OF CONTENTS

PAGE

EXECUTIVE SUMMARY 452

TABLE OF CONTENTS 456

LIST OF TABLES 457

LIST OF FIGURES 458

1.0 INTRODUCTION 459

2.0 DESCRIPTION OF TRUCK STABILIZING DEVICES 460

- 2.1 Miner Constant Contact Side Bearings 460
- 2.2 Stucki Constant Contact Side Bearings 460
- 2.3 RDI Split Wedges 460

3.0 WHEEL WEAR MEASUREMENTS AFTER 55,000 MILES OF OPERATION 461

4.0 SUMMARY OF WHEEL WEAR RESULTS AFTER 55,000 MILES OF SERVICE 467

5.0 WORN WHEEL PROFILES 468

6.0 WHEEL WEAR MEASUREMENTS AFTER 110,000 MILES OF OPERATION 469

7.0 CONCLUSIONS 471

LIST OF TABLES

NUMBER	DESCRIPTION	PAGE
1	Piggyback Cars Equipped With Roller Type Side Bearings - Wheel Wear Results Obtained With Use Of a Finger Gauge	462
2	Piggyback Cars Equipped With Miner Side Bearings - Wheel Wear Results Obtained With Use Of a Finger Gauge	463
3	Piggyback Cars Equipped With Stucki Side Bearings - Wheel Wear Results Obtained With Use Of a Finger Gauge	464
4	Piggyback Cars Equipped With RDI Split Wedges - Wheel Wear Results Obtained With Use Of a Finger Gauge	465
5	Summary Of Wheel Wear Measurements After Approximately 110,000 Miles Of Operation	466
6	Summary of Wheel Wear Measurements	470

LIST OF FIGURES

NUMBER	DESCRIPTION	PAGE
1	Wheel Profiles Of Piggyback Car CP 504605 After 52,906 Miles Of Revenue Service Operation	472
2	Wheel Profiles Of Piggyback Car CP 505012 After 51,817 Miles Of Revenue Service Operation	473
3	Wheel Profiles Of Piggyback Car CP 504722 After 63,945 Miles Of Revenue Service Operation	474
4	Wheel Profiles Of Piggyback Car CP 504249 After 45,562 Miles of Revenue Service Operation	475
5	Wheel Profiles Of Piggyback Car CP 504599 After 43,464 Miles Of Revenue Service Operation	476
6	Wheel Profiles Of Piggyback Car CP 504019 After 68,220 Miles Of Revenue Service Operation	477
7	Wheel Profiles Of Piggyback Car CP 505345 After 53,126 Miles Of Revenue Service Operation	478
8	Wheel Profiles Of Piggyback Car CP 505618 After 40,000 Miles of Revenue Service Operation	479

1.0 INTRODUCTION

At the request of the Mechanical Department of CP Rail, the Planning and Research Department initiated a program to monitor wheel wear performance of piggyback cars equipped with various types of truck stabilizing devices.

A total of forty (40) test cars were assigned to revenue service testing. All 40 test cars were equipped with new 33 inch AAR profile wheels at test commencement. The 40 test cars constituted four different groups. Three groups of piggyback test cars (10 cars per group) each with a different type of truck stabilizing device and a fourth group (10 cars) with conventional trucks with roller type side bearings were placed in revenue service testing to evaluate the effectiveness of the devices in reducing wheel wear and other truck component wear.

Of the three groups equipped with truck stabilizing devices, two were of the constant contact side bearing type, one Miner and the other Stucki, and the third group had RDI split wedges.

Prior to release of test cars into general service for testing CP Rail Mechanical and shop personnel carried out initial truck and carbody measurements. These measurements included bolster gib clearances, side frame column width and initial friction wedge measurements, and side bearing clearances. Wheels of eight test cars, two from each group, were initially measured by the wheel profilometer while all 40 test cars were initially gauged with an AAR calibrated finger gauge.

This report presents wheel wear results obtained from calibrated finger gauge measurements after 55,000 and 110,000 miles of revenue service testing and also provides worn wheel profiles of typical cars from each group after approximately 55,000 miles of revenue service. A final report will include the results of truck tear down inspection and actual worn wheel profiles after 110,000 miles of revenue service testing.

2.0 DESCRIPTION OF TRUCK STABILIZING DEVICES

2.1 Miner Constant Contact Side Bearings

Miner constant contact side bearings are retrofit components which fit in the existing side bearing cage. It is composed of a metal top cap attached to the rubber component and housed between two metal stops. The elastomeric pad provides a specific preload when deflected to 5-1/16" installed height. The rubber block provides a preload of 5,200 to 5,600 lbs depending upon type of truck i.e. 50 or 70 ton.

2.2 Stucki Constant Contact Side Bearings

Stucki constant contact side bearings consist of replacement components which fit in an existing side bearing cage. These components are: a pair of resilient blocks, a standard 4 inch diameter Stucki roller and a pair of steel cage end closures. The elastomeric pads, which in this case are directly in contact with the carbody wear plate (no metal top), are deflected to 5-1/16" installed height to provide a preload of between 5,000 to 7,000 lbs.

2.3 RDI Split Wedges

RDI split wedges are replacement components for conventional friction wedges of a three piece truck. They can be retrofitted to an existing truck whose bolster is modified with the addition of pyramid shaped members of the bolster gibs in order to provide bearing area with the split wedges.

This arrangement increases the warp stiffness of the truck thus giving increased hunting threshold speed. Tests carried out by the Mechanical Department of CP Rail indicated that initially, when wedges are newly applied, no stiffness improvement is obtained. Tests with a truck equipped with split wedges which have been operating in service and hence have been broken in', show that the truck does in fact exhibit increased frame stiffness.

3.0 WHEEL WEAR MEASUREMENTS AFTER 55,000 MILES OF OPERATION

On completion of approximately 55,000 miles of revenue service operation, all 40 test cars were called to Lachine Intermodal Yard, one group at a time, for inspection and wheel profile measurements.

Representatives from both Miner and Stucki companies were present during this first inspection. They also assisted CP Research and Mechanical personnel in collecting wheel wear measurements. Inspection of Miner and Stucki constant contact side bearings was also carried out jointly.

The RDI trucks were last inspected on September 1984 as they were introduced later to revenue service testing because of a delay in the supply of RDI wedges. No representative from RDI was present during the inspection.

The results of finger gauge measurements carried out on test wheels of four groups of piggyback cars are shown in Tables 1 to 4. Table 1 shows the average flange and tread wear of all wheels of each car, as well as the flange and tread wear rates for each car between zero and approximately 55,000 miles of service. Tables 2, 3 and 4 show the same results for the groups of cars equipped with Miner, Stucki and RDI split wedges respectively.

To compute average flange and tread wear for each car, all wheel wear data were considered. As mileages of test cars within a group were not all identical, and in order to be able to establish a base to compare wheel wear performance of cars within the same group and comparative performance between groups, every test car's flange and tread wear rate per 10,000 miles of service was established and is shown in Tables 1 to 4. An overall flange and tread wear as well as wear rates were also established for each of the 4 test groups. The results are summarized in Table 5.

TABLE 1: Piggyback Cars Equipped With Roller Type Side Bearings - Wheel Wear Results Obtained With the Use of a Finger Gauge

Test Car	Car Number	Accumulated Mileage	Average Flange Wear (Inches)	Average Tread Wear (Inches)	Flange Wear Per 10,000 Miles	Tread Wea Per 10,000 Miles
01	CP 504605	52,906	.055	.105	.0104	.0198
02	CP 505012	51,817	.093	.076	.0179	.0147
03	CP 505170	57,413	.092	.105	.0160	.0182
04	CP 505054	50,775	.053	.148	.0104	.0291
05	CP 505505	40,953	.078	.105	.0190	.0256
06	CP 505004	26,851	.100	.043	.0372	.0160
07	CP 505005	38,796	.103	.086	.0265	.0221
08	CP 505519	48,810	.084	.117	.0172	.0239
09	CP 504483	69,115	.134	.088	.0194	.0127
10	CP 505217	65,702	.097	.100	.0148	.0152
Average of All Test Cars in This Group		52,920	.089	.106	.0168	.0201

Notes:

1. Data obtained during first scheduled piggyback car inspection carried out in July 1984 at CP Rail's Lachine Intermodal Yard.
2. Data from test car CP 505004 was not included in computations of group average wheel wear because of relatively low mileage.

TABLE 2: Piggyback Cars Equipped With Miner Side Bearings - Wheel Wear Results Obtained With the Use of a Finger Gauge

Test Car	Car Number	Accumulated Mileage	Average Flange Wear (Inches)	Average Tread Wear (Inches)	Flange Wear Per 10,000 Miles	Tread Wear Per 10,000 Miles
11	CP 504722	63,945	.147	.093	.0229	.0146
12	CP 504249	45,562	.156	.123	.0342	.0270
13	CP 505295	53,177	.147	.061	.0276	.0114
14	CP 504159	56,530	.109	.082	.0193	.0145
15	CP 505330	41,503	.122	.078	.0294	.0188
16	CP 505986	54,665	.100	.127	.0183	.0232
17	CP 505620	50,289	.134	.105	.0266	.0209
18	CP 505309	54,307	.097	.115	.0178	.0211
19	CP 505080	48,053	.106	.098	.0220	.0204
20	CP 505283	49,870	.093	.092	.0188	.0184
Average of All Test Cars In This Group		51,790	.121	.097	.0237	.0190

Note: Data obtained during first scheduled piggyback car inspection carried out in June 1984 at CP Rail's Lachine Intermodal Yard.

TABLE 3: Piggyback Cars Equipped With Stucki Side Bearings - Wheel Wear Results Obtained With the Use of a Finger Gauge

Test Car	Car Number	Accumulated Mileage	Average Flange Wear (Inches)	Average Tread Wear (Inches)	Flange Wear Per 10,000 Miles	Tread Wea Per 10,00 Miles
21	CP 504599	43,464	.100	.123	.0230	.0283
22	CP 504019	68,220	.081	.182	.0119	.0266
23	CP 505063	42,835	.087	.056	.0204	.0130
24	CP 505209	67,082	.126	.060	.0188	.0090
25	CP 505160	62,466	.103	.097	.0165	.0155
26	CP 505376	55,765	.091	.092	.0163	.0165
27	CP 505280	49,349	.081	.171	.0164	.0346
28	CP 505247	47,238	.119	.072	.0251	.0152
29	CP 505314	63,222	.087	.109	.0138	.0173
30	CP 504061	53,169	.117	.068	.0220	.0128
Average of All Test Cars In This Group		55,281	.099	.103	.0184	.0188

Note: Data obtained during first scheduled piggyback car inspection carried out in June 1984 at CP Rail's Lachine Intermodal Yard.

TABLE 4: Piggyback Cars Equipped With RDI Split Wedges - Wheel Wear Results Obtained With the Use of a Finger Gauge

Test Car	Car Number	Accumulated Mileage	Average Flange Wear (Inches)	Average Tread Wear (Inches)	Flange Wear Per 10,000 Miles	Tread Wear Per 10,000 Miles
31	CP 505345	53,126	.140	.066	.0263	.0124
32	CP 505618	39,565	.140	.053	.0353	.0134
33	CP 505552	62,388	.139	.055	.0222	.0090
34	CP 505621	69,353	.170	.082	.0245	.0118
35	CP 505567	60,660	.159	.060	.0262	.0099
36	CP 505590	61,003	.131	.068	.0215	.0111
37	CP 505249	69,719	.165	.084	.0236	.0120
38	CP 505208	56,875	.159	.076	.0279	.0133
39	CP 505117	54,840	.135	.062	.0246	.0114
40	CP 505332	42,295	.150	.074	.0354	.0175
Average of All Test Cars In This Group		56,982	.149	.068	.02675	.0120

Note: Data obtained during first scheduled piggyback car inspection carried out on this group of test cars in September 1984 at CP Rail's Lachine Intermodal Yard.

TABLE 5: Summary of Wheel Wear Measurements
After Approximately 55,000 Miles of Operation

Test Group	Average Mileage	Flange Wear (Inches)	Tread Wear (Inches)	Avg. Flange Wear Rate Per 10,000 Miles	Avg. Tread Wear Rate Per 10,000 Miles
Conventional Side Bearings	52,920	.089	.106	.0168	.0201
Miner Side Bearings	51,790	.123	.098	.0237	.0190
Stucki Side Bearings	55,281	.102	.104	.0184	.0188
RDI Split Wedges	56,982	.152	.068	.02675	.0120

4.0 SUMMARY OF WHEEL WEAR RESULTS AFTER 55,000 MILES OF SERVICE

Wheel wear results obtained from calibrated finger gauge measurements after approximately 55,000 miles of revenue service operation are shown, in Table 5, for each group of cars.

From these results the following observations can be made after 55,000 miles of revenue service operation:

- Trucks with RDI split wedges exhibited a 40% reduction in tread wear but a 60% increase in flange wear compared to conventional trucks. As most 33 inch wheels presently in piggyback service are condemned for high flange (high speed tangent track operation), a reduction in tread wear is considered a definite improvement. However, wheels of trucks equipped with RDI split wedges experienced accelerated flange wear and therefore it is expected that these wheels will be condemned for flange limit exceedence. Unless the flange wear rate is drastically reduced at higher mileages (see section on wear rates between 55,000 and 110,000 miles), the RDI wedges are considered to offer no benefit overall.

- Miner and Stucki constant contact side bearings performed nearly identically with respect to tread wear. Compared to cars equipped with conventional roller type side bearings, there was a very slight tread wear reduction.

- Flange wear on cars equipped with Miner constant contact side bearings was higher than that on Stucki cars. Both Miner and Stucki car wheels exhibited higher flange wear than cars equipped with conventional roller type side bearings.

Wheel wear results obtained after 55,000 miles of service operation show that none of the stabilizing devices provide significantly better wheel wear results except for the RDI retrofit which appeared to have reduced tread wear at the expense of increased flange wear.

The results of wheel wear after an additional 65,000 miles of revenue service operation were somewhat different as described in the next section. Hence the above mentioned summary observations only apply to the initial 55,000 miles of operation. Wear rates differ at higher mileages thus providing a somewhat different picture of the relative performance of the three groups of test cars in relation to the reference group equipped with conventional roller type side bearings.

5.0 WORN WHEEL PROFILES

Out of the forty (40) test cars, eight cars (2 from each group) were monitored for wheel wear utilizing the CP Research Department wheel profilometer.

Initial new wheel profiles on 32 wheelsets with roller bearings and new 33 inch AAR profile wheels were collected by Research personnel at Weston Shops. These wheelsets were identified by marking left and right hand wheels and test car numbers for application on appropriate piggyback test cars.

During first and second truck inspections worn wheel profiles were also collected by CP Research personnel. Worn wheel profiles from the eight cars after approximately 55,000 miles of revenue service were processed and are presented in Figures 1 to 8. Worn wheel profiles at higher mileages (up to 118,000 miles) will be presented in the final report of this study together with results of a truck tear down inspection scheduled to be carried out in the fall of 1985.

From the results of the wheel profiles shown in Figures 1 to 8 it can be clearly observed that the tread wear on wheels of the RDI retrofit trucks is considerably lower than the other two groups equipped with constant contact side bearings. The conventional car wheels exhibited fairly uniform wheel tread and flange wear patterns whereas cars equipped with constant contact side bearings had one or more wheels exhibiting somewhat higher wheel wear as compared to the rest of wheels in that group. The reason for this is not known, however, it is suspected that it may be the result of a skewed truck position, perhaps due to an alignment problem with the constant contact device.

6.0 WHEEL WEAR MEASUREMENTS OBTAINED AFTER APPROXIMATELY 110,000 MILES OF OPERATION

The test cars were inspected by CP Research and Mechanical Department personnel from March to May, 1985 after having accumulated 113,000, 118,000, 118,000 and 108,000 miles on the conventional, Miner, Stucki and RDI cars, respectively. Wheel profilometer and calibrated finger gauge measurements were made. The finger gauge measurements are reported here; wheel profilometer information will be reported in the final report, with truck tear down and inspection information.

Table 6 shows the results of wheel wear measurements performed after about 55,000 and 110,000 miles for each of the groups of cars being tested.

TABLE 6: Summary of Wheel Wear Measurements

				Average Flange Wear Rate		Average Tread Wear Rate	
Test Group	Average Mileage	Flange Wear (Inches)	Tread Wear (Inches)	Zero-55,000 (Miles)	55,000-110,000 (Miles)	Zero-55,000 (Miles)	55,000-110,000 (Miles)
Conventional	113,000	.091	.178	.0168	.0003	.0201	.0120
Miner	118,000	.138	.202	.0237	.0022	.0190	.0157
Stucki	118,000	.098	.183	.0184	zero	.0188	.0126
RDI	108,000	.147	.142	.0267	zero	.0120	.0145

7.0 CONCLUSIONS (After Approximately 110,000 Miles of Service Operation)

1. With respect to flange wear rates between 55,000 and 110,000 miles, a significant reduction in the rate of wear has occurred on all groups of test cars. Only the Miner cars, and conventional cars to a lesser extent, exhibited a limited amount of additional flange wear between 55,000 and 110,000 miles.

2. With respect to total amount of flange metal loss after approximately 110,000 miles of revenue service operation, the RDI cars have the largest amount of flange metal loss. It should be noted that accelerated flange wear on RDI car wheels occurred during the first 55,000 miles of operation.

3. In terms of tread wear rate all test groups, with the exception of the RDI split wedge group, have had a reduction in the rate of tread wear between 55,000 and 110,000 miles of operation. The most significant reduction in the rate of tread wear was observed on conventional cars where the rate decreased by 40% between 55,000 and 110,000 miles of operation.

4. Within the groups of cars equipped with constant contact side bearings, the Stucki cars exhibited a 33% reduction in tread wear rate compared to 17% reduction for the Miner cars between 55,000 and 110,000 miles of operation. The RDI cars on the other hand, exhibited a 21% increase in tread wear rate between 55,000 and 110,000 miles of operation.

5. With respect to total amount of tread metal loss after approximately 110,000 miles of operation, cars equipped with constant contact side bearings and reference cars with conventional side bearings have equivalent amount of tread metal loss. The RDI cars still show the lowest amounts of tread metal removal because of the significantly lower tread wear rate experienced during the first 55,000 miles of operation.

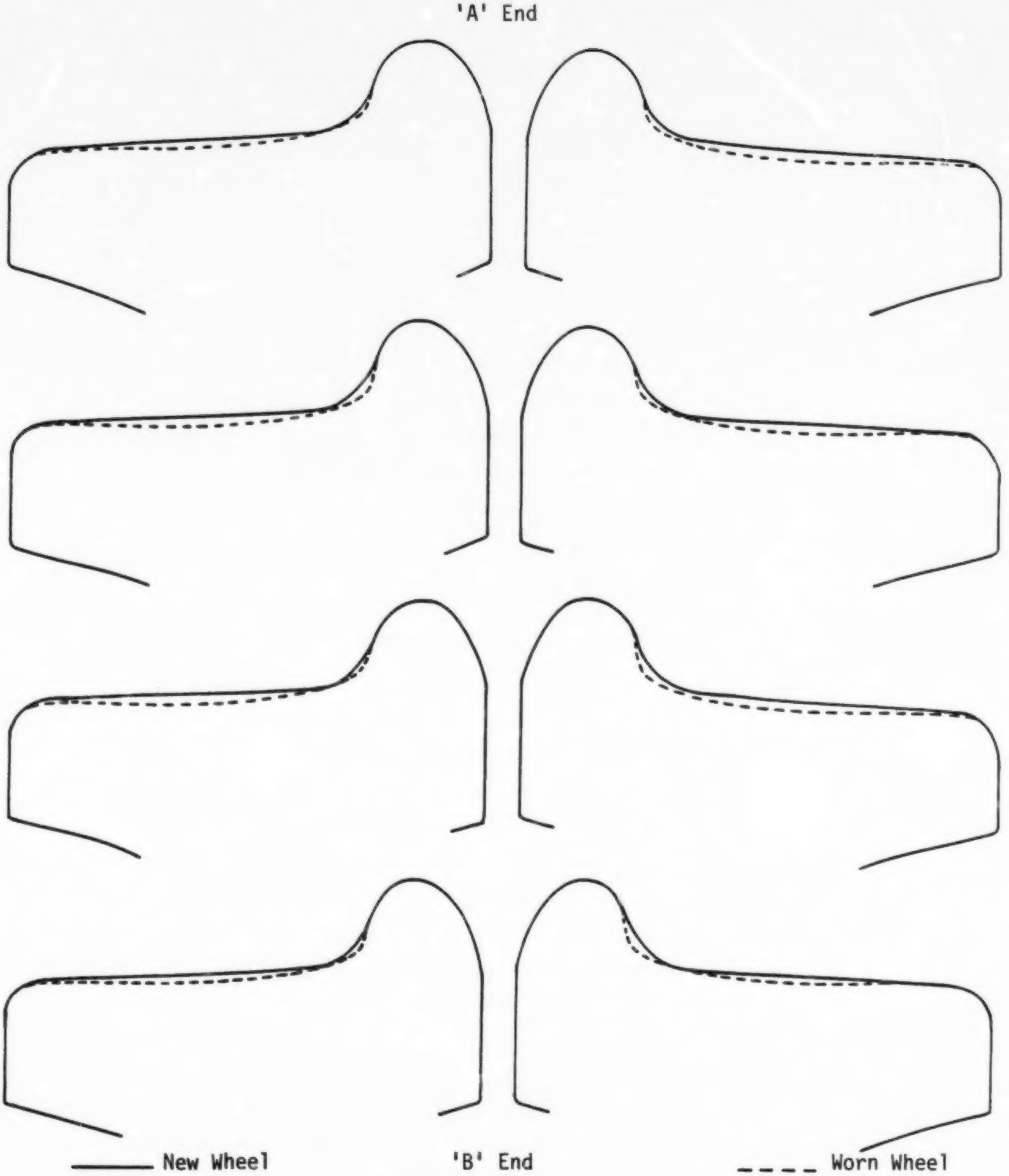
'A' End
New Wheel
'B' End
Worn Wheel

Car Number: CP 504605 Test Car: 01 Group: Conventional

Figure 1: Wheel Profiles of Piggyback Car CP 504605
After 52,906 Miles of Revenue Service Operation

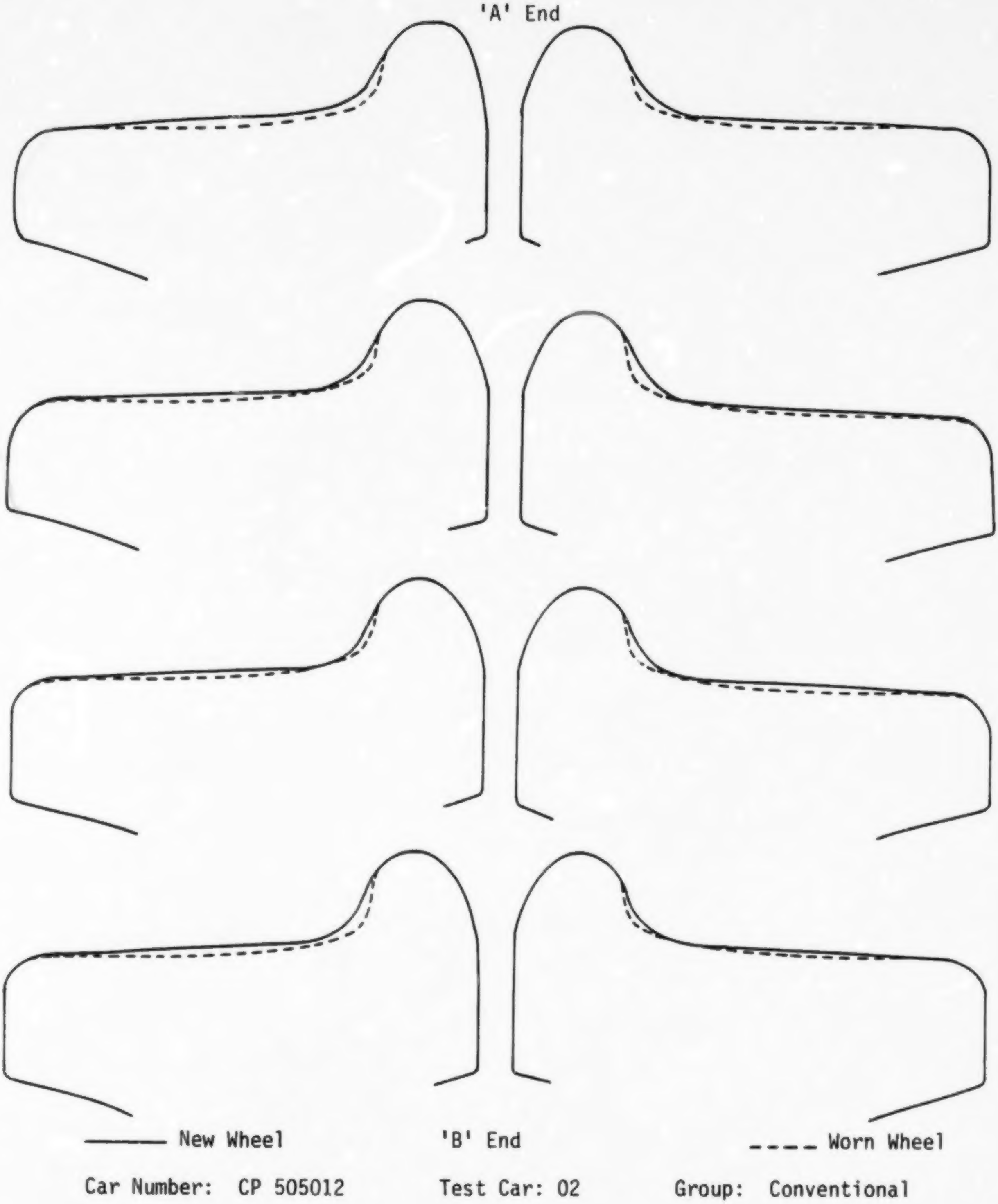
'A' End
New Wheel
'B' End
Worn Wheel
Car Number: CP 505012
Test Car: 02
Group: Conventional

Figure 2: Wheel Profiles of Piggyback Car CP 505012
After 51,817 Miles of Revenue Service Operation

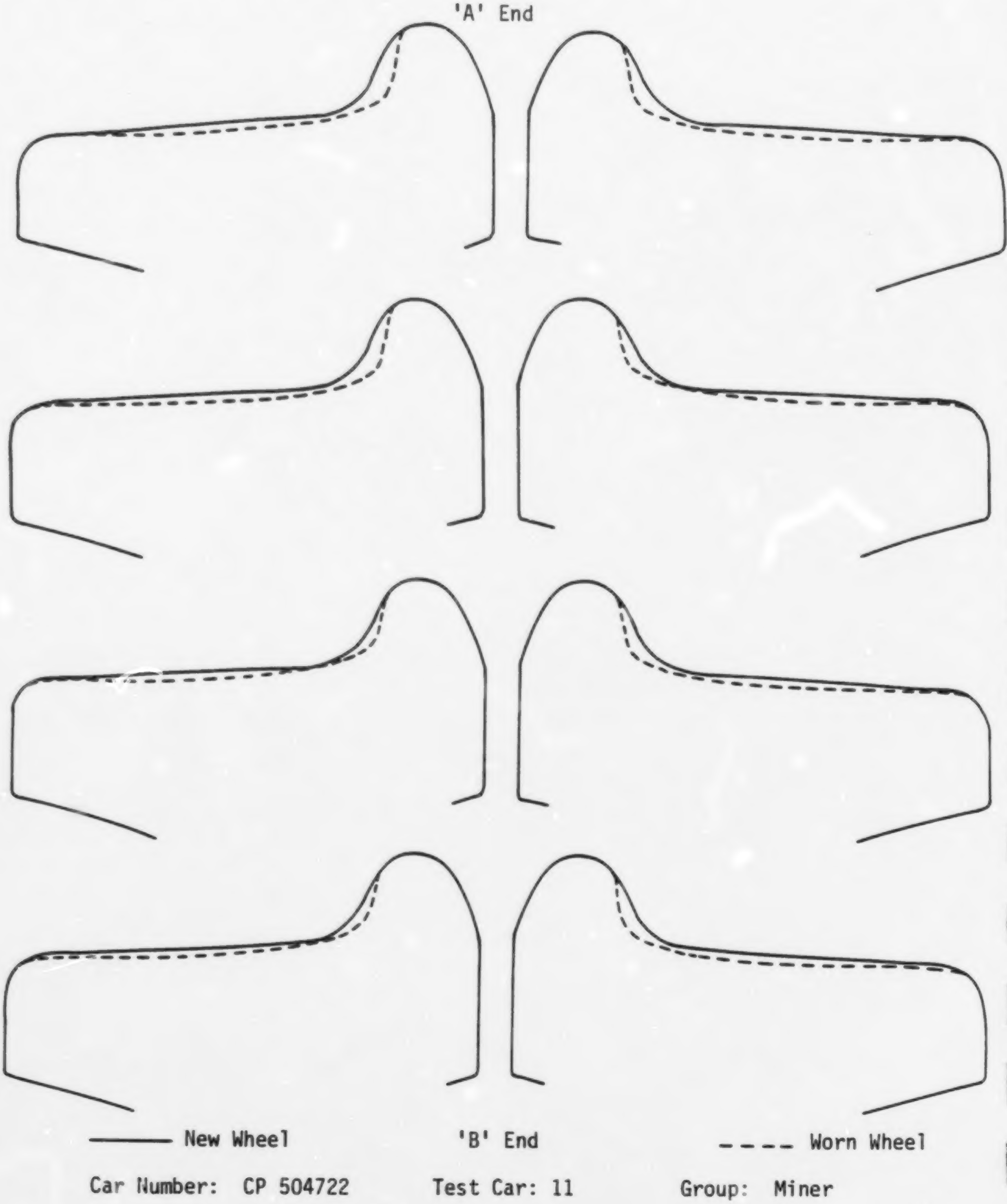
'A' End
New Wheel
'B' End
Worn Wheel
Car Number: CP 504722
Test Car: 11
Group: Miner

Figure 3: Wheel Profiles of Piggyback Car CP 504722
After 63,945 Miles of Revenue Service Operation

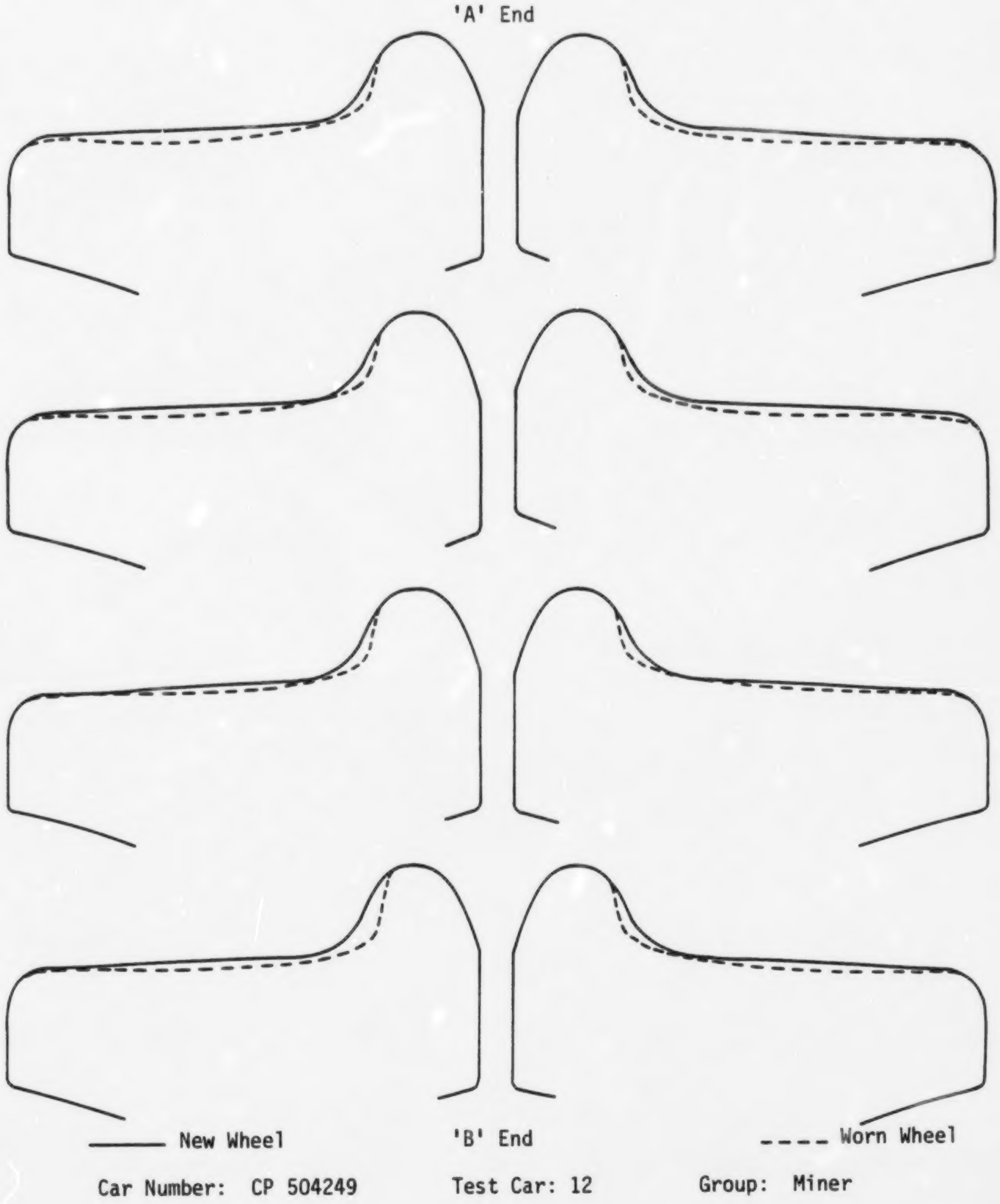
'A' End
New Wheel
'B' End
---- Worn Wheel
Car Number: CP 504249
Test Car: 12
Group: Miner

Figure 4: Wheel Profiles of Piggyback Car CP 504249
After 45,562 Miles of Revenue Service Operation

'A' End

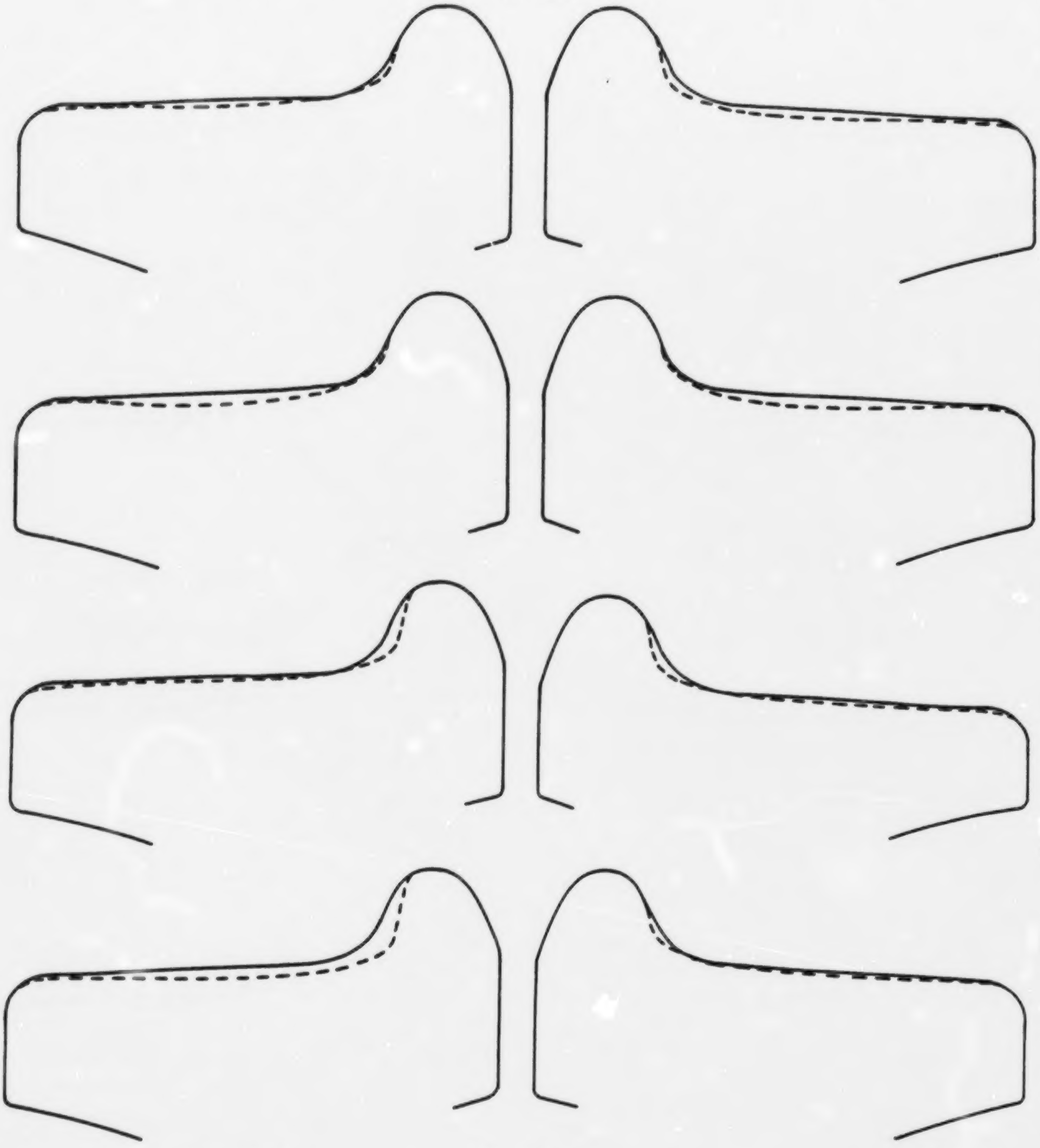

——— New Wheel
'B' End
- - - - Worn Wheel

Car Number: CP 504599 Test Car: 21 Group: Stucki

Figure 5: Wheel Profiles of Piggyback Car CP 504599
After 43,464 Miles of Revenue Service Operation

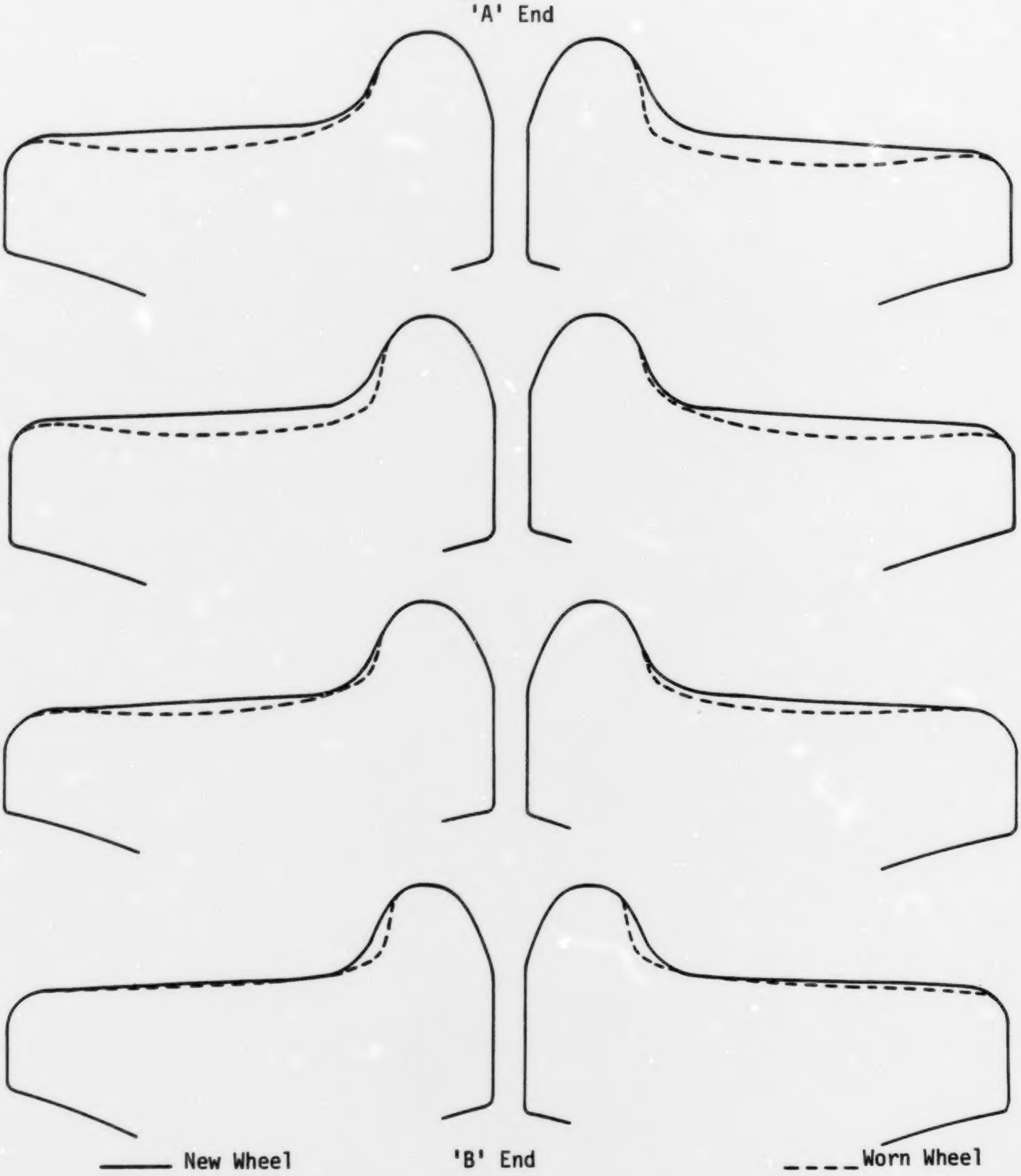
'A' End
New Wheel
'B' End
Worn Wheel

Car Number: CP 504019 Test Car: 22 Group: Stucki

Figure 6: Wheel Profiles of Piggyback Car CP 504019 After 68,220 Miles of Revenue Service Operation

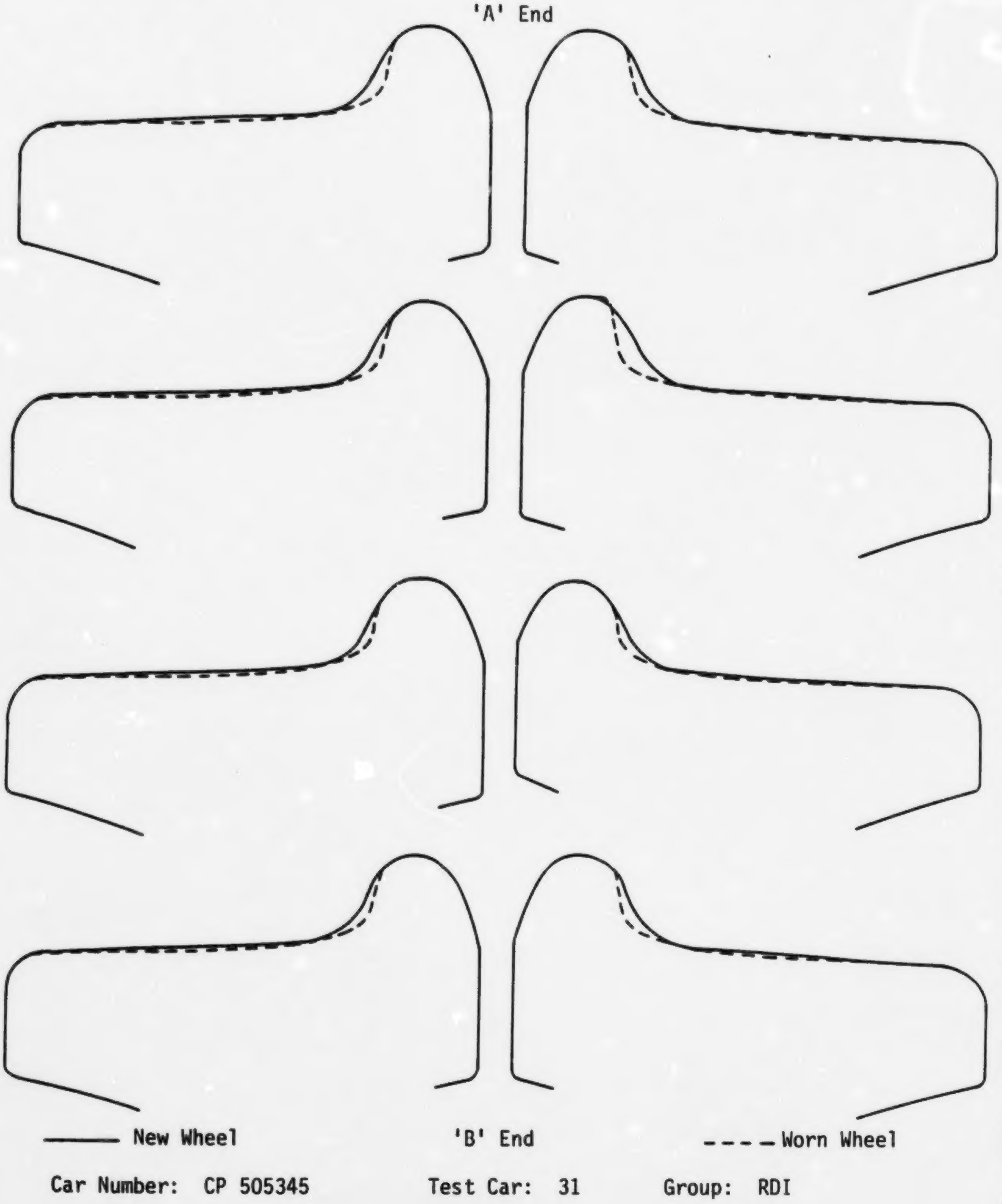
'A' End
New Wheel
'B' End
Worn Wheel
Car Number: CP 505345
Test Car: 31
Group: RDI

Figure 7: Wheel Profiles of Piggyback Car CP 505345
After 53,126 Miles of Revenue Service Testing

'A' End

L4/R4 Worn Wheel Profiles Not Available

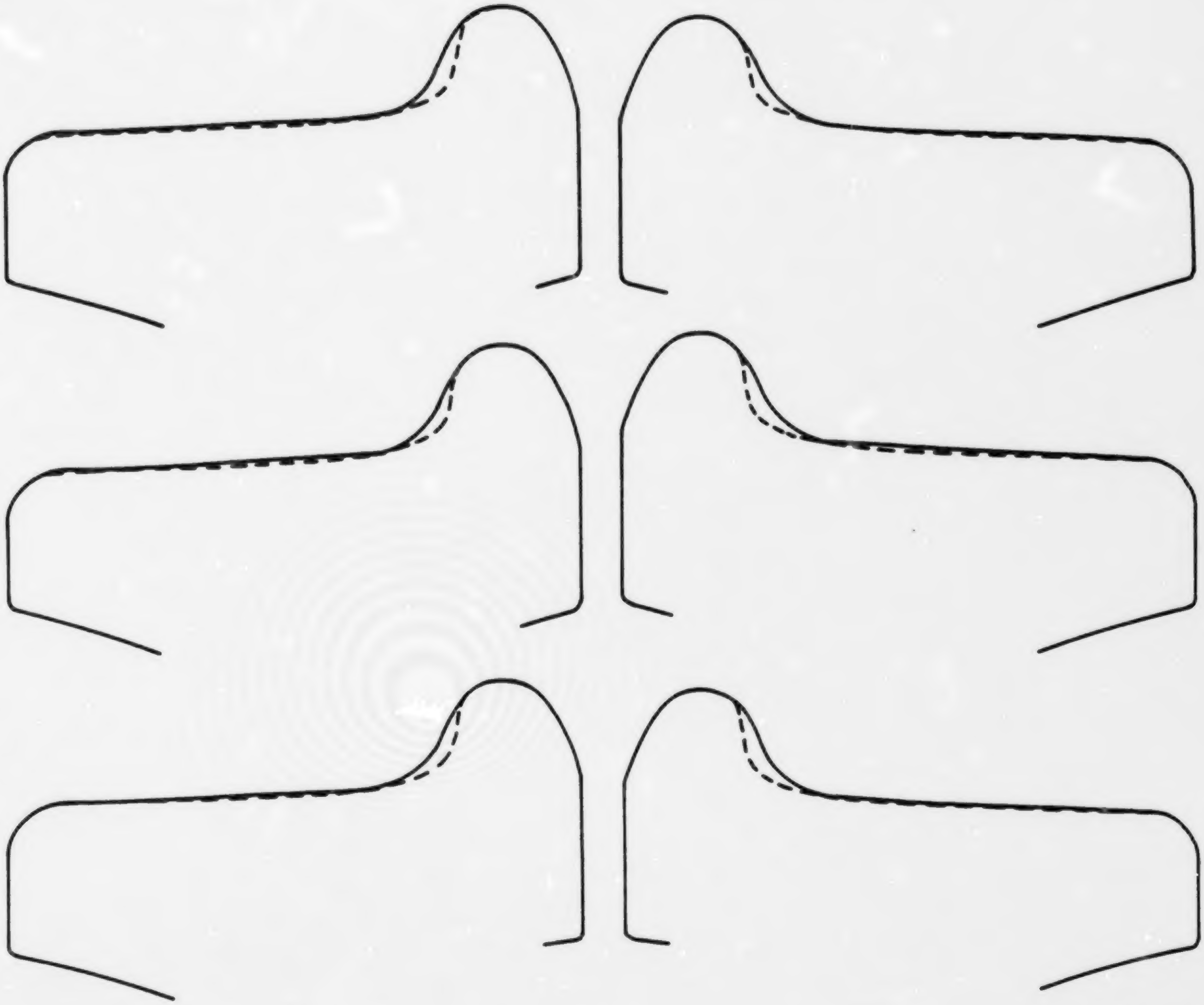

——— New Wheel   'B' End   ----Worn Wheel

Car Number: CP 505618   Test Car: 32   Group: RDI

Figure 8: Wheel Profiles of Piggyback Car CP 505618
After 40,000 Miles of Revenue Service Testing